Magdalena Stolarska
Nicoleta Tarfulea
Editors

Cell Movement

Modeling and Applications

Birkhäuser

Modeling and Simulation in Science, Engineering and Technology

More information about this series at

Magdalena Stolarska • Nicoleta Tarfulea
Editors

Cell Movement

Modeling and Applications

Birkhäuser

Editors
Magdalena Stolarska
Mathematics
University of St. Thomas
Saint Paul, MN, USA

Nicoleta Tarfulea
Mathematics
Purdue University Northwest
Hammond, IN, USA

To Halina and Andrei.

Preface

The English philosopher George Henry Lewes once stated, "A cell is regarded as the true biological atom." While it is true that biological cells are most often part of a whole, they are also extraordinary entities whose individual roles allow the whole multicellular organism to function. Many individual cellular functions are based on the ability of the cell to move, either from one part of the multicellular organism to another or by changing shape. Several canonical examples of cell movement include remodeling of damaged tissue by fibroblasts in wound healing, neutrophil and macrophage localization to an infection in immune response, and in more dire situations, the detachment of a tumor cell from a primary tumor and its relocalization to another portion of the body in cancer metastasis. These few examples illustrate the importance of understanding the process of cellular motility.

The movement of individual cells is a very complex process. In order to move, a cell must be able to locally deform itself by reorganizing its cytoskeleton, attach to its surrounding microenvironment, sense the biochemical and mechanical properties of this microenvironment, and adjust intracellular processes accordingly. The ability to perform these steps requires the coordination of many intracellular components and processes, and despite huge advances in experimental methods, mathematical modeling has continued to be essential in understanding how the coordination is achieved. The advances in experimental techniques over the last decade have provided modelers with new information that has been incorporated into models, and as a result, mathematical models have grown increasing complex. In addition, new experiments have allowed models to focus more on specific cell types and more detailed processes within cells.

In this special volume, we focus on highlighting recently developed modeling approaches and applications of models to better understand the coordination of intracellular processes. The intended audience of this special volume are graduate students and researchers that have a familiarity with some areas of modeling in cell motility and wish to expand their level of understanding of other modeling approaches. We have organized the book according to a flow of topics that we felt was appropriate and describe below. However, the chapters do not have to be read in any particular order.

We aim to present a breadth of models applied to a variety of cell types. One of the most widely studied applications of cell motility is cancer, and two of the chapters in this book discuss modeling cell motility in cancer. Shuttleworth and Trucu describe a model in which a continuum approach with a free boundary is used to track tumor progression on an extracellular matrix (ECM) of varying density. It has been established that heterogeneity in tumor cell types can play a critical role in tumor growth and persistence; Shuttleworth and Trucu address heterogeneity in their continuum model. Kim *et al.* discuss multiple modeling approaches that can be used to better understand mechano-chemical interactions in glioblastoma multiforme, a highly aggressive brain cancer. One novel methodology described in Kim *et al.* is the hybrid model, in which individual cells are modeled as deformable ellipses, while a continuum approach is used to model the evolution of critical biochemical components. The mechanical interaction of individual cells with their microenvironment has been shown to play a critical role in signaling in cancer and other cell types, and He and Jiang write about a general method that can be used to model the interaction of individual deformable cells with a rigid three-dimensional ECM.

Statistical methods play a critical role in modeling cell movements. From comparison with experimental data, researchers often know what the output of a model should be. However, it is often difficult to determine the input parameters that are needed to obtain a given output. Furthermore, if input parameters are available, it is not always clear how accurate these inputs are. Bowman and coworkers describe a highly parallelizable transitional Markov chain Monte Carlo method that helps address these questions. How is the movement of an individual (particle, cell, or animal) related to the movement of the collective (membrane, tissue, population) is another question of interest. Painter and Hillen provide an introduction of how position-jump and velocity-jump processes, which describe the random motion of individuals, can lead to a continuum description at the population level. Xue adds to this introduction by describing a model in which the velocity-jump process integrates intracellular signaling in the context of bacterial cell movement.

While much of the modeling work focuses on eukaryotic cell motility and cell crawling, cells can also translocate via flagellar movement. A canonical example of this is the sperm cell. Simons and Olson provide a review of various modeling frameworks used to understand sperm motility. Also, while some researchers focus on modeling whole cell movement, modeling subcellular components that are required for a cell to move is also necessary. Holz *et al.* review models of the most fundamental component of eukaryotic cell motion, actin in the lamellipodium. This chapter focuses on continuum models that describe the transport and reaction of actin and its regulatory proteins within a single cell. Cell movement encompasses more than cell crawling. A cell's motile machinery is highly involved in other processes such as membrane trafficking. Vasan and coworkers review models that shed light on the interaction of cytoskeletal movements and protein machinery during endocytosis. They focus on models that describe a portion of the cell membrane that is undergoing an endocytic event.

In the nine chapters included in this special volume, we describe stochastic, deterministic, continuum, and discrete modeling approaches. We include models of a variety of individual cell types as well as collective cell motion. Our hope is that the reader can get a sense of the different techniques used to understand various aspects of cell movement, as well as the appropriate uses, benefits, and limitations of a given methodology. At the same time, we recognize that the work on modeling cell movement is extensive, and our aim in this special volume is to provide only a small subset of the recent methodology in modeling of cell motility and of the application of these models.

We would like to acknowledge the various people that over the years have helped us cultivate our desire to understand the processes involved in cell movements, most notably Hans Othmer, who has served as a very influential mentor to both of us. We also thank the authors for working with us in making this volume possible and the reviewers for their thoughtful comments. The creation of this volume was partially supported by a grant from the Simons Foundation (#429449 to Nicoleta E. Tarfulea).

Saint Paul, MN, USA   Magdalena A. Stolarska
Hammond, IN, USA   Nicoleta E. Tarfulea
June 2018

Contents

List of Contributors

Matthew Akamatsu Department of Molecular and Cell Biology, University of California, 94720 Berkeley, CA, USA

Clark Bowman Present address: Department of Mathematics, University of Michigan, 48109 Ann Arbor, MI, USA

Division of Applied Mathematics, Brown University, Providence, RI, 02912, USA

Xiuxiu He Department of Mathematics, Georgia State University, Atlanta, GA, 30303, USA

Thomas Hillen Department of Mathematical and Statistical Sciences, University of Alberta, Edmonton, Alberta T6G 2G1, Canada

Danielle Holz Department of Physics, Lehigh University, Bethlehem, PA 18015, USA

Hyejin Jeon Molecular and Translational Neuroimaging Lab, Department of Radiology, Seoul National University College of Medicine, 28 Yeongeon-dong, Jongno-gu, Seoul, 110-744, Republic of Korea

Yi Jiang Department of Mathematics, Georgia State University, Atlanta, GA, 30303, USA

Yangjin Kim Department of Mathematics, Konkuk University, 120 Neungdong-ro, Gwangjin-gu, Seoul, 05029, Republic of Korea

Karen Larson Division of Applied Mathematics, Brown University, Providence, RI, 02912, USA

Sean Lawler Department of Neurosurgery, Brigham and Women's Hospital and Harvard Medical School, Boston, MA, 02115, USA

Donggu Lee Department of Mathematics, Konkuk University, 120 Neungdong-ro, Gwangjin-gu, Seoul, 05029, Republic of Korea

Junho Lee Department of Mathematics, Konkuk University, 120 Neungdong-ro, Gwangjin-gu, Seoul, 05029, Republic of Korea

Wanho Lee National Institute for Mathematical Sciences, 70, Yuseong-daero 1689 beon-gil, Yuseong-gu, Daejeon, 34047, Republic of Korea

Sookkyung Lim Department of Mathematical Sciences, University of Cincinnati, Cincinnati, OH, 45221, USA

Anastasios Matzavinos Division of Applied Mathematics, Brown University, Providence, RI, 02912, USA

Laura M. McMillen Department of Physics, Lehigh University, Bethlehem, PA, 18015, USA

Sarah D. Olson Department of Mathematical Sciences, Worcester Polytechnic Institute, Worcester, MA, 01609, USA

Kevin J. Painter Department of Mathematics & Maxwell Institute, Heriot-Watt University, Edinburgh, UK

Dipartimento di Scienze Matematiche, Politecnico di Torino, Italy

Padmini Rangamani Department of Mechanical and Aerospace Engineering & Department of Bioengineering, University of California, San Diego, CA, 92093, USA

Soyeon Roh Department of Biological Sciences, Carnegie Mellon University, Pittsburgh, PA, 15213, USA

Alexander Roitershtein Department of Mathematics, Iowa State University, Ames, IA, 50011, USA

Gillian L. Ryan Department of Physics, Kettering University, Flint, MI, 48504, USA

Johannes Schöneberg Department of Molecular and Cell Biology, University of California, 94720 Berkeley, CA, USA

Robyn Shuttleworth Division of Mathematics, University of Dundee, Scotland, DD1 4HN, UK

Julie E. Simons Department of Sciences & Mathematics, California Maritime Academy, Vallejo, CA, 94590, USA

Derek Stein Department of Physics, Brown University, 02912 Providence, RI, USA

Dumitru Trucu Division of Mathematics, University of Dundee, Scotland, DD1 4HN, UK

Ritvik Vasan Department of Mechanical and Aerospace Engineering, University of California, San Diego, CA, 92093, USA

Dimitrios Vavylonis Department of Physics, Lehigh University, Bethlehem, PA, 18015, USA

Chuan Xue Department of Mathematics, Ohio State University, Columbus, OH, 43210, USA

Two-Scale Moving Boundary Dynamics of Cancer Invasion: Heterotypic Cell Populations' Evolution in Heterogeneous ECM

Robyn Shuttleworth and Dumitru Trucu

Abstract Cancer cell invasion, recognised as one of the hallmarks of cancer, is a complex process involving the secretion of matrix-degrading enzymes that have the ability to degrade the surrounding extracellular matrix (ECM). Combined with cell proliferation and migration, and changes in cell-cell and cell-matrix adhesion, the tumour is able to spread into the surrounding tissue. The multiscale character of this process is highlighted here through the double feedback link between the cell-scale molecular processes and those occurring at the tissue level. In this chapter, we build on the multiscale moving boundary framework proposed in Trucu et al. (Multiscale Model Simul 11(1):309–335, 2013) by developing the modelling of the tissue-scale dynamics to include cell-cell and cell-matrix adhesion in a heterogeneous cancer cell population. To that end, we consider here two cancer cell sub-populations, namely a primary tumour cell distribution and a second cancer cell sub-population that arises due to mutations from the primary tumour cells and exhibits higher malignancy. We explore the multiscale moving boundary dynamics of this heterogeneous tumour cell population in the presence of cell-adhesion at the tissue-scale and matrix degrading enzyme molecular processes considered at cell-scale. Using computational simulations we examine the effect of different levels of adhesion and matrix remodelling on the invasion of cancer cells.

1 Introduction

Cancer invasion of tissue is a complicated, multiscale process which plays an essential role in tumour progression. Through a combination of adhesion, secretion of various matrix degrading enzymes, right from the early stages, cancer cells acquire the ability to spread locally and invade the surrounding tissue; this is further exacerbated by later secretion of growth factors that lead to the angiogenesis process

R. Shuttleworth (✉) · D. Trucu
Division of Mathematics, University of Dundee, DD1 4HN Dundee, Scotland, UK
e-mail: r.shuttleworth@dundee.ac.uk; trucu@maths.dundee.ac.uk

that paves the way for metastatic spread, leading to the creation of secondary tumours at different locations in the human body [17]. These new colonies are known as metastases, or secondary tumours, and are the cause of 90% of human cancer deaths [10]. The most common site for breast cancer metastasis, for example, is the bone, followed by the liver and lungs [31]. Once a tumour has invaded the bone or any of these other vital organs, it is fatal and cannot be cured, and only treated by various forms of cancer therapy such as surgical intervention, chemotherapy and radiation [28].

1.1 Biological Background

Recognised as one of the hallmarks of cancer [17], cancer invasion is a key process in tumour development that uses a combination of cell-cell and cell-matrix adhesion, alongside the secretion of proteolytic enzymes to degrade the surrounding tissue and this way expand on the affected area. This enables the cells at the invasive edge of the tumour to colonise new, initially healthy regions of the peritumoural tissue, where in the first instance there is no restriction in nutrients or changes in tissue structure. The ultimate success of invasion relies heavily on the capabilities of the other hallmarks of cancer [17], namely the ability to sustain proliferative signalling, to evade growth suppressors, to enable limitless replicative potential, to induce angiogenesis and to resist cell death. After a decade of further research on cancer, a wider understanding of its processes sparked the addition of another four hallmarks [18] to the original six, namely the ability to avoid immune destruction, the ability to deregulate cellular energetics, tumour-promoting inflammation, along with genetic instability and mutation.

A malignant tumour is comprised of a complex community of cells (fibroblasts, endothelial cells, stromal cells), all of which are mixed in with the extra-cellular matrix (ECM). The extra-cellular matrix is a key biological structure that not only provides support to surrounding cells and tissues [21], but also acts as a framework in which the cells can communicate and exercise spatial movement. The formation of the ECM is an essential process, particularly in wound healing and tumour invasion. The ECM is comprised of a variety of secreted proteins which can vary depending on the type of tissue or the location in which we are investigating. Such components include collagen fibres and elastin which provide necessary structure and elasticity of the ECM, glycoproteins such as fibronectin, laminins and proteoglycans which bind to the collagens and to receptors on the cell surface.

Cells bind to the ECM through cell-matrix adhesion [23]. This process is regulated by a family of specific molecules on the cell surface known as cell adhesion molecules (CAM) that enable the binding process to various ECM components. These give rise to conditions in which the tumour microenvironment contributes towards cell migration within the surrounding tissue. The migratory character of the invading cells is further strengthened through the loss of cell-cell adhesion that

causes these particular tumour cells to become even more motile and spread further in the tissue [9]. An important role in cell-cell adhesion is played by the cell-cell signalling pathways based on the interactions between the distribution of calcium-sensing receptors and Ca^{2+} ions from the extracellular matrix [20]. In normal, healthy cells, this calcium-dependent cell-cell adhesion process is mediated by a large family of transmembrane glycoproteins known as cadherins. Cadherins are split into many groups, the most relevant being known as E-cadherins. In order for normal cellular adhesion to take place, E-cadherin will form binds with proteins found inside the cell known as catenins, most typically the β-catenin, forming an E-cadherin/catenin complex. Any alteration to the function of β-catenin will result in the loss of ability of the E-cadherin to initiate cell-cell adhesion [32]. The direct correlation between this calcium-based cell signalling mechanism and the regulation of E-cadherin and β-catenin was first discovered in colon carcinoma [7]. This loss of cell-cell adhesion paired with a quick spread of the cells due to enhanced cell-matrix adhesion [6] enables these cancerous cells to invade the surrounding tissue [12].

Finally, a key player in the invasion process is the over-production and secretion of proteolytic enzymes. These enzymes can be categorised as matrix-degrading enzymes (MDEs) with such sub-groups as matrix metalloproteinases (MMPs) [26] and the urokinase-type plasminogen activator (uPA). The interaction of these enzymes with the ECM components results in the degradation and remodelling of the ECM. MDEs have the ability to open migratory pathways and alter cell-cell and cell-matrix adhesion properties. One of the first MMPs to interact with the ECM is the membrane-tethered MT1-MMP. Once in the stroma, MT1-MMP will begin to cleave collagen type I into smaller pieces. As well as cleaving, MT1-MMP has another role in that it can activate pro-MMP-2. Molecules of pro-MMP-2 present in the extra-cellular matrix are recruited by the cancer cells and cleaved by MT1-MMP to promote MMP-2 activation. Once activated, MMP-2 is then available to breakdown the previously cleaved smaller pieces of collagen type I, as well as degrade the surrounding fibres in order to create a path in which the cancer cells can advance.

1.2 Mathematical Models of Cancer Invasion

The past few decades have witnessed great interest in the mathematical modelling of cancer invasion [5, 8, 11, 34]. There are many models which investigate different aspects of cancer invasion, particularly using *in vitro* models; however, the *in vivo* process is much more complicated and less understood. *In vivo* models capture the complexity of tumour spread; however, it is very difficult to visualise the individual steps of invasion. On the other hand, *in vitro* models are easier to construct and they allow us to control a lot of the experimental values we obtain and this allows for easier quantitative analysis. One disadvantage to *in vitro* models however is the inability to see the global effect of invasion, i.e., *in vitro* models only contain a partial expression of the interactions between the cancer cells and the ECM [22].

Great effort has been made to understand the interactions that are occurring during the invasion process, and the experiments, both *in vivo* and *in vitro*, have helped to advance this knowledge. Links between cell migration processes and MMPs that are produced by the cancer cells have been discovered [24], as well as links between cell migration and the structure of the extracellular matrix [33]. There has been many attempts to model these interactions, using both continuum and discrete models; however, these are "one-scale" based models and do not consider the overall aspects of a multiscale invasion model.

The model proposed in [3] describes the invasion of tissue by cancer cells whilst considering the tumour cells, tissue (extracellular matrix) and matrix-degrading enzymes. There are two models proposed, the first a continuum model which considers the tumour mass as a whole, and a second individual-based model to investigate the invasive effects on the level of individual cells. The continuum model here describes how the tumour cells respond to haptotactic effects produced within the ECM. It has been shown that the tumour cells will split into two groups, one driven by random migration and the other spurred by haptotaxis. The individual-cell based model confirms this and it is concluded that haptotaxis is important for cancer cell invasion.

The first continuum approach for modelling cell-cell adhesion was proposed in [4] which considers the directed movement of cells in response to the adhesive forces made through binding. The PDE model in [3] was used as a basis for the models in [16] where a continuum model of cancer cell invasion was derived which accounts for both cell-cell and cell-matrix adhesion. These models used non-local terms for both cell-cell and cell-matrix adhesion and they introduced the notion of adhesive flux and cell sensing radius, which was to detect the immediate spatial environment. Analytical results of these models were proved by [12] using a system of nonlinear, non-local partial integro-differential equations describing the spatio-temporal dynamics of cancer invasion. The behaviours of cancer cells under different adhesion coefficients were stated.

A model describing the mesenchymal motion of cells in a fibre network was developed by [19]. Mesenchymal migration involves significant matrix remodelling, where the cell will leave a trail of aligned fibres along its path. Both mesoscopic (individual based) and macroscopic (population based) models were described and these both form a good foundation for modelling on heterogenous orientated environments. This approach was continued by [25] using an individual-cell based model where two different forms of cell migration were investigated. Here it is shown that in terms of mesenchymal migration, the actions of both contact-guidance and ECM remodelling are sufficient processes for invasion to occur.

All of these models have been proposed at a single scale level and do not incorporate a multiscale approach. Multiscale modelling of cancer invasion has only recently become an area of interest, where the first instance can be seen in [2]. Here, three scales were identified; extracellular, cellular and subcellular, and the effect of the microenvironment on tumour development was explored. It is shown

how the three different biological scales can overlap and work together to form a more concise model of tumour invasion. Multiscale modelling was then utilised in [27] where focus lay on the interactions between E-cadherin and β-catenin and how cell migration may control cell adhesion was investigated. Both intracellular and extracellular dynamics were considered, with the conclusion that the tumour cells themselves are facilitating progression.

More recently, a multiscale moving boundary method of tumour invasion was proposed in [29] using three scale modelling; macroscale occurring at the tissue level, microscale occurring at a cellular level and a naturally arising third scale which is used to characterise the invasive boundary of the tumour. We propose a model which builds on this original framework [29] in order to incorporate the adhesive nature of cancer cells [15] with both themselves and the surrounding microenvironment. This multiscale modelling will focus on exploring the evolution of tumour morphology whose importance is justified by clinical considerations, namely that it is not necessarily the overall size but the morphology of the tumour that creates huge surgical challenges. This is mainly due to the deficiencies in all current imaging techniques, which are only able to capture between 65% and 90% of the tumour, enabling the real possibility of not resecting the true extent of the tumour during the surgical process by leaving behind small but complicated leading-edge tumour morphological patterns that are not captured by the imaging, which subsequently lead to an aggressive tumour relapse.

2 The Multiscale Modelling Approach

We will now briefly describe the multiscale framework initially introduced in [29] for modelling cancer cell invasion and then develop the macroscopic dynamics incorporating cell-adhesion. Cancer invasion occurs at many spatial and temporal scales. The multiscale framework introduced in [29] was developed to consider detailed interactions taking place at the cellular- and tissue-scales alongside the linking between these different scales.

Within a maximal environmental tissue cube Y, at initial time t_0, $\Omega(t_0)$ represents the snapshot of the tumour domain where the combined distributions of cancer cells $c_1(t, x)$ and $c_2(t, x)$ exercise their dynamics, with c_1 and c_2 representing the sub-populations 1 (primary tumour cells) and 2 (representing mutated cells), and their combined vector being denoted by $\mathbf{c}(t, x) = [c_1(t, x), c_2(t, x)]$ (as illustrated in Figure 1). The tumour cell population exercise their activity within a supporting density of ECM that is denoted here with $v(t, x)$, and for compact notation, we will consider the combined vector of cancer cells, $\mathbf{c}$ and ECM, v, defined as

$$\mathbf{u}(t, x) := (\mathbf{c}(t, x)^T, v(t, x))^T.$$

Fig. 1 Schematic diagram showing the spatial cubic region Y centred at the origin in $\mathbb{R}^3$. The solid green lines represent the family of macroscopic ϵY cubes placed on the boundary of the tumour $\partial \Omega(t_0)$, and the pale pink region represents the initial mass of cancer cells $\Omega(t_0)$.
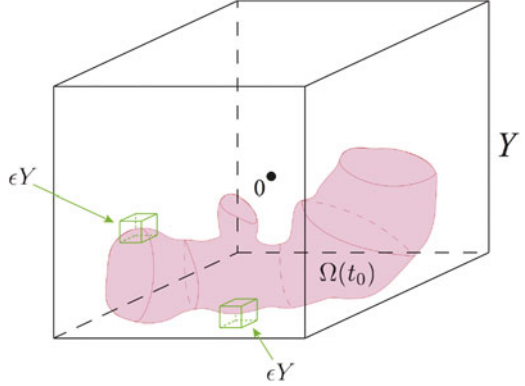
The spatial considerations play an important role in this model. We assume that the concentration of MDEs occupy a negligible amount of space within the tissue scale tumour, and similar to the approach in [15], we shall define the *volume fraction of occupied space* as

$$\rho(t, x) \equiv \rho(\mathbf{u}(t, x)) := \vartheta_v v(t, x) + \vartheta_c \sum_{n=1}^{2} c_n(t, x)$$

where ϑ_v represents the fraction of physical space occupied by the ECM and ϑ_c is the fraction of physical space occupied by c_n.

However, while for the purpose of this work, at the tissue scales (macroscale) we consider only cancer cells and ECM, the crucial activity of the MDEs and their dynamics is described at cell-scale (microscale) by accounting for spatial dynamics of proteolytic processes that occur along the invasive edge of the tumour.

2.1 Macroscale Dynamics

The dynamics of the two cell populations are similar in flavour. In the presence of a logistic proliferation law, per unit time, the primary tumour cells $c_1(t, x)$ are assumed to exercise spatial movement that is a combined effect of local Brownian movement (approximated here through diffusion) and cell adhesion, and lose some of the cell population through certain level of mutation towards a second more motile and aggressive population $c_2(t, x)$. Once mutations have started occurring, under the presence of a logistic proliferation law, population c_2 begin its own dynamics, and so per unit time, this is also experiencing a spatial redistribution dictated by a local Brownian movement (approximated again through diffusion) and cell adhesion. Therefore, mathematically, the dynamics can be re-casted as

$$\frac{\partial c_1}{\partial t} = \nabla \cdot [D_1 \nabla c_1 - c_1 \mathscr{A}_1(t, x, \mathbf{u}(t, \cdot))] + \mu_1 c_1 (1 - \rho(\mathbf{u})) - M_1(t, \mathbf{u}) c_1,$$

$$\frac{\partial c_2}{\partial t} = \nabla \cdot [D_2 \nabla c_2 - c_2 \mathscr{A}_2(t, x, \mathbf{u}(t, \cdot))] + \mu_2 c_2 (1 - \rho(\mathbf{u})) + M_1(t, \mathbf{u}) c_1. \tag{1}$$

where: D_n, $n = 1, 2$ are the non-negative diffusion coefficients; $\mathscr{A}_n(t, x, \mathbf{u}(t, \cdot))$ is the non-local term accounting for cell adhesion incorporating both cell-cell and cell-matrix adhesion; μ_n describes the proliferation coefficient, here; and M_1 the final term describes the mutation from $c_1(t, x)$. To account for the physical space available and avoid overcrowding, we adopt here the proliferation term $1 - \rho(\mathbf{u})$ introduced in [16]. Furthermore, the non-local term $\mathscr{A}_n(t, x, \mathbf{u}(t, \cdot))$, known as the adhesive flux, has a form of the type proposed in [15, 16], and is given as

$$\mathscr{A}_n(t, x, \mathbf{u}(t, \cdot))$$
$$= \frac{1}{R} \int_{\mathbf{B}(0,R)} \mathbf{n}(y) \cdot \mathscr{K}(||y||_2) \cdot g_n(t, \mathbf{u}(t, x + y)) \chi_{\Omega(t)}(x + y) \, dy, \quad n = 1, 2. \tag{2}$$

This describes the motion of cells due to both cell-cell and cell matrix adhesion, which occurs as a result of the forces produced when adhesion bonds are both produced and broken. Here $R > 0$ is the *sensing radius* of cell-cell and cell matrix interactions, $\mathbf{B}(0, R) \subset \mathbb{R}^2$ denotes the usual ball centred at zero and of radius R, and $\chi_{\Omega(t)}(\cdot)$ represents the characteristic function of $\Omega(t)$. At any time instance t, for any $x \in \Omega(t)$, the set $x + \mathbf{B}(0, R)$ is known as the *sensing region* on which all the cells distributed at x, interact and form or break adhesion bonds with the cells located at $y \in \mathbf{B}(x, R) \cap \Omega(t)$. Further, $\mathbf{n}(y)$ denote the unit vector pointing from x to $x + y$, which is given by

$$\mathbf{n}(y) := \begin{cases} y/||y||_2 & \text{if} \quad y \in B(0, R) \setminus \{(0, 0)\}, \\ (0, 0) & \text{otherwise.} \end{cases} \tag{3}$$

The radially dependent spatial kernel $\mathscr{K}(\cdot)$ enable us to account for spatial distribution of the cells for both cell-cell and cell matrix adhesion within the sensing region $\mathbf{B}(x, R)$, and in the simulations we specifically use the form of $\mathscr{K}(\cdot)$ proposed in [16], namely

$$\mathscr{K}(r) := 1 - \frac{r}{R}, \tag{4}$$

where r is the radial distance between the centre point x and $y \in \mathbf{B}(x, R)$. This implies that for points in the sensing region $\mathbf{B}(x, R)$, as the distance r from x increases, the influence on adhesion-driven migration decreases. The adhesion function $\mathbf{g}(t, \mathbf{u}(t, x + y))$ describes the local cell-cell and cell matrix adhesion. This

explores the adhesion velocity of the cells at x is in the direction at which the cells can form the most bonds both among themselves and with components of the ECM within the sensing region around x. Here, $g_i(t, \mathbf{u}(t, x + y))$, $i = 1, 2$ denotes the i-th component of

$$\mathbf{g}(t, \mathbf{u}) = [\mathbf{S}_{cc}\mathbf{c} + \mathbf{S}_{cv}v] \cdot (1 - \rho(\mathbf{u}))^+, \tag{5}$$

and represents the cell-cell and cell matrix adhesion properties for population i, which are explicitly enable via the associated cell-cell and cell-matrix adhesion matrices, $\mathbf{S}_{cc}, \mathbf{S}_{cv} \in \mathbb{R}^{2,2}$, given by

$$\mathbf{S}_{cc} = \begin{bmatrix} S_{c_1,c_1} & S_{c_1,c_2} \\ S_{c_2,c_1} & S_{c_2,c_2} \end{bmatrix} \quad \text{and} \quad \mathbf{S}_{cv} = \begin{bmatrix} S_{c_1,v} & 0 \\ 0 & S_{c_2,v} \end{bmatrix}.$$

Furthermore, the overcrowding of the cell population and ECM is avoided through the term $(1 - \rho(\mathbf{u}))^+ := \max\{(1 - \rho(\mathbf{u})), 0\}$, which ensures that if a point in the domain is already overcrowded (with cells and/or ECM), then that space point does not contribute towards biasing the tumour cells migration due to adhesion.

As a tumour becomes increasingly malignant, it can obtain the ability to mutate to a more aggressive form of cancer cell. For this reason, $M_1(t, \mathbf{u})$ represents the mutation rate from population 1 to population 2. This mutation term is modelled as in [1, 15], namely

$$M_1(t, \mathbf{u}) = \delta H(t - t_{1,2}) \cdot H(v(t, x) - v_{\min}),$$

where $H(\cdot)$ denotes the usual Heaviside function and explore the fact that mutations from the primary tumour occur at a rate $\delta > 0$ after a certain time $t_{1,2}$ and in the presence of a minimal level v_{min} of ECM.

Within the tissue level, we must account the activity of the surrounding environment of the tumour, the extra-cellular matrix. Per unit time, the ECM exhibits degradation in the presence of cancer cells, along with a general remodelling of itself. Thus, this dynamics can be described mathematically as

$$\frac{\partial v}{\partial t} = -\gamma \mathbf{c} + \omega(1 - \rho(\mathbf{u})), \tag{6}$$

where γ is the degradation coefficient multiplied by the current cancer cell distributions, and ω is the remodelling constant; here the matrix remodelling is controlled by the volume filling factor $(1 - \rho(\mathbf{u}))$. Biological evidence suggests that the remodelling of the ECM is not only an essential role of development and wound healing, but also in the development of cancer, contributing to processes such as metastasis and tumour cell invasion [14].
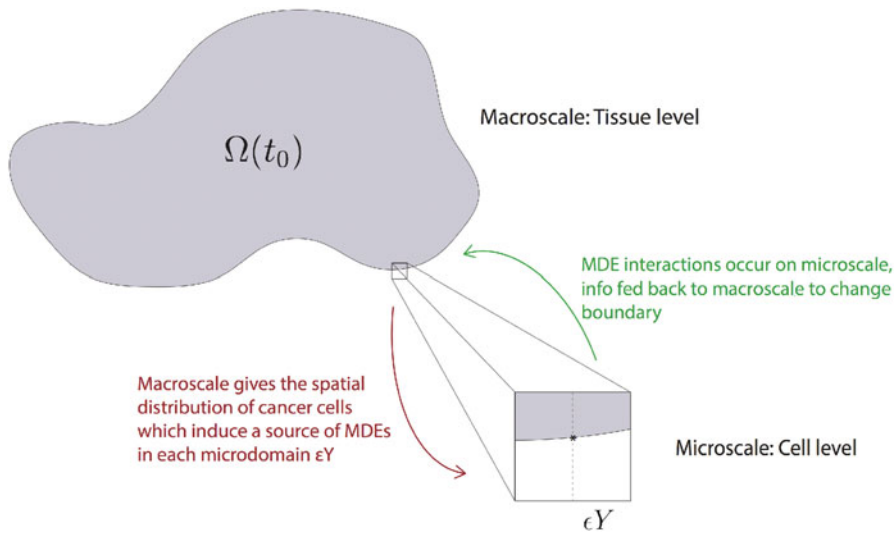
Fig. 2 Schematic of macro-micro interactions.

2.2 Top-Down Tissue- to Cell-Scale Link and the Resulting Microscopic Dynamics

As discussed previously, cancer cell invasion is a multiscale process in which the micro-dynamics of the matrix-degrading enzymes (MDEs) are responsible for the degradation of the ECM. The macroscopic processes defined by the equations (1) and (6) give rise to a microscale dynamics occurring along the invasive edge of the tumour, which, in turn, causes the macroscale boundary of the tumour to advance further into the healthy tissue, as schematically illustrated in Figure 2.

The MDEs, such as matrix metalloproteinases (MMPs) of type 2, are produced within the cancer cells and distributed on the outer proliferating rim of the tumour, with their activity occurring within the area directly surrounding the tumour. Specifically, during a time interval $[t_0, t_0 + \Delta t]$, the cancer cells arriving within the outer proliferating rim of the tumour secrete these MDEs giving rise to a source of such proteolytic enzymes that then exercise a cross-interface transport process within a cell-scale (microscale) size neighbourhood of $\partial \Omega(t_0)$, this way getting to interact directly and as a consequence significantly alter the ECM density that it meets in the peritumoural region. Hence, proceeding as described in [29], we denote by $\epsilon > 0$ the size of the microscale and we explore this MDEs micro-dynamics on an appropriate $\epsilon-$size neighbourhood of $\partial \Omega(t_0)$ given as the complete cover enabled by a union of half-way overlapping micro-cubes ϵY centred at the tumour

interface. Thus, while assuming that we have no source for the cell-scale dynamics being formed outside $\Omega(t_0)$, at each instance $\tau \in [0, \Delta t]$ of the microdynamics and at each given microscale point $y \in \epsilon Y \cap \Omega(t_0)$ the source of MDEs is arising as a collective contribution of the cells from the outer proliferating rim that is located within a given distance $\delta > 0$ with respect to y. Therefore, denoting the source by $f_{\epsilon Y}(y, \tau)$, this is mathematically formulated as

1. $$f_{\epsilon Y}(y, \tau) = \frac{1}{\lambda(\mathbf{B}(y, \delta) \cap \Omega(t_0))} \int_{\mathbf{B}(y, \delta) \cap \Omega(t_0)} \alpha_1 c_1(x, t_0 + \tau)$$
$$+ \alpha_2 c_2(x, t_0 + \tau) dx, \quad y \in \epsilon Y \cap \Omega(t_0), \tag{7}$$

2. $$f_{\epsilon Y}(y, \tau) = 0, \quad y \in \epsilon Y \setminus \left(\Omega(t_0) + \{z \in Y | \, ||z||_2 < \gamma\}\right),$$

where $\lambda(\cdot)$ is the standard Lebesgue measure on $\mathbb{R}^2$, $\mathbf{B}(y, \delta) := \{x \in Y | \, ||y - x||_\infty \leq \delta\}$, α_i, $i = 1, 2$ are MDEs secretion rates by each of the two cell sub-populations, and γ is a small parameter enabling us to capture a sharp but smooth decay to 0 of the MDEs source immediately outside the tumour boundary.

Finally, as the ϵ-size neighbourhood of $\partial\Omega(t_0)$ given by the bundle of half-way overlapping micro-cubes ϵY enables a decoupling of the micro-dynamics on individual ϵYs, in the presence of the source (7), we assume in this work that the MDEs are simply locally diffusing. Hence, denoting the density for MDEs by $m(y, \tau)$, in each ϵY the micro-dynamics exercised by the MDEs is described by:

$$\frac{\partial m}{\partial \tau} = \Delta m + f_{\epsilon Y}(y, \tau), \qquad y \in \epsilon Y, \ \tau \in [0, \Delta t]. \tag{8}$$

Macroscopic boundary movement induced by microscale. During their micro-dynamics, the MDEs interact with the ECM components in the peritumoural region captured by each ϵY. As described in [29], according to the spatial distribution of their advancing front on $\epsilon Y \setminus \Omega(t_0)$, the MDE cause specific spatial patterns of degradation of the ECM components that determine completely a direction of movement $\eta_{\epsilon Y}$ and displacement magnitude $\xi_{\epsilon Y}$ for the tumour boundary progression within each ϵY. As illustrated schematically in Figure 3, this choreographic movement of the tumour boundary captured by the micro-domain ϵY is represented back at macroscale through the relocation of the tumour boundary midpoint $x^*_{\epsilon Y}$, which is located at the intersection of $\partial\Omega(t_0) \cap \epsilon Y$ with the median of ϵY perpendicular to the side of ϵY inside the cancer region, this being chosen as the inner most point in this intersection with respect to the cancer region. Thus, following the derivation in [29], using an appropriately chosen dyadic decomposition of ϵY in a union of small dyadic cubes $\{D_l\}_{i=1, p_{\epsilon Y}}$, with $p_{\epsilon Y} := 2^{k_{\epsilon Y}}$, that ensure uniformity of the approach across all the boundary
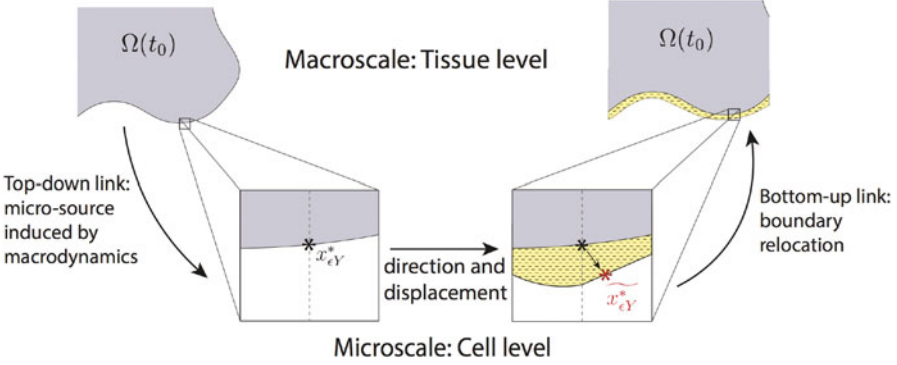
Fig. 3 Schematic of one macro-micro stage in the multiscale process. The projected ϵY cube from macro- to microscale with boundary point reallocation occurring through the micro dynamics and the new relocated boundary position projected back into the macroscopic scale at the tissue level.

micro-domains ϵY, the direction of movement $\eta_{\epsilon Y}$ and displacement magnitude $\xi_{\epsilon Y}$ for the point $x^*_{\epsilon Y}$ are determined mathematically, and are given by

$$\eta_{\epsilon Y} = x^*_{\epsilon Y} + \nu \sum_{l \in \mathscr{I}^*_{\epsilon Y}} \left(\int_{\mathscr{D}_l} m(y, \tau_f) \, dy \right) (y^*_l - x^*_{\epsilon Y}),$$

$$\xi_{\epsilon Y} = \sum_{l \in \mathscr{I}^*_{\epsilon Y}} \frac{\int_{\mathscr{D}_l} m(y, \tau_f) \, dy}{\sum_{l \in \mathscr{I}^*_{\epsilon Y}} \int_{\mathscr{D}_l} m(y, \tau_f) \, dy} |\overrightarrow{x^*_{\epsilon Y} y_l}|.$$

where, $\mathscr{I}^*_{\epsilon Y}$ are the family of indices of the dyadic cubes that track the tip of the advancing MDEs front in ϵY, and y_l represents the barycentre of D_l for any $l \in \mathscr{I}^*_{\epsilon Y}$.

Although a movement direction and displacement have been derived for each $x^*_{\epsilon Y}$, movement will only occur if the ECM degradation is of a certain local strength. The strength of this local ECM degradation is explored through the transitional probability q^* defined in [29] and it is a quantification of the amount of MDE in $\epsilon Y \setminus \Omega(t_0)$ relative to the total amount of MDE in the micro domain ϵY. Therefore the midpoint $x^*_{\epsilon Y}$ will only move to a new spatial position if and only if $q^*(x^*_{\epsilon Y}) := q^*(\epsilon Y \setminus \Omega(t_0))$ exceeds a certain threshold $\omega_{\epsilon Y} \in (0, 1)$ that captures local peritumoural tissue characteristics. Hence, we find that the new invasive boundary $\partial \Omega(t_0 + \Delta t)$ will be an interpolation of the new locations for the points that exercised the movement and those boundary points $x^*_{\epsilon Y}$ that did not move. The invasion process will continue on the newly expanded domain $\Omega(t_0 + \Delta t)$ with a new set of macro-micro stage dynamics on the next multiscale time step $[t_0 + \Delta t, t_0 + 2\Delta t]$. The initial conditions on the expanded domain $\Omega(t_0 + \Delta t)$ are determined by the solution at the final time of the previous invasion step, as detailed in [29].

2.3 Summary of the Global Multiscale Model

At each stage of the invasion process, the macroscale dynamics govern the spatial distributions of both cancer cell populations and the ECM density. The initial distribution of cancer cells $\Omega(t_0)$ induces a source of MDEs (7) on the boundary at each microdomain ϵY. The microscopic dynamics induce a change in the boundary position as illustrated in Figure 3. This movement is then translated back into the macroscale, where the new spatial positions of the boundary $\widetilde{x_{\epsilon Y}^*}$ are interpolated with the spatial positions that could not be moved and a new invading edge is obtained as illustrated in Figures 2 and 3. The next macro-micro stage will then proceed using the solution from the previous step as the new initial conditions and invasion will continue. Once the invasion process has advanced, mutations will begin to occur between cell populations. The mutated population c_2 carries a higher malignancy than population c_1, thus it secretes a higher volume of MDEs, which in turn will allow the second population to advance quicker.

3 Numerical Approaches and Simulations

The numerical scheme developed for the multiscale model described above is structured on two big components corresponding to the macro- and microscales processes involved, namely: (1) a finite differences based macro-solver that addresses the macro-dynamics; and (2) a finite element micro-solver exploring the micro-dynamics that is based on a standard approach involving bilinear shape functions on a squared mesh for each micro-domain. As the macro-solver involves a special treatment for the adhesion terms $\mathscr{A}_n$, in the following we will highlight the main features that this involves.

3.1 Brief Description of Scheme Developed for the Macroscale Solver

As already mentioned above, an important aspect within the macroscopic part of our solver is the numerical approach for the adhesive fluxes $\mathscr{A}_n$ (that explores the effects of cell-cell and cell-matrix adhesion of population c_n), which involves off-grid computations and we address these as follows. We decompose the sensing region $\mathbf{B}(x, R)$ in $s2^m$ annulus radial sectors $\mathscr{S}_1, \ldots, \mathscr{S}_{2^m}$ (obtained by intersecting s annuli with 2^m uniform radial sectors of $\mathbf{B}(x, R)$, as shown in Figure 4, with the radius of the central circle taken small enough so that this is neglected in the subsequent computation steps). Then, for each S_l, we evaluate the total population c_1, total population c_2 and the total ECM mass distributed on $\mathscr{S}_l$ that are given by
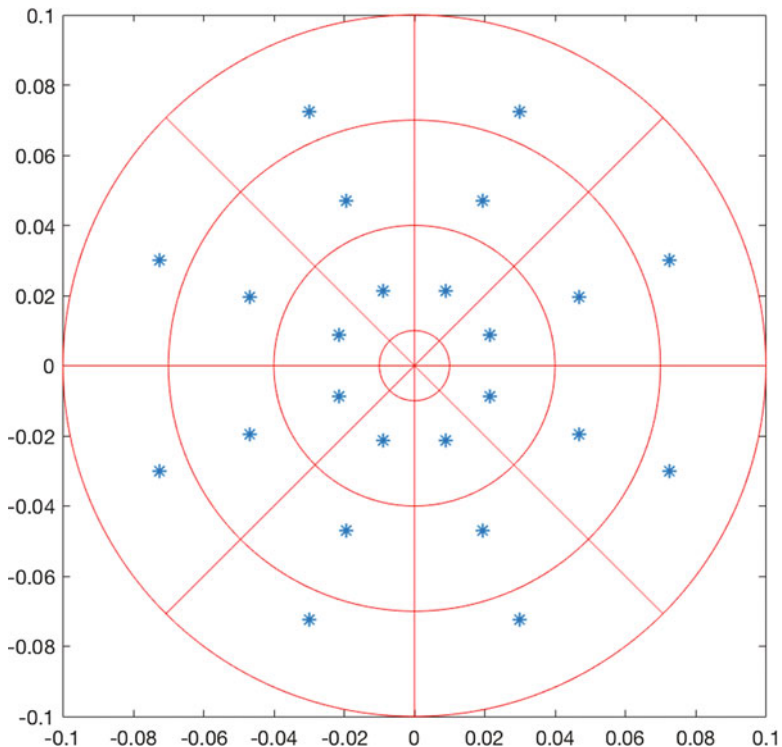
Fig. 4 Sensing region $\mathbf{B}(x, R)$ approximated by the annulus radial sectors with the barycentre $\mathbf{b}_{\mathscr{S}_l}$ associated with each sector $\mathscr{S}_l$ highlighted with a blue dot.

$$\omega_{\mathscr{S}_l, c_1}(t) := \frac{1}{\lambda(\mathscr{S}_l)} \int\limits_{\mathscr{S}_l} c_1(t, x)dx, \quad \omega_{\mathscr{S}_l, c_2}(t) := \frac{1}{\lambda(\mathscr{S}_l)} \int\limits_{\mathscr{S}_l} c_2(t, x)dx,$$

$$and \quad \omega_{\mathscr{S}_l, v}(t) := \frac{1}{\lambda(\mathscr{S}_l)} \int\limits_{\mathscr{S}_l} v(t, x)dx,$$

respectively. Finally, denoting by $\mathbf{b}_{\mathscr{S}_l}$ the barycentre of $\mathscr{S}_l$, $\forall l = 1, \ldots, s2^m$ and evaluating the unit vector $\mathbf{n}(\mathbf{b}_{\mathscr{S}_l}) := \frac{\mathbf{b}_{\mathscr{S}_l} - x}{\|\mathbf{b}_{\mathscr{S}_l} - x\|_2}$, the adhesion flux $\mathscr{A}_n$, $n = 1, 2$, is approximated by

$$\mathscr{A}_n(t, x, \mathbf{u}(t, \cdot)) = \sum_{\substack{l=1 \\ \mathbf{b}_{\mathscr{S}_l} \cap \Omega(t_0) \neq \emptyset}}^{s2^m} \frac{\lambda(\mathscr{S}_l)}{R} \mathbf{n}(\mathbf{b}_{\mathscr{S}_l}) \cdot \mathscr{K}(\mathbf{b}_{\mathscr{S}_l}) g_n(\tilde{\mathbf{u}}(t, \mathbf{b}_{\mathscr{S}_l}))$$

where

$$\tilde{\mathbf{u}}(t, \mathbf{b}_{\mathscr{S}_l}) := [\omega_{\mathscr{S}_l, c_1}(t), \omega_{\mathscr{S}_l, c_2}(t), \omega_{\mathscr{S}_l, v}(t)]^T$$

and

$$g_n(\tilde{\mathbf{u}}(t, \mathbf{b}_{\mathscr{S}_l})) = [\mathbf{S}_{cc}[\omega_{\mathscr{S}_l, c_1}(t), \omega_{\mathscr{S}_l, c_2}(t)]^T + \mathbf{S}_{cv}\omega_{\mathscr{S}_l, v}(t)] \cdot (1 - \rho(\tilde{\mathbf{u}}(t, \mathbf{b}_{\mathscr{S}_l})))^+$$

For the actual implementation, we discretise the entire domain Y by considering a uniform spatial mesh of size h, i.e., $\Delta x = \Delta y = h$ as well as the time interval $[t_0, t_0 + \Delta t]$ into k uniformly distributed time steps, i.e., $\delta_\tau = \frac{\Delta t}{k}$. In order to approximate the reaction-diffusion equations (1), we develop a predictor-corrector in time scheme; whilst the term $\nabla \cdot [\nabla c_n - c_n \mathscr{A}_n(t, x, \mathbf{u}(t, \cdot))]$ will be approximated by a second-order mid-point rule.

In brief, for any time step of index $p = 0, \dots, k$ and for the spatial nodes (i, j), where $i = 1, \dots, q$, $j = 1, \dots, q$ are the indices for the $x-$ and y-direction, respectively, we introduce the midpoint approximations as:

$$\begin{cases} c^p_{n,i,j+\frac{1}{2}} := \frac{c^p_{n,i,j} + c^p_{n,i,j+1}}{2} \\ c^p_{n,i,j-\frac{1}{2}} := \frac{c^p_{n,i,j} + c^p_{n,i,j-1}}{2} \\ c^p_{n,i+\frac{1}{2},j} := \frac{c^p_{n,i,j} + c^p_{n,i+1,j}}{2} \\ c^p_{n,i-\frac{1}{2},j} := \frac{c^p_{n,i,j} + c^p_{n,i-1,j}}{2} \end{cases} \quad \text{and} \quad \begin{cases} \mathscr{A}^p_{n,i,j+\frac{1}{2}} := \frac{\mathscr{A}^p_{n,i,j} + \mathscr{A}^p_{n,i,j+1}}{2} \\ \mathscr{A}^p_{n,i,j-\frac{1}{2}} := \frac{\mathscr{A}^p_{n,i,j} + \mathscr{A}^p_{n,i,j-1}}{2} \\ \mathscr{A}^p_{n,i+\frac{1}{2},j} := \frac{\mathscr{A}^p_{n,i,j} + \mathscr{A}^p_{n,i+1,j}}{2} \\ \mathscr{A}^p_{n,i-\frac{1}{2},j} := \frac{\mathscr{A}^p_{n,i,j} + \mathscr{A}^p_{n,i-1,j}}{2} \end{cases}$$

We also have the following notation for the central differences:

$$\begin{cases} [c_{n,y}]^p_{i,j+\frac{1}{2}} = \frac{c^p_{n,i,j+1} - c^p_{n,i,j}}{\Delta y} \\ [c_{n,y}]^p_{i,j-\frac{1}{2}} := \frac{c^p_{n,i,j} - c^p_{n,i,j-1}}{\Delta y} \\ [c_{n,x}]^p_{i+\frac{1}{2},j} = \frac{c^p_{n,i+1,j} - c^p_{n,i,j}}{\Delta x} \\ [c_{n,x}]^p_{i-\frac{1}{2},j} := \frac{c^p_{n,i,j} - c^p_{n,i-1,j}}{\Delta x} \end{cases}$$

Using this notation, the approximation for (ignoring the constant parameters at the moment) $\nabla \cdot [\nabla c_n - c_n \mathscr{A}_n(t, x, \mathbf{u}(t, \cdot))]$ in (1) is as follows:

$$\nabla \cdot [\nabla c_n - c_n \mathscr{A}_n(t, x, \mathbf{u}(t, \cdot))]$$

$$= \text{div}[\nabla c_n - c_n \mathscr{A}_n(t, x, \mathbf{u}(t, \cdot))]^p_{i,j}$$

$$\simeq \frac{[c_{n,x}]^p_{i+\frac{1}{2},j} - [c_{n,x}]^p_{i-\frac{1}{2},j} - c^p_{n,i+\frac{1}{2},j} \cdot \mathscr{A}^p_{n,i+\frac{1}{2},j} + c^p_{n,i-\frac{1}{2},j} \cdot \mathscr{A}^p_{n,i-\frac{1}{2},j}}{\Delta x} \quad (9)$$

$$+ \frac{[c_{n,y}]^p_{i,j+\frac{1}{2}} - [c_{n,y}]^p_{i,j-\frac{1}{2}} - c^p_{n,i,j+\frac{1}{2}} \cdot \mathscr{A}^p_{n,i,j+\frac{1}{2}} + c^p_{n,i,j-\frac{1}{2}} \cdot \mathscr{A}^p_{n,i,j-\frac{1}{2}}}{\Delta y}$$

For the time discretisation of equation (6), following [29], we have used a predictor-corrector method, where the predictor is given by a second-order Adams-Bashforth scheme and the corrector uses a second-order trapezoidal approximation.

3.2 Simulations in Two Spatial Dimensions

To explore numerically multiscale model of cancer invasion given in (1)–(8), we consider region $Y := [0, 4] \times [0, 4]$ discretised uniformly with macroscopic spatial step size $h = 0.03125$, while the time step is taken here as $\delta_\tau = 10^{-3}$. Assuming that initially population c_2 has no distribution and population c_1 occupies a region $\Omega(0) := \mathbf{B}((2, 2), 0.5)$ positioned at the centre of the domain Y. The initial condition for cancer cell population c_1 is taken as in [29] and is given by

$$c_1(0, x) = 0.5 \left(\exp \left(-\frac{||x - (2, 2)||_2^2}{0.03} \right) - \exp(-28.125) \right) \left(\chi_{\mathbf{B}((2,2),0.5-\gamma)} * \psi_\gamma \right),$$

where ψ_γ is the mollifier defined in [29] with $\gamma << \frac{\Delta x}{3}$. Population c_2 initially has zero density, so $c_2(0, x) = 0$ and we assume a heterogeneous distribution for the initial ECM density based on the initial condition proposed in [15] and given by

$$v(0, x) = \min \left\{ h(x_1, x_2), \frac{1 - \vartheta_c c(0, x)}{\vartheta_v} \right\}, \tag{10}$$

where

$$h(x_1, x_2) = \frac{1}{2} + \frac{1}{2} \sin(\zeta x_1 x_2)^3 \cdot \sin(\zeta \frac{x_2}{x_1}), \tag{11}$$

with

$$(x_1, x_2) = \frac{1}{3}(x + 1.5) \in [0, 1]^2 \text{ for } x \in D, \quad \zeta = 7\pi.$$

Here we consider the volume fraction of cells and ECM to be $\vartheta_c \in [\frac{\pi}{6}, 1]$ and $\vartheta_v \in [0, \frac{5\pi}{6}]$. The initial condition for MDEs is $m(0, x) = 0.5c_1(0, x)$; however, since this closely resembles the profile of the cancer cell distribution, we shall not present the simulation results of MDE concentration. The initial conditions of the combined cell populations and ECM density can be seen in Figure 5.

Throughout these simulations, unless otherwise stated, we use the following parameter set for the non-dimensionalised system of equations (1) and (6), which were estimated based on those used in [15], namely:

$$\mathscr{P}: \quad \begin{aligned} & D_1 = 10^{-3}, \ D_2 = 10^{-3}, \ \gamma = 2, \ t_{1,2} = 10, \ \delta = 0.3, \\ & \mu_1 = 0.25, \ \mu_2 = 0.25, \ \omega = 0, \ v_{\min} = 0.3 \end{aligned}$$
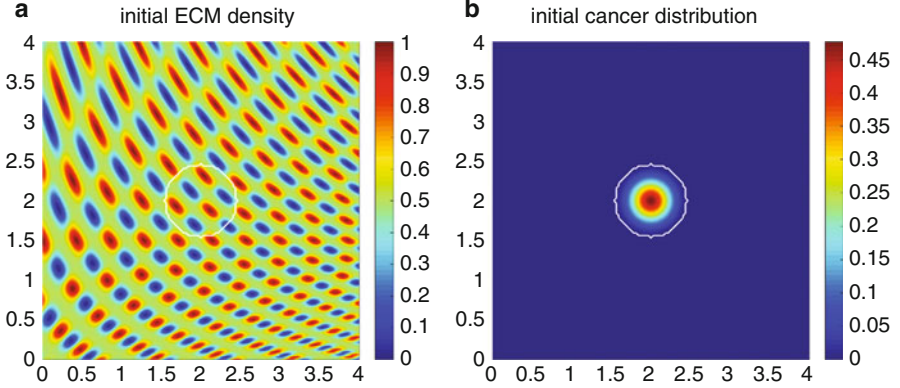
Fig. 5 Initial conditions of the density of ECM (a) and the distribution of cancer cells (b) with the invasive boundary of the tumour represented by the white contour.

We also have here the adhesive strengths matrices $\mathbf{S}_{cc}$ and $\mathbf{S}_{cv}$ given by

$$\mathbf{S}_{cc} = \begin{pmatrix} 0.5 & 0 \\ 0 & 0.3 \end{pmatrix} \quad \text{and} \quad \mathbf{S}_{cv} = \begin{pmatrix} 0.3 & 0 \\ 0 & 0.6 \end{pmatrix}. \tag{12}$$

Initially, we have no cross-adhesion occurring, so $S_{c_1,c_2} = 0 = S_{c_2,c_1}$.

Figure 7 gives simulations using the initial conditions and parameter set $\mathscr{P}$ as stated above. They are shown at stages $25\Delta t$, $50\Delta t$ and $75\Delta t$. Here, we also show the simulations at stage $10\Delta t$, Figure 6, the stage at which mutations occur. By this stage, population c_1 has degraded and lowered the density of the ECM in which the initial cancer distribution was placed. The threshold on which mutations can occur, δ, is higher than the resulting density of ECM; thus when mutations occur, they only take place on the outer edge of the tumour, where $\delta > 0$, as the ECM density is too low inside to support the mutations. The white contour shows the proliferating boundary of the tumour, which at this stage has consistently expanded outwards into the ECM. Due to the initial conditions of the ECM, there are patches of high and low density areas throughout the domain. These patches vary in distance and size from one another, which reflects a non-symmetric microenvironment for the cells. The pattern of the advancing front of the tumour loosely follows this pattern of ECM. Where there are dense patches of low density we see slower cancer progression; this is because there is a lower overall density of matrix for the cells to adhere.

After 25 macro-micro stages, $25\Delta t$, population c_1 and c_2 are both increasing in density, with population c_1 changing shape as the cells continue to mutate. As the tumour spreads, a larger region of ECM is degraded, which is shown in the plot for ECM.
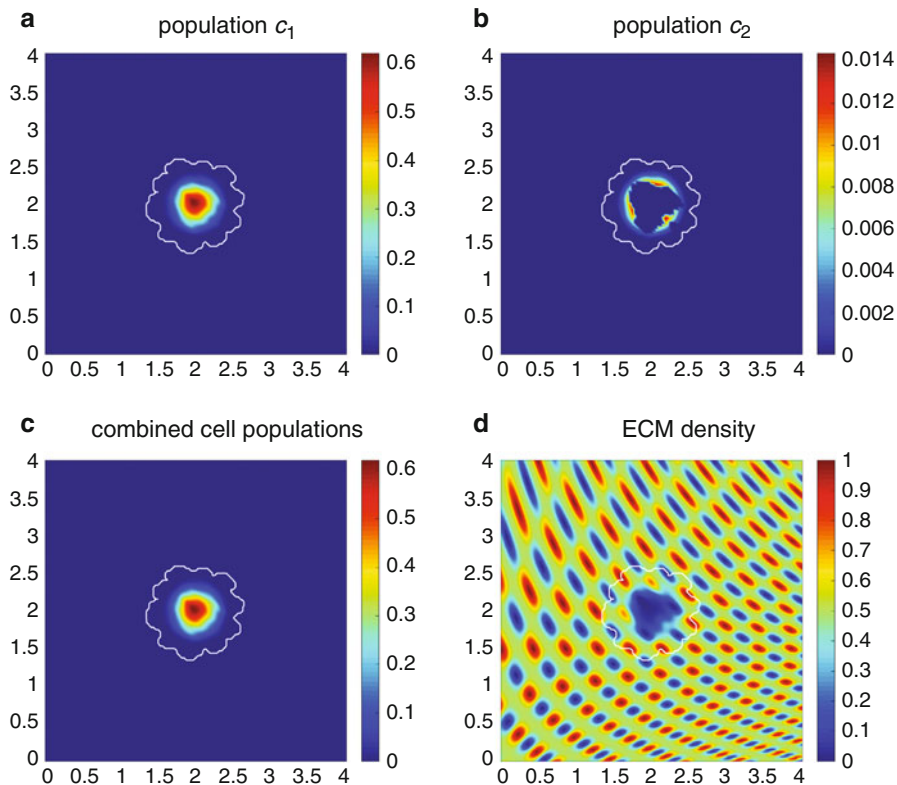
Fig. 6 Simulation results of model at stage $10\Delta t$ when the mutations from population c_1 start to occur.

As the cancer continues to invade, a wider region of the ECM is destroyed and the proliferating edge of the tumour continues to reach outwards, see stages $50\Delta t$ and $75\Delta t$ in Figure 7. The invasive edge of the tumour loosely follows the pattern of ECM at each stage, and small islands start to appear over low density patches of ECM. These islands have zero ECM density and hence cause the cancer cells to be slow to invade as there is an insufficient level of ECM for which the cells can adhere. This pattern of the boundary is due to the multiscale nature of the invasion process, where the macro-dynamics govern the source of the MDEs on the invading edge and then movement of the boundary is determined in each boundary cube ϵY by the resulting micro-dynamics. The MDEs produced by the cancer cells can only degrade locally; this becoming apparent from the resulting ECM plots.

We now want to consider the effect of matrix remodelling on the progression of cancer. Figure 8 shows simulations again using the parameter set $\mathscr{P}$, but this time with the ECM remodelling rate ω being increased from 0 to 0.04. Here we see that the spread of cancer is ultimately covering a larger area than in the absence of remodelling (Figure 7). Population c_2 displays a much larger spread of density
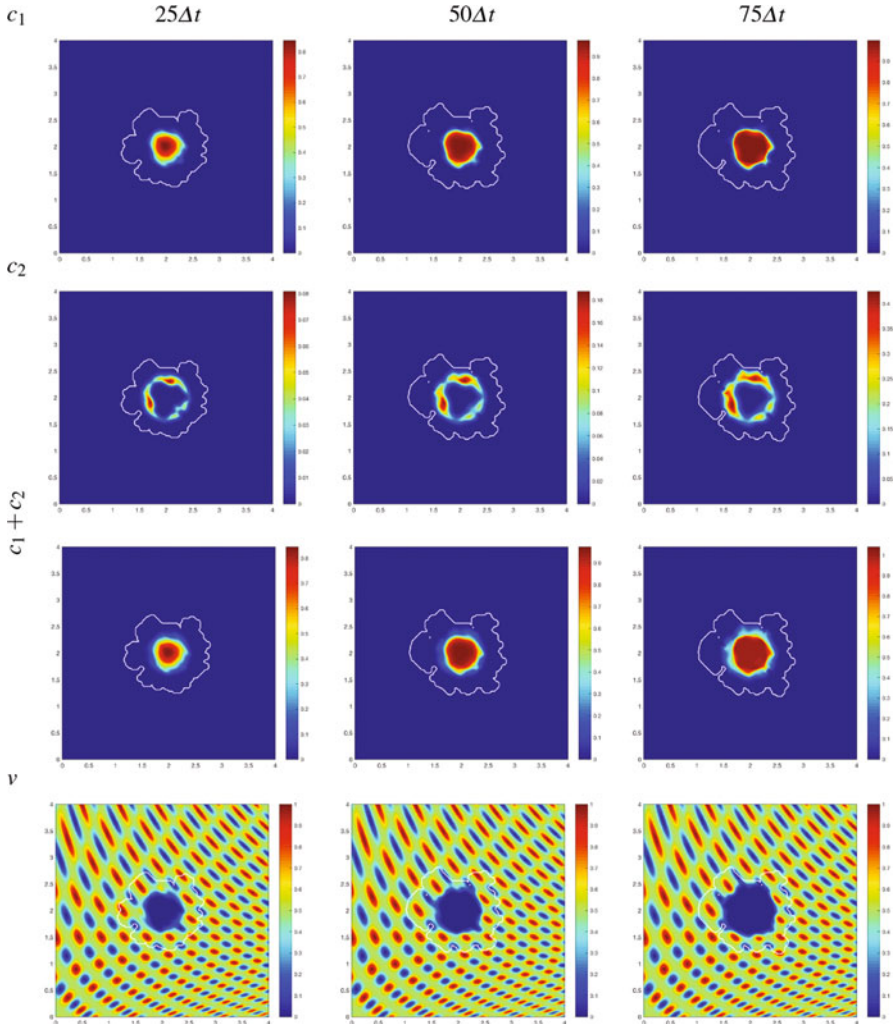
Fig. 7 Simulation results of model using the parameter set $\mathscr{P}$ and adhesion matrices (12). Plots of both cancer populations c_1 and c_2, as well as the combined cancer distributions and the ECM densities at stages $25\Delta t$, $50\Delta t$ and $75\Delta t$.

surrounding population c_1 than in the absence of ECM remodelling. The increased density of ECM surrounding the cells gives more opportunity for adherence and opens a greater number of pathways in which the cells can invade. The boundary of the cancer is following the pattern of the ECM more consistently than in Figure 7, this is due to the higher density of the remodelled ECM allowing for stronger adhesive qualities between the cancer cells and ECM. We can again see the invasion
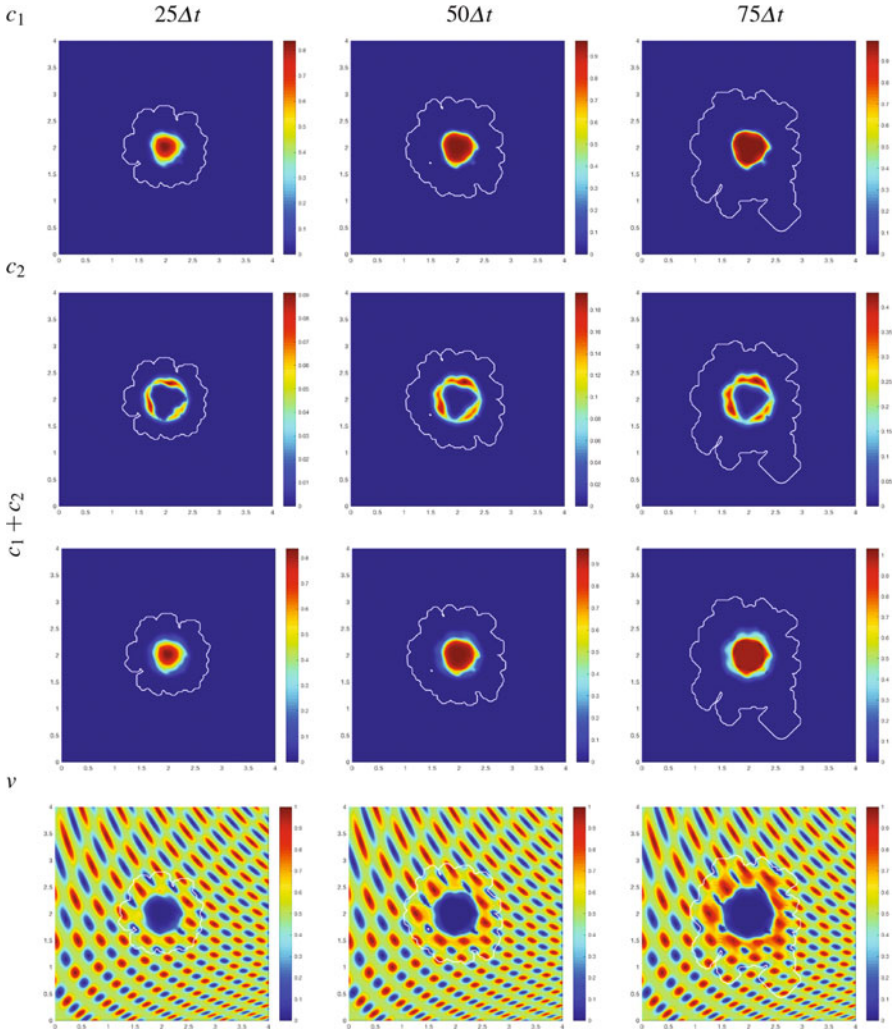
Fig. 8 Simulation results of model with ECM remodelling introduced, $\omega = 0.04$, with the same parameter set $\mathscr{P}$ and adhesion matrices as in Figure 7.

briefly halted at patches of lower density, but this is for a shorter period than before, with the islands being fully invaded by the later stages.

Figure 9 gives simulations where the cell-matrix adhesion between cancer cell population c_1 and the ECM, $S_{c_1,v}$, has been increased from 0.3 to 0.5 and the cell-matrix adhesion between cell population c_2 and the ECM, $S_{c_2,v}$, has been decreased from 0.6 to 0.5, i.e., the adhesion rate between the cells and matrix are equal for both populations. The proliferating edge of the tumour is lobular in the way it follows the pattern of the ECM, much like the simulations in Figure 7, with protrusions pushing
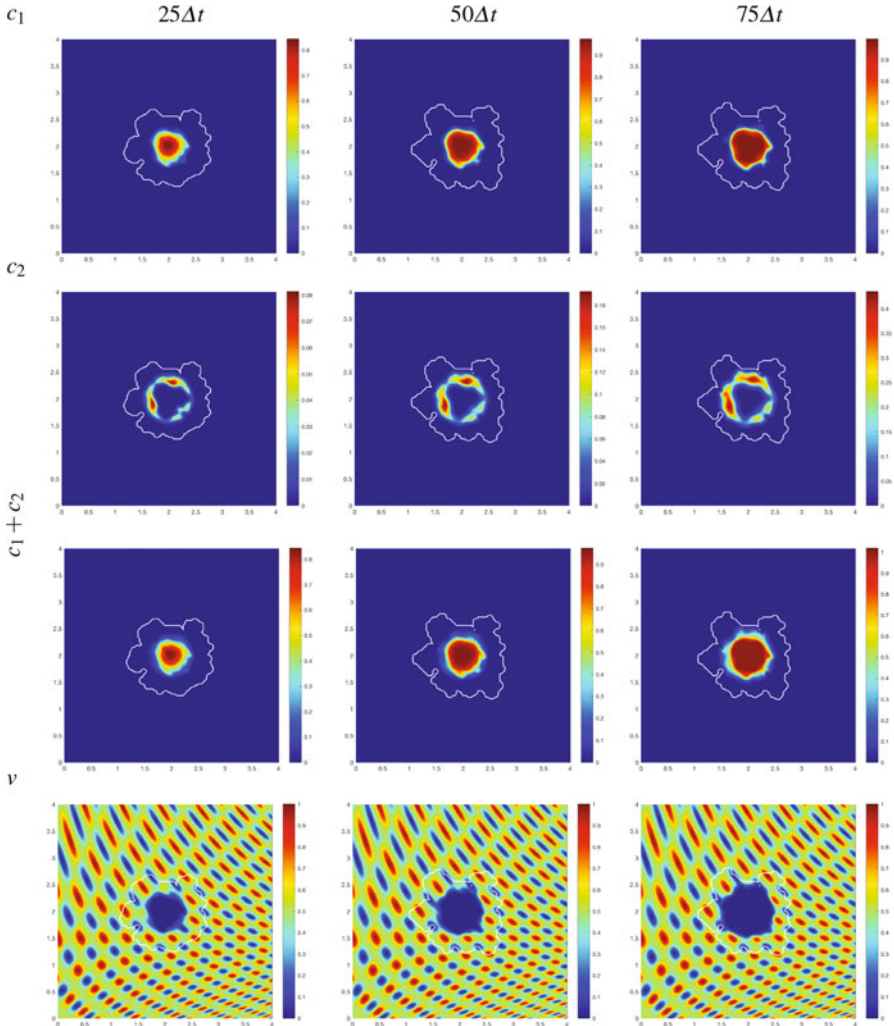
Fig. 9 Simulation results of model with parameter set $\mathscr{P}$ and $S_{c_1,v} = 0.5 = S_{c_2,v}$.

out in the direction of high density areas of the matrix. Although the cell-matrix adhesion term is now equal for both populations, the S_{c_1,c_1} and S_{c_2,c_2} have remained the same, thus we do not see a great change in the profile of the levels of cancer cell densities of the main body of the tumour itself, but we instead see a difference in the pattern of the invading edge of the tumour, due to the further spread of the lower levels of these densities closer to the invasive edge of the tumour. The increase in adhesion between population c_1 and the matrix sees the invading boundary stick closer to the main body of the tumour, particularly to population c_2.

Finally, we investigate the effects of cell-cell adhesion and in particular cross-adhesion. Cross-adhesion is when different cancer cell populations adhere to one another. Here we set $S_{c_1,c_2} = S_{c_2,c_1}$ as both populations will have the same rate of adherence to each other. We look at the case using parameter set $\mathscr{P}$ and the adhesion matrices

$$\mathbf{S}_{cc} = \begin{pmatrix} 0.5 & 0.5 \\ 0.5 & 0.3 \end{pmatrix} \quad \text{and} \quad \mathbf{S}_{cv} = \begin{pmatrix} 0.3 & 0 \\ 0 & 0.6 \end{pmatrix}, \tag{13}$$

Our simulations in this case, shown in Figure 10, exhibit the same general morphology of the tumour boundary as in results with no cross-adhesion present, mainly due to the fact that in this work both cancer cell population are assumed to degrade the ECM at the same rate. However, the difference with respect to the no cross-adhesion case is emphasised by the spatial distribution of the two cancer cell populations within the main body of the tumour. Population c_1 remains consistent with results computed in Figure 7; however, population c_2 exhibits different behaviour. We can distinguish now two higher density patches of c_2 densities which do not spread away from the significantly high levels of c_1 cell density and rather build up in their immediate proximity. Combining the cell populations now gives an increasingly contained spread of the tumour. This result is to be expected because the cells are now more inclined to stick together, rather than invade outwards, and although the adherence between cell populations has increased, their adhesion towards the matrix has stayed the same; hence we observe no difference in the movement of the boundary. This difference is also consistent with the other no cross-adhesion cases considered in Figures 8 and 9.

3.3 Sensitivity to Initial Conditions

To address sensitivity with respect to initial data, we present and discuss here the results of four different sets of initial conditions for the ECM that are induced (10) with (11) by function h given in (14), which are gradually convergent towards the case of homogeneous ECM. Figure 11(a) illustrates a homogenous ECM induced in (10) by the limit case for h that we obtain as $n \to \infty$, namely $h(x_1, x_2) = \frac{1}{2}$. Figures 11(b) and 11(c) use the initial condition (10), where the equation for $h(x_1, x_2)$ is changed to

$$h(x_1, x_2) = \frac{1}{2} + \frac{1}{2^n} \, \sin(\zeta x_1 x_2)^3 \cdot \sin(\zeta \frac{x_2}{x_1}), \tag{14}$$

with $n = 3, 5$ for Figures 11(b) and 11(c), respectively. Using this form effectively flattens down the high density regions of the heterogeneous ECM, making it progressively closer to a homogeneous case, who exhibits a symmetric growth. Finally, Figure 11(d) shows the simulations using the initial conditions (10) with (11), as in Figure 7. The main body of the tumour remains similar from each initial condition
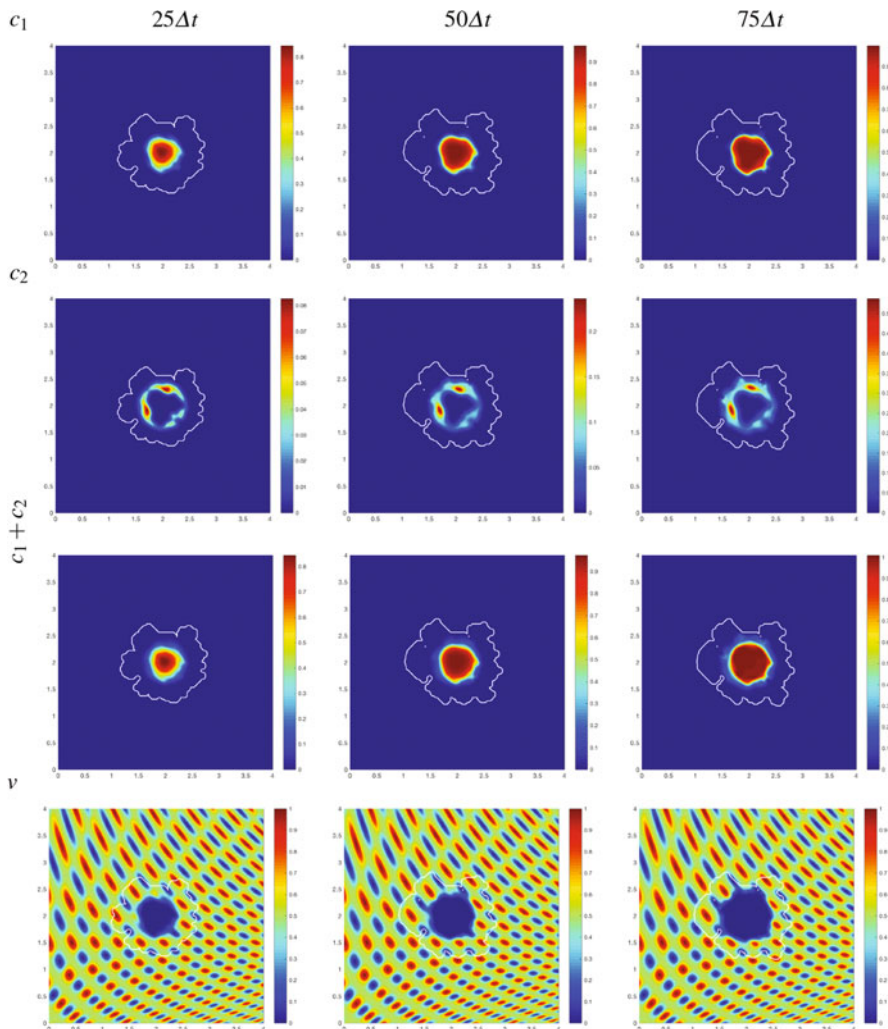
Fig. 10 Simulation results of model with parameter set $\mathscr{P}$ with cross-adhesion coefficient $S_{c_1,c_2} = 0.5 = S_{c_2,c_1}$.

of ECM as all coefficients remain the same as in the no cross-adhesion case shown in Figure 7. The differences between the invading boundaries are clearly visible, ranging from a symmetric expansion of the boundary for homogeneous initial conditions to a fingering leading edge for heterogeneous conditions. We conclude that as the initial condition for the ECM becomes increasingly heterogeneous, the proliferating edge of the tumour becomes consistently more lobular in its invasion.
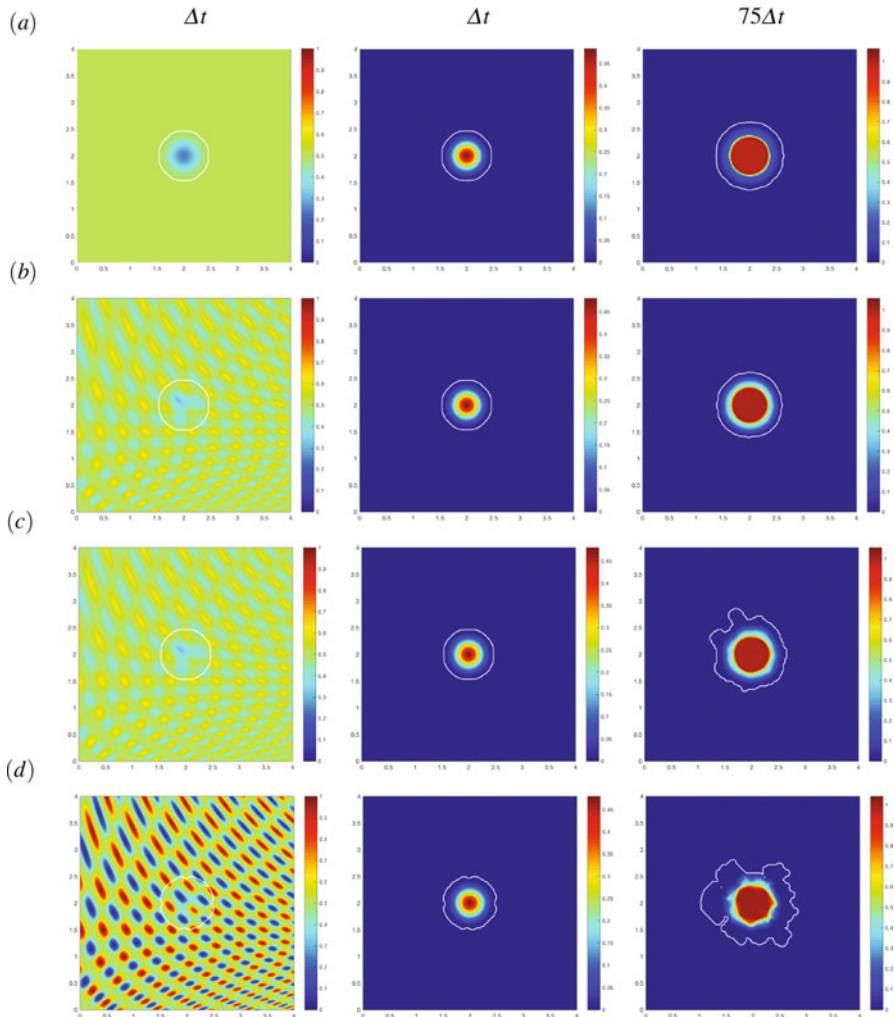
Fig. 11 Simulation results showing different initial conditions for the ECM. Plots showing ECM and the combined cancer distribution at their initial stage Δt, and the tumour at final stage $75\Delta t$.

4 Conclusions

We have presented a multiscale moving boundary model which builds on previous framework proposed by [29] by exploring adhesive dynamics [15] between a heterogeneous cancer cell population and the surrounding microenvironment. This considers both the macroscale dynamics of two cancer cell sub-populations within the ECM and their influence on the microscale MDEs molecular dynamics occurring at the cell-scale along the invasive edge of the tumour. This macro-micro top-down

link is given here via the source of MDEs that are secreted by the cancer cells from both c_1 and c_2 sub-populations arriving within the outer proliferating rim of the tumour. In turn, the micro-dynamics occurring on the cell-scale enables a micro-macro feedback in the form of a bottom-up link by providing the movement direction and displacement magnitude of the tumour boundary.

Comparing with results from the previous framework proposed in [29], we have shown that the inclusion of cell-cell and cell-matrix adhesion changes the way in which the cancer progresses. The computational results presented in this chapter have shown that the initial tumour region exercises greater movement than in the absence of adhesive qualities. We then incorporate another cell population and further explore the interactions between both cancer cell populations and their microenvironment. We have shown that in the presence of ECM remodelling, there is a greater spread of cancer cells as there is more opportunity for adherence which allows the cells to move. Increased cell-matrix adhesion, in particular between c_1 and v, has shown that a change in cell-matrix adhesion will not necessarily change the main body of the tumour, but it induces a change in the invading boundary, becoming very lobular when following the pattern of the ECM. Adding cross-adhesion to these models has shown how the different cell populations mix with one another and exhibits a denser region of population c_2 which remain in the proximity of highest regions of c_1 density. Finally, we investigated the effects of varying initial conditions of ECM, starting with a homogeneous distribution and becoming increasingly heterogenous. We have concluded that as the initial ECM distribution increases in heterogeneity, the proliferating boundary of the tumour becomes more lobular.

To gain further understanding of how cancer cells invade, focus must be placed on the surrounding microenvironment. The extracellular matrix is made from many different components, most of which play a vital role in cancer invasion. The main component of the ECM is collagen, particularly collagen type I which provides the matrix with its structure and flexibility. Investigations into the mesenchymal motion of tumour cells [13, 19, 25] shows that the difference between *undirected* and *directed* fibres is of high importance. Undirected fibres are symmetrical along their axes and their direction is identical at both ends, an example of this type of fibre would be collagen in the human body. Unlike undirected fibres, directed fibres are unsymmetrical and can be distinguished at both ends. Recent work considering fibres by [30], focussed on directed fibres, has highlighted differences between directed and undirected fibres using a one-dimensional model. The addition of fibres, directed or undirected, into the multiscale model would greatly change the pattern of invasion. Several other components of the ECM such as fibronectin, laminin and a variety of different MMPs are also vital in tumour invasion and a greater mathematical understanding of these would allow for an overall better understanding of cancer progression.

References

1. Andasari V, Gerisch A, Lolas G, South A, Chaplain MAJ (2011) Mathematical modeling of cancer cell invasion of tissue: biological insight from mathematical analysis and computational simulation. J Math Biol 63(1):141–171

2. Anderson A, Rejniak K, Gerlee P, Quaranta V (2007) Modelling of cancer growth, evolution and invasion: Bridging scales and models. Math Model Nat Phenom 2(3):1–29

3. Anderson ARA, Chaplain MAJ, Newman EL, Steele RJC, Thompson AM (2000) Mathematical modelling of tumour invasion and metastasis. J Theor Med 2(2):129–154, doi10.1080/10273660008833042

4. Armstrong NJ, Painter KJ, Sherratt JA (2006) A continuum approach to modelling cell-cell adhesion. J Theor Biol 243(1):98–113

5. Bellomo N, Angelis ED, Preziosi L (2002) Multiscale modelling and mathematical problems related to tumour evolution and medical therapy. J Theor Biol 58:3719–3727

6. Berrier AL, Yamada KM (2007) Cell-matrix adhesion. J Cell Physiol 213(3):565–573, doi10.1002/jcp.21237

7. Bhagavathula N, Hanosh AW, Nerusu KC, Appelman H, Chakrabarty S, Varani J (2007) Regulation of e-cadherin and β-catenin by Ca^{2+} in colon carcinoma is dependent on calcium-sensing receptor expression and function. Int J Cancer 121:1455–1462, doi10.1002/ijc.22858

8. Byrne HM, Preziosi L (2004) Modelling solid tumour growth using the theory of mixtures. Math Med Biol 20:341–366, doi10.1093/imammb/20.4.341

9. Cavallaro U, Christofori G (2001) Cell adhesion in tumor invasion and metastasis: loss of the glue is not enough. Biochimica et Biophysica Acta (BBA) - Reviews on Cancer 1552(1):39–45, doi10.1016/S0304-419X(01)00038-5

10. Chaffer CL, Weinberg RA (2011) A perspective on cancer cell metastasis. Science 331(6024):1559–1564

11. Chaplain MA (1996) Avascular growth, angiogenesis and vascular growth in solid tumours: The mathematical modelling of the stages of tumour development. Math Comput Model 23(6):47–87

12. Chaplain MAJ, Lachowicz M, Szymańska Z, Wrzosek D (2011) Mathematical modelling of cancer invasion: The importance of cell-cell adhesion and cell-matrix adhesion. Math Mod Meth Appl S 21:719–743, doi10.1142/S0218202511005192

13. Chauviere A, Hillen T, Preziosi L (2007) Modeling cell movement in anisotropic and heterogeneous network tissues. Netw Heterog Media 2(2):333–357

14. Cox TR, Erler JT (2011) Remodeling and homeostasis of the extracellular matrix: implications for fibrotic diseases and cancer. Disease Models and Mechanisms 4(2):165–178

15. Domschke P, Trucu D, Gerisch A, Chaplain M (2014) Mathematical modelling of cancer invasion: Implications of cell adhesion variability for tumour infiltrative growth patterns. J Theor Biol 361:41–60

16. Gerisch A, Chaplain M (2008) Mathematical modelling of cancer cell invasion of tissue: Local and non-local models and the effect of adhesion. J Theor Biol 250:684–704

17. Hanahan D, Weinberg RA (2000) The hallmarks of cancer. Cell 100:57–70, doi10.1016/S0092-8674(00)81683-9

18. Hanahan D, Weinberg RA (2011) The hallmarks of cancer: The next generation. Cell 144:646–674

19. Hillen T (2006) M5 mesoscopic and macroscopic models for mesenchymal motion. Journal of Mathematical Biology 53(4):585–616, doi10.1007/s00285-006-0017-y

20. Hills CE, Younis MYG, Bennett J, Siamantouras E, Liu KK, Squires PE (2012) Calcium-sensing receptor activation increases cell-cell adhesion and -cell function. Cell Physiol Biochem 30(3):575–586, doi10.1159/000341439

21. Holle AW, Young JL, Spatz JP (2016) In vitro cancer cell–ecm interactions inform in vivo cancer treatment. Advanced Drug Delivery Reviews 97(Supplement C):270–279, doi10.1016/j.addr.2015.10.007

22. Katt ME, Placone AL, Wong AD, Xu ZS, Searson PC (2016) In vitro tumor models: Advantages, disadvantages, variables, and selecting the right platform. Frontiers in Bioengineering and Biotechnology 4(12)
23. Lodish H, Berk A, Zipursky S (2000) Molecular Cell Biology, 4th edn. W.H.Freeman
24. Nabeshima K, Inoue T, Shimao Y, Sameshima T (2002) Matrix metalloproteinases in tumor invasion: Role for cell migration. Pathology International 52(4):255–264
25. Painter KJ (2008) Modelling cell migration strategies in the extracellular matrix. Journal of Mathematical Biology 58(4):511, doi10.1007/s00285-008-0217-8
26. Parsons SL, Watson SA, Brown PD, Collins HM, Steele RJ (1997) Matrix metalloproteinases. Brit J Surg 84(2):160–166, doi10.1046/j.1365-2168.1997.02719.x
27. Ramis-Conde I, Drasdo D, Anderson AR, Chaplain MA (2008) Modeling the influence of the e-cadherin-beta-catenin pathway in cancer cell invasion: a multiscale approach. Biophys J 95(1):155–165
28. Shah D, Tseng W, Martinez S (2012) Treatment options for metaplastic breast cancer. ISRN Oncology 2012
29. Trucu D, Lin P, Chaplain MAJ, Wang Y (2013) A multiscale moving boundary model arising in cancer invasion. Multiscale Model Simul 11(1):309–335
30. Wang Z, Hillen T, Li M (2008) Mesenchymal motion models in one dimension. SIAM J Appl Math 69(2):375–397
31. Weigelt B, Peterse JL, van't Veer LJ (2005) Breast cancer metastasis: markers and models. Nat Rev Cancer 5(8):591–602
32. Wijnhoven B, Dinjens W, Pignatelli M (2000) E-cadherin-catenin cell-cell adhesion complex and human cancer. Brit J Surg 87(8):992–1005
33. Yamaguchi H, Wyckoff J, Condeelis J (2005) Cell migration in tumors. Current Opinion in Cell Biology 17(5):559–564, doi10.1016/j.ceb.2005.08.002
34. Yang H (2012) Mathematical modelling of solid cancer growth with angiogenesis. Theor Biol and Med Mod 9(2)

The Role of Microenvironment in Regulation of Cell Infiltration in Glioblastoma

Yangjin Kim, Wanho Lee, Hyejin Jeon, Sookkyung Lim, Soyeon Roh, Donggu Lee, Junho Lee, and Sean Lawler

Abstract Glioblastoma multiforme (GBM) is one of the deadliest human cancers and is characterized by fast growth and aggressive invasion. GBM also communicates with microglia and macrophages which are recruited by tumor cells to facilitate growth and invasion. In this study we investigate the biochemical and cell-mechanical interactions between the glioma cells and the microenvironment including resident glial cells and M1/M2 microglia that enhance tumor invasion. We develop various types of mathematical models that involve reaction-diffusion

Y. Kim (✉) · D. Lee · J. Lee
Department of Mathematics, Konkuk University, 120 Neungdong-ro, 05029 Gwangjin-gu, Seoul, Republic of Korea
e-mail: ahyouhappy@konkuk.ac.kr; donggu9211@gmail.com; juneho2222@gmail.com

W. Lee
National Institute for Mathematical Sciences, 70, Yuseong-daero 1689 beon-gil, 34047 Yuseong-gu, Daejeon, Republic of Korea
e-mail: wlee@nims.re.kr

H. Jeon
Molecular and Translational Neuroimaging Lab, Department of Radiology, Seoul National University College of Medicine, 28 Yeongeon-dong, Jongno-gu, Seoul, 110–744, Republic of Korea
e-mail: jhjisthebest@gmail.com

S. Lim
Department of Mathematical Sciences, University of Cincinnati, 4199 French Hall West, 45221 Cincinnati, OH, USA
e-mail: limsg@ucmail.uc.edu

S. Roh
Department of Biological Sciences, Carnegie Mellon University, 5000 Forbes Avenue, 15213 Pittsburgh, PA, USA
e-mail: soyeonroh@gmail.com

S. Lawler
Department of Neurosurgery, Brigham and Women's Hospital and Harvard Medical School, 4 Black-fan Circle, HIM 930A Boston, MA, 02115
e-mail: SLAWLER@bwh.harvard.edu

27

equations or multi-scale hybrid models for the important components in this mutual interaction. In particular, we investigate the dynamics of intracellular signaling including miR-451 and AMPK, biochemical interaction of a glioma with M1/M2 microglia via CSF-1-EGF-TGF-β signaling, and glioma cell infiltration through the narrow intercellular space via the regulation of myosin II. We show that these models can replicate the key features of the experimental findings and make novel predictions to guide future experiments aimed at the development of new anti-invasive strategies.

1   Introduction

Cancer invasion is a complex evolutionary process controlled by mutual interactions between a tumor and selective pressures from the tumor microenvironment (TME). (See Figure 1). Glioblastoma multiforme (GBM) is the most aggressive form of primary brain tumors with a very poor survival rate [11]. Diffuse infiltration of glioma cells into normal surrounding brain tissue is one of the major obstacles for the treatment failure because these cells escape surgery and can lead to recurrence. There is little understanding of how the bio-chemical and -mechanical signal pathways from the TME interact to affect tumor invasion. Here we review recent developments in mathematical models of anti-invasion strategies in order to address several aspects of this question in the context of brain tumors.
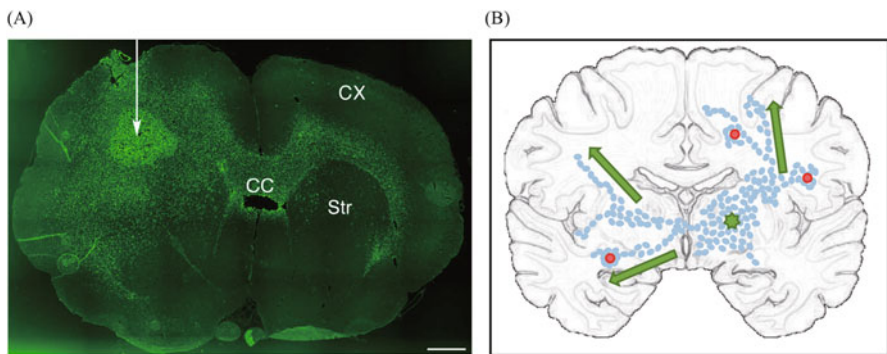
Fig. 1 Glioma cell infiltration in a complex brain microenvironment (A) Invasive Human glioma xenografts. Glioma cells have spread across the corpus callosum (CC) to the contralateral white matter located between cortex (CX) and striatum (Str) in a rat. Green = staining for human nuclear antigen for the location of human tumor cells. White arrow = the location of the site of tumor inoculation. Reprinted from Beadle C, Assanah M, Monzo P, Vallee R, Rosenfield S, et al. (2008) The role of myosin II in glioma invasion of the brain. Mol Biol Cell 19: 3357–3368 [5] under a CC BY license, with permission from American Society for Cell Biology, original copyright 2008. (B) A schematic diagram of diffuse infiltration of tumor cells in brain. Red circle = blood vessels (BVs), green star = active tumor growth, arrow = glioma cells migrating along white matter tracts.
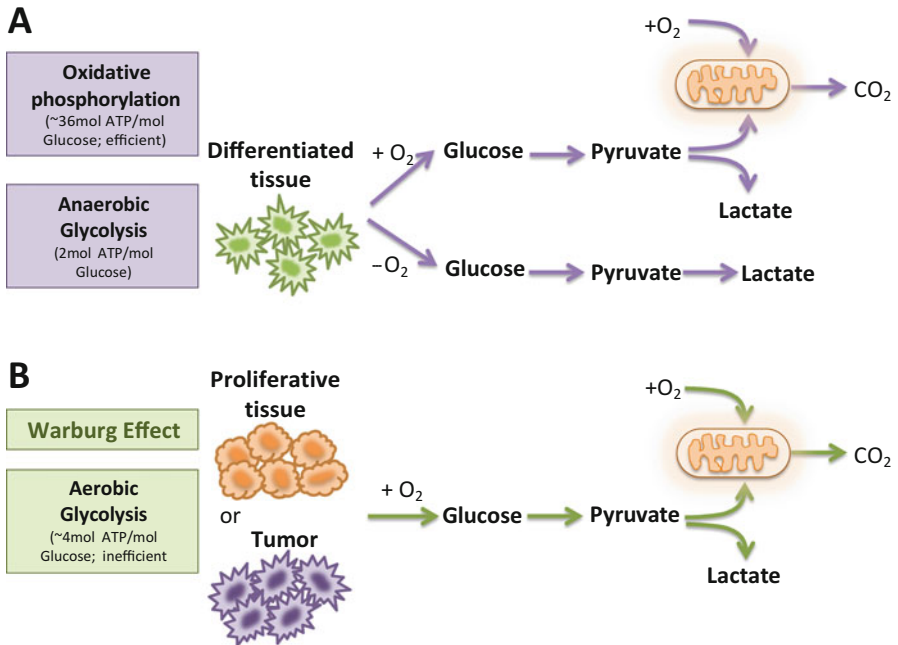
Fig. 2 Warburg effect in glioma Schematics of oxidative phosphorylation and anaerobic (or aerobic) glycolysis [32, 37, 45, 99].

2 Glioma Invasion

Differentiated cells favor the energy efficient tricarboxylic acid (TCA) cycle (Figure 2A), whereas tumor cells favor the less energy efficient process of glycolysis [32] (Figure 2B). This switch allows tumor cells to direct their metabolism towards biosynthetic processes needed for rapid cell growth, rather than generation of ATP [37]. Because glycolysis consumes less oxygen than the TCA cycle, cancer cells do not have to depend so much on oxygen for energy in the hostile (hypoxic) intra-tumoral microenvironment [25, 37]. One of the most important cellular pathways regulating responses to energy status is the AMP-activated protein kinase (AMPK) cascade which is turned on in times of low glucose enabling cell survival under these conditions [60]. Godlewski *et al.* [28] found that normal (high) glucose levels increase expression of the microRNA miR-451 and decrease AMPK activities, resulting in active proliferation while low glucose levels down-regulate miR-451 and enhance AMPK activities, which in turn induces cell motility [26, 27, 65]. See Figure 3.
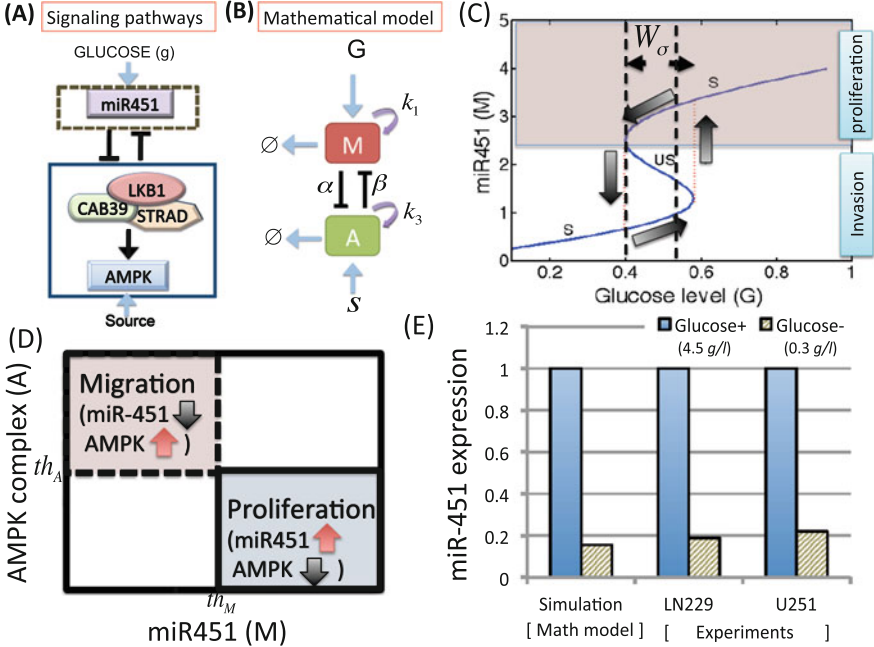
Fig. 3 (A) Signaling network of miR451-AMPK signaling pathways in cell migration and proliferation [26, 28]. (B) Schematic of a mathematical model [45]: miR-451 level and activity of AMPK complex (CAB39/LKB1/AMPK) are represented by "M" and "A," respectively. (C) High and low glucose levels (G) provide an on-off switch of the miR-451 expression level, determining cell proliferation or migration [45]. The intermediate G level induces a window of bi-stability ($W_\sigma = [\sigma_w^\dagger, \sigma_w^\ddagger]$) where the initial status of miR-451 and AMPK complex determines cell fate. (D) A diagram of proliferative ($M > th_M$, $A < th_A$) and migratory ($M < th_M$, $A > th_A$) phase in the M-A plane based on up- and down-regulation of miR-451 and AMPK complex [44]. (E) Simulation and experiments [28]: The relative quantification of miR-451 expression levels in response to high (+, 4.5 g/l) and low (−, 0.3 g/l) glucose injections.

2.1 Control of Glioma Infiltration via a miR-451-AMPK-mTOR

The signaling pathway of miR-451-AMPK can be simplified from the complex network as in Figure 3A and it can be further simplified as a system of differential equations with two variables corresponding to miR-451 and the AMPK complex, see Figure 3B. Governing equations of the miR-451-AMPK signaling in a nondimensional form are as follows:

$$\frac{dM}{dt} = G + \frac{k_1 k_2^2}{k_2^2 + \alpha A^2} - M, \qquad (1)$$

$$\epsilon \frac{dA}{dt} = S + \frac{k_3 k_4^2}{k_4^2 + \beta M^2} - A, \qquad (2)$$

Table 1 Parameters that are used in the core control model (miR-451-AMPK system).

Parameter	Description	Value[a]	Refs
k_1	miR-451 autocatalytic production rate	4.0	[44, 45]
k_2	Hill-type coefficient	1.0	[44, 45]
α	Inhibition strength of miR-451 by AMPK complex	1.6	[44, 45]
k_3	AMPK autocatalytic production rate	4.0	[44, 45]
k_4	Hill-type coefficient	1.0	[44, 45]
β	Inhibition strength of AMPK complex by miR-451	1.0	[44, 45]
S	Signaling source of AMPK	0.2	[44, 45]
ϵ	Scaling factor (slow dynamics)	0.02	[2, 16, 24, 44, 45]
th_M	Threshold of miR-451 for invasion/growth switch	2.0	[44, 45]

[a]Dimensionless value

where parameters are given in Table 1. When the miR-451-AMPK system (1)–(2) is in equilibrium, we can find the steady state of the miR-451 level (M) as a function of glucose amounts (G) where G is a bifurcation parameter as shown in Figure 3C. By observing the dynamic structure of the model, one can find that high levels of miR-451 (and low AMPK activity) in the stable upper branch induce cell proliferation in response to the high glucose level while the low miR-451 levels (and high AMPK activities) in the stable lower branch lead to cell migration in response to low glucose injection. However, the intermediate level of glucose may lead to a bi-stability region where microenvironmental factors may induce either proliferation or migration based on the history of the condition. In Figure 3D, we define two distinctive regions (the migratory region $\mathbb{T}_m$ (dotted pink box and the proliferative region $\mathbb{T}_p$ (blue solid box)) based on activities of those molecules:

$$\mathbb{T}_m = \{(M, A) \in \mathbb{R}^2 : M < th_M, \ A > th_A\} \tag{3}$$

$$\mathbb{T}_p = \{(M, A) \in \mathbb{R}^2 : M > th_M, \ A < th_A\}. \tag{4}$$

Our model predicts a significant reduction in miR-451 levels in response to high (4.5 g/l; blue in Figure 3E) and low (0.3 g/l; gray in Figure 3E) glucose injection doses, which are in good agreement with experimental results in LN229 and U251 glioma cell lines [28].

2.2 PDE Model

The simple model in the previous section can be extended to incorporate more components and diffusion process in time and space. Governing equations for the tumor density ($n(x, t)$), concentrations of the ECM ($\rho(x, t)$), MMP ($P(x, t)$), glucose ($G(x, t)$), miR-451 ($M(x, t)$), and AMPK ($A(x, t)$) are given by [45]

$$\frac{\partial n}{\partial t} = \left[D_n \Delta n - \nabla \cdot \left(\chi_n \frac{n \nabla G}{\sqrt{1 + \lambda_G |\nabla G|^2}} \right) - \nabla \cdot \left(\chi_n^1 \frac{n \nabla \rho}{\sqrt{1 + \lambda_\rho |\nabla \rho|^2}} \right) \right] I_{M < th_M}$$

$$+ \lambda_{11} n (1 - n/n_0) I_{M > th_M}, \tag{5}$$

$$\frac{\partial \rho}{\partial t} = -\lambda_{21} P \rho + \lambda_{22} \rho (1 - \rho/\rho_0), \tag{6}$$

$$\frac{\partial P}{\partial t} = D_P \Delta P + \lambda_{31} n \rho - \lambda_{32} P, \tag{7}$$

$$\frac{\partial G}{\partial t} = D_G \Delta G - \lambda_{41} \, nG + \sum_{j=0}^{N-1} \lambda_{42} I_j, \tag{8}$$

$$\frac{\partial M}{\partial t} = (G + \frac{k_1 k_2^2}{k_2^2 + \alpha A^2} - M) \frac{n}{n_0}, \tag{9}$$

$$\epsilon \frac{\partial A}{\partial t} = (S + \frac{k_3 k_4^2}{k_4^2 + \beta M^2} - A) \frac{n}{n_0}, \tag{10}$$

where $I_{\{\cdot\}}(x)$ is the indicator function, giving 1 under the condition $\{\cdot\}$, and 0 otherwise. Parameter values are given in Table 2. The first three terms in Equation (5) represent random motility, chemotaxis, and haptotaxis, respectively, for the tumor cell in $\mathbb{T}_m$.

The mathematical model can be used to make hypotheses regarding overall growth patterns of a tumor spheroid under the periodic (Figure 4A) and steady-state glucose supply conditions with the same amount of glucose [45]. While a cycle of high and low glucose levels induce high (or low AMPK) and low (or high AMPK) miR-451 activities, leading to a cycle of growth and invasion of the tumor cells, the steady supply of glucose leads to slow but constant growth (Figure 4). The model predicted that the oscillations in glucose levels increase the overall growth of the tumor through the core control system.

2.3 Hybrid Model

Our multi-scale hybrid model includes several aspects: (1) intracellular pathways, (2) a *lattice-free* cell-based mechanical model, (3) a reaction-diffusion model of extracellular biochemical players such as oxygen and glucose. A schematic of the hybrid model is shown in Figure 5.

The growth and movement of individual cells is based on the models developed by Dallon and Othmer [17] (DO model) and Kim *et al.* [46, 47]. The model essentially takes into account the following forces: (i) the active forces $\mathbf{T}_i$ exerted on the substrate or neighboring cells and the reaction force ($\mathbf{M}_{j,i}$), (ii) the dynamic drag forces from adhesion with cells in the neighborhood, (iii) static friction force $\mathbf{S}_{j,i}$ for rigid attachment between involved cells or between a cell and the substrate.

Table 2 Parameters that are used in the PDE model [45].

Parameter	Description	Dimensional value	Refs
D_n	Random motility of tumor cells	10^{-11} cm^2/s	[41]
D_P	Diffusion coefficient of MMPs	5×10^{-11} cm^2/s	[41, 81, 86]
D_G	Diffusion coefficient of glucose	2.31×10^{-7} cm^2/s	[41, 80], Estimated
λ_{11}	Tumor cell growth rate	1.112×10^{-4} s^{-1}	[64, 83], Estimated
n_0	Carrying capacity of tumor cells	1.0×10^{-3} g/cm^3	Estimated
λ_{21}	ECM degradation rate	1.41×10^3 cm^{3}g^{-1}s^{-1}	[41],TW
λ_{22}	ECM release/reconstruction rate	5.0×10^{-5}s^{-1}	[41],TW
ρ_0	ECM carrying capacity	1.0×10^{-3} g/cm^3	[35, 41, 89]
λ_{31}	MMP production rate	6.95×10^{-5} cm^{3}g^{-1}s^{-1}	Estimated
λ_{32}	MMP decay rate	5.0×10^{-5} s^{-1}	[41], Estimated
λ_{41}	Glucose consumption rate	0.3 cm^3/(g.s).	[57, 83], TW
λ_{42}	Glucose injection rate	1.25×10^{-6} g/(cm^3.s)	Estimated
χ_n	Chemotactic sensitivity parameter	1.86×10^{-7} cm^{5}g^{-1}s^{-1}	Estimated
χ_n^1	Haptotactic parameter	4.17×10^{-5} cm^5/(g.s)	[41], Estimated
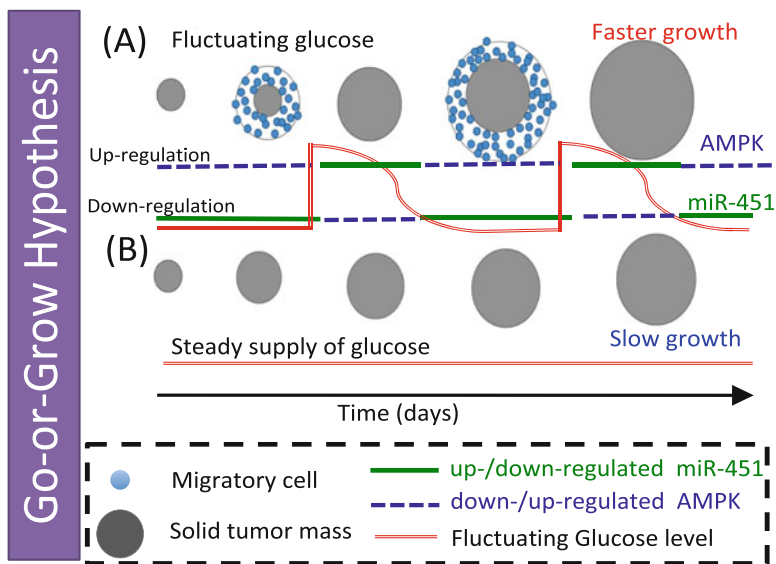
Fig. 4 Theoretical glucose-induced "go"-"grow" hypothesis. (A) the cycles of invasion and growth in response to periodic glucose injection. (B) Monotonic growth induced by steady glucose supply. Our mathematical model predicts that fluctuating glucose leads to faster growth of the tumor through miR-451-AMPK regulation [45].

(See DO for a more detailed discussion of all forces involved.) The total force on the ith cell is then governed by

$$\mathbf{F}_i = \sum_{j \in \mathcal{N}_i^a} \mathbf{M}_{j,i} + \sum_{j \in \mathcal{N}_i^a} \mathbf{T}_i + \sum_{j \in \mathcal{N}_i^d} \mu_{ij}(\mathbf{v}_j - \mathbf{v}_i) + \sum_{j \in \mathcal{N}_i^s} \mathbf{S}_{j,i} \qquad (11)$$
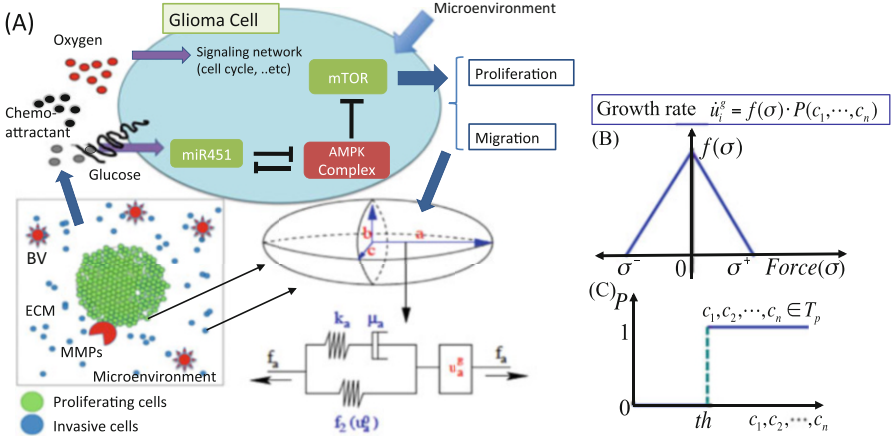
Fig. 5 A schematic of hybrid models in gliomas [38, 43, 44]. (A, Top) Intracellular dynamics (such as miR451, AMPK, mTOR, and cell cycle) in response to diffusible molecules (oxygen, glucose, and chemoattractant) at a cell site. Up- or down-regulation of these intracellular variables determines the cell fate, such as proliferation or migration. (A, Bottom, Left) Domain of the mathematical model: Tumor cells have either proliferating (green) or migratory phase (blue) based on status of intracellular molecules. Migratory cells may secrete MMPs for degradation of thick ECM in response to biochemical or mechanical signals from the surrounding microenvironment including BVs. (A, Bottom, Right) Changes in the length of the a-axis of a glioma cell (the ellipsoid) under a given force (f_a; arrow) consist of two modules: (i) the passive change in the first module (a Maxwell element in parallel with a non-linear spring) (ii) the change due to the active growth (u_a^g). (B) The mechanical growth function $f(\sigma)$ in submodule of the growth rate ($(u_i^g)' = f(\sigma)P(c_1, c_2, \cdots, c_n)$) is defined so that tumor cells can grow under sufficiently small compressive and tensile forces in a nonlinear fashion [46] (C) Proliferation function (P) as a function of intracellular variables ($c_1, c_2, \cdots, c_n$) which gives 1 ($c_1, c_2, \cdots, c_n \in \mathbb{T}_p$) or 0 ($c_1, c_2, \cdots, c_n \in \mathbb{T}_m$) for activation and suppression of the biochemical growth control switch.

where $\mathcal{N}_i^a$ denotes the neighbors of i, including the substrate, upon which it can exert traction, $\mathcal{N}_i^d$ is the set of cells (which includes solid substrate and extracellular matrix) that interact with i via a frictional force, and $\mathcal{N}_i^s$ represents the set of cells that statically bind to cell i. These force balance equations allow us to calculate all forces involved and track down locations of all cells in addition to biophysical response of the cells. These forces are expressed in terms of cell velocity ($\mathbf{v}_i$) which can be used for displacement of the cells for comparison with the experimental data. The governing equations of the length of the i-th axis, $i = \mathbf{a}, \mathbf{b}, \mathbf{c}$, of a cell are

$$u_i = u_i^0 + u_i^g, \tag{12}$$

$$\frac{du_i^0}{dt} = \left(\frac{k_i}{\mu_i}[f_i(t) + \bar{p} - f_2(u_i^0)] + \frac{df_i}{dt} \right) \times \left(f_2'(u_i^0) + k_i \right)^{-1}, \tag{13}$$

where u_i is the change in the length of the ith axis, u_i^0 and u_i^g are the changes in the length of the ith axis due to a change in the passive and growth element, respectively,

f_i is the magnitude of the force applied at each end, f_2 is the nonlinear spring force from the spring in parallel, k_i is the spring constant for the spring in the Maxwell element, μ_i is the viscous coefficient of the dashpot, $\bar{p}$ is the force due to pressure. The specific form and details of the function f_2 are given in [17]. It is assumed that the passive response is incompressible [46, 47], leading to the volume constraint for u_a^0, u_b^0, and u_c^0, $\left(\frac{du_a^0}{dt}\right)(u_b^0 + b_0^*)(u_c^0 + c_0^*) + (u_a^0 + a_0^*)\left(\frac{du_b^0}{dt}\right)(u_c^0 + c_0^*) + (u_a^0 + a_0^*)(u_b^0 + b_0^*)\left(\frac{du_c^0}{dt}\right) = 0$, where $a_0^* = a_0 + u_a^g, b_0^* = b_0 + u_b^g, c_0^* = c_0 + u_c^g$, and a_0, b_0, and c_0 are the initial lengths of three axes.

We consider two kinds of glioma cells involved: proliferative and migratory. The cells are treated as oriented ellipsoids with cytoplasm considered as an incompressible, viscoelastic solid [17, 46]. We take the multiplicative form of the growth rate function for the i-th axis of a cell given by

$$(u_i^g)' = f(\sigma)P(c_1, c_2, \cdots, c_n)$$

where σ is the mechanical force acting on the cell and P is a function of intracellular variables c_i, $i = 1, \ldots, n$ (Figure 5C) such as RAS and sMAD in breast cancer models [42, 47], miR451 (M), AMPK (A), mTOR (R), and other molecules involved in the cell cycle in glioma models [38, 43, 44]. The growth function $f(\sigma)$ is defined so that tumor cells can grow under sufficiently small compressive and tensile forces in a nonlinear fashion [46] (Figure 5B). Here, we assume that the glioma cell proliferation is determined by the core control module: $P(M, A) = 1$ in $\mathbb{T}_p$-phase in Equation (4), and 0 in $\mathbb{T}_m$-phase in Equation (3) [38, 44]. (This was generalized to include mTOR regulation in [43]). The active traction force $\mathbf{T}_i^a$ for migratory cell i is given by

$$\mathbf{T}_i^a = \phi(M, A)\left(\psi_1 \mathbf{d}_r + \psi_2 \frac{\nabla G}{\sqrt{K_G + |\nabla G|^2}} + \psi_3 \frac{\nabla C}{\sqrt{K_C + |\nabla C|^2}}\right) \equiv \phi(M, A)\mathbf{T}_{i,g}$$

(14)

where $\mathbf{d}_r$ is a unit vector of the random moving direction, G, C are the concentration of glucose and a chemoattractant, and ψ_1, ψ_2, ψ_3 are scaling factors of weight distribution ($\psi_1, \psi_2, \psi_3 \in [0, 1]$; $\psi_1 + \psi_2 + \psi_3 = 1$). Here, the indicator function $\phi(M, A)$ is given by

$$\phi(M, A) = \begin{cases} r_n F_0 & \text{if cell } \in \mathbb{T}_m \text{ without physical constraints,} \\ 0 & \text{otherwise,} \end{cases}$$

(15)

where F_0 is the basal magnitude of the active force ($0 \leq |\mathbf{T}_i| \leq F_0$) and r_n is a random number in [0.8, 1.2]. Therefore, the active force is completely turned off for proliferative cells ($\mathbb{T}_p$), cells under physical constraints (a cell completely surrounded by neighboring cells), or in the absence of chemotactic signal ($\nabla C = 0$).
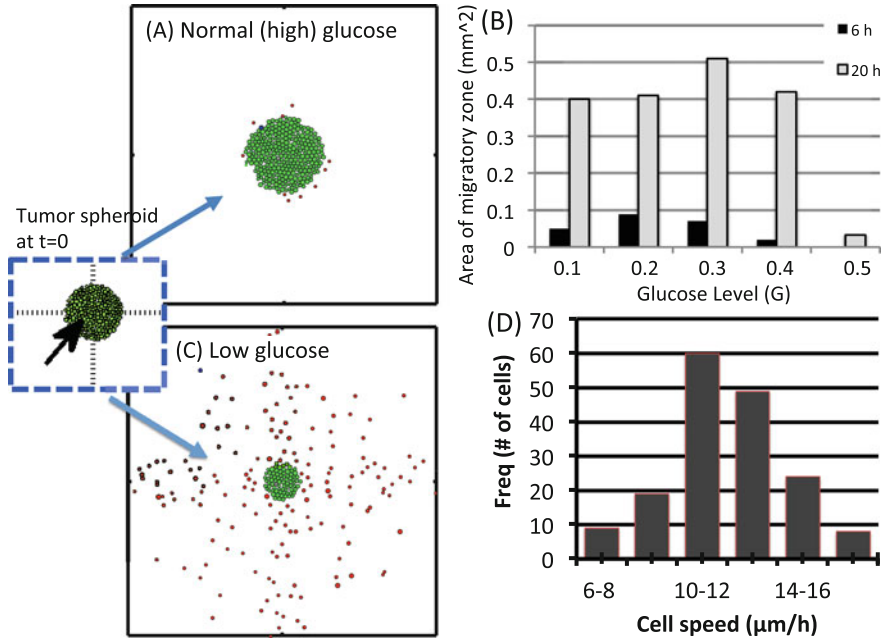
Fig. 6 Spatial dynamics of a hybrid model [44] (A,C) Spatial growth-invasion patterns of tumor spheroid shown in response to normal (A) and low (C) glucose levels at $t = 32h$. Initial condition of the tumor spheroid was given the left-middle panel. (B) The area of the migratory zone in response to various glucose levels ($G_0 = 0.1$-0.5) at $t = 6, 20$ h, respectively. (D) A distribution (frequency) of average cell speeds from the model.

A system of PDEs are coupled to this *lattice-free* cell-based model by taking into account diffusion, reaction, consumption, intravenous injection, and natural decay of oxygen and glucose, transport of a chemoattractant after injection, ECM degradation by proteolytic activities of MMPs [38, 43, 44].

We first investigated the invasion dynamics of a glioma spheroid in response to high and low glucose levels. Figures 6A, C shows spatial growth-invasion patterns of glioma cells at final time $t = 32$ h in response to high ($G_0 = 0.6$) and low ($G_0 = 0.2$) glucose levels, respectively, through the regulation of the corresponding miR-451-AMPK activities at each cell site. While the high glucose level induces a growth-dominated pattern (Figure 6A), glucose withdrawal leads to active invasion from the surface of the growing tumor spheroid (Figure 6C), which is in good agreement with experimental results [28]. However, one should note that some cells inside the tumor core did not migrate due to the surrounding physical constraints (neighboring cells) despite the down-regulation of miR-451 and increased AMPK activities and have to be free from the physical constraints for shedding [44]. This

reduction of cell motility in response to the down-regulated miR-451 level from glucose withdrawal was also observed in [28]. Various cell speeds of tumor cells were reported in the literature depending on many factors such as growth factors and cell culture conditions [44]. In glioma cell lines, the speed was measured to be in the range of 15–20 µm/h in 3D glioblastoma culture and 39–45 µm/h in 2D free culture [36], 15–48 µm/h in collagen I ECM [35], and 15–25 µm/h in glioblastoma with/without α-actinin isoforms [85]. Calculated speeds in the mathematical model are in good agreement with these experimental data (Figure 6D).

We first applied a localization strategy to eradicate invasive glioma cells. Figures 7A–D shows spatial profiles of the invasive glioma cells at $t =$ 0, 100, 200, 240 h, respectively, after first surgery at $t = 0$ followed by injection of a chemoattractant near the resected area (circle). Figures 7E–H shows spatial profiles of glucose (Figure 7E), chemoattractant (Figure 7F), ECM (Figure 7G), and MMP (Figure 7H) at the corresponding time frames. While migratory glioma cells migrate back to the brain tissue near the original resection site, some of those cells are attracted to BVs due to high glucose-induced *chemotaxis* and switch from the migratory phase ($\mathbb{T}_m$) to the proliferative phase ($\mathbb{T}_p$) due to overexpression of miR-451 and mTOR activation. Figure 7I shows time courses of the concentrations of core control module (miR-451, AMPK, and mTOR) at a cell site (cell id=33; arrowhead in Figure 7J) in response to fluctuating (but high) glucose levels due to its proximity to BVs. Overexpression of miR-451 and active proliferation of glioma cells near BVs were observed in experiments [28]. Figures 7J–K shows close-up patterns of growth-invasion of glioma cells in smaller subframes ($[0.05, 0.2] \times [0.55, 0.65]$ in (E-F); $[0.14, 0.16] \times [0.58, 0.61]$ in (K)). This trapped cell (blue cell in the blue box in Figure 7J) near a BV (Figure 7K) settles in a comfortable environment and grows while some other invasive cells (red cells in Figure 7J) migrate toward (black arrows) the resection site. While invasive tumor cells after surgery may not be detected by conventional devices such as MRI at a clinic due to its low image resolution, a localized mass of tumor cells may be detected, suggesting a possible second surgery and increasing the possibility of glioma eradication. However, one would have to handle those growing cells near BV sites. Therefore, in order to improve the localization strategies, a combination therapy is necessary, *i.e.,* by using S-phase-targeting chemo-drugs in addition to localization of the cells, one may be able to eradicate growing cancer cells near BVs [43]. The study also found that the random motility of glioma cells and the distance of dispersed cells from the resection sites also affect the anti-tumor efficacy of the localization strategies [43]. Figure 8 shows saltatory movement patterns of a migratory cell, cell speed (Figure 8A), and direction change (Figure 8B), in the presence of random motility. These fluctuating speeds [21, 35, 36, 85] and saltatory patterns in the movement direction are observed in the experimental scenarios [21].
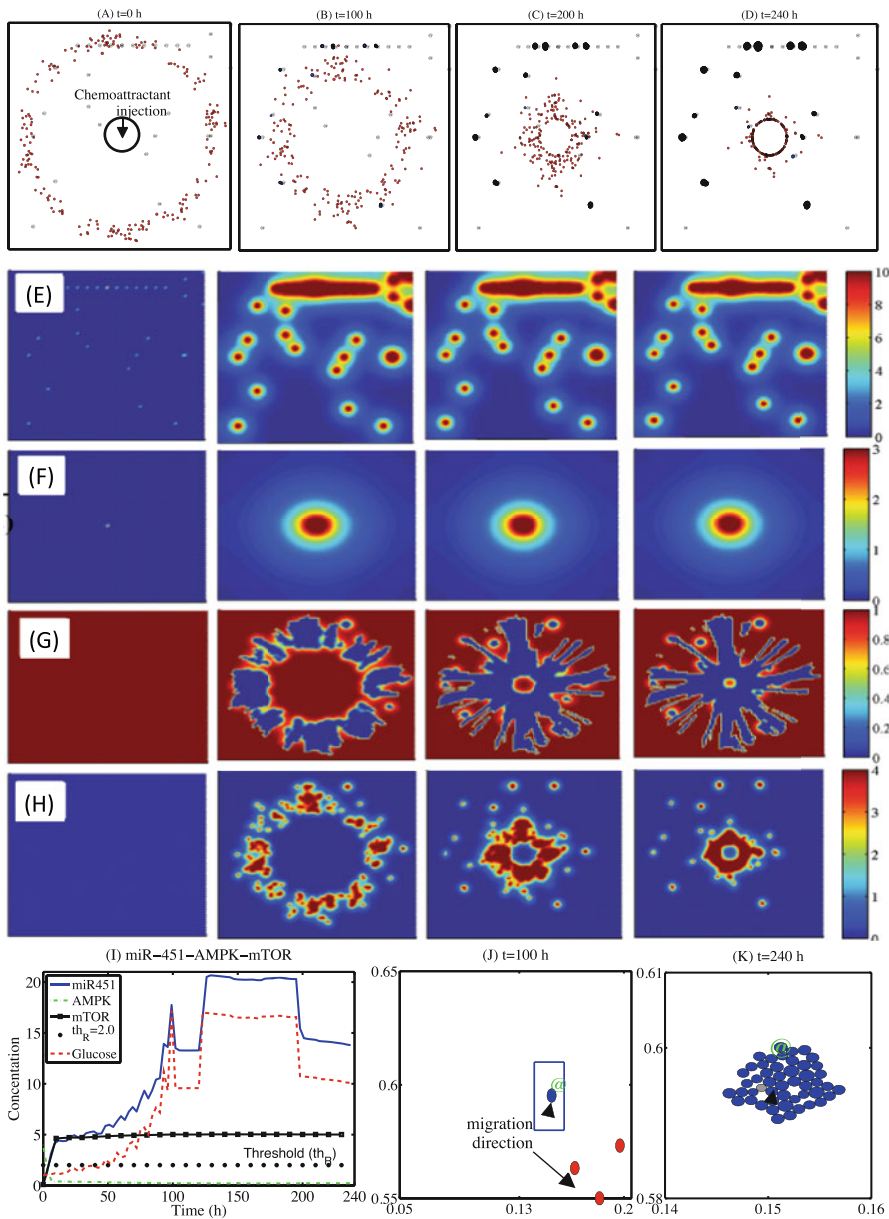
Fig. 7 A proposed anti-invasive therapeutic strategy: *localization* **of** *invisible* **invasive cells after a conventional surgery [43].** A combination of chemoattractants are injected on the periphery of the resection site (circle in (A)) after a conventional surgery to localize the invasive cells in the microenvironment. (A-D) Spatial profiles of tumor cells at $t = 0$ (A), 100 (B), 200 (C), 240 (D) h after a surgery at $t = 0$h. Some of the responsive migratory glioma cells form a cellular mass near the original resection site for another surgery after 10 days. However, some of the migratory cells attracted to BVs can still grow. Domain size $= [0, 1]^2$. (E-H) Spatial profiles

3 Role of M1/M2 Microglia in Regulation of Glioma Invasion

3.1 Introduction

Transforming growth factor beta (TGF-β) with its receptor is one of the signaling factors involved in maintenance of tissue homeostasis and also mediates tumor growth [3] via phosphorylation of transcription factors in the SMAD family [63]. TGF-β also stimulates glioma cell migration [100] in a co-culture with M1/M2 microglia, leading to the development of a stem-cell-like glioma sub-population [102]. Glioma infiltrating macrophages/microglia require colony stimulating factor-1 (CSF-1) for survival, and mediate the phenotypic M1$\rightarrow$ M2 switch [76]. Epidermal growth factor (EGF) is also known to induce tumor cell proliferation via RAS/MAP kinase signaling [39, 48, 52, 62, 104]. This is but one step in a signaling feedback loop in which CSF-1 secreted by glioma cells induces microglia/macrophages to express EGF and infiltrate the tumor, and the EGF and TGF-β in turn induce tumor cell invasion. Blocking the CSF receptor [15, 50] or MMP-2 [61] on microglia can suppress active dispersal of GBM cells. Many mechanical and biochemical processes underlie the complex mutual interaction between a tumor and other cells in microenvironment but we focus on the interaction of a glioma with M1/M2 microglia via CSF-1, EGF, TGF-β, and MMPs (Figure 9).

3.2 Mathematical Model

The mathematical model involves the densities of tumor cells ($n(\mathbf{x}, t)$) and microglia (M1 type ($m_1(\mathbf{x}, t)$ and M2 type $m_2(\mathbf{x}, t)$), and concentrations of the extracellular matrix ($\rho(\mathbf{x}, t)$), CSF-1 ($C(\mathbf{x}, t)$), EGF ($E(\mathbf{x}, t)$), TGF-β ($G(\mathbf{x}, t)$), and MMPs ($P(\mathbf{x}, t)$). In Figure 10A, we show the geometries of the experimental setting (Boyden transwell invasion assay [100]). Glioma cells suspended in the upper chamber interact with microglia or medium alone (control) in the lower chamber. A semi-permeable membrane coated with thick extracellular matrix (Matrigel) was placed in the filter between upper and lower chamber. In response to microglia-induced TGF-β, tumor cells invade the lower chamber through the holes of 12 μm diameter by proteolytic degradation of the ECM. The number of these invasive cells on the lower surface of the membrane was counted after 36 h with and without

---

Fig. 7 (continued) of glucose (E),chemoattractant (F), ECM (G), and MMP (H) that correspond to (A-D). (I) A time course of the core control system (miR-451, AMPK, mTOR) in response to fluctuating glucose levels (dotted red) at a cell site (arrow in (J)) near a BV. (J-K) Spatial profiles of a subset of migratory cells at $t = 100, 240$ h, which transited from the migratory phase ($\mathbb{T}_m$) to a growth phase ($\mathbb{T}_p$) due to high glucose levels from BVs. Red circles=migratory cells, blue circles=growing cells, @=BV.
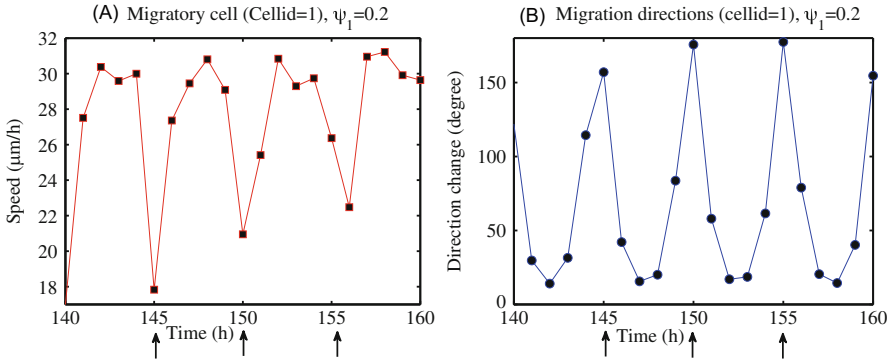
Fig. 8 saltatory migratory patterns in glioma cells [43]. (A,B) Time courses of cell speed (A) and direction changes (angle in (B)) of a migratory glioma cell over sub-time interval [140, 160] in the presence of random motility ($\psi_1 = 0.2$). Black arrows = the location and corresponding times at which the cell changed the migration direction.
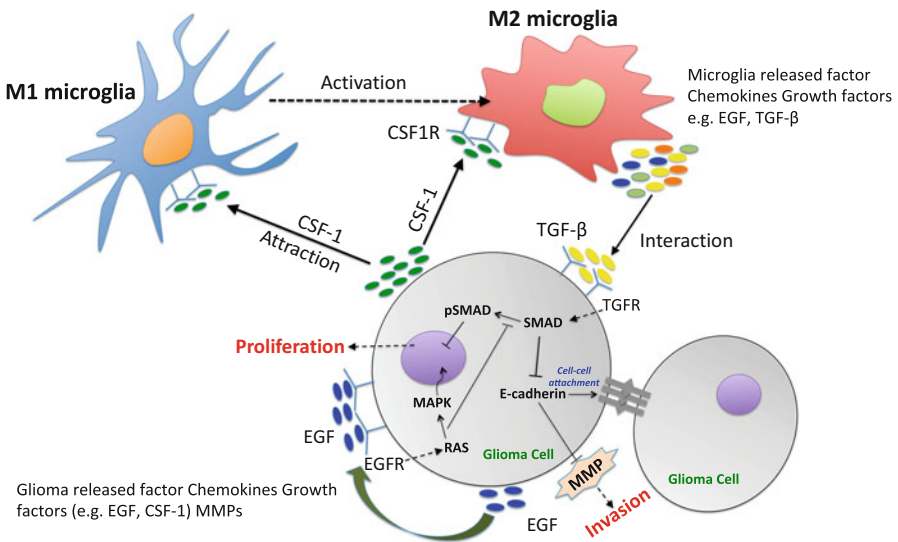
Fig. 9 Interaction of a glioma cell with M1/M2 microglia via CSF-1, EGF, and TGF-β signaling pathways in the control of tumor invasion in glioblastoma. In normal cells, these signaling levels are balanced to maintain homeostasis, but in glioma microenvironment increased secretion of CSF-1 by glioma cells induces the phenotypic changes in microglia (M1→M2 type) and promotes their secretion of EGF. This disrupts the control mechanism of proliferation and inhibition by partially interfering the TGF-β-Smad intracellular pathway, leading to active proliferation and aggressive invasion.
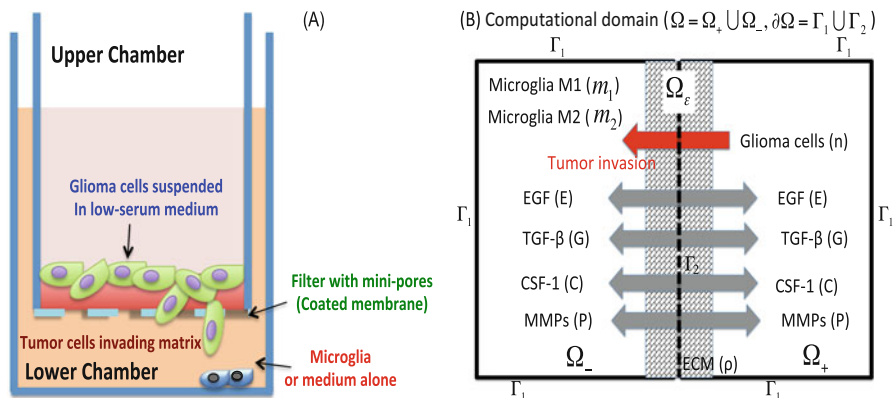
Fig. 10 (A) Illustration of Boyden transwell invasion assay [100]. (B) A schematic of the representation of the computational assay chamber.

microglia in the lower chamber. Figure 10B shows a schematic of the representation of the computational assay chamber ($\Omega = \Omega_+ \cup \Omega_-$) with two kinds of boundaries ($\Gamma = \Gamma_1 \cup \Gamma_2$; outer boundary ($\Gamma_1$) and interface boundary (Γ_2)) and ECM coating (Ω_ϵ) near the interface. EGF, TGF-β , CSF-1, MMP, and glioma cells can cross the membrane (Γ_2), but neither type of microglia (M1 & M2) can cross it. Initially the tumor cells and both types of microglia reside in the upper (Ω_+) and lower (Ω_-) chamber, respectively.

The governing equations are as follows [40]:

$$\frac{\partial n}{\partial t} = \nabla \cdot \left(D_n \nabla n \right) - \nabla \cdot \left(\chi_n \, n \, \frac{\nabla G}{\sigma_G + \lambda_G |\nabla G|} \right) - \nabla \cdot \left(\chi_n^1 \, n \, \frac{\nabla \rho}{\sigma_\rho + \lambda_\rho |\nabla \rho|} \right)$$
$$+ \left(a_1 + a_E \frac{E^l}{k_E^l + E^l} \right) n \left(1 - \frac{n}{\kappa} \right), \tag{16}$$

$$\frac{\partial m_1}{\partial t} = \nabla \cdot \left(D_1 \nabla m_1 \right) + a_2 m_1 - a_3 \, C \, m_1, \tag{17}$$

$$\frac{\partial m_2}{\partial t} = \nabla \cdot \left(D_2 \nabla m_2 \right) - \nabla \cdot \left(\chi_m \, m_2 \, \frac{\nabla C}{\sigma_C + \lambda_C |\nabla C|} \right) + a_3 \, C \, m_1 + a_4 \, m_2, \tag{18}$$

$$\frac{\partial \rho}{\partial t} = -d_\rho P \, n, \tag{19}$$

$$\frac{\partial C}{\partial t} = \nabla \cdot \left(D_C \nabla C \right) + a_5 \, n - d_C C, \tag{20}$$

$$\frac{\partial E}{\partial t} = \nabla \cdot \left(D_E \nabla E \right) + (a_6 \, m_1 + B_1 a_6 \, m_2) - d_E E, \tag{21}$$

$$\frac{\partial G}{\partial t} = \nabla \cdot \left(D_G \nabla G \right) + (a_7 m_1 + B_2 a_7 m_2) - d_G G, \tag{22}$$

Table 3 Parameters used in the model [40].

Par	Description	Dimensional Value	Reference
Random motility/diffusion coefficients (cm^2s^{-1})			
D_n	Random motility of glioma cells	1.0×10^{-9}	[7, 23, 73]
D_1	Random motility of M1 cells	1.7×10^{-10}	[7, 23, 73], Estimated
D_2	Random motility of GIM M2 cells	1.7×10^{-9}	[7, 23, 73], Estimated
D_C	Diffusion coefficient of CSF-1	2.0×10^{-6}	[9, 12, 69, 70, 92]
D_E	Diffusion coefficient of EGF	1.66×10^{-6}	[94]
D_G	Diffusion coefficient of TGF-β	1.0×10^{-6}	[8, 49, 101]
D_P	Diffusion coefficient of MMP	5.0×10^{-10}	[81, 86], Estimated
Decay/degradation rates			
d_C	Natural decay rate of CSF-1	$4.8\times10^{-5}\ \text{s}^{-1}$	[4, 30, 93]
d_E	Natural decay rate of EGF	$8.02\times10^{-6}\ \text{s}^{-1}$	[53]
d_G	Natural decay rate of TGF-β	$8.02\times10^{-6}\ \text{s}^{-1}$	[48], Estimated
d_ρ	ECM degradation by cells via MMP	$2.25\times10^{5}\text{cm}^3\text{g}^{-1}\text{s}^{-1}$	[39], Estimated
d_P	Natural decay rate of MMP	$5.0\times10^{-5}\ \text{s}^{-1}$	[41]
Production rates			
a_1	Proliferation rate of glioma cells	$3.1\times10^{-5}\ \text{s}^{-1}$	Estimated
a_E	EGF-mediated proliferation rate	$3.0\times10^{-6}\ \text{s}^{-1}$	Estimated
k_E	Tumor cell proliferation parameter	$3.319\times10^{-9}\ gcm^{-3}$	Estimated
κ	Tumor cell carrying capacity	$4.0\times10^{4}\ \text{cells/cm}^3$	Estimated
a_2	Proliferation rate of M1 type	$4.38\times10^{-6}\ \text{s}^{-1}$	[54], Estimated
a_3	Transform rate from M1 type to M2 type	$9.0\times10^{2}\ \text{cm}^3\text{g}^{-1}\text{s}^{-1}$	Estimated
a_4	Proliferation rate of GAM M2 type	$1.26\times10^{-6}\ \text{s}^{-1}$	[54], Estimated
a_5	Proliferation rate of CSF-1 by glioma cells	$1.4\times10^{-6}\ \text{s}^{-1}$	[68, 96]
a_6	Production rate of EGF from M1 type	$8.7\times10^{-9}\ \text{s}^{-1}$	[10, 86, 90], Estimated
B_1	Production rate of EGF from M2 type	$1\le B_1 \le10$	Estimated
a_7	Production rate of TGF-β from M1 type	$3.1\times10^{-8}\ s^{-1}$	[97, 98]
B_2	Production rate of TGF-β from M2 type	$2\le B_2 \le3\ (B_2 = 3)$	[100]
a_9	Production rate of MMPs by tumor cells	$5.61\times10^{-5}\ \text{cm}^3\text{g}^{-1}\text{s}^{-1}$	Estimated

<div align="right">(continued)</div>

Table 3 (continued)

Par	Description	Dimensional Value	Reference
Movement parameters (chemotaxis, haptotaxis)			
χ_n	Chemotactic sensitivity of glioma cells to EGF	$2.83 \times 10^{-9}\ cm^2 s^{-1}$	[73, 90]
σ_G	Chemotactic parameter of glioma cells	$5.0 \times 10^{-8}\ g/cm^4$	Estimated
λ_G	Chemotactic parameter of glioma cells	1.0	Estimated
χ_n^1	Haptotactic sensitivity	$3.5 \times 10^{-7}\ cm^2 s^{-1}$	[20, 66, 71], Estimated
σ_ρ	Haptotactic parameter of glioma cells	$1.0 \times 10^{-2} g/cm^4$	Estimated
λ_ρ	Haptotactic parameter of glioma cells	1.0	Estimated
χ_m	Chemotactic sensitivity of GAM to TGF-β	$1.1 \times 10^{-9}\ cm^2 s^{-1}$	[1], Estimated
σ_C	Chemotactic parameter of M2 cells	$5.0 \times 10^{-7}\ g/cm^4$	Estimated
λ_C	Chemotactic parameter of M2 cells	1.0	Estimated
Membrane parameters			
γ_i	Permeability of cells ($i = 1, 2, 3$)	5–200	[48], Estimated
γ_i	Permeability of chemicals (CSF-1, EGF, TGF-β, MMP)	50–900	[48], Estimated
μ	ECM width	0.6	Estimated

$$\frac{\partial P}{\partial t} = \nabla \cdot \left(D_P \nabla P\right) + a_9 n(1 + B_3 I_{\{G>th_G\}})\rho - d_P P, \tag{23}$$

where $I_{\{G>th_G\}} = 0$ if $G > th_G$, and $= 0$ otherwise, and parameter values are given in Table 3. We have Neumann boundary conditions (flux $J = 0$) on the exterior boundary Γ_1

$$\left(D_n \nabla n - \chi_n\, n\, \frac{\nabla G}{\sigma_G + \lambda_G |\nabla G|} - \chi_n^1\, n\, \frac{\nabla \rho}{\sigma_\rho + \lambda_\rho |\nabla \rho|}\right) \cdot \nu = 0, \tag{24}$$

$$\left(D_1 \nabla m_1\right) \cdot \nu = 0, \quad \left(D_2 \nabla m_2 - \chi_m\, m_2\, \frac{\nabla C}{\sigma_C + \lambda_C |\nabla C|}\right) \cdot \nu = 0, \tag{25}$$

$$\left(D_C \nabla C\right) \cdot \nu = 0, \quad \left(D_E \nabla E\right) \cdot \nu = 0, \quad \left(D_G \nabla G\right) \cdot \nu = 0, \quad \left(D_P \nabla P\right) \cdot \nu = 0,$$

where ν is the unit outer normal vector. The membrane is permeable to all variables $(n, m_1, m_2, C, E, G, P)$, but not freely so. We describe the flux (J) at Γ_2 for these variables $u = (n, m_1, m_2, C, E, G, P)$ as $J^+ = J^-$, $J^+ + \gamma_i(u^+ - u^-) = 0$ where

$$u(x) = \begin{cases} u^+(x) & \text{if } x > 0 \\ u^-(x) & \text{if } x < 0 \end{cases} \tag{26}$$

and the parameter γ_i ($i = 1, \cdots, 8$) is determined by the size and density of the membrane holes (see [22] for the derivation of these boundary conditions by homogenization). If the size of the holes in the membrane is increased (or decreased), the membrane becomes more (or less) permeable, and γ_i increases (or decreases).

3.3 Application of the Model

In Figure 11, we investigate the effect of M1/M2 microglia and a TGF-β neutralizing antibody on tumor invasion in Boyden invasion chamber. In the experiments, Wesolowska *et al.* [100] found that (i) the presence of microglial cells in the lower chamber (Neg/9+microglia) increased the number of migratory glioma cells (>2-fold) compared to the control (Neg/9). (ii) the neutralizing antibody (Ab) against TGF-β by a knockdown of TGF-β type II receptor (TβIIR) by plasmid-transcribed shRNA abrogated the migration-promoting effect of microglia by inhibiting transcriptional responses from TGF-β signaling. The simulation results are in good agreement with these experimental results. In the simulations, the
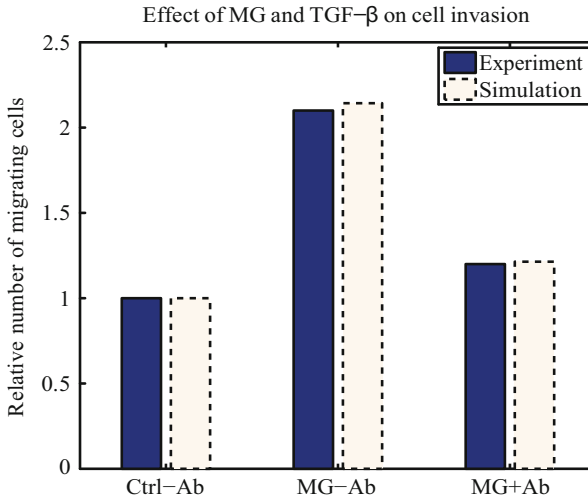
Fig. 11 Effect of MG and TGF-β on tumor cell invasion. Plot shows the relative number of migrating glioma cells in the absence (Ctrl) or presence (MG) of microglia after introducing anti-TGF-β mAb at final time from simulation (blue solid box) and experimental data from the invasion assay in [100] (yellow dashed box). In the absence of antibody, the number of invading tumor cells in the presence of microglia (MG-Ab) in the lower chamber more than doubled relative to controls (Ctrl-Ab). However, in the presence of TGF-β antibody (MG+Ab), fewer tumor cells invade the lower chamber, bringing the invasive tumor population back to control levels (Ctrl-Ab). Therefore, a neutralizing antibody against TGF-β can abrogate the migration-boosting effects of microglia as shown experimentally [100].
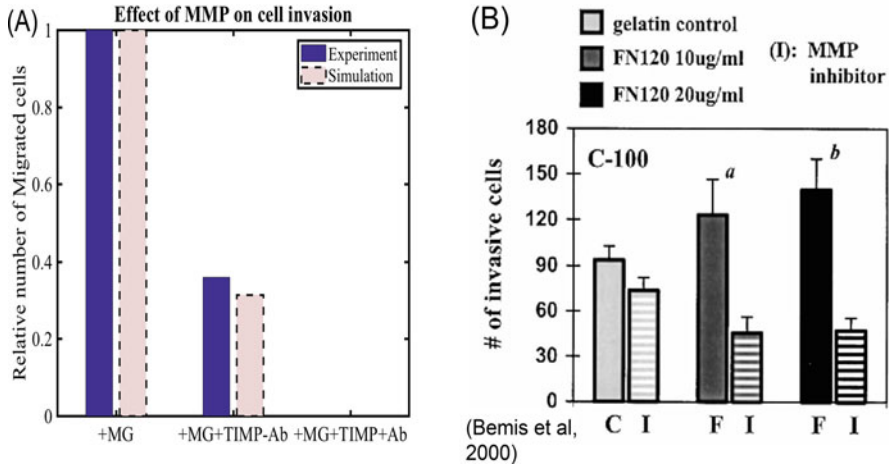
Fig. 12 Effect of MMP inhibitor (TIMP) and combined therapy (TIMP+Ab). (A) Relative population of migratory tumor cells when MMP secretion was suppressed by TIMP in the absence (+MG+TIMP-Ab) and presence (+MG+TIMP+Ab) of antibody against TGF-β antibody relative to the control (+MG; no MMP inhibitor). When proteolytic activity of tumor cells near the ECM boundary is inhibited (a_9 =0), the number of invasive tumor cells is decreased (69% reduction) in the absence of TGF-β antibody and further introduction of TGF-β antibody leads to almost complete blocking of invasion toward the lower chamber (> 99% reduction). (B) Experimental data illustrating the number of invasive cells for a cancer cell line (C-100), in the absence and presence of TIMP (MMP inhibitor) on various fibronectin levels (0, 10, 20 µg/ml) (figure from Bemis *et al.* [6] with permission).

number of migrating glioma cells doubled in the presence of microglia in the lower chamber (MG-Ab in Figure 11) relative to the control (Ctrl-Ab in Figure 11) but the tumor invasion was inhibited in the presence of TGF-β antibody (MG+Ab in Figure 11) relative to controls (MG-Ab in Figure 11). However, one should note that TGF-β blocking is not sufficient to completely suppress the aggressive invasion of glioma cells, since they invade the lower chamber even in the absence of microglia [59, 100].

In Figure 12A, we investigated the effect of MMP blocking on tumor invasion by reducing the MMP production rate (a_9). The model predicted a significant reduction in the population of invasive tumor cells in the lower chamber ($\sim$70%; +MG+TIMP-Ab) relative to controls (+MG). This is in good agreement with the classical experimental results by Bemis and Schedin [6] (Figure 12B) where an MMP inhibitor called TIMP inhibited the tumor cell invasion by more than 50% in a Boyden invasion assay. Since TIMP is only able to partially block the tumor cell invasion and the TGF-β antibody was suggested to block microglia-induced invasion [74, 100] (also see Figure 11), we tested the effect of combination of TIMP and TGF-β antibody on tumor invasion. The model predicts that the combination therapy with TIMP and TGF-β antibody almost completely blocked (> 99%) the glioma cell invasion (+MG+TIMP+Ab in Figure 12A). These *in silico* experiments

suggest that the combination therapy may be used as a new therapeutic strategy for preventing glioma cell infiltration in the tumor microenvironment where stromal cells such as microglia and macrophages interact with glioma cells.

4 The Role of Myosin II in Glioma Infiltration Through Narrow Intercellular Spaces

Migratory glioma cells in a complex microenvironment have to execute many cellular and biomechanical processes including branching at its distal leading end, the dilatation of the centrosome and its associated microtubules [95], nucleus deformation [5], and the contraction of acto-myosin II at the rear, resulting in the saltatory net movement (Figure 13). In this study, we consider myosin II-mediated cell migration through intercellular spaces between resident glial cells in the tumor microenvironment.

4.1 Mathematical Model of Cell-Mechanics

The immersed boundary (IB) method [72] allows one to model and simulate the interaction between the fluid and elastic structures. Using the IB method here, we consider two types of cells, a glioma cell and normal resident cells, which are
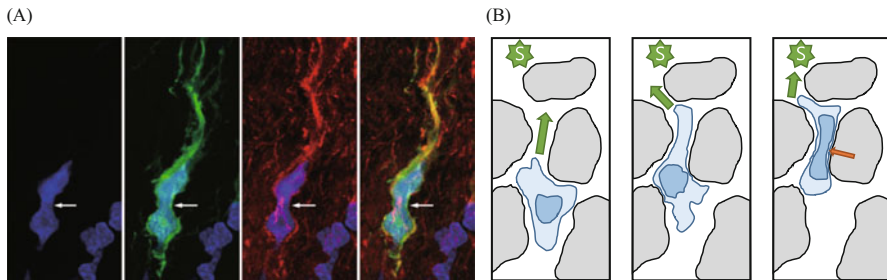
Fig. 13 Nucleus deformation during cell infiltration in a complex brain microenvironment (A) Experimental data showing simultaneous deformation of both nucleus and cell body during glioma cell infiltration through normal glial cells in a PDGF-driven glioma model [5]. Plot shows a human glioma cell with staining of nuclear DAPI in (1st panel, blue), GFP (2nd panel, green), myosin IIB (3rd panel, red), and the merged image (4th). In particular, it shows strong red immunostaining for myosin IIB, illustrating upregulation of myosin II in the course of the nucleus deformation. White arrows = focal deformation of the nucleus and cell body. Reprinted from Beadle C, Assanah M, Monzo P, Vallee R, Rosenfield S, et al. (2008) The role of myosin II in glioma invasion of the brain. Mol Biol Cell 19: 3357–3368 [5] under a CC BY license, with permission from American Society for Cell Biology, original copyright 2008. (B) A schematic of glioma cell (blue curves with nucleus) migration through the narrow intercellular space between normal cells in the brain in response to chemotactic signal (green star; 'S') [5].

assumed to be immersed in a viscous fluid. This migratory glioma cell is represented by nodes and double elastic closed loops: an inner and outer loop for the nucleus and the cell basal membrane, respectively. Each resident cell is represented by a single elastic curve that is tethered to the tissue. See Figure 14A.

Let $X(s, t) = X^{Gm}(s, t) \bigcup X^{Gn}(s, t) \bigcup X^N(s, t)$ be the configuration of tumor cells and glial cells at time t, where s represents a moving curvilinear coordinate. Here, X^{Gm}, X^{Gn}, X^N represent the membrane of a glioma cell, the nucleus of the glioma cell, and the membrane of resident cells, respectively. The coupled system of equations of motion is given as follows:

$$\rho \left(\frac{\partial \boldsymbol{u}}{\partial t} + \boldsymbol{u} \cdot \nabla \boldsymbol{u} \right) = -\nabla p + \mu \Delta \boldsymbol{u} + \boldsymbol{f}, \tag{27}$$

$$\nabla \cdot \boldsymbol{u} = 0, \tag{28}$$

$$\boldsymbol{f}(\boldsymbol{x}, t) = \int \boldsymbol{F}(s, t) \delta(\boldsymbol{x} - X(s, t)) ds, \tag{29}$$

$$\frac{\partial X(s, t)}{\partial t} = \int \boldsymbol{u}(\boldsymbol{x}, t) \, \delta(\boldsymbol{x} - X(s, t)) d\boldsymbol{x}, \tag{30}$$

$$\boldsymbol{F} = \boldsymbol{F}_{\mathrm{e}}^{Gm} + \boldsymbol{F}_{\mathrm{e}}^{Gn} + \boldsymbol{F}_{\mathrm{e}}^{N} + \boldsymbol{F}_{\mathrm{t}}^{Gm} + \boldsymbol{F}_{\mathrm{t}}^{N} + \boldsymbol{F}_{\mathrm{a}}^{Gm}, \tag{31}$$

$$\boldsymbol{F}_{\mathrm{e}}^{Gm} = \frac{\partial E^{Gm}}{\partial X^{Gm}}, \quad \boldsymbol{F}_{\mathrm{e}}^{Gn} = \frac{\partial E^{Gn}}{\partial X^{Gn}}, \quad \boldsymbol{F}_{\mathrm{e}}^{N} = \frac{\partial E^{N}}{\partial X^{N}}, \quad \boldsymbol{F}_{\mathrm{t}}^{N} = c_{\mathrm{t}}^{N}(\boldsymbol{Z}^{N} - X^{N}), \tag{32}$$

$$\boldsymbol{F}_{\mathrm{t}}^{Gm} = \begin{cases} c_{\mathrm{t}}^{Gm}(\boldsymbol{Z}_{r}^{Gm} - X_{r}^{Gm}), & \text{during elongation step} \\ c_{\mathrm{t}}^{Gm}(\boldsymbol{Z}_{f}^{Gm} - X_{f}^{Gm}), & \text{during retraction step} \end{cases} \tag{33}$$

$$\boldsymbol{F}_{\mathrm{a}}^{Gm} = \begin{cases} c_{\mathrm{a}}\boldsymbol{d}, & \text{during elongation step} \\ 0 & \text{during retraction step} \end{cases} \tag{34}$$

Fluid Equations (27)–(28) are the incompressible Navier-Stokes equations, where $\boldsymbol{u}(\boldsymbol{x}, t)$ is the fluid velocity, $p(\boldsymbol{x}, t)$ is the fluid pressure, and $\boldsymbol{f}(\boldsymbol{x}, t)$ is the applied fluid force density defined on a fixed Cartesian coordinate system, where $\boldsymbol{x} = (x_1, x_2)$. Here $\boldsymbol{F}(s, t)$ is the force density which acts on the fluid by the immersed boundary. There are six contributions to $\boldsymbol{F}$: the elastic force densities $\boldsymbol{F}_{\mathrm{e}}^{Gm}$, $\boldsymbol{F}_{\mathrm{e}}^{Gn}$, $\boldsymbol{F}_{\mathrm{e}}^{N}$ from the glioma cell membrane, the nucleus inside the glioma cell, and the normal cell membrane, respectively, the tethered force density $\boldsymbol{F}_{\mathrm{t}}^{Gm}$ acting on the part of the glioma cell membrane, the tethered force density $\boldsymbol{F}_{\mathrm{t}}^{N}$ from the normal cell membrane, and the active force density $\boldsymbol{F}_{\mathrm{a}}^{Gm}$ of the glioma cell membrane for migration. E^{Gm}, E^{Gn}, and E^{N} are the elastic stretching energy functionals with respect to the configurations X^{Gm}, X^{Gn}, and X^{N}, respectively. The constant parameters ρ and μ are the fluid density and the fluid viscosity, respectively.
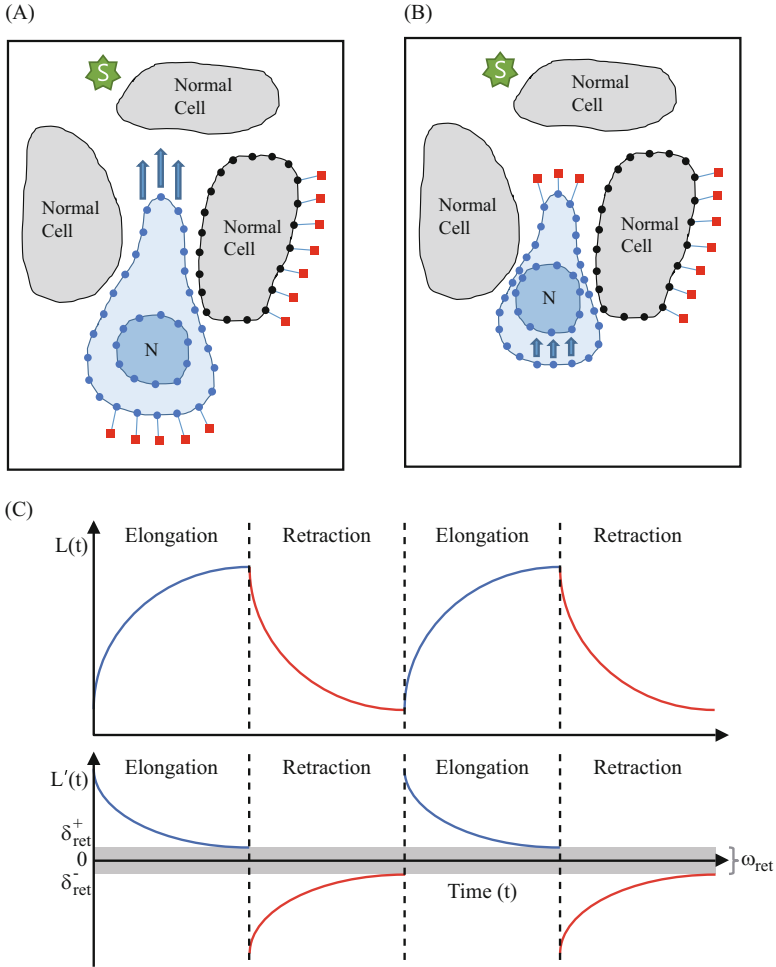
Fig. 14 Schematics of the mathematical model. (A,B) A schematic of glioma cell infiltration through narrow intercellular space between resident cells through elongation (A) and retraction (B) steps in response to chemotactic stimulus (green star (S)). The shape of a glioma cell is represented by two closed curves (the outer cell boundary and the nucleus boundary ('N')), consisting of elastic springs connected by nodes. Resident glial cells (black lines) are treated in a similar way but without the nucleus. Normal cells are tethered in the tissue (red box). In the elongation step, the rear of the glioma cell is attached to the substrate by strong adhesion and active force is generated at the leading edge. During the retraction step, the cell pulls both the nucleus and the cell body forward by generating attachment onto the substrate at the front and releasing the adhesion of the rear of the cell body. (C) Schematics of changes in the cell length ($L(t)$) and the rate of change in cell length ($L'(t)$) during the cycle of the elongation and retraction steps [56].

During the elongation step, the leading edge of the glioma cell protrudes while attaching the rear to the substrate, and infiltrate the intercellular gap by deforming both the nucleus and cell membrane via the myosin II dynamics. Then, in the followed retraction step, the fully elongated cell releases the attachment at the rear and forms new adhesion sites at the front, pulling the back of the cell and finishing a movement cycle. We consider a chemical reaction $[m_f] + [a] \underset{k_{-1}}{\overset{k_1}{\rightleftharpoons}} [m_b]$ for concentrations of actin ($[a]$), the free ($[m_f]$) and bound ($[m_b]$) myosin II with a total concentration $[m_T] = [m_f] + [m_b] \equiv$ constant. These governing equations of mechanics (27)–(34) are coupled with the following equations for dynamics of myosin II and chemoattractant

$$\frac{d[m_b]}{dt} = k_1[m_f][a] - k_{-1}[m_b] = k_1[m_T][a] - (k_1[a] + k_{-1})[m_b], \quad (35)$$

$$\frac{\partial C}{\partial t} = D_C \Delta C + \lambda_{in}^C I_{\Omega_\epsilon} - \mu_C C. \quad (36)$$

Here, actin concentration is proportional to the microenvironmental pressure (p) in the intercellular space and the stiffening rate of nucleus ($r_{[m_b]}$) is inversely proportional to the bound myosin II level: $r_{[m_b]} = k_s \frac{(1/[m_b])^n}{(K_{mb})^n + (1/[m_b])^n} + k_{min}^s$, ($k_s, K_{mb}, k_{min} \in \mathbb{R}^+, n \in \mathbb{Z}^+$). Parameter values are given in Table 4.

4.2 Effect of Myosin II on Deformation of Nucleus for Cell Infiltration

In Figure 15, we investigate the biomechanical dynamics of a glioma cell and its nucleus in wild type and myosin II knockdown (MYOII-KD). Figures 15A and B shows the movement profiles of a migratory tumor cell (blue double circles) through two resident glial cells (black dashed circles) in the wild type (Figure 15A) and MYOII-KD (Figure 15B) at four different times $t = 0, 20, 60, 80 \, min$. While the glioma cell squeezes through the resident glial cells by deforming nucleus and cell membrane in response to a chemotactic source (red star) in the wild type (Figure 15A), the cell is unable to migrate between two normal brain cells in the MYOII-KD case due to stiff nucleus. Figures 15C and D shows the length of cell body (solid blue curves) and nucleus (dotted red curves) in the wild type and MYOII-KD, respectively. It is evident that myosin II is crucial for efficient infiltration between normal cells as shown experimentally [5].

Table 4 Parameters used in this work [56].

Par	Description	Value	References
IB method			
$l \times l$	Fluid domain	0.1 mm×0.1 mm	
$N \times N$	Grid size	512×512	
μ	Fluid viscosity	2.7 g/(cm·s)	[44]
ρ	Fluid density	1.35 g/cm^3	[19, 78]
$\triangle t$	Time step	0.004 s	
r^G	Radius of a glioma cell	5 μm	[38, 43, 44]
r^N	Radius of a normal cell	8 μm	[38, 43, 44]
c_e^{Gm}	Elastic stiffness of a glioma cell	3.8×10^{-5} g·cm/s^2	Estimated
$c_e^{Gn,b}$	Basal elastic stiffness of the nucleus	3.8×10^{-5} g·cm/s^2	Estimated
c_e^N	Elastic stiffness of a normal cell	0.0023 g·cm/s^2	Estimated
c_t^{Gm}	Tethered stiffness of a glioma cell membrane	1500 g/cm·s^2	Estimated
c_t^N	Tethered stiffness of a normal cell	400 g/cm·s^2	Estimated
χ	The basal active force strength	0.7	Estimated
λ_s	Chemotactic parameter	20 (s^2/g)^2	Estimated
Myosin II model			
R_s	Sensing radius for (mechanical pressure)	4.69 μm	[41]
R_s^c	Sensing radius (chemotaxis)	0.4 μm	[41]
k_1	Association rate (bound myosin II)	0.002 μM^{-1}s^{-1}	[82], Estimated
k_{-1}	Dissociation rate (bound myosin II)	0.0001 s^{-1}	[82], Estimated
$[m_T]$	Total myosin II concentration	1 μM	[31]
k_p	Myosin-pressure sensitivity (wild type)	0.9 μM·s^2/(g·cm)	Estimated
	Myosin-pressure sensitivity (MYOII-KD)	0.045 μM·s^2/(g·cm)	Estimated
n	Hill coefficient (myosin reaction)	10	Estimated
K_{mb}	Reciprocal of the critical threshold	1.8 μM^{-1}	Estimated
k_s	Nucleus-myosin constant	5	Estimated
k_s^{min}	Nucleus-myosin constant	0.1	Estimated
Reaction-diffusion (chemoattractant)			
D_C	Diffusion coefficient	2.15×10^{-6} cm^2/s	[39, 48, 94], Estimated
λ_{in}^C	Chemoattractant source	8.2×10^{-1} g/(cm^3.s)	[48]
μ_C	Decay rate	1.0×10^{-6} s^{-1}	[39, 48, 53], Estimated
Therapeutic drugs			
I_B	Injection rate of blebbistatin	5×10^{-2} μM/s	Estimated
μ_B	Decay rate of blebbistatin	5.13×10^{-4} s^{-1}	[29, 43, 75]
α	Degradation rate of the bound myosin II by blebbistatin	1.0×10^{-4} s^{-1} (μM)$^{-1}$	Estimated
μ_D	Decay rate of drugs targeting actin-myosin association	5.13×10^{-4} s^{-1}	[29, 43, 75]
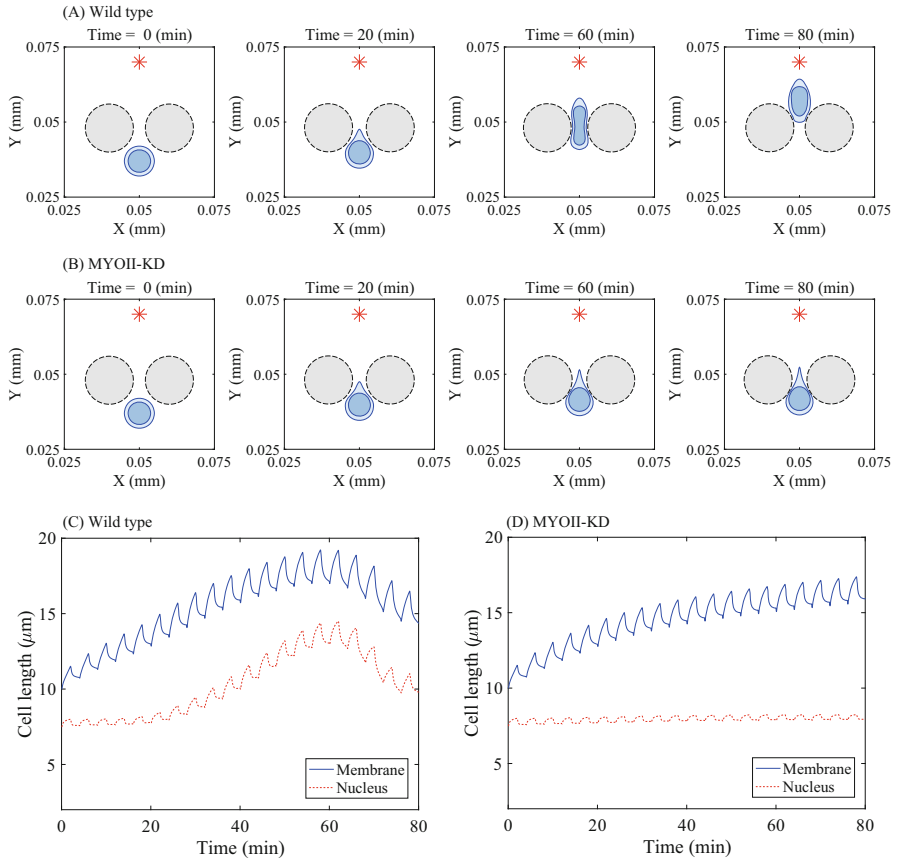
Fig. 15 Dynamics of cell infiltration in wild type and MYOII-KD tumor cells. (A,B) Time evolution of profiles of infiltrating glioma cells (blue circles) between two normal glial cells (black circle) in the wild type (A) and myosin II knock-down case (MYOII-KD; (B)) at $t = 0, 20, 60, 80\ min$. (C,D) Time courses of the length of cell body (blue solid) and nucleus (red dotted), respectively in the wild type (C) and MYOII-KD (D).

4.3 Application of the Model

Glioma cells have to adapt to the harsh biophysical conditions such as narrow inter-cellular paths between resident normal cells prescribed in a zig-zag fashion(black dashed circles in Figure 16A). In Figure 16A we show a time profile of a migratory glioma cell (solid double circles) at $t =$0 (red solid), 1 (blue solid), 6 (purple solid), 16 (green solid) h. The cell determines its migration direction effectively based on the chemical gradient from the chemotactic signal (red star) located in the top of the domain. Figure 16C shows the change in the migration direction of the cell (the angles from the vertical axis) in the presence of normal cells shown in Figure 16A.
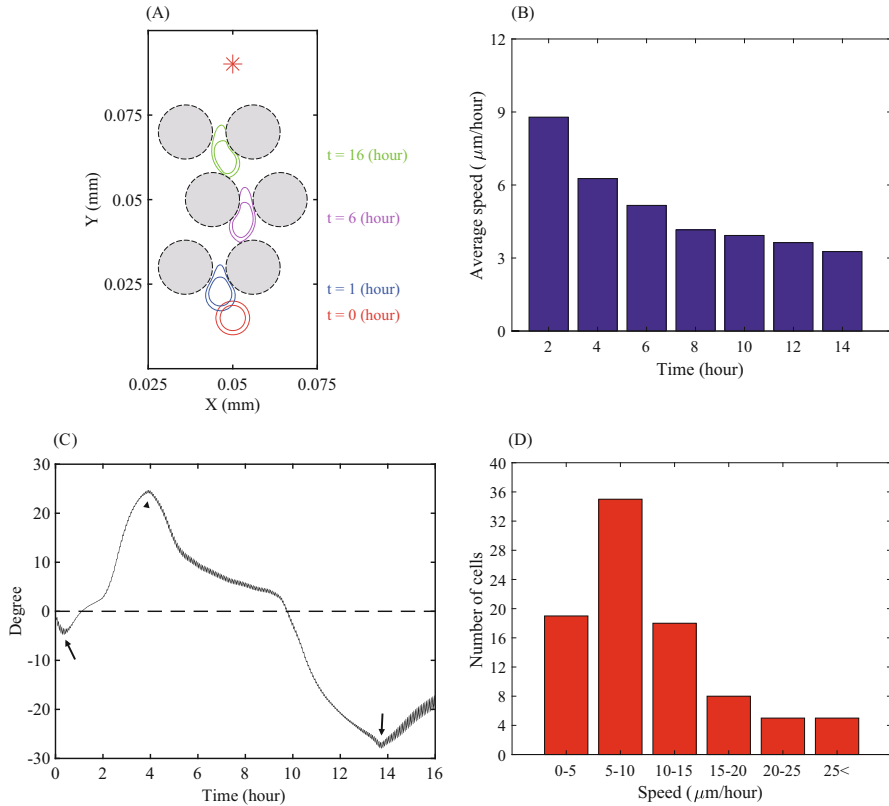
Fig. 16 Glioma cell infiltration through narrow intercellular spaces in a complex microenvironment. (A) A profile of the migratory tumor cell through normal cells (dashed filled circles) at $t = 0$ (red solid), 1 (blue solid), 6 (purple solid), 16 (green solid) h [56]. The normal glial cells were placed in a zig-zag fashion and a chemotactic source was located at the top of the domain (red star). (B) Time courses of the averaged speed of the glioma cell in (A). (C) Time courses of direction change (angle from the vertical axis) of the migratory glioma cell (A) [56]. Positive (negative) values indicate that the cell moves in the north-east (north-west) direction. The cell is attracted toward the chemotactic source (red star in (A)) through *chemotaxis* and changes its moving direction at three time points (black arrows and arrowhead). (D) A distribution of the average speeds of migratory rat glioma cells in experiments [5].

This illustrates a constant, periodic deformation of the cell body and nucleus in response to the gradient of the chemoattractant. In our simulations, the glioma cell needs to deform its nucleus as well as cell membrane for the infiltration process through the narrow gaps and cell speed was in the low range, 3–9 μm/h (Figure 16B) among observed experimental data. Indeed, these low values are in good agreement with experimental speed of rat glioma cells under the same biophysical conditions [5] (Figure 16D).
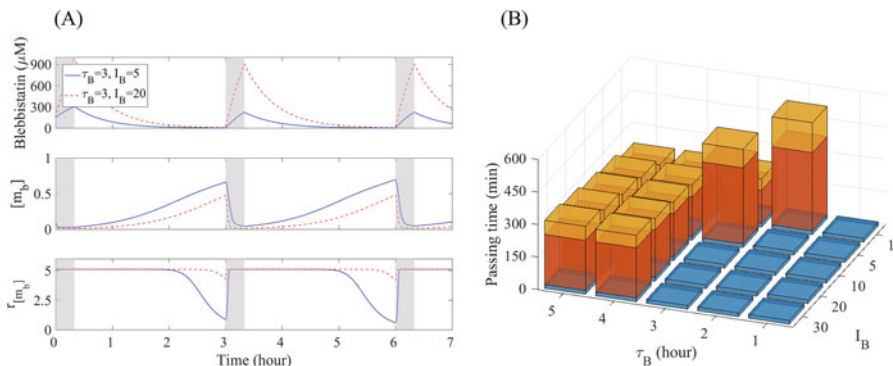
Fig. 17 Anti-invasion strategies by using blebbistatin. (A) Time courses of the concentrations of blebbistatin and bound myosin II ($[m_b]$), and stiffening rate of nucleus ($r_{[m_b]}$) in response to injected blebbistatin at high ($\tau_B = 3$, $I_B = 20$) and low ($\tau_B = 3$, $I_B = 5$) doses. In response to the relatively low blebbistatin concentration ($I_B = 5$; blue solid curve), the bound myosin II level is still high, resulting in lowered stiffening rate of the nucleus and tumor cell infiltration through the narrow intercellular space. On the other hand, a high level of blebbistatin ($I_B = 20$; red dotted curve) keeps nucleus stiff enough to prevent deformation of nucleus, blocking cell infiltration through the narrow gap. (B) Passing time of the cell through the intercellular gap between two normal cells for various injection strength ($I_B = 1, 5, 10, 20, 30$) and dose schedules ($\tau_B = 1, 2, 3, 4, 5$ h) [56]. *Blue= non-invasive tumor cell, red = the tumor cell in the process of migration through the gap, yellow = complete infiltration of the tumor cell.

In Figure 17, we investigate the effect of blebbistatin, a cell-permeable suppressor of class-II myosins, on glioma infiltration. While blocking of ligands such as EGF and PDGF has been inefficient due to redundancy of its downstream signal transduction pathways [18, 77], blebbistatin emerged as an anti-invasion target [34, 67] due to its high selectivity and affinity toward myosin II [51] at a point of convergence of many upstream signaling networks. A new equation for blebbistatin dynamics ($B(t)$) and bound myosin II [m_b] is

$$\frac{dB}{dt} = \sum_{j=1}^{N_B} I_B(H_{t_j} - H_{t_j + \frac{1}{3}}) - \mu_B B, \tag{37}$$

$$\frac{d[m_b]}{dt} = k_1[m_T][a] - (k_1[a] + k_{-1})[m_b] - \alpha B[m_b], \tag{38}$$

where I_B is the injection strength and H is a Heaviside function, in which the injection is given for the first $\frac{1}{3}$ h of every cycle $\tau_B = t_{j+1} - t_j$ ($\geq \frac{1}{3}$ h), $j = 0, \ldots, N_B - 1$, where N_B is the total number of blebbistatin injections and $t_0 = 0$. μ_B is the natural decay rate of blebbistatin, and α is the consumption rate of the bound myosin isoform by blebbistatin. The initial condition was set to be 150 μM [51]. Figure 17A shows the dynamics of the acto-myosin system in response to two different doses of blebbistatin ($I_B = 5, 20$) with a fixed dose schedule ($\tau_B = 3$ h).

In response to the relatively low dose ($I_B = 5$), the high level of bound myosin II is maintained and the stiffening rate of the nucleus is lowered (blue solid curves), resulting in glioma cell invasion. On the other hand, the increased dose ($I_B = 20$) suppresses activities of the bound myosin II but keeps the strong stiffening rate (red dotted curves), blocking glioma cell infiltration. Figure 17B shows passing time of a glioma cell through a narrow gap between two glial cells for various injection strength ($I_B = 1, 5, 10, 20, 30$) and schedules ($\tau_B = 1, 2, 3, 4, 5$) of blebbistatin. The model predicts that the larger (or smaller) injection interval and low (or high) dose would lead to cell invasion (or block invasiveness of the tumor cells). Despite relatively small side effects and toxicity of blebbistatin, administration of blebbistatin need to be taken with precautions [91]. Therefore, an optimal dose schedule is necessary to achieve maximal blocking of glioma infiltration but with minimal dose amount and feasible administration schedule at a clinic. In our simulations, the optimal treatment would be obtained when $\tau_B = 2$, $I_B = 5$.

5   Discussion

Tumor cell migration and proliferation depend on the type and origin of tumor cells and on the tumor microenvironment. In this review, we focused on the dynamics of highly invasive glioma cells. One of the major challenges in treatment of GBM is that by the time the disease is diagnosed these cancerous cells have already invaded the surrounding brain tissue, resulting in critical recurrence and the poor survival rate. Infiltrating glioma cells like the guerilla warriors with specific characteristics [14] were shown to be cultured from biopsies up to $4cm$ away from the main tumor [87]. Therefore, it is critical to understand the fundamental mechanism of invasion. As a first step, we first developed an intracellular model of the miR-451-AMPK core control system which controls the migration and proliferation of glioma cells. Based on biological observations, we developed a PDE model [45] and analyzed the invasion-growth patterns of glioma cells and verified a major prediction of the model experimentally [28]. The model also suggested that anti-invasion drugs which either upregulate miR-451 expression or inhibit other components of the CAB39/AMPK pathway, will slow down cell invasion. The miR-451 and the downstream signaling molecules (AMPK [103], mTOR) were experimentally identified as an anti-tumor target in colorectal carcinoma [13, 58]. The hybrid model was able to predict detailed specific migration patterns at the cellular level and microscale quantification such as cell speeds and saltatory patterns that are in good agreement with the experiments [21, 35, 36, 85]. The model suggested anti-invasion therapeutic strategies such as *localization* [38, 44] and combination therapy (localization+chemodrugs) in the presence of dense BV networks [43]. Multiple microsurgical resections of GBM have been shown to be useful and effective [33]. In order to optimize the schedule of glucose dose and drugs in the strategies, optimal control theories have been applied to the problem [79, 84].

In Section 3, we investigated the role of M1/M2 microglia in regulation of glioma cell invasion through the paracrine signaling including CSF-1, EGF, TGF-β, and MMP [40]. Although the details of the $M1 \rightarrow M2$ transition in gliomas are not fully understood, our model predicts the role of these stromal cells in promoting glioma invasion *in vitro* and suggested several hypotheses on anti-invasion strategies. Cell–cell signaling is an integral but complex process in tumor growth and invasion, since many mutations and chromosomal changes affect these signaling pathways involving growth factors or cytokines. The presence of astrocytes was shown both experimentally [88] and theoretically [55] to work as a secondary wall against glioma infiltration, and further studies need to investigate the role of the continuous spectrum of the $M1 \rightarrow M2$ transition and interactions among those stromal cells in the regulation of glioma invasion.

In Section 4, we investigated glioma cell infiltration through a narrow intercellular gap between resident brain cells [56], which is a complex process that involves deformation of nucleus and membrane of the cell via the tight regulation of acto-myosin dynamics [5]. In the same vein of *localization* strategies in Section 2, we developed the detailed multi-scale biomechanical mathematical model to study the role of myosin II in regulation of cell infiltration in response to a chemotactic source in the presence of resident cells. A better understanding of fundamental cell motility in tumor microenvironment may lead to the development of new anti-invasion drugs that target these myosin II bundles.

Currently, there are limited resources of experimentation and understanding of the mutual interactions between the glioma cells and the stromal cells in the microenvironment. Thus, mathematical studies on the effects of these complex interactions on glioma invasion, and on the sensitivity of the model predictions to kinetic key parameters, may provide insights to guide real experiments aimed at the development of new anti-tumor therapeutic strategies.

References

1. R. Abe, S.C. Donnelly, T. Peng, R. Bucala, and C.N. Metz. Peripheral blood fibrocytes: differentiation pathway and migration to wound sites. *J. Immunol.*, 166(12):7556–62, 2001.

2. B.D. Aguda, Y. Kim, M.G. Hunter, A. Friedman, and C.B. Marsh. MicroRNA regulation of a cancer network: Consequences of the feedback loops involving miR-17-92, E2F, and Myc. *PNAS*, 105(50):19678–19683, 2008.

3. Judit Anido, Andrea Sáez-Borderías, Alba Gonzàlez-Juncà, Laura Rodón, Gerard Folch, Maria A Carmona, Rosa M Prieto-Sánchez, Ignasi Barba, Elena Martínez-Sáez, Ludmila Prudkin, et al. Tgf-β receptor inhibitors target the cd44 high/id1 high glioma-initiating cell population in human glioblastoma. *Cancer cell*, 18(6):655–668, 2010.

4. A. Bartocci, D.S. Mastrogiannis, G. Migliorati, R.J. Stockert, A.W. Wolkoff, and E.R. Stanley. Macrophages specifically regulate the concentration of their own growth factor in the circulation. *Natl Acad Sci U S A*, 84(17):6179–83, 1987.
5. C. Beadle, M.C. Assanah, P. Monzo, R. Vallee, S.S. Rosenfield, and P. Canoll. The role of myosin II in glioma invasion of the brain. *Mol. Biol. Cell*, 19:3357–3368, 2008.
6. L.T. Bemis and P. Schedin. Reproductive state of rat mammary gland stroma modulates human breast cancer cell migration and invasion. *Cancer Res*, 60(13):3414–8, 2000.
7. D. Bray. *Cell movements*. New York: Gerland, 1992.
8. D.R. Brown. Dependence of neurones on astrocytes in a coculture system renders neurones sensitive to transforming growth factor beta1-induced glutamate toxicity. *J Neurochem*, 72(3):943–53, 1999.
9. J.J. Casciari, S.V. Sotirchos, and R.M. Sutherland. Glucose diffusivity in multicellular tumor spheroids. *Cancer Research*, 48(14):3905–3909, 1988.
10. M. A. J. Chaplain. Avascular growth, angiogenesis and vascular growth in solid tumours: The mathematical modeling of the stages of tumour development. *Mathl. Comput. Modeling*, 23(6):47–87, 1996.
11. N.A. Charles, E.C. Holland, R. Gilbertson, R. Glass, and H. Kettenmann. The brain tumor microenvironment. *Glia*, 59:1169–1180, 2011.
12. D. Chen, J.M. Roda, C.B. Marsh, T.D. Eubank, and A. Friedman. Hypoxia inducible factors-mediated inhibition of cancer by GM-CSF: a mathematical model. *Bull Math Biol*, 74(11):2752–2777, 2012.
13. M.B Chen, M.X. Wei, J.Y. Han, X.Y. Wu, C. Li, J. Wang, W. Shen, and P.H. Lu. MicroRNA-451 regulates AMPK/mTORC1 signaling and fascin1 expression in HT-29 colorectal cancer. *Cellular signalling*, 26(1):102–109, 2014.
14. A. Claes, A.J. Idema, and P. Wesseling. Diffuse glioma growth: a guerilla war. *Acta Neuropathologica*, 114(5):443–458, 2007.
15. Salvatore J Coniglio, Eliseo Eugenin, Kostantin Dobrenis, E Richard Stanley, Brian L West, Marc H Symons, and Jeffrey E Segall. Microglial stimulation of glioblastoma invasion involves epidermal growth factor receptor (EGFR) and colony stimulating factor 1 receptor (CSF-1R) signaling. *Molecular medicine*, 18(3):519, 2012.
16. B.E. Crute, K. Seefeld, J. Gamble, B.E. Kemp, and L.A. Witters. Functional domains of the alpha1 catalytic subunit of the AMP-activated protein kinase. *J Biol Chem*, 273(52):35347–54, 1998.
17. J. C. Dallon and H. G. Othmer. How cellular movement determines the collective force generated by the dictyostelium discoideum slug. *J. Theor. Biol.*, 231:203–222, 2004.
18. J.F. de Groot and M.R. Gilbert. New molecular targets in malignant gliomas. *Curr Opin Neurol*, 20:712–718, 2007.
19. Micah Dembo and Francis Harlow. Cell motion, contractile networks, and the physics of interpenetrating reactive flow. *Biophys. J*, 50:109–121, 1986.
20. R.B. Dickinson and R.T. Tranquillo. A stochastic model for adhesion-mediated cell random motility and haptotaxis. *J Math Biol*, 31(6):563–600, 1993.
21. Azadeh Farin, Satoshi O. Suzuki, Michael Weiker, James E. Goldman, Jeffrey N. Bruce, and Peter Canoll. Transplanted glioma cells migrate and proliferate on host brain vasculature: a dynamic analysis. *Glia*, 53(8):799–808, June 2006.
22. A. Friedman, C. Huang, and J. Yong. Effective permeability of the boundary of a domain. *Commun. In Partial differential equations*, 20(1&2):59–102, 1995.
23. E.A. Gaffney, K. Pugh, P.K. Maini, and F. Arnold. Investigating a simple model of cutaneous wound healing angiogenesis. *J Math Biol*, 45(4):337–74, 2002.
24. M.P. Gantier, C.E. McCoy, I. Rusinova, D. Saulep, D. Wang, D. Xu, A.T. Irving, M.A. Behlke, P.J. Hertzog, F. Mackay, and B.R. Williams. Analysis of microRNA turnover in mammalian cells following Dicer1 ablation. *Nucleic Acids Res*, 39(13):5692–703, 2011.
25. R.A. Gatenby and R.J. Gillies. Why do cancers have high aerobic glycolysis? *Nat Rev Cancer*, 4(11):891–9, 2004.

26. J. Godlewski, A. Bronisz, M.O. Nowicki, E.A. Chiocca, and S. Lawler. microRNA-451: A conditional switch controlling glioma cell proliferation and migration. *Cell Cycle*, 9(14):2742–8, 2010.

27. J. Godlewski, H.B. Newton, E.A. Chiocca, and S.E. Lawler. MicroRNAs and glioblastoma; the stem cell connection. *Cell Death Differ*, 17(2):221–8, 2010.

28. J. Godlewski, M.O. Nowicki, A. Bronisz, G. Nuovo J. Palatini, M. D. Lay, J.V. Brocklyn, M.C. Ostrowski, E.A. Chiocca, and S.E. Lawler. MircroRNA-451 regulates LKB1/AMPK signaling and allows adaptation to metabolic stress in glioma cells. *Molecular Cell*, 37:620–632, 2010.

29. K. Gordon. Mathematical modelling of cell-cycle-dependent chemotherapy drugs-implications for cancer treatment. *Ph.D. Thesis, University of Dundee, Dundee.*, pages –, 2006.

30. D.J. Gow, K.A. Sauter, C. Pridans, L. Moffat, A. Sehgal, B.M. Stutchfield, S. Raza, P.M. Beard, Y.T. Tsai, G. Bainbridge, P.L. Boner, G. Fici, D. Garcia-Tapia, R.A. Martin, T. Oliphant, J.A. Shelly, R. Tiwari, T.L. Wilson, L.B. Smith, N.A. Mabbott, and D.A. Hume. Characterisation of a novel fc conjugate of macrophage colony-stimulating factor. *Molecular Therapy*, 22(9):1580–1592, 2014.

31. M.E. Gracheva and H.G. Othmer. A continuum model of motility in ameboid cells. *Bull. Math. Biol.*, 66:167–194, 2004.

32. M.G. Vander Heiden, L.C. Cantley, and C.B. Thompson. Understanding the Warburg effect: the metabolic requirements of cell proliferation. *Science*, 324(5930):1029–33, 2009.

33. B. Hong, B. Wiese, M. Bremer, H.E. Heissler, F. Heidenreich, J.K. Krauss, and M. Nakamura. Multiple microsurgical resections for repeated recurrence of glioblastoma multiforme. *Am J Clin Oncol*, 36(3):261–268, 2013.

34. S. Ivkovic, C. Beadle, S. Noticewal, S.C. Massey, K.R. Swanson, L.N. Toro, A.R. Bresnick, P. Canoll, and S.S. Rosenfelda. Direct inhibition of myosin II effectively blocks glioma invasion in the presence of multiple motogens. *Mol Biol Cell*, 23(4):533–542, 2012.

35. L.J. Kaufman, C.P. Brangwynne, K.E. Kasza, E. Filippidi, V.D. Gordon, T.S. Deisboeck, and D.A. Weitz. Glioma expansion in collagen i matrices: Analyzing collagen concentration-dependent growth and motility patterns. *Biophys. J. BioFAST*, 89:635–650, 2005.

36. H.D. Kim, T.W. Guo, A.P. Wu, A. Wells, F.B. Gertler, and D.A. Lauffenburger. Epidermal growth factor-induced enhancement of glioblastoma cell migration in 3D arises from an intrinsic increase in speed but an extrinsic matrix and proteolysis-dependent increase in persistence. *Mol Biol Cell*, 19:4249–4259, 2008.

37. J.W. Kim and C.V. Dang. Cancer's molecular sweet tooth and the Warburg effect. *Cancer Res*, 66(18):8927–30, 2006.

38. Y. Kim. Regulation of cell proliferation and migration in glioblastoma: New therapeutic approach. *Frontiers in Molecular and Cellular Oncology*, 3:53, 2013.

39. Y. Kim and A. Friedman. Interaction of tumor with its microenvironment : A mathematical model. *Bull. Math. Biol.*, 72(5):1029–1068, 2010.

40. Y. Kim, H. Jeon, and H.G. Othmer. The role of the tumor microenvironment in glioblastoma: A mathematical model. *IEEE Trans Biomed Eng*, 64(3):519–527, 2017.

41. Y. Kim, S. Lawler, M.O. Nowicki, E.A Chiocca, and A. Friedman. A mathematical model of brain tumor : pattern formation of glioma cells outside the tumor spheroid core. *J. Theo. Biol.*, 260:359–371, 2009.

42. Y. Kim and H.G. Othmer. A hybrid model of tumor-stromal interactions in breast cancer. *Bull Math Biol*, 75:1304–1350, 2013.

43. Y. Kim, G. Powathil, H. Kang, D. Trucu, H. Kim, S. Lawler, and M. Chaplain. Strategies of eradicating glioma cells: A multi-scale mathematical model with miR-451-AMPK-mTOR control. *PLoS One*, 10(1):e0114370, 2015.

44. Y. Kim and S. Roh. A hybrid model for cell proliferation and migration in glioblastoma. *Discrete and Continuous Dynamical Systems-B*, 18(4):969–1015, 2013.

45. Y. Kim, S. Roh, S. Lawler, and A. Friedman. miR451 and AMPK/MARK mutual antagonism in glioma cells migration and proliferation. *PLoS One*, 6(12):e28293, 2011.

46. Y. Kim, M. Stolarska, and H.G. Othmer. A hybrid model for tumor spheroid growth in vitro I: Theoretical development and early results. *Math. Models Methods in Appl Scis*, 17:1773–1798, 2007.
47. Y. Kim, M. Stolarska, and H.G. Othmer. The role of the microenvironment in tumor growth and invasion. *Prog Biophys Mol Biol*, 106:353–379, 2011.
48. Y. Kim, J. Wallace, F. Li, M. Ostrowski, and A. Friedman. Transformed epithelial cells and fibroblasts/myofibroblasts interaction in breast tumor: a mathematical model and experiments. *J. Math. Biol.*, 61(3):401–421, 2010.
49. S. Koka, J.B. Vance, and G.I. Maze. Bone growth factors: potential for use as an osseointegration enhancement technique (oet). *J West Soc Periodontol Periodontal Abstr*, 43(3):97–104, 1995.
50. Yoshihiro Komohara, Yukio Fujiwara, Koji Ohnishi, and Motohiro Takeya. Tumor-associated macrophages: Potential therapeutic targets for anti-cancer therapy. *Advanced drug delivery reviews*, 2015.
51. M. Kovacs, J. Toth, C. Hetenyi, A. Malnasi-Csizmadia, and J.R. Sellers. Mechanism of blebbistatin inhibition of myosin II. *JOURNAL OF BIOLOGICAL CHEMISTRY*, 279(34):35557–35563, 2004.
52. M. Kretzschmar. Transforming growth factor-beta and breast cancer: Transforming growth factor-beta/smad signaling defects and cancer. *Breast Cancer Res*, 2(2):107–115, 2000.
53. J.E. Kudlow, C.Y. Cheung, and J.D. Bjorge. Epidermal growth factor stimulates the synthesis of its own receptor in a human breast cancer cell line. *J Biol Chem*, 261(9):4134–8, 1986.
54. L.A. Kunz-Schughart, S. Wenninger, T. Neumeier, P. Seidl, and R. Knuechel. Three-dimensional tissue structure affects sensitivity of fibroblasts to tgf-beta 1. *Am J Physiol Cell Physiol*, 284(1):C209–19, 2003.
55. H.G. Lee and Y. Kim. The role of the microenvironment in regulation of cspg-driven invasive and non-invasive tumor growth in glioblastoma. *Japan J. Indust. Appl. Math.*, 32(3):771–805, 2016.
56. W. Lee, S. Lim, and Y. Kim. The role of myosin II in glioma invasion: A mathematical model. *PLoS One*, 12(2):e0171312, 2017.
57. C.K. Li. The glucose distribution in 9l rat brain multicell tumor spheroids and its effect on cell necrosis. *Cancer*, 50(10):2066–73, 1982.
58. H.Y. Li, Y. Zhang, J.H Cai, and H.L. Bian. MicroRNA-451 inhibits growth of human colorectal carcinoma cells via downregulation of PI3K/AKT pathway. *Asian Pacific Journal of Cancer Prevention*, 14(6):3631–3634, 2013.
59. W. Li and M.B. Graeber. The molecular profile of microglia under the influence of glioma. *Neuro Oncol*, 14:958–978, 2012.
60. S.C. Lin and D.G. Hardie. AMPK: Sensing Glucose as well as Cellular Energy Status. *Cell Metab*, 27(2):299–313, 2018.
61. D.S. Markovic, R. Glass, M. Synowitz, N. Van Rooijen, and H. Kettenmann. Microglia stimulate the invasiveness of glioma cells by increasing the activity of metalloprotease-2. *J Neuropathol Exp Neurol*, 64:754–762, 2005.
62. J. Massague. Tgf-beta signal transduction. *Annual Review of Biochemistry*, 67(1):753, 1998.
63. J. Massagué. TGF [beta] in cancer. *Cell*, 134(2):215–230, 2008.
64. J. Mercapide, .R. Cicco, J.S. Castresana, and A.J. Klein-Szanto. Stromelysin-1/matrix metalloproteinase-3 (mmp-3) expression accounts for invasive properties of human astrocytoma cell lines. *Int J Cancer*, 106(5):676–82, 2003.
65. H.G. Moller, A.P. Rasmussen, H.H. Andersen, K.B. Johnsen, M. Henriksen, and M. Duroux. A systematic review of microrna in glioblastoma multiforme: micro-modulators in the mesenchymal mode of migration and invasion. *Mol Neurobiol*, 47(1):131–44, 2013.
66. P. Namy, J. Ohayon, and P. Tracqui. Critical conditions for pattern formation and in vitro tubulogenesis driven by cellular traction fields. *J Theor Biol*, 227(1):103–20, 2004.
67. A.K. Newell-Litwa, R. Horwitz, and M.L. Lamers. Non-muscle myosin II in disease: mechanisms and therapeutic opportunities. *Dis Model Mech*, 8(12):1495–1515, 2015.

68. H. Oren, N. Duman, H. Abacioglu, H. Ozkan, and G. Irken. Association between serum macrophage colony-stimulating factor levels and monocyte and thrombocyte counts in healthy, hypoxic, and septic term neonates. *Pediatrics*, 108(2):329–332, 2001.

69. M. R. Owen and J. A. Sherratt. Pattern formation and spatiotemporal irregularity in a model for macrophage-tumour interaction. *J. Theor. Biol.*, 189:63–80, 1997.

70. M.R. Owen, H.M. Byrne, and C.E. Lewis. Mathematical modelling of the use of macrophages as vehicles for drug delivery to hypoxic tumour sites. *Journal of Theoretical Biology*, 226(4):377–391, 2004.

71. A.J. Perumpanani and H.M. Byrne. Extracellular matrix concentration exerts selection pressure on invasive cells. *Eur J Cancer*, 35(8):1274–80, 1999.

72. C. Peskin. The immersed boundary method. *Acta Numerica*, 11:479–517, 2002.

73. G. J. Pettet, H. M. Byrne, D. L. S. McElwain, and J. Norbury. A model of wound healing angiogenesis in soft-tissue. *Math. Bios*, 136:35–64, 1996.

74. J. Pinkas and B.A. Teicher. Tgf-beta in cancer and as a therapeutic target. *Biochem Pharmacol*, 72(5):523–9, 2006.

75. G.G. Powathil, K.E. Gordon, L.A. Hill, and M.A. Chaplain. Modelling the effects of cell-cycle heterogeneity on the response of a solid tumour to chemotherapy: Biological insights from a hybrid multiscale cellular automaton model. *J Theor Biol*, 308:1–19, 2012.

76. S.M. Pyonteck, L. Akkari, A.J. Schuhmacher, R.L. Bowman, L. Sevenich, D.F. Quail, O.C. Olson, M.L. Quick, J.T. Huse, V. Teijeiro, M. Setty, C.S. Leslie, Y. Oei, A. Pedraza, J. Zhang, C.W. Brennan, J.C. Sutton, E.C. Holland, D. Daniel, and J.A. Joyce. CSF-1R inhibition alters macrophage polarization and blocks glioma progression. *Nat Med*, 19(10):1264–72, 2013.

77. D.A. Reardon, K.L. Fink, T. Mikkelsen, T.F. Cloughesy, A. O'Neill, S. Plotkin, M. Glantz, P. Ravin, J.J. Raizer, K.M. Rich, D. Schiff, W.R. Shapiro, S. Burdette-Radoux, E.J. Dropcho, S.M. Wittemer, J. Nippgen, M. Picard, and L.B. Nabors. Randomized phase II study of cilengitide, and integrin-targeting arginine-glycine-aspartic acid peptide, in recurrent glioblastoma multiforme. *J Clin Oncol*, 26:5610–5617, 2008.

78. K.A. Rejniak and R.H. Dillon. A single cell-based model of the ductal tumour microarchitecture. *Computational and Mathematical Methods in Medicine*, 8(1):51–69, 2007.

79. A.A.V. Los Reyes, E. Jung, and Y. Kim. Optimal control strategies of eradicating invisible glioblastoma cells after conventional surgery. *J. Roy Soc Interface*, 12:20141392, 2015.

80. Z. Rong, U. Cheema, and P. Vadgama. Needle enzyme electrode based glucose diffusive transport measurement in a collagen gel and validation of a simulation model. *Analyst*, 131(7):816–21, 2006.

81. S. Saffarian, I.E. Collier, B.L. Marmer, E.L. Elson, and G. Goldberg. Interstitial collagenase is a brownian ratchet driven by proteolysis of collagen. *Science*, 306(5693):108–11, 2004.

82. Y. Sakamoto, S. Prudhomme, and M. H. Zaman. Viscoelastic gel-strip model for the simulation of migrating cells. *Annals of Biomedical Engineering*, 39(11):2735–2749, 2011.

83. L.M. Sander and T.S. Deisboeck. Growth patterns of microscopic brain tumors. *Phys. Rev. E*, 66:051901, 2002.

84. H. Schattler, Y. Kim, U. Ledzewicz, A.A.d. los Reyes V, and E. Jung. On the control of cell migration and proliferation in glioblastoma. *Proceeding of the IEEE Conference on Decision and Control,*, 978-1-4673-5716-6/13:1810–1815, 2013.

85. S. Sen, M. Dong, and S. Kumar. Isoform-specific contributions of a-cctinin to glioma cell mechanobiology. *PLoS One*, 4(12):e8427, 2009.

86. J. A. Sherratt and J. D. Murray. Models of epidermal wound healing. *Proc.R. Soc.Lond.*, B241:29–36, 1990.

87. D.L. Silbergeld and M.R. Chicoine. Isolation and characterization of human malignant glioma cells from histologically normal brain. *J Neurosurg*, 86(3):525–31, 1997.

88. Daniel J Silver, Florian A Siebzehnrubl, Michela J Schildts, Anthony T Yachnis, George M Smith, Amy A Smith, Bjorn Scheffler, Brent A Reynolds, Jerry Silver, and Dennis A Steindler. Chondroitin sulfate proteoglycans potently inhibit invasion and serve as a central organizer of the brain tumor microenvironment. *The Journal of Neuroscience*, 33(39):15603–15617, 2013.

89. A.M. Stein, T. Demuth, D. Mobley, M. Berens, and L.M. Sander. A mathematical model of glioblastoma tumor spheroid invasion in a three-dimensional in vitro experiment. *Biophys J*, 92(1):356–65, 2007.

90. C. L. Stokes and D. A. Lauffenburger. Analysis of the roles of microvessel endothelial cell random motility and chemotaxis in angiogenesis. *J. theor. Biol*, 152:377–403, 1991.

91. L.M. Swift, H. Asfour, N.G. Posnack, A. Arutunyan, M.W. Kay, and N. Sarvazyan. Properties of blebbistatin for cardiac optical mapping and other imaging applications. *Pflugers Arch.*, 464(5):503–512, 2012.

92. B. Szomolay, T.D. Eubank, R.D. Roberts, C.B. Marsh, and A. Friedman. Modeling the inhibition of breast cancer growth by GM-CSF. *J. Theor Biol*, 303:141–151, 2012.

93. S. Tang, H. Liu, G. Chen, Q. Roa, and Y. Geng. Internalization and half-life of membrane-bound macrophage colony-stimulating factor. *Chinese Sc Bull*, 45:1697–1703, 2000.

94. R.G. Thorne, S. Hrabetov, and C. Nicholson. Diffusion of epidermal growth factor in rat brain extracellular space measured by integrative optical imaging. *J Neurophysiol*, 92(6):3471–81, 2004.

95. J-W. Tsai, K. H. Bremner, and R. B. Vallee. Dual subcellular roles for lis1 and dynein in radial neuronal migration in live brain tissue. *Nat. Neurosci.*, 10:970–979, 2007.

96. J.C. Utting, A.M. Flanagan, A. Brandao-Burch, I.R. Orriss, and T.R. Arnett. Hypoxia stimulates osteoclast formation from human peripheral blood. *Cell Biochem Funct*, 28(5):374–380, 2010.

97. M.M. Valter, O.D. Wiestler, and T. Pietsch. Differential control of vegf synthesis and secretion in human glioma cells by il-1 and egf. *International Journal of Developmental Neuroscience*, 17(5–6):565–577, 1999.

98. L.M. Wakefield, D.M. Smith, T. Masui, C.C. Harris, and M.B. Sporn. Distribution and modulation of the cellular receptor for transforming growth factor-beta. *J Cell Biol*, 105(2):965–75, 1987.

99. O. Warburg. On the origin of cancer cells. *Science*, 123(3191):309–14, 1956.

100. A. Wesolowska, A. Kwiatkowska, L. Slomnicki, M. Dembinski, A. Master, M. Sliwa, K. Franciszkiewicz, S. Chouaib, and B. Kaminska. Microglia-derived TGF-beta as an important regulator of glioblastoma invasion–an inhibition of TGF-beta-dependent effects by shRNA against human TGF-beta type ii receptor. *Oncogene*, 27(7):918–30, 2008.

101. E.A. Woodcock, S.L. Land, and R.K. Andrews. A low affinity, low molecular weight endothelin-a receptor present in neonatal rat heart. *Clin Exp Pharmacol Physiol*, 20(5):331–4, 1993.

102. Xian-zong Ye, Sen-lin Xu, Yan-hong Xin, Shi-cang Yu, Yi-fang Ping, Lu Chen, Hua-liang Xiao, Bin Wang, Liang Yi, Qing-liang Wang, et al. Tumor-associated microglia/macrophages enhance the invasion of glioma stem-like cells via tgf-β1 signaling pathway. *The Journal of Immunology*, 189(1):444–453, 2012.

103. B.B. Zhang, G. Zhou, and C. Li. AMPK: an emerging drug target for diabetes and the metabolic syndrome. *Cell metabolism*, 9(5):407–416, 2009.

104. Z. Zi, Z. Feng, D. A. Chapnick, M. Dahl, D. Deng, E. Klipp, A. Moustakas, and Xuedong Liu. Quantitative analysis of transient and sustained transforming growth factor-beta signaling dynamics. *Molecular Systems Biology*, 7(492):1–12, 2011.

A Multiscale Model of Cell Migration in Three-Dimensional Extracellular Matrix

Xiuxiu He and Yi Jiang

Abstract Cell migration in a three-dimensional (3D) extracellular matrix (ECM) is one of the key biological processes. Yet many fundamental questions remain unanswered. In this chapter, we introduce a modeling framework for a 3D, element-based, multiscale cell migration model. This model takes into account the mechanosensing signaling pathway, cell morphological dynamics, and cell-ECM interactions. To integrate the mechanochemical dynamics, we developed an implicit integration method to calculate forces for the elements and a moving boundary reaction-diffusion solver. The model is partially tested for cell migration on a curved substrate. Further development is needed to couple the cell model with a mechanical ECM model. This model can be used to test hypotheses of cell-ECM interactions and cell migration in tissue environment.

1 Introduction

Cell migration through 3D ECM is one of the most fundamental processes of living systems that underlies tissue formation, maintenance and regeneration, as well as pathological conditions including cancer invasion. Cells can change their behavior and switch their migration pattern depending on the local ECM. The critical questions: "What are the key ECM and cell characteristics that determine the migration pattern?" and, "Can we predict and manipulate the patterns of migration and resulting ECM remodeling by manipulating the ECM architecture?" are still unanswered.

Most of our understanding of cell migration is cell-centered, coming from assays of cell migration on a two-dimensional (2D) flat substrate. Cell migration is a cyclic multi-step process consisting of (1) actin polymerization-dependent protrusion at

X. He · Y. Jiang (✉)

Department of Mathematics, Georgia State University, 25 Park Place NE STE 1400, 30303 Atlanta, GA, USA

e-mail: xhe9@student.gsu.edu; yjiang12@gsu.edu

the leading edge; (2) integrin-mediated adhesion to ECM; (3) actomyosin-mediated contraction of the cell body increasing longitudinal tension that leads to rear retraction and translocation of the cell body, and (4) contact-dependent ECM cleavage by cell surface proteases [1]. Cell migration through a dense 3D ECM, in contrast to 2D migration, is possible only when the cell generates sufficient tractions to overcome the steric hindrance of the surroundings [2].

Many recent technological advances in super-resolution microscopies [7–9] to visualize the cytoskeleton, the cell, the ECM structures, 3D traction force microscopies to quantify the cell-substrate interactions [10, 11], as well as in engineered substrate geometry [2–5] have offered new tools to investigate 3D migration mechanisms. A mathematical and computational model of 3D cell-ECM interaction is needed to integrate all the new experimental observations to help mechanistically dissect cell migration strategies in 3D. Cell 3D migration also is physicochemical variable and "tunable" [6]. The actin cytoskeleton adapts its 3D organization in response to changes in the ECM, differences in cell mechanics, and the extent to which focal adhesions are present. Cells migrate through an ECM barrier either by changing their shape or by altering the ECM structure through proteolysis. There has been a growing need for a model that can capture the essential processes and interactions of 3D migration, such that the different migration patterns, e.g., the mesenchymal to amoeboid transition, are emergent from the cell interacting with the local ECM environment.

Many mathematical models of cell migration exist in the literature, but very few have considered realistic biomechanics. Most mathematical models of cell migration have been in 2D. Mogliner et al. [14] have modeled the integration of the spatial and temporal organization of multiple forces, including actin-driven protrusion of the cell membrane, membrane tension, cell-substrate adhesion, and myosin-mediated contraction of the actin network to understand the shape and movement of keratocyte [14] . Levine et al. [15] further described the cell's cytoskeleton as a viscous, compressible fluid driven by active stresses from actin polymerization and myosin contraction, which reproduced the long time scales of keratocyte and fibroblast migration on which the cytoskeleton can rearrange [16]. These 2D models did not consider the interaction with the ECM environment. Several models of cell-ECM coupling also exist. Most notable is probably the anisotropic biphasic theory of tissue equivalent mechanics [17], where cell seeded collagen gel was modeled as two continuous phases that interpenetrate each other: the viscoelastic fiber network phase and fluid phase. The model accounted for the biomechanical feedback between cell behavior and evolving network alignment. The continuous mechanics however does not treat the nonaffine local deformations. The model was extended to compare cell migration and cell traction through quantifying cell traction [18]. At the tissue scale, Bauer et al. [19] studied ECM topography as the contact guidance for endothelial cell migration during angiogenesis, but did not consider biomechanics. Zaman et al. [20] have developed a model of cell migration in ECM environment with different ligand, cell integrin receptor levels, and pore size, but did not consider ECM remodeling. Tozluoglu et al. [21] developed a cell blebbing model that took into account actin protrusion, actomyosin contraction, membrane

tension, and substrate adhesion. The model emphasized that the geometry of ECM determines cell migration pattern, but considered neither ECM mechanics nor remodeling. Also Lepzelter et al. [37] modeled 3D environment with explicit fibers, focusing on how the overall stiffness and ligand concentration influence the cell motility persistence, again did not consider ECM remodeling. He et al. [38] studied how substrate curvature regulates cell migration morphology and motility through developing 3D element-based cell model. A recent review [39] summarized the recent advances in the modeling of ECM biomechanics, cell migration, and cell-ECM interactions in the context of cancer invasion.

Our grand goal is to develop a cell migration model that can interact mechanically and chemically with the 3D ECM, and can adapt its migration pattern realistically as a function of the local ECM structure and mechanics. While it has been well accepted that 3D cell migration is in many ways different from 2D, and that physical properties of the ECM such as stiffness, crosslinking, and pore size affect 3D migration [22–26], how cells detect the mechanical properties of the matrix and switch their migration mode accordingly is still unresolved [27]. Furthermore, as cells move along, around, and through the network of ECM fibers, they remodel the structure of the fiber network, which also changes the mechanical property and in turn modulate the cell migration patterns. Many mathematical models for ECM biomechanics exist, thanks to its importance in connective tissue and tissue engineering. These models range from molecular dynamics of collagen molecules to bulk properties of fiber networks [28–34]. Because our goal is to understand how cells interact with collagen networks with different ECM architectures, neither atomic molecular dynamics nor continuous models will work. We have developed a 3D elastic computational fiber network model and parameterized it with *in vitro* collagen experiments [35]. Using this model, we simulated mechanical testing of fiber networks and examine the mechanical properties of fiber networks with varying density, alignment, and crosslinking.

In this chapter, we present a 3D multiscale cell migration model framework with a cell signaling cascade that is coupled to the 3D ECM biomechanical model.

2 Three-Dimensional Multiscale Cell Migration Model

At the cellular scale, the element-based cell model specifies the cell membrane, cytoskeleton, and nucleus (Figure 1). We model cell membrane using membrane elements similar to those in Newman's subcellular element model [12], where a pair-wise Morse potential between elements describes their interactions. The Morse potential

$$V(r) = D(1 - e^{(-a(r-r_e))})^2 \tag{1}$$

where r is the distance between elements, r_e is the equilibrium distance, and D is the potential well depth, is a better approximation than elastic springs as it explicitly includes the effect of bond breaking, which is necessary for simulating the cell membrane dynamics that could have large deformations. Each membrane element is connected to the nucleus through an elastic cytoskeleton string, and the nucleus is a semi-rigid sphere that can deform slightly when pushed and pulled by the cytoskeletal strings (Figure 1).

At the molecular scale, each membrane element carries integrins. Integrin can bind to nearby ECM to form focal adhesion and initiate cell polarity, which leads to the signaling cascade down the mechanosensing pathway to regulate the actin cytoskeleton dynamics. We use a highly simplified mechanosensing signaling network (low right corner of Figure 1), which includes integrin binding activated Rho1, Rac/Arp2/3 pathways. Activation of Rho1 leads to actomyosin bundle formation, while activation of Rac/Arp2/3 leads to actin polymerization. The spatiotemporal dynamics of these molecules are described using a set of reaction-diffusion equations. The resulting spatial distributions of filament actin (F-actin) and actomyosin drive the dynamics of the cytoskeletal strings: high concentration of F-actin leads to fiber elongation and high concentration of actomyosin leads to fiber shortening. At the same time, the high density of actomyosin also leads to integrin clustering, which in turn strengthens focal adhesion by stabilizing the nascent integrin bindings. Each membrane element then integrates the forces from the string (cytoskeleton force), from its neighboring elements (membrane tension), and the integrin-ECM binding (focal adhesion), to determine its motion. The motion of the elements determines cell shape as well as the migration dynamics.

At the tissue scale, this cell model can be embedded in a 3D ECM model. The mechanical binding between integrin and ECM ligand and the signaling cascade is described above. This model framework and the following implicit integration method can also easily allow for proteolytic interaction between the cell and the ECM in this rather flexible model framework.

2.1 Mechanical Element-Based Cell Model

The equations of motion for membrane elements α_i is:

$$\dot{\mathbf{y}}_{\alpha_i} = \boldsymbol{\mu}_{\alpha_i} - \nabla_{\alpha_i} \sum_{\beta_i \neq \alpha_i} V(|\mathbf{y}_{\alpha_i} - \mathbf{y}_{\beta_i}|) - \nabla_{\alpha_i} \sum_{j \in N_{\alpha_i}} P_j + \boldsymbol{\rho}_\alpha, \qquad (2)$$

where $\boldsymbol{\mu}$ is Gaussian-distributed random noise that reflects the underlying fluctuations of cytoskeleton, V is the Morse potential (Equation 1), P is the elastic energy in cytoskeletal structure connected to α_i, and ρ is the protrusion or contraction force
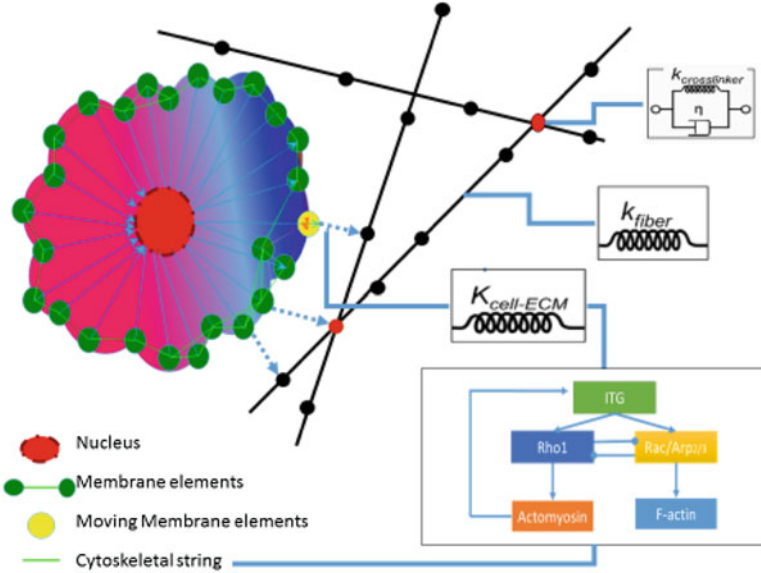
Fig. 1 Schematic of the 3D multiscale cell-ECM model: a cell consists of membrane elements that interact through a Morse potential, a deformable nucleus, and cytoskeletal strings that can protrude and contract as regulated by local F-actin and Actomyosin concentrations. The viscoelastic ECM model (black fibers with red crosslinker treated as bead-and-springs) provides not only the binding sites for cells, but also the mechanical coupling for cell membrane elements. The cell-ECM mechanical coupling initiates the maturation steps of Integrin (ITG)-Ligand (ECM) binding. Stable Integrin-ligand binding leads to the signaling cascade through Rac and Rho (lower right corner) that determines the actin and myosin dynamics. F-actin and Actomyosin activities dictate the time-dependent elongation and contraction of cytoskeletal strings.

associated with local concentration of molecules in the signaling cascade (low right corner of Figure 1). As the cell membrane is represented as membrane element, the model is capable of capturing complicated morphological dynamics with multiscale interactions and geometric constrains.

We assume that inertial effects can be ignored in the over-damped environment of a live cell. Part of the mechanics at molecular scale, e.g. mediated by motor proteins or initiation of actin polymerization, are dominated by Brownian motion, which has been modeled using the Langevin equation [36]. The motion of membrane element also experiences a frictional drag. Hence the velocity of the membrane element **v** is

$$\mathbf{v}_{\alpha_i} = \kappa \dot{\mathbf{y}}_{\alpha_i} \tag{3}$$

$$= \mathbf{F}(\mathbf{y}, \mathbf{L}, \boldsymbol{\rho}, \boldsymbol{\mu}) \tag{4}$$

$$= \mathbf{f}_1(\mathbf{y}) + \mathbf{f}_2(\mathbf{L}) + \mathbf{f}_3(\boldsymbol{\rho}) + \mathbf{f}_4(\boldsymbol{\mu}), \tag{5}$$

where κ is the drag coefficient, $\mathbf{y}$ is the positions of all elements in 3D, and $\mathbf{L}$ represents the elastic deformation of cytoskeletal string. The Langevin Equation (2) can incorporate other signaling cascade or intracellular interactions associated with migration, for example chemotaxis and durotaxis. To avoid the potential stability issues with explicit integration methods, we introduce the following implicit numerical integration method, in which we simplify the complex interactions.

$$\mathbf{y}_{t+\Delta_t} = \mathbf{y}_t + \Delta_t \cdot \mathbf{F}_{t+\Delta_t} \tag{6}$$

$$\mathbf{F}_{t+\Delta_t} = \mathbf{F}_t + (\mathbf{y}_{t+\Delta_t} - \mathbf{y}_t) \cdot \mathbf{F}'_{\mathbf{y}_t}. \tag{7}$$

$$\mathbf{F}'_{\mathbf{y}_t} = \mathbf{f}'_1(\mathbf{y}_t) + \mathbf{f}'_2(\mathbf{y}_t) + \mathbf{f}'_3(\boldsymbol{\rho}_t) + \mathbf{f}'_4(\boldsymbol{\mu}_t) \tag{8}$$

Therefore we have

$$\mathbf{y}_{t+\Delta_t} - \mathbf{y}_t = \Delta_t \cdot \frac{\mathbf{F}_t}{\mathbf{I} - \Delta_t \cdot \mathbf{F}'_{\mathbf{y}_t}} \tag{9}$$

$$= (\frac{\mathbf{I}}{\Delta_t} - \mathbf{F}'_{\mathbf{y}_t})^{-1} \mathbf{F}_t, \tag{10}$$

where $\mathbf{F} = \sum_{k=1,\ldots 4} \mathbf{f}$, $\mathbf{F}_t = \mathbf{F}(\mathbf{y}_t)$, $\mathbf{F}'_{\mathbf{y}_t}$ is derivative of $\mathbf{F}$ with respect to $\mathbf{y}$.

The first force arises from the inter-elemental potential and can be rewritten as

$$\mathbf{f}_1(\mathbf{y}_t) = \nabla_{\alpha_i} \sum_{\beta_i \neq \alpha_i} V(|\mathbf{y}_{\alpha_i} - \mathbf{y}_{\beta_i}|). \tag{11}$$

Let $r_{\alpha_i,\beta_i} = |\mathbf{y}_{\alpha_i} - \mathbf{y}_{\beta_i}|$. We consider the gradient of $\mathbf{f}_1(\mathbf{y}_t)$ with respect to $x_{\mathbf{y}_t}$ where $\mathbf{y}_t = (x_{\mathbf{y}_t}, \ y_{\mathbf{y}_t}, \ z_{\mathbf{y}_t})$ is 3D position of the membrane element.

$$\mathbf{f}'_1(\mathbf{y}_t)_{x_{\mathbf{y}_t}} = (\nabla_{\alpha_i} \sum_{\beta_i \neq \alpha_i} V(|\mathbf{y}_{\alpha_i} - \mathbf{y}_{\beta_i}|)_{x_{\mathbf{y}_t}} \tag{12}$$

$$= \sum_{\beta_i \neq \alpha_i} (\nabla_{\alpha_i} (V(|\mathbf{y}_{\alpha_i} - \mathbf{y}_{\beta_i}|))_{r_{\alpha_i,\beta_i}} \cdot (r_{\alpha_i,\beta_i})_{x_{\mathbf{y}_t}} \tag{13}$$

Equivalently, because $(r_{\alpha_i,\beta_i})_{x_{\mathbf{y}_t}} = r_{\alpha_i,\beta_i}^{-\frac{1}{2}}(x_{\mathbf{y}_{\alpha_i} t} - x_{\mathbf{y}_{\beta_i} t})$, we have

$$\mathbf{f}'_1(\mathbf{y}_t)_{\mathbf{y}_t} = \sum_{\beta_i \neq \alpha_i} r_{\alpha_i,\beta_i}^{-\frac{1}{2}} (\nabla_{\alpha_i} (V(|\mathbf{y}_{\alpha_i} - \mathbf{y}_{\beta_i}|))_{r_{\alpha_i,\beta_i}} \cdot (\mathbf{y}_{\alpha_i} - \mathbf{y}_{\beta_i}) \tag{14}$$

Similarly, the force from the elastic cytoskeletal strings is

$$\mathbf{f}_2(\mathbf{y}_t) = -k(\mathbf{y}_t - \mathbf{y}_{eq}) \tag{15}$$

$$\mathbf{f}_2'(\mathbf{y}_t)_{x_{\mathbf{y}_t}} = -k \cdot \frac{x_{\mathbf{y}_t}}{|x_{\mathbf{y}_t}|}, \tag{16}$$

which leads to

$$\mathbf{f}_2'(\mathbf{y}_t)_{\mathbf{y}_t} = -k \cdot \frac{\mathbf{y}_t}{||\mathbf{y}_t||_2} \tag{17}$$

Moreover, $\mathbf{f}_4(\mu)$ is motion from Gaussian-distributed random variate with zero mean and is independent of the positions of elements $\mathbf{y}_{\alpha_i}$, therefore $\mathbf{f}_4'(\mu)_{\mathbf{y}_t} = 0$, which is the same for $\mathbf{f}_3'(\boldsymbol{\rho})_{\mathbf{y}_t}$.

Taken together, $\mathbf{F}_{\mathbf{y}_t}'$ for each membrane element in Equation (7) is

$$\mathbf{F}'(\mathbf{y}_t, \boldsymbol{\rho}, \mu)_{\mathbf{y}_t} = -\sum_{\beta_i \neq \alpha_i} r_{\alpha_i, \beta_i}^{-\frac{1}{2}} (\nabla_{\alpha_i}(V(|\mathbf{y}_{\alpha_i} - \mathbf{y}_{\beta_i}|))_{r_{\alpha_i, \beta_i}} \cdot (\mathbf{y}_{\alpha_i} - \mathbf{y}_{\beta_i}) - k \cdot \frac{\mathbf{y}_t}{||\mathbf{y}_t||_2}. \tag{18}$$

This method has been tested and implemented in parallel for simulating 3D cell migration on curved substrate [38]. We used this 3D cell migration model to simulate cell migration on both convex and concave substrates. We showed that cell spreads out more on a more convex surface, while cell migration is more persistent on the more concave surfaces (Figure 2).

2.2 Mechanochemical Cytoskeletal Dynamics

As illustrated in Figure 1, we integrate the mechanics of integrin-ECM binding and cytoskeletal with the actin cytoskeletal dynamics through the combination of reaction-diffusion equations and element-based modeling. The number, status, and duration of integrin binding determines the strength of a focal adhesion [13]. The local concentrations of F-actin and actomyosin prescribe the elongation and contraction of cytoskeletal fibers. Both focal adhesion and the elongation/contraction of cytoskeletal fibers then contribute to the equation of motion of the MEs. Motion of the MEs then determines cell shape dynamics and migration behavior (Figure 3).
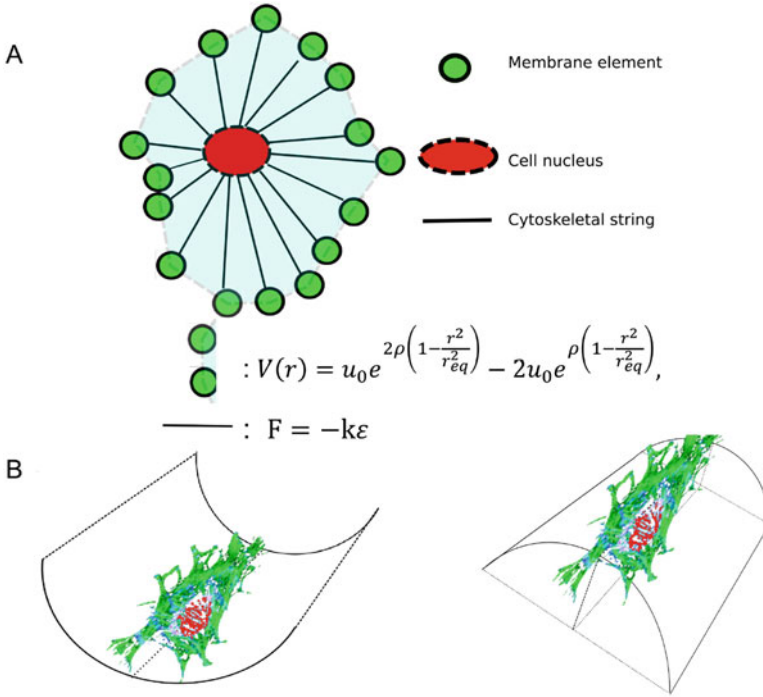
Fig. 2 Schematic of the 3D cell model (A) and single cell migration on substrate with (B) negative (lower left) and positive (lower right) curvature. (Adapted from [38] with permission.)
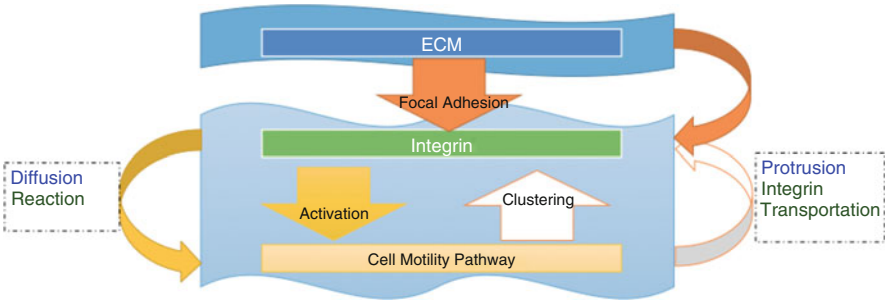
Fig. 3 Schematic of mechanochemical integration. Integrin binding with ECM forms focal adhesion, which activates mechanosensing signaling pathway. The spatiotemporal concentration dynamics of the molecules in the mechanosensing pathway, modeled as a reaction-diffusion system, determine the protrusion and contraction of the cytoskeletal fibers as well as integrin clustering.

For each node in our simplified signaling network, the concentration follows a general diffusion-reaction equation:

$$\frac{\partial \mathbf{C}}{\partial t} = \nabla(D\nabla\mathbf{C}) + \mathbf{R} \tag{19}$$

where $\mathbf{C}$ is the concentration and D is the diffusion coefficient. The reaction kinetics $\mathbf{R}$ includes:

$$\frac{\partial N}{\partial t} = k_{aN} L I - k_{dN} N + k_{dS} S - k_{as} N \tag{20}$$

$$\frac{\partial S}{\partial t} = k_{aS} N - k_{dN} S \tag{21}$$

$$\frac{\partial R}{\partial t} = \frac{I_R + \alpha_{SR} S}{1 + (\frac{\rho}{\beta_\rho})^{n_1}} (\frac{R_i}{R_{tot}}) - \delta_R R \tag{22}$$

$$\frac{\partial \rho}{\partial t} = \frac{I_\rho + \alpha_{S\rho} S}{1 + (\frac{R}{\beta_R})^{n_2}} (\frac{\rho_i}{\rho_{tot}}) - \delta_\rho \rho \tag{23}$$

$$\frac{\partial AcM}{\partial t} = (I_{AcM} + \alpha_\rho \rho) \frac{AcM_i}{AcM_{tot}} - \delta_{AcM} AcM \tag{24}$$

$$\frac{\partial Fa}{\partial t} = (I_{Fa} + \alpha_R R) \frac{Fa_i}{Fa_{tot}} - \delta_{Fa} Fa \tag{25}$$

$$\frac{\partial I}{\partial t} = \frac{k_1 I_0}{k_2 + AcM} + \frac{k_3 L_0}{k_4 + L} - k_5 I, \tag{26}$$

where L is ECM ligand, I is integrin, N is nascent integrin binding, and S is stable integrin binding. The first two equations describe the stabilization or maturation of focal adhesion:

$$\text{Ligand(L)} + \text{Integrin(I)} \underset{d_{dN}}{\overset{k_{aN}}{\rightleftharpoons}} \text{Nascent} - \text{binding (N)} \underset{d_{dS}}{\overset{k_{aS}}{\rightleftharpoons}} \text{Stable} - \text{binding(S)} \tag{27}$$
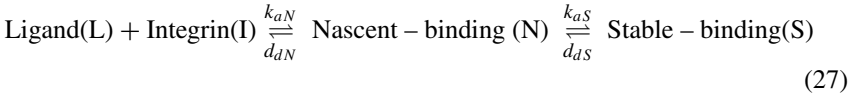
In the rest of the equations, ρ is Rho1, R is Rac/Arp2/3, AcM is actomyosin, and Fa is F-actin, with their respective kinetic rates k and decay constants δ.

The challenge for solving the reaction diffusion equations is that as cell migrates, the domain to solve the equations changes constantly, i.e., a moving boundary problem. However, there has not been a reaction-diffusion solver with moving boundary conditions with mechanics. StochSS [40, 43] is a stochastic biochemical network simulator without spatial temporal biochemical aspect. Simmune [41] uses a non-deformable cube volume element to simulate cell-cell and cell-ECM interactions based on Cellular Potts model. Vcell [42] and Simmune are able to build 3D mesh from microscopic images; however, without a fast 3D moving boundary reaction-diffusion solver, they are currently not capable of simulating cell morphology and ECM deformation.

We introduce a novel 3D moving boundary reaction-diffusion solver, where the volume discretization and volume adaption are designed to take advantage of the discrete cell MEs and the cytoskeletal string structure. The volume discretization takes place in two steps. First we triangulate the cell surface formed by MEs; as
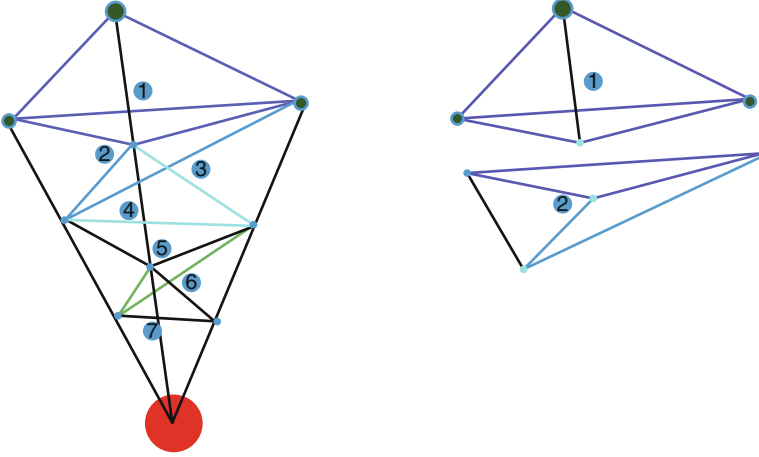
Fig. 4 Schematic diagram of volume discretization. The membrane elements of a cell surface triangle and the cytoskeletal strings connecting them to the nucleus define a tetrahedron. To discretize the tetrahedron further, fixed number of points are added along each cytoskeletal string.

the cell nucleus and MEs are connected through the cytoskeletal fibers, the three MEs of a triangle and the fibers and the nucleus surface define the tetrahedrons that discretize the 3D cell (Figure 4 left). Second we define discretization points along each cytoskeletal string. The points are further apart closer to the nucleus than to the cell surface, such that the discretized tetrahedra have roughly equal volumes. Vertices of tetrahedron are either MEs or points along cytoskeleton strings. As the cell moves, positions of the vertices move with membrane and string deformation (Figure 2A). When the tetrahedra are small enough and the time step of integration is small enough, we can assume that within the tetrahedron the amount of molecules involved in the volume adaption remains homogeneous within each step.

The diffusion term can be discretized using the 3D analog of Crank-Nicholson scheme, based on the Locally One-Dimensional (LOD) method:

$$\frac{\partial C}{\partial t} = D[\frac{\partial^2 C}{\partial x^2} + \frac{\partial^2 C}{\partial y^2} + \frac{\partial^2 C}{\partial z^2}]. \tag{28}$$

Let $v_x \equiv D\frac{\Delta t}{\Delta x^2}$, $v_y \equiv D\frac{\Delta t}{\Delta y^2}$, and $v_z \equiv D\frac{\Delta t}{\Delta z^2}$.

$$(1 - \frac{v_x}{2}\delta_x^2 - \frac{v_y}{2}\delta_y^2 - \frac{v_z}{2}\delta_z^2)C^{n+1} = (1 + \frac{v_x}{2}\delta_x^2 + \frac{v_y}{2}\delta_y^2 + \frac{v_z}{2}\delta_z^2)C^n \tag{29}$$

The factorization of the scheme is

$$(1 - \frac{v_x}{2}\delta_x^2)(1 - \frac{v_y}{2}\delta_y^2)(1 - \frac{v_z}{2}\delta_z^2)C^{n+1} = (1 + \frac{v_x}{2}\delta_x^2)(1 + \frac{v_y}{2}\delta_y^2)(1 + \frac{v_z}{2}\delta_z^2)C^n \tag{30}$$

Fig. 5 Schematic of volume adaption. V_1^- (before) and V_1^+ (after).
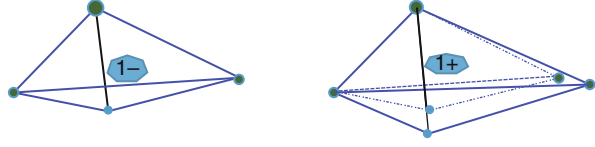
The truncation error of this method is $T = O(\Delta t^2) + O(\Delta x^2) + O(\Delta y^2) + O(\Delta z^2)$. The method is always stable. We implement this scheme by breaking it down to three steps:

$$\begin{cases} (1 - \frac{A_x}{2})C^{n*} = (1 + \frac{A_x}{2} + A_y + A_z)C^n \\ (1 - \frac{A_y}{2})C^{n**} = C^{n*} - \frac{A_y}{2}C^n \\ (1 - \frac{A_z}{2})C^{n+1} = C^{n**} - \frac{A_z}{2}C^n \end{cases} \tag{31}$$

Each time step, the system is solved for all tetrahedra by combining the reaction and diffusion calculations. Then as the MEs and fibers adapt mechanically, the concentrations for the next time step depend on the new locations of the tetrahedra:

$$C_i^+ = \frac{1}{V_+}\{C_i \parallel V_i^+ \cap V_i^- \parallel + \sum_{j \in N(i)} C_j \parallel V_i^+ \cap V_j^- \parallel\} \tag{32}$$

When the time step is small enough, the new tetrahedron V_i^+ overlaps significantly with the old V_i^- (Figure 5). We need to calculate the intersection between two convex tetrahedra. Therefore the problem becomes solving the following system for $V^+ \cap V^-$, where V^+ has vertices $P_1^+, P_2^+, P_3^+, P_4^+$ and V^- has vertices $P_1^-, P_2^-, P_3^-, P_4^-$.

The procedures are the following:

- Find the vertex set $S = \{P_i^- : i = 1, \ldots, 4\}$.

- If S has 4 elements, $V^- \subset V^+$. $V^+ \cap V^- = V^-$.

- If S has 3 elements, $S = \{P_1, P_2, P_3\}$. Let $\overline{S} = \{P\}$. Compute PP_i intersects any face of V^+ that does not contain vertex $\in S$. That is, computing three lines intersect with one plane and get the split point to add to S.

- If S has 2 elements, $S = \{P_1, P_2\}$. Let $\overline{S} = \{P_3, P_4\}$. Compute P_iP_j, $i \in \{1, 2\}$, $j \in \{3, 4\}$ intersect with the opposite face of corner P_i. That is, computing line-face intersection for four times. Add new split points to S.

- If S has one elements, $S = \{P\}$. Let $\overline{S} = \{P_1, P_2, P_3\}$. Compute PP_i intersect with the opposite face of P, then add the split points to S.

- If S has 0 elements,

$$a_{m1}^{j}x + a_{m2}^{j}y + a_{m3}^{j}z = b_{m}^{j} \tag{33}$$

$$a_{p1}^{i}x + a_{p2}^{i}y + a_{p3}^{i}z = b_{p}^{i} \tag{34}$$

$$a_{q1}^{i}x + a_{q2}^{i}y + a_{q3}^{i}z = b_{q}^{i} \tag{35}$$

where m is the face index of tetrahedron j and $\{p, \quad q\}$ is a pair of faces of tetrahedron i. With the solution of both cases, we have all vertices of the intersection $V^{+} \cap V^{-}$. It is then trivial to solve for the volume because it is convex.

$$\begin{bmatrix} 1 \\ x \\ y \\ z \end{bmatrix} = \begin{bmatrix} 1 & 1 & 1 & 1 \\ x_1 & x_2 & x_3 & x_4 \\ y_1 & y_2 & y_3 & y_4 \\ z_1 & z_2 & z_3 & z_4 \end{bmatrix} \begin{bmatrix} \zeta_1 \\ \zeta_2 \\ \zeta_3 \\ \zeta_4 \end{bmatrix} \tag{36}$$

$$\zeta_1 + \zeta_2 + \zeta_3 + \zeta_4 = 1, \forall (x, \quad y, \quad z) \in \Omega^{e} \tag{37}$$

ζ_i is the volume of the sub-tetrahedron spanned by the point $(x, \quad y, \quad z)$ and the face opposite the i-th corner. The above 4×4 matrix is called *Jacobian* matrix of the tetrahedron. Explicit inversion gives

$$\begin{bmatrix} \zeta_1 \\ \zeta_2 \\ \zeta_3 \\ \zeta_4 \end{bmatrix} = \frac{1}{6V} \begin{bmatrix} 6V_{01} & y_{42}z_{32} - y_{32}y_{42} & x_{32}z_{42} - x_{42}z_{32} & x_{42}y_{32} - x_{32}y_{42} \\ 6V_{02} & y_{31}z_{43} - y_{34}z_{13} & x_{43}z_{31} - x_{13}z_{34} & x_{31}y_{43} - x_{34}y_{13} \\ 6V_{03} & y_{24}z_{14} - y_{14}z_{24} & x_{14}z_{24} - x_{24}z_{14} & x_{24}y_{14} - x_{14}y_{24} \\ 6V_{04} & y_{13}z_{21} - y_{12}z_{31} & x_{12}z_{13} - x_{31}z_{12} & x_{13}y_{21} - x_{12}y_{31} \end{bmatrix} \begin{bmatrix} 1 \\ x \\ y \\ z \end{bmatrix} \tag{38}$$

where $x_{ij} = x_i - x_j$, $y_{ij} = y_i - y_j$, and $z_{ij} = z_i - z_j$. The first column entries are explicitly given by

$$6V_{01} = x_2(y_3z_4 - y_4z_3) + x_3(y_4z_2 - y_2z_4) + x_4(y_2z_3 - y_3z_2). \tag{39}$$

$$6V_{02} = x_1(y_4z_3 - y_3z_4) + x_3(y_1z_4 - y_4z_1) + x_4(y_3z_1 - y_1z_3). \tag{40}$$

$$6V_{03} = x_1(y_2z_4 - y_4z_2) + x_2(y_4z_1 - y_1z_4) + x_4(y_1z_2 - y_2z_1). \tag{41}$$

$$6V_{04} = x_1(y_3z_2 - y_2z_3) + x_2(y_1z_3 - y_3z_1) + x_3(y_2z_1 - y_1z_2). \tag{42}$$

This novel design for solving the reaction-diffusion equations with moving boundary conditions is motivated by the discrete nature of our element-based model. The movement of cell membrane elements is updated by solving Equation (2), which is based on the solution of Equations (19). The two are integrated using the moving boundary reaction-diffusion interface (as shown in Figure 3). Within our model design, this method is more efficient than other finite volume methods, e.g., a finite volume procedure [45] that treats mechanical-chemical responses such as load-velocity relations, because the volume elements can be calculated and updated analytically.

Alternatively, we could use a moving grid finite element method [46, 47]. Continuously changing boundaries can be readily handled by moving grid implementations with few changes to the finite element methodology, at least when grid motion is prescribed. In many biological contexts, however, the grid motion cannot be prescribed. A novel moving grid finite element method [44], where solution and the grid movement are both unknown that have to be solved for simultaneously. In most cases the solution of the partial differential equation and the grid movement are expanded in a piecewise linear finite element approximation space and then the least squares residual is minimized with respect to the time derivatives of the two unknowns. This method thus yields both the solution and the grid movement simultaneously. This method was applied to solve a reaction-diffusion system where the boundary is deformed continuously in some prescribed fashion (in most cases to mimic biological experiments) [44] in 2D.

3 Discussion

Cell migration requires coordination of processes across multiscales: the molecular regulation of the cytoskeleton dynamics, the membrane biophysical properties, and the interaction with the extracellular environment. We have developed a multiscale element-based 3D single cell model, which integrates biomechanics and cell singling, as well as biomechanics and biochemical interactions with the 3D ECM. Mechanical interactions between integrin and ligand, within the actin cytoskeletal structure, between the membrane elements and the cytoskeleton, are coupled to the kinetics of the mechanosensing pathway. We in addition propose a set of numerical treatments for the mechanochemical coupling at both the molecular and cellular scales.

This model necessarily contains a large number of parameters, many of which are available either from either direct experimental measurements (e.g., kinetic rates) or estimates (e.g., diffusion coefficients). The key parameters in our model are the simplified mechanochemical integration, i.e., the elongation and shortening of cytoskeletal fibers as a function of the local concentration of F-actin and actomyosin. The parameters for these rules could be fitted from experimental data with high resolution spatiotemporal actin cytoskeleton dynamics, e.g., using the lattice light sheet super-resolution microscopy [48]. Alternatively, these parameters could be derived from finer resolution molecular dynamics simulations, for example using a computational model for mechanochemical simulations of active networks (MEDYAN) [49].

Among the key processes of cell migration, ECM degradation by matrix metalloproteinase (MMP) is not always active. Processes related to MMP degradation are highly complex, e.g., degradation in the form of actin-rich invadopodia is found to be regulated by secretion of exosomes containing ECM [50]. Such proteolytic processes can be included either as rules or as kinetic equations when rate parameters are available. In addition, intracellular fluid dynamics has been

proposed to be important in regulating migration for cells in confined geometries [5]. Our modeling framework has the capability of further extending the reaction-diffusion equations to reaction-diffusion-advection equations.

Our flexible modeling framework has only been implemented for single cell migration on curved substrates [38]. Further research is needed to couple our cell migration model with mechanically realistic ECM model [35]. Many questions regarding cell migration in 3D ECM could be addressed, and experimentally testable hypotheses generated, using such a modeling framework.

References

1. Friedl, P., Alexander, S. (2011). Cancer invasion and the microenvironment: plasticity and reciprocity. Cell, **147**(5), 992–1009.
2. Califano, J.P. and Reinhart-King, C.A. (2008). A balance of substrate mechanics and matrix chemistry regulates endothelial cell network assembly. Cellular and Molecular Bioengineering, **1**(2–3), p. 122.
3. Driscoll, M.K., Sun, X., Guven, C., Fourkas, J.T. and Losert, W. (2014). Cellular contact guidance through dynamic sensing of nanotopography. ACS nano, **8**(4), pp. 3546–3555.
4. Kim, D.H., Provenzano, P.P., Smith, C.L. and Levchenko, A. (2012). Matrix nanotopography as a regulator of cell function. J Cell Biol, **197**(3), pp. 351–360.
5. Stroka, K.M., Jiang, H., Chen, S.H., Tong, Z., Wirtz, D., Sun, S.X. and Konstantopoulos, K. (2014). Water permeation drives tumor cell migration in confined microenvironments. Cell, **157**(3), pp. 611–623.
6. Friedl, P. and Wolf, K. (2009). Plasticity of cell migration: a multiscale tuning model. The Journal of cell biology, pp. jcb-200909003.
7. Xu F, Zhang M, He W, Han R, Xue F, Liu Z, Zhang F, Lippincott-Schwartz J, Xu P. (2017). Live cell single molecule-guided Bayesian localization super resolution microscopy. Cell research, **27**(5), 713.
8. Chen, B.C., Legant, W.R., Wang, K., Shao, L., Milkie, D.E., Davidson, M.W., Janetopoulos, C., Wu, X.S., Hammer, J.A., Liu, Z. and English, B.P. (2014). Lattice light-sheet microscopy: imaging molecules to embryos at high spatiotemporal resolution. Science, **346**(6208), p.1257998.
9. Lee, B., Konen, J., Wilkinson, S., Marcus, A.I. and Jiang, Y. (2017). Local alignment vectors reveal cancer cell-induced ECM fiber remodeling dynamics. Scientific reports, **7**, p.39498.
10. Oakes, P.W., Wagner, E., Brand, C.A., Probst, D., Linke, M., Schwarz, U.S., Glotzer, M. and Gardel, M.L. (2017). Optogenetic control of RhoA reveals zyxin-mediated elasticity of stress fibres. Nature Communications, **8**, p.15817.
11. Franck, C., Maskarinec, S.A., Tirrell, D.A. and Ravichandran, G. (2011). Three-dimensional traction force microscopy: a new tool for quantifying cell-matrix interactions. PloS one, **6**(3), p.e17833.
12. Newman, TJ. (2005). Modeling multicellular systems using subcellular elements, J. Math Biosci Eng, **2** (3) , pp. 611–622
13. Gallant, N.D., Michael, K.E. and Garcia, A.J. (2005). Cell adhesion strengthening: contributions of adhesive area, integrin binding, and focal adhesion assembly. Molecular biology of the cell, **16**(9), pp. 4329–4340.
14. Barnhart, E.L., Lee, K.C., Keren, K., Mogilner, A. and Theriot, J.A. (2011). An adhesion-dependent switch between mechanisms that determine motile cell shape. PLoS biology, **9**(5), p.e1001059.

15. Shao, D., Levine, H. and Rappel, W.J. (2012). Coupling actin flow, adhesion, and morphology in a computational cell motility model. Proceedings of the National Academy of Sciences, **109**(18), pp. 6851–6856.
16. Rubinstein, B., Fournier, M.F., Jacobson, K., Verkhovsky, A.B. and Mogilner, A. (2009). Actin-myosin viscoelastic flow in the keratocyte lamellipod. Biophysical journal, **97**(7), pp. 1853–1863.
17. Checa, S., Rausch, M.K., Petersen, A., Kuhl, E. and Duda, G.N. (2015). The emergence of extracellular matrix mechanics and cell traction forces as important regulators of cellular self-organization. Biomechanics and modeling in mechanobiology, **14**(1), pp. 1–13.
18. Shreiber, D.I., Barocas, V.H. and Tranquillo, R.T. (2003). Temporal variations in cell migration and traction during fibroblast-mediated gel compaction. Biophysical journal, **84**(6), pp. 4102–4114.
19. Bauer, A.L., Jackson, T.L. and Jiang, Y. (2009). Topography of extracellular matrix mediates vascular morphogenesis and migration speeds in angiogenesis. PLoS computational biology, **5**(7), p.e1000445.
20. Zaman, M.H., Trapani, L.M., Sieminski, A.L., MacKellar, D., Gong, H., Kamm, R.D., Wells, A., Lauffenburger, D.A. and Matsudaira, P. (2006). Migration of tumor cells in 3D matrices is governed by matrix stiffness along with cell-matrix adhesion and proteolysis. Proceedings of the National Academy of Sciences, **103**(29), pp. 10889–10894.
21. Tozluo?lu, M., Tournier, A.L., Jenkins, R.P., Hooper, S., Bates, P.A. and Sahai, E. (2013). Matrix geometry determines optimal cancer cell migration strategy and modulates response to interventions. Nature cell biology, **15**(7), p.751.
22. Nelson, C.M. and Bissell, M.J. (2006). Of extracellular matrix, scaffolds, and signaling: tissue architecture regulates development, homeostasis, and cancer. Annu. Rev. Cell Dev. Biol., **22**, pp. 287–309.
23. Yamada, K.M. and Cukierman, E. (2007). Modeling tissue morphogenesis and cancer in 3D. Cell, **130**(4), pp. 601–610.
24. Grinnell, F. and Petroll, W.M. (2010). Cell motility and mechanics in three-dimensional collagen matrices. Annual review of cell and developmental biology, **26**, pp. 335–361.
25. DuFort, C.C., Paszek, M.J. and Weaver, V.M. 2011. Balancing forces: architectural control of mechanotransduction. Nature reviews Molecular cell biology, **12**(5), p.308.
26. Baker, B.M. and Chen, C.S. (2012). Deconstructing the third dimension?how 3D culture microenvironments alter cellular cues. J Cell Sci, **125**(13), pp. 3015–3024.
27. Petrie, R.J., Gavara, N., Chadwick, R.S. and Yamada, K.M., 2012. Nonpolarized signaling reveals two distinct modes of 3D cell migration. J Cell Biol, **197**(3), pp. 439–455.
28. Buehler, M.J. (2006). Atomistic and continuum modeling of mechanical properties of collagen: elasticity, fracture, and self-assembly. Journal of Materials Research, **21**(8), pp. 1947–1961.
29. Buehler, M.J. (2006). Nature designs tough collagen: explaining the nanostructure of collagen fibrils. Proceedings of the National Academy of Sciences, **103**(33), pp. 12285–12290.
30. Gautieri, A., Vesentini, S., Redaelli, A. and Buehler, M.J. (2011). Hierarchical structure and nanomechanics of collagen microfibrils from the atomistic scale up. Nano letters, **11**(2), pp. 757–766.
31. Broedersz, C.P., Storm, C. and MacKintosh, F.C. (2008). Nonlinear elasticity of composite networks of stiff biopolymers with flexible linkers. Physical review letters, **101**(11), p.118103.
32. Rubinstein, M. and Panyukov, S. (1997). Nonaffine deformation and elasticity of polymer networks. Macromolecules, **30**(25), pp. 8036–8044.
33. Stein, A.M., Vader, D.A., Weitz, D.A. and Sander, L.M. (2011). The micromechanics of three?dimensional collagen?I gels. Complexity, **16**(4), pp. 22–28.
34. Head, D.A., Levine, A.J. and MacKintosh, F.C. (2003). Distinct regimes of elastic response and deformation modes of cross-linked cytoskeletal and semiflexible polymer networks. Physical Review E, **68**(6), p.061907.
35. Lee, B., Zhou, X., Riching, K., Eliceiri, K.W., Keely, P.J., Guelcher, S.A., Weaver, A.M. and Jiang, Y. (2014). A three-dimensional computational model of collagen network mechanics. PloS one, **9**(11), p.e111896.

36. Mogilner, A., Elston, T.C., Wang, H. and Oster, G. (2002). Molecular motors: theory. In Computational cell biology (pp. 320–353). Springer, New York, NY.
37. Lepzelter, D. and M.H. Zaman. (2014). Modeling persistence in mesenchymal cell motility using explicit fibers. Langmuir, **30**(19): p. 5506–9.
38. He, X. and Jiang, Y. (2017). Substrate curvature regulates cell migration. Physical biology, **14**(3), p.035006.
39. He, X., Lee, B., Jiang, Y. (2016). Cell-ECM interactions in tumor invasion. In Systems Biology of Tumor Microenvironment (pp. 73–91). Springer, Cham.
40. Silin, D. and T. Patzek. (2006). Pore space morphology analysis using maximal inscribed spheres. Physica A: Statistical Mechanics and its Applications, **371**(2): p. 336–360
41. Angermann, B.R., et al. (2012). Computational modeling of cellular signaling processes embedded into dynamic spatial contexts. Nature methods, **9**(3): p. 283–9
42. Loew, L.M. and J.C. Schaff. (2001). The Virtual Cell: a software environment for computational cell biology. Trends in biotechnology, **19**(10): p. 401–6
43. StochSS.http://www.stochss.org (2014)
44. Madzvamuse, A., Maini, P.K. and Wathen, A.J. (2005). A moving grid finite element method for the simulation of pattern generation by Turing models on growing domains. Journal of Scientific Computing, **24**(2), pp. 247–262.
45. Xing, J., Wang, H. and Oster, G. (2005). From continuum Fokker-Planck models to discrete kinetic models. Biophysical journal, 89(3), pp. 1551–1563.
46. Baines, M. J. (1994). Moving Finite Elements, Monographs on Numerical Analysis, Clarendon, Press, Oxford.
47. Miller, K. and Miller, R.N. (1981). Moving finite elements. I. SIAM Journal on Numerical Analysis, **18**(6), pp. 1019–1032.
48. Chen, B., Legand, W.R., Wang, K., et al., (2014). Lattice light-sheet microscopy: Imaging molecules to embryos at high spatiotemporal resolution. Science, **346**, 6200.
49. Popov, K., Komianos, J. and Papoian, G.A. (2016). MEDYAN: mechanochemical simulations of contraction and polarity alignment in actomyosin networks. PLoS computational biology, **12**(4), p.e1004877.
50. Sung, B.H., Ketova, T., Hoshino, D., Zijlstra, A. and Weaver, A.M. (2015). Directional cell movement through tissues is controlled by exosome secretion. Nature communications, **6**, p.7164.

Bayesian Uncertainty Quantification for Particle-Based Simulation of Lipid Bilayer Membranes

Clark Bowman, Karen Larson, Alexander Roitershtein, Derek Stein, and Anastasios Matzavinos

Abstract A number of problems of interest in applied mathematics and biology involve the quantification of uncertainty in computational and real-world models. A recent approach to Bayesian uncertainty quantification using transitional Markov chain Monte Carlo (TMCMC) is extremely parallelizable and has opened the door to a variety of applications which were previously too computationally intensive to be practical. In this chapter, we first explore the machinery required to understand and implement Bayesian uncertainty quantification using TMCMC. We then describe dissipative particle dynamics, a computational particle simulation method which is suitable for modeling biological structures on the subcellular level, and develop an example simulation of a lipid membrane in fluid. Finally, we apply the algorithm to a basic model of uncertainty in our lipid simulation, effectively recovering a target set of parameters (along with distributions corresponding to the uncertainty) and demonstrating the practicality of Bayesian uncertainty quantification for complex particle simulations.

C. Bowman (✉)
Present address: Department of Mathematics, University of Michigan, 48109 Ann Arbor, MI, USA

Division of Applied Mathematics, Brown University, 02912 Providence, RI, USA
e-mail: clarkbow@umich.edu

K. Larson · A. Matzavinos
Division of Applied Mathematics, Brown University, 02912 Providence, RI, USA
e-mail: karen_larson@brown.edu; matzavinos@brown.edu

A. Roitershtein
Department of Mathematics, Iowa State University, 50011 Ames, Iowa, USA
e-mail: roiterst@iastate.edu

D. Stein
Department of Physics, Brown University, 02912 Providence, RI, USA
e-mail: derek_stein@brown.edu

1   Introduction

Mathematical models are vital to the study of complex systems such as biological cells [22, 26, 33, 35]. The ground truth is often unknown, and the sheer number of components may prove computational and analytic approaches to be infeasible, even when the underlying mechanics are well understood. In these scenarios, the comparative simplicity of models affords tractability at the cost of introducing uncertainty.

The most basic question that can be asked of a model is the forward problem: given a particular input, what output will be produced from the system? Supposing the model is deterministic, this question may seem straightforward – the model must simply be applied and the output observed. Yet there are many potential sources of uncertainty: the output may be subject to measurement error, or the model may depend on parameters which are themselves uncertain (see, e.g., [2, 40]), thereby propagating uncertainty forward. In the case where the model is itself stochastic (e.g., a branching process model of a disease), uncertainty may be a fundamental aspect of the system dynamics [1, 41]. The broad field which describes the mathematical treatment of models in the presence of uncertainty is often referred to as *uncertainty quantification* (UQ) [14, 21, 32].

The mathematical treatment of uncertainty in this context may be trivial – for example, accounting for a measurement error in the output (e.g., a Gaussian noise term) may be as simple as executing the forward problem, then adding a Gaussian random variable. In this case, the forward problem is solved only once, so the resulting distribution is easily sampled from, even when the model itself has considerable complexity.

Conversely, many other problems become significantly more difficult when uncertainty is introduced [41]. The classical inverse problem is one such example: what input (or set of inputs) yields a particular output? Especially if the model is complex, the model itself is unlikely to be invertible; moreover, depending on the form of the uncertainty, the set of inputs which must be considered can be prohibitively large [36]. To illustrate, consider that in the previous example of additive Gaussian noise, which is among the simplest models of measurement uncertainty, the entire input space could feasibly have produced any particular output, so long as the Gaussian noise chanced to be exactly the difference between the true output and the target output. Even if the input space is finite, the number of times the model must be applied makes this "solution" impractical for all but the simplest and most efficient models.

The Bayesian approach to this parameter estimation problem, i.e., Bayesian uncertainty quantification, attempts to leverage tools from Bayesian statistics to make the problem more tractable [4, 40]. As will be explored in Section 2, there are a variety of approaches to sampling from high-dimensional and complex distributions in the Bayesian setting [7]. As the goal of parameter estimation is the probability distribution corresponding to the relative likelihood of particular parameter values generating the observed output, this machinery is readily applied.

The main goal of this chapter is to introduce a particular recent approach to Bayesian parameter estimation which is practical even for comparatively expensive models, such as those necessary to study the dynamics of biological cells in atomistic detail. Rather than running the forward problem for a prohibitively large set of parameters, the algorithm uses a Markov chain Monte Carlo approach which evaluates the problem only at a discrete set of points. More importantly, the specific algorithm used, known as transitional Markov chain Monte Carlo (TMCMC), is massively parallelizable, and so the high cost of the model can be offset by the ability to execute many copies of the model simultaneously [3, 6, 8, 14].

To demonstrate the effectiveness of this approach, we introduce in Section 3 an example simulation of a lipid bilayer membrane, which plays a sizeable role in the motility of, e.g., eukaryotic organisms. Using a particular type of particle simulation known as dissipative particle dynamics [18, 24], we model both the lipids and fluid directly, and the membrane is held together only by the inter-molecular forces between the tails of the lipids and the surrounding water. Two free parameters are selected as input and are passed to the model on initialization, while the simulation output is calculated directly from the particle positions via a time-averaging procedure. The resulting model has considerable complexity and is moderately expensive – by standard Markov chain Monte Carlo approaches, Bayesian uncertainty quantification in such a setting is not feasible.

In Section 4, the parallelized TMCMC approach is applied to the membrane particle simulation in the context of a simple error prediction model which corrupts the output with additive Gaussian noise. To check that the resulting samples are reasonable, they are compared with a known set of parameters which was used to generate the target output. In all cases tested, the reference parameter values are assigned reasonably high probability under the sampled posterior. Namely, Bayesian parameter estimation is feasible for an example particle simulation with tens of thousands of particles, and so may have applications to a wide range of problems in mathematical and cellular biology, whose models are often too expensive to apply naïve methods.

2 Bayesian Uncertainty Quantification and Sampling Methods

2.1 Bayesian Uncertainty Quantification

To approach the parameter estimation problem using a Bayesian methodology such as TMCMC, we must first formally introduce the Bayesian formulation of uncertainty quantification [4]. The hallmark of Bayesian statistics is the assumption of prior distributions for unknown parameters – in other words, probabilities are a representation of degrees of belief; any knowledge of the unknowns *a priori*, whether from previous experience or from physical limitations, informs belief in the parameter values even before a statistical model is applied [36].

In the context of parameter estimation, the unknown parameters are the inputs to some mathematical model M (including not only model parameters, but also initial conditions, boundary conditions, etc.), which then produces a set of output quantities governed by the form of the model. A simple bacterial growth model, for example, might be parametrized by the probability p that a particular bacterium divides in a certain time period, but would also take as input the number X_0 of bacteria present at time 0. The Bayesian assumption is that the n inputs, jointly parametrized by $\boldsymbol{\theta} \in \mathbb{R}^n$, are random variables with joint prior density $\pi(\boldsymbol{\theta}|M)$.

Given a particular set of inputs $\boldsymbol{\theta}$, the model M produces a set of m data, referred to jointly as $\mathbf{D} \in \mathbb{R}^m$, according to some likelihood $p(\mathbf{D}|\boldsymbol{\theta}, M)$ – this is the content of the model itself, i.e., the mapping from inputs to outputs, which is probabilistic owing to uncertainties and stochasticity in the model M. The parameter estimation problem instead targets the posterior $p(\boldsymbol{\theta}|\mathbf{D}, M)$, i.e., the mapping from the outputs back to the inputs, which is also informed by the prior beliefs $\pi(\boldsymbol{\theta}|M)$. In this setting, $\mathbf{D}$ is known and $\boldsymbol{\theta}$ is unknown, and so it should be stressed that $p(\mathbf{D}|\boldsymbol{\theta}, M)$ is purposefully referred to as a likelihood since it is *not* a distribution in $\boldsymbol{\theta}$.

Using Bayes' theorem, the posterior distribution can be computed as

$$p(\boldsymbol{\theta}|\mathbf{D}, M) = \frac{p(\mathbf{D}|\boldsymbol{\theta}, M)\pi(\boldsymbol{\theta}|M)}{\rho(\mathbf{D}|M)}, \tag{1}$$

which additionally introduces the evidence $\rho(\mathbf{D}|M)$ of the model class, given by the multi-dimensional integral

$$\rho(\mathbf{D}|M) = \int_{\mathbb{R}^n} p(\mathbf{D}|\boldsymbol{\theta}, M)\pi(\boldsymbol{\theta}|M)d\boldsymbol{\theta}.$$

In the case where the model M is one particular model in a parametrized class of models, the evidence $\rho(\mathbf{D}|M)$ functions as a measure of the degree to which the model matches the observed data, thereby playing a critical role in model selection [5, 37]. For the parameter estimation problem, however, it should be noted that ρ does not depend on $\boldsymbol{\theta}$, and so its role in this chapter is simply to function as a normalization constant for the posterior.

To proceed further, assumptions must be made about the specific form of the likelihood $p(\mathbf{D}|\boldsymbol{\theta}, M)$. Here, we will assume that the measured data $\mathbf{D}$ are generated according to the following model prediction equation:

$$\mathbf{D} = g(\boldsymbol{\theta}|M) + \mathbf{e}, \tag{2}$$

where $g(\boldsymbol{\theta}|M)$ is the predicted output for a specific set of parameters $\boldsymbol{\theta}$ and $\mathbf{e}$ is a prediction error due to, e.g., measurement, computational, or modeling errors. Specifically, we will make the simplifying assumption that the error $\mathbf{e}$ is normally distributed with zero mean and covariance matrix $\boldsymbol{\Sigma}$, which may involve additional unknown parameters. Since g is assumed deterministic, it follows that $\mathbf{D}$ is also

normally distributed, and so the likelihood $p(\mathbf{D}|\boldsymbol{\theta}, M)$ of the observed data can be written as

$$p(\mathbf{D}|\boldsymbol{\theta}, M) = \frac{|\boldsymbol{\Sigma}(\boldsymbol{\theta})|^{-1/2}}{(2\pi)^{m/2}} \exp\left[-\frac{1}{2} J(\boldsymbol{\theta}, \mathbf{D}|M) \right], \tag{3}$$

where

$$J(\boldsymbol{\theta}, \mathbf{D}|M) = [\mathbf{D} - g(\boldsymbol{\theta}|M)]^T \boldsymbol{\Sigma}^{-1}(\boldsymbol{\theta})[\mathbf{D} - g(\boldsymbol{\theta}|M)]$$

is the weighted measure of fit between the model predictions and the measured data, $|\cdot|$ denotes determinant, and the parameter set $\boldsymbol{\theta}$ is augmented to include any unknown parameters in the covariance matrix $\boldsymbol{\Sigma}$ [5, 38]. It follows that sets of parameters $\boldsymbol{\theta}$ which reduce $J(\boldsymbol{\theta}, \mathbf{D}|M)$, which is often called the "fitness" of the parameter set $\boldsymbol{\theta}$ to the data $\mathbf{D}$, generally increase the likelihood; thus, the most likely sets of parameters (before consideration of the prior $\pi(\boldsymbol{\theta}|M)$) can be intuitively recognized as those whose output most closely matches the observed data.

While this explicit form of the likelihood can be straightforwardly calculated for any chosen set of parameters $\boldsymbol{\theta}$, each evaluation must reference the model prediction function g, which may be computationally intensive (e.g., a particle simulation). Since the parameters are assumed to be real-valued and the noise $\mathbf{e}$ spans the entire output space, computing the complete posterior $p(\boldsymbol{\theta}|\mathbf{D}, M)$ would then require an infinite number of evaluations of g. By formulating the problem in a Bayesian context, however, we gain access to the Bayesian statistician's toolkit, which contains a number of methods for approximately sampling such distributions: in particular, the class of Monte Carlo algorithms known as Markov chain Monte Carlo (MCMC).

2.2 Markov Chain Monte Carlo (MCMC)

As we have defined it, the major goal of parameter estimation is the recovery of the posterior distribution $p(\boldsymbol{\theta}|\mathbf{D}, M)$. Via (1), there are two distributions which must be known in order to achieve this goal (the evidence ρ does not depend on $\boldsymbol{\theta}$ and so, in this context, simply functions as a normalizing constant). The first is the prior $\pi(\boldsymbol{\theta}|M)$ associated with the parameters $\boldsymbol{\theta}$ in a given model class – tautologically, this is "easy," since it is (by definition) prior knowledge. The second component is more difficult: the likelihood $p(\mathbf{D}|\boldsymbol{\theta}, M)$ must also be known. As has been mentioned, the explicit form of the likelihood can only be poked at by observing specific realizations of the forward problem.

Given infinite time, it would be possible to recover the likelihood by evaluating the model prediction function g for every valid set of parameters $\boldsymbol{\theta}$. To approach the problem in a feasible, finite time, we instead turn to a set of stochastic sampling methods which have become omnipresent as computers have become more efficient: Markov chain Monte Carlo, often referred to as MCMC [4, 36]. Such methods rely

on constructing Markov chains which have as their invariant distribution a specific distribution of interest (in the context of the parameter estimation problem, the posterior $p(\boldsymbol{\theta}|\mathbf{D}, M)$). There are a number of practical issues which surround the application of MCMC to parameter estimation: to understand the nature of these difficulties, and the ways in which they are addressed in the context of Bayesian UQ, we briefly review a subset of relevant MCMC algorithms.

The most fundamental such algorithm is the Metropolis algorithm [4]. Let $p(\cdot)$ be a target distribution defined on a state space S, and suppose a function $f \propto p$ is known (this is not as absurd an assumption as it might sound at first glance – in the Bayesian framework, if p is a posterior distribution, then a likelihood function can serve the role of f). Begin with any initial guess $X_0 \in S$. The Metropolis algorithm functions by iteratively calculating a new value X_{k+1} given the current value X_k in such a way that, as $k \to \infty$, the distribution of X_k approaches p. In this way, simply calculating the values X_k up to some large k produces approximate samples from p.

The specific method for updating the guesses X_k is to make a proposal Y, chosen at random according to a symmetric proposal distribution $q(\cdot, X_k)$ (e.g., a multivariate Gaussian centered at X_k). The algorithm then chooses whether to accept the proposal (in which case $X_{k+1} = Y$) or reject it (in which case $X_{k+1} = X_k$). By choosing the acceptance probability to be the ratio $f(Y)/f(X_k)$, the invariant distribution of the chain becomes the target distribution p. Convergence to the stationary distribution can be proven easily if q is chosen carefully – in the case of a Gaussian, its infinite support makes possible the transition to any state x with $p(x) > 0$ (irreducibility), while the possibility of rejecting a proposal ensures aperiodicity [34].

Even this basic algorithm appears to have ready applications to the parameter estimation problem. Choosing the invariant distribution p to be the posterior $p(\boldsymbol{\theta}|\mathbf{D}, M)$, along with a standard proposal distribution q (a multivariate Gaussian will work for real-valued parameters), the only difficulty seems to be the calculation of some $f \propto p$ – this is the same problem as was encountered initially, where the likelihood function is not known, and it is not computationally feasible to estimate the likelihood over the entire parameter space. The key is that the Metropolis algorithm does not rely on the general form of f, but instead only relies on the calculation of f at various points chosen according to the proposal distribution q. Supposing the algorithm provides a guess Y for the set of parameters, the likelihood $f(Y) = p(\mathbf{D}|Y, M)$ can be estimated as in (3), assuming output is generated according to the model prediction equation (2).

The main difficulty of this approach has been alluded to already – the convergence to the stationary distribution is asymptotic, and the time to convergence can vary greatly (depending on q, the dimensionality, and the form of the likelihood). Specifically, the algorithm may get "stuck" sampling from a region where the fit appears to be locally optimal for long times, as the probability of transitioning to other regions of high density may be extremely low (this is known as a probabilistic *bottleneck*). This problem can be seen in Figure 1, which uses the Metropolis algorithm to approach a simple toy problem in one dimension. The result is that approximate sampling from the posterior $p(\boldsymbol{\theta}|\mathbf{D}, M)$ may require running the chain for longer than is computationally feasible.
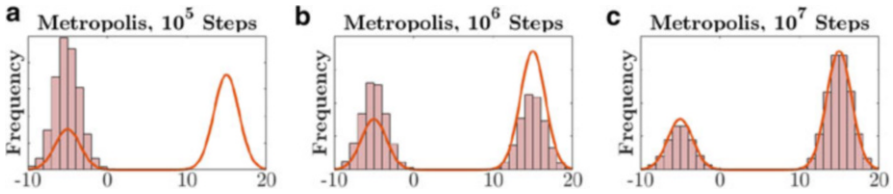
Fig. 1 The Metropolis algorithm applied to the density $p(x) \propto 0.3e^{-0.2(x+5)^2} + 0.7e^{-0.2(x-15)^2}$ (solid curve). The proposal distribution used is a Gaussian with $\sigma = 4$. Shown are the most recent 10% of samples after the specific number of steps. (a) For short times, the chain gets "stuck" in the smaller peak, unable to cross the bottleneck to explore the full distribution. (b) For intermediate times, although the distribution is explored fully, the chain does not spend the correct proportion of time in each peak. (c) For large times, convergence to the invariant distribution is guaranteed via irreducibility and aperiodicity of the chain.

Naïvely, one way to address this problem would be to choose an extremely broad proposal distribution q, thereby allowing the chain to jump across bottlenecks in a single step. Unfortunately, this has the second effect of greatly increasing the number of proposals which are rejected. Instead, we borrow ideas from a second MCMC method which is more robust to the problem of probabilistic bottlenecks. Simulated annealing is an approach to nonconvex optimization which introduces a *cooling schedule* to ensure that, in the short term, the chain can transition across regions where the likelihood may be extremely low [15, 16, 30, 34].

Simulated annealing bears a strong resemblance to the Metropolis algorithm; it functions by making iterative proposals with a carefully chosen probability of acceptance. Unlike the Metropolis algorithm, the probability depends on the iteration k, such that the probability of transitioning to a region of low probability is much higher when k is small. The acceptance probability is often stated in terms of a temperature $T(k)$ which is monotonically decreasing, owing to its connections to the role of temperature in statistical mechanics (and begetting the term "cooling schedule"). The common explicit acceptance probability $\exp((\log f(Y) - \log f(X_k))/T(k))$ coincides with the Metropolis algorithm in the case that $T(k) = 1$, and so simulated annealing can be thought of as a generalization of Metropolis [15, 30, 36].

Since the transition probability depends on k, the chain $\{X_k\}$ no longer has an invariant distribution. Instead, each step of the chain has its own unique "invariant distribution" p_k. As k increases, $T(k)$ decreases, and if T falls to zero, the weak limit of the p_k should put its entire mass at the global maximum value of f (this is why simulated annealing is effective at optimization). Conversely, for small k, a large temperature greatly increases the probability of accepting a transition to a region where f is much smaller. If the cooling schedule is chosen to scale appropriately, it can thus be very effective at facilitating transitions across bottlenecks like that of Figure 1. A simple application of simulated annealing to the toy sampling problem can be seen in Figure 2.

The specific MCMC algorithm which will be applied to the Bayesian parameter estimation problem, known as transitional Markov chain Monte Carlo (TMCMC),
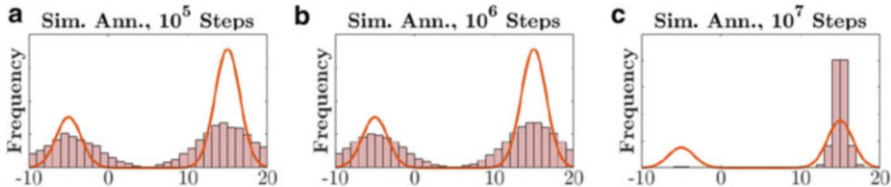
Fig. 2 Simulated annealing with cooling schedule $T(k) = 5(1 - 10^{-7}k)$ for the toy problem of Figure 1. Again, the proposal distribution used is a zero-mean Gaussian with $\sigma = 4$. Shown are the most recent 10% of samples after the specific number of steps. (a, b) Even for short times, the high temperature smooths the target distribution, allowing sampling from both peaks. (c) As the temperature falls to zero, the distribution clusters around the global maximum.

makes use of the ideas central to both of these algorithms [14, 40]. Each step of the chain uses the Metropolis algorithm to draw approximate samples from a target intermediate distribution, while the parent chain uses a cooling schedule to *transition* from the prior to the posterior, much as simulated annealing transitions from smoothed to peaked. The specifics of TMCMC, as well as its explicit implementation in the UQ framework, are detailed in Section 2.3.

2.3   Transitional Markov Chain Monte Carlo (TMCMC)

As mentioned in the previous section, MCMC algorithms are often used to generate approximate samples from high-dimensional and complex posterior distributions. While basic algorithms like Metropolis and simulated annealing will function in this regard, more efficient algorithms which improve the convergence rate are more useful in practice, since the convergence times of MCMC algorithms for some distributions (especially those with bottlenecks) can be quite long. Although there do exist more efficient methods with proven convergence results (in particular, delayed rejection adaptive Metropolis (DRAM) [13] and differential evolution random sampling MC (DREAM) [39] are commonly used), we will use here the TMCMC algorithm, which has the computational advantage of being massively parallelizable due to its use of a large number of independent Markov chains [8, 14, 40].

Like simulated annealing, TMCMC attempts to avoid probabilistic bottlenecks by transitioning to the target distribution from a broad initial distribution (in this case, the prior $\pi(\boldsymbol{\theta}|M)$) that allows the chain to explore regions of low probability. To accomplish this, a series of intermediate probability densities are constructed iteratively:

$$f_j(\boldsymbol{\theta}) \sim [p(\mathbf{D}|\boldsymbol{\theta}, M)]^{q_j} \cdot \pi(\boldsymbol{\theta}|M), \quad j = 0, \ldots, \lambda$$

$$0 = q_0 < q_1 < \ldots < q_\lambda = 1.$$

Note that f_0 is simply the prior distribution, while f_λ is the posterior distribution (i.e., the product of the prior and likelihood, as in (1), up to the normalization constant $\rho(\mathbf{D}|M)$).

The basic idea of TMCMC is as follows: begin with a collection of samples from the prior distribution (which is easy, so long as the prior has a simple form such as a Gaussian or uniform distribution). Then, iteratively resample in such a way that the samples at each step j correspond to the intermediate density f_j. At the conclusion of the algorithm, the samples will be asymptotically distributed as f_λ (the posterior), with greater accuracy for small step sizes and large numbers of samples. During each iteration, the resampling procedure involves the use of a large number of independent Markov chains which are evolved using the Metropolis algorithm; since the chains are independent, the algorithm is easily parallelizable, and so the potentially expensive cost of evaluating the likelihood $p(\mathbf{D}|\boldsymbol{\theta}, M)$ is offset by the ability to run multiple evaluations concurrently.

The algorithm (Algorithm 1, below) begins by taking N_0 samples $\boldsymbol{\theta}_{0,k}$ (indexed first by generation, then by sample number) from the prior distribution $f_0(\boldsymbol{\theta}) = \pi(\boldsymbol{\theta}|M)$. For each stage j of the algorithm, it uses the current set of samples to evaluate the plausibility weights $w(\boldsymbol{\theta}_{j,k})$ as

$$w(\boldsymbol{\theta}_{j,k}) = \frac{f_{j+1}(\boldsymbol{\theta}_{j,k})}{f_j(\boldsymbol{\theta}_{j,k})} = [p(\mathbf{D}|M, \boldsymbol{\theta}_{j,k})]^{q_{j+1}-q_j}.$$

Note that since the plausibility weights are calculated as the likelihood raised to a nonnegative power, the observed data $\mathbf{D}$ is more likely to have come from sampled parameters $\boldsymbol{\theta}_{j,k}$ with higher plausibility weights (thus begetting the term). q_{j+1} has not yet been defined; the choice of q_{j+1} is what determines how smoothly the

---

Algorithm 1 TMCMC

1: **procedure** TMCMC Ref. [14]
2: BEGIN, SET $j = 0, q_0 = 0$
3: **Generate** $\{\boldsymbol{\theta}_{0,k}, k = 1, \ldots, N_0\}$ from prior $f_0(\boldsymbol{\theta}) = \pi(\boldsymbol{\theta}|M)$ and compute likelihood $p(\mathbf{D}|\boldsymbol{\theta}_{0,k}, M)$ for each sample.
4: *loop*:
5: **WHILE** $q_{j+1} \leq 1$ **DO:**
6:     **Analyze** samples $\{\theta_{j,k}, k = 1, \ldots, N_j\}$ to determine q_{j+1}, weights $\overline{w}(\boldsymbol{\theta}_{j,k})$, covariance $\boldsymbol{\Sigma}_j$, and estimator S_j of $\mathbb{E}[w(\boldsymbol{\theta}_{j,k})]$.
7:     **Resample** based on samples available in stage j in order to generate samples for stage $j + 1$ and compute likelihood $p(\mathbf{D}|\boldsymbol{\theta}_{j+1,k}, M)$ for each.
8:     **if** $q_{j+1} > 1$ **then**
9:         BREAK,
10:     **else**
11:         $j = j + 1$
12:         **goto** *loop*.
13:     **end**
14: **END**

prior distribution transitions to the posterior distribution (with a smoother transition coming at the cost of increased computational requirements). Recent literature suggests that q_{j+1} be chosen to make the covariance of the plausibility weights at stage j smaller than a tolerance covariance, recommending the specific value 1.0 [8, 14].

The algorithm then calculates the average S_j of the plausibility weights, the normalized plausibility weights $\overline{w}(\boldsymbol{\theta}_{j,k})$, and the scaled covariance $\boldsymbol{\Sigma}_j$ of the $\boldsymbol{\theta}_{j,k}$, which will be used to generate the next generation of samples $\boldsymbol{\theta}_{j+1,k}$:

$$S_j = \frac{1}{N_j} \sum_{k=1}^{N_j} w(\boldsymbol{\theta}_{j,k}),$$

$$\overline{w}(\boldsymbol{\theta}_{j,k}) = w(\boldsymbol{\theta}_{j,k}) / \sum_{k=1}^{N_j} w(\boldsymbol{\theta}_{j,k}) = w(\boldsymbol{\theta}_{j,k})/(N_j S_j),$$

$$\boldsymbol{\Sigma}_j = \beta^2 \sum_{k=1}^{N_j} \overline{w}(\boldsymbol{\theta}_{j,k})[\boldsymbol{\theta}_{j,k} - \boldsymbol{\mu}_j][\boldsymbol{\theta}_{j,k} - \boldsymbol{\mu}_j]^T.$$

Here, $\boldsymbol{\Sigma}_j$ is calculated using the sample mean $\boldsymbol{\mu}_j$ of the $\boldsymbol{\theta}_{j,k}$ and a scaling factor β.

As an aside, it is worth noting that the product of the S_j, i.e.,

$$S = \prod_{j=0}^{\lambda-1} S_j,$$

is an asymptotically unbiased estimator of the evidence $\rho(\mathbf{D}|M)$ [8], and so TMCMC is especially efficient for model selection (see Section 2.1).

The algorithm then independently generates N_{j+1} samples $\hat{\boldsymbol{\theta}}_{j+1,k}$ by choosing randomly among the current set of samples $\{\boldsymbol{\theta}_{j,k}\}$ such that $\hat{\boldsymbol{\theta}}_{j+1,\ell} = \boldsymbol{\theta}_{j,k}$ with probability $\overline{w}(\boldsymbol{\theta}_{j,k})$. Since the samples are chosen independently, there is the possibility of selecting the same sample from the current generation multiple times – call $n_{j+1,k}$ the number of times that $\boldsymbol{\theta}_{j,k}$ is chosen (which could range from 0 to N_{j+1}). Each unique sample is used as the starting point of an independent Markov chain whose behavior is governed by the Metropolis algorithm with target distribution f_j and a proposal distribution normally distributed with covariance $\boldsymbol{\Sigma}_j$ and centered at the current value. The scaling parameter β thus plays the role of controlling the rejection rate and jump size; recent literature recommends $\beta = 0.2$ [2, 8].

Finally, the samples $\boldsymbol{\theta}_{j+1,k}$ are drawn from the Markov chains, with each sample being the value obtained by stepping a chain forward once. $n_{j+1,k}$ samples are drawn from the chain which started at $\boldsymbol{\theta}_{j,k}$, yielding N_{j+1} samples total. At this

point, the iteration j is complete, and the algorithm either moves forward to generation $j + 1$ or terminates if $q_{j+1} > 1$.

With the approach established, it remains only to apply the TMCMC approach to the Bayesian UQ setting in the context of a sample problem. In what follows, we describe a particle simulation method with broad applications to cell biology, along with a specific implementation which models a lipid membrane and fluid. The results of applying the TMCMC algorithm to this model appear in Section 4.

3   A Biological Model: 2D Lipid Bilayer Membrane

Bayesian uncertainty quantification is agnostic to its forward problem: it functions exclusively with respect to the parameter space and the problem output. Historically, the high-dimensional optimization literature has largely focused on the particular forward problem of a (usually very complicated) function evaluation via, e.g., convex optimization methods or simulated annealing. In this chapter, we show that the general Bayesian framework (and its ability to discern *distributions*, rather than just critical points) can be applied to a much more complicated system, namely, the output of a comparatively expensive particle simulation. It follows that Bayesian uncertainty quantification has a number of applications in molecular biology, where particle simulations are both feasible and revealing of dynamics which are difficult to study experimentally or with simpler models.

The simplest and most widely used class of particle simulations is *molecular dynamics*, i.e., the direct simulation of atoms or molecules via Newton's laws [18, 23]. Molecular dynamics simulations operate by writing a large coupled system of ordinary differential equations which track the locations of particles, then stepping time forward in discrete steps (usually via a finite difference scheme). Since all particles are modeled explicitly and all pairwise forces (e.g., the Lennard-Jones potential between neutral particles or Coulomb potential between charged particles) are included, molecular dynamics is often considered a ground truth for systems where such simulations are computationally feasible. Conversely, since each atom or molecule is tracked individually, the cost of such simulations grows massively with the scale of the system. For many systems on the order of biological cells, where the number of molecules may be in the billions, current computing power is not sufficient for practical simulation via molecular dynamics [18].

There are a number of approaches for bridging the basic idea of particle simulation to the so-called "mesoscale," the spatial scale between the realms of molecular dynamics and continuum methods. One common approach, referred to as Brownian dynamics, does not explicitly model fluid particles, instead modeling only the solute, which is usually the material of interest. Forces which would be exerted on the solute by the solvent are incorporated via Gaussian force terms. As fluid usually composes the bulk of such simulations, Brownian dynamics simulations are orders of magnitude cheaper than comparable simulations using molecular dynamics. However, since the fluid particles are not modeled explicitly,

nonequilibrium phenomena in the fluid, e.g., microflows, may be lost. In systems where such flows may dictate important properties of the mechanics, Brownian dynamics simulations may not be appropriate.

We utilize here the method of dissipative particle dynamics (DPD), a second mesoscale approach which continues to explicitly model the fluid [18, 24]. Instead, the improvement in computational efficiency is derived from rescaling the particles themselves: rather than modeling individual atoms or molecules, the DPD method tracks the movement of "dissipative particles," which correspond to clumps of many atoms or molecules. This coarse-graining introduces a number of physical problems. Most notably, clumps of particles, which comprise mostly empty space, should be able to pass through each other, but should experience varying forces depending on the degree to which they overlap. To address these difficulties, the dissipative particles interact via artificial forces, chosen to achieve target physical properties and to obey the correct hydrodynamic behavior on aggregate [9, 31]. Comparisons with Navier-Stokes and molecular dynamics simulations have shown the dissipative particle dynamics method to produce accurate results for a variety of simple- and complex-geometry flows [19].

Dissipative particle dynamics excels at modeling mesoscopic biological systems, as both solute and solvent can be modeled with dissipative particles with varying forces and coefficients. In addition, the reduced number of particles due to the coarseness of the method make DPD feasible for many applications. In this section, we describe explicitly the DPD formulation and the forces it comprises, then use the DPD method to implement an example of a biological application: a simulation of a lipid bilayer membrane immersed in water.

3.1   The Dissipative Particle Dynamics (DPD) Method

In general, since DPD forces are defined on a pairwise basis between particles, they can be used in conjunction with other sets of forces by selectively applying each force only to the desired interactions. Here, for the sake of notational simplicity, we will analyze a system consisting of dissipative particles alone. Let the mass and velocity of particle i be given by m_i and $\mathbf{v}_i$, respectively. The equation of motion for particle i can be written as

$$m_i \frac{d\mathbf{v}_i}{dt} = \sum_{j \neq i} \mathbf{F}_{ij}^C + \sum_{j \neq i} \mathbf{F}_{ij}^D + \sum_{j \neq i} \mathbf{F}_{ij}^F, \tag{4}$$

where $\mathbf{F}_{ij}^C$ is a conservative force deriving from a potential exerted on particle i by the j-th particle, $\mathbf{F}_{ij}^D$ is a dissipative force due to the exchange of momentum, and $\mathbf{F}_{ij}^R$ is a random force inducing the random motion of particles.

Intuitively, the three forces of the DPD interaction follow from the nature of the dissipative particles as "clumps" of atoms and molecules. When two particles are
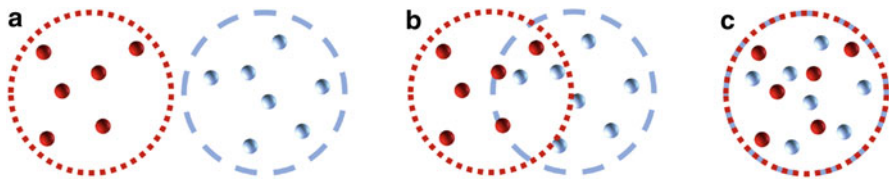
Fig. 3 Schematic of DPD particles and their degree of interaction. Moving from (a) to (c), the dissipative particles move together until completely overlapping. Despite occupying the same location in space, their component atoms need not overlap, and so the repulsive potential should not diverge.

moved closer together, more of their components become close enough to interact, and so the particles should increasingly repulse each other. However, since the dissipative particles are mostly empty space, this repulsion should not diverge as they are forced together, since the component molecules could avoid overlap even if their parent dissipative particles occupy the exact same location. This justifies a soft conservative force – pairwise repulsion that does not diverge as the interparticle separation $\mathbf{r}_{ij} = \mathbf{r}_i - \mathbf{r}_j \to 0$ (Figure 3).

In addition to center-to-center repulsion due to the degree of overlap, particles should also exhibit drag when passing through each other at nonzero velocity. The component atoms and molecules of each particle would be driven together, and the resulting collisions would impart a greater force than if the parent particles were simply held at a fixed distance. This "drag" between particles should thus scale with two different factors: the velocity (affecting the energy imparted when components collide) and the degree of overlap (affecting the number of collisions). This justifies a dissipative force which depends on both the relative velocity $\mathbf{v}_{ij} = \mathbf{v}_i - \mathbf{v}_j$ of particle i with respect to particle j and on the interparticle separation $\mathbf{r}_{ij}$.

Finally, there should be some correction for the positions and velocities of the components, which are not tracked. Atoms and molecules within the dissipative particles interact in Brownian-like fashion, and so the interaction between particles should have a random component to account for the ensemble of component velocities. This justifies a random force which scales with the temperature T of the system, since higher temperatures increase the magnitude of the Brownian-style interaction between the molecules in each dissipative particle. Note that, like the other two forces, the random force $\mathbf{F}_{ij}^R$ is a force between two particles, and does not affect individual particles in isolation – though the atoms and molecules within a single dissipative particle also interact, any exchange of momentum does not affect the momentum of the dissipative particle which contains them.

Defined in this fashion, the forces are consistent with Galilean invariance, as they depend only on the relative positions and velocities of the particles. On physical grounds, it is also assumed that the dissipative force $\mathbf{F}_{ij}^D$ depends linearly on the momentum and the random force $\mathbf{F}_{ij}^R$ is independent of the momentum (see, e.g., [9] or [18] for a more detailed discussion of these assumptions). The following

functional forms for $\mathbf{F}_{ij}^D$ and $\mathbf{F}_{ij}^R$ satisfy these assumptions and are usually adopted in the context of the DPD methodology:

$$\begin{cases} \mathbf{F}_{ij}^D = -\gamma \, w_D\big(|\mathbf{r}_{ij}|\big)(\mathbf{e}_{ij} \cdot \mathbf{v}_{ij})\mathbf{e}_{ij}, \\ \mathbf{F}_{ij}^R = \sigma \, w_R\big(|\mathbf{r}_{ij}|\big)\mathbf{e}_{ij}\xi_{ij}, \end{cases} \tag{5}$$

where $\mathbf{e}_{ij} = \mathbf{r}_{ij}/|\mathbf{r}_{ij}|$ is the center-to-center unit vector, $w_D(\cdot)$ and $w_R(\cdot)$ are arbitrary weighting functions describing the scaling of each force with the interparticle distance $|\mathbf{r}_{ij}|$, γ and σ are adjustable coefficients of interaction, and ξ_{ij} is a Gaussian white-noise term with

$$\mathbb{E}\,\xi_{ij}(t) = 0 \text{ and } \mathbb{E}\big(\xi_{ij}(t)\xi_{k\ell}(\tau)\big) = (\delta_{ik}\delta_{j\ell} + \delta_{i\ell}\delta_{jk})\delta(t - \tau),$$

where the δ terms are defined as usual, i.e., δ_{ik} is equal to one if $i = k$ and zero otherwise, and $\delta(t - \tau)$ is the Dirac distribution. In order to ensure that the total momentum is conserved, it is assumed that $\xi_{ij}(t) = \xi_{ji}(t)$ for all $t > 0$.

By substituting (5) into (4) we obtain a system of stochastic differential equations that form the core of the DPD approach:

$$\begin{cases} d\mathbf{r}_i = \mathbf{v}_i dt \\ d\mathbf{v}_i = \dfrac{1}{m_i} \left(\displaystyle\sum_{j \neq i} \mathbf{F}_{ij}^C(\mathbf{r}_{ij}) - \sum_{j \neq i} \gamma \, w_D\big(|\mathbf{r}_{ij}|\big)(\mathbf{e}_{ij} \cdot \mathbf{v}_{ij})\mathbf{e}_{ij} \right) dt \\ \qquad + \dfrac{1}{m_i} \displaystyle\sum_{j \neq i} \sigma \, w_R\big(|\mathbf{r}_{ij}|\big)\mathbf{e}_{ij} \, dW_{ij} \end{cases} \tag{6}$$

where for each i, j, W_{ij} is a Wiener process and $W_{ij} = W_{ji}$.

To ensure the system is properly thermostatted, it should be checked that the long-time asymptotics converge to the Gibbs canonical ensemble of particles interacting via the conservative force alone at a target temperature T – in other words, the dissipative force (which removes energy from the system) and random force (which can influence the energy in either direction) should be balanced such that, on average, the behavior is what would be predicted for particles bouncing around at the specified temperature. Español and Warren [9] proved this result for *any* conservative force field $\mathbf{F}_{ij}^C$ given that the following two conditions, which relate the dissipative and random forces (and are thus referred to as the fluctuation-dissipation conditions), are satisfied:

$$\begin{cases} w_D\big(|\mathbf{r}_{ij}|\big) = w_R^2\big(|\mathbf{r}_{ij}|\big) \\ \sigma^2 = 2\gamma k_B T. \end{cases} \tag{7}$$

The process of implementing the DPD method, in net, thus consists of numerically approximating the solution of (6) while ensuring that the conditions in (7) are satisfied. There are a number of free parameters which can be tuned to yield desired physical properties and types of interaction. The conservative force between i and j is most commonly taken to decay linearly from a specified value a_{ij} to zero at a distance of r_{ij}^c, making a_{ij} the conservative coefficient (i.e., coefficient of repulsion) and r_{ij}^c a cutoff radius. The weighting function $w_D(\cdot)$ (and thus $w_R(\cdot)$ via fluctuation-dissipation) are also usually taken to fall to zero at the cutoff radius r_{ij}^c. A final important parameter is the coefficient γ_{ij} of dissipative interaction, which can influence physical properties such as viscosity. Many physical observables have been derived in terms of these free parameters (see, e.g., [27]), and so a fluid with certain desired properties such as compressibility or viscosity can be simulated accurately.

Actual simulation by the DPD method usually utilizes a finite difference scheme (in particular, the velocity-Verlet method). Various explicit numerical implementations of the DPD method are detailed in [18]. Here, we chose to code the DPD membrane simulation using the LAMMPS molecular dynamics package, an open-source C++ framework for particle simulations [28].

3.2 Simulation Setup and Parameters

The sample simulation proposed here is the modeling of a finite patch of lipid bilayer membrane composed of lipids with hydrophobic and hydrophilic parts. One of the chief advantages of modeling such a system with dissipative particle dynamics is the difference in spatial scale between solute and solvent: a typical lipid is many times larger than a single water molecule, and so their interaction may be challenging to model by conventional means. In a coarse-grained method such as DPD, the lipid might be modeled as a bead-spring chain, with the beads (i.e., DPD particles) corresponding to different sections of the lipid. Conversely, a DPD particle modeling the solvent, depending on choice of scale, might model several water molecules. In this way, the actual particles which interact via DPD potentials are of similar scale, and their interactions can be easily adjusted via the DPD force coefficients, e.g., the conservative coefficient a_{ij} or dissipative coefficient γ_{ij} between particles i and j.

The principle (and easiest to conceptualize) mode of interaction between particles is via the conservative force, which dictates the repulsion between coarse-grained clumps as a function of their degree of overlap. We define three types of DPD particle: the fluid, the hydrophilic lipid head particles, and the hydrophobic lipid tail particles. Achieving hydrophobicity in the lipid tails is possible by adjusting the strength of conservative interactions such that the repulsion between two tail particles is less than that between one tail and one fluid particle. Similarly, hydrophilicity can be achieved by choosing the repulsion between one head and one fluid particle to be less than that between one head and one tail particle.

Table 1 Pairwise coefficients for DPD membrane

a_{ij}	Head	Tail	Water	γ_{ij}	Head	Tail	Water	r_{ij}^c	Head	Tail	Water
Head	15.0	50.0	35.0	Head	4.5	9.0	4.5	Head	2.5	1.75	1.75
Tail	50.0	15.0	75.0	Tail	9.0	4.5	20.0	Tail	1.75	1.0	1.0
Water	35.0	75.0	25.0	Water	4.5	20.0	4.5	Water	1.75	1.0	1.0

Fig. 4 Schematic of a lipid with one head particle (red) and two tails comprising six tail particles each (gray). Bonds are shown as thin rods. The angle between tails, labeled ϕ, minimizes energy at a specified neutral angle ϕ_0.
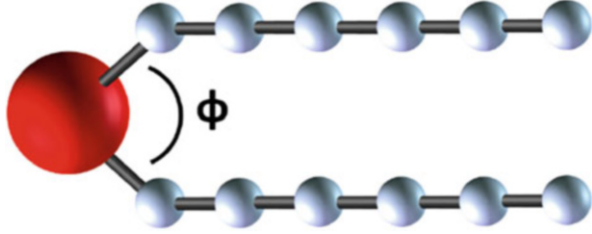
The specific values chosen for this simulation, which appear in Table 1, are adapted from existing literature on DPD membranes [11] as well as the compressibility argument for water in [12]. Values are given in nondimensionalized units, as is common in DPD literature: see [29] for a description of the Lennard-Jones units used. If desired, all measurable quantities can be scaled to real units by physical arguments.

Each lipid is composed of a single lipid head connected to two lipid tails of six particles each via harmonic bonds, each of which uses the spring potential $E_{ij} = 64(r_{ij} - 0.5)^2$ so that the neutral length of a bond is 0.5. Three-body potentials $E_{ijk} = 50(1 - \cos(\phi_{ijk} - \phi_0))$ are imposed along consecutive bonds to provide stiffness, where ϕ_{ijk} is the angle between bonds ij and jk and ϕ_0 is the resting angle. This facilitates specification of the neutral angle between the membrane tails, i.e., the angle preferentially formed between the line segments connecting the head particle to the first particle in each tail, labeled as ϕ in Figure 4. The neutral angle between tail bonds is fixed at $180°$.

The membrane of [11] uses multiple head particles to account for the relative size of the hydrophilic head as compared to the hydrophobic tails. Here, we instead adjust the effective size of the head particle by changing the cutoff radius between different types of particles. The pairwise potential radii can be seen in Table 1. The masses are adjusted accordingly, so that a particle effectively 2.5 times larger in one dimension has a mass $2.5^3 = 15.625$ times greater, with the fluid particles having unit mass.

Lipids are placed in a two-dimensional 96×64 periodic simulation box in two adjacent rows with the head particles toward the outside, as in Figure 5(a). The separation between lipids, spacing between tail particles within a lipid, and total length of the membrane patch are free parameters, here chosen to be 0.8, 0.5, and 64, respectively. The remainder of the simulation box is filled with fluid particles, placed on the vertices of a square lattice with edge length 2.0. The system is then evolved in time using a velocity-Verlet scheme (see, e.g., [27]) with timestep
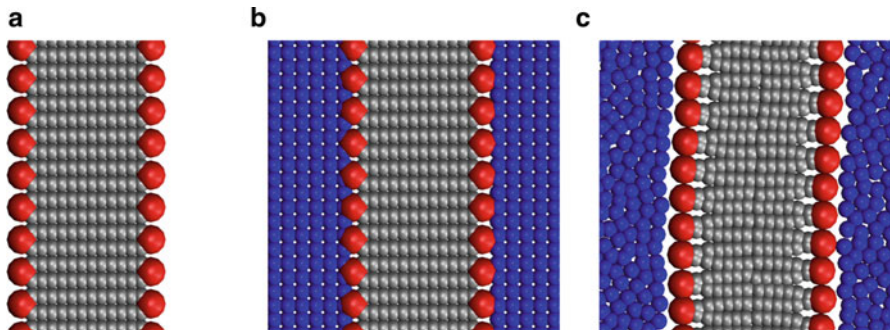
Fig. 5 (a) Membrane initialization. Head particles (red) line the outside; each has two lipid tails of six tail particles (gray) directed inward. (b) Fluid initialization. Water particles are placed on the vertices of a square lattice outside the membrane. (c) Membrane after 2500 steps.
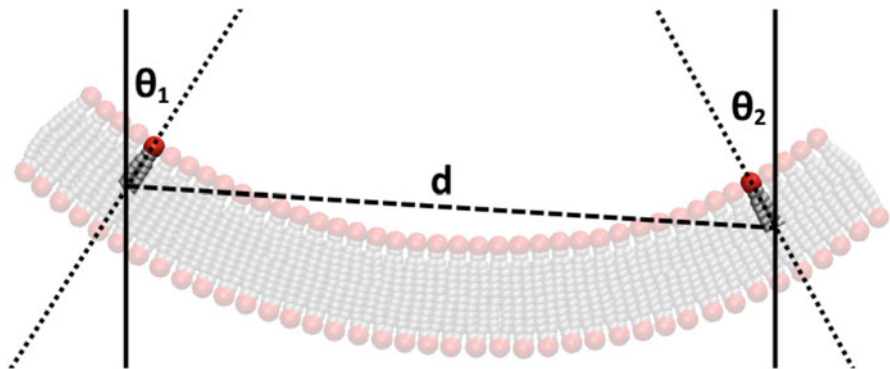
Fig. 6 Schematic of tracked lipids and method for determination of curvature. Angles are with respect to a fixed reference angle (here shown as vertical lines) and can thus be negative. The derivation for approximate curvature κ relies only on the absolute difference $|\theta_2 - \theta_1|$ and tail-to-tail distance d.

0.03 and nondimensional temperature 0.1. The phases of initialization and resulting membrane at time $t = 75$ appear in Figure 5.

To be used as a forward problem where Bayesian uncertainty quantification can be applied, the input and output spaces must be specified. Here, we choose the output to be the equilibrium curvature of the membrane, as measured from the particle simulation. Within the upper layer, two lipids, five molecules from the membrane edge on either side, are chosen to be tracked (see Figure 6). In each timestep and for each of the two tracked lipids, the position of the head particle and the average position of the furthermost tail particles are used to compute the angle (relative to vertical; denoted θ_1 and θ_2 for first and second tracked lipid, resp.) and location along the bilayer interface.

The radius of the circle which passes through the given points and subtends the difference in angles $|\theta_2 - \theta_1|$ over that span is given in terms of the distance d between the points as

$$R = \frac{2}{d} \sin \left| \frac{\theta_2 - \theta_1}{2} \right|,$$

and the curvature (assuming it is constant along the membrane) is approximated as

$$\kappa \approx \frac{1}{R} = \frac{d}{2 \sin \left| \frac{\theta_2 - \theta_1}{2} \right|}.$$

After an equilibration period of 20000 steps, the curvature is measured at each timestep for the following 30000 steps, with the average curvature over this period used as the one-dimensional output of the simulation. A single serial run of the simulation, which tracks ~ 15000 dissipative particles, requires five to ten minutes on an Intel Xeon E5–2670.

There are a number of different biological phenomena which affect the curvature of lipid membranes in eukaryotic phyla; one such mechanism is differences in lipid structure (e.g., tail length or angle) between monolayers [10, 17, 25]. As these structural differences are easily incorporated into the bead-spring model lipids, we choose a set of parameter values describing the lipid shape – specifically, the set of possible neutral angles between lipid tails (ϕ_0 in Figure 4) on the top and bottom layers of the membrane, specified separately – as the parameter space for the forward model. Increasing ϕ_0 in one lipid layer causes the layer to lengthen as the tails are forced further apart, altering the net curvature of the membrane. Given a target curvature, Bayesian statistics can be used to find the probability distribution in the parameter space which describes the set of parameters which, when accounting for noise in measurement and in the stochasticity of the simulation, could yield the target output. The specific application of Bayesian uncertainty quantification to the model membrane system is described in Section 4.

4 Uncertainty Quantification for Particle Simulations

In the previous section, we developed a computational model for a lipid membrane using dissipative particle dynamics. We additionally described a target observable, namely, the curvature κ of the membrane, and detailed a method of measurement. Although a variety of free parameters may affect the membrane curvature, we isolated two parameters to examine: the resting angle between lipid tails in the top and bottom layers, denoted ϕ_t and ϕ_b, respectively. (Since there is no meaningful

notion of direction as might be imposed by, e.g., gravity, top and bottom are defined with respect to the y axis at initialization, where the top layer is in the $-y$ direction.)

In Section 2.1, we described a framework for Bayesian uncertainty quantification in the context of the model prediction equation (2), reproduced below:

$$\mathbf{D} = g(\boldsymbol{\theta}|M) + \mathbf{e}$$

Namely, we assume there exists a function g which, given a particular model M, deterministically maps the parameter space to the output space, and that observable measurement of the output is corrupted by additive Gaussian noise $\mathbf{e}$, which has zero mean and covariance matrix $\boldsymbol{\Sigma}$. In the context of the membrane model, it may be useful intuitively to think of g as the mapping from the parameter space to the mean curvature, while the noise $\mathbf{e}$ corresponds to a hypothetical measurement or modeling error which might have a Gaussian form. We are specifically interested in the subset of Bayesian UQ known as parameter estimation: given a reference curvature κ^* (and assuming, as an example, uniform priors on the lipid tail angles ϕ_t and ϕ_b over some reasonable range), what is the form of the posterior $p(\boldsymbol{\theta}|\kappa^*, M)$?

It is worth noting that we make no assumptions about the covariance $\boldsymbol{\Sigma}$ of the additive noise. Moreover, it is clear that $\boldsymbol{\Sigma}$ should have a significant effect on the posterior distribution. Consider the following example: with a reference curvature $\kappa^* = 0.1$, running the simulation with a particular set of angles $\boldsymbol{\theta}_1$ yielded a mean curvature $\kappa_1 = 0.11$, while a simulation with a second set of angles $\boldsymbol{\theta}_2$ yielded a mean curvature $\kappa_2 = 0.105$. If $|\boldsymbol{\Sigma}|$ were known to be very small, e.g., $|\boldsymbol{\Sigma}| = 10^{-9}$, then the likelihood of the parameters $\boldsymbol{\theta}_2$ should be much greater – being hundreds of standard deviations further from the reference value κ^* is comparatively unlikely. Conversely, if $|\boldsymbol{\Sigma}|$ were known to be very large, e.g., $|\boldsymbol{\Sigma}| = 1$, then the likelihoods of both sets of parameters should be nearly equal – given such a large measurement error in the reference curvature and the proximity of $\boldsymbol{\theta}_1$ and $\boldsymbol{\theta}_2$, either is similarly plausible. A natural way of incorporating this effect is to augment the input space with a parametrization of $\boldsymbol{\Sigma}$, as detailed in Section 2.1. In the context of the membrane simulation, the result is a parameter space of dimensionality $n = 3$ which incorporates the two model parameters (ϕ_t and ϕ_b) as well as the standard deviation s of the measurement error $\mathbf{e}$ (since the output – curvature – is one dimensional, $\boldsymbol{\Sigma}$ is scalar, and so we will hereafter refer only to the estimated standard deviation s and reference standard deviation $\sigma = \sqrt{\boldsymbol{\Sigma}}$ of the noise).

The following sets of results were sampled using a particular high-performance parallel version of TMCMC known as $\Pi 4U$ [14]. In each case, the prior distribution $\pi(\boldsymbol{\theta}|M)$ is taken to be uniform over $[0, 120] \times [0, 120] \times [0, 0.001] \in \mathbb{R}^3$ (the first two parameters, ϕ_t and ϕ_b, are specified in degrees; the third parameter, s, is specified in units of curvature).

Targeting arbitrarily chosen reference curvatures, it would be difficult to evaluate the effectiveness of the algorithm in recovering a meaningful distribution, since we would not *a priori* have any notion of whether the approximate posterior actually

generated curvatures close to the specified value. For this reason, we instead use target curvatures derived from arbitrarily chosen angles ϕ_t^* and ϕ_b^*. In order that the generated curvature be consistent with (2), a sample from the Gaussian noise term **e** (with reference standard deviation σ, here chosen arbitrarily as $\sigma \approx 10^{-5}$) is added to κ^*. In this way, it is possible to check that the recovered approximate posterior contains (and ideally is centered near) the set of values which originally generated the reference curvature κ^* via (2). For each of the following sets of results, we specify the reference angles ϕ_t^* and ϕ_b^* which were used to generate the target curvature via one run of the particle simulation. It should be noted that the uniform prior, which assigns equal mass to a wide range of potential parameter values, is fixed before the generation of κ^* – the Bayesian framework does not have any information *a priori* about which parameter values are more or less likely.

4.1 Parameter Estimation Results

The first set of UQ results used reference angles $\phi_t^* = 100$ and $\phi_b^* = 20$, which yielded a curvature of $\kappa^* = 0.03834$ via the model prediction equation with noise level $\sigma \approx 10^{-5}$. Results from the algorithm appear in Figure 7 (see caption for a description of the various subfigures). Since curvature does not have a notion of direction, the resulting joint posterior of (ϕ_t, ϕ_b) (center left subfigure) is symmetric about the diagonal. Note that, when one neutral angle is small, changing said angle has little effect on the curvature; the left flank of the upper curve is nearly flat, as is the lower flank of the bottom curve. Conversely, when the magnitudes of both angles are large, the distribution pulls away from the diagonal – once the smaller angle becomes sufficiently similar in magnitude to the larger, the membrane curvature begins to decrease, and so achieving a target positive curvature requires the larger angle to increase further. Since ϕ_b^* and ϕ_t^* are both assigned high probability (up to symmetry), the algorithm was effective at recovering the reference angles.

Unsurprisingly, the parameter s corresponding to the noise term **e** was not recovered to great accuracy. The model prediction equation (2) makes the assumption of a deterministic prediction function g; the dissipative particle dynamics simulation, which is inherently stochastic, fails this assumption, although the issue is somewhat circumvented by the time-averaging approach taken to the measurement of the curvature. Conversely, this means that the recovered distribution of s corresponds in some sense to the underlying noise of the DPD approach, which may be of interest in its own right (for a more rigorous treatment of the modeling uncertainty inherent to particle simulations, see [2]).

A second set of results, shown in Figure 8, used $\phi_t^* = 80$ and $\phi_b^* = 20$, yielding a target curvature of $\kappa^* = 0.02087$. Again, the reference angles were assigned high probability under the posterior, and so the algorithm was effective at parameter recovery. As in the previous set of results, the leftmost region of the joint posterior is close to horizontal, suggesting that small neutral angles are comparatively unimportant in determining the curvature. There are two factors
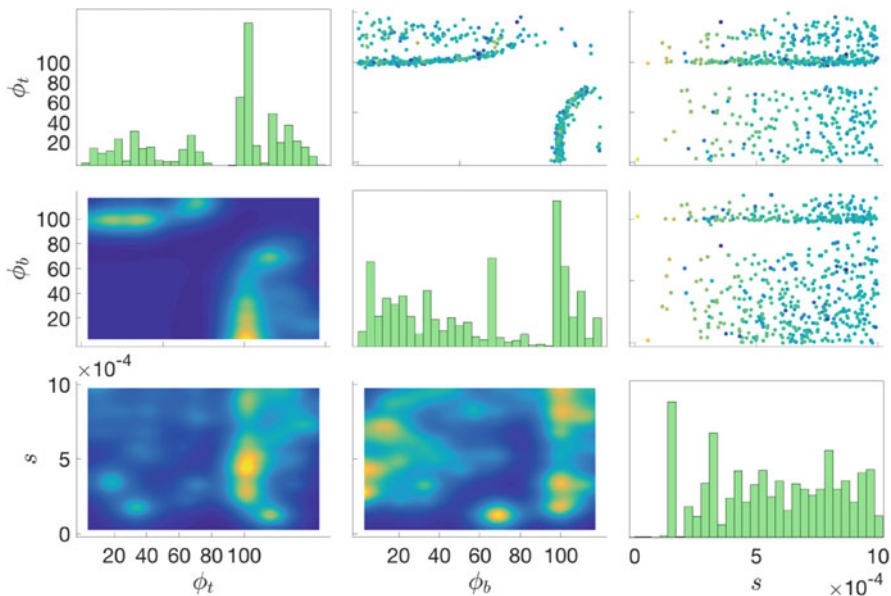
Fig. 7 5000 samples from approximate posterior with $\phi_t^* = 100$, $\phi_b^* = 20$ ($\kappa^* = 0.03834$). Histograms on the major diagonal are the empirical marginal distributions of ϕ_t, ϕ_b, s, from left to right. Plots in the upper right are the empirical joint distributions of pairs of parameters; the specific parameters and values appear in the margin. Shaded plots in the lower left are smoothed representations of the joint posterior, color-coded by probability – blue (low) to yellow (high).

which contribute to this behavior: first, the lipid tails do have some repulsion to each other, and so (even in the absence of fluid) a lipid with neutral angle 0 would not actually have overlapping tails at equilibrium. In this way, the energy of extremely small angles may be dominated by the short-scale repulsion between tails. Second, the potential imposed is harmonic, and so scales with $(\phi - \phi_0)^2$. As a result, when already close to equilibrium, small perturbations in the lipid angle yield correspondingly small changes in the energy.

The shape of the posterior is markedly different in the case where the reference curvature is very small (i.e., the desired membrane is nearly flat). Figure 9 shows the results of the UQ algorithm for identical reference angles $\phi_t^* = \phi_b^* = 20$. (Due to thermal fluctuations, along with the fact that curvature is nonnegative, the time-averaged reference curvature obtained was actually nonzero: $\kappa^* = 0.001480$.) The joint distribution of (ϕ_t, ϕ_b) loosely follows the diagonal, as should be the case by symmetry. Interestingly, the distribution becomes considerably narrower as the neutral angles increase in magnitude. Namely, to achieve a very small reference curvature using large angles, the angles must be extremely close to each other. This is a direct result of the quadratic scaling of the harmonic energy: since the lipids in a flat membrane are restricted to relatively small angles, each lipid angle is far from equilibrium, and so even small perturbations in the neutral angle on one side would significantly upset the balance between the lipid layers.
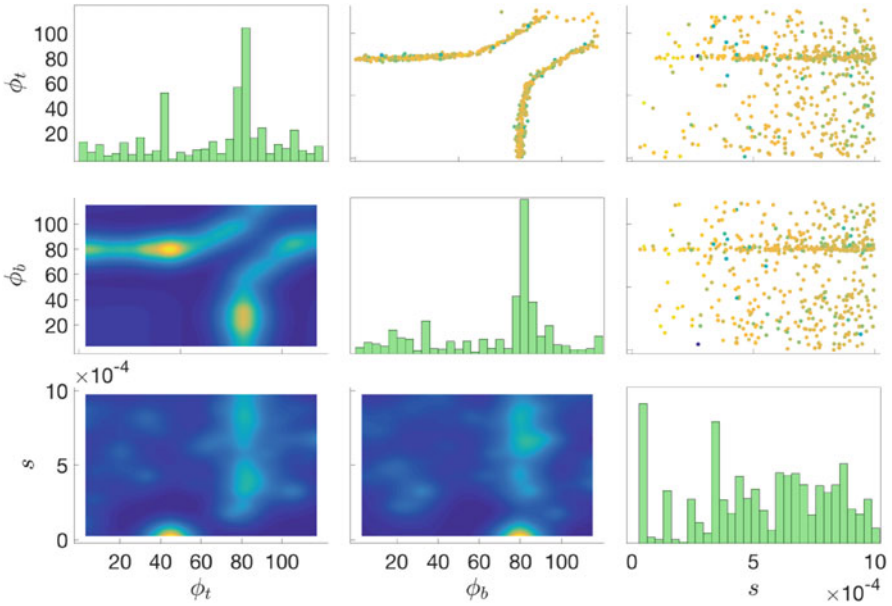
Fig. 8 5000 samples from approximate posterior with $\phi_t^* = 80$, $\phi_b^* = 20$ ($\kappa^* = 0.02087$). See Figure 7 for description of subfigures.
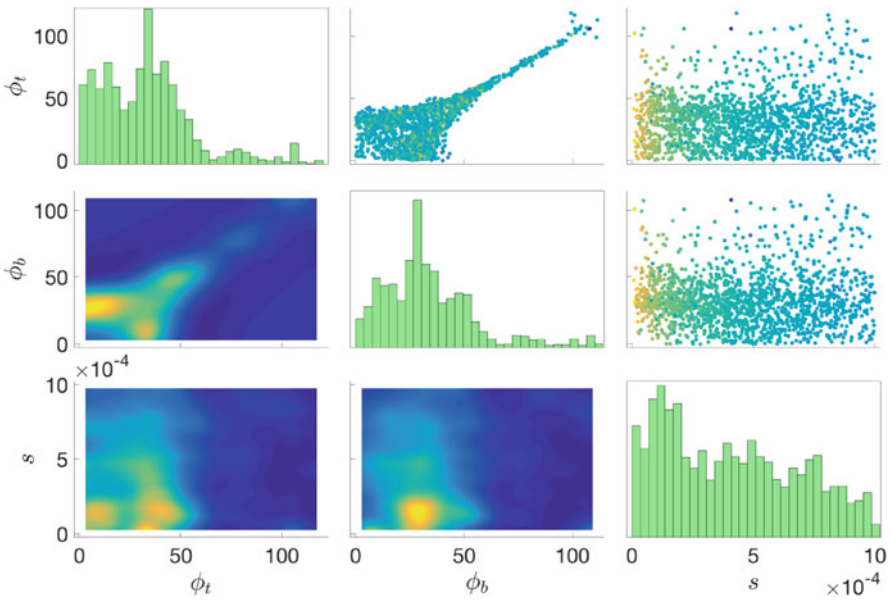
Fig. 9 5000 samples from approximate posterior with $\phi_t^* = 20$, $\phi_b^* = 20$ ($\kappa^* = 0.001480$). See Figure 7 for description of subfigures.
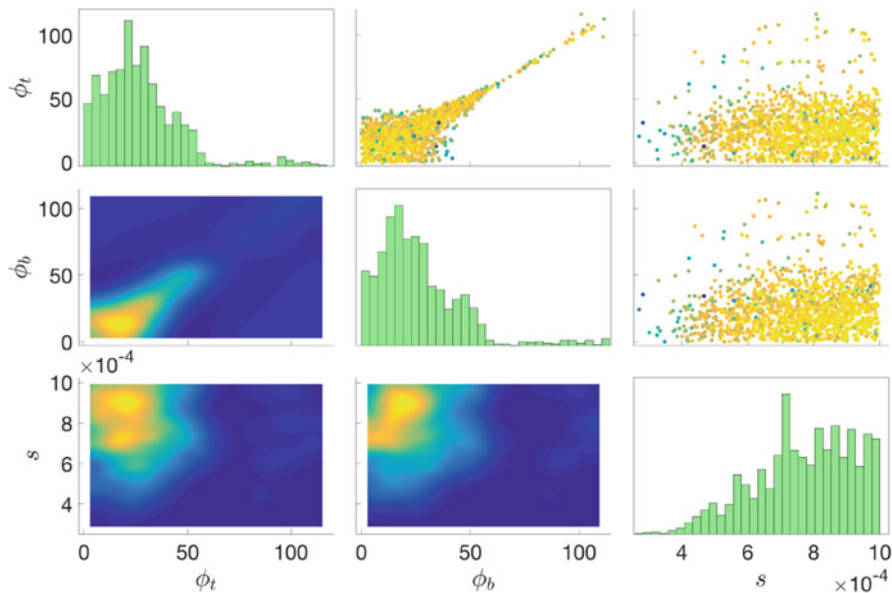
Fig. 10 5000 samples from approximate posterior with $\kappa^* = 0$. See Figure 7 for description of subfigures.

For small angles, the distribution is more broad; for extremely small values, the fact that the reference curvature was nonzero is evident (specifically, the joint distribution of (ϕ_t, ϕ_b) splits away from the diagonal as the angles approach zero). The smaller angles result in lipids being closer to equilibrium, thereby reducing the magnitude of the energy shift when the neutral angle on one side is perturbed. Although it peaks elsewhere, the posterior does put significant mass on the reference angles $\phi_t^* = \phi_b^* = 20$.

As a point of comparison, Figure 10 presents the results of a second run directly setting the target curvature κ^* to zero. Unlike Figure 9, the joint of (ϕ_t, ϕ_b) here does contain the diagonal (top middle). Because the flat membrane becomes very unstable as the angles are increased on both sides, the posterior appears borderline invisible in that region.

5 Discussion

In the three cases presented here, Bayesian UQ via TMCMC was found to be effective at recovering the reference parameters, along with classifying the uncertainty via approximate sampling from the posterior. It is worth restating, in somewhat broader terms, why this result is significant and how it may be applied to general computational models in cellular biology.

The cell membrane is a central structure in many forms of cell motility, and the simulation method described in Section 3.2 has significant complexity and nontrivial dynamics. Nonetheless, it should be thought of as a stand-in for an even more complex problem, whose input and output may be very high dimensional. For example, a computational model of a prokaryote might consider a broad range of parameters such as the oscillation rate, flexibility, and length of the flagella, the rigidity and size of the cell body, and the temperature and viscosity of the surrounding fluid; a model of a eukaryote might include the density, (de-)polymerization rate, and aspects of the structure of the actin cytoskeleton. Both models may be interested in output such as the speed and trajectory of cell motion, or the robustness of motility to external influences such as fluid flow or obstacles.

Parameter estimation as we have presented it is simply a generalization of the inverse problem: suppose in these examples that we know the comparable output of experiment, or are targeting a specific behavior that is known to have biological relevance. What can be inferred about the input space, i.e., what parameters would generate such behavior? Moreover, what is the degree of uncertainty in these inferences? For extremely complex models as in these examples, many questions in this vein are intractable through naïve methods. The distribution of parameters cannot be sampled exactly, and approximate sampling methods such as Metropolis may require too many evaluations of an already expensive model, or may introduce other problems such as probabilistic bottlenecks.

The most important aspect of the TMCMC approach to Bayesian uncertainty quantification described in Section 2.3 is its parallelizability. Because each generation of the algorithm generates many approximate samples from the target intermediate distribution, the chains can be run simultaneously; with modern parallel architectures growing increasingly more powerful and efficient, this marks an improvement in the computational tractability of uncertainty quantification of many orders of magnitude. As shown in the previous section, this allows for practical uncertainty quantification even for complex particle simulations.

Since this efficient parallel implementation of TMCMC can be applied to an effective black box, this method is accessible to a broad range of existing models in mathematical and cellular biology. In particular, the DPD method described in Section 3.1 has already been applied to a number of complicated mesoscopic systems [20] which could be examined under the lens of uncertainty quantification.

Computational Details

High-performance uncertainty quantification results from Section 4.1 were obtained from parallel runs on 184 Intel Xeon E5-2670 cores (2.6 GHz). TMCMC in Figures 7 and 8 converged after six generations, with total runtimes of 47.22 and 47.38 h (34.00 and 34.11 s per sample), respectively. TMCMC in Figures 9 and 10 converged after five generations, with total runtimes of 36.98 and 37.02 h (26.63 and 26.65 s per sample), respectively.

References

1. D.F. Anderson and T.G. Kurtz, *Stochastic Analysis of Biochemical Systems.* (Springer, New York, 2015)
2. P. Angelikopoulos, C. Papadimitriou, and P. Koumoutsakos: Bayesian uncertainty quantification and propagation in molecular dynamics simulations: A high performance computing framework. J. Chem. Phys. **137**, 144103 (2012)
3. P. Angelikopoulos, C. Papadimitriou, and P. Koumoutsakos: X-TMCMC: Adaptive Kriging for Bayesian inverse modeling. Comput. Methods Appl. Mech. Engrg. **289**, 409–428 (2015)
4. D. Barber, *Bayesian Reasoning and Machine Learning.* (Cambridge University Press, 2012)
5. J.L. Beck, K.V. Yuen: Model selection using response measurements: Bayesian probabilistic approach. J. Eng. Mech. **130** (2) 192–203 (2004)
6. Z. Chen, K. Larson, C. Bowman, P. Hadjidoukas, C. Papadimitriou, P. Koumoutsakos, and A. Matzavinos: Data-driven prediction and origin identification of epidemics in population networks. Submitted. (2018)
7. B. Efron and T. Hastie, *Computer Age Statistical Inference: Algorithms, Evidence, and Data Science.* (Cambridge University Press, 2016)
8. J.Y. Ching, Y.C. Chen: Transitional Markov chain Monte Carlo method for Bayesian model updating, model class selection, and model averaging. J. Eng. Mech. **133** 816–832 (2007)
9. P. Español and P. Warren: Statistical mechanics of dissipative particle dynamics. Europhys. Lett. **30**, 191–196 (1995)
10. V.A. Frolov. A.V. Shnyrova, and J. Zimmerberg. Lipid polymorphisms and membrane shape. CSH Perspect. Biol. **3** (11): a004747 (2011)
11. L. Gao, J. Shillcock, and R. Lipowsky: Improved dissipative particle dynamics simulations of lipid bilayers. J. Chem. Phys. **126**, 015101 (2007)
12. R.D. Groot and P.B. Warren: Dissipative particle dynamics – bridging the gap between atomistic and mesoscopic simulations. J. Chem. Phys. **107**, 4423–4435 (1997)
13. H. Haario, M. Laine, A. Mira and E. Saksman: DRAM: Efficient adaptive MCMC. Stat. Comput. **16**, 339–354 (2006)
14. P.E. Hadjidoukas, P. Angelikopoulos, C. Papadimitriou, P. Koumoutsakos: Π4U: A high performance computing framework for Bayesian uncertainty quantification of complex models. J. Comput. Phys. **284** 1–21 (2015)
15. B. Hajek: Cooling schedules for optimal annealing. Math. Oper. Res. **13** (2), 311–329 (1988)
16. R. Holley and D. Stroock: Simulated annealing via Sobolev inequalities. Comm. Math. Phys. **115** (4), 553–569 (1988)
17. I.K. Jarsch, F. Daste, and J.L. Gallop. Membrane curvature in cell biology: an integration of molecular mechanisms. J. Cell. Biol. **214** (4) 375–387 (2016)
18. G. Karniadakis, A. Beskok, and N. Aluru, *Microflows and Nanoflows: Fundamentals and Simulation.* (Springer, New York, 2005)
19. E. Keaveny, I. Pivkin, M. Maxey, and G. Karniadakis: A comparative study between dissipative particle dynamics and molecular dynamics for simple- and complex-geometry flows. J. Chem. Phys. **123**, 104107 (2005)

20. D. Kim, C. Bowman, J.T. Del Bonis-O'Donnell, A. Matzavinos, and D. Stein: Giant acceleration of DNA diffusion in an array of entropic barriers. Phys. Rev. Lett. **118**, 048002 (2017)
21. O.P. Le Maître and O.M. Knio, *Spectral Methods for Uncertainty Quantification.* (Springer, New York, 2010)
22. H. Lei and G.E. Karniadakis: Probing vasoocclusion phenomena in sickle cell anemia via mesoscopic simulations. PNAS **110** (28), 211–227 (2013)
23. B. Leimkuhler and C. Matthews, *Molecular Dynamics: With Deterministic and Stochastic Numerical Methods.* (Springer, New York, 2015)
24. B. Leimkuhler and X. Shang: On the numerical treatment of dissipative particle dynamics and related systems. Journal of Computational Physics **280**, 72–95 (2015)
25. H. Matsuo et al. Role of LBPA and Alix in multivesicular liposome formation and endosome organization. Science **303** 531534 (2004)
26. F. Milde, G. Tauriello, H. Haberkern, and P. Koumoutsakos: SEM++: A particle model of cellular growth, signaling and migration. Comp. Part. Mech. **1** (2), 211–227 (2014)
27. N. Phan-Thien, *Understanding Viscoelasticity: An Introduction to Rheology,* 2nd edn. (Springer, Berlin, 2013)
28. S. Plimpton, Fast parallel algorithms for short-range molecular dynamics. J. Comp. Phys. 117, 1–19 (1995)
29. D. C. Rapaport, *The Art of Molecular Dynamics Simulation,* 2nd edn. (Cambridge, UK, 2004)
30. P. Salamon, P. Sibani, and R. Frost, *Facts, Conjectures, and Improvements for Simulated Annealing.* (SIAM, 2002)
31. T. Shardlow and Y. Yan: Geometric ergodicity for dissipative particle dynamics. Stoch. Dyn. **6**, 123–154 (2006)
32. R. Smith, *Uncertainty Quantification: Theory, Implementation, and Applications.* (Society for Industrial and Applied Mathematics, Philadelphia, 2014)
33. M.A. Stolarska, Y. Kim, H.G. Othmer: Multi-scale models of cell and tissue dynamics. Phil. Trans. R. Soc. A **367**, 3525–3553 (2009)
34. D. Stroock, *An Introduction to Markov Processes,* 2nd edn. (Springer, 2014)
35. Y.-H. Tang, L. Lu, H. Li, C. Evangelinos, L. Grinberg, V. Sachdeva, and G.E. Karniadakis: OpenRBC: A fast simulator of red blood cells at protein resolution. Biophysical Journal **112** (10), 2030–2037 (2017)
36. A. Tarantola, *Inverse Problem Theory and Methods for Model Parameter Estimation.* (Society for Industrial and Applied Mathematics, Philadelphia, 2005)
37. K.-V. Yuen,*Bayesian Methods for Structural Dynamics and Civil Engineering.* (Wiley Verlag, 2010)
38. M.W. Vanik, J.L. Beck, S.K. Au: Bayesian probabilistic approach to structural health monitoring. J. Eng. Mech. **126**, 738–745 (2000)
39. A. Vrugt, C. J. F. ter Braak, C. G. H. Diks, B. A. Robinson, J. M. Hyman, and D. Higdon: Accelerating Markov Chain Monte Carlo Simulation by Differential Evolution with Self-Adaptive Randomized Subspace Sampling, Int. J. Non. Sci. Num. Sim. **10**, 273 (2011).
40. S. Wu, P. Angelikopoulos, C. Papadimitriou, R. Moser, and P. Koumoutsakos: A hierarchical Bayesian framework for force field selection in molecular dynamics simulations. Phil. Trans. R. Soc. A **374**, 20150032 (2016)
41. D. Xiu, *Numerical Methods for Stochastic Computations: A Spectral Method Approach.* (Princeton University Press, 2010)

From Random Walks to Fully Anisotropic Diffusion Models for Cell and Animal Movement

Kevin J. Painter and Thomas Hillen

Abstract This chapter provides an introduction on how anisotropic diffusion models can be derived from position-jump and velocity-jump random walks. We show how the availability of measurement data can guide the choice of the appropriate model. We further present two new applications, respectively to cell movement on micro-fabricated surfaces and magnetic compass orientation by sea turtle hatchlings.

1   Introduction

Getting from point A to point B is a daily challenge, although for the most part our movement patterns are routine – staggering from bedroom to bathroom, from home to work, from office to coffee pot – and we switch into autopilot, following the course hard-wired into our conscious. Sometimes we may find ourselves in an unusual place attempting to reach an unfamiliar goal, yet even then navigation is straightforward when armed with a smartphone and network connection.

Cells and animals do not have the technological aids at our disposal yet frequently need to migrate through their environment, sometimes independently, sometimes collectively: the solo navigations of recently fledged albatrosses across thousands of kilometres of southern oceans, or the collective movements of cells as they move into developing tissues and organs offer particularly astonishing examples. Given the myriad of potential factors – chemicals, electric, magnetic and gravitational fields, topography and physical structure of the environment,

K. J. Painter (✉)
Department of Mathematics & Maxwell Institute, Heriot-Watt University, Edinburgh, UK

Dipartimento di Scienze Matematiche, Politecnico di Torino, Italy
e-mail: K.Painter@hw.ac.uk

T. Hillen
University of Alberta, Edmonton, Alberta T6G 2G1, Canada
e-mail: thillen@ualberta.ca

etc. – a key question, whether posed by ecologists, cell biologists, microbiologists or oncologists, is exactly what cues signal to the cells or organisms along their paths.

Mathematical and computational modelling offer the means to address such questions, via encapsulating a biological process into its essentials. Yet choosing an approach and setting up a model to begin with is far from a trivial task. Inevitably this will come down to the knowledge and data we have and the nature of the problem we are trying to address. One major determinant in the modelling choice will be the *biological scale* of the problem. Consider a population-scale problem such as predicting the spatial spread of a cancer to aid diagnosis and treatment. While we may have some understanding of the underlying biological processes at a cellular level (e.g. enhanced proliferation and invasion of cells into healthy tissue), the primary scale of interest is typically a macroscopic one at the time of treatment: the scale of the cancer (centimetres) is significantly greater than the microscopic cells from which it is formed. In such instances, an efficient and oft-used solution is to blur the population into a convenient density distribution and propose a suitable evolution equation (such as a partial differential equation) for its change over space and time [36, 37, 48].

Macroscopic approaches such as these have formed a bedrock for mathematical modelling over many years, providing insight into a wide variety of fundamental processes. When the only data we have is similarly macroscopic, such as an MRI (magnetic resonance imaging) scan indicating the spatial extent of a cancer's growth, a macroscopic model makes sense: fitting the model to approximated densities determined from the scan offers a method of validation and parameter estimation [56]. But what if the available data is at the level of the individual? Can we relate a model posed at a macroscopic level to an individual's movement? These questions are clearly crucial when we consider technological advances in our capacity to track molecules, cells or organisms: individual molecules can be tagged and followed via single particle tracking (SPT) as they skate across the cell membrane [52]; labelled cells can be followed via sophisticated imaging while migrating through a complicated tissue environment [59]; attaching a global positioning system (GPS) to an animal can allow it to be followed even if it travels across oceans and continents [7]. Clearly, the data provided by such methods can shed significant light on the fundamental mechanisms of movement. For modellers, a significant challenge is raised: how can we best exploit all forms of available data to obtain better models, both at the level of individuals and populations?

To motivate the rest of this chapter, we consider two very different applications, respectively, in cell movement and turtle hatchling navigation. Both applications have a similar fundamental question (what are the guidance cues that determine navigation?), but offer distinct examples for the type of data that may be at hand for model parametrisation/formulation. In the case of cell movement we have a tabulated summary of population-averaged behaviour. For turtles we have individual-level data, an orientation for each tested hatchling in a sample. The analytical models we proceed to describe can be fitted to each of the datasets, in each case shedding light on the problem.

1.1 Dataset A: Cell Movement on Microfabricated Substrates

The development, maintenance and repair of our bodies requires that various cells migrate through complex tissue environments; in tumour invasion, these same mechanisms can facilitate the rapid dispersal and spread of malignant cells into neighbouring healthy tissue [19]. Various extracellular factors contribute to cell guidance, ranging from extracellular molecules (e.g. chemoattractants and repellents), direct signals from other cells (e.g. contact inhibition of locomotion) and the oriented movement of cells along aligned structures [20, 42]. This latter form of oriented movement is generally termed contact guidance [14] and, while principally described in the context of movement along the long bundles of collagen fibres characteristic of connective tissue, can also occur during the movement of cells along axonal tracts of the central nervous system or crawling along blood capillaries [17]. Contact guidance has been identified in various cell populations, including fibroblasts [13], immune cells [59] and various cancerous populations [16, 49].

The capacity of environmental anisotropy to influence cell orientation/movement can be studied by tracing cell paths when plated on micro-fabricated structures. To illustrate the data available from such experiments we analyse those in Jeon et al. [25], where a two-dimensional substratum is formed with a rectangular array of orthogonal micro-ridges, see Figure 1 (left). Inter-ridge lengths in the x- and y-directions are, respectively, denoted W and L, with the former set at 12, 24 or 48 μm and the latter set to generate $W : L$ ratios of $1 : 2$, $1 : 4$ or $1 : \infty$ (the last case corresponding to an absence of ridges in the $x-$direction). Ridge heights were set at 3 μm, with further tests conducted at 10 μm and a control case without any ridges. NIH373 fibroblast cells were plated on these substrates: a population characterised by its mesenchymal movement with cells extending long protrusions to probe the environment. Cells clearly align to the micro-ridges, generating anisotropic movement (see Figure 1, top right and bottom row) under anisotropic arrangements. Data from individual tracking was summarised at a macroscopic level (averaged over the population) in terms of mean speeds and directional bias, reproduced in Table 1. In Section 4.1 we will use this data to parametrise an anisotropic diffusion model that describes cell spread for different anisotropies in the substratum.

1.2 Dataset B: Magnetic Navigation in Loggerhead Hatchlings

Maritime navigation is undeniably hazardous. The frequent lack of visible landmass, turbulent currents and dramatic meteorological conditions resulted in frequent positional misreckoning (and shipwrecking) during the early ages of maritime traffic, stimulating governments of the time to propose prizes for a method of accurately establishing longitudinal coordinates. John Harrison's marine chronometer marked a pivotal moment in the transition towards (relatively) safe navigation [53]. Marine animals, of course, do not rely on such aids but many species routinely undertake
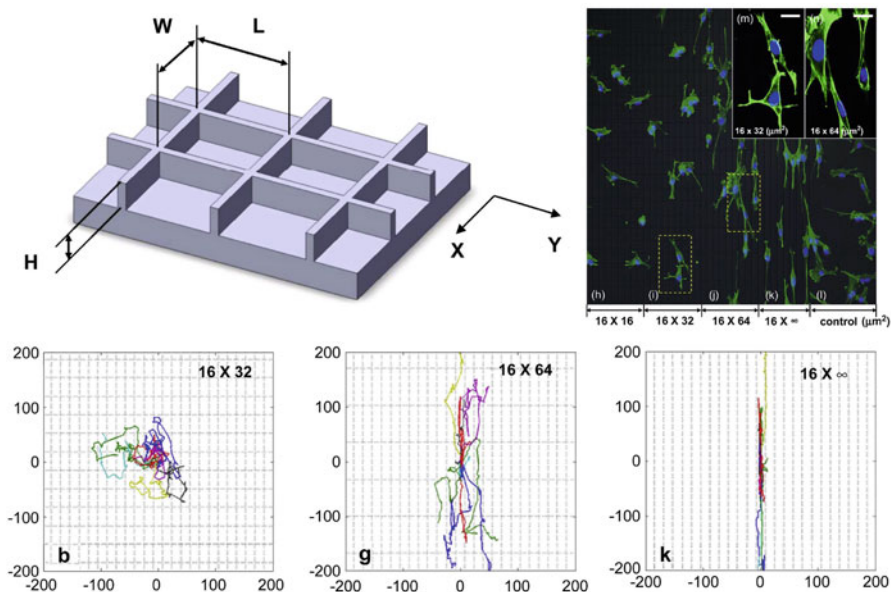
Fig. 1 Top Left: schematic of the micro-ridge substrate. Top Right: typical observation of cell movement on an anisotropic substrate, where the micro-ridges are in different aspect ratios. Bottom: cell tracks observed for different environmental anisotropies. Horizontal and vertical axes represent microns. Figures reprinted from Biomaterials, volume 31, Jeon, H., Hidai, H., Hwang, D.J., Healy, K.E. and Grigoropoulos, C.P., "The effect of microscale anisotropic cross patterns on fibroblast migration", pp. 4286–4295 (2010), with permission from Elsevier.

Table 1 Reproduction of the movement data from Jeon et al. [25] for fibroblast cells migrating on a micro-ridged substratum.

Case	Ridge height	x-velocity $v_x \pm$error	y-velocity $v_y \pm$ error	Speed $\pm$ error
(μm$\times\mu$m)	(μm)	(μm/min)	(μm/min)	(μm/min)
12 x 24	3	0.38±0.015	0.58±0.025	0.78±0.027
12 x 48	3	0.28±0.014	0.9±0.045	1.01±0.045
12 x ∞	3	0.08±0.005	0.56±0.029	0.59±0.029
16 x 32	3	0.48±0.021	0.65±0.026	0.9±0.03
16 x 64	3	0.31±0.015	0.87±0.038	1.0±0.039
16 x ∞	3	0.12±0.007	0.8±0.036	0.84±0.036
24 x 48	3	0.26±0.015	0.42±0.024	0.55±0.027
24 x 96	3	0.2±0.012	0.49±0.02	0.58±0.022
24 x ∞	3	0.12±0.007	0.48±0.027	0.52±0.028
12 x 24	10	0.33±0.016	0.46±0.024	0.65±0.026
12 x 48	10	0.18±0.013	0.76±0.044	0.83±0.046
12 x ∞	10	0.04±0.003	0.60±0.032	0.61±0.032
Control	0	0.38±0.019	0.41±0.033	0.63±0.025

long marine journeys [29], with one of the most phenomenal belonging to the loggerhead turtle (*Caretta caretta*). North Atlantic loggerhead hatchlings dash to the ocean from eggs laid at various nesting beaches and undergo a period of "frantic" swimming that transports them from the dangerous coastal waters to ocean circulatory currents such as the Gulf Stream. They subsequently embark on a years to decades long period of open ocean migration, remaining within the warmer waters of the Sargasso Sea and the North Atlantic Subtropical Gyre, the circular current system that surrounds it (Figure 2). As adults, they continue to navigate between feeding grounds or back to nesting beaches.

Considering the small size of hatchlings and juveniles, sustained swimming is energetically demanding and there is clear benefit to simply drifting within the convenient conveyor belt of the North Atlantic Gyre. Yet, such simplistic behaviour could come with a risk if the stream branches, such as in the North Atlantic where it splits into separate streams heading south (towards the warmer waters of the Azores) or north (into the colder waters of Ireland and the North Atlantic), Figure 2; drifting into the latter could transport turtles into perilously cold waters. Consequently, it is likely that some degree of positional awareness and navigation is employed and an increasing volume of evidence has emerged on the potential for turtles to follow a magnetic compass [28], exploiting the information provided by the Earth's magnetic field. Such a capacity would clearly be advantageous: despite its diurnal and secular variation, magnetic field information is always available (unlike, say, celestial cues).

To investigate this hypothesis, Lohmann and colleagues (see [28] for a review) devised a laboratory experiment that monitors how hatchling orientation changes when exposed to distinct magnetic fields. Briefly, a turtle is placed in a large water-tank while harnessed and tethered to an electronic monitor that computes its swimming direction. The tank is surrounded by a coil system capable of replicating specific geomagnetic fields, such as those found at distinct points along a turtle's typical migratory route. Following an acclimatisation period, the mean swimming direction over a 5-min period is recorded for each turtle, generating orientation data at an individual level. In Figure 2 we reproduce the data summarised in [28] (itself summarising the collection of studies found in [15, 27, 50]). Specifically, magnetic fields were reproduced for different points along the North Atlantic Gyre and, for each location, the (mean) orientation of each tested turtle is binned into a circular histogram. The key inference from these studies is that hatchlings indeed show subtle changes to their preferred swimming direction, consistent with an orientation that optimises remaining within the Gyre. In Section 4.2 we will use this data to parametrise stochastic and continuous models, assessing the capacity for oriented swimming to maintain successful circulation of hatchlings.

1.3 Outline

In the next section (Section 2) we introduce advection-diffusion equations and the fully anistotropic advection-diffusion framework. We introduce *position-jump* and *velocity-jump* random walks as two alternative stochastic models for oriented
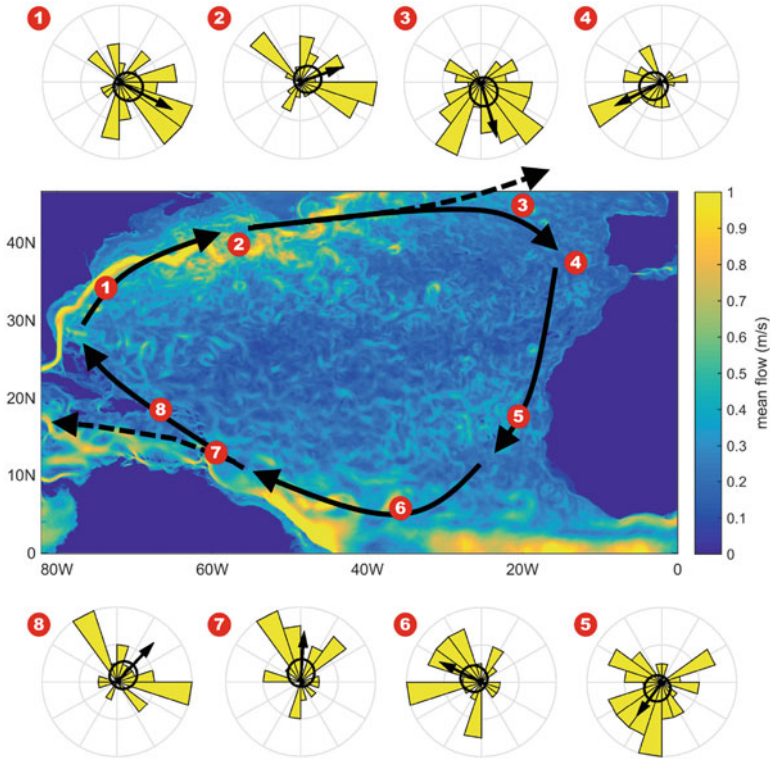
Fig. 2 The North Atlantic Gyre (Black arrows) is a circular system of currents, formed by the Gulf Stream, the North Atlantic Current, the Canary Current and the North Equatorial Current. For North Atlantic loggerhead turtles, such as those hatching along Florida beaches, remaining inside the region enclosed by the Gyre is optimal for access to suitable feeding grounds (e.g. the Sargasso Sea, the Azores) and to avoid straying into perilously cold waters (e.g. far North Atlantic) or unfamiliar geographic regions (far from traditional nesting/feeding sites). Two potentially hazardous points are indicated by the North Easterly point (3) and the South Westerly point (7): here, currents split into northerly/southerly streams for (3) and northerly/westerly streams for (7). Circular histograms reproduce the hatchling orientation data from [28], where (1–8) correspond to the locations where the magnetic field was reproduced in an experimental arena. When this data is fitted to the von Mises distribution, equation (11), a clear bias emerges, with the dominant direction and concentration strength reflected by the arrow direction and length (concentration parameters κ range from 0.67 for dataset 5 to 0.91 for dataset 1). Clearly, the unimodal von Mises distribution may not always be an "optimal" distribution: for example, datasets 2 and 8 may be more convincingly fitted by a multimodal form, such as linear combinations of von Mises distributions. Given the present study aims and the limited sample sizes, we restrict our fitting to the unimodal von Mises distribution.

movement, and show how these models can be parametrised by translating between individual-level and population-level measurements via circular statistics. In Section 3 we give detailed derivations of the fully anistotropic advection-diffusion model, starting from either a position-jump or velocity-jump process. In Section 4

we return to the two applications/datasets described above. While each dataset offers a rather distinct set of summary statistics, we show how they can both be incorporated within our framework to parametrise models.

2 Basic Tools

Here we outline the basic set of tools that we employ to model and analyse population spread in an anisotropic/oriented environment: advection-diffusion equations, scaling limits for random walks, position-jump and velocity-jump random walks and directional statistics. We note that the derivations of the following sections require a copious notation, spanning scalar, vector and tensor/matrix quantities. To help the reader keep track, we use normal face fonts for scalar quantities (e.g. $t, p, u \ldots$), bold faces for vectors (e.g. $\mathbf{a}, \mathbf{n}, \mathbf{v} \ldots$) and double struck ($\mathbb{D}, \mathbb{V} \ldots$) for tensors and matrices. Much of the material here is of an elementary textbook nature, and we limit references as follows: for more information on the use of advection-diffusion equations in biology, see, for example, [35, 37]; for more information and perspectives on random walks and their continuous approximations in biological systems, see, for example, [9, 22, 38, 39, 41, 46, 47]; for more information on the theory and use of directional statistics in biology, see [2, 31].

2.1 Advection-Diffusion Equations

Advection-diffusion equations (AD equations) occupy a prominent position in biological movement modelling [35, 37]. Firstly, AD equations have a relatively straightforward and intuitive form and their long history has generated numerous methods for their analysis. Secondly, AD equations can arise as a limiting form from more realistic/detailed models: they can be derived from discrete and continuous random walks [38], from stochastic differential equations [18] and from individual based models [12]. Thirdly, they have shown to be powerful models capable of describing a wide range of applications in areas as diverse as microbiology [11], ecology [30, 34], physiology [26] and medicine [45]. In short, AD equations describe the basic elements of a movement process.

In the simplest case we restrict to a one-dimensional line and consider a constant drift velocity a and constant diffusion coefficient $d > 0$. The AD equation for some population density $u(x, t)$, where x denotes position along the line and t describes time, is given by

$$u_t + au_x = du_{xx} \tag{1}$$

where the index notation denotes partial derivatives.
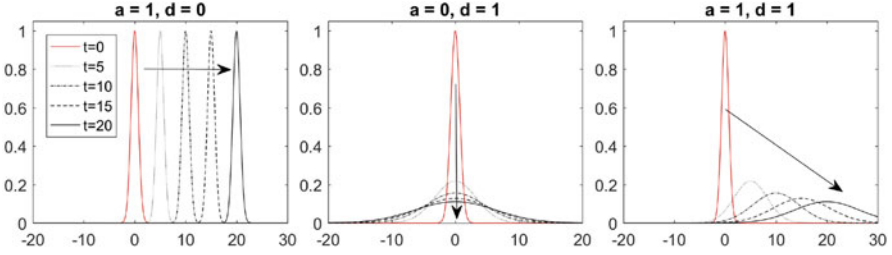
Fig. 3 Typical solutions of the basic diffusion-advection equation (1). Initial conditions are $u(x, 0) = e^{-x^2}$ and solutions shown for (left to right): pure advection; pure diffusion; diffusion-advection.

In the absence of diffusion ($d = 0$), we have $u_t + au_x = 0$ and solutions are of the form $u(x - at)$, describing movement with constant speed a. If $a > 0$ this movement is to the right and if $a < 0$ to the left (see Figure 3 left). In the absence of advection ($a = 0$) we obtain a pure heat (or diffusion) equation $u_t = du_{xx}$: solutions disperse (Figure 3 middle) and (for $x \in \mathbb{R}$) the fundamental solution is

$$u(x, t) = \frac{1}{\sqrt{4\pi dt}} e^{-x^2/4dt}.$$

Taking both terms together ($a \neq 0, d > 0$) the population is transported with velocity a while simultaneously spreading due to diffusion (Figure 3 right).

While the basic elements of directed movement (via a) and spatial spread (via d) are already contained in (1), questions arise concerning their specific choices related to biological observations/properties: How does the direction and thickness of nano-grooves translate to advection/diffusion terms? How can we link datasets on turtle headings to these parameters? To answer questions like these we need to generalise the above AD equations (1) in a number of ways:

- advection and diffusion coefficients will more generally depend on space and time;
- we need to explore AD equations in higher space dimensions, in particular two dimensions for the examples studied here;
- as we shall see, any underlying anisotropy or oriented information in the environment can affect both advection and diffusion, necessitating usage of an anisotropic formulation with $n \times n$ diffusion tensor $\mathbb{D}(\mathbf{x}, t)$.

Instead of (1) we will therefore consider the *fully anisotropic advection-diffusion equation* (FAAD equation):

$$u_t + \nabla \cdot (\mathbf{a}(\mathbf{x}, t)u) = \nabla\nabla : (\mathbb{D}(\mathbf{x}, t)u). \tag{2}$$

Note that because the advective velocity $\mathbf{a}(\mathbf{x}, t)$ now depends on space, it appears inside the divergence such that $u_t + \nabla \cdot (\mathbf{a}(\mathbf{x}, t)u) = 0$ is a conservation law. The new anisotropic diffusion term in (2) demands special attention. The colon notation (:) used here denotes the contraction of two tensors, and generates a summation across the full suite (i.e. including mixed) of second order derivatives:

$$\nabla\nabla : (\mathbb{D}(\mathbf{x}, t)u) = \sum_{i, j=1}^{n} \frac{\partial}{\partial x_i} \frac{\partial}{\partial x_j} (\mathbb{D}^{ij}(\mathbf{x}, t)u(\mathbf{x}, t)). \tag{3}$$

Note moreover that this term can be expanded into

$$\nabla\nabla : (\mathbb{D}u) = \nabla \cdot (\mathbb{D}\nabla u) + \nabla \cdot ((\nabla \cdot \mathbb{D})u),$$

which reveals a standard (Fickian-type) anisotropic diffusion term along with an advection term with velocity $\nabla \cdot \mathbb{D}$. As we will show below, the term (3) arises naturally from a detailed random walk description for moving biological agents. We also note that this term can confer some advantages over the standard Fickian anisotropic diffusion form $(\nabla \cdot (\mathbb{D}\nabla u))$: in particular, (3) can allow local maxima and minima to form in the population density steady state distribution, consistent with certain biological observations. Before we move on to this we first show how explicit expressions can be obtained for drift and diffusion terms, correlating to the inputs into an individual-level random walk, and introduce scaling methods in the process.

2.2 Scaling Limits for a Simple Random Walk

Consider an unfortunate hare confined to a life of consecutive and equispaced hops left or right along an infinite one-dimensional road. This animal's convenient movement path can be characterised by a probability density function $p(x, t)$, denoting the probability of the hare being at position x at time t. We set δ to be the hop length, q and $1 - q$ as the probabilities of a jump to the right or left and introduce τ as the (assumed constant) time between consecutive hops. To determine an equation for $p(x, t + \tau)$ we need to calculate the probability of finding the individual at x at time $= t + \tau$. Clearly this will only be possible if the individual has jumped right from position $x - \delta$, or left from $x + \delta$, at time t. As a result, we have the discrete *Master equation*

$$p(x, t + \tau) = qp(x - \delta, t) + (1 - q)p(x + \delta, t). \tag{4}$$

How can we determine a continuous limit for this discrete equation? The first step is to reinterpret p as a continuous probability distribution and then expand the

left-hand side about (x, t) as a function of t in powers of τ, and the right-hand side terms as functions of x in powers of δ. After removing the arguments (x, t) for clarity, we find

$$p + \tau p_t + \frac{\tau^2}{2} p_{tt} + \ldots = q \left(p - \delta p_x + \frac{\delta^2}{2} p_{xx} - \ldots \right)$$

$$+ (1 - q) \left(p + \delta p_x + \frac{\delta^2}{2} p_{xx} + \ldots \right),$$

where the subscripts denote partial derivatives. Simplifying, we obtain

$$p_t(x, t) = \frac{\delta}{\tau}(1 - 2q)p_x(x, t) + \frac{\delta^2}{2\tau} p_{xx}(x, t) + O(\tau, \frac{\delta^3}{2\tau}). \tag{5}$$

Glancing at Equation (5) hints at the continuous model, where we see that the *leading terms* form an advection-diffusion equation,

$$p_t(x, t) = -ap_x(x, t) + dp_{xx}(x, t) \tag{6}$$

with

$$a = \frac{\delta}{\tau}(2q - 1) \quad \text{and} \quad d = \frac{\delta^2}{2\tau}.$$

However, to do this more formally we must think carefully about different *scalings*, corresponding to distinct limiting scenarios as $\delta, \tau \to 0$ and $q \to 1/2$. We will present three choices: others certainly exist, yet the majority do not lead to a useful limit equation. In other words, if δ, τ and q do not scale as indicated below, then the above does not provide an appropriate method for deriving a useful continuous model. Note that for each of these scalings, all of the hidden lower order terms of equation (5) limit to zero and are henceforth excluded from consideration.

(a) Suppose $\delta, \tau \to 0$ such that $\frac{\delta}{\tau} \to \alpha = $ constant. This describes a *hyperbolic scaling*. Hence, $\frac{\delta^2}{\tau} \to 0$, and the diffusive term vanishes. Thus, we are left with a simple *transport equation*

$$p_t + ap_x = 0,$$

where the advective velocity is $a = \alpha(2q - 1)$. We can see from this that the advective speed reaches a maximum of α when $q = 0$ or 1, which corresponds to always choosing left or always choosing right: i.e., there will be no doubling back.

(b) Suppose $\delta, \tau \to 0$ such that $\frac{\delta^2}{\tau} \to 2d = $ constant. This describes a *parabolic scaling*. Here we can consider two cases:

(b.1) If $q = \frac{1}{2}$. Here we have $a = 0$ and we hence obtain a pure *diffusion equation*

$$p_t = dp_{xx}.$$

(b.2) If $q \rightarrow \frac{1}{2}$ in such a way that $\frac{\delta}{\tau}(2q - 1) \rightarrow a$, and $\frac{\delta^2}{2\tau} \rightarrow d$, then the scaling results in the *advection-diffusion equation*

$$p_t + ap_x = dp_{xx} \, . \tag{7}$$

Summarising:

- When δ and τ scale in the same way, then we obtain a pure transport equation. This case is called *drift dominated*.
- When $\delta^2 \sim \tau$, we have the *diffusion dominated* case.
- Only if $q - \frac{1}{2} \sim \delta$ do we get both terms, an advection and a diffusion term (*mixed case*). In this case we exactly derive our simple one-dimensional AD equation (1), but now we have a connection from the macroscopic parameters a and d to the statistical inputs of the underlying random walk process (q, δ, τ).

The question of which scaling to apply will typically come down to the appropriate relationship between the *macroscopic* and the *individual* spatial and temporal scales: i.e. between the scales of the individual movement process and the scale of the problem. For example, for the hops of a hare their frequency may take place on a timescale of seconds, over a distance of several centimetres. For modelling purposes, we may be interested in the dynamics of the system over observational scales ranging from minutes and metres to years and kilometres. The comparison between these scales provides the key to the appropriate scaling.

It is important to note that we have, in fact, only derived a continuous limiting equation for the probability distribution of finding an individual at position x at time t. Can we directly relate p to a density function u that describes the distribution of a population? Formally, this would require that the jumpers are stochastically independent, i.e. that any interactions between population members can be (reasonably) ignored. This would, quite obviously, be a strong assumption if applied generally and its validity demands careful assessment [46, 54]. Accounting for population interactions will significantly complicate the proceedings (often to the point of intractability) and we shall therefore restrict to stochastically independent jumpers in the context of this chapter: effectively, we directly interchange the probability distribution p with the population density distribution u.

2.3   Classes of Biological Random Walks

In the above example we considered an *uncorrelated position-jump random walk on a discrete and regular one-dimensional lattice* for our underlying movement process: moves were uncorrelated, in that the decision of which direction to take did not depend on the previous decision(s), movement occurred through positional jumps in space that ignored explicit description of passage between successive points, and were of fixed length, so that the path was localised to equally spaced points along a one-dimensional line.
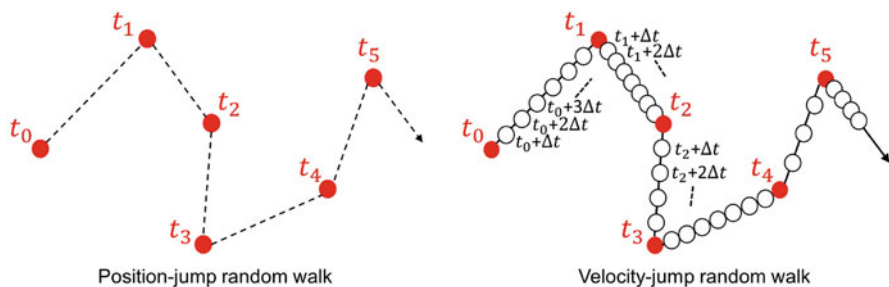
Fig. 4 Schematic illustrating position-jump and velocity-jump random walks. (Left) In the position-jump process, the particle makes instantaneous jumps through space at discrete times $t_0, t_1, t_2, \ldots$ (Right) In the velocity-jump process, the particle makes instantaneous velocity-changes at discrete times $t_0, t_1, t_2, \ldots$ (red circles), but subsequently moves continuously through space with a fixed velocity in the intervening times (white circles).

More generally, two popular random walk descriptions for biological movement are the *position-jump* and *velocity-jump* random walk processes. These descriptions have been introduced to biological modelling by Othmer, Dunbar and Alt [38] and subsequently proven to be powerful and popular approaches. In the simpler position-jump process, the random walker jumps discretely from point to point according to certain jump probabilities (Figure 4 left); the one-dimensional random walk discussed above provides a particularly simple example. The more sophisticated velocity-jump process assumes piecewise continuous movement through space, with random walkers changing their velocity (or heading) during *turns* (Figure 4 right). Choosing an appropriate random walk description involves a balancing of their respective advantages: for example, while the velocity-jump approach benefits from its more natural representation of biological movement, the subsequent derivation of a continuous limiting equation is somewhat more complicated.

2.3.1 Position-Jump Processes

Moving beyond our simple random walk above, a more general position-jump random walk assumes movement proceeds through a sequence of positional jumps in space, interspersed according to some characteristic mean waiting time. Such instantaneous transitions are clearly somewhat unrealistic in the context of biological movement, yet given the discrete nature of many datasets (for example, satellite tracking of an animal in which its path is recorded through its spatial coordinate at discrete times) a position-jump model can often be justified as a reasonable approximation [5, 57].

Position-jump random walks can be alternatively stated via a discrete or continuous time master equation [38], and here we consider the former form. Specifically, we consider a population of stochastically independent jumpers performing a discrete time random walk, starting at $t = 0$ and making jumps at fixed times separated

by time step τ. We introduce a redistribution kernel $K(\mathbf{y}, \mathbf{x}, t)$, a probability density function for a jump from position $\mathbf{x}$ to $\mathbf{y}$ at time t. Note that, as a probability, we have $K \geq 0$.

The difference in the population density at $\mathbf{x}$ between times t and $t + \tau$ will be determined by summing all jumps into position $\mathbf{x}$ and subtracting all those away from position $\mathbf{x}$, i.e. by the equation

$$u(\mathbf{x}, t + \tau) - u(\mathbf{x}, t) = \int_{D^{\mathbf{x}}} K(\mathbf{x}, \mathbf{y}, t)u(\mathbf{y}, t) - K(\mathbf{y}, \mathbf{x}, t)u(\mathbf{x}, t)d\mu(\mathbf{y}) . \qquad (8)$$

In the above, $(D^{\mathbf{x}}, \mu(\mathbf{y}))$ is a measure space. The above is general for random walks including jumps of various step lengths, or cases where movement occurs in continuous space or is restricted to discrete jumps between regularly or irregularly arranged nodes. The set $D^{\mathbf{x}}$ determines the set of destination/incoming sites for position $\mathbf{x}$, i.e. the set of points $\mathbf{y} \in D^{\mathbf{x}}$ from which jumps into or out of $\mathbf{x}$ can be made, with $\mu(\mathbf{y})$ its associated measure. For example, if jumps can be made in any direction and any distance up to length h, then $D^{\mathbf{x}}$ becomes the ball centred on $\mathbf{x}$ of radius h and the associated measure is the standard Lebesgue measure. If jumps can be made in any direction, but are restricted to a fixed length h, then $D^{\mathbf{x}}$ will be the sphere of radius h centred on $\mathbf{x}$ and the associated measure is the surface Lebesgue measure. When movements become restricted to a set of nodes, $D^{\mathbf{x}}$ becomes a finite or infinite set of discrete positions with a corresponding discrete measure.

The choice of redistribution kernel K is a key modelling decision, and allows various potential factors to be incorporated: for example, K could incorporate an impact due to environmental anisotropy or navigating cues that bias jumps into particular headings. The redistribution kernel is taken to be a probability measure, i.e.

$$\int_{D^{\mathbf{x}}} K(\mathbf{y}, \mathbf{x}, t)d\mu(y) = 1 .$$

The above excludes spatio-temporal variation in the rate that jumps are made. However, it is noted that this is distinct from variation in staying at the same site, since $D^{\mathbf{x}}$ could include $\mathbf{x}$ and remaining would correspond to $K(\mathbf{x}, \mathbf{x}, t) > 0$.

2.3.2 Velocity-Jump Processes

In velocity-jump random walks, movement consists of smooth runs with constant velocity interspersed by (instantaneous) reorientations [38]. For stochastically independent walkers, the individual-scale velocity-jump random walk can be formulated as an individual-scale continuous *transport equation*. Transport models form a powerful and relatively new tool in the modelling and analysis of animal and cell movement [21, 37, 40, 47], although they have a long history in continuum

mechanics (where they are usually referred to as kinetic equations) [3, 8]. As a result, various tools and techniques have been developed and in particular the scaling techniques that allow their approximation to a reduced (and hopefully simpler) macroscopic model [22, 47]. Consequently, the transport equation can be thought of as a bridge that connects the individual random walk to a fully continuous macroscopic model.

The reapplication of transport equations to biological processes has grown from seminal work of the 1980s (see [1, 38]) as an approach for modelling biological movement, whether by cells or organisms. Transport equations typically refer to mathematical models in which the particles of interest are structured by their position in space, time and velocity. In words, the transport equation for animal/cell movement takes the intuitively simple form:

Rate of change of population   Change due to   Change due to
    moving with velocity **v**   = movement through + turning into or out
        at position **x** time t space   of velocity **v**

Formally, if we define by $p(\mathbf{v}, \mathbf{x}, t)$ to be the density of the population moving with velocity $\mathbf{v} \in V$ at position $\mathbf{x}$ and time t, then

$$p_t(\mathbf{v}, \mathbf{x}, t) + \mathbf{v} \cdot \nabla p(\mathbf{v}, \mathbf{x}, t) = \mathcal{L} p(\mathbf{v}, \mathbf{x}, t), \tag{9}$$

where $\mathcal{L}$ denotes a *turning operator* that describes the process of velocity switching[1]. For the velocity space $V \subset \mathbb{R}^n$ we take $V = [s_1, s_2] \times S^{n-1}$, where $0 \leq s_1 \leq s_2 < \infty$, s_1 and s_2 define the lower and upper bounds for organism movement speed[2] and S^{n-1} defines the unit sphere.

The choice of $\mathcal{L}$ forms a key modelling decision, and an oft-used form is the integral operator representation [38]:

$$\mathcal{L} p(\mathbf{v}, \mathbf{x}, t) = -\mu p(\mathbf{v}, \mathbf{x}, t) + \mu \int_V T(\mathbf{v}, \mathbf{v}', \mathbf{x}, t) p(\mathbf{v}, \mathbf{x}, t) d\mathbf{v}', \tag{10}$$

where the first term on the right-hand side gives the rate at which particles switch away from velocity **v** and the second term denotes the switching into velocity **v** from all other velocities. The parameter μ is the *turning rate*, with $1/\mu$ the *mean run time* between individual turns. The turning kernel $T(\mathbf{v}, \mathbf{v}', \mathbf{x}, t) \geq 0$ denotes the switching into velocity **v** for a turn made at position **x** and time t, given some previous velocity $\mathbf{v}'$. Mass conservation demands

---

[1] We note that this particular form assumes there is no net force on the particles, and thus no inertia on them.

[2] It is worth noting that this is a key distinction from the kinetic theory of gas molecules, where $V = \mathbb{R}^n$ permits (at least theoretically) individual molecules to acquire infinite momentum [8].

$$\int_V T(\mathbf{v}, \mathbf{v}', \mathbf{x}, t) d\mathbf{v} = 1$$

and consequently T denotes a probability measure over V. As for the redistribution kernel in the position-jump process, its choice is a major consideration: for example, orientation signals from the environment at $\mathbf{x}$ and time t, or the inclusion of persistence in the previous direction $\mathbf{v}'$.

2.4 Directional Statistics

Each of the position-jump and velocity-jump processes above relies on various biological inputs: mean waiting times, speeds, turning rates and redistribution kernels. It is through these inputs that the random walk can be linked to biological datasets, and not least significant are the kernels K and T, which, respectively, describe probability distribution functions for either the redistribution kernel for a positional jump from some position $\mathbf{x}$ to a position $\mathbf{y}$ or a change of velocity from $\mathbf{v}'$ to $\mathbf{v}$. Fundamentally, each distribution encapsulates an orientating "choice" of the animal or cell and we now turn to consider some suitable representations.

Typical datasets for cell movement and animal navigation problems relate to orientations/headings in space and handling such data demands a review of some concepts from directional statistics [31]. In two dimensions, directional (or circular) statistics involves consideration of data on orientations that can be expressed with respect to some angle α relative to a given x-direction. The problem of directly transposing the definitions of regular (linear) statistics to circular statistics becomes immediately apparent with even its simplest concepts: for a set of angles uniformly distributed across the circle, what meaning would the (linear) mean angle of this dataset have?

In general we consider the set of directions on the n-dimensional sphere, i.e. the set of unit vectors $\mathbf{n} \in S^{n-1}$. A directional distribution is then a probability distribution $q(\mathbf{n})$ defined over S^{n-1}, i.e. one satisfying

$$q(\mathbf{n}) \geq 0 \quad \text{and} \quad \int_{S^{n-1}} q(\mathbf{n}) d\mathbf{n} = 1 \,.$$

Of particular importance for our work are the first and second moments of q, respectively the expectation $\mathbf{E}_q$ and variance–covariance matrix $\mathbb{V}_q$ (which we will often refer to simply as the variance):

$$\mathbf{E}_q = \int_{S^{n-1}} \mathbf{n} q(\mathbf{n}) d\mathbf{n},$$

$$\mathbb{V}_q = \int_{S^{n-1}} (\mathbf{n} - \mathbf{E}_q)(\mathbf{n} - \mathbf{E}_q)^T q(\mathbf{n}) d\mathbf{n}.$$
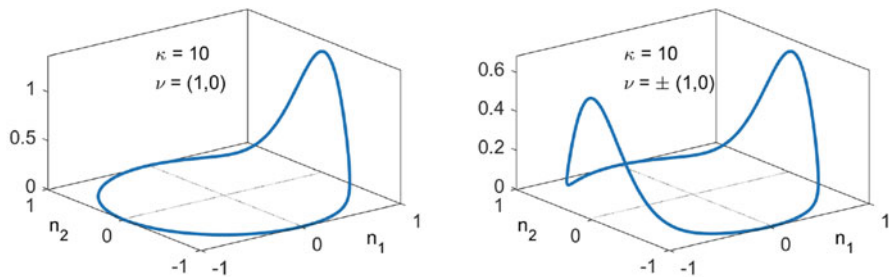
Fig. 5 Left: The unimodal von Mises distribution as a function of $\mathbf{n} = (n_1, n_2)^T \in S^1$ with a peak at $\mathbf{v} = (1, 0)^T$. Right: The bimodal von Mises distribution q_{vM} as a function of $\mathbf{n} \in S^1$ with peaks at $\mathbf{v} = \pm(1, 0)^T$. In these plots we set $\kappa = 10$.

In two dimensions, distributions will be defined on the unit circle, i.e. $\mathbf{n} \in S^1$. The simplest example is the uniform distribution, $q(\mathbf{n}) = \frac{1}{2\pi}$, although this has obviously limited usage in cases where data shows clear clustering/structure.

Given the enormous importance of the normal distribution in linear statistics, it is clearly desirable to define a similar concept for circular statistics. While the wrapped normal distribution offers the most direct analogue, the normal distribution's prominent position in circular statistics is filled instead by its sibling, the *von Mises distribution* [2, 31], which benefits from its more analytically tractable form; the subtle differences between the wrapped normal and von Mises distribution are unlikely to be differentiated within the context of typical (noisy) biological datasets. Suppose we have some dominant/preferred direction $\mathbf{v} \in S^1$, then the von Mises distribution is given by

$$q_{vM}(\mathbf{n}, \mathbf{v}, \kappa) = \frac{1}{2\pi I_0(\kappa)} e^{\kappa \mathbf{n} \cdot \mathbf{v}} \tag{11}$$

for $\mathbf{n} \in S^1$. Here κ denotes the *concentration parameter* and $I_0(\kappa)$ ($I_j(\kappa)$) denotes the modified Bessel function of first kind of order 0 (order j). The von Mises distribution is illustrated in Figure 5 on the left.

It is, of course, equally possible to write down the von Mises distribution in terms of polar angles. Denoting α to be the angle of $\mathbf{n}$ and ϕ to be the angle of $\mathbf{v}$ (i.e. the *dominant angle*), then we can write

$$q_{vM}(\alpha, \phi, \kappa) = \frac{1}{2\pi I_0(\kappa)} e^{\kappa \cos(\alpha - \phi)} .$$

The above form is more common, particularly in the biological literature [32], but it is less useful for computations and can be notationally more cumbersome. Hence we work with the coordinate free form (11) when possible.

As for the normal distribution on the line, the von Mises distribution on the circle is the workhorse of planar directional statistics [2, 31]. It can be derived from random walks, diffusion equations and energy principles, and has applications in earth sciences, physics, biology, medicine, and elsewhere. It is used for data fitting and hypothesis testing of directional data, and we will use it here for our modelling of biological movement. The first and second moments of (11) have been computed in [23] (amongst elsewhere) and are given by

$$\mathbf{E}_{q_{vM}} = \frac{I_1(\kappa)}{I_0(\kappa)} \, \boldsymbol{\nu} \, ; \tag{12}$$

$$\mathbb{V}_{q_{vM}} = \frac{1}{2} \left(1 - \frac{I_2(\kappa)}{I_0(\kappa)} \right) \mathbb{I}_2 + \left(\frac{I_2(\kappa)}{I_0(\kappa)} - \left(\frac{I_1(\kappa)}{I_0(\kappa)} \right)^2 \right) \boldsymbol{\nu}\boldsymbol{\nu}^T \, . \tag{13}$$

Note that $\mathbb{I}_2$ denotes the 2×2 identity matrix, and $\boldsymbol{\nu}\boldsymbol{\nu}^T$ denotes the dyadic product of two vectors (in tensor notation $\boldsymbol{\nu} \otimes \boldsymbol{\nu}$).

Many biological datasets possess multimodal structure and we note that the von Mises distribution can be extended to describe such instances, for example through simple linear combinations of (11); the moments correspondingly follow from linear combinations of (12–13). A particularly useful case emerges for axially symmetric directional information, such as the spreading of cells along nanogrooves or animal movement along linear environment structures such as seismic lines [33]. In such cases we can define a bimodal von Mises distributions with equal sized local maxima at $\pm\boldsymbol{\nu}$. As shown in [23], we find that for given $\boldsymbol{\nu} \in S^1$ the bimodal von Mises distribution

$$q_{bvM}(\mathbf{n}, \boldsymbol{\nu}, \kappa) = \frac{1}{4\pi \, I_0(\kappa)} \left(e^{\kappa \mathbf{n} \cdot \boldsymbol{\nu}} + e^{-\kappa \mathbf{n} \cdot \boldsymbol{\nu}} \right), \tag{14}$$

has moments

$$\mathbf{E}_{q_{bvM}} = \mathbf{0} \, , \tag{15}$$

$$\mathbb{V}_{q_{bvM}} = \frac{1}{2} \left(1 - \frac{I_2(\kappa)}{I_0(\kappa)} \right) \mathbb{I}_2 + \frac{I_2(\kappa)}{I_0(\kappa)} \boldsymbol{\nu}\boldsymbol{\nu}^T . \tag{16}$$

An illustration of the bimodal von Mises distribution is shown in Figure 5 on the right.

For the present chapter we exclusively concentrate on two-dimensional applications, however it is worth remarking that extensions can be made to three dimensions. The equivalent of the von Mises distribution in three dimensions is called the *Fisher distribution* and is given by

$$q_F(\mathbf{n}, \boldsymbol{\nu}, \kappa) = \frac{\kappa}{4\pi \, \sinh(\kappa)} e^{\kappa \mathbf{n} \cdot \boldsymbol{\nu}}, \qquad \mathbf{n} \in S^2. \tag{17}$$

Again, first and second moments have been previously calculated for this distribution (see [23]), given by

$$\mathbf{E}_{q_F} = \left(\coth \kappa - \frac{1}{\kappa} \right) \boldsymbol{v}, \tag{18}$$

$$\mathbb{V}_{q_F} = \left(\frac{\coth \kappa}{\kappa} - \frac{1}{\kappa^2} \right) \mathbb{I} + \left(1 - \frac{\coth \kappa}{\kappa} + \frac{2}{\kappa^2} - \coth^2 \kappa \right) \boldsymbol{v}\boldsymbol{v}^T. \tag{19}$$

3 Derivation of Fully Anisotropic Advection-Diffusion Equations

Here we present two derivations of the FAAD model (2), respectively, from a position-jump and velocity-jump process. We will find that both the macroscopic drift velocity **a** and the diffusion tensor $\mathbb{D}$ depend on statistical properties of the parameters in the corresponding random walk model. Hence, the choice of an appropriate model can be linked to the available data: if we can compute mean and variance of species locations, then the position-jump framework applies (see our cell movement example); if the data allow estimates for mean speeds, mean directions and their variances, then the velocity-jump process is perhaps a better choice (see the sea-turtle example).

3.1 Position-Jump Derivation

For the position-jump derivation we will make a number of convenient restrictions:

1. we assume random walks in which the jumps can occur in any direction (i.e. lattice-free), but are restricted to fixed length δ.
2. we assume the jump is *myopic* (or short-sighted).

The first restriction determines that the set D in equation (8) simply becomes the sphere of radius δ. The myopic nature of the jump implies that the heading is based only on environmental information obtained at the present site, i.e. at $(\mathbf{x}, t)$ for a walker at position $\mathbf{x}$ at time t; alternatives could involve, as an example, a dependence on information at the destination site, or a comparison between the current and destination site [55].

   The consequence of these assumptions is that our redistribution kernels can be written in terms of a directional distribution for choosing direction $\mathbf{n} \in S^{n-1}$, i.e. $K(\mathbf{y}, \mathbf{x}, t) = k(\mathbf{n}, \mathbf{x}, t)$ where $\mathbf{n}$ is in the direction $\frac{\mathbf{y}-\mathbf{x}}{|\mathbf{y}-\mathbf{x}|}$ and the Master equation becomes

$$u(\mathbf{x}, t + \tau) - u(\mathbf{x}, t) = \int_{S^{n-1}} k(\mathbf{n}, \mathbf{x} - \delta\mathbf{n}, t)u(\mathbf{x} - \delta\mathbf{n}, t) - k(\mathbf{n}, \mathbf{x}, t)u(\mathbf{x}, t)d\mathbf{n}.$$
(20)

At this point it is interesting to quickly consider the connection to the one-dimensional case (4) that was studied earlier. In the one-dimensional case we have only two headings, $\mathbf{n} \in \{-1, 1\}$. Hence we define

$$k(\mathbf{n}, x, t) = q\delta_0(-1 - \mathbf{n}) + (1 - q)\delta_0(1 - \mathbf{n}),$$

where δ_0 denotes the Dirac-delta distribution. Then (20) becomes

$$u(x, t + \tau) = qu(x - \delta, t) + (1 - q)u(x + \delta, t),$$

which is exactly (4).

For small values of δ and τ we expand the right-hand side of equation (20) about $\mathbf{x}$ and the left-hand side about t to obtain

$$\frac{\partial u}{\partial t} + O(\tau) = \frac{\delta}{\tau} \int_{S^{n-1}} -\mathbf{n} \cdot \nabla (ku) + \frac{\delta}{2} (\mathbf{n} \cdot \nabla)^2 (ku) + O(\delta^2)d\mathbf{n},$$

$$= -\frac{\delta}{\tau} \left(\nabla \cdot \int_{S^{n-1}} \mathbf{n} (ku) d\mathbf{n} \right) + \frac{\delta^2}{2\tau} \left(\nabla\nabla : \int_{S_{n-1}} \mathbf{n}\mathbf{n}^T k d\mathbf{n} \right) u + O(\delta^3/\tau),$$

where we use the colon notation (:) which denotes the contraction of two tensors as

$$A : B = \sum_{i,j=1}^{n} a_{ij}b_{ij}, \qquad A, B \in \mathbb{R}^{n \times n}.$$

As discussed in Section 2.2, distinct scalings generate different continuous limits and we again consider both the drift and diffusion dominated scenarios.

- (drift dominated) if $\delta, \tau \to 0$ such that $\lim_{\delta,\tau\to 0} \frac{\delta}{\tau} = c$ (constant) we have the hyperbolic model

$$\frac{\partial u}{\partial t} + \nabla \cdot (\mathbf{a}(\mathbf{x}, t)u) = 0,$$

  where $\mathbf{a}(\mathbf{x}, t) = c \int_{S^{n-1}} \mathbf{n}k(\mathbf{n}, x, t)d\mathbf{n}$ (i.e. the advection is proportional to the first moment of k).

- if $\delta, \tau \to 0$ such that $\lim_{\delta,\tau\to 0} \frac{\delta^2}{2\tau} = d$ then we have two cases

  - (diffusion dominated) if $\int_{S^{n-1}} \mathbf{n}k d\mathbf{n} = 0$ then we have

$$\frac{\partial u}{\partial t} = \nabla\nabla : (\mathbb{D}(\mathbf{x}, t)u),$$

    where $\mathbb{D}(\mathbf{x}, t)$ is the $n \times n$ matrix defined by $\mathbb{D}(\mathbf{x}, t) = d \int_{S^{n-1}} \mathbf{n}\mathbf{n}^T k(\mathbf{n}, \mathbf{x}, t)d\mathbf{n}$.

– (drift-diffusion). If $\lim_{\delta,\tau \to 0} \frac{\delta^2}{2\tau} = d$ and $\lim_{\delta,\tau \to 0} \frac{\delta}{\tau} \int_{S^{n-1}} \mathbf{n} k d\mathbf{n} \sim c\delta$, we have

$$\frac{\partial u}{\partial t} + \nabla \cdot (\mathbf{a}(\mathbf{x}, t)u) = \nabla\nabla : (\mathbb{D}(\mathbf{x}, t)u),$$

with

$$\mathbf{a}(\mathbf{x}, t) = c \int_{S^{n-1}} \mathbf{n} k(\mathbf{n}, \mathbf{x}, t)d\mathbf{n},$$

$$\mathbb{D}(\mathbf{x}, t) = d \int_{S^{n-1}} (\mathbf{n} - \mathbf{a}(\mathbf{x}, t))(\mathbf{n} - \mathbf{a}(\mathbf{x}, t))^T k(\mathbf{n}, \mathbf{x}, t)d\mathbf{n}.$$

The final form is particularly relevant, as it is exactly the FAAD model we introduced earlier. In this case, we now have a connection to the advection velocity and diffusion tensor terms from the underlying statistical inputs $k(\mathbf{n}, x, t)$ of a random walk process.

3.2 Velocity-Jump Derivation

To facilitate the derivation we consider a simplified form of transport equation. Specifically, we assume that the turning kernel does not depend on the previous velocity $\mathbf{v}'$, i.e.

$$T(\mathbf{v}, \mathbf{v}', \mathbf{x}, t) = T(\mathbf{v}, \mathbf{x}, t).$$

Using this choice in (10) for (9) we have the considerably simpler form

$$p_t(\mathbf{v}, \mathbf{x}, t) + \mathbf{v} \cdot \nabla p(\mathbf{v}, \mathbf{x}, t) = -\mu p(\mathbf{v}, \mathbf{x}, t) + T(\mathbf{v}, \mathbf{x}, t)u(\mathbf{x}, t), \qquad (21)$$

where we have defined the macroscopic density

$$u(\mathbf{x}, t) = \int_V p(\mathbf{v}, \mathbf{x}, t)d\mathbf{v}. \qquad (22)$$

The process from here is to derive an evolution equation for the macroscopic density $u(\mathbf{x}, t)$, which can be achieved through a variety of scaling techniques, including parabolic scaling, hyperbolic scaling and moment closure. For a detailed treatment for model (21) we refer to our earlier paper [22] and we summarise one such choice here: moment closure.

3.2.1 Moment Closure Method

In a moment closure approach, the idea is to identify statistically meaningful quantities related to p and T, such as expectations and variances. We remind ourselves that the formulation demands that the turning distribution $T(\mathbf{v}, \mathbf{x}, t)$ is a probability measure, i.e.

$$T(\mathbf{v}, \mathbf{x}, t) \geq 0, \qquad \int_V T(\mathbf{v}, \mathbf{x}, t)d\mathbf{v} = 1,$$

and we consider its expectation $\mathbf{E}_T$ and variance $\mathbb{V}_T$,

$$\mathbf{E}_T(\mathbf{x}, t) = \int_V \mathbf{v}T(\mathbf{v}, \mathbf{x}, t)d\mathbf{v},$$

$$\mathbb{V}_T(\mathbf{x}, t) := \int_V (\mathbf{v} - \mathbf{E}_T(\mathbf{x}, t))(\mathbf{v} - \mathbf{E}_T(\mathbf{x}, t))^T T(\mathbf{v}, \mathbf{x}, t)d\mathbf{v}. \qquad (23)$$

$\mathbf{E}_T(\mathbf{x}, t)$ describes the mean new velocity vector for the turning kernel, while $\mathbb{V}_T(\mathbf{x}, t)$ is its variance–covariance matrix.

We now introduce the same quantities for $p(\mathbf{v}, \mathbf{x}, t)$, although we note that p in itself is not a probability measure, since $\int_V p(\mathbf{v}, \mathbf{x}, t)d\mathbf{v} = u(\mathbf{x}, t)$ is not necessarily equal to one. But we can normalise, introducing $\hat{p}$ via the equation

$$u(\mathbf{x}, t)\hat{p}(\mathbf{v}, \mathbf{x}, t) = p(\mathbf{v}, \mathbf{x}, t)$$

and noting that $\int_V \hat{p}(\mathbf{v}, \mathbf{x}, t)d\mathbf{v} = 1$. We subsequently introduce the expectation and variances

$$\mathbf{E}_{\hat{p}}(\mathbf{x}, t) = \int_V \mathbf{v}\hat{p}(\mathbf{v}, \mathbf{x}, t)d\mathbf{v},$$

$$\mathbb{V}_{\hat{p}}(\mathbf{x}, t) = \int_V (\mathbf{v} - \mathbf{E}_{\hat{p}}(\mathbf{x}, t))(\mathbf{v} - \mathbf{E}_{\hat{p}}(\mathbf{x}, t))^T \hat{p}(\mathbf{v}, \mathbf{x}, t)d\mathbf{v}.$$

Then, $\mathbf{E}_{\hat{p}}$ defines the mean velocity of the normalised population while $\mathbb{V}_{\hat{p}}$ is its variance–covariance matrix. In terms of the original population density p, we can write

$$\int_V \mathbf{v}p(\mathbf{v}, \mathbf{x}, t)d\mathbf{v} = \mathbf{E}_{\hat{p}}(\mathbf{x}, t)u(\mathbf{x}, t), \qquad (24)$$

$$\int_V (\mathbf{v} - \mathbf{E}_{\hat{p}}(\mathbf{x}, t))(\mathbf{v} - \mathbf{E}_{\hat{p}}(\mathbf{x}, t))^T p(\mathbf{v}, \mathbf{x}, t)d\mathbf{v} = \mathbb{V}_{\hat{p}}(\mathbf{x}, t)u(\mathbf{x}, t). \qquad (25)$$

Next we explain the moment closure method itself. We can derive equations for the expectation and variance introduced above, and it turns out that the equation

for the expectation (first moment) depends on the variance (second moment) while
the equation for the variance depends on a third moment, etc. Effectively we obtain
an infinite hierarchy of moment equations, where each new equation depends on
a next higher moment. To obtain a usable model, the sequence of equations must
be cut somewhere, a process termed *moment closure*. Generally, choosing the right
closure condition is a work of art and many plausible approaches are available in the
literature [8, 20]. Here we will choose a standard method that uses the equilibrium
distribution and cut at the second moment to obtain a single equation of type (2) for
the mass density $u(\mathbf{x}, t)$.

Let us start by integrating equation (21) over V and express each term with
respect to the corresponding moments. Note that hereon we omit the arguments
for readability.

$$\int_V p_t d\mathbf{v} + \int_V \nabla \cdot \mathbf{v} p \, d\mathbf{v} = -\mu \int_V p \, d\mathbf{v} + \mu \int_V T \, d\mathbf{v} \, u,$$

which can equivalently be written as

$$u_t + \nabla \cdot (\mathbf{E}_{\hat{p}} u) = -\mu u + \mu u = 0.$$

Hence our first equation is a conservation law

$$u_t + \nabla \cdot (\mathbf{E}_{\hat{p}} u) = 0. \tag{26}$$

As a next step we multiply (21) by $\mathbf{v}$ and again integrate over V. We obtain

$$\int_V \mathbf{v} u_t d\mathbf{v} + \int \mathbf{v}(\nabla \cdot \mathbf{v} p) d\mathbf{v} = -\mu \int_V \mathbf{v} p \, d\mathbf{v} + \mu \int_V \mathbf{v} T \, d\mathbf{v} \, u,$$

which can be equivalently written as

$$(\mathbf{E}_{\hat{p}} u)_t + \nabla \cdot \int_V \mathbf{v}\mathbf{v}^T p \, d\mathbf{v} = \mu(\mathbf{E}_T - \mathbf{E}_{\hat{p}})u. \tag{27}$$

We write the second moment $\int \mathbf{v}\mathbf{v}^T p d\mathbf{v}$ in terms of the variance of $\hat{p}$, i.e.

$$\mathbb{V}_{\hat{p}} u = \int_V (\mathbf{v} - \mathbf{E}_{\hat{p}})(\mathbf{v} - \mathbf{E}_{\hat{p}})^T p d\mathbf{v},$$

$$= \int_V \mathbf{v}\mathbf{v}^T p d\mathbf{v} - 2 \int_V \mathbf{v}\mathbf{E}_{\hat{p}}^T p d\mathbf{v} + \mathbf{E}_{\hat{p}} \mathbf{E}_{\hat{p}}^T u.$$

Hence

$$\int_V \mathbf{v}\mathbf{v}^T p d\mathbf{v} = \mathbb{V}_{\hat{p}} u + \mathbf{E}_{\hat{p}} \mathbf{E}_{\hat{p}}^T u.$$

We use this expression in (27) and obtain the equation for the expectation:

$$(\mathbf{E}_{\hat{p}}u)_t + \nabla \cdot (\mathbf{E}_{\hat{p}}\mathbf{E}_{\hat{p}}^T u) = -\nabla \cdot (\mathbb{V}_{\hat{p}}u) + \mu(\mathbf{E}_T - \mathbf{E}_{\hat{p}})u. \quad (28)$$

So far we have simply integrated and introduced a few fancy variables for $\mathbf{E}_{\hat{p}}$, $\mathbb{V}_{\hat{p}}$, etc. The next step is to present two critical assumptions that allow us to close the system:

(a1) Moment closure – the variance $\mathbb{V}_{\hat{p}}$ is computed from the equilibrium distribution p_e: $\mathbb{V}_{\hat{p}} \approx \mathbb{V}_{\hat{p}_e}$.

(a2) Fast flux relaxation – the equation (28) for the expectation $\mathbf{E}_{\hat{p}}$ is in quasi-equilibrium.

It is noted that the above assumptions were originally conceived in a physical context, namely the kinetic theory of dilute gases [8]. The extent to which these can be directly translated to biological particles, such as cells and organisms, is uncertain and a goal for further investigations: within the present article we simply take them as stated. The first assumption has proven to be useful in a number of studies. The second assumption effectively stipulates that, *at the space/time scales* of the macroscopic model, the particle instantaneously respond to local information: reasonable, say, for an organism switching direction multiple times a day but studied over a macroscopic scale of months to years.

The equilibrium distribution p_e can be computed from the condition $\mathscr{L}p_e = 0$ where $\mathscr{L}$ is the integral operator from (10). In our case

$$\mathscr{L}p = \mu(Tu - p) = 0$$

is solved by the equilibrium distribution,

$$p_e(\mathbf{v}, \mathbf{x}, t) = u(\mathbf{x}, t)T(\mathbf{v}, \mathbf{x}, t).$$

This equilibrium distribution has the expectation

$$\mathbf{E}_{\hat{p}_e}u = \int_V \mathbf{v}p_e d\mathbf{v} = \int_V \mathbf{v}uT \ d\mathbf{v} = \mathbf{E}_T u. \quad (29)$$

Now we approximate the highest order term, the variance as

$$\mathbb{V}_{\hat{p}} \approx \mathbb{V}_{\hat{p}_e} = \int_V (\mathbf{v} - \mathbf{E}_{\hat{p}_e})(\mathbf{v} - \mathbf{E}_{\hat{p}_e})^T uT \ d\mathbf{v} = \mathbb{V}_T u. \quad (30)$$

In assumption (a2) we postulate that the equation (28) is in quasi-steady state, i.e.

$$\mathbf{0} \approx -\nabla \cdot (\mathbb{V}_{\hat{p}}u) + \mu(\mathbf{E}_T - \mathbf{E}_{\hat{p}})u,$$

and, substituting the moment closure (30), we find the approximation

$$\mathbf{E}_{\hat{p}}u \approx -\frac{1}{\mu}\nabla \cdot (\mathbb{V}_T u) + \mathbf{E}_T u\,. \tag{31}$$

Finally, we substitute (31) into the conservation law (26) and we assume that the approximation is good (i.e. we replace $\approx$ with $=$) to obtain a closed system

$$u_t + \nabla \cdot (\mathbf{E}_T u) = \frac{1}{\mu}\nabla\nabla : (\mathbb{V}_T u)\,. \tag{32}$$

This closed equation is exactly the fully anisotropic advection-diffusion equation (FAAD) in (2) with

$$\mathbf{a}(\mathbf{x}, t) = \mathbf{E}_T(\mathbf{x}, t) \quad \text{and} \quad \mathbb{D}(\mathbf{x}, t) = \frac{1}{\mu}\mathbb{V}_T(\mathbf{x}, t). \tag{33}$$

Let us consider two special cases of this derivation.

Example 1 (Directional Distributions) Some further simplifications can be used to relate turning directly to a directional distribution. Let us restrict movement to a single speed, i.e. $V = sS^{n-1}$, where s is the mean speed and S^{n-1} is the n-dimensional sphere. Hence, $\mathbf{v} = s\mathbf{n}$ where $\mathbf{n} \in S^{n-1}$ defines the directional heading. We can therefore simply define T in terms of a directional distribution, say q, for choosing some heading $\mathbf{n} \in S^{n-1}$. Specifically,

$$T(\mathbf{v}, \mathbf{x}, t) := \frac{q(\mathbf{n}, \mathbf{x}, t)}{s^{n-1}}\,, \tag{34}$$

where the s^{n-1} factor results from moving between a distribution over V to one over S^{n-1}. Subsequently, advection and diffusion tensors for (2) will be given by

$$\mathbf{a}(\mathbf{x}, t) = s\mathbf{E}_q(\mathbf{x}, t) = s\int_{S^{n-1}} \mathbf{n}q(\mathbf{n}, \mathbf{x}, t)d\mathbf{n}\,, \tag{35}$$

$$\mathbb{D}(\mathbf{x}, t) = \frac{s^2}{\mu}\mathbb{V}_q(\mathbf{x}, t) = \frac{s^2}{\mu}\int_{S^{n-1}} (\mathbf{n} - \mathbf{E}_q)(\mathbf{n} - \mathbf{E}_q)^T q d\mathbf{n}\,. \tag{36}$$

Notice that for the von-Mises and Fisher distributions discussed earlier, we have already computed expectation and variances: i.e., they are ready to be used.

Example 2 (including external drift) The above derivation can also be applied to the case of particles that are drifting in an external velocity field $\mathbf{b}(\mathbf{x}, t) \in \mathbb{R}^n$, for example turtles transported in ocean currents or insects blown by the wind. If particles are inactive, their heading is exactly the direction of the external flow field

$\mathbf{b}(\mathbf{x}, t)$, in which case the directional distribution used for the turning kernel would be a point measure

$$T(\mathbf{v}, \mathbf{x}, t) = \delta_{\mathbf{b}(\mathbf{x},t)}(\mathbf{v}).$$

Then, expectation and variances can be calculated as

$$\mathbf{E}_T(\mathbf{x}, t) = \mathbf{b}(\mathbf{x}, t) \quad \text{and} \quad \mathbb{V}_T(\mathbf{x}, t) = 0.$$

The above macroscopic limit is a pure drift equation

$$u_t + \nabla \cdot (\mathbf{b}(\mathbf{x}, t)u) = 0. \tag{37}$$

Note that the same equation arises if we simply assume that a force proportional to $\mathbf{b}$ acts on cells, where the cells have no inertia. In that case we also get a drift of the form $\mathbf{b}(x, t)$. For situations in which we have a population of actively navigating/moving particles immersed in an external velocity field we can simply combine the two cases of (35), (36) and (37) to obtain

$$u_t + \nabla \cdot ((\mathbf{a}(\mathbf{x}, t) + \mathbf{b}(\mathbf{x}, t))u) = \nabla\nabla : (\mathbb{D}(\mathbf{x}, t)u). \tag{38}$$

Indeed, this case was used to analyse sea turtle data in [43].

4   Applications to Cell/Animal Orientation Datasets

We illustrate the methodology through our two motivating applications. In each case we take as a starting point an individual-based description for oriented movement: an underlying velocity-jump process for the random walk. This initial description arises naturally, given our fundamental knowledge of particle behaviours: cells on fabricated substrates reveal alignment and orientation according to the substrate anisotropy (Figure 1); datasets for turtles are based according to their mean swimming orientation when subjected to specific magnetic fields (Figure 2). We remark that in each application a two-dimensional approximation ($n = 2$) is reasonable: cells migrate across the two-dimensional substrate and the diving capabilities of young turtles restrict their movements to the ocean surface [10]. Simulation methods are provided in the Appendix.

The two applications differ not only in their field of study but also with respect to the "usable data". For cell movement we consider a tabulated summary of responses for distinct micro-ridge substrates, Table 1. This is data at a population-averaged level, and we do not have explicit data on each individual cell's orientating response. Nevertheless, we can still use this data to directly parametrise our model, which

is done directly at the FAAD level that arises as a continuous approximation of the individual model. In the case of hatchling movements, a circular dataset is available for the mean heading of each tested turtle in samples exposed to distinct navigation fields. In this case, we can directly parametrise the von Mises distribution that describes an individual's orientation response, and subsequently scale to a macroscopic FAAD equation in order to collect population-level measurements.

4.1 Application A: Cell Movement on Microfabricated Structures

The data of Jeon et al. [25] in Table 1 are at a population level: the mean x-velocity ($v_x \pm v_{x,error}$), mean y-velocity ($v_y \pm v_{y,error}$) and mean speed ($s \pm s_{error}$), where velocity components are measured according to absolute values. To relate these to the parametrisation of (2), we first remark on some particulars induced by the anisotropic arrangement. Firstly, the dominant drift velocity $\mathbf{a} = 0$, since the environment is essentially bidirectional and, on average, equal numbers of cells will be found travelling up or down (left or right). Secondly, the substratum is anisotropic but spatially homogeneous, and hence the diffusion tensor $\mathbb{D}$ is constant in space. Finally, anisotropies coincide with the coordinate axes, so $\mathbb{D}$ becomes a diagonal matrix

$$\mathbb{D} = \begin{pmatrix} \lambda_x & 0 \\ 0 & \lambda_y \end{pmatrix}, \tag{39}$$

with two eigenvalues λ_x and λ_y.

Given that $\mathbb{D}$ is constant in space, the fully anisotropic diffusion model becomes identical to the standard anisotropic diffusion equation:

$$u_t = \nabla \cdot \mathbb{D} \nabla u. \tag{40}$$

Hence we can exploit results relating to the above. Firstly, the fundamental solution of (40) is the Gaussian distribution with covariance matrix $\mathbb{D}$:

$$u(\mathbf{x}, t) = \frac{1}{2\pi t \sqrt{\text{Det}\mathbb{D}}} \exp\left(-\frac{1}{4t}\mathbf{x}^T \mathbb{D}^{-1}\mathbf{x}\right) \tag{41}$$

(in two spatial dimensions), where the set

$$E_c := \{\mathbf{x} : \mathbf{x}^T \mathbb{D}^{-1}\mathbf{x} = c\}$$

gives the set of locations for which there is an equal probability of finding a random mover that started at the origin. This set defines a *diffusion ellipse*, with semi-axes of lengths $\sqrt{\lambda_x}$ and $\sqrt{\lambda_y}$, respectively, and provides one way to graphically visualise

the anisotropy of $\mathbb{D}$. A second method is the *diffusion peanut*, which is the image of the map $\mathbf{w} \mapsto \mathbf{w}^T \mathbb{D} \mathbf{w}$ for $\mathbf{w} \in S^1$, and relates to the mean-squared displacement in direction $\mathbf{w}$, $\sigma_{\mathbf{w}}^2$, via $\sigma_{\mathbf{w}}^2 = 2t\mathbf{w}^T \mathbb{D} \mathbf{w}$ [45]. This gives rise to the *apparent diffusion coefficient in direction* $\mathbf{w}$,

$$\text{ADC}_{\mathbf{w}} := \frac{\sigma_{\mathbf{w}}^2}{2t} = \mathbf{w}^T \mathbb{D} \mathbf{w} \,.$$

In particular, given coordinate directions $(1, 0)^T$ and $(0, 1)^T$, we find that the mean squared displacements in x- and y-directions will be $2t\lambda_x$ and $2t\lambda_y$ respectively. This provides the key for using the data in Table 1: given the mean velocities in x and y directions and taking a unit time step of 1 min, we convert to mean displacements for the x and y directions and in turn estimate the λ's in (39), the values of which are listed in Table 2 for each experimental setting. To illustrate some of the anisotropies graphically, we plot diffusion ellipses and peanuts for the three cases 16×32, 16×64 and $16 \times \infty$ in Figure 6. As the structure is stretched along the $y-$ direction we observe progressively thinned-out ellipses/pinched peanuts, reflecting restricted movement along this axis.

For turning rates of the order of 2.5/min and a tracking timeframe of 400 min, each cell turns on average 1000 times across its track. Given an average speed of 0.5 μm/min, each particle travels about 200 μm in this timeframe, suggesting this to be a suitably macroscopic scale. We subsequently plot solutions to the FAAD model on this spatial and temporal scale, plotting the evolving distribution for 10 individuals presumed to have started at the origin. Exploiting the spatially uniform nature of the environment, solutions will simply be governed by the fundamental solution (41), which we plot in Figure 7 at $t = 100$ and $t = 400$ for the same three cases 16×32, 16×64 and $16 \times \infty$. Consistent with the diffusion ellipses, the highest degree of environmental anisotropy generates a quasi-one-dimensional spread of the cells along the y-axis. We note that there is no direct information in [25] that allows us to directly compare these plots to their data, and therefore this represents a prediction of the expected population distribution.

We can turn the argument full circle and use the measured data to estimate cell movement parameters that would be required in the underlying velocity-jump process: speed s, turning rate μ, and concentration parameter κ of the bimodal von-Mises distribution (14). We should note that this is predicated on an *assumption* of the individual-level behaviour: i.e., that cells orient according to a bimodal von-Mises distribution. In the absence of specific individual-level data, this is of course impossible to state with certainty, yet it is nevertheless instructive to show how we can "reverse the process".

Recall that, given the symmetric/bidirectional scenario, the drift velocity $\mathbf{a} = 0$ and the macroscopic model becomes the pure fully anisotropic diffusion equation

$$u_t = \nabla\nabla : (\mathbb{D}u) \,,$$

Table 2 Speed and diffusion coefficients λ_x and λ_y from the data from Jeon et al. [25]. We also list the values for the turning rate μ, and the concentration parameter κ of a corresponding bi-modal von-Mises distribution.

Case	Ridge height	Speed ± error	$\lambda_x \pm$ error	$\lambda_y \pm$ error	Turning rate	Anisotropy
(μm× μm)	(μm)	(μm/min)	(μm^2/min)	(μm^2/min)	(/min)	parameter
12 x 24	3	0.78±0.027	0.072±0.0057	0.17±0.015	2.53	2.57
12 x 48	3	1.01±0.045	0.039±0.0039	0.41±0.041	2.29	10.79
12 x ∞	3	0.59±0.029	0.0032±0.00040	0.16±0.016	2.17	49.49
16 x 32	3	0.9±0.03	0.12±0.010	0.21±0.017	2.48	1.96
16 x 64	3	1.0±0.039	0.048±0.0047	0.38±0.033	2.34	8.32
16 x ∞	3	0.84±0.0072	0.0072±0.00080	0.32±0.029	2.15	44.84
24 x 48	3	0.55±0.027	0.034±0.0039	0.088±0.010	2.47	2.89
24 x 96	3	0.58±0.022	0.020±0.0024	0.12±0.0098	2.40	6.42
24 x ∞	3	0.52±0.028	0.0072±0.00084	0.12±0.013	2.20	16.47
12 x 24	10	0.65±0.026	0.055±0.0053	0.11±0.011	2.63	2.10
12 x 48	10	0.83±0.046	0.016±0.0023	0.29±0.033	2.25	18.28
12 x ∞	10	0.61±0.032	0.00081±0.00012	0.18±0.019	2.05	224.22
Control	0	0.63±0.025	0.072±0.0072	0.085±0.014	2.53	0.83
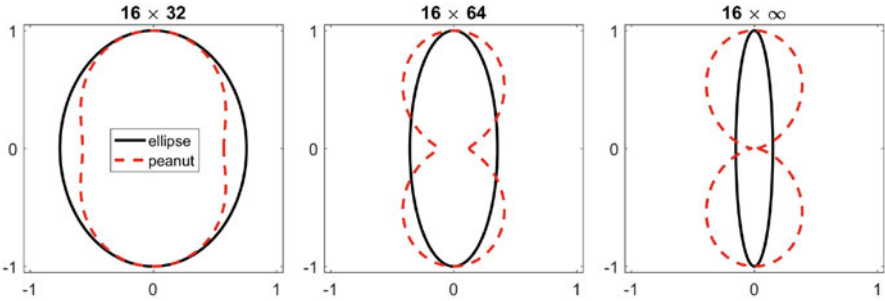
Fig. 6 Diffusion ellipses (black solid line) and peanuts (red-dashed line) representing the anisotropic cell migration for the 16×32, 16×64 and $16 \times \infty$ micro-ridge arrangements, see Table 2. Note that we renormalise the longer axes to aid comparison between their respective shapes.

with diffusion tensor from (36)

$$\mathbb{D} = \frac{s^2}{\mu} \mathbb{V}_q = \frac{s^2}{2\mu} \left(1 - \frac{I_2(\kappa)}{I_0(\kappa)} \right) \mathbb{I}_2 + \frac{s^2}{\mu} \frac{I_2(\kappa)}{I_0(\kappa)} \boldsymbol{v} \boldsymbol{v}^T. \tag{42}$$

For now let us write the diffusion tensor in (42) as

$$\mathbb{D} = k_1 \mathbb{I}_2 + k_2 \boldsymbol{v} \boldsymbol{v}^T, \qquad k_1 = \frac{s^2}{2\mu} \left(1 - \frac{I_2(\kappa)}{I_0(\kappa)} \right), \qquad k_2 = \frac{s^2}{\mu} \frac{I_2(\kappa)}{I_0(\kappa)}. \tag{43}$$
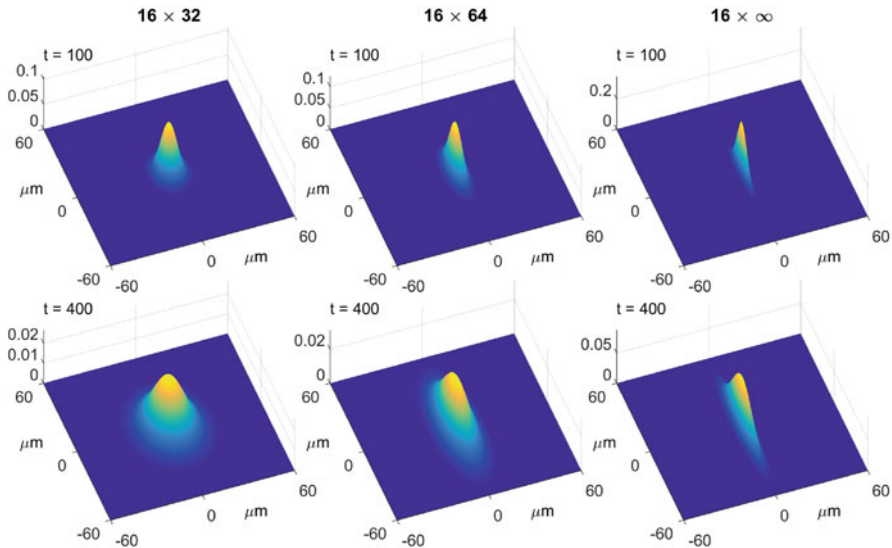
Fig. 7 Population distributions $u(\mathbf{x}, t)$ plotted at (top row) $t = 100$ and (bottom row) $t = 400$ for 10 cells initiated at $\mathbf{x} = \mathbf{0}$.

Since the primary direction of anisotropy is in the y-direction, we have $\boldsymbol{v} = (0, 1)^T$ and can explicitly compute

$$\mathbb{D} = \begin{pmatrix} k_1 & 0 \\ 0 & k_1 + k_2 \end{pmatrix} = \begin{pmatrix} \lambda_x & 0 \\ 0 & \lambda_y \end{pmatrix},$$

where we employed (39) for the second equality. Therefore, we obtain two equations relating k_1, k_2 and λ_x, λ_y:

$$k_1 = \lambda_x \qquad k_1 + k_2 = \lambda_y.$$

Using the expressions for k_1 and k_2 in (43) we find $\mathrm{tr}\mathbb{D} = \lambda_x + \lambda_y = \frac{s^2}{\mu}$, which gives

$$\mu = \frac{s^2}{\lambda_x + \lambda_y}. \tag{44}$$

The corresponding values for the turning rate μ are listed in Table 2. Furthermore we can use the previous relations to compute

$$\frac{I_2(\kappa)}{I_0(\kappa)} = \frac{\mu(\lambda_y - \lambda_x)}{s^2}. \tag{45}$$
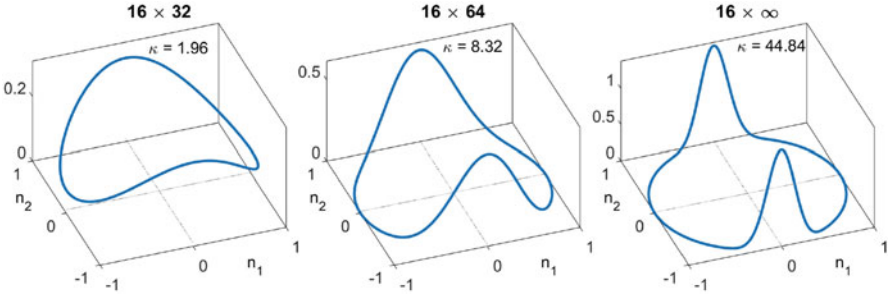
Fig. 8 Bimodal von Mises distributions for the turning distributions of stochastic velocity-jump random walks corresponding to the macroscopic cases in Figure 7.

Determining concentration (or anisotropy) parameter κ demands inverting the ratio of modified Bessel functions $I_2(\kappa)/I_0(\kappa)$, a monotonically increasing function from 0 to 1 for $\kappa \in [0, \infty)$. We use Wolfram Alpha to invert this function for our data and list the corresponding values in Table 2.

The turning rate μ is surprisingly consistent between the different experiments, which may reflect that this parameter is (relatively) independent of the form of the substratum (for example, determined mainly by intracellular factors). The anisotropy parameter κ, however, varies over several orders of magnitude with the most anisotropic cases corresponding to those without ridges in the x-direction, as expected. Graphical illustrations of the bimodal von Mises distribution for the three cases 16×32, 16×64 and $16 \times \infty$ are provided in Figure 8. Higher ridges (10 µm) offer even more guidance and, consequently, larger anisotropy: including an extreme of $\kappa = 224$. This upper value effectively reduces the bimodal von Mises distribution to a pair of Delta functions in opposite directions, so that movement is almost completely confined to the one-dimensional y-direction.

4.2 Application B: Magnetic Navigation in Loggerhead Hatchlings

Our second application considers hatchling loggerhead turtle navigation, investigating the extent to which oriented swimming keeps them within the relative safety of the North Atlantic Gyre. Specifically, we extend the agent-based simulation study of [51], exploiting the computational advantages of the FAAD model to investigate how different amounts of oriented swimming help to maintain turtle trajectories. We specifically focus on two critical regions of the Gyre as follows.

- (NE) a north east Gyre location corresponding to a "corridor" along its north-eastern sector, the region where it breaks into northerly (perilous) and southerly moving streams. We centre this region on the point marked 3 in Figure 2, with its corresponding dataset providing the parameters for orientation.

- (SW) a south west Gyre location corresponding to a region of the Carribean, where the Gyre branches into a more northerly stream that remains within the Gyre, or continues west into the Gulf of Mexico. We centre this region on point 7 in Figure 2, with its corresponding dataset providing the parameters for orientation.

In each case we quantitatively assess the extent to which hatchling turtles that are continuously immersed at some point inside (NE) or (SW) tend to maintain a trajectory within the Gyre. Specifically, for each region (NE) and (SW) we numerically solve the FAAD equation, as extended to incorporate both an additional drift (as derived above, see equation (38)) due to currents and a constant (in time) source representing hatchlings entering the region under investigation. Specifically, defining $u(\mathbf{x}, t)$ to be the hatchling turtle density, we solve

$$u(\mathbf{x}, t)_t + \nabla \cdot ((\mathbf{a}(\mathbf{x}, t) + \mathbf{b}(\mathbf{x}, t)) u(\mathbf{x}, t)) = \nabla\nabla : (\mathbb{D}(\mathbf{x}, t) u(\mathbf{x}, t)) + \gamma \delta_{\mathbf{x}_0}(\mathbf{x}), \quad (46)$$

where, in addition to previous definitions, γ represents the rate at which new hatchlings enter the system and $\delta_{\mathbf{x}_0}$ is the 2D Dirac delta function. The point $\mathbf{x}_0$ defines the "immersion site" and we set $\mathbf{x}_0 = (25°W, 44.5°N)$ for (NE) and $\mathbf{x}_0 = (56.5°W, 8°N)$ for (SW), respectively denoting points upwards of the general current direction for the regions. Encountered currents $\mathbf{b}(\mathbf{x}, t)$ can vary considerably over time, and we therefore inject hatchlings continuously into the corridor across a full calender year (taken to be 2016). Our restriction to the two-dimensional ocean surface follows from the poor diving abilities of young marine turtles: a maximum dive of the order of 1–2 metres for loggerhead hatchlings [10].

We define a "success" and a "failure" boundary for each region, removing turtles if they hit either of these boundaries and tracking over time the total numbers that have done so. In the context of the continuous model, this corresponds to setting absorbing boundary conditions along two boundaries. For the (NE) region we define the success boundary along the 42.5°N line and the failure boundary along 46.5°N line; the more northerly line represents turtles moving towards cooler waters and straying from the southerly shifting Gyre. For (SW) the success boundary is set along 18°N line and the failure boundary marked by 64.5°W; success is implied by a northerly shift with the Gyre, while failure is marked by a westward shift towards the Gulf of Mexico. Of course, the lack of any data makes any such notion of success or failure moot and we cannot equate these boundaries with survival probabilities: they simply provide a proxy to track the tendency to remain within the Gyre.

To close the computational regions we consider two further boundaries with reflective boundary conditions associated with them, so that there is no net loss across these boundaries. For (NE) we consider the lines 28°W/12°W, and for (SW) the lines 54.5°W/8°N. Note that these lines are all reasonably far from the initial injection site such that, in practice, the vast majority of turtles end up becoming absorbed by one of the success/failure boundaries before hitting one of the reflective boundaries.

4.2.1   Data and Parametrisation

The model demands two specific components that can be drawn from biological data: the ocean currents $\mathbf{b}(\mathbf{x}, t)$ for the passive drift vector field and navigation/movement parameters for hatchling active movement. Velocity fields for ocean currents are obtained from HYCOM (the global HYbrid Coordinate Ocean Model, [6]), an ocean forecasting model forced by wind speed, heat flux and numerous other factors that has been subsequently assimilated with field measurements (from satellites, floats, moored buoys, etc.) to generate post-validated output. The resolution of HYCOM data ($1/12°$ and day to day) allows it to reproduce both the large scale persistent currents and localised phenomena such as eddies. Note that the surface/near-surface swimming behaviour of young turtles allows us to restrict to the (2D) upper-most layer of HYCOM datasets. HYCOM data for each of regions (NE) and (SW) was downloaded from http://pdrc.soest.hawaii.edu/data/data.php, accessed during June/July 2017. Note that for computations, HYCOM data has been interpolated from its native resolutions ($1/12°$ and day-day) to the spatial/temporal resolution required by the numerical code via standard linear interpolation schemes.

Defining the active movement component to motion requires specifying the speed/turning rate (s, λ) parameters and the concentration/dominant direction $(\kappa, \mathbf{v})$ parameters demanded by the von Mises distribution. Hatchlings are capable of sustaining speeds of 0.72 km/h (see [51] and references therein) and, based on this, we suppose the average daily swim length varies from 0–10 km/day, corresponding to between 0 and $\sim$14 h per day of active swimming. Of course, whether a hatchling would be capable of maintaining active swimming at the upper end of this spectrum is somewhat debatable. For the turning rate, we assume a value of 50 per day, although it is noted that modifying this parameter has very little bearing on the overall results. Given this turning rate and assuming each turtle remains in the simulated region for the order of 100 days, we obtain an average of 5000 turns per trajectory. For average swimming speeds ranging between 0–10 km/day, turtles swim up to 1000 km over the simulation timecourse, implying spatial scales of the order 100–1000 km as suitably macroscopic. We remark that the comparisons between the individual and continuous simulations suggest the veracity of the continuous limit as a suitable approximation.

Concentration parameters/dominant directions can be drawn directly from the hatchling orientation datasets illustrated in Figure 2. For region (NE) we utilise the dataset indicated by position 3: fitting a von Mises distribution via standard methods (e.g., see, [2]) allows us to obtain estimates $\kappa_{NE} \approx 0.874$ and $\mathbf{v}_{NE} \approx (0.307, -0.952)$, the latter representing a true bearing of 162°. The region (SW) employs position 7 and yields $\kappa_{SW} \approx 0.797$ and $\mathbf{v}_{SW} \approx (0.070, 0.998)$, representing a true bearing of 4°. We assume these values are constant in space and time over the respective regions.
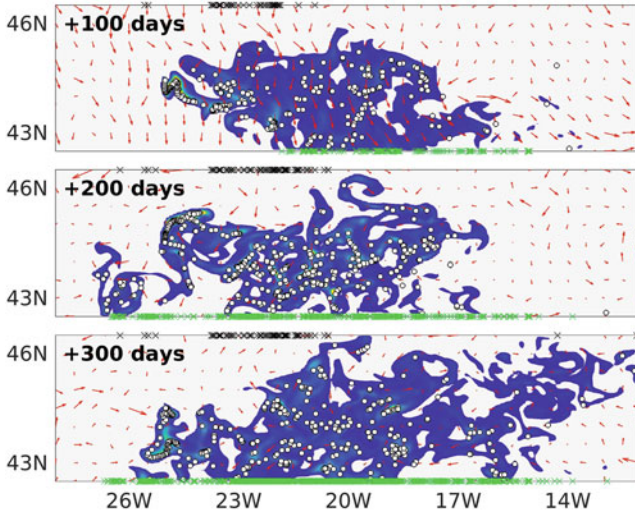
Fig. 9 Comparison between the FAAD model (46) and individual-based stochastic simulations of the velocity-jump model for the problem of North Atlantic turtle hatchling movement. In each frame we plot both the continuous population density distribution $u(\mathbf{x}, t)$ (reflected by the colour map, where grey indicates negligible density and blue to yellow reflects increasing density) and the individual dots generated by the velocity-jump simulations. Here, top and bottom boundaries, respectively, define the "failure" and "success" boundaries, and the individual particles are colour coded according to whether they are still moving (white dots) or have hit either the failure (black crosses) or success (green crosses) boundary. Underlying ocean currents are indicated by the red arrows. For this simulation we use region (NE) and release particles continuously from position $\mathbf{x}_0 = (25°W, 44.5°N)$ with $\gamma = 5$/day. The total daily swim is set at $s = 2$ km/day, with $\lambda = 50$/day, $\kappa_{NE} \approx 0.874$ and $\mathbf{\nu}_{NE} \approx (0.307, -0.952)$. Note that the von Mises distribution for these values is visualised by the dashed red line in the inset figure to the left-hand frame of Figure 11. Simulations (in terms of ocean currents utilised) start on 01/01/2016 (midnight) with solutions displayed on the days following as indicated.

4.2.2 Results

In Figure 9 we compare the density distribution predicted by the parametrised FAAD model (46) with a particle distribution obtained through individual-based simulations of the stochastic velocity-jump process. The close correlation between the continuous density distribution (as reflected by the colourmap) and the distribution of individual particles (white dots) indicates that the FAAD model provides a highly acceptable approximation for the turtle distribution. Further simulations (not shown) confirm this close correspondence, and we therefore exploit the FAAD model for its computational advantages in the subsequent simulations.

Figure 10 compares density distributions for the same region at the same time points under three choices for the amount of active swimming: 0 km/day (i.e. only passive drifting occurs), 2 km/day and 10 km/day. A shift towards a greater amount
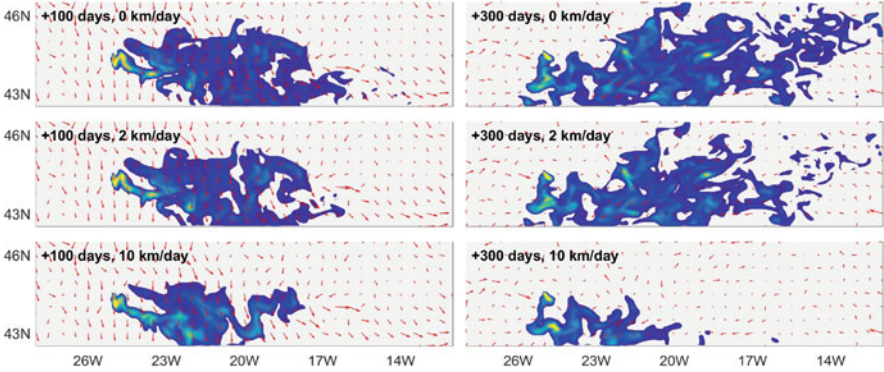
Fig. 10 Comparison of population density distributions under varying amounts of active swimming per day. In each frame we plot the turtle density distribution (colour density map, as described in Figure 9) at the two separate times (left) +100 days and (right) +300 days for (top row) $s = 0$ km/day, (middle row) $s = 2$ km/day and (bottom row) $s = 10$ km/day. The strength and direction of ocean currents is indicated by the red arrows. All other parameters and details as in Figure 9.

of active swimming has a clear impact on the density distribution, pushing it in an expected southerly direction such that a greater density becomes absorbed by the "success" boundary.

Finally, we plot the results from a more extended analysis, following a parameter sweep for each of the two regions, classifying the data obtained in terms of the following simple "success measure":

$$\text{Success at time T} = \frac{\text{Total density hitting success boundary by time T}}{\text{Total density hitting success and failure boundaries by time T}}.$$

The above clearly approaches 1 for a successful population and 0 for an unsuccessful population. In the simulations here we set $T = 500$ for a population continuously released at $\mathbf{x}_0$ from $t = 0$ (midnight, 01/01/2016) to the end of 2016 ($t = 366$); the continuation until $T = 500$ ensures that by the end of the simulation only a negligible fraction of the released population has failed to hit one of the absorbing boundaries. Simulations are plotted in Figure 11 for each of the two regions, under a range of daily active swimming distances and for three values of the concentration parameter: the value obtained by the data fitting and perturbations of $\times 2$ and $\times 1/2$ these values. The simulations clearly show that increasing the amount of active swimming, or increasing the certainty of orientation, nudges a greater proportion of the population towards the successful boundary, supporting the hypothesis that oriented responses can help maintain hatchling movement within the Gyre (e.g. [28, 51]). Extensions of the study to consider movement throughout the full circulatory path would allow more detailed evaluations into the extent to which oriented swims aid route maintenance: we remark that this would be a focus for a future study and refer to [28] for such an analysis for an individual-based model.
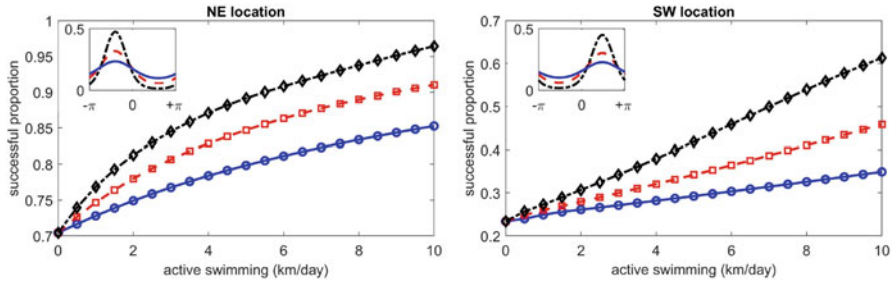
Fig. 11 Success is plotted as a function of daily swimming distance for the two regions and for different concentration parameters. All other parameters and details as in Figure 9. Red dashed line indicates a choice of κ as taken directly from the data fitting, with blue solid and black dot-dashed respectively showing choices of $\times 2$ and $\times 1/2$ these values. Insets plot the corresponding von Mises distributions used for each simulation set.

5 Conclusions

In this chapter we have described the use of fully anisotropic advection-diffusion models as a way of modelling animal and cell movement behaviour. We have described the derivation of these models from two fundamental stochastic random walks, position-jump and velocity-jump processes, thereby connecting the macroscopic parameters and terms to the statistical inputs at the individual level. Utilising two distinct datasets, we have shown how the models can be parametrised either directly at the population level or by starting at the individual/stochastic random walk model. Beyond the applications presented here, we note that similar methods have been applied in a number of other applications in ecology and cell movement, including seismic-line following behaviour of wolves and caribou populations [22, 33], butterfly hilltopping [44] and anisotropic glioma growth [45, 56].

6 Appendix: Numerical methods

Stochastic Velocity-Jump Process

The stochastic random walk simulations assume each individual performs a velocity-jump random walk in either a static (cell movement) or flowing (turtles) medium. Particle motion therefore derives from an oriented and active movement

component that describes the individual's self-motility (crawling, swimming, flying, etc.), the details of which are encoded in the velocity-jump random walk, and a passive drift due to movement of the medium (e.g. air or water flow). The passive drift is described by a velocity vector field $\mathbf{b}(\mathbf{x}, t)$ ($\mathbf{x}$ is position and t is time) that could be either imposed (e.g. obtained from public-domain datasets) or separately modelled (e.g. Navier-Stokes equation). Note that we implicitly assume that the individuals have negligible impact on the flow of the surrounding medium.

For an individual i at position $\mathbf{x}_i(t)$ and time t, travelling with active velocity $\mathbf{v}_i(t) = s(\cos \alpha_i(t), \sin \alpha_i(t))$ where angle $\alpha_i(t)$ denotes the active heading, then at time $t + \Delta t$ (where Δt is small) we have:

$$\mathbf{x}_i(t + \Delta t) = \mathbf{x}_i(t) + \Delta t (\mathbf{v}_i(t) + \mathbf{b}(\mathbf{x}_i, t)) ;$$
$$\mathbf{v}_i(t + \Delta t) = \begin{cases} \mathbf{v}_i'(t + \Delta t) \text{ with probability } \lambda \Delta t , \\ \mathbf{v}_i(t) \qquad \text{otherwise} . \end{cases} \qquad (47)$$

where $\mathbf{v}_i'(t + \Delta t)$ is the new velocity chosen at time $t + \Delta t$ if a reorientation has occurred, randomly chosen according to the given probability distribution for the turning kernel of the velocity jump random walk.

The time discretisation Δt used in simulation is suitably small, in the sense that simulations conducted with smaller timesteps generate near identical results. For the selection of new active headings via the von Mises distribution we employ code (circ_vmrnd.m) from the circular statistics toolbox [4]. Currents and the inputs required for the active heading choice are interpolated from the native spatial/temporal resolutions in the saved variables to the individual particle's continuous position $\mathbf{x}$ and time t via a simple linear interpolation scheme.

Continuous Model

As described earlier, moment closure analysis for the velocity-jump random walk generates a continuous model of FAAD form

$$u(\mathbf{x}, t)_t + \nabla \cdot ((\mathbf{a}(\mathbf{x}, t) + \mathbf{b}(\mathbf{x}, t)) u(t, \mathbf{x})) = \nabla\nabla : (\mathbb{D}(\mathbf{x}, t) u(\mathbf{x}, t)) . \qquad (48)$$

where $\mathbf{a}(\mathbf{x}, t)$ and $\mathbb{D}(\mathbf{x}, t)$ depend on the statistical inputs of the random walk (mean speed, turning rates, moments of the turning distribution).

Numerical methods for solving (48) are adapted from our previous studies (e.g. see [43]). We adopt a simple Method of Lines (MOL) approach, first discretising in space (using a fixed lattice of space Δx) to create a large system of ordinary differential equations (ODEs) which are subsequently integrated over time. The "fully anisotropic" diffusion term is expanded into an advective and standard anisotropic-diffusion component. This advective component, along with advection terms arising from ocean currents and active directional swimming, is solved via

a third-order upwinding scheme, augmented by flux-limiting to ensure positivity of solutions (e.g., see [24]). The choice of finite-difference discretisation for the anisotropic diffusion term is more specific: naive discretisations can lead to numerical instability for sufficiently anisotropic scenarios (high κ values). The method of [58] allows greater flexibility in the choice of κ: in this scheme, finite difference derivatives are calculated and combined along distinct axial directions: the axes of the discretisation lattice and the major and minor axes of the ellipse corresponding to the anisotropic diffusion tensor. Under the moderate levels of anisotropy encountered here we obtain a stable scheme. Time discretisation here is performed via a simple forward Euler method with a suitably small time step.

References

1. Alt, W.: Biased random walk model for chemotaxis and related diffusion approximation. J. Math. Biol. **9**, 147–177 (1980)
2. Batschelet, E.: Circular Statistics in Biology. Academic Press, London (1981)
3. Bellomo, N., Schiavo, M.: Lecture Notes on the Mathematical Theory of Generalized Boltzmann Methods. World Scientific, Singapore (2000)
4. Berens, P.: Circstat: a MATLAB toolbox for circular statistics. J. Stat. Softw. **31**, 1–21 (2009)
5. Berg, H.: Random Walks in Biology. Princeton University Press (1983)
6. Bleck, R.: An oceanic general circulation model framed in hybrid isopycnic-cartesian coordinates. Ocean Mod. **4**, 55–88 (2002)
7. Cagnacci, F., Boitani, L., Powell, R.A., Boyce, M.S.: Animal ecology meets GPS-based radiotelemetry: a perfect storm of opportunities and challenges. Phil. Trans. R. Soc. B **365**, 21572162 (2010)
8. Cercignani, C., Illner, R., Pulvirenti, M.: The Mathematical Theory of Diluted Gases. Springer, New York (1994)
9. Codling, E.A., Plank, M.J., Benhamou, S.: Random walk models in biology. J. Roy. Soc. Interface **5**, 813–834 (2008)
10. Davenport, J. and Clough, W.: Swimming and diving in young loggerhead sea turtles (*Caretta caretta L.*). Copeia, **1986**, 53–57 (1986)
11. Dawes, A., Iron, D.: Cortical geometry may influence placement of interface between par protein domains in early caenorhabditis elegans embryos. J. Theor. Bio. **333**, 27–37 (2013)
12. Deutsch, A., Dormann, S.: Cellular Automaton Modeling of Biological Pattern Formation: Characterization, Applications, and Analysis. Birkaeuser, Boston (2005)
13. Dickinson, R.B., Guido, S., Tranquillo, R.T.: Biased cell migration of fibroblasts exhibiting contact guidance in oriented collagen gels. Ann. Biomed. Eng. **22**, 342–356 (1994)
14. Dunn, G.A., Heath, J.P.: A new hypothesis of contact guidance in tissue cells. Exp. Cell Res. **101**, 1–14 (1976)
15. Fuxjager, M.J., Eastwood, B.S., Lohmann, K.J.: Orientation of hatchling loggerhead sea turtles to regional magnetic fields along a transoceanic migratory pathway. J. Exp. Biol. **214**, 2504–2508 (2011)
16. Gritsenko, P., Ilina, O., Friedl, P.: Interstitial guidance of cancer invasion. J. Pathol. **226**, 185–199 (2012)
17. Gritsenko, P., Leenders, W., Friedl, P.: Recapitulating in vivo-like plasticity of glioma cell invasion along blood vessels and in astrocyte-rich stroma. Histochem. Cell Biol. (2017). doi: 10.1007/s00418-017-1604-2
18. Hadeler, K., Hillen, T., Lutscher, F.: The Langevin or Klein-Kramers approach to biological modeling. Math. Models Meth. Appl. Sci. **14**(10), 1561–1583 (2004)

19. Hanahan, D., Weinberg, R.: Hallmarks of cancer: The next generation. Cell **144**, 646–674 (2011)
20. Hillen, T.: M^5 mesoscopic and macroscopic models for mesenchymal motion. J. Math. Biol. **53**, 585–616 (2006)
21. Hillen, T., Othmer, H.: The diffusion limit of transport equations derived from velocity jump processes. SIAM J. Appl. Math. **61**, 751–775 (2000)
22. Hillen, T., Painter, K.J.: Transport models for movement in oriented habitats and anisotropic diffusion. In: Lewis, M., Maini, P., Petrovskii,S. (Eds.), Dispersal, Individual Movement and Spatial Ecology: A Mathematical Perspective. Springer,Heidelberg. p. 46 (2013)
23. Hillen, T., Painter, K.J., Swan, A.C., Murtha, A.D.: Moments of von Mises and Fisher distributions and applications. Math. Biosci. & Eng **14**, 673–694 (2017)
24. Hundsdorfer, W., Verwer, J.G.: Numerical solution of time-dependent advection-diffusion-reaction equations, vol. 33. Springer Science & Business Media (2003)
25. Jeon, H., Hidai, H., Hwang, D.J., Healy, K.E., Grigoropoulos, C.P.: The effect of microscale anisotropic cross patterns on fibroblast migration. Biomaterials **31**, 4286–4295 (2010)
26. Keener, J., Sneyd, J.: Mathematical Physiology. Springer (1994)
27. Lohmann, K.J., Cain, S.D., Dodge, S.A., Lohmann, C.M.F.: Regional magnetic fields as navigational markers for sea turtles. Science **294**, 364–366 (2001)
28. Lohmann, K.J., Putman, N.F., Lohmann, C.M.F.: The magnetic map of hatchling loggerhead sea turtles. Curr. Opin. Neurobiol. **22**, 336–342 (2012)
29. Luschi, P.: Long-distance animal migrations in the oceanic environment: orientation and navigation correlates. ISRN Zool. (2013)
30. Lutscher, F., Pachepsky, E., Lewis, M.: The effect of dispersal patterns on stream populations. SIAM J. Appl. Math. **65**, 1305–1327 (2005)
31. Mardia, K., Jupp, P.: Directional Statistics. Wiley and Sons (2000)
32. McKenzie, H., Lewis, M., Merrill, E.: First passage time analysis of animal movement and insights into the functional response. Bull. Math. Biol. **71**, 107–129 (2009)
33. McKenzie, H.W., Merrill, E.H., Spiteri, R.J., Lewis, M.A.: How linear features alter predator movement and the functional response. Interface focus **2**, 205–216 (2012)
34. Moorcroft, P., Lewis, M.: Mechanistic Home Range Analysis. Princeton University Press, Princeton (2006)
35. Murray, J.D.: Mathematical Biology. I: An Introduction, 3rd edn. Springer-Verlag, New York (2002)
36. Murray, J.D.: Mathematical biology II: Spatial models and biochemical applications, Springer-Verlag, New York (2003)
37. Okubo, A., Levin, S.: Diffusion and Ecological Problems: Modern Perspectives. Springer (2002)
38. Othmer, H.G., Dunbar, S., Alt, W.: Models of dispersal in biological systems. J. Math. Biol. **26**, 263–298 (1988)
39. Othmer, H.G., Stevens, A: Aggregation, blowup, and collapse: the ABC's of taxis in reinforced random walks. SIAM J. Appl. Math., **57**, 1044–1081 (1997).
40. Othmer, H.G., Hillen, T.: The diffusion limit of transport equations II: Chemotaxis equations. SIAM J. Appl. Math. **62**, 1122–1250 (2002)
41. Othmer, H.G., Xue, C.: The mathematical analysis of biological aggregation and dispersal: progress, problems and perspectives. In: Lewis, M., Maini, P., Petrovskii, S. (Eds.), Dispersal, Individual Movement and Spatial Ecology: A Mathematical Perspective. Springer,Heidelberg. 79–127 (2013)
42. Painter, K.J.: Modelling migration strategies in the extracellular matrix. J. Math. Biol. **58**, 511–543 (2009)
43. Painter, K.J., Hillen, T.: Navigating the flow: Individual and continuum models for homing in flowing environments. Royal Soc. Interface **12**, 20150,647 (2015)
44. Painter, K.J.: Multiscale models for movement in oriented environments and their application to hilltopping in butterflies. Theor. Ecol. **7**, 53–75 (2014)

45. Painter, K.J., Hillen, T.: Mathematical modelling of glioma growth: the use of diffusion tensor imaging (DTI) data to predict the anisotropic pathways of cancer invasion. J. Theor. Biol. **323**, 25–39 (2013)
46. Patlak, C.: Random walk with persistence and external bias. Bull. Math. Biophys. **15**, 311–338 (1953)
47. Perthame, B.: Transport Equations in Biology. Birkhäuser (2007)
48. Preziosi, L. (ed.): Cancer Modelling and Simulation. Chapman Hall/CRC Press (2003)
49. Provenzano, P.P., Eliceiri, K.W., Campbell, J.M., Inman, D.R., White, J.G., Keely, P.J.: Collagen reorganization at the tumor-stromal interface facilitates local invasion. BMC medicine **4**, 38 (2006)
50. Putman, N.F., Endres, C.S., Lohmann, C.M.F., Lohmann, K.J.: Longitude perception and bicoordinate magnetic maps in sea turtles. Curr. Biol. **21**, 463–466 (2011)
51. Putman, N.F., Verley, P., Shay, T.J., Lohmann, K.J.: Simulating transoceanic migrations of young loggerhead sea turtles: merging magnetic navigation behavior with an ocean circulation model. J. Exp. Biol. **215**, 1863–1870 (2012)
52. Saxton, M.J., Jacobson, K.: Single-particle tracking: applications to membrane dynamics. Ann. Rev. Biophys. & Biomol. Struct. **26**, 373–399 (1997)
53. Sobel, D.: Longitude: The true story of a lone genius who solved the greatest scientific problem of his time. Bloomsbury Publishing USA (1995)
54. Stevens, A.: The derivation of chemotaxis-equations as limit dynamics of moderately interacting stochastic many particle systems. SIAM J. Appl. Math. **61**(1), 183–212 (2000)
55. Stevens, A., Othmer, H.G.: Aggregation, blowup, and collapse: the ABC's of taxis in reinforced random walks. SIAM J. Appl. Math. **57**, 1044–1081 (1997)
56. Swan, A., Hillen, T., Bowman, J.C., Murtha, A.D.: A patient-specific anisotropic diffusion model for brain tumour spread. Bull. Math. Biol. pp. 1–33 (2017)
57. Turchin, P.: Quantitative Analysis of Movement. Sinauer Assoc., Sunderland (1998)
58. Weickert, J.: Anisotropic diffusion in image processing. Teubner, Stuttgart (1998)
59. Wolf, K., Müller, R., Borgmann, S., Bröcker, E.B., Friedl, P.: Amoeboid shape change and contact guidance: T-lymphocyte crawling through fibrillar collagen is independent of matrix remodeling by MMPs and other proteases. Blood **102**, 3262–3269 (2003)

Bacterial Chemotaxis: A Classic Example of Multiscale Modeling in Biology

Chuan Xue

Abstract Both individual-based models and PDE models have been developed to describe the active movement of cell populations in various contexts. Individual-based models can faithfully replicate the detailed mechanisms of cell signaling and movement but are computationally intensive. PDE models are amenable for fast computation and mathematical analysis but are often based on phenomenological descriptions of macroscopic cell fluxes. Multiscale methods must be developed to elucidate the connections between individual-based models and PDE models in order to combine the strengths of these approaches. This chapter summarizes recent progress in connecting individual-based models and PDE models for chemotaxis of bacterial populations, which is a classic example for multiscale modeling in biology. The application scope and limitations of the Keller-Segel chemotaxis equation **are** also discussed.

1 Introduction

Active cell movement plays a crucial role in the life of living organisms, and in many situations the movement is guided by extracellular chemical signals. Sperm cells swim long distances to fertilize an egg, and this process is directed by chemical substances released from the outer surface of the egg [1]. Neutrophils and fibroblasts move into a wound to stop infection and rebuild the tissue, and this process is orchestrated by a number of chemical signals [2]. Cancer cells can migrate away from a primary tumor to invade other tissues and cause cancer metastasis [3]. In bioremediation, bacteria are used to clean waste water because they migrate towards certain toxins and degrade them [4]. The directed movement of cells or organisms in response to extracellular chemical signals is called "chemotaxis."

C. Xue (✉)
Department of Mathematics, Ohio State University, 43210 Columbus, OH, USA
e-mail: cxue@math.osu.edu

143

To understand the role of chemotaxis in multicellular processes, it is crucial to develop quantitative and predictive mathematical models to describe chemotaxis of cell populations. Detailed individual-based models have been developed to incorporate data in cell signaling, movement, as well as cell-cell interaction. This approach can faithfully replicate the biology, but due to the large number of cells involved and the complexity of the intracellular dynamics, they are computationally intensive and frequently become intractable. Alternatively, simplified PDE models have also been used to describe the spatial-temporal dynamics of the cell densities. This approach is appealing and convenient because of the variety of mathematical tools available in simulation and analysis of PDE models. However, these models often rely on phenomenological assumptions of cell fluxes which cannot be easily justified experimentally. Multiscale methods to embed data at the cellular and subcellular processes into PDE models of the cell population dynamics must be developed to combine the strengths of these two approaches.

Significant progress has been made along this line for bacterial chemotaxis, which is the most basic and best understood form of chemotaxis. In this chapter, I review results that focus on the derivation of PDE models for bacterial chemotaxis from individual-based models that describe single cell movement as a velocity jump process and integrates intracellular signaling as an internal ODE system. Through numerical examples, I illustrate the application scope and limitations of the well-known Patlak-Keller-Segel chemotaxis equation in modeling the bacteria population dynamics. The mathematical framework developed for bacterial chemotaxis can be extended to similar biological systems and serve as a classic example for multiscale modeling in biology.

2   Biological Background

Chemotaxis of run-and-tumble bacteria has been extensively studied over the past 50 years. Examples of such bacteria include *Escherichia*, *Salmonella*, *Bacillus*, *Rhodobacter*, and *Pseudomonas* [5–8]. Among them the best understood is the model system *Escherichia coli* [8–10], which is described below in detail. Chemotaxis of other bacteria is similar but not identical to that of *E. coli*.

2.1   Single Cell Movement

E. coli has a cylindrical cell body that is 1–2 μm long and several helical flagella that project away from the cell body in all directions. Each flagellum can be rotated by a flagellar motor embedded in the cell membrane either clockwise or counterclockwise. If all the flagella are rotated counterclockwise (CCW), they form a single bundle and push the cell forward in a long smooth "run" at a speed $s = 10$–30 μm/s; if some flagella are rotated clockwise (CW), these flagella disengage

from the bundle causing the cell to stop and "tumble" in place. The cell moves by randomly alternating smooth runs and reorienting tumbles. In the absence of a chemical signal gradient, the mean run time is 1 s and mean tumble time is 0.1 s. However, if the cell is exposed to a signal gradient, it alters the rotation pattern of each flagellar motor so that the run time is extended when the cell moves up (down) the gradient of a chemoattractant (chemorepellent).

2.2 Intracellular Signaling

The rotation of a flagellar motor is controlled by the intracellular chemotaxis pathway shown in Figure 1. The transmembrane chemoreceptors form stable ternary complexes with the signaling proteins CheA and CheW, and cluster at one pole
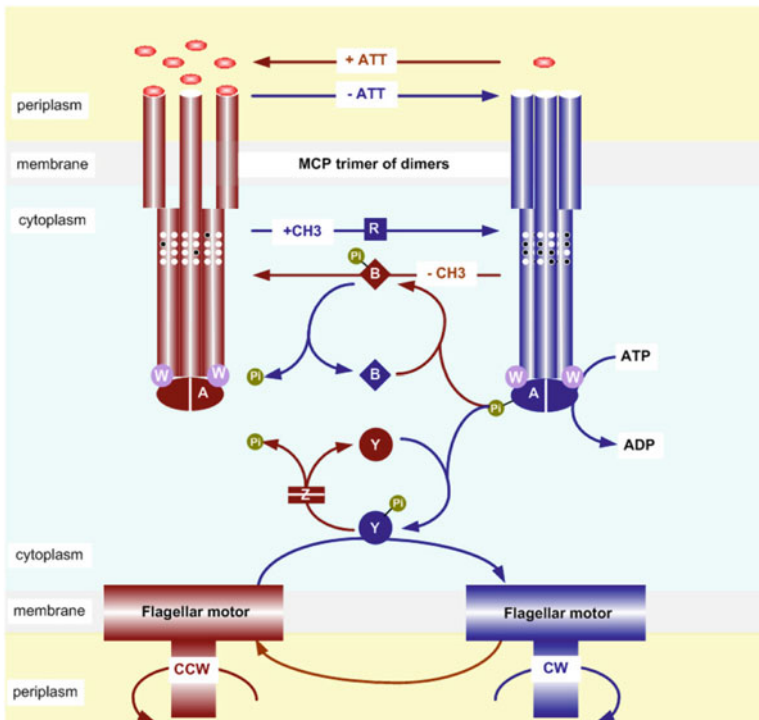
Fig. 1 The chemotaxis signaling pathway for the model bacterium *E. coli*. Transmembrane chemoreceptors function as trimers of dimers with ligand-binding domains on the peri-plasmic side and signaling domains on the cytoplasmic side. Methylation sites of receptors appear as white dots on the receptors. The cytoplasmic signaling proteins are represented by single letters, e.g., A = CheA. Red (blue) components promote CCW (CW) rotation of flagellar motors. Reprinted from [11] with permission.

of the cell body. CheA is an auto-kinase, and its activity is reduced if attractant molecules bind to the associated receptor but can be restored if the methylation level of the receptor increases. CheA is also a kinase for the response regulators CheY and CheB. The phosphorylated form CheYp binds to the flagella motor, which increases the probability of CW rotation and triggers tumbling. CheBp and CheR change the methylation state of the receptor at a slower rate: CheR methylates it and CheBp demethylates it.

Upon ligand binding, the kinase activity of CheA is reduced, thus CheYp decreases rapidly, and the cell tends to run for longer. This process, called excitation, occurs within fractions of seconds. Simultaneously, CheBp is reduced but CheR is not affected, thus the receptor methylation level increases, until the activity of CheA is restored to its pre-stimulus level. This process, called adaptation, takes seconds to minutes, depending on the nature of the signal. We note that excitation and adaptation are two concurrent processes that affect each other, specifically, adaptation acts as a negative feedback to excitation and allows the cell to subtract away background signal and respond to further signal changes.

Bacterial chemotaxis involves multiple time scales. Ligand binding to chemoreceptors on the cell membrane, change of kinase activity, and phosphorylation reactions inside a cell occur within fractions of seconds. Methylation and demethylation of the receptors that cause adaptation of a cell occur on a time scale of seconds. The adaptation time scale is the slowest time scale for intracellular dynamics. It is intrinsically determined by the intracellular signaling network and reflects the time scale of methylation and demethylation.

3   Individual-Based Models

Chemotaxis plays a critical role in self-organization patterns formed in bacterial colonies, e.g., traveling bands, aggregates, swarm rings [12–16]. To understand the interplay of different mechanisms in the pattern formation process, individual-based models have been developed to couple descriptions of single cell movement (Section 3.1) and cell signaling (Section 3.2), as well as cell growth and the dynamics of extracellular signals [17–19].

When the cell density is sufficiently low, cell-cell mechanical interactions can be neglected and cell movement can be modeled as velocity jump processes without collisions. This situation may still involve a large population of cells. For example, in case that the cell volume fraction is 0.1% and the medium has dimension 1cm $\times$ 1cm $\times$ 1mm, assume that the volume of a single cell is approximately $1\mu m^3$, then the number of cells is approximately 10^8. When the cell density becomes high, cells can also interact with each other through the surrounding fluid. Individual-based models have been developed for such situations by treating cells as particles without intracellular dynamics [20–27]. Our review focuses on the low cell density situation.

3.1 Single Cell Movement Modeled as a Velocity Jump Process

The run-and-tumble movement of a single cell is frequently modeled as a velocity-jump process [17, 28, 29]. A velocity jump process is a stochastic process in which the velocity of an individual jumps instantaneously at random time points. The velocity jumps can be characterized by two quantities: a turning rate function which specifies when the next velocity jump occurs and a turning kernel which specifies the probability density of the new velocity given the velocity prior to the jump.

3.1.1 A Base Model

For bacterial chemotaxis, the mean tumble time is much smaller than the mean run time, thus the tumbling phase of the cell movement is usually ignored. The speed of the cell is usually assumed to be constant, and thus the velocity space is a sphere

$$V = s_0 \partial B_0^1, \tag{1}$$

where s_0 is the typical speed of the cell and ∂B_0^1 is the unit sphere centered at the origin.

Under this simplification, the cell movement can be modeled as a sequence of runs connected by instantaneous reorientations. Because CheYp binding suppresses CCW rotation of the flagella which in turn induce tumbling, the turning rate λ is an increasing function of intracellular CheYp concentration y_p, i.e.,

$$\lambda = \lambda(y_p). \tag{2}$$

The turning kernel is usually assumed to only depend on the angle between $\mathbf{v}$ and $\mathbf{v}'$, denoted as θ,

$$T(\mathbf{v}, \mathbf{v}') = h(\theta). \tag{3}$$

Recordings of cell trajectories in free space shows that *E. coli* has a slight directional persistence towards the previous direction after a tumble [30, 31], thus $h(\theta)$ is a decreasing function. To conserve probability, one must have

$$\int_V T(\mathbf{v}, \mathbf{v}') d\mathbf{v} = 1. \tag{4}$$

Under the above assumptions, the movement of a single cell is described by the following SDE system

$$\begin{cases} d\mathbf{x} = \mathbf{v} dt, \\ d\mathbf{v} = (\zeta - \mathbf{v}) dY(t, \lambda), \end{cases} \tag{5}$$

where ζ is a random variable with probability density given by $T(\cdot, \mathbf{v})$ and $Y(t, \lambda)$ is an inhomogeneous Poisson process with intensity given by $\lambda(y_p)$. The system is coupled with equations for cell signaling through the variable y_p.

3.1.2 Inclusion of Cell Tumbling

More detailed models have been developed to incorporate a finite tumbling phase explicitly. This was achieved by describing the cell movement as a velocity jump process with a moving state and a resting state. Denote the rate for a running cell to stop and tumble by λ and the rate for a tumbling cell to start running by μ, i.e.,

$$\text{Run} \underset{\mu}{\overset{\lambda}{\rightleftharpoons}} \text{Tumble.}$$
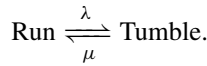
The transition rates λ and μ depend on the rotation state of all the flagella around the cell body, which in turn depends on intracellular CheYp concentration y_p. Thus one has

$$\lambda = \lambda(y_p), \qquad \mu = \mu(y_p).$$

The switching behavior of a single flagellum between CW and CCW rotations has been measured under different CheYp concentrations in [32]. Specifically, experimental data was collected on the CW bias (P_{CW}) and the switching frequency (F) of a single flagellar motor (Figure 2A-B, dots), which revealed the ultrasensitivity of the motor to CheYp.

Assume the direction switches between CCW and CW are first order reactions with rates λ_f and μ_f, i.e.,

$$\text{CCW} \underset{\mu_f}{\overset{\lambda_f}{\rightleftharpoons}} \text{CW.}$$
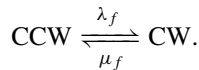
The Cluzel data on P_{CW} and F can then be transformed into data for λ_f and μ_f (Figure 2C-D, dots). The transformation is based on the relations

$$\lambda_f (1 - P_{CW}) = \mu_f P_{CW}, \quad F = \frac{2\lambda_f \mu_f}{\lambda_f + \mu_f}.$$

or equivalently,

$$\lambda_f = \frac{F}{2(1 - P_{CW})}, \quad \mu_f = \frac{F}{2P_{CW}}.$$

This data can be fitted by requiring λ_f to be an increasing function of y_p and μ_f a decreasing function of y_p (Figure 2). The fitting in [33] leads to

$$\lambda_f = a_1 \exp(b_1 Y_p),$$
$$\mu_f = a_2 \exp\left(-(b_2 - Y_p)^4/c\right),$$

(6)

where a_1, b_1, a_2, b_2, and c are constants given in the caption of Figure 2. Please note that these fitting results (solid curves) are much better than the original fitting method suggested in [32], which fits P_{CW} by a Hill function with hill coefficient 10.3 and $K_m = 3.1\ \mu M$ and the derivative of the function for F (dashed curves).
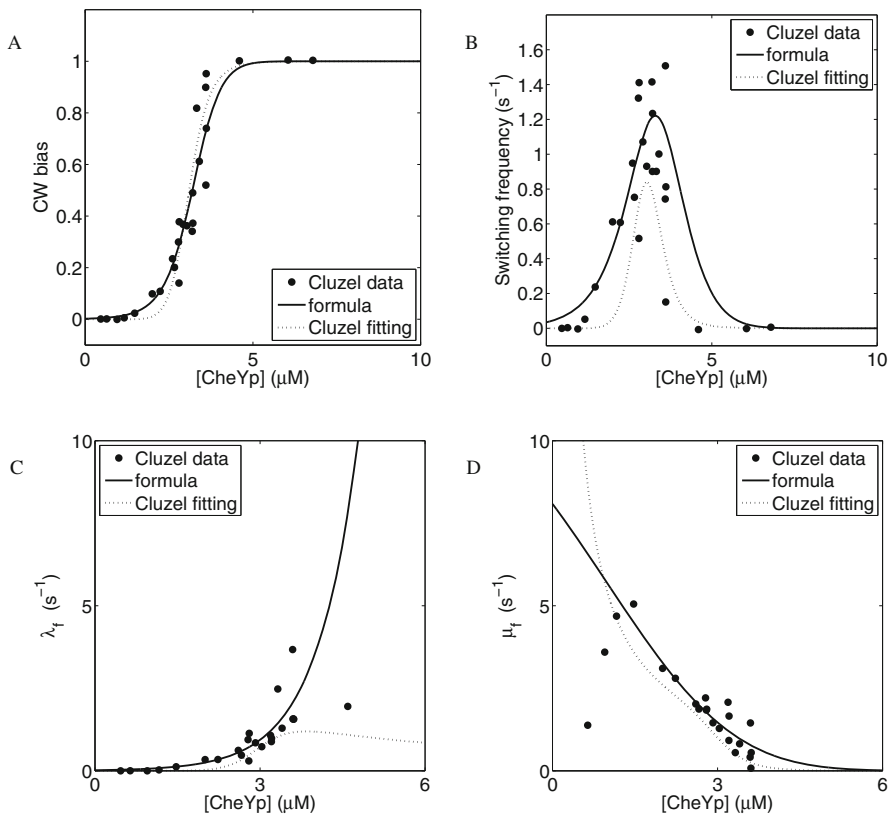
Fig. 2 Parameter fitting for the transition rates λ_f and μ_f as a function of CheYp (y_p). The dots are from experimental data extracted from Figure 2 in [32]. The solid lines are calculated using the formula (6). Parameters: $a_1 = 0.0174001\ s^{-1}$, $b_1 = 1.32887\ \mu M^{-1}$, $a_2 = 12.0809\ s^{-1}$, $b_2 = -5.83762\ \mu M$, $c = 2892.12$. The dotted lines are calculated using the original fitting method suggested in [32].

To calculate the cell-level rates λ and μ, one way is to use a voting process: assume that all the flagella of a cell rotate independently and if the majority of them rotate CCW simultaneously then the cell runs forward, otherwise it tumbles in place [19]. In reality different flagella can interact with each other through the surrounding fluid, and the significance of the hydrodynamic interaction needs to be investigated in the future.

Assume that each cell has n_f flagella and in order for a cell to "run" at least w flagella are needed to rotate CCW simultaneously. The probability of having exactly i flagella rotating CCW is

$$P^i_{CCW} = \binom{n_f}{i} \left(\frac{\mu_f}{\lambda_f + \mu_f} \right)^i \left(\frac{\lambda_f}{\lambda_f + \mu_f} \right)^{n_f - i}. \tag{7}$$

The probability for the cell to be in the run and tumble states are given by

$$P_{run} = \sum_{i=w}^{n_f} P^i_{CCW}, \quad P_{tumble} = 1 - P_{run}. \tag{8}$$

The probability for multiple flagella switching rotation simultaneously at a specific time is much smaller than that for a single one. Hence, the transition from run to tumble primarily occurs when the cell has exactly w flagella rotating CCW and one of them switches to CW, i.e.,

$$\lambda = w\lambda_f \cdot \frac{P^w_{CCW}}{P_{run}}. \tag{9}$$

Similar argument leads to

$$\mu = (n_f - w + 1)\mu_f \cdot \frac{P^{w-1}_{CCW}}{P_{tumble}}. \tag{10}$$

Figure 3 plots these rates determined with $n_f = 8$ and $w = 5$ and the time fraction that a cell spent running. It shows that the multi-flagella voting process help increase the sensitivity of the cell movement to intracellular CheYp level. It also showed that if the internal CheYp is perturbed far away from its baseline level ($\sim 3\ \mu M$), then the cell can be locked in the run or tumble state.
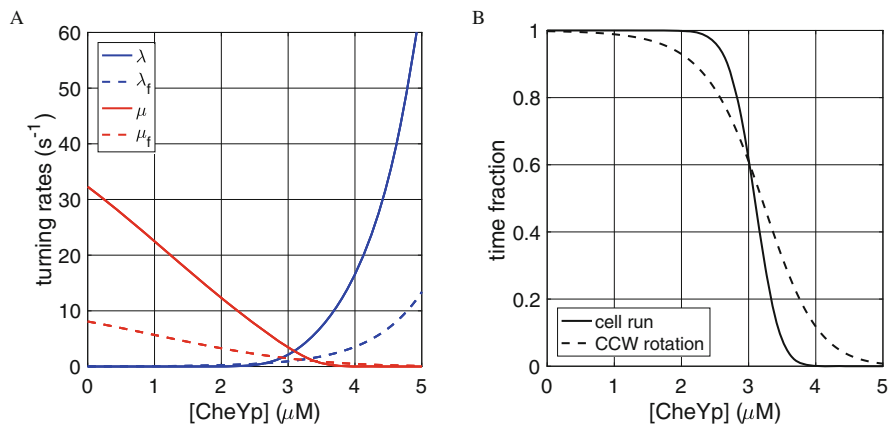
Fig. 3 A. The transition rates λ and μ as a function of CheYp determined by the voting process. B. Time fraction of cell running and flagella CCW rotation. Parameters: $n_f = 8$, $w = 5$.

3.2 Intracellular Signaling Modeled by an Internal ODE System

Extensive effort has been put into modeling the intracellular chemotactic signaling of *E. coli* in the past 50 years, and the hand-in-hand interplay between experiments and modeling has led to profound quantitative understanding of the signaling dynamics (see reviews [34, 35]). These models usually adopt a system of ODEs to track the concentrations of intracellular proteins over time.

$$\frac{d\mathbf{y}}{dt} = \mathbf{f}(\mathbf{y}, S(\mathbf{x}, t)), \tag{11}$$

Here $\mathbf{x} \in \mathbb{R}^N$ is the cell position, and $S(\mathbf{x}, t)$ is the extracellular signal along the cell trajectory. To simulate a large population of cells, often a simplified ODE model was used for intracellular signaling instead. A key requirement of the model is that it must contain one variable that demonstrates the fast excitation and slow adaptation behavior as of CheYp. The intracellular CheYp concentration y_p is either an explicit equation in the system or represented as a function of the variable $\mathbf{y}$. In either case, one has

$$y_p = y_p(\mathbf{y}). \tag{12}$$

3.2.1   A Cartoon Model

The simplest dynamical system of this kind is the linear cartoon model used in [36, 37],

$$
\begin{aligned}
\frac{dy_1}{dt} &= \frac{S - y_1 - y_2}{t_e}, \\
\frac{dy_2}{dt} &= \frac{S - y_2}{t_a},
\end{aligned}
\tag{13}
$$

where $t_e \ll t_a$ are the excitation and adaptation time constants. Here y_1 is the variable that excites and fully adapts to its steady state 0 after a step signal change, and y_p can be identified as $-y_1$. This cartoon model has facilitated the development of multiscale methods to derive PDE models for cell population dynamics, which will be discussed in Section 4.

3.2.2   A Coarse-Grained Model

A conceptual model that incorporates the main structure of the excitation-adaptation network was introduced in [38]. The wiring diagram is given in Figure 4A. S is the external signal measured by the fraction of receptor occupancy. E is the excitation process representing the phosphorylation of CheY by CheA$_p$. A is the adaptation process representing the phosphorylation of CheB by CheA$_p$. The reaction between E and A can be identified as the regulation of CheA activity by CheB$_p$ through demethylation.

Denote the concentrations of E and A by y_1 and y_2. Using mass action kinetics, one has

$$
\begin{aligned}
\frac{dy_1}{dt} &= k_0 + k_s S - \mu_e y_1 y_2, \\
\frac{dy_2}{dt} &= k_0 + k_s S - \mu_a y_2.
\end{aligned}
\tag{14}
$$

Given a step signal change, y_1 changes rapidly and adapts slowly to its pre-stimulus level (Figure 4B). In this model, y_p can be identified as $-y_1$.

3.2.3   A Detailed Model for *E. coli* Chemotaxis

A comprehensive model for *E. coli* intracellular signaling was introduced to study cell population dynamics in [38]. The model is based on the full signaling network in Figure 1 and a simplified version of trimers-of-dimers model proposed in [11] using quasi-steady state approximations of fast reactions and mean field approximations of the methylation level of the receptors.
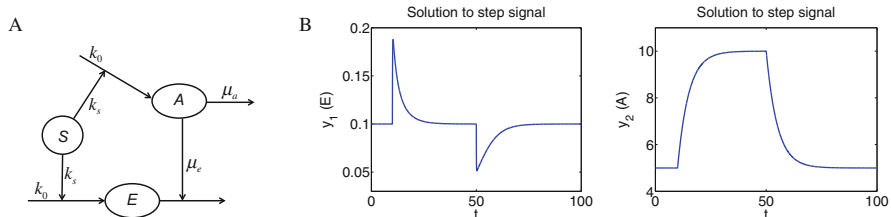
Fig. 4 The coarse-grained model. (A) The wiring diagram. (B) Solution of the model given step changes of the signal from 0 to 1 at $t = 10$ and from 1 to 0 at $t = 50$. Parameters used are nondimensional: $k_0 = 1$, $k_s = 1$, $\mu_a = 0.2$, $\mu_e = 2$. Reproduced from [38] with permission.

Denote the mean methylation level of the chemoreceptors by m and the external signal concentration by S. The equation of m is governed by the methylation and demethylation reactions mediated by CheR (R) and CheB$_p$ (B_p),

$$\frac{dm}{dt} = k_R R\left(1 - A(m, S)\right) - k_{Bp} B_p A(m, S). \tag{15}$$

Here $A(m, S)$ is the mean receptor activity

$$A(m, S) = \frac{1}{1 + \exp\left[N_r f(m, S)\right]}, \tag{16}$$

with

$$f(m, S) = \alpha(m_0 - m) + \log(1 + S/K_i) - \log(1 + S/K_a). \tag{17}$$

CheR concentration R is given by

$$R = \frac{R_t}{1 + K_R T_t(1 - A(m, S))}. \tag{18}$$

CheB$_p$ concentration B_p is implicitly given by a system of algebraic equations of B_p, Y_p (concentration of CheY$_p$), and T_p (concentration of CheAp-associated receptors) obtained by assuming quasi-steady states of these proteins,

$$k_A\left(T_t A(m, S) - T_p\right) - k_Y Y T_p - k_B B T_p = 0,$$
$$k_Y Y T_p - \mu_Y Y_p - k_Z Z Y_p = 0, \tag{19}$$
$$k_B B T_p - \mu_B B_p = 0,$$
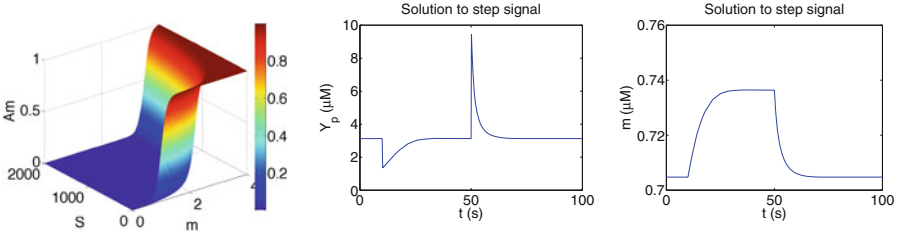
Fig. 5 The detailed model for *E. coli* chemotaxis. A: the function $A(m, S)$. B and C: solution of Y_p and m given step changes of the signal from 0 to 1 μM at $t = 10$ s and from 1 μM to 0 at $t = 50$ s. Parameter used: $m_0 = 1$, $\alpha = 1.7$, $K_i = 18$, $K_a = 3$, $N_r = 6$, $Y_t = 18$ μM, $B_t = 2$ μM, $R_t = 0.3$ μM, $Z_t = 1.1$ μM, $T_t = 5/3$ μM, $k_R = 3.82 \times 10^{-2} \text{s}^{-1}$, $k_{Bp} = 3.25 \text{s}^{-1}$, $k_A = 100 \text{s}^{-1}$, $k_Y = 130$ μM^{-1}s^{-1}, $k_B = 7.5$ μM^{-1}s^{-1}, $k_Z = 8.45$ μM^{-1}s^{-1}, $\mu_Y = 0.1 \text{s}^{-1}$, $\mu_B = 1 \text{s}^{-1}$, $K_Z = 1$ μM^{-1}, $K_Y = 0.65$ μM^{-1}, $K_{Bp} = 6.5$ μM^{-1}, $K_B = 0.25$ μM^{-1}, $K_R = 0.15$ μM^{-1}. Reproduced from [38] with permission.

where

$$Y = \frac{Y_t - (1 + K_Z Z)Y_p}{1 + K_Y T_p},$$

$$Z = \frac{z}{1 + K_Z Y_p}, \tag{20}$$

$$B = \frac{B_t - (1 + K_{Bp} T_t A(m))B_p}{1 + K_B T_p}.$$

In this model y_p is simply given by the CheYp concentration Y_p. The function $A(m, S)$ and the solution subject to a step signal change are plotted in Figure 5. A sample code of this model can be obtained online at [39].

4   From Individual-Based Models to PDE Models

PDE models have been used extensively to describe chemotactic movement of cell populations in biological and biomedical applications [40–45]. A fundamental challenge faced by modelers is to determine under what conditions these models provide a good approximation to the underlying biological process and how to accurately estimate the parameters in the PDEs. To address this problem, mathematical analysis must be developed to elucidate the connections of PDE models and individual-based models.

Significant progress has been made along this line in the context of bacterial chemotaxis, the simplest form of chemotaxis among all cell types. Macroscopic PDEs have been derived from the individual-based models described in Section 3.

4.1 The Patlak-Keller-Segel Equation for Chemotaxis in Small Signal Gradients

When the cell density is low, the most popular PDE approach for chemotaxis is to use the classical Patlak-Keller-Segel (PKS) equation (or a variation of it) to describe the evolution of the cell density

$$\frac{\partial n}{\partial t} = \nabla \cdot \left(D_n \nabla n - \chi n \nabla S \right), \tag{21}$$

where $n = n(\boldsymbol{x}, t)$ is the cell density, $S = S(\boldsymbol{x}, t)$ is the signal concentration, D_n is the effective diffusion coefficient, and $\chi = \chi(S, \nabla S, n, \ldots)$ is the chemotactic sensitivity. Similar equations have also been used to describe cell movement towards other signals, e.g., mechanical signals, light, and heat.

Equation (21) has been formally derived for bacterial chemotaxis. The underlying assumption is that the external signal $S(\boldsymbol{x}, t)$ changes slow enough along cell trajectories such that intracellular signaling is close to equilibrium. A primitive form of this condition was first introduced in [36, 37] as the "shallow gradient assumption" and later elaborated in [38] as the "small signal variation assumption." This assumption leads to time scale separation of intracellular signaling and external signal variation, which justifies the application of perturbation method with the small parameter being the ratio of different time scales.

The derivation in early works [46–49] does not incorporate intracellular signaling explicitly; instead, the turning rates of the velocity jump processes depend directly on the external signal. Built upon these methods, the derivation in more recent works incorporated intracellular signaling by ODE systems described in Section 3.2 [36–38, 50].

4.1.1 Derivation with Intracellular Dynamics Given by the Cartoon Model (13)

In [36, 37], Equation (21) was derived from the individual-based model with the linear cartoon model (13) for intracellular signaling and the linear turning rate

$$\lambda = \lambda_0 - a_1 y_1$$

for cell movement. The key ideas of the derivation is presented below.

Consider cell movement in 1D and assume that the external signal does not change over time, i.e., $S = S(x)$. Let $z = y_2 - S$ and pass y_1 to its quasi-steady state, then

$$\frac{dz}{dt} = -\frac{z}{t_a} \mp s_0 S_x,$$

$$\lambda = \lambda_0 + a_1 z, \tag{22}$$

where minus should be used for right-moving cells and plus should be used for left-moving cells.

Let $p^\pm = p^\pm(x, z, t)$ be the density of cells at position x with internal state z and velocity $\pm s_0$ at time t. Assume that cells are unbiased in choosing new directions of movement after tumbling, then one has

$$\frac{\partial p^+}{\partial t} + s_0 \frac{\partial p^+}{\partial x} + \frac{\partial}{\partial z}\left[\left(-\frac{z}{t_a} - s_0 S_x(x)\right) p^+\right] = \frac{1}{2}(\lambda_0 + a_1 z)\left(-p^+ + p^-\right),$$

$$\frac{\partial p^-}{\partial t} - s_0 \frac{\partial p^-}{\partial x} + \frac{\partial}{\partial z}\left[\left(-\frac{z}{t_a} + s_0 S_x(x)\right) p^-\right] = \frac{1}{2}(\lambda_0 + a_1 z)\left(p^+ - p^-\right). \tag{23}$$

The macroscopic cell density is given by

$$n(x, t) = \int_{\mathbb{R}} (p^+ + p^-)dz.$$

To obtain approximating equations for $n(x, t)$, one needs to integrate the system (23) over the internal variable z. Denote

$$j(x, t) = \int_{\mathbb{R}} s_0(p^+ - p^-)dz,$$

$$n_k(x, t) = \int_{\mathbb{R}} z^k(p^+ + p^-)dz,$$

$$j_k(x, t) = \int_{\mathbb{R}} z^k s_0(p^+ - p^-)dz, \quad k \geq 1,$$

where $n(x, t)$ and $j(x, t)$ are the macroscopic cell density and flux.

Taking the sum and difference of the two components of (23) and integrating over z, one obtains

$$\frac{\partial n}{\partial t} + \frac{\partial j}{\partial x} = 0,$$

$$\frac{\partial j}{\partial t} + s_0^2 \frac{\partial n}{\partial x} = -\lambda_0 j - a_1 j_1, \tag{24}$$

Multiplying (23) by z and then performing the same calculations, one obtains

$$
\begin{aligned}
\frac{\partial n_1}{\partial t} + \frac{\partial j_1}{\partial x} &= -S_x(x)j - \frac{1}{t_a}n_1, \\
\frac{\partial j_1}{\partial t} + s_0^2\frac{\partial n_1}{\partial x} &= -s_0^2 S_x(x)n - \left(\lambda_0 + \frac{1}{t_a}\right)j_1 - a_1 j_2,
\end{aligned}
\tag{25}
$$

The moment-flux system (24) and (25) is not closed because the 2nd-order moment j_2 in (25) is unknown. To obtain a closed moment-flux system, j_2 must be estimated as a function of lower-order moments. If we approximate y_2 by its quasi-steady state in Equation (13), then $z = y_2 - S(x) \approx 0$, leading to the moment closure assumption

$$
j_2 = \int_{\mathbb{R}} z^2 s_0(p^+ - p^-)\mathrm{d}z \approx 0.
\tag{26}
$$

This estimation is justified if the external signal changes slowly along the cell trajectory, in which case the internal states of the cells are only slightly perturbed away from equilibrium. The closed moment-flux system (24)–(26) represents a macroscopic model for the bacterial population dynamics.

Using the diffusion space and time scale, the system (24)–(26) can be rewritten as

$$
\begin{aligned}
\varepsilon^2 \frac{\partial n}{\partial t} + \varepsilon \frac{\partial j}{\partial x} &= 0, \\
\varepsilon^2 \frac{\partial j}{\partial t} + \varepsilon s_0^2 \frac{\partial n}{\partial x} &= -\lambda_0 j - a_1 j_1, \\
\varepsilon^2 \frac{\partial n_1}{\partial t} + \varepsilon \frac{\partial j_1}{\partial x} &= -\varepsilon S_x(x)j - \frac{1}{t_a}n_1, \\
\varepsilon^2 \frac{\partial j_1}{\partial t} + \varepsilon s_0^2 \frac{\partial n_1}{\partial x} &= -\varepsilon s_0^2 S_x(x)n - \left(\lambda_0 + \frac{1}{t_a}\right)j_1,
\end{aligned}
\tag{27}
$$

Here the small parameter ε can be regarded as the ratio of the time scale for intracellular adaptation t_a and the time scale for detected external signal variation $T_s = a_1 s_0 S_x/\lambda_0$.

Using the Hilbert expansion $u(x,t) = \sum_{j=0}^{\infty} \varepsilon^j u^j(x,t)$ for each variable and matching terms with the same order of ε, the 1D form of Equation (21) was derived from (27) for $n^0(x,t) = n(x,t) + \mathcal{O}(\varepsilon)$:

$$
\partial_t n^0 = \partial_x \left(D_n \partial_x n^0 - \chi n^0 \partial_x S \right),
\tag{28}
$$

where

$$
D_n = s_0^2/\lambda_0, \qquad \chi = \frac{a_1 s_0^2 t_a}{\lambda_0(1 + \lambda_0 t_a)}.
\tag{29}
$$

Alternative moment closure methods were also suggested in [36] based on quasi-steady state approximations of z. Replacing one or both z in the definition of j_2 by its quasi-steady state $z_{qss} = \mp s_0 S_x(x) t_a$, "−" for right-moving cells (p^+) and "+" for left-moving cells (p^-), one obtains

$$j_2 \approx -s_0^2 S_x(x) t_a n_1, \tag{30}$$

or

$$j_2 \approx s_0^2 S_x(x)^2 t_a^2 j. \tag{31}$$

Under these closure assumptions, the system (24), (25) reduces to the same PKS equation.

In [50], a new method was developed to accommodate a nonlinear turning frequency given by the expansion

$$\lambda(z) = \lambda_0 + \sum_{i=1}^{\infty} a_i z^i. \tag{32}$$

The derivation did not involve any moment closure step, but instead employed regular perturbation to the infinite moment system for n, j, n_k, and j_k with $k \geq 1$ on the diffusion space and time scale. Perturbation of an infinite moment system involves the inversion of an infinite matrix operator that is not feasible in general. In this case, a special technique was developed utilizing the structure of the equations. With these extensions, the resulting PKS model has the following parameters

$$D_n = \frac{s_0^2}{N\lambda_0}, \qquad \chi = \frac{a_1 s_0^2 t_a}{N\lambda_0(1 + \lambda_0 t_a)}, \tag{33}$$

where $N = 3$ is the space dimension.

4.1.2 Derivation with the General ODE Model (11) for Cell Signaling

In [38], mathematical analysis was developed to derive the PKS equation from individual-based models with cell signaling given by the general ODE system (11).

Given the base model for cell movement, Equation (21) was derived with the following formula for D_n and χ

$$
\begin{aligned}
D_n &= \frac{s_0^2}{N\lambda_0(1 - \psi_d)}, \\
\chi &= \frac{s_0^2}{N\lambda_0} \left[(\nabla_y \lambda)|_{y=\bar{y}(S)} \cdot \left(\lambda_0(1 - \psi_d) I_q - (\nabla_y \mathbf{f})|_{y=\bar{y}(S)} \right)^{-1} \frac{d\bar{y}(S)}{dS} \right].
\end{aligned}
\tag{34}
$$

Here N is the space dimension, $\lambda = \lambda(y_p(\mathbf{y}))$, $\lambda_0 = \lambda(\bar{\mathbf{y}})$, $\bar{\mathbf{y}}(S)$ is the adapted state satisfying $\mathbf{f}(\bar{\mathbf{y}}, S) = 0$, I_q is the $q \times q$ identity matrix, q is the dimension of the internal variable, and ψ_d is the index of directional persistence given by

$$\psi_d = \left(\mathbf{v}' \cdot \int_V T(\mathbf{v}, \mathbf{v}')\mathbf{v}\mathrm{d}\mathbf{v}\right)\Big/ s_0^2. \tag{35}$$

The derivation was based on a small signal variation assumption, which essentially assumes $t_a \ll T_s$, where t_a is the adaptation time scale intrinsically determined by the intracellular signaling network, and T_s is the time scale for the external signal variation interpreted by a cell. For the general ODE model, t_a and T_s can be approximated as

$$t_a \sim 1\Big/ \min_{0 \le S \le S_{\max}} \left|\sigma_m\left((\nabla_{\mathbf{y}}\mathbf{f})|_{\mathbf{y}=\bar{\mathbf{y}}(S)}\right)\right|, \tag{36}$$

$$T_s \sim 1\Big/ \max_{\substack{0 \le S \le S_{\max} \\ \mathbf{v} \in V}} \lambda_0^{-1} \left\|\nabla_{\mathbf{y}}\lambda|_{\mathbf{y}=\bar{\mathbf{y}}(S)}\right\| \cdot \left\|\frac{\mathrm{d}\bar{\mathbf{y}}(S)}{\mathrm{d}S}\dot{S}\right\|, \tag{37}$$

where σ_m takes the maximum real part of the eigenvalues of a matrix.

The formula (34) provides a means to embed the detailed biochemistry of intracellular signaling into macroscopic PDEs for the population. It is the first set of general formulas that represent the quantities D_n and χ in terms of the structure and kinetics of the intracellular signaling network. When applied to the cartoon model (13), it reduces to the same formula as in previous works. When applied to the coarse-grained model (14), it leads to a logarithmic chemotactic sensitivity that depends on the signal S

$$\chi = \frac{\chi_0}{S + \alpha_0}. \tag{38}$$

In other words, the macroscopic drift of the population is proportional to the gradient of the logarithm of the signal

$$\mathbf{u}_s \equiv \chi \nabla S = \nabla \log(S + \alpha_0). \tag{39}$$

The logarithmic sensing mechanism was observed experimentally in [51]. These analyses suggest that the origin of the logarithmic sensing mechanism is the structure of the intracellular network [38].

When applied to the detailed model (15)–(20), the general formula predicted a logarithmic sensitivity with $\chi_0 = 9.50 \times 10^{-2}$ mm/s and $\alpha_0 = 17.67$ μM, comparable with experimental measurements. Due to the complicated form of the intracellular dynamics, the formula (34) was evaluated numerically with the derivatives approximated using a fourth-order accurate scheme and then fitted using the function (38) (Figure 6).
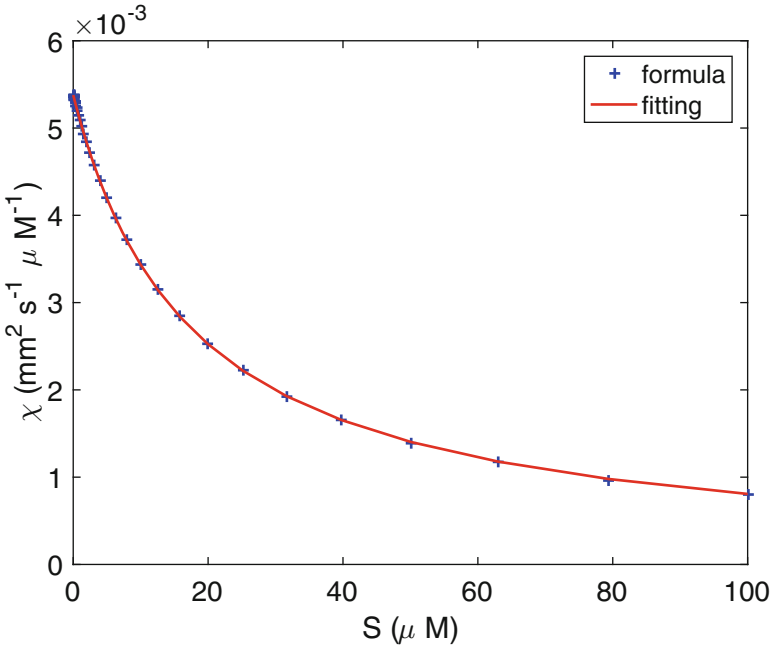
Fig. 6 Logarithmic sensitivity of *E. coli* predicted by the individual-based model with (15)–(20). The blue crosses are calculated using numerical approximations of the formula (34). The red line is the best fitting to the function (38). Parameters used: $\chi_0 = 9.50 \times 10^{-2}$mm/s, $\alpha_0 = 17.67$ μM.

4.1.3 Limitations of PKS Models

The PKS equation (21) provides an accurate approximation of the individual-based model when the external signal changes slowly along cell trajectories, but breaks down when the external signal changes fast, regardless of the form of the intracellular dynamics. This was shown by extensive numerical comparisons of the cell density dynamics predicted by the PKS equation and the corresponding individual-based model using different kinds of signal functions [38, 52]. PDE models derived in [53] have similar limitations as the PKS model.

Consider cell movement in a domain $x \in [0, 8]$ mm with a static exponential ramp signal

$$S = \begin{cases} e^{a(x-1)} & 0 \leq x \leq 4, \\ e^{3a} & 4 < x \leq 8. \end{cases} \tag{40}$$

Assume that initially cells form an aggregate in the region $x \in [1, 2]$, and set the initial cell distribution to be

$$n(x, 0) = \frac{3\pi}{4} \left| \sin(\pi x) \right|^3 \chi_{1 < x < 2}, \tag{41}$$

where $\chi_{1 < x < 2}$ is the characteristic function. Let

$$\lambda = \lambda_0 + \tanh\left(b(Y_p(m) - \bar{Y}_p)\right), \quad T(\mathbf{v}, \mathbf{v}') = \frac{1}{|V|}, \qquad V = s_0 \partial B_0^1. \tag{42}$$

where $\lambda_0 = 1\mathrm{s}^{-1}$, $b = 5\mathrm{s}^{-1}\,\mu\mathrm{M}^{-1}$ and $s_0 = 20\,\mu\mathrm{m/s}$.

Figure 7 plots the cell density dynamics predicted by the individual-based model with (15)–(20) and the corresponding PKS model. If the signal gradient is small ($a = 0.2mm^{-1}$), the two approaches match tightly (Figure 7A); but if the signal gradient becomes large ($a = 0.5 \mathrm{\ mm}^{-1}$), the two approaches deviate significantly (Figure 7B). The latter situation often occurs in self-organized population dynamics [54]. A key feature when the PKS approximation breaks down is the fat distribution of the intracellular states as shown in Figure 8.
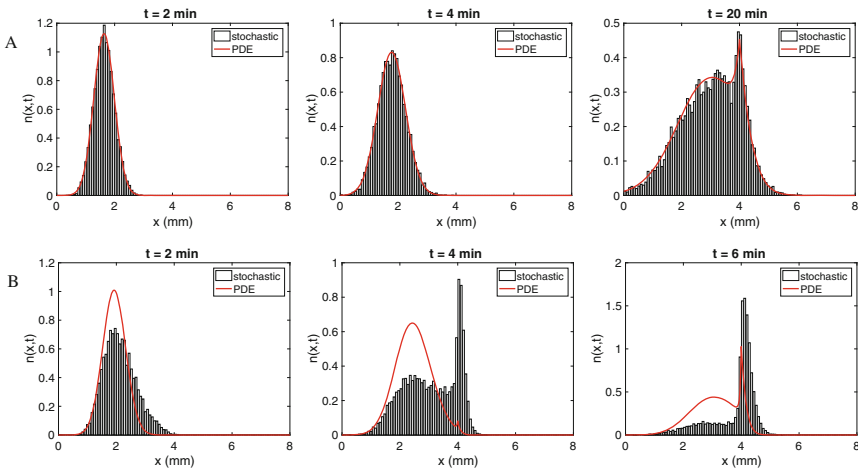
Fig. 7 Comparison of the PKS equation with the underlying individual-based model for bacterial chemotaxis in small signal gradient with $a = 0.2 \mathrm{\ mm}^{-1}$ (A) and large signal gradient with $a = 0.5 \mathrm{\ mm}^{-1}$ (B). Bars: stochastic simulations of the individual-based model with (15)–(20). Curves: solutions of the corresponding PKS model.
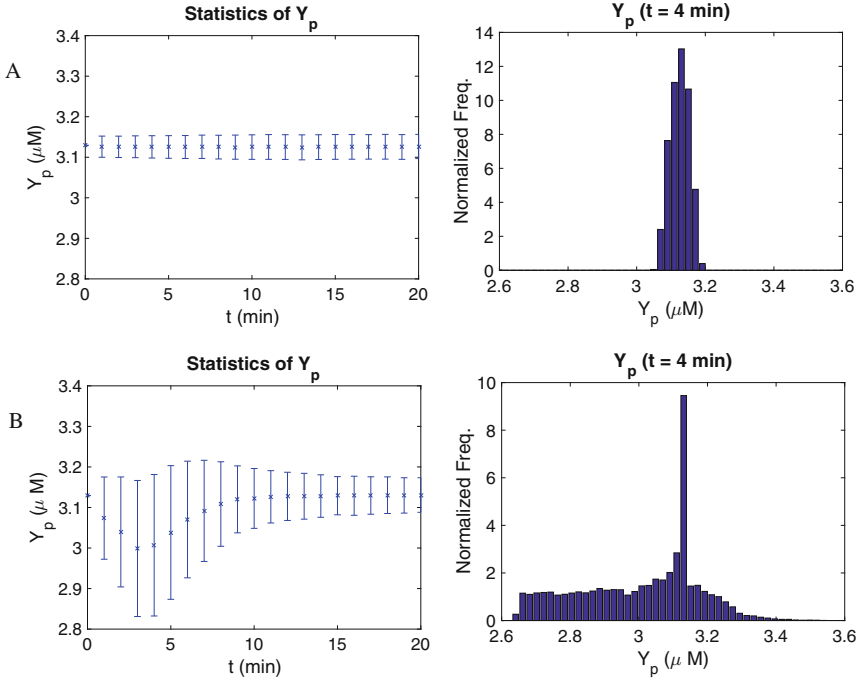
Fig. 8 Statistics of intracellular CheYp given small signal gradient with $a = 0.2$ mm^{-1} (A) and large signal gradient with $a = 0.5$ mm^{-1} (B). Left: mean and standard deviation of y_p over the whole population as a function of time. Right: distribution of y_p at $t = 4$ min.

4.2 Moment-Flux Models for Chemotaxis in Large Signal Gradients

When cells are exposed to large signal gradient, their intracellular state can be far from steady state and broadly distributed. Macroscopic PDE models for such situations must include information on the distribution of the intracellular states in order to accurately describe the population dynamics.

In [52], a hierarchy of moment-flux models that are suitable for bacterial chemotaxis in large gradient was derived from the individual-based model with the cartoon intracellular dynamics (13) and nonlinear turning rate (32). The models consist of a system of hyperbolic equations for n, j and several internal-state moments n_k and j_k with $k \leq K$. The moments n_k and j_k enclose the distribution of the internal state and its deviation from equilibrium.

Consider the example with cell signaling described by the simplified cartoon model (22) and cell movement subject to a time-independent signal. Multiplying (23) by 1 and z^k/k for all $k \geq 1$, integrating over z, and taking the sum and difference of the two components, we obtain (24) and the following moment equations

$$\frac{1}{k}\frac{\partial n_k}{\partial t} + \frac{1}{k}\frac{\partial j_k}{\partial x} = \left[-S_x j_{k-1} - \frac{1}{t_a}n_k \right], \qquad k \geq 1$$

$$\frac{1}{k}\frac{\partial j_k}{\partial t} + \frac{s_0^2}{k}\frac{\partial n_k}{\partial x} = \left[-s_0^2 S_x(x)n_{k-1} - \frac{1}{t_a}j_k \right] - \frac{1}{k}(\lambda_0 j_k + a_1 j_{k+1}), \ k \geq 1.$$

$$(43)$$

The system for $k = 1$ is identical to (25).

The k-th order moment equations (43) have the factor $1/k$ in all terms except the terms in the square brackets, which suggests that high-order moments in z equilibrate relatively fast. The moment closure method in [52] is to pick an integer K large enough such that $1/(K+1) \ll 1$ and set

$$-S_x(x)j_{k-1} - \frac{1}{t_a}n_k = 0 \qquad \forall k > K,$$

$$-s_0^2 S_x(x)n_{k-1} - \frac{1}{t_a}j_k = 0 \qquad \forall k > K.$$

$$(44)$$

This assumption is equivalent to setting

$$j_{K+1} = -s_0^2 S_x(x)t_a n_K. \tag{45}$$

With this approximation, the infinite system (24) and (43) reduces to a closed moment system of moment equations for $(n, j, n_1, j_1, \cdots, n_K, j_K)^T$.

Numerical simulations showed that as K increases, the moment-flux models become more accurate in approximating the population dynamics governed by the individual-based model (Figure 9). The models with $K = 3$ and 4 show a tight match to the individual-based model, while the PKS equation and the moment-flux models with $K = 1$ deviate from the individual-based model significantly. Note that the moment closure (45) with $K = 1$ reduces to the moment closure (30) which was used for the case with small signal gradient. Because the number of equations of the model $(2K + 2)$ increases with K, it is desirable to use K as small as possible to reduce computational cost.

4.3 Open Problems

There are several open problems raised by previous multiscale analysis. The moment-flux models in [52] were derived using the linear cartoon model for intracellular signaling. The method needs to be extended to include intrinsic
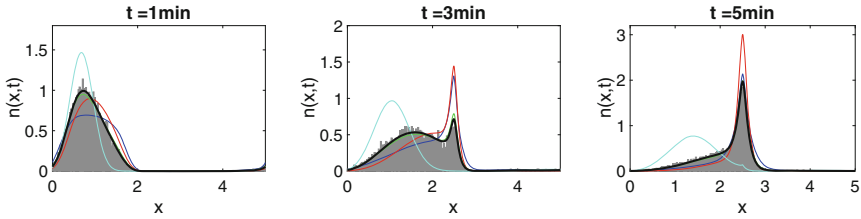
Fig. 9 Comparison of the moment-flux model, the PKS model, and the underlying individual-based model with (22). The signal is given by $S(x) = \mu L/2 - \mu|x - L/2|$ with $L = 5$ mm and $\mu = 4.5$, which does not satisfy the small signal variation assumption. The gray bar plot is a single realization of the individual-based model with 10^4 cells. The blue, red, green, and black curves are the numerical solutions of the moment-flux models with order $K = 1, 2, 3, 4$. The cyan curve is the solution of the PKS model.

nonlinearities of the intracellular dynamics, e.g., as in (14) or (15)–(20). For cases in which the signal gradient only becomes large in part of the domain, hybrid methods that bridge individual-based models and PDE models can be developed. This is desirable especially in 3D, in which case simulations of the hyperbolic moment-flux models become very time-consuming.

5   Summary

This chapter summarizes the multiscale modeling framework used for bacterial chemotaxis and the major breakthroughs in deriving PDE models from individual-based models in this context. Analyses and simulations revealed that the PKS equation is accurate in approximating the population dynamics when cell movement is subject to small signal gradients, but it breaks down if the signal gradient becomes large. For the former case, detailed formulas were derived for the macroscopic parameters in the PKS equation in terms of measurable parameters that describe single cell signaling and movement. For the latter case, a hallmark is the broad distribution of the intracellular state over the whole population and alternative moment-flux PDE models could be used instead. This review is not to reiterate all relevant results in the literature, but written with enough detail so that it can be easily understood by researchers and graduate students with a diverse background. The hope is that the modeling methods developed for bacterial chemotaxis can be used or extended to address other multiscale problems in biology.

References

1. Sean P Cook, Charles J Brokaw, Charles H Muller, and Donner F Babcock. Sperm chemotaxis: egg peptides control cytosolic calcium to regulate flagellar responses. *Developmental biology*, 165(1):10–19, 1994.

2. Robert F Diegelmann, Melissa C Evans, et al. Wound healing: an overview of acute, fibrotic and delayed healing. *Front Biosci*, 9(1):283–289, 2004.

3. P. Friedl and D. Gilmour. Collective cell migration in morphogenesis, regeneration and cancer. *Nat Rev Mol Cell Biol*, 10(7):445–457, Jul 2009.

4. G. Pandey and R. K. Jain. Bacterial chemotaxis toward environmental pollutants: role in bioremediation. *Appl Environ Microbiol*, 68(12):5789–5795, Dec 2002.

5. J. P. Armitage, T. P. Pitta, M. A. Vigeant, H. L. Packer, and R. M. Ford. Transformations in flagellar structure of rhodobacter sphaeroides and possible relationship to changes in swimming speed. *J Bacteriol*, 181(16):4825–4833, Aug 1999.

6. K. J. Duffy and R. M. Ford. Turn angle and run time distributions characterize swimming behavior for pseudomonas putida. *J Bacteriol*, 179(4):1428–1430, Feb 1997.

7. C. V. Rao, J. R. Kirby, and A. P. Arkin. Design and diversity in bacterial chemotaxis: a comparative study in *Escherichia coli* and *Bacillus subtilis*. *PLoS Biol*, 2(2):E49, Feb 2004.

8. G. L. Hazelbauer. Bacterial chemotaxis: the early years of molecular studies. *Annu Rev Microbiol*, 66:285–303, Oct 2012.

9. D. E. Koshland. *Bacterial Chemotaxis as a Model Behavioral System*. Raven Press, New York, 1980.

10. H. C. Berg. *Random Walks in Biology*. Princeton University Press, 1983.

11. X. Xin and H. G. Othmer. A "trimer of dimers"-based model for the chemotactic signal transduction network in bacterial chemotaxis. *Bull Math Biol*, 74(10):2339–2382, Oct 2012.

12. J. Adler. Chemotaxis in bacteria. *SCIENCE*, 153:708–716, 1966.

13. Julius Adler. Effect of amino acids and oxygen on chemotaxis in escherichia coli. *Journal of bacteriology*, 92(1):121–129, 1966.

14. Julius Adler. Chemotaxis in bacteria. *Annual review of biochemistry*, 44(1):341–356, 1975.

15. E. O. Budrene and H. C. Berg. Complex patterns formed by motile cells of *Escherichia coli*. *Nature*, 349(6310):630–633, February 1991.

16. E. O. Budrene and H. C. Berg. Dynamics of formation of symmetrical patterns by chemotactic bacteria. *Nature*, 376(6535):49–53, 1995.

17. C. Xue, E. O. Budrene, and H. G. Othmer. Radial and spiral stream formation in *Proteus mirabilis* colonies. *PLoS Comput Biol*, 7(12):e1002332, 12 2011.

18. B. Franz, C. Xue, K. J. Painter, and R. Erban. Travelling waves in hybrid chemotaxis models. *Bull Math Biol*, 76(2):377–400, Feb 2014.

19. X. Xue, C. Xue, and M. Tang. The role of intracellular signaling in the stripe formation in engineered *E. coli* populations. *submitted*, 2017.

20. A Decoene, A Lorz, S Martin, B Maury, and M Tang. Simulation of self-propelled chemotactic bacteria in a stokes flow. In *ESAIM: proceedings*, volume 30, pages 104–123. EDP Sciences, 2010.

21. A. Decoene, S. Martin, and B. Maury. Microscopic modelling of active bacterial suspensions. *Mathematical Modelling of Natural Phenomena*, 6:98–129, 2011.

22. Robert Dillon, Lisa Fauci, and III Donald Gaver. A microscale model of bacterial swimming, chemotaxis and substrate transport. *Journal of Theoretical Biology*, 177(4):325–340, 1995.

23. Heather Flores, Edgar Lobaton, Stefan Méndez-Diez, Svetlana Tlupova, and Ricardo Cortez. A study of bacterial flagellar bundling. *Bulletin of Mathematical Biology*, 67(1):137–168, 2005.

24. J. P. Hernández-Ortiz, Ch. G. Stoltz, and M. D. Graham. Transport and collective dynamics in suspensions of confined swimming particles. *Physical Review Letters*, 95:204501, 2005. (doi:10.1103/PhysRevLett.95.204501).

25. J. P. Hernández-Ortiz, P. T. Underhill, and M. D. Graham. Dynamics of confined suspensions of swimming particles. *J. Phys.: Condens. Matter*, 21(20):204107, 2009.

26. S. D. Ryan, B. M. Haines, L. Berlyand, F. Ziebert, and I. S. Aranson. Viscosity of bacterial suspensions: Hydrodynamic interactions and self-induced noise. *Physical Review E*, 83(050904(R)), 2011.

27. S. D. Ryan, A. Sokolov, L. Berlyand, and I. S. Aranson. Correlation properties of collective motion in bacterial suspensions. *New Journal of Physics*, 15:105021, 2013.

28. H. G. Othmer, S. R. Dunbar, and W. Alt. Models of dispersal in biological systems. *J. Math. Biol.*, 26(3):263–298, 1988.

29. H. Othmer and C. Xue. The mathematical analysis of biological aggregation and dispersal: progress, problems and perspectives. In M. Lewis, P. Maini, and S. Petrovskii, editors, *Dispersal, individual movement and spatial ecology: A mathematical perspective*. Springer, 2013.

30. H. C. Berg and D. Brown. Chemotaxis in *Escherichia Coli* analyzed by three-dimensional tracking. *Nature*, 239:502–507, 1972.

31. R. M. Macnab. Sensing the environment: Bacterial chemotaxis. In R. Goldberg, editor, *Biological Regulation and Development*, pages 377–412, New York, 1980. Plenum Press.

32. P. Cluzel, M. Surette, and S. Leibler. An ultrasensitive bacterial motor revealed by monitoring signaling proteins in single cells. *Science*, 287:1652–1655, 2000.

33. Clinton H Durney. A two-component model for bacterial chemotaxis, 2013.

34. H. G. Othmer, X. Xin, and C. Xue. Excitation and adaptation in bacteria-a model signal transduction system that controls taxis and spatial pattern formation. *Int J Mol Sci*, 14(5):9205–9248, 2013.

35. M. J. Tindall, S. L. Porter, P. K. Maini, G. Gaglia, and J. P. Armitage. Overview of mathematical approaches used to model bacterial chemotaxis I: the single cell. *Bull Math Biol*, 70(6):1525–1569, Aug 2008.

36. R. Erban and H. G. Othmer. From individual to collective behavior in bacterial chemotaxis. *SIAM J. Appl. Math.*, 65(2):361–391, 2004.

37. R. Erban and H. Othmer. From signal transduction to spatial pattern formation in *E. coli*: A paradigm for multiscale modeling in biology. *Multiscale Modeling & Simulation* 3(2):362–394, 2005.

38. C. Xue. Macroscopic equations for bacterial chemotaxis: integration of detailed biochemistry of cell signaling. *J Math Biol*, 70(1–2):1–44, Jan 2015.

39. https://people.math.osu.edu/xue.41/pub.html.

40. C. S. Patlak. Random walk with persistence and external bias. *Bull. of Math. Biophys.*, 15:311–338, 1953.

41. E. F. Keller and L. A. Segel. Initiation of slime mold aggregation viewed as an instability. *J. Theor. Biol.*, 26:399–415, 1970.

42. E. F. Keller and L. A. Segel. Model for chemotaxis. *J. Theor. Biol.*, 30:225–234, 1971.

43. E. F. Keller and L. A. Segel. Traveling bands of chemotactic bacteria: A theoretical analysis. *J. Theor. Biol.*, 30:235–248, 1971.

44. Benoit Perthame. Pde models for chemotactic movements: parabolic, hyperbolic and kinetic. *Applications of Mathematics*, 49(6):539–564, 2004.

45. M. J. Tindall, P. K. Maini, S. L. Porter, and J. P. Armitage. Overview of mathematical approaches used to model bacterial chemotaxis II: bacterial populations. *Bull Math Biol*, 70(6):1570–1607, Aug 2008.

46. Mercedes A Rivero, Robert T Tranquillo, Helen M Buettner, and Douglas A Lauffenburger. Transport models for chemotactic cell populations based on individual cell behavior. *Chemical engineering science*, 44(12):2881–2897, 1989.

47. T. Hillen and H. G. Othmer. The diffusion limit of transport equations derived from velocity-jump processes. *SIAM J. Appl. Math.*, 61(3):751–775, 2000.

48. H. G. Othmer and T. Hillen. The diffusion limit of transport equations II: chemotaxis equations. *SIAM J. Appl. Math.*, 62:1222–1250, 2002.

49. F. A. C. C. Chalub, P. A. Markowich, B. Perthame, and C. Schmeiser. Kinetic models for chemotaxis and their drift-diffusion limits. *Monatshefte für Mathematik*, 142(1):123–141, 2004.

50. C. Xue and H. G. Othmer. Multiscale models of taxis-driven patterning in bacterial populations. *SIAM J. Appl. Math.*, 70(1):133–167, 2009.
51. Yevgeniy V. Kalinin, Lili Jiang, Yuhai Tu, and Mingming Wu. Logarithmic sensing in *Escherichia coli* bacterial chemotaxis. *Biophys J*, 96(6):2439–2448, Mar 2009.
52. C. Xue and X. Yang. Moment-flux models for bacterial chemotaxis in large signal gradients. *J Math Biol*, 73(4):977–1000, 2016.
53. J. E. Simons and P. A. Milewski. The volcano effect in bacterial chemotaxis. *Mathematical and Computer Modelling*, 53(7–8):1374–1388, 2011.
54. B. Franz, C. Xue, K. Painter, and R. Erban. Travelling waves in hybrid chemotaxis models. *Bull. Math. Biol.*, 2014.

Sperm Motility: Models for Dynamic Behavior in Complex Environments

Julie E. Simons and Sarah D. Olson

Abstract Sperm–often considered the most diverse cell type known–present unique challenges for modeling frameworks. Responsible for fertilizing the egg, sperm are not only necessary for sexual reproduction, but also increasingly important to study given rising rates of infertility. In this review, we summarize aspects of sperm motility and interactions, which make it unique in comparison to other cells. The journey of a sperm involves swimming in different fluid environments, where emergent trajectories and waveforms are coupled to the fluid properties such as viscosity, the mechanics of the flagellum, as well as the relevant biochemistry. We emphasize that there is a range of modeling frameworks, each of which can bring an understanding to fundamental aspects of sperm motility, such as how a particular fluid or interaction with another swimmer can alter swimming speeds and trajectories. In order to study the emergent flagellar waveforms of sperm and compare to experiments, it is important to have accurate models of the relevant surfaces and interactions to capture the correct and relevant hydrodynamics. We discuss current challenges and describe aspects of sperm motility that models can elucidate in the future, ultimately to help solve the puzzle of how the sperm is able to reach and fertilize the egg.

1 Introduction

Cellular movement is a ubiquitous and dynamic process that takes on many different modes, depending on the particular cell type and the surrounding environment

J. E. Simons (✉)
Department of Sciences & Mathematics, California Maritime Academy, 200 Maritime Academy Drive, Vallejo, CA 94950, USA
e-mail: jsimons@csum.edu

S. D. Olson
Department of Mathematical Sciences, Worcester Polytechnic Institute, Worcester, MA 01609, USA
e-mail: sdolson@wpi.edu

[183]. In the context of spermatozoon (the sperm cell), motility is vital for sexual reproduction and a strong indicator of fertility [58]. Using a single flagellum, sperm must navigate a wide range of environments and their motility patterns must change in response to various chemical and physical cues, as shown in Figure 1. These changing motility patterns are required not only to successfully reach the egg, but also to break through the surface of the egg to begin the process of fertilization. This process is necessary for the survival of sexually reproducing species, and is therefore subject to strong evolutionary pressures [15].

This can be contrasted with other cellular motility behaviors. While sperm swim, other cell types may exhibit a complex gliding or crawling motion, possibly along confining tracks in the tissue [137, 149]. This gliding or crawling motion is vital in processes such as morphogenesis (development of an organism) and wound healing, where cells migrate over a long distance and are able to sense the microenvironment through chemical signals and physical communication [5, 129, 202]. Some cells must change their shape during cell division as well as during navigation in confined spaces. For example, Amoebae are able to move along a substrate by extending structures called pseudopodia [183]. In many animal cells, such shape changes

(a) Changes in sea urchin flagellar waveform as viscosity is increased going from (A)-(C), reproduced from [206] with permission of The Company of Biologists LTD.
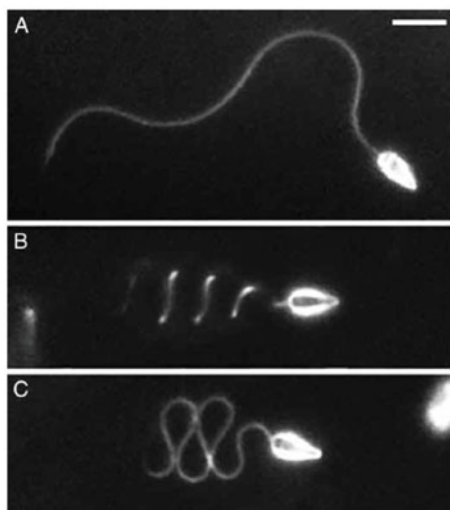
(b) Experimental trajectories of sperm from sea urchin and mice are tracked over time, when responding to different chemical stimuli, reproduced from [35] and licensed through creative commons (CC BY).
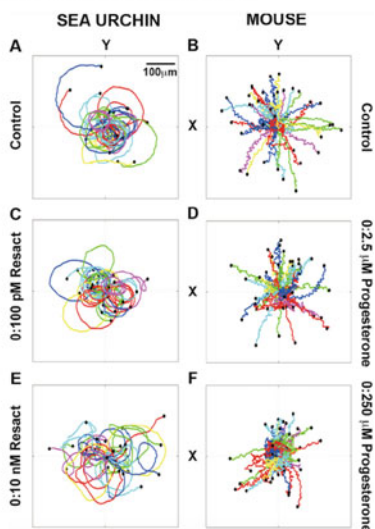
Fig. 1 Examples of experimental observations of sperm motility patterns, demonstrating how motility behaviors change depending on the environment the sperm encounters. Not only does the sperm modulate its waveform, as demonstrated in panel (a), but such changes can also result in changes in trajectories (as in panel (b)) and thus can affect the ability of the sperm to effectively migrate.

are driven by internal forces generated by polymerization of actin, along with the movement of microtubules and intermediate filaments within the cytoplasm [5, 19, 69].

While these descriptions highlight differences in motility behaviors, all cells are subject to similar physical laws that dictate what motility patterns are possible. Locomotion at the cellular scale is unique: as E.M. Purcell explained in his now famous paper, *Life at Low Reynolds Number* [156], cells require novel mechanisms (notably, asymmetry in motion) in order to successfully move in a world that lacks inertial forces. This means that if a cell stops moving or exerting forces, there is no acceleration and the cell body would immediately cease moving due to the external forces, including a viscous or resistive force from the surrounding fluid or the substrate they are moving on. The successful and efficient migration of a single cell or group of cells is a direct result of the generation of internal forces coupled with chemical signaling [69, 129].

Flagellated cells contain one or more flagella, specialized whip-like structures that are able to aid in the movement of the cell. In the photosensitive green algae known as *Chlamydomonas*, two anterior flagella beat in a coordinated fashion to move or swim away from light. Bacteria can have one or more flagella attached to the cell body. Due to a motor at the base of each bacterial flagellum, the flagella are able to rotate, sometimes forming coordinated bundles, thereby propelling the cell body forward [13, 14]. This allows bacteria to swim towards higher concentrations of food sources [1, 178, 179] and efficiently move in different conditions such as the mucus layer that coats the stomach and in biofilms containing extracellular polymeric substances [23, 34, 68]. Sperm cells have a single elastic flagellum that propagates bending along its length, propelling the sperm forward through different fluid environments that include swimming through or around mucus, cells, hormones, and other large proteins [63, 166, 193]. In contrast to animal cells where actin dynamics control the changing cell shape, the bending of the sperm flagellum is driven by dynein, a molecular motor protein that is moving along microtubules within the flagellum [120, 207].

Sperm are unique in that their one and only function is to reach and fertilize the ovum (egg), which often involves swimming a distance greater than 1000 times their own length [76, 193]. Of the millions that start the journey, only a few will reach the site of fertilization [189]; it is thought that the various chemical and physical cues could act as a filter, allowing the forward progression of only healthy sperm [124, 171, 193]. Along the way, mammalian sperm undergo the process of maturation called capacitation [38, 204]. This includes the ability of the sperm to exhibit hyperactive motility, corresponding to highly asymmetric flagellar bending and increased intracellular calcium [157, 188, 189, 193], which is known to be necessary for the sperm to reach the egg. In the female reproductive tract, sperm respond to changes in the fluid viscosity, chemical cues, and geometry of the channels as they navigate through different regions by modulating their motility patterns. Figure 1 shows several examples of how sea urchin and mouse sperm may change their motility behavior depending on their physical environment. Another example is when sperm enter the oviduct; initially, sperm are thought to be held in a reservoir until chemical cues around the time of ovulation initiate capacitation

[188, 193]. Sperm can then change their waveform to the hyperactive motility pattern, as well as shed proteins along the sperm head, both of which are thought to assist the sperm in pulling off of the epithelial wall and swimming towards the egg [189].

How exactly does the sperm find the egg? There are still many questions related to the steering and guidance of sperm, in terms of the relevance of different factors at different locations. Hypothesized mechanisms involve different types of *taxes*–motion in response to a stimulus–and there is considerable debate about whether these are long or short range guidance mechanisms for sperm. For example, chemotaxis (chemically mediated motion, see Figure 1b) [22, 36, 59, 180] and thermotaxis (temperature-mediated motion) [8–10] are potential short range mechanisms whereas rheotaxis (fluid flow-mediated motion) [108, 131] is thought to be a long range mechanism. The biased motion towards or away from stimuli is due to a change in flagellar beating. Thus, the beat pattern may be modulated by chemical, temporal, and background fluid flow properties of the surroundings. However, changes in flagellar bending can also be caused by responses to variations in the confined geometry of their local environment, fluid properties such as viscosity, and interactions with other sperm [63, 110, 176, 206, 208, 209].

Frameworks to model different aspects of sperm motility continue to evolve as new experimental data becomes available. On one end of the modeling spectrum, continuum frameworks describing systems of differential equations are used to describe evolving densities of sperm populations. These models are useful for studying the macroscopic effects of preferential motion towards or away from chemical signals or other environmental cues. Some models have focused on accurately modeling force generation and movement of the flagellum and its elements, while others have used minimal models of the structure with more detailed and accurate models of the fluid environment. These models can provide a method to investigate situations where biological experimental capabilities are limited–for example, force measurements along the cell body over time–but also scenarios where cellular motility does not occur properly.

The power of modeling is to identify and understand potential targets to increase motility in sperm that are deficient, or to identify targets that would prevent sperm from reaching the egg. These targets are vital for developing fertility solutions. As observed from the complex coupling of chemical and physical cues, systematically understanding sperm motility, on multiple scales, will provide insight into the complicated movements we observe. Modeling approaches can test experimental hypotheses as well as propose future experimental studies. But there are many other outcomes from these studies that extend beyond the world of fertility. In understanding sperm motility, we not only gain insight into the general process of cellular motility, but these insights can be harnessed to model surfaces covered with cilia (which are structurally similar to flagella) such as the lungs [54, 126], as well as inform the development of devices such as artificial microswimmers that can be used in applications as varied as drug delivery and bio-sensing [66].

2   Historical Context for Modeling Frameworks

Mathematical models for sperm motility date back to early twentieth century investigations of viscous flows near rigid bodies. While sperm are not rigid bodies, portions of the sperm body may be modeled as rigid, and the environment sperm encounter is characterized as viscous, with almost no inertial effects. Sperm flagella are the source of the motion of sperm, and these are slender tubular structures that tend to beat with a primarily planar waveform, though helical waveforms have been observed as well (see Figure 1a) [203, 209]. Due to the planar nature of their waveforms, sperm are an ideal cell type for studying flagellar motility from a mathematical modeling perspective and sperm have been the inspiration for many studies of the hydrodynamics of viscous fluids near waving boundaries, since the sperm flagellum could be viewed as a finite waving boundary in a fluid.

Mathematical investigations of sperm motility started with the studies of G.I. Taylor in the early 1950s [194, 195]. These studies modeled the flagellum of organisms like sperm as oscillating infinite sheets or cylinders and were used to investigate the energetics and phase-locking mechanisms from a hydrodynamical perspective. Shortly after this, theories were developed to measure forces and velocities in viscous fluid flow around slender bodies like flagella [80, 82]. These studies idealized the flagellum as a slender body (narrow in width compared to its length), which could be approximated as a series of rigid cylinders connected end to end. In this way, the motion of either finite or infinite filaments was modeled by considering the motion of each cylinder separately. The goal of these models was to construct solutions that are consistent with the fluid equations and result in small cross sections of the slender body that are moving with the same velocity.

Results from the early work in [80] is now known as resistive force theory (or local drag theory), in which coefficients that give a proportional relationship between force and velocity can be calculated based on parameters given by the geometry of the body and its waveform. Resistive force theory is a simple mathematical approach to modeling sperm motility, because it provides a direct link between velocities and forces without any other computations. However, it is a coarse approximation that relies upon the assumption that if the body is divided into cylindrical elements, each element does not interact with any other.

In response to this, slender body theory was developed. As first described in [82], distributions of forces and torques along the centerline of the slender body were considered instead of focusing on the motion of the surface of elements or pieces of the flagellum. Slender body theory was refined over the next several decades to more accurately incorporate interactions between elements of the flagellum and to deal with singularity issues with solutions near the ends of the flagellum [12, 45, 85, 104, 105, 109, 117, 118]. For reviews of these theories, see [105, 112].

Ultimately, these mathematical theories have shed light upon idealized behavior of oscillating filaments and sheets, but computational models and simulations are necessary to understand the more complicated waveforms observed in sperm, interactions with surfaces and between sperm, effects of biologically realistic

fluid models that incorporate elasticity and obstacles, and how morphology affects sperm motility. In order to accomplish this, methods that are robust to changes in waveform, incorporating surfaces and other boundaries, and complex fluids– which often have no closed-form solutions and must be computationally simulated themselves–are now at the forefront of sperm motility models. While these more recent computational approaches still rely upon the concepts developed in resistive force theory or slender body theory to model the flagellar hydrodynamics, current work seeks to elucidate the diverse sperm motility behavior observed in physiologically relevant biological settings, where motion is not fixed but rather a dynamic, emergent behavior with many feedback mechanisms.

3 Modeling Motion in Viscous Fluids

When studying sperm motility in a viscous fluid, a critical nondimensional ratio characterizing the relative importance of inertial to viscous effects is the Reynolds number, $Re = \rho UL/\mu$. Here, ρ is the fluid density, μ is the dynamic viscosity, and U and V are characteristic length and velocity scales, respectively. When using the viscosity of water and characteristic scales for human sperm, we have $Re \sim 10^{-3}$. Thus, we consider their environment as viscosity-dominated and inertia can be neglected. Many studies have used the incompressible Stokes Equations,

$$\mathbf{0} = \mu \Delta \mathbf{u} - \nabla p + \mathbf{f}, \tag{1a}$$

$$0 = \nabla \cdot \mathbf{u}, \tag{1b}$$

to study swimmers in viscous, incompressible fluids at zero Reynolds number. Here, $\mathbf{f}$ is the force density that the swimmer exerts on the fluid, which will be further described below and in Section 5. The fluid velocity is $\mathbf{u}$, μ is the dynamic viscosity, and p is the pressure. The classical Navier-Stokes equations for incompressible fluids would have an inertial term, $\rho D\mathbf{u}/Dt$ with material derivative D/Dt on the left-hand side of (1a). However, in a zero Reynolds number Stokesian regime, the left-hand side is zero since inertial terms are assumed to be negligible. The incompressibility condition or conservation of mass is given in (1b).

We have a governing equation for the fluid, but the study of moving objects in fluids requires a formulation for how we represent the object and how the object interacts with the fluid. Is the fluid pushing on the object? Is the object pushing on the fluid? What happens at the interface between the object and the fluid? The answers to these questions lie in both the experimental setting and the modeling framework.

From Newton's third law of motion, we know that for every action, there is an equal and opposite reaction. Thus, when there is fluid flow resulting from external properties (for instance, flux of fluid through a channel due to a pumping mechanism upstream or downstream, or peristaltic flow due to boundary contractions), the fluid

will move and so will any free object surrounded by the fluid in motion. On the other hand, nonpassive objects like motile cells will exert forces upon the fluid in order to navigate through their environment. In most biologically realistic scenarios, both of these effects are present. In the case of reproduction, the egg is a passive object whereas sperm are actively generating forces to navigate and swim towards the egg [190, 193].

One significant modeling consideration for objects in fluids is how to connect two effects: how the fluid acts upon the object and how the object acts upon the fluid. Alternatively, this can be framed as how the fluid reacts to the object and how the object reacts to the fluid. The general framework used is to assume that at the surface of any object in a fluid, a no-slip condition must be satisfied [92]. This effectively means that, due to frictional forces, the velocity of the fluid at the surface of an object must match the velocity of the surface itself, and no fluid can pass through the surface nor move along the surface tangentially. For a moving cell like a sperm body, this means that at the interface between the surface and the fluid, both the fluid and the surface must move with the same velocity. If these conditions were violated, fluid might flow through an object like the sperm body. While it is true that the membrane surfaces of cells are not entirely impermeable, such effects are minute and would have a negligible contribution to the motility of the entire cell.

There are several models for connecting the forces the sperm is exerting with the fluid motion itself. In an Eulerian approach, one could assume the fluid lies in a particular domain, which could be discretized as necessary for computations (for instance, in a Cartesian grid). The sperm body is viewed as an immersed boundary or structure in that domain. Because this boundary is freely moving, it will not lie on the exact grid of the fluid domain. Therefore, any forces exerted along the length of the boundary will be distributed on the discretized domain (grid elements) surrounding the boundary. Once these forces are distributed onto the fluid domain, a numerical fluid solver can be used to calculate the fluid velocities at all points in the domain. After these velocities are found, one can interpolate the flow field to find the approximate velocity of the immersed boundary. The immersed boundary can then be moved according to these interpolated velocities along its length and the process can be repeated. This is called the immersed boundary method and was pioneered by Charles Peskin [152, 153].

Direct Lagrangian approaches to relate the motion of the sperm and the surrounding fluid are possible if analytical solutions to the fluid equations are known. While this is not possible in the Navier-Stokes equations, the incompressible Stokes equations given in (1a)-(1b) do have known analytical solutions in a variety of domains. For instance, suppose there is a point force $\mathbf{F}$ at position $\mathbf{X}_0$ in an infinite 3D domain. If the force density at a point $\mathbf{x}$ in the fluid is $\mathbf{f}(\mathbf{x}) = \mathbf{F}\delta(\|\mathbf{x} - \mathbf{X}_0\|)$ where δ is the Dirac delta function, then the solution to the incompressible Stokes equations is known as a Stokeslet:

$$\mathbf{u}(\mathbf{x}) = \frac{1}{8\pi\mu}\left(\frac{\mathbf{F}}{r} + \frac{(\mathbf{F}\cdot(\mathbf{x}-\mathbf{X}_0))(\mathbf{x}-\mathbf{X}_0)}{r^3}\right), \tag{2}$$

where $r = \|\mathbf{x} - \mathbf{X}_0\|$. The Stokeslet is an exact fundamental solution that is everywhere incompressible for a given force density $\mathbf{f}$. It is important to note that there is a singularity at $r = 0$, the location of the point force, which makes evaluation of the Stokeslet at $r = 0$ impossible. Other fundamental solutions can be derived [18]; for example, the rotlet is the fundamental solution to a point torque in Stokes flow. Solutions can also be derived for other physical fluid domains such as the half space near a plane wall or fluid near the surface of a sphere [17, 18, 138].

Equation (2) gives a direct relationship between the velocity field $\mathbf{u}(\mathbf{x})$ and a point force $\mathbf{F}$ located at $\mathbf{X}_0$. This means that if one specifies the point force, the velocity field may be calculated directly. Conversely, if one specifies the velocity at a position, one can recover the force required to generate that velocity. It is this relationship in the Stokeslet approach that enables a Lagrangian framework to be used to model motion in a viscous fluid. Due to linearity of the Stokes equations in (1a)–(1b), if there are multiple forces, one can simply add solutions together to obtain a solution for a *distribution* of point forces or torques. Moreover, solutions such as the Stokeslet and rotlet provide a way to connect velocity with forces and torques directly. In the case of the Stokeslet, for instance, one can either find the velocity field $\mathbf{u}(\mathbf{x})$ given a distribution of point forces, or conversely, find the forces that would be required to give rise to a given distribution of velocities at specific points. Depending on the application or modeling framework, one of these approaches may be more appropriate than the other.

Ultimately, one must decide how to connect the underlying flagellar motility model with the physical concepts of velocities and forces and torques in the system. In this context, motility arises from the beating of the sperm flagellum. As discussed in Section 2, mathematical treatments of flagellar motion often rely upon resistive force theory or slender body theory. From a computational perspective, resistive force theory provides a straightforward way to calculate forces from velocities and vice versa, but is limited in that it assumes that elements (or pieces) of the flagellum do not affect the rest of the flagellum. On the other hand, if one uses the more accurate slender body theory, which relies upon singularity solutions to the incompressible Stokes Equations in (1a)–(1b), the singular nature of the solutions is problematic for computational methods. Using nonlocal slender body theory to overcome these issues has also been shown to be computationally intractable, as shown in [198], where the authors introduced a regularization parameter to the singular solution to address this issue.

If, instead, one regularizes the force *distribution* from the beginning, using a regularized delta function instead of the singular Dirac delta function, one can derive what is known as a regularized Stokeslet [40, 42]. There are many possible choices for a regularized Dirac delta function, but the resulting regularized Stokelet will take a form such as:

$$\mathbf{u}(\mathbf{x}) = \frac{\mathbf{F}(r^2 + 2\epsilon^2) + (\mathbf{F} \cdot (\mathbf{x} - \mathbf{X}_0))(\mathbf{x} - \mathbf{X}_0)}{8\pi(r^2 + \epsilon^2)^{3/2}} \tag{3}$$

where $\epsilon > 0$ is a regularization parameter, assumed to be small. This approach provides a non-singular solution to the incompressible Stokes equations given in (1a)–(1b); by simply taking the regularization parameter $\epsilon \to 0$, the singular Stokeslet solution is recovered. This method has also been shown to be consistent with the slender body theories of Lighthill and Keller-Rubinow in the limit as $\epsilon \to 0$ [44].

Through the use of regularized fundamental solutions, we can now view the problem in a completely Lagrangian framework because there is no need for a fluid grid or interpolation. We will have an exact solution for velocity and pressure given regularized forces (and regularized torques or other quantities, if necessary) that can be evaluated on the structure as well as anywhere in the fluid domain. Additionally, regularized fundamental solutions for different fluid domains have been derived using the method of images (see [2, 211] for further details) as well as for triply and doubly periodic domains [43, 113, 114]. Crucially, the regularized fundamental solutions to solve the Stokes equation are a good choice for slender bodies as they have been shown to match well with experiments [21, 107, 163] and swimming speeds for a flagellum compare well with small amplitude theoretical results [141, 144, 194, 195].

4   Representing the Sperm

In Section 3, we gave an overview of how we view a sperm as an immersed structure in a fluid. As the sperm swims, it exerts forces upon the fluid, and the fluid moves. The sperm body can also be moved by the fluid itself and react to its environment. This description provides a context for the interaction between the sperm and the fluid. In this section, we will focus on models for the sperm body itself, which is depicted in Figure 2. Any model of sperm motility must allow for the flagellum to beat or otherwise generate propulsive forces to move the sperm body through the fluid.

The simplest representation is to think of the sperm as a single point where systems of differential equations or an agent-based model are then used to update the location of each sperm body. These types of models have been used in other cellular motility contexts as well. In the differential equation modeling framework, the curvature of the trajectory can be coupled to a chemoattractant concentration [70, 96], and such chemotactic behavior has been shown to be a robust navigation strategy for a large range of parameters [70]. Other models have coupled the differential equations to a background fluid flow [29, 108] and hypothesized that reorientation in the flow, due to a transverse velocity component, is related to a preferred handedness in the flagellar beat [108]. Agent-based models have explored sperm motility within a realistic 3D geometry based on medical imaging of the female reproductive tract [30, 31]. These models can be validated or compared to experimental data that is able to track the trajectories of sperm under different experimental conditions (e.g., Figure 1b) [35, 184, 185].

Other studies have focused on the long range fluid flow and interactions of many swimmers where they are represented as a "pusher," meaning the swimmers push fluid away from their bodies. Note that this representation can also be used more generally–beyond sperm–for microswimmers such as bacteria and the flow induced by a pusher can be accounted for in terms of a simplified fundamental solution corresponding to a dipole. The interactions of many can be easily simulated, possibly accounting for interactions with walls or other boundaries [112, 127, 167, 168]. As an extension of the "pusher" model, swimmers such as sperm have been studied using a "two-sphere model" or a "dumb bell" model where the sperm is represented as two points, one for the head and one for the flagellum [2, 4, 84]. Again, the point of these models is to simulate the large scale flow structure to understand at what concentration of swimmers certain patterns such as local vortices occur [167, 168]. These studies have also been used to demonstrate that swimmers will aggregate near a wall or surface, simply due to hydrodynamic effects, which can help to explain similar experimental observations [50, 127, 165].

Perhaps the largest class of models for sperm motility rely upon modeling the beating flagellum itself. The elastic flagellum is on average 30–200 microns [47], and has a cylindrical shape that tapers in radius towards the flagellum tip (end). As depicted in Figure 2, within the flagellum there are nine sets of microtubule doublets (inextensible and stiff rods) on the outer part of the structure that run along the length of the flagellum [120, 203, 207]. Many species of sperm exhibit mainly planar motion, which is attributed to the fusing of microtubules 5 and 6, which defines the beat plane as perpendicular to the central pair. There is also a central pair of microtubules, giving the 9+2 structure characteristic of the axoneme, which is also found in cilia. The bending of the flagellum is propagated along the length by the coordinated turning on and off of dynein motors, which are active force generators [81, 203]. Dyneins reach across and grab the adjacent microtubule; this causes the microtubule doublets to slide relative to one another, generating bending. The exact mechanism of how dyneins work in a coordinated fashion to create a propagating waveform is not completely understood [207]. However, it is known that coordinated activation of dyneins on doublets 1–4 bend the axoneme in one direction, which in turn allows the dyneins on doublets 6–9 to initiate activation and start to bend the axoneme in the other direction while the dyneins on doublets 1–4 are deactivating.

To model the flagellum, one can focus on the structural components that comprise the flagellum or just the waveform of the flagellum itself. For instance, one can consider the flagellum as an oscillating thin filament whose centerline is used as the location of forces or velocities of interest. While this may be considered a coarse approximation to model the flagellum, it can be used to effectively model motility. Moreover, even though many models have used a centerline approach to represent the flagellum, there are still ways to account for the flagellar structure in such a simplified framework. For example, since the flagellum tapers in radius towards the end, the stiffness decreases along the length [170]. To account for this, models
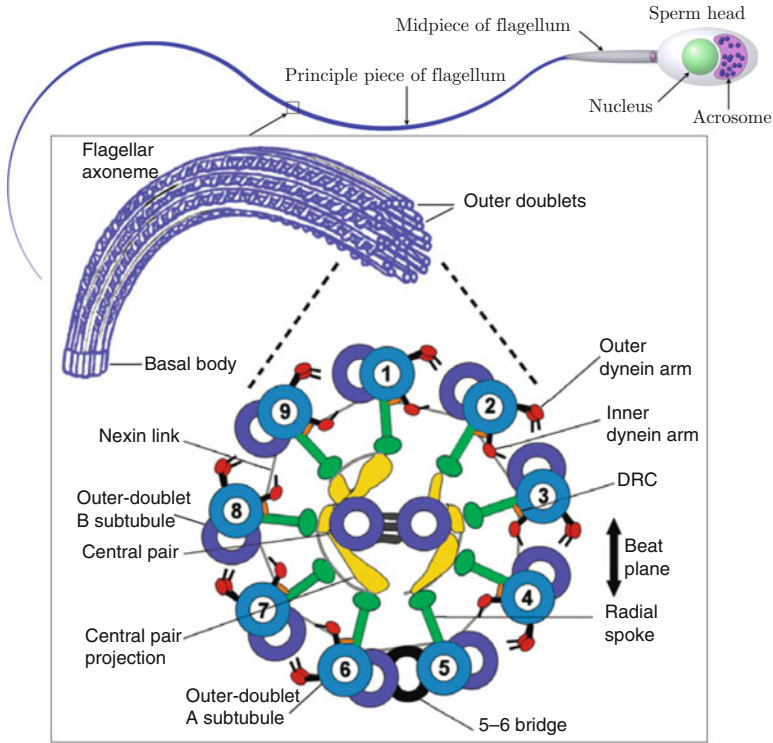
Fig. 2 Depiction of a typical sperm cell structure (top), with cross section showing the internal structure of the axoneme of the flagellum in the box. Dynein motors are the active force generators and the nexin links are elastic linkages or accessory structures. The flexural rigidity of the axoneme is imparted by the 9 sets of microtubule doublets that run along the length of the flagellum. The image in the box is reproduced with permission from *Journal of Cell Science* [120].

have incorporated a variable stiffness along the length, which leads to different trajectories in model simulations [146]. Other models have coupled movement of the centerline to the evolving calcium concentration [145, 146, 174], known to be important for hyperactivated motility, which consists of highly asymmetrical and high amplitude bending of the flagellum. In Section 5, we will discuss different types of models that account for the bending of the flagellum in more detail.

Many models for sperm motility focus on the flagellar motion alone, but the sperm head can also be incorporated. This is a passive cell body containing the DNA, which is attached to the base of the flagellum. The cell body varies in both shape and size depending on the particular species. Bull sperm are known for a paddle or oar shaped head with a length of around 8 microns, whereas mouse sperm have an additional apical hook and sea urchin sperm have an ellipsoidal head [11, 47]. Accounting for the cell body will certainly have an effect on the resulting fluid flow and trajectories, but this definitely has an associated computational cost. The

cell body is often discretized as a number of points that are connected via a network of stiff springs [64] or the cell body could be represented with the method of images if it is assumed spherical [211].

In laboratory settings, headless sperm are still able to swim since the cell body does not contribute to propulsion [131]. In [101], there is a detailed description of how neglecting the sperm head will result in a swimming speed with an error of approximately 20%. Additionally, the torque of the head is three orders of magnitude lower than the flagellum [101]. Thus, if one is interested in precise speeds and angular velocities, the cell body should be accounted for. However, if the modeling question lends itself to understanding fundamental interactions of many swimmers or accounting for detailed biochemistry, the results for "headless" models will be of the right order of magnitude.

5   Modeling Flagellar Bending

For sperm to effectively swim, their flagellum must undulate or bend. As mentioned in Section 4, bending is known to come from the action of dynein motors along the length of the axoneme. There are several models that have been proposed to account for the activation of dynein and bending of the flagellum, these include sliding filament models [25–28] and the Geometric Clutch Hypothesis [120–123]. A simplified model of the axoneme with a curvature threshold model for planar bending has been developed in 2D, where the simulations account for the relevant fluid dynamics and the flagella were able to exhibit coordinated flagellar bending [51–53, 214]. Since the detailed axonemal structure of dyneins, microtubules, and other accessory structures shown in Figure 2 is not always computationally feasible, many studies have approximated the flagellum with a series of cylinders or a centerline, as depicted in Figure 3. Such simplified representations of the flagellum have been shown to agree well with experiments in terms of swimming speeds and the trajectory of a single sperm [77, 146].

These cylinder or centerline representations of the flagellum can actuate flagellar bending using two main approaches. One uses prescribed flagellar motion and the other is an elastohydrodynamic model where the flagellum is elastic and its waveform is an emergent or developing property of the coupled system. The former is an idealized model of swimming where we can prescribe flagellar motion and understand how swimming speeds vary for different assumed parameters such as the amplitude or frequency. The latter approach has an emergent waveform that will vary based on the type of fluid, elastic properties of the swimmer, and interactions with a wall or other neighboring swimmers. Emergent flagellar bending is important because experimental observations have illustrated that sperm waveforms and trajectories are an emergent property of the nonlinear system coupling the fluid, biochemistry, surface interactions, and the mechanics of bending [63, 76, 209]. In particular, flagellar waveforms have been observed to range from planar to helical
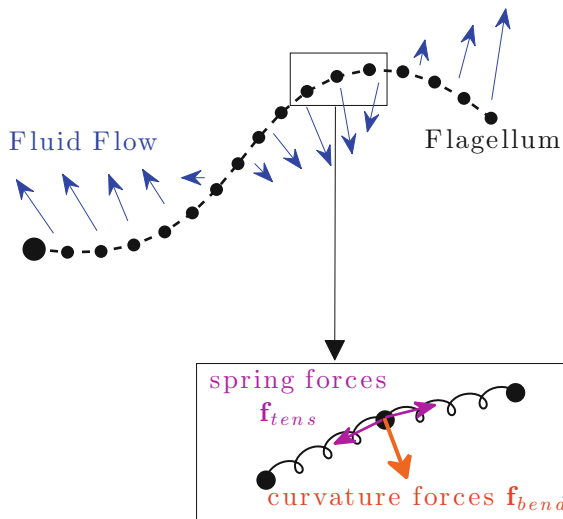
Fig. 3 Schematic of a centerline of a flagellum. After discretizing the centerline for computational approaches, each point (denoted by black dots) may experience bending forces ($\mathbf{f}_{bend}$) that actuate the motion of the flagellum and may experience tensile forces ($\mathbf{f}_{tens}$) from connections with neighboring points. Depending on the model, these two forces may be calculated and then used to find the fluid velocity field, or a prescribed motion of the flagellum could be used to calculate the total force at each point.

as viscosity varies (shown in Figure 1a), and trajectories can vary based on chemical stimuli in the fluid (shown in Figure 1b) [56, 160, 184, 185, 206, 209].

5.1 Prescribed Waveforms

For prescribed motion with a centerline representation, one option is to extract the motion directly from experimental data, as done recently in [99]. A more typical setup is to consider an undulating flagellum of length L given as

$$x(s, t) = s, \qquad y(s, t) = a \sin(ks - \omega t), \qquad z(s, t) = b \cos(ks - \omega t), \qquad (4)$$

for $0 < s < L$ where s is a parameter initialized as arclength, the wavenumber is $k = 2\pi/\lambda$ for wavelength λ, the bending amplitudes in y and z are given by a and b, and ω is the constant angular frequency. A planar waveform can be studied simply by letting $b = 0$. At any given time $t \geq 0$, the velocity of the flagellum is calculated by

$$u_b(s, t) = 0, \qquad v_b(s, t) = -a\omega \cos(ks - \omega t), \qquad w_b(s, t) = b\omega \sin(ks - \omega t), \quad (5)$$

where u_b, v_b, and w_b are the velocity components of x, y, and z, respectively.

Using the waveform in Equation (4), studies have considered infinite-length swimmers with small amplitude using asymptotic analysis. For swimmers with either planar or helical bending in a Newtonian flow, analysis has shown that swimming speed scales quadratically with amplitude [169, 194, 195]. When modeling finite-length swimmers, the total velocity $\mathbf{V}$ includes the velocity from the prescribed flagellar beat $\mathbf{u}_b(\mathbf{x}) = (u_b, v_b, w_b)$, translation $\mathbf{U}_0 = (U_0^x, U_0^y, U_0^z)$, and rotation $\boldsymbol{\Omega}_0 = (\Omega_0^x, \Omega_0^y, \Omega_0^z)$ as:

$$\mathbf{V} = \mathbf{u}_b(\mathbf{x}) + \mathbf{U}_0 + \boldsymbol{\Omega}_0 \times \mathbf{x}. \tag{6}$$

When prescribing the velocity of the flagellar beat with $\mathbf{u}_b$, one can solve for the velocities with additional conservation laws, which are generally a force-free and torque-free condition when modeling a zero-thrust swimmer in a viscous, incompressible flow.

Using this type of an approach, swimming speeds of finite-length filaments with planar waveforms [77, 79, 85, 86, 91] and with helical waveforms [39, 86] have been examined using various approximations to understand the "optimal" waveform that maximizes speed and minimizes power. Simulations have shown that for a variety of wavenumbers, a smaller normalized head radius (ratio of head radius and swimmer length) results in an increased swimming speed and a decrease in inverse hydrodynamic efficiency [77, 85]. Other computational models have been used to study the trajectory of a finite-length swimmer over a longer period of time using a prescribed waveform. Since the rotational and translational velocity of the flagellum in space can depend on other factors, several studies have used this method and also accounted for a wall to understand how trajectories vary in the presence of a wall [77, 100, 101, 147, 175].

5.2 Emergent Waveforms

The other type of model is one where the dynamics of the elastic flagellum are not prescribed but are an emergent property of the fluid-structure interaction. One approach is to use the sliding filament model [25, 27, 161] and to simplify the hydrodynamic interactions using resistive force theory [71, 80]. In this type of model, the flagellum is idealized as a pair of elastic filaments that slide relative to one another and a governing equation can be derived for the location of the flagellar centerline [32, 87]. The movement of the sliding filaments is controlled by the choice of internal shear stress (or force); one study chose a simple traveling wave where it was determined that interesting buckling instabilities can occur in the elastic flagellum when nonlinearities were accounted for [75].

Instead of using resistive force theory, one can use a computational method to solve for the resulting fluid flow when the emergent flagellar bending of the swimmer is determined in terms of bending and tensile forces. As shown in Figure 3, one can discretize the flagellar centerline as a series of points. Most immersed

boundary approaches idealize the elastic flagellum as a series of interconnected springs [64, 153]. As the flagellum is bending, this will give rise to local bending forces $\mathbf{f}_{bend}$ due to changes in curvature and local tensile forces $\mathbf{f}_{tens}$ as the springs comprising the inextensible flagellum are being stretched. One could derive functional forms for these forces based on phenomenological models accounting for the detailed structure of the axoneme, including the active force generation of the dyneins that leads to bending [51–53]. A more simplified version of this type of model would be to prescribe sinusoidal forcings–that are not dependent upon the current configuration–along the length of the flagellum, as in [125].

An alternate approach to determine bending and tensile forces is to propose an energy functional where in general, the swimmer will tend to minimize this elastic energy. The variational derivative of the energy functional would then determine the forces that the swimmer exerts on the surrounding fluid [153]. Modeling the elastic flagellum as an Euler elastica is a common approach [64, 65, 196], consisting of two energy functionals (conditions) where one corresponds to a tensile energy (stiffness or effective inextensibility of the swimmer) and the other is a bending energy related to the preferred curvature. The Euler elastica energy E is given as

$$E = \varepsilon_T + \varepsilon_B = \int_\Gamma \left(S_T \left[\left\| \frac{\partial \mathbf{X}}{\partial s} \right\| - 1 \right]^2 \right) ds + \int_\Gamma \left(S_B \left[\frac{\partial \Theta}{\partial s} - \zeta(s, t) \right]^2 \right) ds. \tag{7}$$

Here, Γ is the curve corresponding to the centerline of the swimmer, s is a parameter initialized as arclength, t is time, $\mathbf{X}(s, t)$ is the centerline of the swimmer, and Θ is the shear angle with respect to the first point of the centerline (towards the head or basal end). The preferred curvature is $\zeta(s, t)$ and is generally chosen to be some type of a propagating sinusoidal waveform (planar), similar to the curvature observed in experiments of human sperm [176]. The coefficients S_T and S_B are the tensile and bending stiffness coefficients. For larger values of the coefficients S_T and S_B, the conditions are more strictly enforced. In addition, the stiffness coefficients can be matched to experimental values obtained for the stiffness of a flagellum [146, 151, 170]. In this model, deviations between the preferred curvature and the current curvature generate force ($\mathbf{f}_{bend} = -\partial \varepsilon_B / \partial \mathbf{X}$); the flagellum will tend to maintain the preferred curvature but due to energy dissipation in the fluid or interactions with other nearby swimmers or boundaries, the achieved flagellar beat may differ from the preferred one.

Many models have used an energy functional with a preferred curvature or bending component to study emergent trajectories and waveforms of sperm in different fluid environments [61, 64, 142, 144, 146, 173, 174, 214]. For example, in [142], it was observed that even though two swimmers may have two different preferred waveforms, when they have attracted, the beats will synchronize and conform to each other due to hydrodynamic interactions (see Figure 8a and Section 7). This approach has been used to study the emergent flagellar beating of swimmers when near a plane wall [61, 174] as well as when coupling the preferred curvature to a dynamic intracellular calcium concentration [140, 146, 173].

In order to capture phenomena such as rolling and out of plane rotations due to wall interactions and background flow, a sperm representation must be used that allows for nonplanar movements. Recently, the planar waveform preferred curvature model using the Euler elastica energy formulation has been extended to be fully 3D where deviations from a planar waveform are penalized, and helical trajectories are observed [173]. Another approach is to model the swimmer's centerline as a Kirchhoff rod given as $\mathbf{X}(s, t)$ where a corresponding orthonormal director basis $\{\mathbf{D}^1, \mathbf{D}^2, \mathbf{D}^3\}$ at each point on the swimmer is accounted for in order to capture twist, and hence rolling [119, 141, 144]. A Darboux vector for the orthonormal basis is used, which is a rotation of the Frenet frame such that $\mathbf{D}^3$ is aligned with the tangent vector while $\mathbf{D}^1$ and $\mathbf{D}^2$ are perpendicular to the axis of the rod, capturing the twist. The elastic energy E for the rod given by $\Gamma = \mathbf{X}(s, t)$ and $\{\mathbf{D}^1, \mathbf{D}^2, \mathbf{D}^3\}$ is

$$
E = \underbrace{\int_\Gamma a_1 \left(\frac{\partial \mathbf{D}^2}{\partial s} \cdot \mathbf{D}^3 - \kappa_1 \right)^2 ds}_{\varepsilon_{bend,1}} + \underbrace{\int_\Gamma a_2 \left(\frac{\partial \mathbf{D}^3}{\partial s} \cdot \mathbf{D}^1 - \kappa_2 \right)^2 ds}_{\varepsilon_{bend,2}} + \underbrace{\int_\Gamma a_3 \left(\frac{\partial \mathbf{D}^1}{\partial s} \cdot \mathbf{D}^2 - \kappa_3 \right)^2 ds}_{\varepsilon_{twist}}
$$

$$
+ \underbrace{\int_\Gamma b_1 \left(\mathbf{D}^1 \cdot \frac{\partial \mathbf{X}}{\partial s} \right)^2 ds}_{\varepsilon_{shear,1}} + \underbrace{\int_\Gamma b_2 \left(\mathbf{D}^2 \cdot \frac{\partial \mathbf{X}}{\partial s} \right)^2 ds}_{\varepsilon_{shear,2}} + \underbrace{\int_\Gamma b_3 \left(\mathbf{D}^3 \cdot \frac{\partial \mathbf{X}}{\partial s} - 1 \right)^2 ds}_{\varepsilon_{stretch}} .
$$

(8)

The energy components ($\varepsilon_{bend,1}$, etc.) are divided up between bending, stretching, twisting, and shear in the different axes along the rod. The parameters of the curve are defined as follows: κ_1 is the geodesic curvature, κ_2 is the normal curvature, and κ_3 is twist. In order to have a temporal and spatially dependent preferred curvature, we determine a preferred curvature κ_1 and κ_2 that correspond to a propagating wave [33, 89].

Recently, the computational method solving for the Stokes flow due to forces and torque from a Kirchhoff rod using regularized fundamental solutions was developed [144]. The swimming speeds of the Kirchhoff rod with a propagating wave of curvature matched well with asymptotic swimming speeds for infinite-length, small amplitude planar, and helical waveforms [141, 144]. This model is now being used to study interactions of swimmers with a wall [94, 97] as well as to further investigate emergent trajectories for planar, quasi-planar, and helical preferred flagellar beats that are coupled to an evolving cytosolic calcium concentration [33]. In Figure 4, the swimmers are initialized at the same location at $t = 0$ and results are shown for the time interval of $t = 14$–15 s. We assume a preferred helical beatform as in Equation (4), and calculate the corresponding preferred curvature and twist (κ_i for $i = 1, 2, 3$ in Equation (8)) for two cases. The first case assumes a constant amplitude (no calcium coupling) as shown in Figure 4(a)–(b) and the second case shown in Figure 4(c)–(d) corresponds to a nonconstant amplitude that is coupled to the calcium concentration within the flagellum, representative of hyperactivated
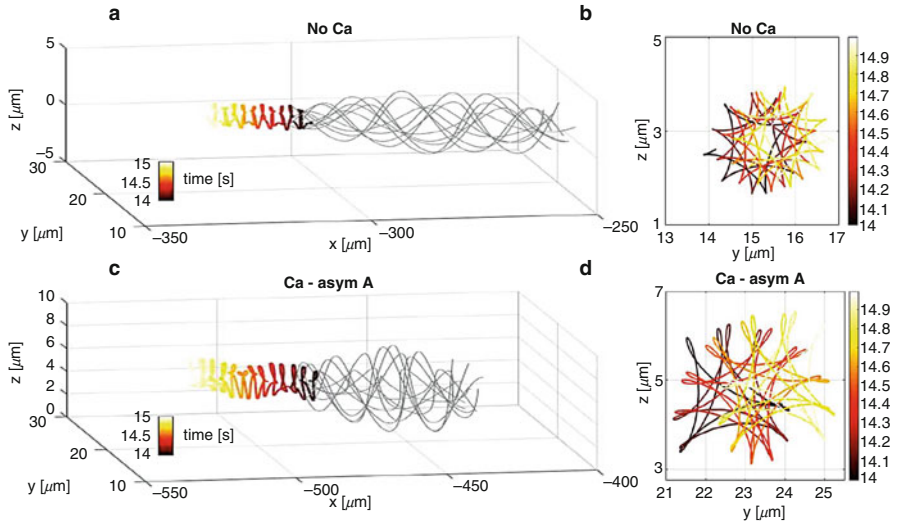
Fig. 4 Emergent waveforms and trajectories from a computational model using a Kirchhoff rod framework that was developed in [33]. In the top row, (a)–(b), the preferred curvature corresponds to a propagating wave of constant amplitude whereas (c)–(d) has curvature coupled to an evolving calcium concentration allowing for a nonconstant amplitude. The color bar corresponds to time and displays the 3D trajectory of the head in (a) and (b), where (c) and (d) give the zoomed in 2D trajectory in the y-z plane. In (a) and (c), the snapshots of the flagellum are superimposed at the same point.

sperm motility. In Figure 4, we note that the calcium coupling to the beatform in (c)–(d) has a swimmer that is able to swim further in the 15 s time interval. In addition, 3D and 2D emergent trajectories shown in Figure 4 resemble 3D experimental observations of helical trajectories and chiral ribbons [184, 185] and 2D trajectories projected on the y-z plane are hypotrochoid curves similar to previous experimental observations [206].

6 Interaction with Surfaces

Like many other cells, sperm must navigate complex environments in order to perform their function. What makes this cell type unique is that they traverse such a broad range of environments, as shown in Figure 5, and must dramatically change the way their flagella beat in order to successfully fertilize the egg and pass on their genetic material. One important aspect of this navigation is how to negotiate boundaries, such as the oviductal epithelium or the outer layers of the oocyte.

(a) Image of sperm heads (indi-
cated by arrows) bound to cilia
lining the oviductal epithelium,
reproduced from [146] with per-
mission from Oxford University
Press.

(b) Micrograph of a frozen tissue
section of bovine cervix, repro-
duced from [196] with permission
of The Royal Society of Chem-
istry.

(c) Image of hamster sperm near
an egg, reproduced from [134] and
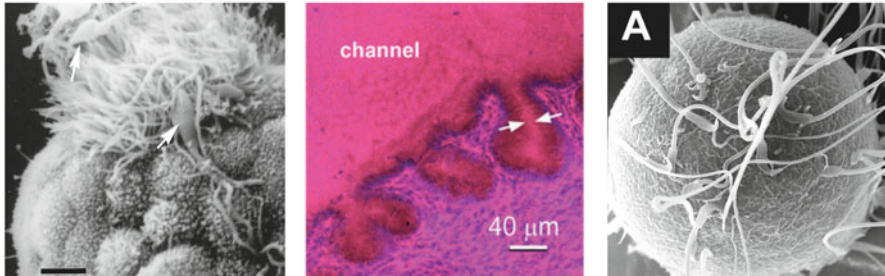licensed through creative com-
mons.

Fig. 5 Experimental images illustrating the different types of surfaces that sperm interact with, which include the oviductal epithelial surfaces in (a), the complex geometry of the cervix in (b), and the outer surface of the egg in (c).

Biologically, interactions with these types of boundaries have been observed or hypothesized to serve one of several purposes:

1. Storage until ovulation,
2. Detachment around the time of ovulation, and
3. Penetration of the oocyte.

Sperm storage happens within the oviduct, either through binding to cilia lining the oviductal epithelium or in what are called oviductal crypts [37, 78, 177, 187]. Figure 5a shows sperm bound to cilia along the oviductal epithelium and Figure 5b shows crypt structures that have been observed with sperm inside them. In some species, sperm may be "stored" in this manner for extended periods of time: from days to weeks to months, depending on the species and mating habits [16]. Detachment from the oviductal epithelium or release from oviductal crypts has been observed around the time of ovulation [193]. In many species, detachment has been shown to require the flagellum to beat hyperactively, meaning asymmetrically with high amplitudes [88, 213]. Penetration of the oocyte (shown in Figure 5c) is one of the most significant steps in sexual reproduction, but requires a complex interaction between the components of what is known as the cumulus-oocyte complex (COC) and the sperm body, which must exhibit hyperactive motility and go through a cascade of biochemical reactions. It is hypothesized that the hyperactive waveform aids in penetration of the layers of the COC [3, 158, 182, 188, 191, 192].

The earliest models of sperm interactions with boundaries involve 2D fluids. For instance, in [64], the authors use the immersed boundary method in a 2D fluid to model the interaction of sperm with boundaries. The results of this work show attraction to boundaries, as has been observed experimentally for quite some time [165]. Later on, slender body theory was used in [175] to show that sperm may

(a) Behavior of sperm near the epithelial wall, beating symmetrically, with ciliary bonds modeled by a spring (see insets). Numbers are placed near the flagellum, indicating the order of time progression. Figure reproduced with permission from Elsevier [171] .

(b) Wave numbers (increasing from top to bottom) affect hydrodynamic attraction (seen by the tendency of sperm to remain at z/L, a constant scaled height above the wall over time where later times are to the left) of sperm near a surface. Reproduced with permission from [172].
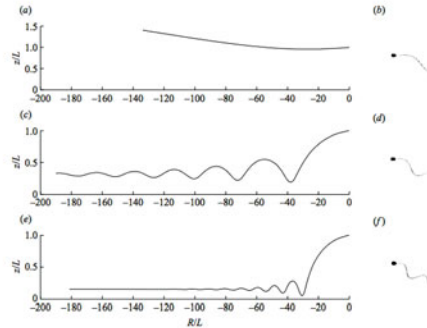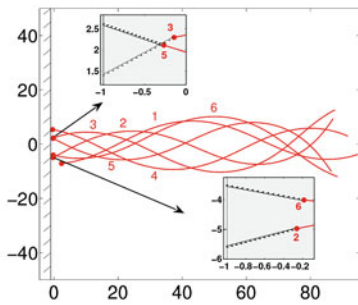
(c) With a 3D waveform, surface attraction may depend on the swimming angle. Figure reproduced with permission from [172].
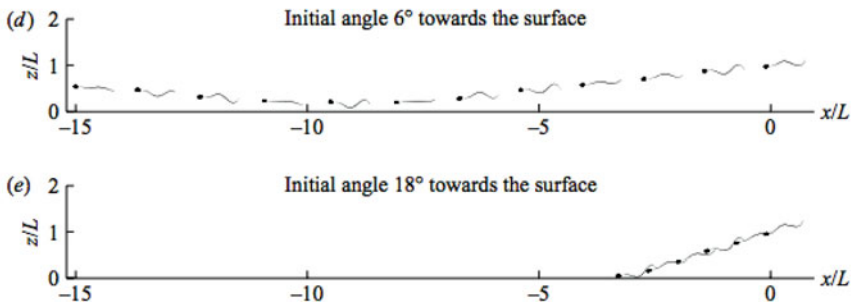
Fig. 6 Interactions with a planar surface, from various mathematical models. In panel (a), a bond to the epithelial surface is modeled. In panel (b) and (c), surface "accumulation" is observed only for particular wavenumbers and angles of approach.

accumulate a certain distance away from a surface depending on the wavenumber of the flagellum (see Figure 6b). This model also showed that sperm may adhere to surfaces depending on their angle of approach when swimming near a surface, as shown in Figure 6c. The authors in [61] used mesoscale hydrodynamics to also show attraction of sperm towards surfaces, with a more robust flagellum model that can interact dynamically with a surface. More recently, in [100], the authors study accumulation heights (where sperm tend to aggregate) near a surface using prescribed kinematics and the boundary element method. They found accumulation heights to be fairly insensitive to morphological effects, and extended previous results on sensitivities to wave numbers.

Important in any interactions of sperm with boundaries or surfaces are binding and unbinding between receptors on the sperm head and either cilia of the

epithelium or the surface of the egg. Additionally, because it has been observed that this binding and unbinding accompanies hyperactive motility [37], models have been used to investigate how hyperactive waveforms are affected when a sperm is near a surface or bound to a surface or point.

In [48], the authors considered a model that calculated the total force generated by a filament with specified kinematics, clamped or freely hinged at the head, and resistive force theory. In this model, the motion of the flagellum was given with the head remaining stationary, as if bound. Their studies showed that hyperactive waveforms enable both pushing and pulling forces at the head, which might give a physical argument for why sperm would swim hyperactively if they are trying to pull away from an epithelial wall instead of swim towards it. These results also suggested that if sperm are bound to a wall via cilia, such bonds might be broken if the sperm can pull away. The effects of a nearby wall was modeled with the wall set a fixed distance from the sperm body, which had only small effects. These minimal effects were likely because the sperm body was not allowed to get close to the wall, a restriction of the modeling framework.

In [174], a freely swimming flagellum with an emergent waveform was placed near a wall modeled by the method of images. The effects of binding to cilia lining the epithelium were modeled as well. In these simulations, without any binding, the flagellum will get stuck along the wall unless it has a sufficiently asymmetric or high amplitude waveform. Moreover, if a bond is modeled, the bond can actually enable the sperm body to overcome surface effects and break free of a surface more freely, though asymmetry and amplitude of the waveform are still important. Figure 6a shows an example of the flagellar behavior over time of a sperm bound to the epithelium, with an elastic bond mimicking the cilia. This model is able to capture a fully dynamic interaction between a surface and a freely swimming flagellum, with the flagellum flattening and unable to swim away when it is too close to a surface, but the model is restricted to particular geometries due to the modeling framework.

The authors in [102] added to this body of work by using the boundary element method to model the sperm, with varying morphologies, to consider adhesion dynamics near surfaces. The authors used a similar bond model to [174], but were able to explore a large range of geometries with respect to the surface. In this setting, hyperactivation did enable detachment from a surface but increased viscosity or elasticity of the fluid weakens this effect. This suggests that sperm must overcome not only surface dynamics, but also fluid properties that are known to vary in different regions of the oviduct. The authors propose that the increased elasticity in the COC would help a hyperactive sperm to actively penetrate the egg instead of pull away from the surface.

Very few models of sperm-egg interactions have been proposed with regards to understanding the role of sperm motility in the fertilization process. Clearly this is an important part of fertilization, but most studies have focused on simple planar surfaces. However, in [98], the authors find that, unlike the attraction observed near planar surfaces, spherical surfaces like the egg do not induce the same hydrodynamic attraction. This would indicate that further mechanisms (such as binding to the surface of the egg) must exist for the sperm to stay near the egg and

eventually penetrate the outer layers. While a complex process of modulating the flagellar waveform, breaking through the outer layers of the COC and binding with the surface of the egg must happen [155], the precise roles of all of these dynamics in egg fertilization have yet to be fully explained.

7 Sperm-Sperm Interactions

Sperm are generally not solitary cells swimming towards an egg. Figure 7 shows several examples of experimental observations of sperm swimming in populations or groups. While sperm counts dwindle as one approaches the egg [186, 205], interactions between sperm can have a significant effect upon their trajectories and ability to reach the egg at all. For instance, in mice, sperm have been observed to form "trains" which travel at faster speeds than individuals [67]. Similar cooperative swimming behavior has been observed in species as diverse as fishflies, echidnas, and possums and may enable groups of sperm to move efficiently towards the egg [83, 106, 134, 135].

Models for understanding the interactions between swimming sperm date back to G.I. Taylor's work in [194], which demonstrated that two parallel sheets will oscillate in-phase to minimize work. These results indicate that, at least in 2D fluids, there may be an energetic argument for swimming in a coordinated fashion. In [64], the

(a) A wood mouse 'sperm train', reprinted with permission from Springer Nature [67].
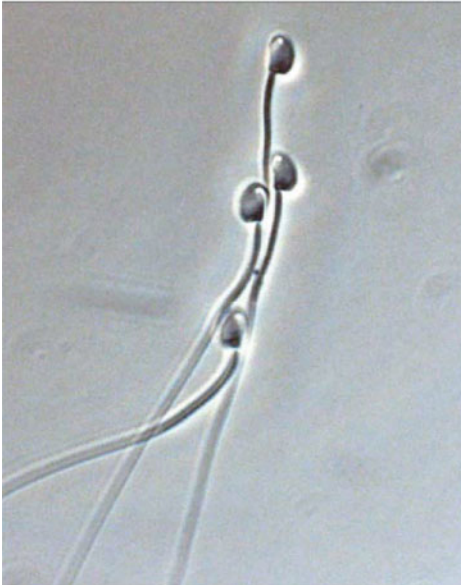
(b) Ant 'sperm bundles', reproduced from [148] with permission of the Royal Society.
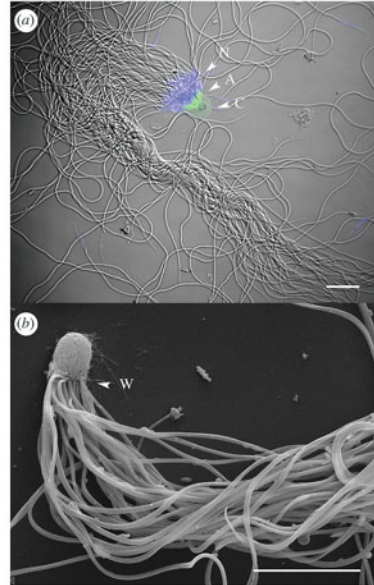
Fig. 7 Examples of experimental observations of sperm swimming in groups or populations.

interaction between two sperm was modeled with flagella of finite length in 2D and phase-locking was also observed. Another model using a 2D fluid found oscillating filaments that synchronize and attract, minimizing energy consumption [214].

In 3D, energy dissipation was found to be minimized when infinite cylindrical filaments oscillate in phase [130]. The authors in [125] modeled two semi-flexible filaments in 3D separated over a range of distances with either coplanar orientations or "transverse" (parallel) orientations. The authors concluded that speeds can increase when two sperm are either coplanar and out of phase or parallel to each other and in phase. Furthermore, power output can increase if two sperm are coplanar and in phase, or parallel and out of phase. This model was limited to short-term simulations where the filaments would not interact too strongly, so that their relative geometrical configuration remained roughly unchanged. Similar results were found for coplanar swimmers, but for simulations that allowed for longer simulations and dynamic interactions between the flagella using a preferred curvature formulation [46].

To compare 2D and 3D fluid models for the interaction of nearby sperm, the authors in [142] showed that coplanar flagella will attract (see Figure 8a) and increase their efficiency in both 2D and 3D. Synchrony occurs faster in 2D, but one observes greater enhancements in velocity and efficiency in 3D. These conclusions give some support for hydrodynamic arguments behind sperm swimming in groups.

A model proposed in [46] investigated how an active bond between two sperm heads might affect velocities, efficiencies, and power. This model mimics that of possum sperm, which fuse at the head and swim as a pair towards the egg. The model reproduced experimental work demonstrating that greater speeds were achieved when sperm paired in this fashion, and the model suggested optimal ranges in the angles of fusion between the sperm heads as well as the phase shift between the two sperm. These optimal ranges coincide with observed configurations in possum sperm.

Long-term dynamic simulations of finite length flagella in a range of 3D configurations are lacking, primarily due to modeling frameworks. The model proposed in [173], derived based on the preferred curvature model of [65, 146], is able to place sperm in any configuration in a fully 3D fluid domain and run long-term simulations. In this work, the authors reproduce the attraction observed in other models when sperm are coplanar, but find that any deviation from a coplanar configuration would, at best, result in only a transient attraction before ultimately swimming apart, as shown in Figure 8b.

This suggests that the cooperative or group swimming behavior observed biologically may not be the result of purely hydrodynamic effects, but also perhaps specific sperm morphology designed to overcome the tendency to swim apart. One example is the possum sperm pairs mentioned above, but there are other examples. For instance, in many rodent species, sperm heads have apical hooks on their heads which have been observed to hook along other sperm tails to create the sperm "train" [95]. The diversity of sperm morphologies and complexity of these interactions for specific species has been widely ignored in the modeling work so far, due to model limitations, but is an active area of study.

(a) Attraction in both 2D and 3D fluids over time, reprinted from [140] with the permission of AIP publishing.

(b) An example of attraction and repulsion observed over time in a fully 3D setting, reprinted from [170] with permission from Elsevier.
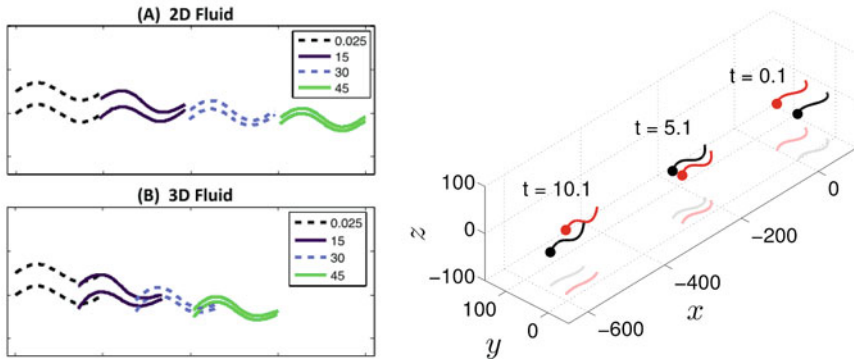
Fig. 8 Example of models for interactions of sperm swimming near each other. Panel (a) shows attraction of coplanar swimmers. Panel (b) shows two non-coplanar sperm attracting initially (at $t = 5.1$) and then repelling (at $t = 10.1$).

8 Background Fluid Flow

As described in Section 3, from Newton's third law of motion, when a fluid moves, so will any free object surrounded by the fluid. Therefore, it is not surprising that the relative magnitude of the flow will effect fertilization success rates. If the background flow was too large, fertilization of the egg would become more difficult since the egg would be rotating and moving, a chemoattractant gradient might not be sensed, and a sperm might be unable to effectively swim against the flow [217]. However, lower to moderate background flows are hypothesized to be a long range guidance mechanism, helping bring the sperm and egg together [131, 216]. These flows are generated by muscle contractions, cilia in the fallopian tubes, and fluid secretion from the oviductal epithelial cells [131, 189, 190, 193]. Uterine flow due to a wave of muscle contractions (peristalsis) helps bring the egg to the uterus and several modeling studies have quantified embryo transport in flows induced by peristalsis [6, 62, 215]. In the female reproductive tract, sperm are swimming in flows as large as one-fifth of their own swimming speed [131, 176]. Similarly, external fertilizers living in coastal ocean environments also experience laminar shear flows [217].

A natural question is whether there is an "optimal" flow rate. Experimental and computational studies can be utilized to study and characterize sperm motility, as well as sperm-egg encounters, at different flow rates. For red abalone sperm, a marine invertebrate, it was observed that the swimming speed, encounter rate, and fertilization success all were highest at the lowest shear tested (0.1 Hz), and decayed as shear increased beyond 0.1 Hz [162, 217]. These experimental results are highlighted in Figure 9a, where assays were done with and without the

(a) Experimental results for sperm-egg encounters and sperm swimming speed for red abalone under different experimental conditions, with largest values at a shear of 0.1, reproduced from [214] with permission of PNAS.
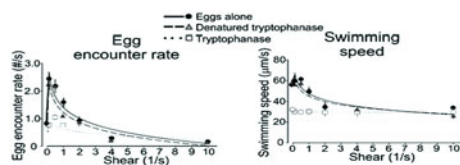
(b) Traces of mouse sperm swimming with (right) and without (left) a background flow where arrows denote swimming direction and the scalebar corresponds to 200 microns, reprinted from [129] with permission of Elsevier.
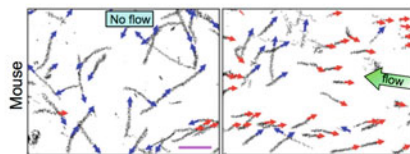
Fig. 9 Experiments illustrating how sperm swimming speeds, swimming direction, and encounters with the egg can change in the presence of a background flow.

presence of a known chemoattractant for red abalone, tryptophan, with background flow. Similarly, experiments with bull, human, and mouse sperm have investigated swimming at different flow rates. In Figure 9b, one can observe how mouse sperm are able to reorient and swim in the direction opposite or against the flow, called positive rheotaxis [108, 131]. Additional experiments have shown that mammalian sperm exhibit positive rheotaxis over a range of fluid viscosities and flows [108, 128], and the time to reorient against the flow is proportional to the flow velocity [60].

As already highlighted in Section 6, mammalian sperm are navigating complex environments and interacting with the surfaces of the oviductal walls. Previous models, without a background flow, have studied sperm accumulation near walls, showing sensitivity to the wavenumber [100]. Hence, recent studies have been focusing on identifying the conditions and particular flagellar beats that allow for positive rheotaxis in the presence of a wall. With the use of microfluidic devices, experiments have shown that fluid flow and microgrooves facilitated migration in the direction opposite of the flow [60, 128, 199].

An earlier study hypothesized that helical flagellar bending is necessary for rheotaxis [131]. Computational models have varied a chirality parameter, which corresponds to having a flagellar beat that ranges from planar to helical, showing that positive rheotaxis does not require a helical beat [101, 147]. Emergent sperm trajectories and flagellar beats are highlighted in Figure 10a where the sperm exhibits positive rheotaxis after reorienting in the flow over time. Since fluid flow may induce rolling or rotation of the sperm flagellum [131], this was investigated with a 3D analysis of flagellar waveforms where it was determined that the cell turning direction is not defined by the rolling direction [29]. The emergent behavior was further studied in a computational model by systematically varying the shear rate and the chirality parameter to understand under what conditions positive rheotaxis would occur. In Figure 10b, each symbol represents a different observed swimming pattern. This phase diagram highlights the interplay of fluid shear, steric surface interactions, and the chirality of the flagellar beat, which has been described in several studies [101, 108, 147].

Even though studies have started to identify the conditions under which a mammalian sperm will exhibit positive rheotaxis, there is still some debate as to

(a) Model results for a sperm swimming in a background flow as scaled time ft increases, reproduced from [145].
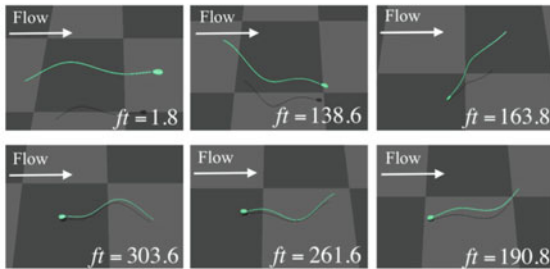
(b) Phase diagram characterizing emergent swimming behaviors, reproduced from [145].
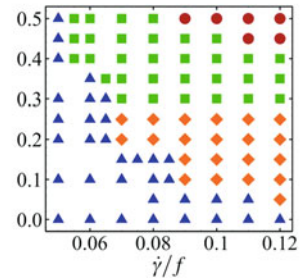
Fig. 10 Simulations illustrating how sperm motility changes in the presence of a background flow. In panel (a), a time series shows a model sperm reorienting to swim against the background fluid flow. In panel (b), swimming is a function of $\dot{\gamma}/f$ (ratio of the shear rate and beat frequency) and chirality parameter (measuring how planar versus helical a flagellar beat is) on the y-axis where squares=upward swimming (against flow), diamonds=periodic tumbling, circles=negative relative velocity, and triangles=downward swimming. The figures are reproduced with permission from the American Physical Society.

whether this is a passive response or an active response. A passive response would correspond to flagellar waveforms or swimming direction changes solely based on hydrodynamic interactions [131]. An active response would include sensing the flow via mechanosensitive channels, which would then initiate a signaling pathway that would result in changes in flagellar waveform causing the sperm to reorient against the flow [60]. An interesting fact is that sea urchin sperm are not biased by fluid flow, nor are CatSper mutant mouse sperm, which possess defective calcium signal transduction [131]. Additional modeling studies where flagellar bending is an emergent property, possibly coupled to evolving chemical concentrations, are necessary to further illuminate how reorientation in a flow occurs.

9 Modeling the Flow: From Viscosity to Elasticity

While sperm reside in a viscous fluid environment, most biological fluids are not homogeneous, and contain varying amounts of polymers and proteins that can be thought of as obstacles that may add elastic effects to the fluid. In the mammalian female reproductive tract, the fluid environment varies with the estrous or menstrual cycle; around ovulation the isthmus epithelium is covered by a dense mucus that then disappears after ovulation [103, 131]. The role of fluid viscosity is also important to consider since mammalian sperm swim in cervical mucus, which can range from 200 to 680 cP in humans [110, 176]. Emergent flagellar waveforms observed when swimming in a gel also depend on whether the sperm is fresh (exhibiting low amplitude, symmetrical beating in control medium) or if the sperm
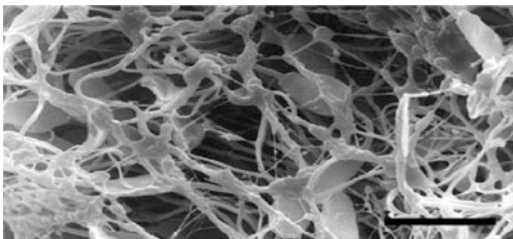
is hyperactivated (having high internal calcium concentration and large amplitude, asymmetrical beating in control medium) [191]. Additionally, in polyacrylamide gels, relative to the control medium, swimming speed is enhanced for hyperactive sperm and in general, attraction and clustering of sperm are enhanced [191, 200].

All of these observations suggest that both viscosity and fluid elasticity play roles in sperm progression, but precisely what these roles are is a complex question. In [110], the authors suggest that viscosity is a control mechanism along the oviduct for sperm selection. Thus, different fluid environments could act to control, aid, or hinder sperm progression. We note that experimental studies which track emergent flagellar waveforms and swimming speeds are both costly and time intensive. Hence, in order to advance our understanding of sperm motility in a variety of fluid environments, models have moved from Stokesian flows to more advanced fluid models to systematically probe a range of model parameters and identify swimming speeds and emergent flagellar waveforms.

As shown in Figure 11, vaginal and cervical fluids contain a network of proteins such as mucin. These networks can act as barriers and/or add elasticity to the fluid. If one wants to account for the additional drag or resistance in the fluid due to a network of polymers, we could use a two-phase fluid model or use the Brinkman equation. In a two-phase fluid model, the volume fractions of the fluid and polymer phase are accounted for at each region in space, where viscous stress tensors account for friction between the phases. Through analysis and simulations, for most cases, it has been shown that swimming speeds in a gel represented as a two phase fluid (elastic polymer network and viscous fluid) decrease in comparison to a single fluid model [57, 72]. However, an enhancement in propulsion was observed when the polymer network was stationary [72].

The other approach is to think of the homogenized fluid flow through a sparse array of fibers or polymers that are stationary [7, 24, 93, 181]. This can be modeled using a Brinkman flow equation, which is the Stokes equation in (1a) with an additional term on the right-hand side. This term is a flow dependent resistance term, $-\mu\alpha\mathbf{u}$, where α is the resistance parameter and is inversely proportional to the permeability. When taking the limit as $\alpha \to 0$, we recover the Stokes equation, which is the case of no obstacles and infinite permeability. The Brinkman equation is effectively a two-phase fluid with a sparse and stationary solid volume fraction. With asymptotics, for a prescribed waveform, it has been shown in 2D and 3D that an infinite-length swimmer has an increased swimming speed in a Brinkman

(a) Comparison of swimming at different resistance parameter $\alpha = 1/\sqrt{\gamma}$ for permeability γ, using the model in [89].

(b) Interactions in a Brinkman fluid, left is $\bar{\alpha} = 1$ and right is $\bar{\alpha} = 10$ for nondimensional resistance parameter $\bar{\alpha} = L/\sqrt{\gamma}$ where L is the swimmer length and γ is permeability. Reprinted from [113], with the permission of AIP Publishing.
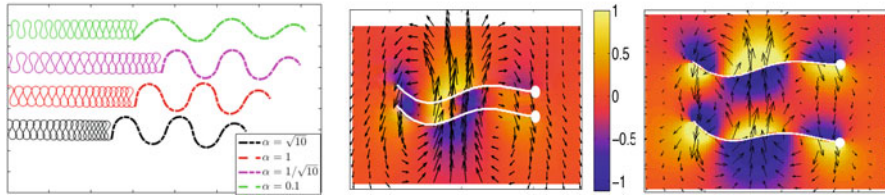
Fig. 12 Simulations of sperm swimming in a Brinkman fluid with varying resistance parameter, which characterizes how the presence of fibers effect the flow.

fluid in comparison to the Stokes case (with no resistance) [90, 116]. The idea of enhanced swimming with additional fibers (higher α) seemed counterintuitive until the formula for work was derived [89]. In order to attain the prescribed amplitude and see this enhancement in swimming speed, the amount of work increases dramatically with α. Thus, most microorganisms and artificial microswimmers may not be able to demonstrate this enhancement over this range of α because there is a finite amount of energy available.

New numerical methods utilizing regularized fundamental solutions have been developed to study swimmers with a preferred curvature model and emergent waveforms in Brinkman fluids [41, 89, 115]. In Figure 12a, for the same preferred waveform, there is a non-monotonic change in emergent flagellar amplitude and swimming speed with respect to the resistance parameter α. The enhanced swimming for $0 < \alpha < 1$ is in a biologically relevant range of fiber volume fractions, showing that the presence of a small to moderate amount of fibers can give a boost in swimming speed. For $\alpha > 1$, the fibers are preventing the swimmer from moving and achieving the preferred waveform. The authors also determined that stiffer swimmers representative of mammalian sperm are able to see an enhancement whereas less stiff swimmers such as marine invertebrate sperm do not see this enhancement, leading to the hypothesis that mammalian sperm have adapted to their fluid environment [89, 115, 143].

One may also wonder how the presence of fibers might change the dynamics of interactions of pairs of swimmers. In Figure 12b, for nondimensional resistance parameter $\bar{\alpha} = L/\sqrt{\gamma}$ with swimmer length L and fluid permeability γ, attraction of two coplanar swimmers is observed for $\bar{\alpha} = 1$ (left panel) and repulsion is observed for $\bar{\alpha} = 10$ (right panel). These results also demonstrate that the presence of the fibers, without additional fluid elasticity, could enhance swimming speed and attraction for low to moderate resistance parameter $\bar{\alpha}$.

When mucus has a high density of proteins, rheological testing has shown that there is no longer a linear relation between stress and strain, making it non-Newtonian [63, 166, 193]. There are several different modeling approaches that can

be used to simulate these types of flows. One approach has been to assume that the polymer network has an effective viscosity that varies as a function of the shear rate and a popular choice is the Carreau model for a shear thinning fluid, where low shear rates capture a Newtonian fluid and higher shear rates correspond to a power-law fluid. For the Carreau fluid model, asymptotic analysis of infinite-length swimming exhibits a decrease in swimming speed relative to the Stokes case [49] whereas swimming was enhanced relative to the Stokes case in numerical simulations for finite-length swimmers [133]. Thus, results suggest that a boost in swimming speed is observed due to shear thinning at the head of the swimmer. The Carreau model works well at moderate shear rates, but it is not able to fully capture and describe the non-Newtonian flow at higher shear rates.

Instead of modifying the viscosity, one can model the polymers or proteins explicitly. The advantage of doing this is that known behaviors of polymers can be incorporated. Importantly, it is known that viscoelastic fluids are characterized by a Newtonian fluid behavior in steady shear, but at higher shears, deformations can cause proteins or polymer chains to exhibit a nonlinear strain response that could be frequency-dependent. One approach to capture this behavior is to model a dynamic network of elastic links immersed in a viscous fluid. Such a network will result in additional forcing terms in the governing equations for the fluid. Depending on the rules governing the links, the elastic link network may be able to account for viscosity and shear thinning [20, 55, 210]. The complex rules governing such polymer dynamics can be computationally expensive, but this method can be used to understand the types of dynamic networks that enhance flagellar swimming. It was found that stiffer networks enhance swimming speeds when the motion is prescribed and swimming efficiency depends heavily on the evolution of the links (whether and how the links can break and reform) as the swimmer progresses through the network [212].

Another approach to model a viscoelastic fluid is to modify the stress term in the governing equations for the fluid so that it accounts for the polymers. The governing equations of zero Reynolds number flow can be expressed as:

$$\nabla \cdot \sigma + \mathbf{f} = \mathbf{0}, \tag{9a}$$

$$\nabla \cdot \mathbf{u} = 0, \tag{9b}$$

where σ is the stress (force per area). The Stokes equations have a linear relation between viscous stress and the local strain:

$$\sigma = -pI + \mu(\nabla \mathbf{u} + \nabla \mathbf{u}^T) \tag{10}$$

where T denotes transpose and I is the identity matrix. Plugging this form of the stress into (9a) gives (1a). Now, to arrive at non-Newtonian flows, the fluid is idealized as a solvent of given constant density ρ and viscosity μ, which has a dilute suspension of polymers immersed in it. The effective extra stress contribution is derived from the transport and distension of these dilute polymers. In the Oldroyd-
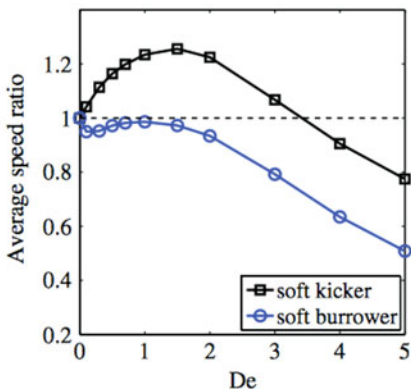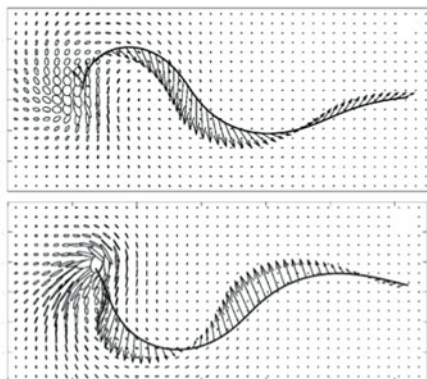
Fig. 13 Simulations results for sperm swimming in a viscoelastic fluid governed by the Oldroyd-B equation.

B model [139], the total stress σ now becomes a sum of the Newtonian fluid stress given in (10) and the stress from the polymers σ_P. The polymeric stress is found by solving the Oldroyd-B constitutive model, containing an upper convected derivative of the viscoelastic stress tensor. Note that most viscoelastic fluids have several polymer relaxation times and the Oldroyd-B model assumes a single, constant relaxation time r_t. When working with the Oldroyd-B model, the nondimensional parameter $De = r_T L/U$ is the Deborah number, which describes the relaxation time of the fluid for characteristic length and velocity scales L and U, respectively.

Swimming speeds of infinite-length swimmers in viscoelastic fluids governed by the Oldroyd-B equations exhibit a decrease in swimming speed relative to the speed in a purely viscous fluid [73, 74, 111]. In contrast, simulations of finite-length swimmers using a preferred curvature model revealed that enhancement in swimming speeds are observed for larger amplitude undulations at $De \sim 1$ [196, 197]. In Figure 13a, the emergent swimming speed is normalized with respect to the swimming speed in a Newtonian fluid and plotted as a function of the Deborah number. Since sperm propel themselves by "kicking" their tails, they are classified as a "kicker," where an enhancement in swimming speed is observed for a certain range of stiffness parameters. This enhancement in swimming speed is due to an accumulation of stress at the end of the tail, as shown in Figure 13b, where the ellipses represent the symmetric portion of the polymeric stress tensor σ_P. Note that in Figure 13a, the "burrower" corresponds to an undulation representative of nematodes such as *C. elegans* and does not have an enhancement in swimming speed in this non-Newtonian flow.

In summary, elasticity can have a range of outcomes. Since stress accumulation at the tips or end of the swimmer can cause an enhancement in swimming speed, anal-

ysis with infinite-length swimmers are not able to capture such effects. Additionally, conflicting experimental results in terms of swimming speed enhancement or slow down have now been unified since the outcome depends on the Deborah number *De*, the stiffness of the swimmer, and the particular undulating waveform of the swimmer [197]. Recent experimental results have observed that sperm interactions and collective swimming are enhanced in viscoelastic fluids [200]; this still remains an open avenue for computational models to understand hydrodynamic efficiency of interactions in these fluids. We point out that most computational studies with non-Newtonian flows are often completed in 2D for ease of computation. However, one must be cautious when interpreting results since the derivatives of the flow could vary greatly when comparing 2D and 3D [132]. Thus, further studies in 3D, as well as additional experiments to identify and verify the correct rheological properties of vaginal and oviductal fluids at multiple time points are needed in order to elucidate the true role that fluid elasticity plays in sperm motility.

Many of these models for viscoelasticity, particularly in the study of finite-length filaments, are recent. As noted earlier, interactions with the egg have not been studied in great detail and part of this is due to the nature of the cumulus oophorus complex surrounding the egg, which consists of cells and a viscoelastic extracellular matrix [159]. It has been shown that removing the cumulus reduces fertility and it is postulated that the cumulus might entrap the sperm [201]. The work in [211] demonstrates how the method of images can be used to model the surface of an egg surrounded by a viscoelastic mesh. While only a preliminary investigation was done into how the viscoelastic mesh would respond to a force applied by a sperm head, future work will certainly help elucidate how sperm motility, interaction with surfaces, and fluid rheology all play concerted roles in fertilization of the egg.

10   Current Challenges and Future Directions

Fertility is one of the most important fields of study in our changing world. As we face uncertainties with population decline of species in some regions and grapple with population control in other areas, an understanding of sexual reproduction and its underlying mechanisms is paramount. Despite a long history of biological investigations and mathematical modeling in male fertility, it has long been an area with limited clinical possibilities beyond observational diagnoses. With advances in both models and experimental capabilities, this is changing.

While this chapter has summarized a great deal of research dating back over 60 years, there are still many open questions and challenges. As mentioned earlier, computational approaches are necessary to meet these challenges and begin to answer these questions. Like any modeling context, there are significant tradeoffs in the level of detail one chooses to use to capture the dynamics of sperm motility. A detailed description of the sperm body itself would certainly lead to a more accurate simulation, but it is often associated with a large computational cost as well as many

parameters and model equations to describe the motion, which might not be fully known. With our ever increasing computational capabilities, models will be able to incorporate more and more detail and simulations will be larger in scale, both spatially and temporally. Beyond computation and the topics discussed in detail in this chapter, there are several areas that warrant future modeling consideration for sperm motility and its role in fertility.

Though basic interactions between sperm and rigid surfaces, or interactions between pairs of sperm in particular geometries have been studied fairly extensively, little has been done to understand sperm motility in more complicated scenarios that include flexible boundaries. This includes interactions within populations–where each sperm may act as a moving boundary for other nearby sperm–or interactions with flexible surfaces mimicking the oviductal epithelium. Flexible boundaries were explored in a 2D fluid channel [64], where results suggested that flexible surfaces might decrease speeds. It is thought that peristalsis caused by oviductal contractions may also aid in sperm progress towards the egg [164], though dynamic 3D models to investigate the oviductal role in sperm transport are lacking. Additionally, more biologically realistic models for the interaction between cilia lining the oviduct and sperm, beyond the work in [102, 174], could be of interest in understanding sperm transport.

Sperm are the most diverse cell type known [154] and sperm morphology, in particular, is extremely varied and has been shown to have significant effects on hydrodynamics [56]. While many models have focused on the sperm flagellum and ignored the sperm head and other structures like the midpiece (the more rigid piece of the flagellum near the head, depicted in Figure 2), there is a growing body of work exploring these features. In [56], the authors consider the effects of adding spherical heads on a flagellum model and varying parameters controlling sizes of the head and tail waveform to find strong effects on the hydrodynamics. More recently, work to move beyond spherical or ellipsoidal heads has been done (for instance, see [175], where the authors use a deformed sphere that captures the principle features of a human sperm head). The exact effects of varying head morphologies remains unclear and if one wants to consider sperm across a broad range of taxa, morphology–as well as species-specific reproductive strategies–will be important to consider.

Most modeling frameworks have relied upon planar waveforms, which is a simplification of the actual waveforms observed. Sperm may have primarily planar waveforms, but sometimes their beat patterns are more helical or have a so-called figure-eight deviation from the plane. And even if the waveform is primarily planar, the environments sperm live in are simply not fully captured by planar models. Thus, models that can react dynamically to the local environment and are robust to fully 3D interactions deserve increasing attention to develop more realistic models of sperm motility [81].

Biochemistry mediates much of the behavior we observe in sperm motility. It is known that calcium and pH levels can modulate motility, as well as more complex biochemical cascades such as the acrosome reaction, which must occur before fertilization. While some work has been done to model biochemical reaction

pathways and their impact upon motility (for instance, see [146, 172]), incorporating more biochemistry and biologically realistic models for reactions happening within the sperm and between sperm and their environment is vital. This includes studying biochemical changes as sperm progress through the oviduct and ultimately modeling interactions with the egg and the cumulus–oophorus complex surrounding the egg, which are generally viewed as gate-keeping mechanisms for successful fertilization.

All models for cellular motility have been developed to explore biological questions which the laboratory setting may not be able to answer. That being said, many recent advances–in microscopy, microfluidic devices, and other techniques–now make it possible to not only observe cellular motility and dynamics in more detail, but also test hypotheses arising from model results and vice versa. Sperm motility is not just an ideal model system for studying cellular motility, but truly a system that can elucidate some of the most complex dynamics we face in the study of cellular locomotion, due to the direct evolutionary outcomes of successful fertilization and the implications for species survival.

References

1. J. Adler. Chemotaxis in bacteria. *Science*, 153(3737):708–716, 1966.
2. J. Ainley, S. Durkin, R. Embid, P. Boindala, and R. Cortez. The method of images for regularized Stokeslets. *J. Comp. Phys.*, 227:4600–4616, 2008.
3. W. Alasmari, S. Costello, J. Correia, S.K. Oxenham, J. Morris, L. Fernandes, J. Ramalho-Santos, J. Kirkman-Brown, F. Michelangeli, S. Publicover, and C.L. Barratt. Ca^{2+} signals generated by catsper and Ca^{2+} stores regulate different behaviors in human sperm. *J. Biol. Chem.*, 288(9):6248–6258, 2013.
4. G.P. Alexander and J.M. Yeomans. Dumb-bell swimmers. *Eur. Phys. Letters*, 83:34006, 2008.
5. R. Ananthakrishnan and A. Ehrlicher. The forces behind cell movement. *Int. J. Biol. Sci.*, 3:303–317, 2007.
6. V. Aranda, R. Cortez, and L. Fauci. A model of Stokesian peristalsis and vesicle transport in a three-dimensional closed cavity. *J. Biomech.*, 48:1631–1638, 2015.
7. J. L. Auriault. On the domain of validity of Brinkman's equation. *Transp. Porous Media*, 79:215–223, 2009.
8. A. Bahat, S.R. Caplan, and M. Eisenbach. Thermotaxis of human sperm cells in extraordinarily shallow temperature gradients over a wide range. *PLOS ONE*, 7:e41915, 2012.
9. A. Bahat and M. Eisenbach. Sperm thermotaxis. *Mol. Cell Endocrinol.*, 252:115–119, 2006.
10. A. Bahat and M. Eisenbach. Human sperm thermotaxis is mediated by phospholipase c and inositol trisphosphate receptor Ca^{2+} channel. *Biol. Reprod.*, 82:606–616, 2010.
11. G.F. Bahr and E. Zeitler. Study of bull spermatozoa: quantitative electron microscopy. *J. Cell Biol.*, 21:175–189, 2006.
12. G.K. Batchelor. Slender-body theory for particles of arbitrary cross-section in stokes flow. *J. Fluid Mech.*, 44(3):419–440, 1970.
13. H.C. Berg. Dynamic properties of bacterial flagellar motors. *Nature*, 249(5452):77–79, 1974.
14. H.C. Berg and R.A. Anderson. Bacteria swim by rotating their flagellar filaments. *Nature*, 245(5425):380–382, 1973.

15. T.R. Birkhead, D.J. Hosken, and S.S. Pitnick. *Sperm biology: an evolutionary perspective*. Academic press, 2008.

16. T.R. Birkhead and A.P. Møller. Sexual selection and the temporal separation of reproductive events: sperm storage data from reptiles, birds and mammals. *Biol. J. Linn. Soc.*, 50(4):295–311, 1993.

17. J.R. Blake. A note on the image system for a Stokeslet in a no-slip boundary. *Proc. Camb. Philos. Soc.*, 70:303–310, 1971.

18. J.R. Blake and A.T. Chwang. Fundamental singularities of viscous flow. *J. Eng. Math.*, 8:23–29, 1974.

19. L. Blanchoin, R. Boujemaa-Paterski, C. Sykes, and J. Plastino. Actin dynamics, architecture, and mechanics in cell motility. *Physiol. Rev.*, 94:235–263, 2014.

20. D.C. Bottino and L.J. Fauci. A computational model of ameboid deformation and locomotion. *Eur. Biophys. J.*, 27:532–539, 1998.

21. E.L. Bouzarth and M.L. Minion. Modeling slender bodies with the method of regularized Stokeslets. *J. Comput. Phys.*, 230(10):3929–3947, May 2011.

22. C. Brenker, N. Goodwin, I. Weyand, N.D. Kashikar, M. Naruse, M. Krahling, A. Muller, U.B. Kaupp, and T. Strunker. The CatSper channel: a polymodal chemosensor in human sperm. *EMBO J.*, 31:1654–1665, 2012.

23. C. Brennen and H. Winet. Fluid mechanics of propulsion by cilia and flagella. *Ann. Rev. Fluid Mech.*, 9:339–398, 1977.

24. H. C. Brinkman. A calculation of the viscous force exerted by a flowing fluid on a dense swarm of particles. *Appl. Sci. Res.*, pages 27–34, 1947.

25. C.J. Brokaw. Bend propagation by a sliding filament model for flagella. *J. Exp. Biol.*, 55:289–304, 1971.

26. C.J. Brokaw. Computer simulation of flagellar movement: I. Demonstration of stable bend propagation and bend initiation by the sliding filament model. *Biophys. J.*, 12:564–568, 1972.

27. C.J. Brokaw. Flagellar movement: a sliding filament model. *Science*, 178(4060):455–462, 1972.

28. C.J. Brokaw. Computer simulation of flagellar movement. VI. Simple curvature-controlled models are incompletely specified. *Biophys. J.*, 48:633–642, 1985.

29. A. Bukatin, I. Kukhtevich, N. Stoop, J. Dunkel, and V. Kantsler. Bimodal rheotactic behavior reflects flagellar beat asymmetry in human sperm cells. *Proc. Natl. Acad. Sci. U.S.A.*, 112:15904–15909, 2015.

30. M. Burkitt, D. Walker, D.M. Romano, and A. Fazeli. Constructing complex 3d biological environments from medical imaging using high performance computing. *IEEE Transac. Computat. Bio. Bioinf.*, 9:643–654, 2012.

31. M. Burkitt, D. Walker, D.M. Romano, and A. Fazeli. Using computational modeling to investigate sperm navigation and behavior in the female reproductive tract. *Theriogenology*, 77:703–716, 2012.

32. S. Camalet and F. Julicher. Generic aspects of axonemal beating. *New J. Phys.*, 2:24.1–23, 2000.

33. L. Carichino and S. D. Olson. Emergent trajectories of 3d sperm motility: comparing asymmetries and force coupling models. *ArXiv e-prints*, 2018. http://adsabs.harvard.edu/abs/2018arXiv180404712C.

34. J.P. Celli, B.S. Turner, N.H. Afdhal, S. Keates, C.P. Ghiran, I .and Kelly, R.H. Ewoldt, G.H. McKinley, P. So, S. Erramilli, and R. Bansil. Helicobacter pylori moves through mucus by reducing mucin viscoelasticity. *Proc. Natl. Acad. Sci. U.S.A.*, 106:1431–14326, 2009.

35. H. Chang, Kim B.J., Y.S. Kim, S.S. Suarez, and M. Wu. Different migration patterns of sea urchin and mouse sperm revealed by a microfluidic chemotaxis device. *PLOS ONE*, 8:e60587, 2013.

36. H. Chang and S.S. Suarez. Rethinking the relationship between hyperactivation and chemotaxis in mammalian sperm. *Biol. Reprod.*, 85:296–305, 2011.

37. H. Chang and S.S. Suarez. Unexpected flagellar movement patterns and epithelial binding behavior of mouse sperm in the oviduct. *Biol. Reprod.*, 86(5), 2012.

38. Y. Chen, M.J. Cann, T.N. Litvin, V. Lourgenko, M.L. Sinclair, L.R. Levin, and J. Buck. Soluble Adenylyl Cyclase as an evolutionarily conserved bicarbonate sensor. *Science*, 289:625–628, 2000.

39. C.J. Coakley and M.E.J. Holwill. Propulsion of micro-organisms by three-dimensional flagellar waves. *J. Theor. Biol.*, 35:525–542, 1972.

40. R. Cortez. The method of regularized stokeslets. *SIAM J. Sci. Comput.*, 23(4):1204–1225, 2001.

41. R. Cortez, B. Cummins, K. Leiderman, and D. Varela. Computation of three-dimensional Brinkman flows using regularized methods. *J. Comput. Phys.*, 229:7609–7624, 2010.

42. R. Cortez, L. Fauci, and A. Medovikov. The method of regularized stokeslets in three dimensions: analysis, validation, and application to helical swimming. *Phys. Fluids*, 17(3):031504, 2005.

43. R. Cortez and F. Hoffmann. A fast numerical method for computing doubly-periodic regularized Stokes flow in 3D. *J. Comp. Phys.*, 258:1–14, 2014.

44. R. Cortez and M. Nicholas. Slender body theory for stokes flows with regularized forces. *Comm. App. Math. Com. Sc.*, 7(1):33–62, 2012.

45. R.G. Cox. The motion of long slender bodies in a viscous fluid part 1. General theory. *J. Fluid Mech.*, 44(4):791–810, 1970.

46. P. Cripe, O. Richfield, and J. Simons. Sperm pairing and measures of efficiency in planar swimming models. *Spora: J. Biomath.*, 2(1):5, 2016.

47. J.M. Cummins and P.F. Woodall. On mammalian sperm dimensions. *J. Reprod. Fertility*, 75(1):153–175, 1985.

48. M.P. Curtis, J.C. Kirkman-Brown, T.J. Connolly, and E.A. Gaffney. Modelling a tethered mammalian sperm cell undergoing hyperactivation. *J. Theor. Biol.*, 309:1–10, 2012.

49. M. Dasgupta, B. Liu, H.C. Fu, M. Berhanu, K.S. Breuer, T.R. Powers, and A. Kudrolli. Speed of a swimming sheet in Newtonian and viscoelastic fluids. *Phys. Rev. E*, 87:013015, 2013.

50. P. Denissenko, V. Kantsler, D.J. Smith, and J. Kirkman-Brown. Human spermatozoa migration in microchannels reveals boundary-following navigation. *Proc. Natl. Acad. Sci. U.S.A.*, 109:8007–8010, 2012.

51. R. Dillon and L. Fauci. An integrative model of internal axoneme mechanics and external fluid dynamics in ciliary beating. *J. Theor. Biol.*, 207:415–430, 2000.

52. R. Dillon, L. Fauci, and C. Omoto. Mathematical modeling of axoneme mechanics and fluid dynamics in ciliary and sperm motility. *Dyn. Contin. Discret. I*, 10:745, 2003.

53. R. H. Dillon, L. J. Fauci, and X. Yang. Sperm motility and multiciliary beating: an integrative mechanical model. *Comput. Math. Apps.*, 52:749–758, 2006.

54. R.H. Dillon, L.J. Fauci, C. Omoto, and X. Yang. Fluid dynamic models of flagellar and ciliary beating. *Ann. N.Y. Acad. Sci.*, 1101(1):494–505, 2007.

55. R.H. Dillon and J. Zhuo. Using the immersed boundary method to model complex fluids-structure interaction in sperm motility. *Discrete Continuous Dyn. Syst. Ser. B*, 15:343, 2011.

56. R.D. Dresdner and D.F. Katz. Relationships of mammalian sperm motility and morphology to hydrodynamic aspects of cell function. *Biol. Reprod.*, 25(5):920–930, 1981.

57. J. Du, J.P. Keener, R.D. Guy, and A.L. Fogelson. Low Reynolds number swimming in viscous two-phase fluids. *Phys. Rev. E*, 85:036304, 2012.

58. J.M. Eimers, E.R. te Velde, R. Gerritse, E.T. Vogelzang, C.W.N. Looman, and J.D.F. Habbema. The prediction of the chance to conceive in subfertile couples. *Fertil. Steril.*, 61(1):44–52, 1994.

59. M. Eisenbach. A hitchhikers guide through advances and conceptual changes in chemotaxis. *J. Cell Physiol.*, 213:574–580, 2007.

60. T. M. El-Sherry, M. Elsayed, H.K. Abdelhafez, and M. Abdelgawad. Characterization of rheotaxis of bull sperm using microfluidics. *Integr. Biol.*, 6:1111–1121, 2014.

61. J. Elgeti, U.B. Kaupp, and G. Gompper. Hydrodynamics of sperm cells near surfaces. *Biophys. J.*, 99(4):1018–1026, 2010.

62. O. Eytan, A. Jaffa, and D. Elad. Peristaltic flow in a tapered channel: application to embryo transport within the uterine cavity. *Med. Eng. Phys.*, 23:473–482, 2001.

63. L.J. Fauci and R. Dillon. Biofluidmechanics of reproduction. *Annu. Rev. Fluid Mech.*, 38:371–394, 2006.
64. L.J. Fauci and A. McDonald. Sperm motility in the presence of boundaries. *Bull. Math. Biol.*, 57(5):679–699, 1995.
65. L.J. Fauci and C.S. Peskin. A computational model of aquatic animal locomotion. *J.Comp. Phys.*, 77(1):85–108, 1988.
66. J. Feng and S.K. Cho. Mini and micro propulsion for medical swimmers (review). *Micromach.*, 5:97–113, 2014.
67. H.S. Fisher and H.E. Hoekstra. Competition drives cooperation among closely related sperm of deer mice. *Nature*, 463(7282):801–803, 2010.
68. H.C. Flemming and J. Wingender. The biofilm matrix. *Nature Rev. Microbiol.*, 8:623–633, 2010.
69. P. Friedl and D. Gilmour. Collective cell migration in morphogenesis, regeneration, and cancer. *Nature Rev. Molec. Cell Biol.*, 10:445–457, 2009.
70. B. M. Friedrich and F. Julicher. Chemotaxis of sperm cells. *Proc. Natl. Acad. Sci. U.S.A.*, 104:13256–61, 2007.
71. B.M. Friedrich, I.H. Riedel-Kruse, J. Howard, and F. Julicher. High-precision tracking of sperm swimming fine structure provides strong test for resistive force theory. *J. Exp. Biol.*, 213:1226–1234, 2010.
72. H. Fu, V. B. Shenoy, and T. R. Powers. Low Reynolds number swimming in gels. *Europhys. Lett.*, 91, 2010.
73. H. Fu, C. W. Wolgemuth, and T. R. Powers. Swimming speeds of filaments in nonlinearly viscoelastic fluids. *Phys. Fluids*, 21:033102, 2009.
74. H.C. Fu, T.R. Powers, and C.W. Wolgemuth. Theory of swimming filaments in viscoelastic media. *Phys. Rev. Lett.*, 99(25):258101, 2007.
75. H. Gadêlha, E.A. Gaffney, D.J. Smith, and J.C. Kirkman-Brown. Nonlinear instability in flagellar dynamics: a novel modulation mechanism in sperm migration? *J. Royal Soc. Int.*, page rsif20100136, 2010.
76. E. A. Gaffney, H. Gadêlha, D. J. Smith, J. R. Blake, and J. C. Kirkman-Brown. Mammalian sperm motility: observation and theory. *Annu. Rev. Fluid. Mech.*, 43:501–528, 2011.
77. E.A. Gillies, R.M. Cannon, R.B. Green, and A.A. Pacey. Hydrodynamic propulsion of human sperm. *J. Fluid Mech.*, 625:445–474, 2009.
78. D.H. Gist and J.M. Jones. Sperm storage within the oviduct of turtles. *J. Morphol.*, 199(3):379–384, 1989.
79. J. Gray. Undulatory propulsion. *J. Cell Sci.*, 94:551–578, 1953.
80. J. Gray and G. Hancock. The propulsion of sea-urchin spermatozoa. *J. Exp. Biol.*, 32:802–814, 1955.
81. A. Guerrero, J. Carneiro, A. Pimentel, C.D. Wood, G. Corkidi, and A. Darszon. Strategies for locating the female gamete: the importance of measuring sperm trajectories in three spatial dimensions. *Molec. Human Reprod.*, 17(8):511–523, 2011.
82. G.J. Hancock. The self-propulsion of microscopic organisms through liquids. *Proc. Royal Soc. London A*, 217:96–121, 1953.
83. F. Hayashi. Insemination through an externally attached spermatophore: bundled sperm and post-copulatory mate guarding by male fishflies (megaloptera: Corydalidae). *J. Insect Physiol.*, 42(9):859–866, 1996.
84. J.P. Hernandez-Ortiz, C.G. Stoltz, and M.D. Graham. Transport and collective dynamics in suspensions of confined swimming particles. *Phys. Rev. Lett.*, 95:204501, 2005.
85. J.J.L. Higdon. A hydrodynamic analysis of flagellar propulsion. *J. Fluid Mech.*, 90(4):685–711, 1979.
86. J.J.L. Higdon. The hydrodynamics analysis of flagellar propulsion: helical waves. *J. Fluid Mech.*, 94:331–351, 1979.
87. M. Hines and J. Blum. Bend propagation in flagella. I. Derivation of equations of motion and their simulation. *Biophys. J.*, 23:41–57, 1978.

88. K. Ho, C.A. Wolff, and S.S. Suarez. CatSper-null mutant spermatozoa are unable to ascend beyond the oviductal reservoir. *Reprod. Fertil. Develop.*, 21(2):345–350, 2009.
89. N. Ho, K. Leiderman, and S.D. Olson. A 3-dimensional model of flagellar swimming in a Brinkman fluid. *ArXiv e-prints*, 2018. http://adsabs.harvard.edu/abs/2018arXiv180406271H.
90. N. Ho, S. D. Olson, and K. Leiderman. Swimming speeds of filaments in viscous fluids with resistance. *Phys. Rev. E*, 93(4):043108, 2016.
91. M.E.J. Holwill and C.A. Miles. Hydrodynamic analysis of non-uniform and flagellar undulations. *J. Theor. Biol.*, 31:25–42, 1972.
92. G. Hou, J. Wang, and A. Layton. Numerical methods for fluid-structure interaction – A review. *Commun. Comput. Phys.*, 12(2):337–377, 2012.
93. I. D. Howells. Drag due to the motion of a Newtonian fluid through a sparse random array of small fixed rigid objects. *J. Fluid Mech.*, 64:449–475, 1974.
94. J. Huang, L. Carichino, and S.D. Olson. Hydrodynamic interactions of actuated elastic filaments near a planar wall with applications to sperm motility. *J. Coupled Syst. Multiscale Dyn.*, In Press.
95. S. Immler, H.D.M. Moore, W.G. Breed, and T.R. Birkhead. By hook or by crook? Morphometry, competition and cooperation in rodent sperm. *PLOS One*, 2(1):e170, 2007.
96. M. Ishikawa, H. Tsutsui, J. Cosson, Y. Oka, and M. Morisawa. Strategies for sperm chemotaxis in the siphonophores and ascidians: A numerical simulation study. *Biol. Bull.*, 206:95–102, 2004.
97. K. Ishimoto and E.A. Gaffney. An elastohydrodynamical simulation study of filament and spermatozoan swimming driven by internal couples. *IMA J. Appl. Math.*, 83:655–679, 2018.
98. K. Ishimoto, J. Cosson, and E.A. Gaffney. A simulation study of sperm motility hydrodynamics near fish eggs and spheres. *J. Theor. Biol.*, 389:187–197, 2016.
99. K. Ishimoto, H. Gadêlha, E.A. Gaffney, D.J. Smith, and J. Kirkman-Brown. Coarse-graining the fluid flow around a human sperm. *Phys. Rev. Lett.*, 118(12):124501, 2017.
100. K. Ishimoto and E.A. Gaffney. A study of spermatozoan swimming stability near a surface. *J. Theor. Biol.*, 360:187–199, 2014.
101. K. Ishimoto and E.A. Gaffney. Fluid flow and sperm guidance: a simulation study of hydrodynamic sperm rheotaxis. *J. Royal Soc. Int.*, 12:20150172, 2015.
102. K. Ishimoto and E.A. Gaffney. Mechanical tuning of mammalian sperm behaviour by hyperactivation, rheology and substrate adhesion: a numerical exploration. *J. Royal Soc. Int.*, 13(124):20160633, 2016.
103. R.P. Jansen. Fallopian tube isthmic mucus and ovum transport. *Science*, 201:349–351, 1978.
104. R.E. Johnson. An improved slender-body theory for stokes flow. *J. Fluid Mech.*, 99(2):411–431, 1980.
105. R.E. Johnson and C.J. Brokaw. Flagellar hydrodynamics. a comparison between resistive-force theory and slender-body theory. *Biophys. J.*, 25(1):113–127, 1979.
106. S.D. Johnston, B. Smith, M. Pyne, D. Stenzel, and W.V. Holt. One-sided ejaculation of echidna sperm bundles. *Am. Nat.*, 170(6):E162–E164, 2007.
107. S. Jung, K. Mareck, L. Fauci, and M.J. Shelley. Rotational dynamics of a superhelix towed in a Stokes fluid. *Phys. Fluids*, 19:103105–1–6, 2007.
108. V. Kantsler, J. Dunkel, M. Blayney, and R.E. Goldstein. Rheotaxis facilitates upstream navigation of mammalian sperm cells. *eLIFE Biophys.*, 3:e020403–1–12, 2014.
109. J.B. Keller and S.I. Rubinow. Slender-body theory for slow viscous flow. *J. Fluid Mech.*, 75(4):705–714, 1976.
110. J.C. Kirkman-Brown and D.J. Smith. Sperm motility: is viscosity fundamental to progress? *Molec. Hum Reprod.*, 17:539–544, 2011.
111. E. Lauga. Propulsion in a viscoelastic fluid. *Phys. Fluids*, 19(8):083104, 2007.
112. E. Lauga and T.R. Powers. The hydrodynamics of swimming microorganisms. *Rep. Prog. Phys.*, 72(9):096601, 2009.
113. K. Leiderman, E. L. Bouzarth, R. Cortez, and A. T. Layton. A regularization method for the numerical solution of periodic Stokes flow. *J. Comput. Phys.*, 236:187–202, 2013.

114. K. Leiderman, E.L. Bouzarth, and H.N. Nguyen. A regularization method for the numerical solution of doubly-periodic Stokes flow. In Layton. A. and S.D. Olson, editors, *Biological Fluid Dynamics: Modeling, Computation, and Applications*, volume 628, pages 73–90, Providence, RI, 2014. A.M.S. Contemp. Math. Series.

115. K. Leiderman and S.D. Olson. Swimming in a two-dimensional brinkman fluid: Computational modeling and regularized solutions. *Phys. Fluids*, 28(2):021902, 2016.

116. A. M. Leshansky. Enhanced low-Reynolds-number propulsion in heterogenous viscous environments. *Phys. Rev. E*, 80, 2009.

117. J. Lighthill. *Mathematical biofluiddynamics*, volume 17. SIAM, 1975.

118. J. Lighthill. Flagellar hydrodynamics. *SIAM Rev.*, 18(2):161–230, 1976.

119. S. Lim, A. Ferent, S. X. Wang, and C. S. Peskin. Dynamics of a closed rod with twist and bend in fluid. *SIAM J. Sci. Comput.*, 31:273–302, 2008.

120. C. B. Lindemann and K. A. Lesich. Flagellar and ciliary beating: the proven and the possible. *J. Cell Sci.*, 123(4):519–528, 2010.

121. C.B. Lindemann. A geometric clutch hypothesis to explain oscillations of the axoneme of cilia and flagella. *J. Theor. Biol.*, 168(2):175–190, 1994.

122. C.B. Lindemann. A model of flagellar and ciliary functioning which uses the forces transverse to the axoneme as the regulator of dynein activation. *Cell Motil. Cytoskel.*, 29:141–154, 1994.

123. C.B. Lindemann. The geometric clutch as a working hypothesis for future research on cilia and flagella. *Ann. N.Y. Acad. Sci.*, 1101(1):477–493, 2007.

124. P.V. Lishko, Y. Kirichok, D. Ren, B. Navarro, J.J. Chung, and D.E. Clapham. The control of male fertility by spermatozoan ion channels. *Annu. Rev. Physiol.*, 74:453–75, 2012.

125. I. Llopis, I. Pagonabarraga, M.C. Lagomarsino, and C.P. Lowe. Cooperative motion of intrinsic and actuated semiflexible swimmers. *Phys. Rev. E*, 87(3):032720, 2013.

126. D.J Lubkin, E.A. Gaffney, and J.R. Blake. A viscoelastic traction layer model of muco-ciliary transport. *Bull. Math. Biol*, 69(1):289–327, 2007.

127. E. Lushi, H. Willard, and R.E. Goldstein. Fluid flows created by swimming bacteria drive self-organization in confined suspensions. *Proc. Natl. Acad. Sci. U.S.A.*, 111:9733–9738, 2014.

128. L. Martinez-Fresneda, J. Costelloe, A. O'Hara, A. Lynch, S. Monsonis-Centelles, D. Newport, and S. Fair. Characterization of the rheotaxis response of bull sperm using a microfluidic device. *Anim. Reprod. Sci.*, 169:109–110, 2016.

129. R. Mayor and S. Etienne-Manneville. The front and rear of collective cell migration. *Nature Revi. Molec. Cell Biol.*, 17:97–109, 2016.

130. C. Mettot and E. Lauga. Energetics of synchronized states in three-dimensional beating flagella. *Phys. Rev. E*, 84(6):061905, 2011.

131. K. Miki and D.E. Clapham. Rheotaxis guides mammalian sperm. *Curr. Biol.*, 23:443–452, 2013.

132. T.D. Montenegro-Johnson. Fake μs: A cautionary tail of shear-thinning locomotion. *Phys. Rev. Fluids*, 2:081101, 2017.

133. T.D. Montenegro-Johnson, D.J. Smith, and D. Loghin. Physics of theologically-enhanced propulsion: different strokes in generalized Stokes. *Phys. Fluids*, 25:081903, 2013.

134. H. Moore, K. Dvorakova, N. Jenkins, and W. Breed. Exceptional sperm cooperation in the wood mouse. *Nature*, 418(6894):174–177, 2002.

135. H.D. Moore and D.A. Taggart. Sperm pairing in the opossum increases the efficiency of sperm movement in a viscous environment. *Biol. Reprod.*, 52(4):947–953, 1995.

136. R.D. Moreno, A.A. Laserre, and C. Barros. Protease activity involvement in the passage of mammalian sperm through the zona pellucida. *Biol. Res.*, 44(2):145–150, 2011.

137. M. Murase. *Dynamics of Cellular Motility*. John Wiley Publishing, 1992.

138. S.D. Nigam and V. Srinivasan. No-slip images in a sphere. *J. Math. Phys. Sci.*, 9:389–398, 1975.

139. J. Oldroyd. On the formulation of rheological equations of state. *Proc. Royal Soc. London A*, 200:523–541, 1950.

140. S.D. Olson. Fluid dynamic model of invertebrate sperm chemotactic motility with varying calcium inputs. *J. Biomech.*, 46(2):329–337, 2013.

141. S.D. Olson. Motion of filaments with planar and helical bending waves in a viscous fluid. In Layton. A. and S.D. Olson, editors, *Biological Fluid Dynamics: Modeling, Computation, and Applications*, pages 109–128, Providence, RI, 2014. A.M.S. Contemp. Math. Series.

142. S.D. Olson and L.J. Fauci. Hydrodynamic interactions of sheets vs filaments: Synchronization, attraction, and alignment. *Phys. Fluids*, 27(12):121901, 2015.

143. S.D. Olson and K. Leiderman. Effect of fluid resistance on symmetric and asymmetric flagellar waveforms. *J. Aero Aqua Bio-mech.*, 4(1):12–17, 2015.

144. S.D. Olson, S. Lim, and R. Cortez. Modeling the dynamics of an elastic rod with intrinsic curvature and twist using a regularized Stokes formulation. *J. Comp. Phys.*, 238:169–187, 2013.

145. S.D. Olson, S.S. Suarez, and L. Fauci. A model of CatSper channel mediated calcium dynamics in mammalian spermatozoa. *Bull. Math. Biol.*, 72:1925–1946, 2010.

146. S.D. Olson, S.S. Suarez, and L.J. Fauci. Coupling biochemistry and hydrodynamics captures hyperactivated sperm motility in a simple flagellar model. *J. Theor. Biol.*, 283(1):203–216, 2011.

147. T Omori and T Ishikawa. Upward swimming of a sperm cell in shear flow. *Phys. Rev. E*, 93:032402, 2016.

148. A.A. Pacey, C.J. Hill, I.W. Scudamore, M.A. Warren, C.L.R. Barratt, and I.D. Cooke. The interaction in vitro of human spermatozoa with epithelial cells from the human uterine (fallopian) tube. *Hum. Reprod.*, 10(2):360–366, 1995.

149. C.D. Paul, P. Mistriotis, and K. Konstantopoulos. Cancer cell motility: lessons from migration in confined spaces. *Nat. Rev. Cancer*, 17:131–140, 2017.

150. M. Pearcy, N. Delescaille, P. Lybaert, and S. Aron. Team swimming in ant spermatozoa. *Biol. Lett.*, 10(6):20140308, 2014.

151. D. W. Pelle, C. J. Brokaw, K. A. Lesich, and C. B. Lindemann. Mechanical properties of the passive sea urchin sperm flagellum. *Cell Motil. Cytoskel.*, 66(9):721–735, 2009.

152. C.S. Peskin. Flow patterns around heart valves: a numerical method. *J. Comput. Phys.*, 10(2):252–271, 1972.

153. C.S. Peskin. The immersed boundary method. *Acta Numer.*, 11:459–517, 2002.

154. S. Pitnick, D.J. Hosken, and T.R. Birkhead. Sperm morphological diversity. In *Sperm Biology*, pages 69–149, Burlington, MA, 2009. Academic Press.

155. P. Primakoff and D.G. Myles. Penetration, adhesion, and fusion in mammalian sperm-egg interaction. *Science*, 296(5576):2183–2185, 2002.

156. E.M. Purcell. Life at low reynolds number. *Amer. J. Phys.*, 45(1):3–11, 1977.

157. H. Qi, M.M. Moran, B. Navarro, J.A. Chong, G. Krapivinsky, L. Krapivinsky, Y. Kirichok, I.S. Ramsey, T.A. Quill, and D.E. Clapham. All four CatSper ion channel proteins are required for male fertility and sperm cell hyperactivated motility. *Proc. Natl. Acad. Sci. U.S.A.*, 104:1219–1223, 2007.

158. T.A. Quill, S.A. Sugden, K.L. Rossi, L.K. Doolittle, R.E. Hammer, and D.L. Garbers. Hyperactivated sperm motility driven by CatSper2 is required for fertilization. *Proc. Natl. Acad. Sci. U.S.A.*, 100(25):14869–14874, 2003.

159. M. Relucenti, R. Heyn, S. Correr, and G. Familiari. Cumulus oophorus extracellular matrix in the human oocyte: a role for adhesive proteins. *Ital. J. Anat. Embryol.*, 110(2):219, 2005.

160. I.H. Riedel, K. Kruse, and J. Howard. A self-organized vortex array of hydrodynamically entrained sperm cells. *Science*, 309:300–303, 2005.

161. I.H. Riedel-Kruse, A. Hilfinger, J. Howard, and F. Julicher. How molecular motors shape the flagellar beat. *Hum. Front. Sci. Prog.*, 1:192–208, 2007.

162. J.A. Riffell and R.K. Zimmer. Sex and flow: the consequences of fluid shear for sperm-egg interactions. *J. Exp. Biol.*, 210:3644–3660, 2007.

163. B. Rodenborn, C.H. Chen, H.L. Swinney, B. Liu, and H.P. Zhang. Propulsion of microorganisms by a helical flagellum. *Proc. Natl. Acad. Sci. U.S.A.*, 110:338–347, 2013.

164. S. Rodriguez-Martinez, H .and Einarsson, B. Larsson, M. Akusu, and I. Settergren. Spontaneous motility of the pig oviduct in vitro. *Biol. Reprod.*, 26(1):98–104, 1982.

165. Rothschild. Non-random distribution of bull spermatozoa in a drop of sperm suspension. *Nature*, 198(488):1221, 1963.

166. J. Rutllant, M. Lopez-Bejar, and F. Lopez-Gatius. Ultrastructural and rheological properties of bovine vaginal fluid and its relation to sperm motility and fertilization: a review. *Reprod. Dom. Anim.*, 40:79–86, 2005.

167. D. Saintillan and M.J. Shelley. Instabilities, pattern formation, and mixing in active suspensions. *Phys. Fluids*, 20:123304, 2008.

168. D. Saintillan and M.J. Shelley. Emergence of coherent structures and large-scale flows in motile suspensions. *J. Roy. Soc. Interface*, 9:571, 2011.

169. M. Sauzade, G. W. Elfring, and E. Lauga. Taylor's swimming sheet: Analysis and improvement of the perturbation series. *Physica D*, 240:1567–1573, 2012.

170. K.A. Schmitz-Lesich and C.B. Lindemann. Direct measurement of the passive stiffness of rat sperm and implications to the mechanism of the calcium response. *Cell Motil. Cytoskel.*, 59:169–179, 2004.

171. K.K. Shukla, A.A. Mahdi, and S. Rajender. Ion channels in sperm physiology and male fertility and infertility. *J. Androl.*, 133:777–788, 2012.

172. J. Simons and L.J. Fauci. A model for the acrosome reaction in mammalian sperm. Bull. Math. Biol., 80:2481–2501, 2018.

173. J. Simons, L. Fauci, and R. Cortez. A fully three-dimensional model of the interaction of driven elastic filaments in a stokes flow with applications to sperm motility. *J. Biomech.*, 48(9):1639–1651, 2015.

174. J. Simons, S.D. Olson, R. Cortez, and L. Fauci. The dynamics of sperm detachment from epithelium in a coupled fluid-biochemical model of hyperactivated motility. *J. Theor. Biol.*, 354:81–94, 2014.

175. D.J. Smith, E.A. Gaffney, J.R. Blake, and J.C. Kirkman-Brown. Human sperm accumulation near surfaces: a simulation study. *J. Fluid Mech.*, 621:289–320, 2009.

176. D.J. Smith, E.A. Gaffney, H. Gadêlha, N. Kapur, and J.C. Kirkman-Brown. Bend propagation in the flagella of migrating human sperm, and its modulation by viscosity. *Cell Motil. Cytoskel.*, 66(4):220–236, 2009.

177. T. Smith and R. Yanagimachi. The viability of hamster spermatozoa stored in the isthmus of the oviduct: the importance of sperm-epithelium contact for sperm survival. *Biol. Reprod.*, 42(3):450–457, 1990.

178. Y. Sowa and R.M. Berry. Bacterial flagellar motor. *Quaterly Rev. Biophys.*, 4:103–132, 2008.

179. O.S. Soyer. The promise of evolutionary systems biology: Lessons from bacterial chemotaxis. *Sci. Signal.*, 3:pe23:1–3, 2010.

180. M. Spehr, G. Gisselmann, A. Poplawski, J.A. Riffell, C.H. Wetzel, R.K. Zimmer, and H. Hatt. Identification of a testicular odorant receptor mediating human sperm chemotaxis. *Science*, 299:2054–2058, 2003.

181. L. Spielman and S. L. Goren. Model for predicting pressure drop and filtration efficiency in fibrous media. *Env. Science Tech.*, 1(4):279–287, 1968.

182. C.R. Stauss, T.J. Votta, and S.S. Suarez. Sperm motility hyperactivation facilitates penetration of the hamster zona pellucida. *Biol. Reprod.*, 53(6):1280–1285, 1995.

183. H. Stebbings. Cell motility. *eLS*, pages 1–6, 2001.

184. T.W. Su, I. Choi, J. Feng, K. Huang, E. McLeod, and A. Ozcan. Sperm trajectories form chiral ribbons. *Sci. Rep.*, 3, 2013.

185. T.W. Su, L. Xue, and A. Ozcan. High-throughput lensfree 3D tracking of human sperms reveals rare statistics of helical trajectories. *Proc. Natl. Acad. Sci. U.S.A.*, 109(40):16018–16022, 2012.

186. S.S. Suarez. Sperm transport and motility in the mouse oviduct: observations in situ. *Biol. Reprod.*, 36(1):203–210, 1987.

187. S.S. Suarez. Regulation of sperm storage and movement in the mammalian oviduct. *Int. J. Dev. Biol.*, 52(5–6):455–462, 2004.

188. S.S. Suarez. Control of hyperactivation in sperm. *Hum. Reprod. Update*, 14(6):647–657, 2008.

189. S.S. Suarez. Regulation of sperm storage and movement in the mammalian oviduct. *Int. J. Dev. Biol.*, 52:455–462, 2008.

190. S.S. Suarez. How do sperm get to the egg? Bioengineering expertise needed! *Exp. Mech.*, 50:1267–1274, 2010.

191. S.S. Suarez and X. Dai. Hyperactivation enhances mouse sperm capacity for penetrating viscoelastic media. *Biol. Reprod.*, 46(4):686–691, 1992.

192. S.S. Suarez, D.F. Katz, D.H. Owen, J.B. Andrew, and R.L. Powell. Evidence for the function of hyperactivated motility in sperm. *Biol. Reprod.*, 44(2):375–381, 1991.

193. S.S. Suarez and A.A. Pacey. Sperm transport in the female reproductive tract. *Hum. Reprod. Update*, 12(1):23–37, 2006.

194. G.I. Taylor. Analysis of the swimming of microscopic organisms. *Proc. Roy. Soc. Lond. Ser. A*, 209:447–461, 1951.

195. G.I. Taylor. Analysis of the swimming of long and narrow animals. *Proc. Roy. Soc. Lond. Ser. A*, 214:158–183, 1952.

196. J. Teran, L. Fauci, and M. Shelley. Viscoelastic fluid response can increase the speed of a free swimmer. *Phys. Rev. Lett.*, 104:038101–4, 2010.

197. B. Thomases and R.D. Guy. Mechanisms of elastic enhancement and hindrance for finite-length undulatory swimmers in viscoelastic fluids. *Phys. Rev. Lett.*, 113:098102, 2014.

198. A.K. Tornberg and M.J. Shelley. Simulating the dynamics and interactions of flexible fibers in stokes flows. *J. Comp. Phys.*, 196:8–40, 2004.

199. C.K. Tung, F. Ardon, A.G. Fiore, S.S. Suarez, and M. Wu. Cooperative roles of biological flow and surface topography in guiding sperm migration revealed by a microfluidic model. *Lab Chip*, 14:1348–1356, 2014.

200. C.K. Tung, C. Lin, B. Harvey, A.G. Fiore, F. Ardon, M. Wu, and S.S. Suarez. Fluid viscoelasticity promotes collective swimming of sperm. *Sci. Rep.*, 7, 2017.

201. A. Van Soom, S. Tanghe, I. De Pauw, D. Maes, and A. De Kruif. Function of the cumulus oophorus before and during mammalian fertilization. *Reprod. Domestic Anim.*, 37(3):144–151, 2002.

202. S.R.K. Vedula, A. Ravasio, C.T. Lim, and B. Ladoux. Collective cell migration: a mechanistic perspective. *Physiol.*, 28:370–379, 2013.

203. G. Vernon and D. Woolley. Basal sliding and the mechanics of oscillation in a mammalian sperm flagellum. *Biophys. J.*, 85(6):3934–3944, 2004.

204. P.E. Visconti, G.D. Moore, J.L. Bailey, D. Pan, P. Leclerc, S. Conors, P. Olds-Clarke, and G.S. Kopf. Capacitation in mouse spermatozoa. II: Capacitation and protein tyrosine phosporylation are regulated by a cAMP-dependent pathway. *Development*, 121:1139–1150, 1995.

205. M. Williams, C.J. Hill, I. Scudamore, B. Dunphy, I.D. Cooke, and C.L.R. Barratt. Physiology: Sperm numbers and distribution within the human fallopian tube around ovulation. *Human Reprod.*, 8(12):2019–2026, 1993.

206. D.M. Woolley. Motility of spermatozoa at surfaces. *Reproduction*, 126:259–270, 2003.

207. D.M. Woolley. Flagellar oscillation: a commentary on proposed mechanisms. *Biol. Rev.*, 85:453–470, 2010.

208. D.M. Woolley, R.F. Crockett, W.D.I. Groom, and S.G. Revell. A study of synchronisation between the flagella of bull spermatozoa, with related observations. *J. Exp. Biol.*, 212:2215–2223, 2009.

209. D.M. Woolley and G.G. Vernon. A study of helical and planar waves on sea urchin sperm flagella, with a theory of how they are generated. *J. Exp. Biol.*, 204(7):1333–1345, 2001.

210. J. Wróbel, R. Cortez, and L. Fauci. Modeling viscoelastic networks in Stokes flow. *Phys. Fluids*, 26:113102, 2014.

211. J.K. Wróbel, R. Cortez, D. Varela, and L. Fauci. Regularized image system for stokes flow outside a solid sphere. *J. Comput. Phys.*, 317:165–184, 2016.
212. J.K. Wróbel, S. Lynch, A. Barrett, L. Fauci, and R. Cortez. Enhanced flagellar swimming through a compliant viscoelastic network in stokes flow. *J. Fluid Mech.*, 792:775–797, 2016.
213. R. Yanagimachi. The movement of golden hamster spermatozoa before and after capacitation. *J. Reprod. Fertil.*, 23(1):193–196, 1970.
214. Y. Yang, J. Elgeti, and G. Gompper. Cooperation of sperm in two dimensions: synchronization, attraction, and aggregation through hydrodynamic interactions. *Phys. Rev. E*, 78:061903–1–9, 2008.
215. S. Yaniv, A. Jaffa, and D. Elad. Modeling embryo transfer in a closed uterine cavity. *J. Biomech. Eng.*, 134:111003–7, 2012.
216. Z. Zhang, J. Liu, J Meriano, C. Ru, S. Xie, J. Luo, and Y. Sun. Human sperm rheotaxis: a passive physical process. *Sci. Reports*, 6:23553, 2016.
217. R.K. Zimmer and J.A. Riffell. Sperm chemotaxis, fluid shear, and the evolution of sexual reproduction. *Proc. Natl. Acad. Sci. U.S.A.*, 108(32):13200–13205, 2011.

Lamellipodia in Stationary and Fluctuating States

Danielle Holz, Laura M. McMillen, Gillian L. Ryan, and Dimitrios Vavylonis

Abstract We review recent mathematical models describing the diffusive transport, reaction, and turnover of actin and regulators at the leading edge of motile cells. These models are motivated by experimental results using cells with flat, steady lamellipodia studied by Single Molecule Speckle microscopy. The same cells can also be made to exhibit protruding and retracting lamellipodia, which demonstrate how changes in actin polymerization lead to changes in the rate of protrusion. The second part of this chapter provides a description of these fluctuations as an excitable actin system pushing against the cell membrane by polymerization.

1 Introduction

Lamellipodia are thin and flat protrusions at the leading edge that allow cells to attach, and move across on flat surfaces. Lamellipodial protrusions have been studied extensively, both due to their importance in cell motility and as model systems of cytoskeletal dynamics [10, 20, 68, 81, 101]. Actin filaments in the lamellipodium form a dynamic network that polymerizes primarily close to the leading edge of the cell, with the filament barbed ends pointing toward the cell membrane. In the dendritic nucleation model, many of these filaments are created as branches off pre-existing filaments [80]. Pushing of the cell front forward is due to the addition of monomers to free barbed ends of the lamellipodial actin network near the cell membrane. The concentration of free barbed ends is regulated by capping proteins. The whole actin network undergoes retrograde flow towards the cell center due to polymerization at the leading edge combined with adhesion and

---

D. Holz · L. M. McMillen · D. Vavylonis (✉)
Department of Physics, Lehigh University, Bethlehem, PA, USA
e-mail: dah414@lehigh.edu; lms211@lehigh.edu; vavylonis@lehigh.edu

G. L. Ryan
Department of Physics, Kettering University, Flint, MI, USA
e-mail: gryan@kettering.edu

myosin contraction at the rear of the lamellipodium [77, 81, 85, 101]. The difference between the rates of polymerization and retrograde flow results in net lamellipodial protrusion or retraction. The actin subunits in the filament that move towards the back of the network break off from the network due to cofilin-induced severing into oligomers. The disassembled pieces further depolymerize and are recycled close to the leading edge.

Many actin regulatory proteins have been characterized in vitro, but precisely how they control actin polymerization and depolymerization across the lamellipodium has not been completely resolved. The majority of actin polymerization in lamellipodia occurs near the leading edge. As the network moves toward the body of the cell by retrograde flow, F-actin is depolymerized and recycled to be used again.

1.1 *Lamellipodium in Homeostasis*

Since all lamellipodial components have to be recycled, the transport of disassembled proteins through the cytoplasm back towards the leading edge is an important component of the kinetics in lamellipodia. Some studies suggested that diffusion is fast enough to deliver actin subunits to the leading edge [49, 99] while others have proposed a role for active transport mechanisms such as myosin-based transport [26] or hydrodynamic flow [108]. Previous theoretical work has shown how diffusion may become limiting, depending on both the value of the diffusion coefficient in the cytoplasm and the spatial distribution of sources and sinks of actin subunits in the cytoplasm [72, 92]. One of the difficulties in directly measuring the existence of gradients of diffuse actin experimentally is that the diffuse population is a small fraction of the actin in filaments. Further, the dynamics in photoactivation or photobleaching experiments reflect a combination of reaction and diffusion that can be hard to disentangle [61, 92].

In the first part of this chapter we discuss recent studies that show how mathematical models based on data obtained by single molecule speckle (SiMS) microscopy can be combined with fluorescence recovery after photobleaching (FRAP) or photoactivation (PA) studies to model the dynamics of the diffuse actin pool [92, 92, 99], capping protein, and Arp2/3 complex. In SiMS, cells contain fluorescently labeled proteins at a concentration sufficiently low to resolve single molecules [102]. If a fluorescent protein is diffusing freely in the lamellipodium, it will appear as a diffuse background or localized cloud, depending on its diffusion coefficient and the exposure time of the camera. When the tagged protein binds to the actin network it appears as a speckle undergoing retrograde flow while it remains bound to the network. Speckle disappearance reflects dissociation of the tagged protein to the diffuse pool. By contrast, cells in FRAP or PA experiments typically contain a large fraction of labeled protein that leads to spatially extended intensity fields, the redistribution of which around an area of interest reflects the combined dynamics of reaction, retrograde flow, and diffusion [92].

1.2 Lamellipodia in Fluctuating States of Protrusion and Retraction

In many cells, usually soon after they spread on a surface and before the onset of directed cell motion, the protrusion of the lamellipodium is followed by retraction [88]. This leads to cycles of protrusion and retraction that are periodic and in some cells organize into traveling waves of protrusion along the cell front and sides [4, 8, 22, 29, 55, 58, 59, 84, 87, 88]. This regular behavior involving fluctuations around a steady state can be used to study how the dynamics of actin polymerization are converted into cell motion [88].

Patterns of protrusions and retractions have been observed in XTC cells from *Xenopus*, which usually adopt a circular shape after introduction to the poly-L-lysine substrate (Figure 4A,B) [88]. The flat lamellipodia within these cells are ideal for quantitative analysis, allowing accurate averaging and calculations of correlations among different components. The retrograde flow rate was approximately constant during protrusion and retraction, suggesting that the changing F-actin localization in these cells stems from variations in the assembly and disassembly of the actin network near the leading edge, as opposed to stemming from changing retrograde flow rates [87].

The observed dynamics are suggestive of excitations driven by noise (i.e., stochastic concentration fluctuations): experimental results of XTC cells from Ryan et al. [87] show cycles of bursts of actin polymerization in a random pattern around the cell, lateral propagation, followed by disassembly. In the second part of this chapter we describe recent models that successfully described these experimental observations.

2 Model of Actin Turnover and FRAP Kinetics in XTC Cells

Numerous experiments provide evidence that actin polymerization and depolymerization occur not just at the leading edge but also throughout the lamellipodium [7, 15, 56, 66, 82, 96, 98, 101]. Most directly, Single Molecule Speckle (SiMS) Microscopy on XTC cells demonstrates single molecules of actin polymerizing throughout the lamellipodium [102] (Figure 1A & D).

In apparent contradiction to the studies above, which indicate an extended distribution of barbed ends across the lamellipodia, fluorescent recovery after photobleaching (FRAP) experiments show that significant fluorescence recovery occurs fast near or at the leading edge, while recovery away from the leading edge occurs with a delay followed by a more rapid increase [38, 52, 73]. This suggests that actin polymerization occurs only very close to the leading edge and that recovery at the back relies on retrograde flow of unbleached monomers from the very front of the leading edge [52, 53]. However, reassociation of the bleached actin within

the bleached area in FRAP experiments may slow down recovery [101] as shown for reaction diffusion models of actin turnover in a spatially homogeneous system without retrograde flow [14, 61, 95].

To address this apparent discrepancy between SiMS and FRAP data, Smith et al. [92] compared models with actin turnover distributed throughout the lamellipodium to FRAP experiments of XTC cells, the same cell type for which SiMS experiments had already been performed. They studied XTC cells that have negligible leading edge protrusion or retraction. While the FRAP recovery in XTC lamellipodia is qualitatively similar to that in other cells [38, 52, 73], these models demonstrated that SiMS and FRAP data do not contradict one another.

Smith et al. developed two models to show that turnover can occur without causing rapid FRAP recovery away from the leading edge. The first model uses diffuse actin that polymerizes and depolymerizes as monomers. FRAP curves simulated with this model are good fits to experiments, but have some different qualitative features. The second model considers two species of diffuse actin that can polymerize and depolymerize throughout the lamellipodium, monomers (G-actin), and oligomers (O-actin). Oligomers are slowly diffusing actin that can anneal to the F-actin network. The presence of a small amount of oligomers further reduces the amount of recovery away from the leading edge in simulated FRAP. The results of this model are in better agreement with both FRAP and SiMS microscopy.

2.1 Model of Actin Profile Based on SiMS Speckle Statistics

In the model by Smith et al. [92], SiMS microscopy data are used to compute the steady-state F-actin concentration profile. This profile is then used to calculate the steady-state G- and O-actin profiles and the corresponding polymerization rates as a function of distance from the leading edge. These reaction rates are then used in a numerical simulation of FRAP.

2.1.1 Calculation of F-Actin Profile

The statistics of single molecules of labeled actin obtained in previous studies of XTC cells (Figure 1A) [91, 102] are an input to the model. The location of speckle appearance events correspond to polymerization and yield an appearance rate, $a(x)$, as a function of distance from leading edge x (Figure 1D) [102]. The units of $a(x)$ in the model are μM/s. To obtain an analytical form for $a(x)$, the appearance curve is approximated with a double exponential:

$$a(x) = G_\infty K \left[A_1 e^{-x/\lambda_1} + A_2 e^{-x/\lambda_2} \right]. \tag{1}$$

The shorter length, λ_1, corresponds to polymerization at the leading edge while the longer length scale, λ_2, corresponds to basal polymerization that occurs throughout
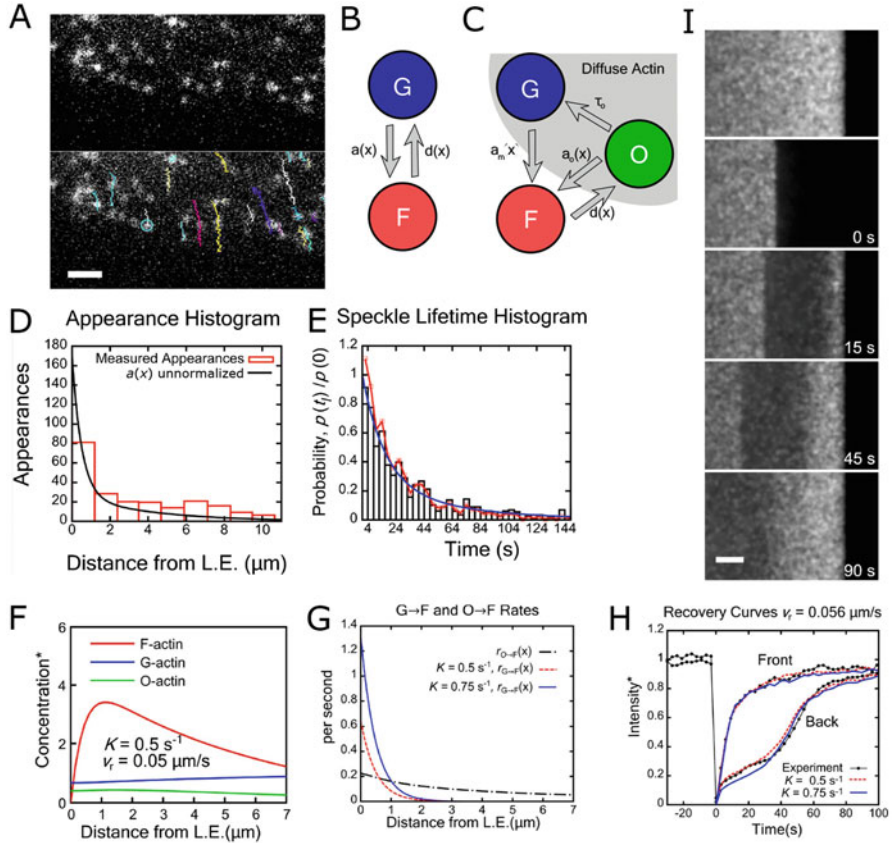
Fig. 1 SiMS experimental data and simulated FRAP. (A) Tracking EGFP-actin speckles in experimental SiMS in XTC cells (reproduced with permission from [91]). (B) Model with F-actin and one species of diffuse G-actin. (C) Model for two-species of diffuse actin (G, oligomeric) and F-actin. (D) Appearance profile for EGFP-actin speckles in XTC cells. (E) Lifetime distribution for EGFP-actin speckles in XTC cells. (F) Simulated concentration profiles for F, G, and O actin as a function of distance from the leading edge. (G) Simulated rates of binding for $G \rightarrow F$ and $O \rightarrow F$. (H) Simulated FRAP curves using a model that includes oligomers. (I) Simulated FRAP using a model that includes oligomers. Panels B-H reproduced with permission from [92].

the lamellipodium. This equation is a phenomenological fit chosen for two reasons: it captures the experimental data, and it yields analytical results in later calculations. The biophysical mechanism that gives rise to the appearance distribution $a(x)$ is not yet fully established. The total rate of appearance is scaled in proportion to the cytoplasmic concentration of labeled actin monomers far from the leading edge, G_∞. For convenience, $A_1 + A_2 = 1$ so K can be used as a parameter that adjusts the total rate of polymerization and the resulting F-actin/G-actin (F/G) ratio. The fit gives $A_1 = 0.84$, $A_2 = 0.16$, $\lambda_1 = 0.5\,\mu m$, $\lambda_2 = 4\,\mu m$ (Figure 1C). While the bin size for appearance data is comparable to λ_1, the distribution of appearance events

within the first 0.5 μm of the leading edge was not crucial for this study. What is
more important is the total number of speckles in the first bin.

Measurements of the speckle lifetime distribution in Figure 1E, $p(t_l)$, give the
probability distribution of the amount of time t_l that each actin subunit spends as
F-actin. The lifetime distribution is approximately constant within the first 3 μm
from the leading edge [91, 102]. The lifetime distribution is adequately described
by a double exponential:

$$p(t_l)/p(0) = C_1 e^{-t_l/\tau_1} + C_2 e^{-t_l/\tau_2}, \tag{2}$$

where $C_1 = 0.741$, $C_2 = 0.259$, $\tau_1 = 16$ s, $\tau_2 = 60$ s. Exponentials were chosen
because they capture the lifetime distribution well. They are also mathematically
convenient since they allow use of exponential statistics in simulations and enable
obtaining analytical results.

The velocity of retrograde flow v_r provides the remaining parameter necessary
to construct an F-actin profile represented by the speckle statistics. Using the
appearance rate $a(x)$ as a source of F-actin yields the steady-state concentration
profile $F(x)$:

$$F(x) = \int_0^\infty Y(x, x')a(x')dx'. \tag{3}$$

The profile $Y(x, x')$ generated by a point source at x' is obtained by considering the
amount of subunits that have a longer lifetime than the time it took to travel from x'
to x via retrograde flow:

$$Y(x, x') = \Theta(x - x')\frac{1}{v_r}\int_{\frac{x-x'}{v_r}}^\infty p(t_l)dt_l, \tag{4}$$

where the prefactor is found by balancing retrograde flow out of x' with amount
created by the point source and Θ is the step function. Retrograde flow rate can be
considered approximately constant within the first 4 μm from the leading edge of
XTC cells [87].

2.1.2 Model with Monomers as Only Diffuse Actin Species

The first model considers actin in two states: F-actin that undergoes retrograde flow,
and G-actin with diffusion coefficient $D = 4$ μm^2/s [25, 49, 61, 108]. G-actin
diffuses freely, polymerizing to become F-actin with rate $a(x)$. A diagram of this
model is shown in Figure 1B where F and G are the only two species in the model.

At steady state, both retrograde flux of F-actin and diffusive flux of G-actin balance the local exchange between F- and G-actin:

$$v_r \frac{\partial F(x)}{\partial x} = -D \frac{\partial^2 G(x)}{\partial x^2} = a(x) - d(x),$$ (5)

where $G(x)$ is the G-actin concentration and $d(x)$ the rate of speckle disappearance. Knowing $F(x)$ from Equation (3), we can solve Equation (5) for the G-actin profile:

$$G(x) = G_\infty - \frac{v_r}{D} \int\limits_x^\infty F(x')dx'.$$ (6)

The value of parameter K determines the F/G ratio since it changes the magnitude (but not the shape) of the F-actin profile. To obtain the steady-state F-actin profile based on SiMs data, we substituted Equations (1) and (2) into (3) and (4). The result of the total amount of F-actin:

$$\int\limits_0^\infty F(x)dx = G_\infty K \sum_{i=1}^2 \sum_{j=1}^2 A_i C_j \tau_j^2 \lambda_i,$$ (7)

demonstrating that the F-actin concentration is directly proportional to parameter K. By substituting Equation (7) into Equation (6) we can calculate the G-actin profile analytically. By increasing K, the G-actin depletion near the leading edge is increased. Increasing the value of the retrograde flow velocity causes a greater depletion of G-actin.

2.1.3 Model with Both Monomers and Oligomers

Actin oligomers could be present in the lamellipodium through cofilin-mediated severing of actin filaments [9, 16, 34, 50] or Arp2/3 complex debranching [12, 60]. The short lifetimes of capping protein speckles in lamellipodia indicate severing of capped filaments [66]. Reassociation of these oligomers to the actin network could be a mechanism for structural reorganization of actin filaments in the lamellipodium [66, 97]. Oligomers with diffusion coefficient $D_O \approx 0.5$ μm²/s and a fluorescent subunit would appear as background noise during exposure in SiMS experiments [91]. If they anneal to the network, they would contribute to speckle appearance events in SiMS experiments. When they dissociate from the network (via severing or debranching) they would contribute to speckle disappearances. Since the diffusion coefficient in the cytoplasm decreases with increasing molecular weight of protein complex [75], such D_O values may represent fragments of order ∼10 actin subunits.

In the model shown in Figure 1C, G-actin monomers can associate into F-actin and F-actin subunits depolymerize into O-actin. Subunits of O-actin can become F-actin or disassemble to G-actin with an average lifetime τ_O. The total appearance rate is separated into oligomers, $a_O(x)$, and monomers, $a_G(x)$, with $a(x) = a_O(x) + a_G(x)$. It is then assumed that O-actin accounts for a majority of appearance events away from the leading edge (corresponding to structural reorganization of actin filaments away from the leading edge through severing and reannealing) while G-actin polymerization contributes to most events close to the leading edge (see [92] for other possibilities). At steady state, similar to Equation (5)

$$v_r \frac{\partial F(x)}{\partial x} = a_O(x) + a_G(x) - d(x), \tag{8}$$

$$D_G \frac{\partial^2 G(x)}{\partial x^2} = a_G(x) - \frac{1}{\tau_O} O(x), \tag{9}$$

$$D_O \frac{\partial^2 O(x)}{\partial x^2} = a_O(x) - d(x) + \frac{1}{\tau_O} O(x), \tag{10}$$

where $D_G = 4 \ \mu m^2/s$ and D_O are the G- and O-actin diffusion coefficients. The F-actin profile is given by the same expression as in Equation (3), so we can substitute in Equation (8) to solve for $d(x)$, which leads to $O(x)$ through Equation (10) to:

$$O(x) = \tau_O \cosh\left(\frac{x}{\sqrt{D_O \tau_O}}\right) \int\limits_0^\infty f(x') \exp\left(\frac{-x'}{\sqrt{D_O \tau_O}}\right) dx'$$

$$-\tau_O \int\limits_0^x f(x') \sinh\left(\frac{x-x'}{\sqrt{D_O \tau_O}}\right) dx', \tag{11}$$

where $f(x) = a_G(x) - v_r \partial F/\partial x$. The G-actin profile can then be solved similar to the model with monomers only, using Equation (9):

$$G(x) = G_\infty - \frac{D_O}{D_G} O(x) - \frac{v_r}{D_G} \int\limits_x^\infty F(x') dx'. \tag{12}$$

An example of calculated profile is shown in Figure 1F, where $D_O = 0.5 \ \mu m^2/s$ and $\tau_O = 20$ s. The profile in Figure 1F is consistent with values of the F/G ratio in the range 2–10 [1, 19, 51, 101]. The total amount of O-actin can be quite low compared to the amount of F and G-actin, while still making a contribution to the total speckle appearance rate. O-actin is generated by F-actin disassembly so it peaks close to the leading edge where the F-actin concentration is larger.

2.2 Particle Simulations

To simulate FRAP recovery, Smith et al. [92] assumed the appearance rate is proportional to the local G-actin or O-actin concentration. In the model with just monomers, the rate at which monomers convert to F-actin is:

$$r_{G \to F}(x) = a(x)/G(x). \tag{13}$$

The O- and G-actin binding rates of the model with oligomers are correspondingly:

$$r_{G \to F}(x) = a_G(x)/G(x), \quad r_{O \to F}(x) = a_O(x)/O(x). \tag{14}$$

Figure 1G shows an example of calculated transition rates for the model with both monomers and oligomers. Estimated values for the concentration of barbed ends are $[B] \approx 1\,\mu M$ [101]. We expect the transition rate to be proportional to the local concentration of free barbed ends. Using $r_{G \to F} = k^+[B]$, the rate constant close to the leading edge is $k^+ \approx 0.6\,\mu M^{-1} s^{-1}$, consistent with previous estimates [101].

The transition rates in Equations (13) and (14) were used in [92] in an off-lattice 2D Monte Carlo simulation with reaction and diffusion of individual subunits. Each subunit was either diffusing (G-actin, O-actin) or undergoing retrograde flow (F-actin). Every time step, Δt (1 ms or smaller), diffuse particles were moved according to the 2D Gaussian diffusion propagator and checked for association to the F-actin. When a monomer transitions to F-actin, its lifetime is picked from the lifetime distribution $p(t_l)$. After an F-actin subunit is moved, its lifetime is compared to the time elapsed since polymerization to check if it should depolymerize and become G-actin. To simulate images, the particles are treated as diffraction-limited spots that diffuse during camera exposure [91]. Bleached particles are removed from the simulation and do not contribute to intensity.

2.3 FRAP Recovery: Comparison of Model Results to Experiments

A simulated FRAP image is shown in Figure 1I where a region of size 5x20 µm is bleached near the leading edge. Figure 1H shows the recovery of intensity at two strips between 0–0.5 µm and 2.5–3 µm ("Front" and "Back") from the leading edge using the model with both monomer and oligomers, plotted against experimental data. The simulated recovery curves are very similar to the experiments, with fast recovery at the front and slower recovery at the back. Good fits were obtained for $K = 0.4$–0.9 s^{-1}, $D_O < 1$ µm^2/s, and $\tau_O < 60$ s The model with oligomers captured two features of the experiment that the monomer-only model does not:

1. Recovery at the back (Figure 1I) is slower in the model with oligomers compared to the monomer-only model. In Figure 1I, the FRAP curve at the back does

not show significant recovery until retrograde flow carries monomers from the leading edge into the back region. For the chosen parameters, oligomers do not diffuse into the bleached region before retrograde flow transports monomers from the leading edge into the region. Two factors contribute: The time required to travel distance of order $3\ \mu$ by free oligomer diffusion is 10 s, but this is slowed down by rebinding of O-actin within the bleached region [95] since $\sqrt{4D_O/r_{O\to F}} = 3.2\ \mu$m; and generation of a new O-actin subunit, from unbleached monomers that polymerize at the leading edge, requires times of order the average speckle lifetime.

2. Unlike in the monomer-only model, the recovery at the front (Figure 1I) does not have a tail at long times. A tail in the front recovery curve occurs in the monomers-only model due to hindered diffusion through the lamellipodium [95]. In the model with oligomers, the region of G-actin polymerization is narrow, and this effect is reduced in magnitude.

The above results support models that include annealing and severing in the lamellipodium [42, 64]. For a more detailed study of the dependence of the FRAP curves on model parameters, we refer the reader to [92]. The above models did not explicitly account for the fact that G-actin monomers can carry different types of nucleotide (ADP or ATP), or that monomers can be bound to profilin, thymosin, or cofilin. It is assumed that the reactions among these different states occur fast enough to be considered quasi-static and also do not modify the diffusion coefficient of bound G-actin [72].

We note that a recent modeling study of lamellipodial actin turnover in keratocyte fragments by Aroush et al. [6] reached different conclusions compared to Smith et al. [92]. These authors concluded that while the actin network disassembles and reassembles throughout the lamellipodium, actin subunits typically diffuse across the entire lamellipodium before reassembling into the network. Aroush et al. also argue that about two-thirds of the lamellipodial actin diffuses in the cytoplasm with nearly uniform density, a much higher fraction of diffuse actin compared to Figure 1F. Future work should address the origin of these discrepancies. A model with the features stated by Aroush et al. (very high concentration of diffuse actin, no local reassembly) would not capture the slow FRAP recovery at the back of the lamellipodium of XTC cells (Figure 1H) or the increase of F-actin intensity starting from the leading edge after photoactivation of actin in the cell middle (Figure 2G below).

3 Model of Actin Turnover and Photoactivation Kinetics in Neuronal Cells

Photoactivation (PA) of fluorescently labeled actin is another way to study subcellular actin transport and reaction. In this section we review an extension of the model of [92] of Section 2, developed in [99], to model PA of neuronal CAD (Cath.a

differentiated) cells. For these cells, the study in [54] suggested an enhancement of G-actin at the leading edge. To account for this enhancement, which could arise from actin monomers bound to the plasma membrane through a profilin-Tβ4-actin complex [99], a membrane-bound G-actin component close to the leading was added to the model (otherwise the G-actin is depleted rather than enhanced near the leading edge, see Figure 1F). In addition to modeling PA kinetics, another aim of the study in [99] was to examine the effect of G-actin sequestering protein thymosin β4 (Tβ4) in facilitating diffusing actin transport (uninterrupted by polymerization) across the cell.

3.1 Model Description

This model includes 3 pools of diffuse protein instead of 2 (Figure 2A). The three pools are: R, which is a recycling component that represents all actin which has been recently depolymerized (which may include oligomers or actin bound to other protein complexes); G_C, which binds reversibly to Tβ4 in the cytoplasm; and G_M, which represents actin diffusing along the membrane, e.g., as membrane-bound profilin-Tβ4-actin. The G_C pool groups together free and Tβ4-bound actin, assuming they are in rapid equilibrium, given the estimated off rate of 2.5 s^{-1} for the Tβ4-actin complex [67]. G_C and G_M also group together actin monomers free or in complex with profilin and does not distinguish between ATP- and ADP-actin. All 3 diffuse pools are able to associate with F-actin; however, F-actin only depolymerizes to the recycled actin in this model.

The appearance rate in this model is split between the three actin pools,

$$a(x) = a_R(x) + a_C(x) + a_M(x). \tag{15}$$

Given the similarities between XTC and neuronal CAD cell lamellipodia, it was assumed that $a(x)$ is given by Equation (1) and the lifetime distribution by Equation (2). The appearances are defined as follows:

$$a_C(x) = K G_\infty A_C e^{-x/\lambda_1}, \ a_M(x) = K G_\infty A_M e^{-x/\lambda_1}, \ a_R(x) = K G_\infty A_R e^{-x/\lambda_2}. \tag{16}$$

Here G_∞ is the concentration of G_C far from the leading edge, K determines the fraction of F to G-actin, and $A_C + A_M + A_R = 1$.

The concentration of actin at steady state, $F(x)$, can be calculated as in Equation (3). The equations that describe the steady-state concentrations of the diffuse components are as follows:

$$D_R \frac{d^2 R(x)}{dx^2} = a_R(x) + \frac{1}{\tau_R} R(x) - d(x), \tag{17}$$

$$D_C \frac{d^2 G_C(x)}{dx^2} = a_C(x) + k(x)G_C(x) - \frac{1}{\tau_{GM}}G_M(x) - \frac{1}{\tau_R}R(x), \qquad (18)$$

$$D_M \frac{D^2 G_M(x)}{dx^2} = a_M(x) - k(x)G_C(x) + \frac{1}{\tau_{GM}}G_M(x). \qquad (19)$$

In these equations D_R, D_C, and D_M are the diffusion coefficients for recycled actin, cytoplasmic actin, and membrane bound actin, respectively. In all these equations, x is the distance from the leading edge. The lifetimes τ_{GM} and τ_R are the times that G_M and R remain in their respective states until they become G_C. The rate $k(x)$ is a spatially dependent rate that G_C becomes G_M.

The binding rate for the recycled actin, R, to become F-actin is $a_R(x)/R(x)$ and similarly for G_M and G_C. These rates were then used in a 2D Monte Carlo particle simulation as in Section 2.2. The system is initialized so that the concentrations matched those found after solving Equations (17)–(19). Simulated concentration profiles are shown in Figure 2B and the parameters used to find these profiles are listed in Table 1. To perform photoactivation on a region, all particles outside of that region are deleted and the remaining particles allowed to move and react.

Table 1 Parameter table for simulated photoactivation of PA-GFP actin.

Parameter	Value	Reference/Justification
D_R	0.5 μm^2/s	Smith et al. 2013 [92]
D_C	3.0 μm^2/s	Measured in [99]
D_M	0.001 μm^2/s	Small value to represent slow diffusion of membrane-bound component G_M
v_r	70 nm/s	Measured in [99]
K	0.25 s^{-1}	Estimated to give a ratio of F-actin to diffuse components as in Figure 2B.
τ_R	20 s	Smith et al. 2013 [92]
τ_M	0.5 s	Smaller than 1 s
A_R	0.16	Smith et al. 2013 [92]
A_C	0.21	Smith et al. 2013 [92], assuming 25 % of polymerization events from the non-recycling pools at the leading edge are due to G_C
A_M	0.63	Smith et al. 2013 [92], assuming 75% of polymerization events from the non-recycling pools at the leading edge are due to G_M
λ_1	0.5 μm	Smith et al. 2013 [92]
λ_2	4 μm	Smith et al. 2013 [92]
$k(x)$	20 s$^{-1}e^{-x/0.5\,\mu m}$	Selected to occur within a narrow region close to the leading edge and with amplitude giving G_M concentration higher than G_C

3.2   Comparison to Photoactivation Experiments

An example of experimental photoactivation of PA-GFP actin from [99] is shown in Figure 2C. This photoactivation is over a 5 by 10 μm region at the leading edge showing the retrograde flow of the actin network and the local recycling of the photoactivated actin in nearby regions (clearer in inverted grayscale image in Figure 2C, bottom panel). The decay of fluorescence in the photoactivated region as it moves inwards by retrograde flow is shown in Figure 2D. Simulations of actin photoactivation over the same size and position as that in the experiment capture the behavior seen in experiments (Figure 2E,F) with rebinding near the photoactivated region as well as similar decay in fluorescence.

Simulations were also used to model photoactivation experiments of actin in the cell center (Figure 2G), which demonstrate the transport dynamics of actin across the lamellipodium. Figure 2H shows the normalized fluorescence response within 1 μm of the leading edge as well as at the center. The fast recovery at the leading edge of the cell brings up the question of whether diffusion is sufficiently fast to transport actin from the cell center to the leading edge in this amount of time. Simulations mimicking cell center photoactivation reproduce the observed dynamics (Figure 2I,J), demonstrating that diffusion is likely sufficient for fast delivery of actin from the cell center to the leading edge.

Another photoactivation experiment involved activating PA-GFP actin in the whole lamellipodium [99]. The fluorescence at the leading edge decayed to about 50% of its original value after 120 s. The authors of [99] suggest that this points to a pool of actin that is recycled within the lamellipodium. Simulations of whole lamellipodium activation using the model of this section reproduce the experimental trace [99]; however, the plateau occurs at the level of total amount of actin photoactivated in the simulation box. Further modeling studies that account for the diffusion through the whole 3D cell volume are needed to better interpret these experimental results.

3.3   Simulations of Cells Without Actin Sequestration by Tβ4

Tβ4 binds to actin monomers, not allowing polymerization. Vitriol et al. [99] performed PA experiments after knocking down (KD) Tβ4, using shRNA. In experiments in which the cell center was photoactivated, a lag in recovery at the leading edge was observed compared to the control case. After varying all parameters in the model that would affect this recovery, the authors found that the model matches experiment after: (1) an increase in the binding rate of G_C at the back of the lamellipodium, and (2) reduction of the diffusion coefficient of G_C by 50%, compared to the control case. From this, the model predicted a less sharp sigmoidal recovery at the back of the lamellipodium (2–3 μm away from the leading edge), which agreed with experimental measurements [99].
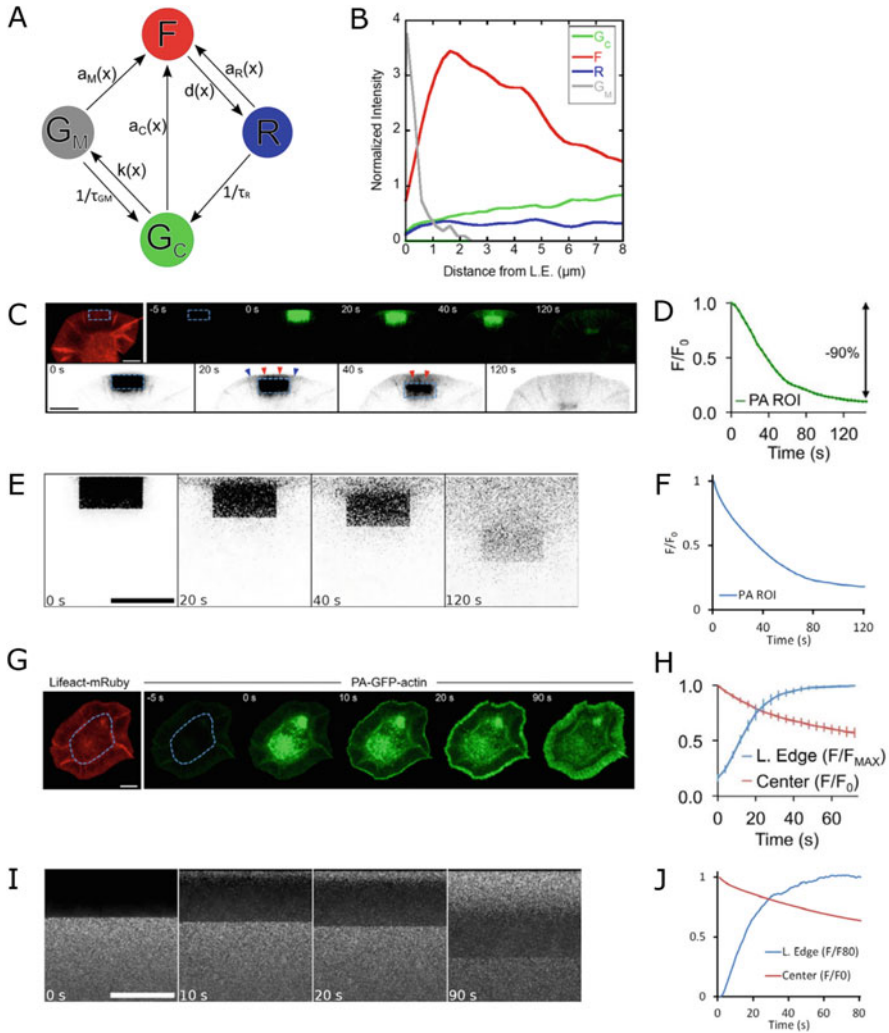
Fig. 2 Experiments and Simulations of Actin Photoactivation (reproduced from [99]). (A) Model with three diffuse species of actin: recycled, cytoplasmic, membrane bound as well as F-actin. The rates depend on distance from leading edge, with membrane binding, $k(x)$, occurring close to the leading edge. (B) Simulated steady-state concentration profile using the model in A. (C) Photoactivation in ROI at cell leading edge. (D) Fluorescence decay in ROI of panel C. (E) Simulated photoactivation of 5 by 10 μm box at the leading edge. (F) Simulated fluorescence decay in activation box of panel E. (G) Cell center actin photoactivation. (H) Fluorescence in cell center and close to leading edge after photoactivation of cell center. (I) Simulated photoactivation of cell center. (J) Simulated fluorescence in cell center and close to the leading edge after photoactivation of cell center. Image scale bars, panels C,E,G: 10 μm; panel I: 8 μm.

The results of the PA simulations and experiments suggested actin within the lamellipodium exists within two pools, one which is bound to Tβ4 and allows for fast diffusion through the lamellipodium and another pool which diffuses slowly and is not bound to Tβ4 [99]. Actin bound to Tβ4 is prevented from binding to actin at the back of the lamellipodium and can diffuse fast through the lamellipodium to the leading edge of the cell where it may associate in a complex with profilin and allow the actin to incorporate into the actin network, perhaps through the aid of formins. Tβ4 aids in this diffusion by sequestering the actin monomers and not allowing them to bind promiscuously to other actin binding proteins throughout the lamellipodial network [99]. The actin that is not bound to Tβ4 (recycling actin, likely actin oligomers) is incorporated into the actin network away from the leading edge. This study showed that a large portion of the actin in the lamellipodium is recycled actin and that it plays an important role in the kinetics of turnover of the network.

4 Model of Capping Protein and Arp2/3 Complex Turnover

Capping protein and the Arp2/3 complex are two of the most important regulators of actin dynamics in cells and in *in vitro* reconstitution experiments [47]. This section summarizes the work in [62] that extends the approach of Smith et al. to capping protein and Arp2/3 complex. For both of these proteins, SiMS and FRAP data have been performed in lamellipodia (albeit by different groups on different cell systems). Similar to the case of diffuse actin, it is possible that both exhibit significant concentration gradients in their diffuse pool. For example, slowly diffusing capping proteins have indeed been observed by SiMS [91], which may reflect capping protein bound to slowly diffusing actin oligomers or to the membrane. The Arp2/3 complex has also been observed to form a slowly diffusing complex with its activators prior to attachment to the actin network [65]. The study by McMillen and Vavylonis [62] addressed these issues.

4.1 Method to Calculate Concentration Profiles

Since proteins in the lamellipodium are frequently associating to larger complexes or binding to the membrane, the simplest model to account for this behavior with two distinct cytoplasmic populations was considered: a fast diffusing cytoplasmic population, C_{fast}, and a slow diffusing cytoplasmic population, C_{slow}. Bound protein (B), which is protein bound to filaments in the actin network, can depolymerize into either C_{fast} with probability s_1 or C_{slow} with probability s_2, where $s_2 = 1 - s_1$. The diffuse protein C_{fast} can become bound protein with spatially dependent rate $r_{C_{fast}}(x)$, and C_{slow} can become bound with spatially dependent rate $r_{C_{slow}}(x)$, where

x is the distance from the leading edge. The diffuse component C_{fast} can become C_{slow} with a lifetime of $\tau_{C\,fast}$, and the component C_{slow} can become C_{fast} with a lifetime of $\tau_{C_{slow}}$.

The appearance profile measured by SiMS was assumed to be the sum of two separate profiles, $a_{C_{fast}}(x)$ and $a_{C_{slow}}(x)$, due to the fast and slow cytoplasmic pools as follows:

$$a(x) = a_{C_{fast}}(x) + a_{C_{slow}}(x). \tag{20}$$

How the profile is split into two components is an assumption of the model. Generally, the speckle appearance profile can be fitted by a double exponential with two length-scales λ_{short} and λ_{long}. We define $C_{fast,\infty}$ and $C_{slow,\infty}$ to be the concentrations of C_{fast} and C_{slow} respectively at distances far from the leading edge of the cell. Using $C_\infty = C_{fast,\infty} + C_{slow,\infty}$ to normalize concentrations, the constant K defines the magnitude of the association reactions:

$$a_{C_{fast}}(x) = K C_\infty \left(A_1^{C_{fast}} e^{-x/\lambda_{short}} + A_2^{C_{fast}} e^{-x/\lambda_{long}} \right) \tag{21}$$

$$a_{C_{slow}}(x) = K C_\infty \left(A_1^{C_{slow}} e^{-x/\lambda_{short}} + A_2^{C_{slow}} e^{-x/\lambda_{long}} \right), \tag{22}$$

where the dimensionless coefficients in Equations (21) and (22) satisfy $A_1^{C_{fast}} + A_2^{C_{fast}} + A_1^{C_{slow}} + A_2^{C_{slow}} = 1$.

In the examples we consider in this section, the lifetime distribution for protein speckles $p(t)$ has weak dependence upon distance from the leading edge, within a range of a few μm [66, 91, 102]. It can be fitted with a single exponential as in Equation (2) where $C_2 = 0$.

The bound protein profile, $B(x)$, can be calculated analytically using the function $Y(x, x')$ of Equation (4) to find the profile of bound protein $B_1(x)$ and $B_2(x)$ due to each of the diffuse species, C_{fast} and C_{slow}, respectively, such that $B(x) = B_1(x) + B_2(x)$, where:

$$B_1(x) = \int_0^\infty Y(x, x') a_{C_{fast}}(x') dx', \quad B_2(x) = \int_0^\infty Y(x, x') a_{C_{slow}}(x') dx'. \tag{23}$$

The steady-state reaction diffusion equations that describe the system are as follows:

$$v_r \frac{\partial B(x)}{\partial x} = a(x) - d(x), \tag{24}$$

$$D_{C_{fast}} \frac{\partial^2 C_{fast}}{\partial x^2} = a_{C_{fast}}(x) - s_1 d(x) + \frac{1}{\tau_{C_{fast}}} C_{fast}(x) - \frac{1}{\tau_{C_{slow}}} C_{slow}(x), \tag{25}$$

$$D_{C_{slow}} \frac{\partial^2 C_{slow}}{\partial x^2} = a_{C_{slow}}(x) - (1-s_1)d(x) + \frac{1}{\tau_{C_{slow}}} C_{slow}(x) - \frac{1}{\tau_{C_{fast}}} C_{fast}(x). \quad (26)$$

Parameters $D_{C_{fast}}$ and $D_{C_{slow}}$ are the diffusion coefficients for C_{fast} and C_{slow} respectively and $d(x)$ is the detachment rate of bound proteins to the cytoplasm, which is found by solving Equation (24), given $a(x)$ and $B(x)$ from Equations (20) and (23). The parameter s_1 is the probability for the bound protein to dissociate into C_{fast}. The concentrations far from the leading edge obey: $C_{slow,\infty}/C_{fast,\infty} = \tau_{C_{slow}}/\tau_{C_{fast}}$. Equations (20)–(26) can be solved numerically to find $C_{fast}(x)/C_{fast,\infty}$ and $C_{slow}(x)/C_{slow,\infty}$ given v_r, $\tau_{C_{fast}}$, $\tau_{C_{slow}}$, $D_{C_{fast}}$, $D_{C_{slow}}$, s_1, and the parameters that define $a_{C_{fast}}(x)$, $a_{C_{slow}}(x)$, and $p(t)$. The method used involves adding time dependence to Equations (25) and (26) and allowing them to relax for a sufficiently long time:

$$\frac{\partial C_{fast}}{\partial t} = D_{C_{fast}} \frac{\partial^2 C_{fast}}{\partial x^2} - a_{C_{fast}}(x) + s_1 d(x) - \frac{1}{\tau_{C_{fast}}} C_{fast}(x) + \frac{1}{\tau_{C_{slow}}} C_{slow}(x),$$
$$(27)$$

$$\frac{\partial C_{fast}}{\partial t} = D_{C_{slow}} \frac{\partial^2 C_{slow}}{\partial x^2} - a_{C_{slow}}(x) + (1-s_1)d(x) - \frac{1}{\tau_{C_{slow}}} C_{slow}(x) + \frac{1}{\tau_{C_{fast}}} C_{fast}(x).$$
$$(28)$$

A no-flux boundary condition is imposed at the leading edge.

4.2 Calculation of Rate Constants and Simulation

The local rates with which the cytoplasmic protein binds to the network from the fast and slow diffusing states (to be used in Monte Carlo particle simulations) can be found using the appearance profiles and the cytoplasmic protein profiles:

$$r_{C_{fast}} = a_{C_{fast}}(x)/C_{fast}(x), \quad r_{C_{slow}} = a_{C_{slow}}(x)/C_{slow}(x). \quad (29)$$

These are the reaction rates for C_{fast} to convert into B_1 and for C_{slow} into B_2. 2D Monte Carlo simulations of independent particles were performed using the method of Smith et al. [92] described previously. The simulation was initialized using the steady-state concentrations evaluated by Equations (27) and (28).

4.3 Application to Capping Protein Dynamics

In [62], the model of Section 4.1 was applied to capping protein, the lamellipodial dynamics of which had been studied in prior studies with both FRAP and SiMS, though in different cell systems. Kapustina et al. [46] analyzed FRAP data of

fibroblast cells expressing EGFP-CapZ in a circular region of diameter 5 μm centered at 5 μm from the leading edge of the cell [100]. They fitted the recovery to a model that used Virtual Cell [70] with various components to find values for the diffusion coefficient of capping protein in the cytoplasm, D=5–10 μm^2/s, and for its lifetime when bound to the actin network, τ = 10 s. These values are different to those measured with SiMS microscopy of XTC cells [66, 91] where capping protein was found to associate over an extended area of the lamellipodium, to have a slowly diffusing cytoplasmic pool with $D \approx 0.5\,\mu$m^2/s and to have a shorter bound lifetime, $\tau \approx$ 2s [66, 91]. While both studies show a short lifetime of bound capping protein compared to the lifetime of polymerized actin (Figure 1E), they indicate quantitatively different transport modes in the lamellipodia. One goal in [62] was finding out if the measured SiMS microscopy parameters from Miyoshi et al. can be used to fit the FRAP data from Kapustina et al. and to study the implications for the concentration profile of capping protein across the lamellipodia.

Two previously proposed possibilities for the reasons behind slow capping protein diffusion were considered: one being that capping protein is bound to severed actin oligomers, the other being that capping protein binds to the membrane. Monte Carlo simulations with bleaching of a 5 μm by 5 μm square region centered 5 μm from the leading edge were compared to the data of Kapustina et al. using a circular bleach region (this difference in shape has only a small effect on the recovery curve). In the simulations for capping protein below, the value for retrograde flow used was v_r= 0.03 μm/s [105].

4.3.1   Model Including Oligomers

The model with oligomers shown in Figure 3A,B is a specific case of the general model of Section 4.1. The motivation for this model is the suggested existence of short actin oligomers in the lamellipodium. If severed actin filaments are capped by capping protein, this could explain why 50% of capping protein has been observed in a slowly diffusing state with diffusion coefficient $\approx 0.5\,\mu$m^2/s [91]. In this model C_fast represents capping protein heterodimers diffusing in the cytoplasm and C_slow represents capping protein heterodimers attached to the barbed end of an actin oligomer diffusing in the cytoplasm. The bound protein can only dissociate into capped oligomers, C_slow, that can either rebind to the network or become uncapped and convert to C_fast.

Both fast and slow diffusing species were assumed to be able to bind to the network, representing capping of free barbed ends and re-binding of oligomers to the lamellipodial network, respectively (Figure 3A,B,E,F). Since SiMS only measures the total appearance profile, an additional assumption in the model was how $a(x)$ is split into $a_{C_\text{fast}}(x)$ and $a_{C_\text{slow}}(x)$. Since the total appearance profile of capping protein can be fit to a double exponential [62], the appearance rates were broken up such that $a_{C_\text{fast}}(x)$ corresponds to the short length scale and $a_{C_\text{slow}}(x)$ to the long length scale:
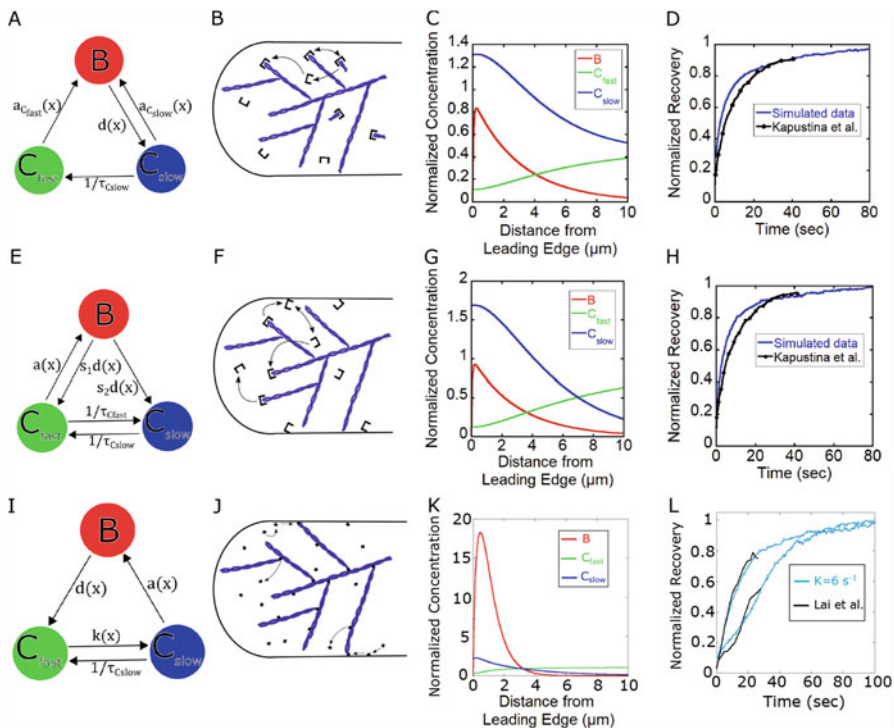
Fig. 3 Modeling FRAP for Capping Protein and Arp2/3 Complex in lamellipodium (reproduced with permission from [62]). (A) Diagram for model of capping protein including oligomers. (B) Cartoon for model of panel A. (C) Simulated steady-state concentration profiles for capping protein model for model in panel A. (D) Simulated FRAP curve of capping protein after bleaching a 5 μm$\times$5 μm box situated 2.5 μm from the leading edge for model of panel A, compared to experimental data in [46]. (E) Diagram for model of capping protein with membrane binding. (F) Cartoon for model of panel B. (G) Simulated steady-state concentration profiles for capping protein model of panel E. (H) Same as panel D but for model of panel E. (I) Diagram for model of Arp2/3 complex with membrane binding. (J) Cartoon for model of panel I. (K) Simulated steady-state concentration profiles for model of panel I. (L) Simulated FRAP curve of Arp2/3 complex after bleaching a 2 μm$\times$4 μm box at the leading edge and monitored 0–1 μm and 1–2 μm from the leading edge, compared to experimental data in [52].

$$a_{C_{\text{fast}}}(x) = K C_\infty A_1 e^{-x/\lambda_{\text{short}}}, \quad a_{C_{\text{slow}}}(x) = K C_\infty A_2 e^{-x/\lambda_{\text{long}}}, \qquad (30)$$

with $A_1 = 0.74$, $A_2 = 0.26$, $\lambda_{\text{short}} = 2.0$ μm, and $\lambda_{\text{long}} = 8.65$ μm. The function $a_{C_{\text{fast}}}(x)$ accounts for the appearances due to C_{fast} close to the leading edge, whereas $a_{C_{\text{slow}}}(x)$ accounts for the appearances due to C_{slow} that are distributed throughout the lamellipodium. Thus, the behavior of capping protein was assumed to follow the behavior of actin oligomer rebinding that contributes to a large fraction of actin speckle appearances at the back of the lamellipodium (Section 2.3).

Parameters in the model were calculated from prior experiments or their range estimated. The lifetime distribution of capping protein bound to the network can be fit with a single exponential with $\tau = 2.0$ s [66]. The lifetime of the capping protein bound to the actin oligomer ($\tau_{C_{\text{slow}}}$) is likely in the range of the lifetime of an actin oligomer, 5–30 s [92]. The diffusion coefficient of the slow component is $D_{C_{\text{slow}}}$ = 0.5 μm^2/s [91], and $D_{C_{\text{fast}}}$ =2–5 μm^2/s is expected which is comparable to the diffusion coefficient of actin monomers [61, 99]. The value of K that influences the ratio of cytoplasmic to bound protein was calculated to give an estimated ratio of cytoplasmic protein to bound protein 2.3 to 1 [62].

Scanning the model parameters within the range described in the preceding paragraph fits to FRAP data were obtained. The simulated FRAP was applied to a steady state initialized with the concentrations found after relaxing Equations (27) and (28) in time. Figure 3C shows the steady-state concentration profiles using K = 0.5 s^{-1}, $D_{C_{\text{fast}}}$ = 2.0 μm^2/s , $D_{C_{\text{slow}}}$ = 0.2 μm^2/s, v_r= 0.03 μm/s, τ = 2.0 s, and $\tau_{C_{\text{slow}}}$ = 13.0 s. In order to obtain good fits to the experimental FRAP data for capping protein, the lifetime $\tau_{C_{\text{slow}}}$ needs to be maximized, and the diffusion coefficient $D_{C_{\text{fast}}}$ needs to be minimized, within the range of values described above and the range that gives nonnegative concentration profiles in the model equations. Figure 3D shows the recovery of the intensity in the bleached region along with the recovery in Kapustina et al. The recovery curve for $D_{C_{\text{slow}}}$ = 0.5 μm^2/s is an overall good fit to the experimental curve; however, the initial recovery is more rapid compared to experiment. The fit can be improved using $D_{C_{\text{slow}}}$ = 0.2 μm^2/s [62].

The above results show that parameters measured with SiMS can be used to model the FRAP data in [46], using a smaller diffusion coefficient $D_{C_{\text{slow}}}$ and faster dissociation time τ compared to [46]. The diffusion of long-lived oligomers out of the bleached region contributes to making the recovery slower initially and a value $\tau_{C_{\text{slow}}} \approx 13$ s is needed for a good fit. This is in agreement with the fact that slowly diffusing speckles can be tracked for a few seconds and thus the lifetime of the slowly diffusing capping protein is likely in the range of 5–30 s [91]. Even though the dissociation time $\tau = 2$ s is small compared to the measured FRAP half-time, the bound species is a small fraction of the total amount.

4.3.2 Model with Membrane Binding

Another way of accounting for slowly diffusing capping protein is considering that capping protein binds and diffuses along the membrane [91]. Membrane binding can occur through a fast-diffusing state in the cytoplasm or by membrane-induced uncapping of capped barbed ends. The model shown in Figure 3E,F is another possible mechanism of why capping protein dissociates so frequently from the actin network and diffuses slowly. CARMIL is a membrane bound protein complex that also binds capping protein and may account for the very short lifetime of capping protein bound to the actin filament [23, 27, 28]. In this model only fast diffusing

cytoplasmic protein is able to become bound (representing capping of barbed ends) so that the appearance rate is:

$$a(x) = a_{C_{\text{fast}}}(x) = K C_\infty \left(A_1 e^{-x/\lambda_{\text{short}}} + A_2 e^{-x/\lambda_{\text{long}}} \right), \tag{31}$$

with $A_1 = 0.74$, $A_2 = 0.26$, $\lambda_{\text{short}} = 2.0$ µm, and $\lambda_{\text{long}} = 8.65$ µm. The bound protein can dissociate into either C_{fast} or C_{slow} and the parameter s_1 is the probability of dissociating into C_{fast}. The fast diffusing capping protein can convert to slow with lifetime $\tau_{C_{\text{fast}}}$ and slow can become fast with lifetime $\tau_{C_{\text{slow}}}$. The model in Figure 3E, F is another specific case of the general model.

The model with membrane binding (Figure 3E) has more parameters compared to the model with oligomers (Figure 3A).

The new parameters are the lifetimes $\tau_{C_{\text{fast}}}$, $\tau_{C_{\text{slow}}}$, and the dissociation probability s_1. As mentioned in Section 4.3.1, the lifetime of the slowly diffusing capping protein is likely in the range of 5–30 s. It was assumed that $\tau_{C_{\text{fast}}} = \tau_{C_{\text{slow}}}$ so that C_{fast} and C_{slow} each correspond to 50% of the concentration far from the leading edge [91]. Figure 3G shows a concentration profile generated with $K = 0.435$ s^{-1}, $D_{C_{\text{fast}}} = 2.0$ µm^2/s, $D_{C_{\text{slow}}} = 0.5$ µm^2/s, $v_r = 0.03$ µm/s, $\tau = 2.0$ s, $\tau_{C_{\text{fast}}} = 5.0$ s, $\tau_{C_{\text{slow}}} = 5.0$ s, $s_1 = 0.1$.

Parameters could be adjusted for the second model to fit the experimental FRAP data. The simulated recovery curves are shown in Figure 3H, along with the experimental data. Both simulated curves with $D_{C_{\text{slow}}} = 0.1$ µm^2/s and $D_{C_{\text{slow}}} = 0.5$ µm^2/s fit the data; however, the smaller diffusion coefficient allows for a better fit. Similar to the model with oligomers, $D_{C_{\text{fast}}}$ needs to be on the lower range of the physically plausible values 2–5 µm^2/s . Parameter s_1 needs to be small compared to unity, otherwise the bleached region recovers too quickly and none of the other parameters are able to slow the recovery down enough to capture what occurs in the experiment. Keeping $\tau_{C_{\text{fast}}} = \tau_{C_{\text{slow}}}$, variation of these two parameters together showed that they also need to be in the range of a few seconds [62].

In conclusion, obtaining a good fit drives this model to a similar kinetic scheme as the model with oligomers, with the majority of the bound protein dissociating into slowly diffusing protein.

4.3.3 Comparison of Two Models for Capping Protein Turnover

The pool of slowly diffusing protein is important to fit FRAP recovery with half-time on the order of 10 s, using a bound lifetime of 2 s. Retrograde flow contributes little to FRAP since the distance traveled by retrograde flow during recovery is small compared to the size of the bleached region. Since both models are driven to similar kinetic transition rates, it is hard to distinguish between them using further FRAP data of either the back or front of the lamellipodium. A clearer difference between the two models can be seen in lamellipodium photoactivation simulations with the

same parameters as for the FRAP data [62]. Both models demonstrate significant concentration gradients of the two diffuse species across the lamellipodium. This prediction of concentration gradients could be tested in future experiments. The origin of this gradient is mainly the local production of slowly diffusing capping protein close to the leading edge. The inward flux of the slowly diffusing population plus the retrograde flow of the bound species must be balanced by the diffusive flux of the fast species at steady state.

4.4 Application to Arp2/3 Complex Dynamics

Both FRAP and SiMS microscopy experiments have been performed to study the kinetics of Arp2/3 complex in the lamellipodium. In FRAP studies by Lai et al. [52], the bleached region was a 2 μm by 4 μm box positioned at the leading edge of a B16-F1 melanoma cell. Recovery was faster at the leading edge of the cell than it was away from the leading edge. While this has been interpreted to suggest that Arp2/3 complex forms branches within a very narrow region close to the leading edge, SiMS experiments using XTC cells (tagging the p40 and p21 subunits) by Miyoshi et al. [66] show distributed speckle appearances 1 μm away from the leading edge and further, and an exponential distribution of speckle lifetimes with $\tau = 18$ s.

McMillen and Vavylonis [62] used modeling to (i) check if the FRAP recovery observed in Lai et al. [52] is consistent with the distributed appearances in Miyoshi et al. [66], and (ii) explore the implications for the concentration profiles of the diffuse species. FRAP of lamellipodia of B16-F1 melanoma cells [52] has similar qualitative features to FRAP of XTC cells (Figure 1) as well as PA of neuronal cells (Figure 2). The simulations below used a profile with distributed appearances that is narrower compared to the profile measured in XTC cells, which have wider lamellipodia compared to the B16-F1 melanoma cells. This appearance profile was calculated to give an Arp2/3 complex concentration profile that matches the concentration profile of the B16-F1 melanoma cells [62].

Using SiMS microscopy, Millius et al. [65] suggested that some Arp2/3 complexes bind to the WAVE complex on the cell membrane of XTC cells and perform a slow diffusion prior to incorporation of the actin network, while other Arp2/3 complexes are recruited directly from the cytosol. Millius et al. observed slowly diffusing speckles of Arp2/3 complex components within a few μm from the leading edge.

The study in [62] thus considered a model with membrane binding of the Arp2/3 complex (Figure 3I,J). The two diffuse species in this model represent Arp2/3 complex in the cytoplasm, C_{fast}, and bound to the membrane, C_{slow}. The bound Arp2/3 complex dissociates into C_{fast} only, representing debranching and dissociation of the Arp2/3 complex from the pointed end. This occurs with the detachment rate $d(x)$ corresponding to bound lifetime τ. This lifetime may

include Arp2/3 complex attachment without branch formation, as observed in single molecule in vitro experiments where bound Arp2/3 complex has bound lifetimes in the range 2–200 s [90].

Binding to the membrane was assumed to occur close to the leading edge with a spatially dependent rate $k(x) = k_m e^{-x/\lambda_m}$ defined by parameters λ_m and k_m. This was achieved in the simulations by using a spatially dependent $\tau_{C_{fast}}$. Spontaneous unbinding occurs with lifetime $\tau_{C_{slow}}$. The appearance profile describing association of membrane-bound Arp2/3 complex to the actin network is given by

$$a(x) = A_1 e^{-x/\lambda_{short}} + A_2 e^{-x/\lambda_{long}} \tag{32}$$

with $A_1 = 0.49$, $A_2 = 0.51$, $\lambda_{short} = 0.08$ μm, and $\lambda_{long} = 0.43$ μm. Using an estimated retrograde flow rate $v_r = 0.04$ μm/s in [52], $D_{C_{slow}} = 0.6$ μm/s^2 (the estimate in Millius et al. [65]) and assuming membrane binding occurs close to the leading edge, $\lambda_m = 0.2$ μm, leaves $D_{C_{fast}}$, K, $\tau_{C_{slow}}$ and k_m as undetermined parameters. Knowing the larger size of the Arp2/3 complex as compared to actin monomers and capping protein, a diffusion coefficient of 2–6 μm^2/s is anticipated.

In the steady-state profile in Figure 3K , $D_C = 3$ μm^2/s , $K = 6.0$ s^{-1}, $\tau_{C_{slow}} = 20$ s, and $k_m = 40$ s^{-1}. With these parameters, the bound protein is sharply peaked close to the leading edge while the fast diffusing protein is small compared to the bound species and slightly depleted at the leading edge.

The model fit the experimental FRAP data by Lai et al. [52], which shows faster recovery at the lamellipodium front as compared to the back. The recovery of simulated FRAP is quantified in Figure 3L where the front recovery curve is taken 0–1 μm from the leading edge, and the back recovery curve is taken 1–2 μm from the leading edge as in Lai et al. [52]. The recovery at the back has a small initial increase due to the diffusion of the cytoplasmic component, followed by a slower recovery. This slower recovery is driven by binding at the back of the lamellipodium and retrograde flow that brings labeled subunits from the cell front. In order to fit the experimental FRAP data the value of K has to be sufficiently high to keep the bound to cytoplasmic ratio sufficiently smaller than unity; otherwise the back of the lamellipodium recovers faster than in experiments. Similarly, decreasing coefficient k_m to a value where the concentration of slowly diffusing species becomes a small fraction of the bound concentration gives a better fit to the FRAP curve at the back. The recovery is also affected by the diffusion coefficient of the fast diffusing species. Values above $D_{C_{fast}} = 2$ μm^2/s give a good fit to the experimental FRAP data.

The results of Figure 3K,L suggest that the diffusing population is a small fraction of the bound. Lewalle et al. [56] also performed FRAP of Arp2/3 complex in lamellipodia and found recovery throughout the lamellipodia pronounced close to the leading edge, consistent with the assumptions in [62]. The fact that the concentration of Arp2/3 complex increases by about 8-fold after stimulation in XTC cells [87] is consistent with the existence of a small fraction of fast-diffusing Arp2/3 complex (presumably the only species present prior to lamellipodia stimulation).

Inspection of the movies in Millius et al. [65] indicates however that the number of slowly diffusing speckles is comparable to the bound population. While the slowly diffusing Arp2/3 complex speckles may also represent Arp2/3 complex bound to debranched actin oligomers (not considered here as a separate species), such a pool would also need to be as small for the model to reproduce the FRAP data. This motivates further studies to investigate if the fraction of diffusible Arp2/3 complex varies by a large factor among cell systems and/or during different stages of stimulation of the same cell.

4.5 Discussion

In this section we described how modeling was used to calculate concentration profiles of capping protein (Figure 3C,G) and Arp2/3 complex (Figure 3K) based on prior SiMS and FRAP data. The predicted gradients in the diffuse pool will have implications on the behavior of the lamellipodium when perturbed from steady state, for example during the stimulation of a protrusion by increase of free barbed end concentration close to the leading edge [62]. Diffusion limitations of capping protein or Arp2/3 complex towards the leading edge could become important upon protrusion initiation.

In the results of Figure 3, the capping protein distribution is broader than that of Arp2/3 complex but both are narrower than F-actin (Figure 1). Other studies using fluorescence speckle microscopy however suggest different length scales for each component with capping protein, Arp2/3 complex, and F-actin having increasingly broader concentration profiles [44]. Future work should examine if these differences are cell-type specific.

Hu and Papoian [39, 40] used a stochastic simulation model that includes physical and chemical interactions for actin, Arp2/3 complex, and capping protein in the lamellipodium to model protrusions. They only allow Arp2/3 complex-mediated activation branching very close to the membrane with diffusion coefficient 20 μm^2/s for all species, larger than what we used here for the fast and slow diffusing pools. One of the findings in Hu and Papoian is a significant dependence of protrusion dynamics on the concentrations of capping protein and Arp2/3 complex. Since cytoplasmic concentration gradients result for slower values of the diffusion coefficients, this effect would provide an additional influence on protrusion dynamics.

The method presented in this section could be generalized to study the diffusive dynamics of other lamellipodia regulators that have been studied with SiMS, including cofilin and AIP1 [97], which collaborate in actin filament severing, VASP [66], and WAVE [65].

5 Model of Lamellipodium Protrusion and Retraction Driven by Fluctuations in Actin Polymerization

5.1 Motivation from Experiment

We now return to the topic of lamellipodial protrusion and retraction of XTC cells mentioned in Section 1.2. In these cells waves of protrusion were accompanied by waves of LifeAct-labeled F-actin accumulation along the lamellipodium [87] (Figure 4B,C,D). This phenomenon belongs to the general class of cellular actin waves [43] and the regularity of protrusions and retractions during cell spreading indicates a process that can be described by a coarse-grained mathematical model.

The magnitude of protrusions and retractions is shown by the distribution of the standard deviation in Figure 4C. The standard deviation was measured along the radial direction in 1-degree intervals along the entire arc-length of the cell. The protrusion velocity was anti-correlated with the total local F-actin concentration measured by integrating LifeAct intensity over a 5 μm distance into the cell (Figure 4E). The time-dependent cross-correlation function (Figure 4E) showed that, on average, the fastest protrusion (retraction) speeds occurred just 10 s after a minimum (maximum) of integrated F-actin intensity at a given position along the arc-length of the cell.

The constant retrograde flow and fluctuating actin polymerization near the membrane in XTC cell lamellipodia is evident in the kymograph of Figure 4B, in which LifeAct forms diagonal lines of high intensity starting at the cell edge. These indicate an F-actin network that forms near the edge of the cell and processes into the cell as time increases to the right. Alternating high and low intensity over time in Figure 4B points to changing actin polymerization. Net actin polymerization near the membrane, as evidenced by increasing intensity, occurs during protrusion, although the total intensity within the lamellipodium is greatest during retraction, consistent with the anti-correlation of Figure 4E [87]. The notion that fluctuations in actin polymerization can drive such dynamics is further supported by the experimental evidence that other cell types treated with blebbistatin continue to protrude and retract periodically, although the period of oscillations may change [11, 30, 106].

5.2 One-Dimensional Model with Excitable Actin Dynamics

The observed dynamics are suggestive of excitations driven by noise. Excitability typically involves the interaction between an activator and an inhibitor: in an excitation, an activator species self-recruits rapidly; this activator in turn recruits an inhibitor that causes the activator to slowly dissipate [63]. Ryan et al. [87] speculate that the anticorrelation of leading-edge velocity with total actin intensity suggests that F-actin acts as an inhibitor. Likely mechanisms for this inhibition
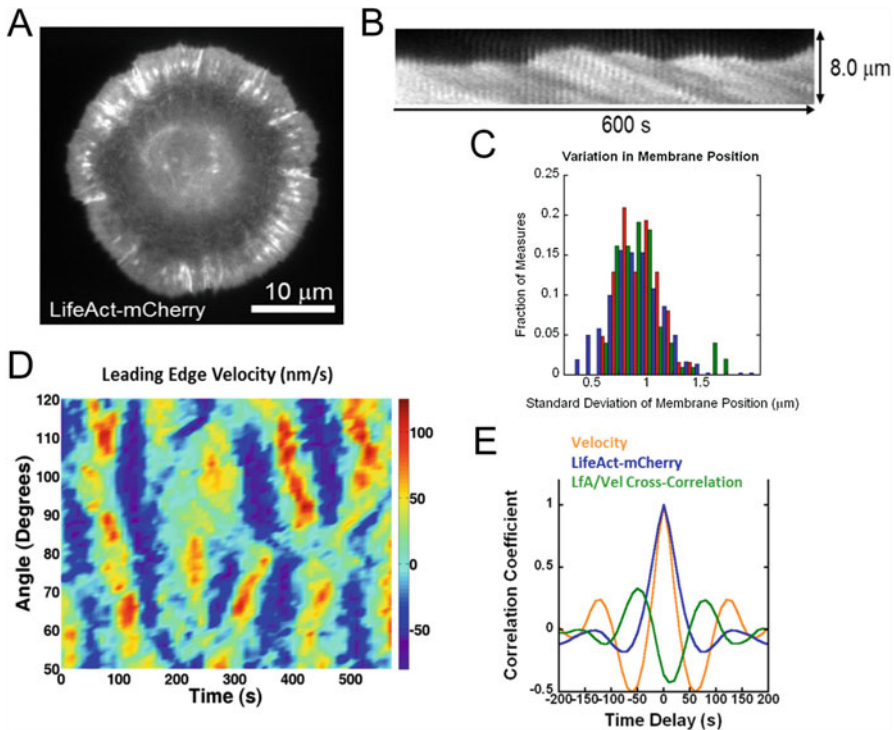
Fig. 4 Experimental observations of leading edge protrusion and retraction (reproduced with permission from [87] and panel C from [86]). (A) An XTC cell expressing actin marker LifeAct-mCherry. (B) Kymograph of segment at leading edge of cell in panel A. F-actin polymerized near the leading edge into the cell via retrograde flow, resulting in diagonal striping of kymograph. (C) Distribution of the standard deviation of the radial membrane position at a fixed angular position for three cells. (D) Leading-edge velocity (with respect to fixed substrate) versus angle and time for cell in Figure 1G of [87]. Positive (negative) velocities indicate protrusion (retraction). The retrograde flow speed for this cell was 74 ± 3 nm/s. (E) Average correlation coefficients for leading-edge velocity autocorrelation, LifeAct-mCherry autocorrelation, and LifeAct-mCherry-velocity cross correlation, versus time at a fixed angular position.

include the formation of actomyosin bundles [5] and adhesions [3] and accumulation of mechanical tension [45, 77]. Many molecules are activator candidates: actin polymerization can be triggered by the Scar/WAVE and WASp proteins that self-recruit on the cell membrane to activate the Arp2/3 complex [36, 76, 79]. Once activated, the Arp2/3 complex generates new barbed ends by nucleating branches off preexisting filaments, thought to lead to autocatalytic dendritic nucleation [71, 93]. Severing of growing filaments could also contribute to diffusive autocatalytic generation of barbed ends [66, 74] through transient association of diffuse cofilin and AIP1 with F-actin [97]. Formin-mediated nucleation of new filaments is another possible activation mechanism [35, 107].
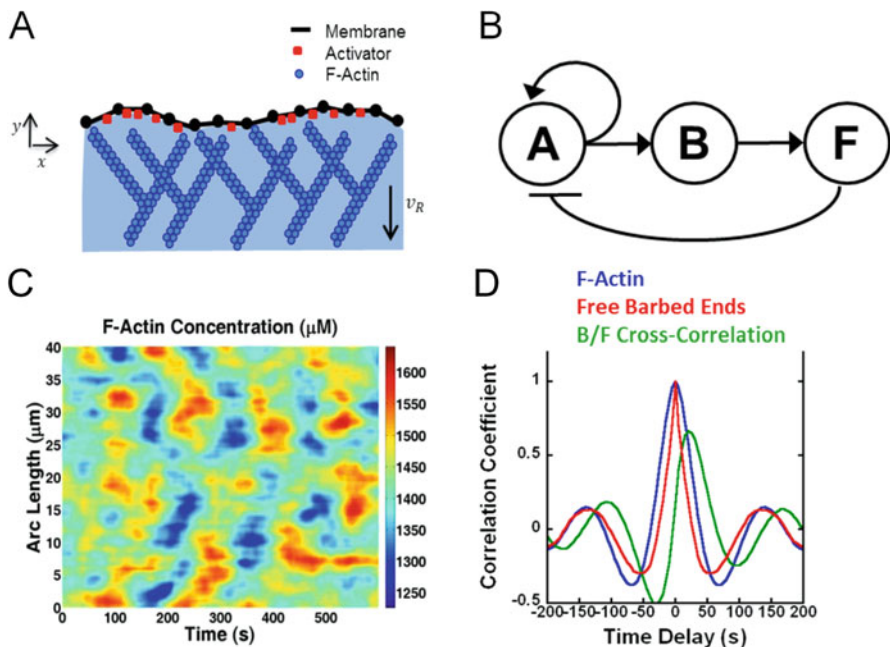
Fig. 5 One-dimensional model for an XTC cell leading edge (panels A, B reproduced with permission from [86] and C, D from [87]). (A) The model includes F-actin, F, activator, A, and free barbed ends, B, along the arc-length of the membrane. (B) Reaction network diagram. Assembly of F is promoted by the autocatalytic activator A which generates free barbed ends. Accumulation of F inhibits A. (C) Simulation results, F-actin concentration vs arc-length and time. (D) Correlation coefficients vs time for free barbed end autocorrelation, F-actin autocorrelation, and cross-correlation between B and F-actin at a given arc-length.

5.2.1 Model that Reproduces Wavelike Propagation

In the one-dimensional model of Ryan et al. [87], the concentrations of a diffusible activator, $A(x, t)$, free barbed ends, $B(x, t)$, and F-actin, $F(x, t)$, are calculated at different positions x along the leading edge over time (Figure 5A). The lamellipodium is modeled in one dimension, each coordinate representing a slice along the arc-length of the leading edge. In this model it is assumed that protrusions and retractions stem from underlying concentration fluctuations in the local actin network and cell membrane displacement is not explicitly considered. Denoting rate constants by k and ρ, the equations governing the concentrations are:

$$\frac{\partial A}{\partial t} = (\rho_0 + \rho_2 A^2)e^{-F/F_S} - k_A^- A + D_A \nabla^2 A + \sigma(x, t), \tag{33}$$

$$\frac{\partial B}{\partial t} = k_B^+ A - k_B^- B, \tag{34}$$

$$\frac{\partial F}{\partial t} = k_F^+ B - k_F^- F. \tag{35}$$

The first term on the right-hand side (rhs) of Equation (33) allows for spontaneous accumulation as well as nonlinear self-recruitment of the activator. A simple quadratic dependence on A is chosen (see Section 5.2.2 below). When F-actin exceeds saturation concentration, F_s, the activator on-rate is reduced. This is the negative feedback in Figure 5B. The second term on the rhs in Equation (33) represents deactivation. Diffusion of the activator (third term on the rhs) along the membrane couples neighboring sites and allows propagation of actin dynamics along the leading edge. The last term in Equation (33) is white noise, $< \sigma(x, t)\sigma(x', t') > = \sigma_0^2 \delta(t-t')\delta(x-x')$ and represents concentration fluctuations [32, 104] that generate excitations by perturbing the system out of its stable state (see Section 5.2.3). Equation (34) describes accumulation of free barbed ends as a result of the activation process. Rate constant k_B^+ describes how fast the activator generates new barbed ends. Rate constant $k_B^- \approx 0.4\text{–}8 \text{ s}^{-1}$ is the rate of free barbed end loss through capping by capping protein [79]. Equation (35) describes change of F-actin as a result of polymerization at free barbed ends and spontaneous disassembly.

Since the capping rate k_B^- is much faster than the frequency of the protrusion and retraction events, generation of barbed ends must be fast enough such that B responds to changes in A quickly. This leads to $B \approx k_B^+ A/k_B^-$ and allows Equation (33) to be rewritten as follows:

$$\frac{\partial B}{\partial t} = (r_0 + r_2 B^2)e^{-F/F_S} - k_A^- B + D_A \nabla^2 B + s(x, t). \tag{36}$$

Here, unknown rate constant k_B^+ is absorbed into the new rate constants r_0 and r_2 and into the amplitude of the noise that is now s_0. Equations (35) and (36) form a closed system in terms of B and F. Details on selecting model parameters are given in Section 5.2.4.

Numerical integration of the model produces spikes of free barbed end concentration, followed by spikes in local F-actin concentration. Figure 5C shows that the model captures the wave-like propagation across sections of the membranes arc-length as well as the magnitude and timescale of the actin fluctuations of Figure 4D.

The F-actin autocorrelation function calculated using the model, shown in Figure 5D, matches the experimental result of Figure 4E. A characteristic feature of the cross-correlation function between B and F is that spikes of B precede those of F, demonstrated by the positive shift of the cross-correlation peak to the right of the origin by approximately 25 s. Without the noise term in Equation (36), for the reference parameter values, point excitations propagate laterally along the membrane before returning to a uniform stationary state (Figure 6A,B). Addition of noise to this steady-state system excites actin randomly along the membrane, so that excitations combine into structures similar to those seen in experiment.
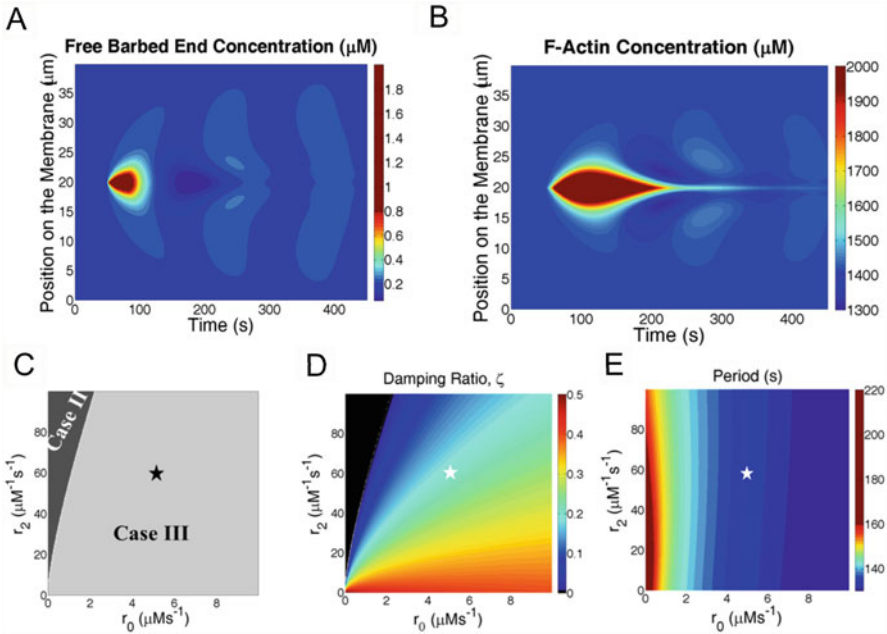
Fig. 6 Model response to point excitation and stability analysis predicts characteristics of model solutions (reproduced from [87]). (A) Free barbed end concentration, generated by localizing noise, $s(t) = 0.1\ \mu\text{M}\ s^{-1}$, at a single point (at $20\ \mu\text{m}$) along the membrane for 1.5 s. Simulations were run with the same parameters as Figure 5, except the noise term was zero outside the region described above. Excitations spread from the region at which noise was applied with a speed $\sim 0.17\ \mu\text{m/s}$. This is similar to the speed of protrusion propagation in Figure 4D. In the presence of multiple sources of noise, excitations combine into transient wave-like patterns. (B) F-Actin concentration corresponding to the free barbed end concentration shown in A. (C) Results of linear stability analysis as function of r_0 and r_2 for wave number $q = 0$. The black star indicates the exact parameters used in Figure 5. Case II (dark gray): unstable oscillatory solutions; Case III (light gray): stable oscillatory solutions. (D) Damping ratio, calculated for regions of parameter space within Case III of panel C (Case II region shown in dark gray). (E) Similar to panel D but displaying period τ for both Case II and Case III solutions.

5.2.2 Choice of Nonlinear Terms

The negative feedback in Equations (33) and (36) uses an exponential cutoff, e^{-F/F_s} that prevents F-actin from accumulating in amounts that far exceeds F_s. Excitations away from steady state are driven by the autocatalytic term $\rho(B) = r_0 + r_2 B^2$ in Equation (36). A quadratic was chosen for the following reason. During an excitation, the concentration of actin near the leading edge approximately doubles (see Figure 4 and 5). A change of similar magnitude is anticipated in

the concentration of free barbed ends. Now the term $\rho(B)e^{-F/F_s}$ should have approximately the same value at both steady state, $B = B^*$ and $F = F^*$, and at the instant in time when the free barbed end concentration is at a maximum, $B \approx 2B^*$ and $F = \alpha F^*$. Since B and F are out of phase leads one to estimate $1.1 < \alpha < 1.5$. Assuming a power law, $\rho(B) \sim B^n$, this would require $2 \leq n \leq 5$. Ryan et al. [87] chose the smallest integer exponent consistent with this requirement. The constant term r_0 in $\rho(B)$ prevents unphysical fixed points with very small concentrations of free barbed ends. This term accounts for filaments created by spontaneous nucleation rather than through autocatalytic feedback.

5.2.3 Linear Stability Analysis

Linear stability analysis can be performed on the model described by Equations (35) and (36) without the noise term in Equation (36). Parameters can be chosen such that the system is in a stable steady-state region, close to the boundary of an unstable region. The addition of a noise term then transiently perturbs the stable state of the system, generating spontaneous excitations.

Stability analysis is performed around a homogeneous steady state $B = B^*$ and $F = F^*$. Fixed points B^* and F^* are defined by the nullclines of a homogeneous system (i.e., no dependence on arc-length distance) $u(B^*, F^*) = v(B^*, F^*) = 0$ where

$$u(B, F) = (r_0 + r_2 B^2)e^{-F/F_s} - k_A^- B, \tag{37}$$

$$v(B, F) = k_F^+ B - k_F^- F. \tag{38}$$

The fixed points can be found numerically. While Equations (37) and (38) can have up to 3 fixed points, for parameter values in [87], there is a single fixed point. Defining $b(x, t) = B(x, t) - B^*$ and $f(x, t) = F(x, t) - F^*$, considering sufficiently small deviations from the fixed point, and Fourier transforming $x \to q$, it is obtained from Equations (35) and (36) (without the noise term):

$$\begin{pmatrix} \dot{b}_q \\ \dot{f}_q \end{pmatrix} = J \begin{pmatrix} b_q \\ f_q \end{pmatrix}, \text{ where } J = \begin{bmatrix} 2r_2 B^* e^{-F^*/F_x} - (k_A^- + D_A q^2) & \frac{r_0 + r_2 B^{*2}}{F_S} e^{-F^*/F_S} \\ k_F^+ & -k_F^- \end{bmatrix}. \tag{39}$$

The characteristic equation is $\lambda^2 - \mathrm{Tr} J \lambda + \det J = 0$. Solving this for λ one finds two wave-number dependent eigenvalues. These eigenvalues can be used to distinguish between parameter sets based on the type of behaviors they elicit within the model. These behaviors can be separated into three distinct cases (note: the remaining of this subsection below corrects a mislabeling in the Supplementary Material of [87]): (I) both eigenvalues real, (II) both eigenvalues complex with positive real components that give unstable solutions to the linearized equation, and (III) both

eigenvalues complex with negative real part that generate stable solutions. Whether eigenvalues are real or complex is determined by the sign of $\text{Tr}(J)^2 - 4\det(J)$.

Case I. Two real eigenvalues occur when $\text{Tr}(J)^2 - 4\det(J) > 0$. Real λ indicate stable or unstable fixed points, depending on the sign of λ.

Case II. Complex eigenvalues with positive real components result from parameter sets in which $\text{Tr}(J)^2 - 4\det(J) < 0$ and $\text{Tr}(J) > 0$. In this case the system has an unstable solution fixed point. However, because Equations (35) and (36) give bounded solutions, the solution would evolve into a limit cycle, in which the system exhibits oscillatory behavior. The period of these oscillations, estimated from the linear stability analysis is $\tau = 2\pi/\text{Im}(\lambda)$.

Case III. Complex eigenvalues with negative real components. These solutions fulfill $\text{Tr}(J)^2 - 4\det(J) < 0$ and $\text{Tr}\, J < 0$. Small q more easily satisfy this condition compared to larger q. If perturbed, such a system will relax back to the stable solution in an oscillatory manner with period $\tau = 2\pi/\text{Im}(\lambda)$. The relaxation rate is described by the dimensionless damping ratio $\zeta = \text{Tr}\, J / 2\sqrt{\det(J)}$.

5.2.4 Selection of Parameters

In [87], the values of k_F^+ and k_F^- were taken from experiment. Five constraints were used to determine the values of r_2, r_0, F_S, k_A^-, and D_A (Table 2). The first two constraints required fixed points with $B^* \approx 0.4\,\mu\text{M}$ and $F^* \approx 1500\,\mu\text{M}$. The value of B^* was chosen because within a band of width $d \sim 2\,\mu\text{m}$ near the leading edge the concentration of free barbed ends is approximately $1\,\mu\text{M}$ [81]. In this model, which does not distinguish distance from the leading edge, this corresponds to a barbed end concentration $1\mu\text{M} \times d/w = 0.4\,\mu\text{M}$, where $w \sim 5\,\mu\text{m}$ is the width of the lamellipodium. The third condition required that the system is in a region of parameter space in which relaxation to steady state occurs with underdamped oscillations, such that the $q = 0$ case of the linear stability analysis lies in a Case III region, but not far from a Case II region. The fourth condition was that the period of oscillation is $\sim 130\,\text{s}$, as observed experimentally. Finally, the diffusion coefficient of the activator was selected to match the width of the spatial correlation function found in experiment.

Figure 6C shows linear stability diagrams for $q = 0$ as a function of two model parameters, r_0 and r_2. These two parameters that are important in controlling the response of the system to stimulation of polymerization (last paragraph in this section) need to be adjusted as they are not directly determined from prior experiments. The star indicates the reference parameter set. Figure 6D displays the damping ratio, ζ as a function of the same parameters as in Figure 6C for $q = 0$. The damping ratio approaches zero close to the region of Case II. Larger values of r_2 increase the strength of the nonlinear positive feedback and bring the system from a stable (Case III) towards an unstable (Case II) region (Figure 6C). Increase of r_0

Table 2 Parameter table for one-dimensional model of lamellipodium protrusion and retraction.

Parameter	Value	Reference/Justification
F_s	200 μM	Chosen to match the constraints of Section 5.2.4.
k_F^+	66 s^{-1}	Estimated in [66].
k_F^-	0.01 s^{-1}	Close to inverse of time required for actin to traverse lamellipodium by retrograde flow.
k_A^-	0.03 s^{-1}	Chosen to match the constraints of Section 5.2.4.
D_A	0.1 μm^{2}s^{-1}	Typical of membrane proteins, also matches width of spatial correlation function in [87].
r_0	5 μMs^{-1}	Chosen to match the constraints of Section 5.2.4.
r_2	600 μM^{-1}s^{-1}	Chosen to match the constraints of Section 5.2.4.
s_0	0.02 μMμm$^{-1/2}$s$^{-1/2}$	Reproduces noise-induced excitations with rate similar to experiments [87].

results in increased damping ζ, thus the value of r_2 must exceed an r_0-dependent threshold for ζ to become sufficiently low. Figure 6E displays the period τ as a function of the same parameters as in Figure 6C for $q = 0$, which is less sensitive to changes in r_2 compared to r_0.

Selecting the value of the diffusion coefficient of the activator, D_A, required that the damping ratio $\zeta(q)$ increases to ~ 1 at a wavenumber $q \approx 1$ μm^{-1}. Activator diffusion coefficient of 0.1 μm^2/s fulfills this and reproduces a width for the spatial correlation function similar to experiment (full-width-half maximum approximately 5.2 μm). A decrease to $D_A = 0.05$ μm^2/s results in a full-width-half-maximum of 3.4 μm, while an increase to $D_A = 0.4$ μm^2/s results in a full-width-half-maximum of 8.8 μm.

Short wavelengths are more strongly damped compared to longer wavelengths. For the reference parameters values, the system switches from an underdamped regime (Case III) to an overdamped case (Case I) at a wavenumber $q = 0.97$ μm^{-1}.

5.2.5 Arp2/3 Complex as Activator and Cell Response to Stimulus

Arp2/3-complex-mediated dendritic growth is autocatalytic: nucleated branches act as nuclei for further branches. Could the Arp2/3 complex be the activator species of the model? Experiments with fluorescently labeled components of the Arp2/3 complex in [87] showed that it accumulates in bursts along the leading edge. These bursts precede maxima of total F-actin amount, indicating a possible role for Arp2/3 complex in the activation process. However, Ryan et al. [87] argued that it is unlikely for it to be the only activator because lateral spreading of Arp2/3 complex-mediated branching would be too slow to cause the observed traveling waves of protrusion: the effective diffusion coefficient calculated by a branching mechanism is 10 times smaller ($D = 0.01$ μm^2/s) than the estimated D value for the activator species.

These numbers support the additional involvement of diffuse proteins such as small GTPases, Scar/WAVE and WASp, and PIP3.

A general feature of the model with excitable dynamics is the synchronized response to a sudden global perturbation. In [87], this was tested by exploring the ability of the model to capture response to chemical stimulants. After hours of remaining on slides, protrusions and retractions subside in XTC cells. Introduction of fetal calf serum (FCS) restores the protrusions and retractions similar to the early stages after introduction to the slide. Figure 7A shows the leading edge of a cell expressing p21-EGFP (a protein in the Arp2/3 complex) and LifeAct-mCherry that is stimulated with FCS at 200 s. The increase in p21-EGFP and LifeAct-Cherry intensity after the addition of FCS is quantified in Figure 7B. The model can capture the FCS response through a sudden increase in rate r_0 and r_2 (Figure 7C). This change reproduces the experimental behavior, most notably the out-of-phase transient oscillations in Arp2/3 complex and F-actin at late times after stimulation. We note other studies in *Dictyostelium* response to cAMP have also been interpreted as an indication of excitability [104].
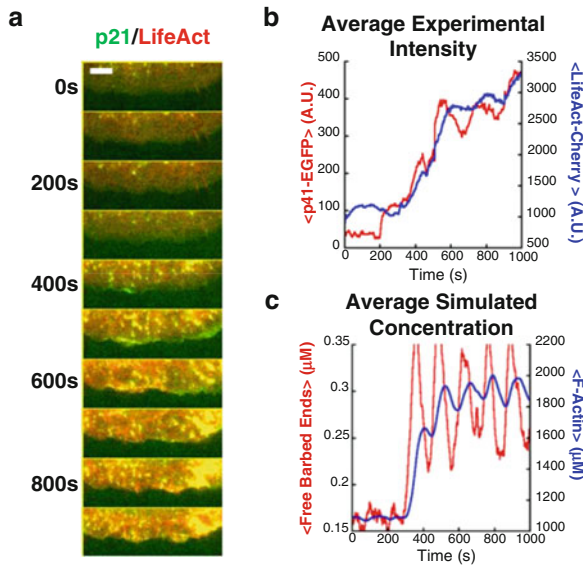
Fig. 7 XTC cell response to FCS and comparison to the model (reproduced with permission from [87]). (A) Montages of leading edge of cell expressing p21-EGFP and LifeAct-mCherry stimulated by FCS at 200 s. The cell had been plated for 4 h. Intensity increases are evident after stimulation. Bar: 5 μm. (B) Intensities of p21-EGFP and LifeAct-mCherry averaged over all angles vs time. (C) Results of model showing concentrations of the free barbed end and F-actin concentrations, averaged over arc-length. Rate constants were functions of time: $r_o(t) = 1\ \mu Ms^{-1} + 24\ \mu Ms^{-1} H(t)$, $r_2(t) = 1\ \mu Ms^{-1} + 624\ \mu Ms^{-1} H(t)$. Here $H(t) = \Theta(t - 250s)t^3/(T^3 + t^3)$, where $T = 220$ s and Θ is the step function.

5.3 Two-Dimensional Model of Lamelipodial Protrusions and Retractions

The one-dimensional model of actin accumulation along the arc-length of the cell described above did not address the movement of the cell membrane. In [86] the model was extended into two dimensions. This enabled two-dimensional aspects of XTC lamellipodia to be captured such as the extent and profile of XTC protrusions as well as F-actin concentration versus distance from the leading edge.

As mentioned in Section 2, F-actin assembly is distributed throughout the lamellipodium, and does not occur solely where actin filaments touch the cell membrane. A 2D model of fluctuations in actin polymerization would have to account for the time-variation of appearance rate $a(y) = A_1 e^{-y/\lambda_1} + A_2 e^{-y/\lambda_2}$ (measuring the rate of new speckle appearance as function of distance from the leading edge), as well as the variations in speckle lifetime (note: unlike Equation (1), y is the direction into the cell). Ryan et al. [86] made a few simplifying approximations. First, they assumed that all the basal speckle appearance events are due to recycling oligomeric actin that break off and reassemble at the back of the lamellipodium [92]. Second, the effective lifetime of F-actin in lamellipodia was approximated by a single exponential with a characteristic time $1/k_F^- = 100$ s. This lifetime is longer than the speckle lifetime due to several dissociation and local recycling events. In this model, fluctuations in actin polymerization arose from fluctuations in the polymerization rate very close to the membrane of the leading edge (i.e., they represent fluctuations of the amplitude of the λ_1 term in Equation (1)). This would be consistent with the assumption of a slowly diffusing membrane-bound activator.

5.3.1 The Model

The leading edge is along the x-axis, with the negative y-axis directed into the cell (neglecting the curvature associated with the shape of the whole cell). The displacement of the membrane along the y-axis is $h(s, t)$, where s is arc-length across the membrane, and, approximately, $s \approx x$. Periodic boundary conditions are applied along the x-axis after a total width 20 µm. The F-actin network in the lamellipodium is assumed to be a rigid network with sufficiently large modulus to be practically incompressible, consistent with the retrograde flow in the lamellipodium of XTC cells being approximately constant through protrusion and retraction cycles [87]. Computer simulations of the model were implemented on a 40 μm wide and 20 to 40 µm tall system. Concentrations were calculated on a lattice grid with membrane movement allowed on a continuum. Results were obtained after an equilibration period.

Barbed-End and F-Actin Concentrations

Free barbed ends of concentration $B(x, t)$ are generated by an autocatalytic membrane-bound activator with concentration $A(x, t)$. The accumulation of the activator is damped as a result of F-actin polymerization at the lamellipodium near the given arc-length position, similar to the 1D model. Random fluctuations in activator concentration can generate excitations by perturbing the system out of its stable state [32, 63, 87, 104]. Denoting rate constants by symbols k and r, and σ' as noise obeying Gaussian statistics with zero mean, the equations are:

$$\frac{\partial A(x, t)}{\partial t} = \left[r_0' + r_2' A(x, t)^2 \right] e^{-\int_{-\infty}^{h(x,t)} F(x,y,t)/F_{sat} dy} - k_A^- A(x, t)$$

$$+ D_A \frac{\partial^2 A(x, t)}{\partial x^2} + \sigma'(x, t), \tag{40}$$

$$\frac{\partial B(x, t)}{\partial t} = k_B^+ A(x, t) - k_B^- B(x, t), \tag{41}$$

$$\frac{\partial F(x, y, t)}{\partial t} = \gamma_{pol}(x, t) k_F^+ B(x, t) \delta[y - h(x, t)] - k_F^- F(x, y, t) + v_R \frac{\partial F(x, y, t)}{\partial y}. \tag{42}$$

Equations (40) and (42) are the two-dimensional extension of (33) and (35). The negative feedback in the first term on the rhs of Equation (40) is now the concentration measured by a line integral from the cell membrane towards the cell middle. The first term on the rhs of Equation (42) describes accumulation of F-actin as a result of polymerization at free barbed ends at the membrane. The polymerization rate is reduced compared to the polymerization rate in the absence of load by unitless reduction factor $\gamma_{pol}(x)$ with values between 0 and 1 that we describe in more detail below ($\gamma_{pol} = 1$ corresponds to polymerization under no load, while $\gamma_{pol} = 0$ corresponds to stalling of polymerization). The second term in the rhs of Equation (42) is the uniform F-actin disassembly rate. The last term in Equation (42) describes constant retrograde flow (v_R is a positive number). Similar to the one-dimensional model, Equations (40) and (41) can be replaced by:

$$\frac{\partial B(x, t)}{\partial t} = \left[r_0 + r_2 B(x, t)^2 \right] e^{-\int_{-\infty}^{h(x,t)} F(x,y,t)/F_{sat} dy} - k_A^- B(x, t)$$

$$+ D_A \frac{\partial^2 B(x, t)}{\partial x^2} + \sigma(x, t). \tag{43}$$

Here, unknown rate constant k_B^+ is absorbed into the new rate constants r_0 and r_2 and into the amplitude of the noise that is now σ_0.

Membrane Motion

The motion of the membrane at the leading edge was assumed to result from the balance of forces due to actin polymerization, f_{pol} , membrane forces due to membrane tension and conserved cell surface area, f_{mem} and frictional forces, f_{fr}, that result from the breaking of links between the cell membrane and the F-actin network [13]. Applying force balance in the y-direction (assuming variation of stresses in the x-direction can be neglected), and using units for f_{pol} , f_{mem} and f_{fr} of force per unit membrane length, one has for a given point on the cell membrane:

$$f_{pol} + f_{mem} + f_{fr} = 0. \tag{44}$$

The viscous resistance of the surrounding medium to the movement of the cell membrane is negligible compared to the forces of actin polymerization and membrane load [24] so it is neglected in Equation (44).

Given a local concentration of free barbed ends, $B(x, t)$, that push against the membrane, the actin filament polymerization rate must adjust to satisfy Equation (44). Assuming that a constant fraction of the actin filament elongation is converted into F-actin network expansion along the y direction, which occurs with rate $\partial h(x, t)/\partial t + v_R$, there exists a force-velocity curve $f_{pol}[B(x, t), \partial h(x, t)/\partial t + v_R]$. The frictional force f_{fr} is also a function of the network expansion rate and the concentration of actin network links with the membrane [13]. The concentration of these links can be assumed to be approximately constant. Alternatively, f_{fr} could be negligible compared to the membrane force f_{mem}. In both cases, solving Equation (44) for the membrane extension rate gives

$$\frac{\partial h(x, t)}{\partial t} = \gamma_{pol} \left[B(x, t), f_{mem}(x, t) \right] v_0 - v_R, \tag{45}$$

where v_0 is the network expansion rate at the leading edge in the absence of resisting force, and function $\gamma_{pol}(B, f_{mem})$, which can be evaluated at any point along the leading edge as a function of time, is the parameter that appeared in Equation (42). Observed maximum protrusion speeds for XTC cells are similar in magnitude to retrograde flow speeds [87] so $v_0 \approx 2v_R$. Forward membrane motion requires a polymerization rate greater than the retrograde flow rate, $\gamma_{pol} > \frac{1}{2}$. When $\gamma_{pol} = \frac{1}{2}$, the system is balanced and the membrane does not move, while $\gamma_{pol} < \frac{1}{2}$ leads to membrane retraction. In the remainder of this subsection we provide expressions for the restorative membrane force, $f_{mem}(x)$, which depends on the shape and extension of the leading edge, and consider two possible functional forms of $\gamma_{pol}(B, f_{mem})$. Equations (42), (43), and (45), together with the following definitions of $f_{mem}(x)$ and $\gamma_{pol}(B, f_{mem})$, provide the complete model.

The membrane force includes two components: a global area-conserving force and a component due to membrane curvature, $f_{mem} = f_{area} + f_{curv}$. Component f_{area} is directed towards the cell center and is the same for all x at any given time;

it depends only on the average extension of the lamellipodium $\langle h \rangle_x$ measured from a reference extension h_{ref}:

$$f_{area} = -k_{mem} \left(\langle h \rangle_x - h_{ref} \right). \tag{46}$$

The constant k_{mem} describes the stiffness associated with uniform increase of the adhered cell radius. The curvature component of the membrane force depends on the membrane curvature $\kappa(x) = \partial^2 h(x, t)/\partial x^2$ at position x:

$$f_{curv}(x) = S\kappa(x), \tag{47}$$

where S is a constant. As both positive and negative membrane curvatures are possible, this force may point inwards or outwards with respect to the center of the cell. The dependence of f_{curv} on the second derivative of h represents the effects of membrane tension [31]. More complex dependencies such as 4th order derivatives that represent elastic bending contributions are not included in Equation (47).

For a large enough lamellipodium segment, fluctuations in $\langle h \rangle_x$ at steady state are very small. Thus f_{area} settles down to an approximately constant value independent of k_{mem} and h_{ref} such that there is no net lamellipodial extension, $\langle \gamma_{pol} \rangle_t \approx \langle \gamma_{pol} \rangle_x \approx \frac{1}{2}$. The values of k_{mem} and S are related to one another since they both include the effects of membrane tension. However, since only changes in S will have a significant impact in the results, k_{mem} and S are treated as independent variables for convenience.

Two functional forms of γ_{pol} were examined, corresponding to exponential (Brownian-ratchet-like) and switch-like force-velocity relationships, respectively. Both models assume that the membrane force is distributed equally among the free barbed ends at the leading edge.

Ratchet Model. In this model each filament end grows with an exponential force-velocity curve as would be expected by a Brownian ratchet mechanism [24, 69, 78],

$$\gamma_{pol}^{ratchet} \left[f_{mem}(x, t), B(x, t) \right] = e^{-\alpha f_{mem}(x,t)/B(x,t)}. \tag{48}$$

In Equation (48) the polymerization rate decreases exponentially with the force per filament, with a scaling factor $\alpha = \delta/k_B T = 0.66 \text{ pN}^{-1}$, where $\delta = 2.7$ nm is the filament elongation length per actin monomer. The ratchet model dictates a gradual change in the actin polymerization rate in response to changes in the ratio of the concentration of free barbed ends and the membrane load. When f_{mem} is approximately constant, a large change in B is required to transition between maximum protrusion rates ($\gamma_{pol} = 1$) and maximum retraction rates ($\gamma_{pol} = 0$).

Switch-like Model. Interactions among filaments and attachment to the membrane [24] may give rise to nonlinearities in the force-velocity curve leading to concave-down force-velocity curves as observed during gliding motility of keratocytes [33, 48, 83], as well as stick-slip behavior (multiple branches in force-velocity relationship) [17, 21, 103]. Ryan et al. [86] did not consider the more-complex possibility of stick-slip behavior, but investigated a concave dependence given by

a Hill function. In a phenomenological description, filament polymerization shifts rapidly from being unencumbered to being stalled upon increasing load:

$$\gamma_{pol}^{switch}\left[f_{mem}(x,t),\,B(x,t)\right]=1-\frac{[\alpha f_{mem}(x,t)/B(x,t)]^n}{K_0^n+[\alpha f_{mem}(x,t)/B(x,t)]^n}. \tag{49}$$

The value $n=10$ was chosen to produce a steep curve and facilitate rapid switching between protrusion and retraction. The constant K_0 determines the location of the inflection point of the Hill function, and was chosen to preserve the fixed point of the model from the ratchet polymerization case ($\gamma_{pol}=\frac{1}{2}$ at the same h_{ref} and f_{mem}/B). This step-like change allows a small change in B to influence a transition between near-maximum protrusion rates and near-maximum retraction rates. Similar dependencies were also assumed in models of actin network growth during protrusion of nerve growth cones [18] and keratocytes [2, 8].

5.3.2 Model Reproduces Features of Protrusion and Retraction Observed in Cells

Both the ratchet and switch-like model produce results that are in qualitative agreement with experiments, with the switch-like model exhibiting a sharper behavior (using parameters in Table 3). This model of force dependence of actin polymerization on membrane load, given by Equation (49), coupled with our model of excitable actin dynamics leads to periodic protrusion and retraction of the model membrane, accompanied by periodic increases in the amount of F-actin (Figure 8A,B). The noise term in Equation (43) generates local spikes of free barbed end concentration that spread across the leading edge, causing

Table 3 Parameters for two-dimensional model of lamellipodium protrusion and retraction. Values for $k_F^-,\,k_A^-,\,D_A$, same as Table 2.

Parameter	Value	Reference/Justification
F_{sat}	$1000\,\mu\mathrm{M}\mu\mathrm{m}$	Corresponds to $200\,\mu\mathrm{M}$ one-dimensional model in Table 2.
k_F^+	$0.224\,\mu\mathrm{Ms}^{-1}$	Corresponds to one-dimensional model with $\gamma_{pol}=1/2$
r_0	$240\,\mu\mathrm{m}^{-1}s^{-1}$	Reproduces period comparable to experiment for switch-like model.
r_2	$0.1\,\mu\mathrm{ms}^{-1}$	Corresponds to $60\,\mu\mathrm{Ms}^{-1}$ of Table 2.
v_r	$0.05\,\mu\mathrm{ms}^{-1}$	Typical retrograde flow rate in XTC cells [87].
n	10	Chosen for concave-down curve.
σ_0	$9.5\,\mu\mathrm{m}^{-1/2}\mathrm{s}^{-1/2}$	Same as the one-dimensional model.
αk_{mem}	$12\,\mu\mathrm{m}^{-2}$	Chosen for computational efficiency, Results are not sensitive to this value.
αS	1	Corresponds to membrane tension $S=1.5$ pN.

membrane protrusion. Actin polymerization rates peak during protrusion, leading to increases in F-actin at the membrane during those events. Accumulation of F-actin subsequently causes a reduction of the barbed end concentration, leading to retraction. Retrograde flow of the actin network distributes the F-actin throughout the lamellipodium over time. Combined with the periodic nature of the polymerization rate, this flow causes striping in the kymographs of Figure 8B.

Since the average value of B corresponds to $\gamma_{pol} = \frac{1}{2}$, fluctuations in B cause the system to switch between 0 (stall, resulting in retraction the speed of retrograde flow) and 1 (maximum polymerization rate, which is about twice the retrograde flow rate). The nonlinearity of the switch-like model around $\gamma_{pol} = \frac{1}{2}$ leads to a sharper change from protrusion to retraction as B fluctuates. Due to the weaker dependence of γ_{pol} on the barbed end concentration B and membrane force f_{mem} near $\gamma_{pol} = \frac{1}{2}$, the ratchet model produces smaller membrane distortions and membrane speeds compared to the switch-like model.

The standard deviation of membrane position depends on the magnitude of the membrane curvature force (Figure 8C). Membrane extension becomes small at the highest value of αS, indicating the increasing resistance of membrane tension to the formation of protrusions and retractions. The membrane shape and kymograph in Figure 8A,B are very similar to those observed experimentally (Figure 4A,B) with a value $\alpha S = 1$.

Similar to the one-dimensional model, the two-dimensional model produces short-range traveling waves of F-actin along the arc-length of the cell, which travel along both directions similar to experiment. For both the switch-like and ratchet models of actin polymerization, the cross-correlation of the total actin concentration and the leading edge velocity is similar to that calculated for experimental measurements of LifeAct-mCherry intensity and leading edge velocity in Figure 4E. The model also reproduces the same sequence of peaks in the cross-correlation, velocity autocorrelation, and LifeAct-mCherry intensity autocorrelation as in Figure 4E at around 100 s, which indicates the period of these signals.

5.3.3   Response of Leading Edge to Membrane Force Perturbation

The two-dimensional model generates predictions for the response of lamellipodia to changes in membrane forces. Circularly shaped XTC cells spread on a substrate transition from a state of stable non-oscillating lamellipodia to a transient state of large protrusions and retractions after treatment with blebbistatin [105]. During this response, the adhered cell surface area increases while no change in the retrograde flow rate within the lamellipodium can be detected. Ryan et al. [86] suggested that the transient reduction in membrane tension after blebbistatin [57] arising from the loss of contraction in the medial cell region, contributes to this behavior, in addition to other changes in biochemical reaction rates.
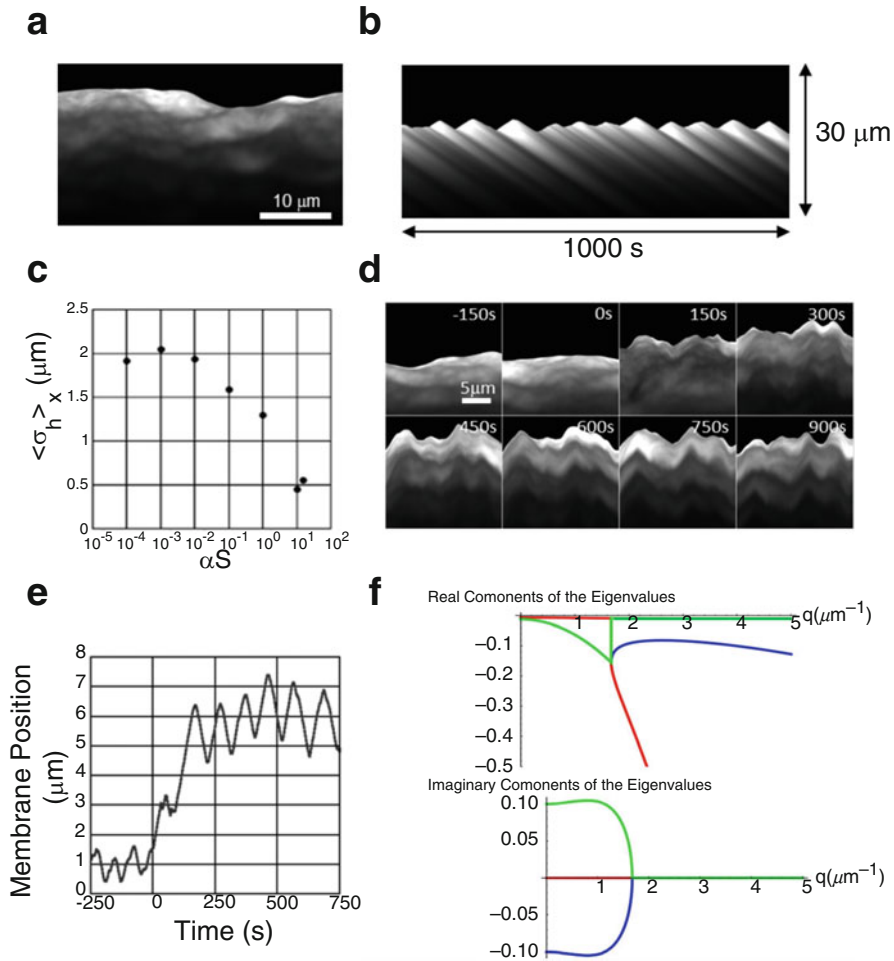
Fig. 8 Results of the 2D lamellipodium (switch-like case). Reproduced with permission from [86] (A) Snapshot for $\alpha S = 1$ with intensity representing F-actin. (B) Kymographs of the F-actin for the same simulation in A. (C) Average standard deviation of membrane position (average over all positions in simulation at steady state, over 500 s) vs membrane curvature force amplitude αS. (D) Simulation of lamellipodium response to global perturbation of membrane forces. Initial conditions same as panel A. At $t = 0$ the membrane force is reduced globally and αS reduced to 0.01. Simulations show the membrane expanding upwards, generating large protrusions and retractions after the perturbation. (E) Average position of leading edge over a 5-µm-wide region of panel D. (F) Linear stability analysis results for switch-like model. Top, real components of the eigenvalues vs wavenumber q. Bottom, imaginary components of eigenvalues. Units of vertical axes in 1/s.

A simulation of a lamellipodium undergoing a perturbation in membrane forces is shown in Figure 8D. Initial conditions were chosen such that the lamellipodium does not exhibit large protrusions and retractions (some fluctuations still remain). When the membrane curvature force and membrane area-conserving force are

reduced simultaneously, the leading edge extends by a few µm and large protrusions and retractions develop, similar to the experiment in [105] (Figure 8E).

In conclusion, both the one- and two- dimensional models predict that the lamellipodium can alternate between non-oscillating and oscillating states through perturbations that influence biochemical rates (Figure 7C) or membrane forces (Figure 8D).

5.3.4   Linear Stability Analysis

To interpret the numerical results, linear stability analysis was performed on Equations (42), (43), and (45) without noise, to study the stability of homogeneous sates in parameter space. The addition of noise during simulation then generates spontaneous excitations by perturbing the stable system. Defining $F_{tot}(x,t) = \int_{-\infty}^{h(x,t)} F(x, y, t)dy$, Equation (42) becomes

$$\frac{\partial F_{tot}(x, t)}{\partial t} = \gamma_{pol}(x, t) k_F^+ B(x, t) - k_F^- F_{tot}(x, t). \tag{50}$$

Assuming a homogeneous steady state (at which $\gamma_{pol} = \frac{1}{2}$ and using $h_{ref} = 0$ µm as the reference point) we find fixed points, $B(x, t) = B^*$, $F_{tot}(x, t) = F^*$, and $h(x, t) = h^*$. These values can be calculated numerically after setting the time derivatives in Equations (43) (without noise), (45) and (50) equal to zero. Considering sufficiently small perturbations around the fixed points and Fourier transforming $x \to q$, one has:

$$\begin{pmatrix} F_{tot} \\ B \\ h \end{pmatrix} = \begin{pmatrix} F^* \\ B^* \\ h^* \end{pmatrix} + J \begin{pmatrix} \delta F \\ \delta B \\ \delta h \end{pmatrix}. \tag{51}$$

The Jacobian J for the switch-like model is:

$$J = \begin{pmatrix} k_F^+ (n+2)/4 & -k_F^- & \frac{nk_F^+(\alpha k_{mem} - \alpha S q^2)}{4K_0} \\ 2B^* r_2 e^{-F^*/F_{sat}} - k_A^- D_A q^2 & \frac{-(r_0 + r_2 B^{*2})}{F_{sat}} e^{-F^*/F_{sat}} & 0 \\ v_R n/(2B^*) & 0 & \frac{v_R n(-\alpha k_{mem} - \alpha S q^2)}{2B^* K_0} \end{pmatrix}, \tag{52}$$

where $K_0 = \alpha k_{mem} h^*/B^*$ and was chosen to preserve the fixed point between both force-velocity models, so that $\gamma_{pol}^{switch} = \gamma_{pol}^{ratchet} = \frac{1}{2}$ occurs at the same fixed point (B^*, F^*, h^*) in both models. The Jacobian for the ratchet model can be calculated similarly.

Solving for the eigenvalues of J, one finds now three instead of two wave-number dependent eigenvalue. Similar to the one-dimensional model, the signs of their real and imaginary parts result in three Cases: (I) non-oscillatory behavior, (II) unstable

oscillatory behavior, and (III) a stable oscillatory behavior. Because the system gives bounded solutions, both cases II and III produce oscillatory behavior with a period given approximately by $\tau = 2\pi/\text{Im}[\lambda(q)]$. Similar to the one-dimensional model, this analysis showed that parameters can be chosen that result in the system being close to the boundary between linearly stable and unstable fixed points.

The stability of the homogeneous state depends on the wavenumber. The real and complex components of the eigenvalues as a function of wavenumber for the switch-like model (for the reference model parameter values) are shown in Figure 8F. For small wavenumbers, the eigenvalues correspond to Case III. With increasing wavenumber, the system progresses into Case I.

5.4 Discussion

This section highlighted how the mechanical and biochemical interactions combine nonlinearly to generate fluctuations in actin polymerization that drive lamellipodial protrusions. The near-constancy of retrograde flow in XTC cells allowed focusing on the kinetics of actin polymerization and force balance at the membrane.

Fluctuations in actin polymerization rate was also the basis of a model of waves in keratocytes [8]; however, these authors did not model explicitly the process of local membrane protrusion. The changing density of free barbed ends in the model of [8] is due to VASP which localizes on barbed ends, in the cytosol or in mature adhesions. A cooperative force-velocity curve similar to the switch model was implemented; however, unlike the model discussed in this chapter, a global constraint on membrane tension allowed only one protrusion to occur in the membrane at a time. Another related model where protrusions are driven by nucleation of new filaments is the one-dimensional model in [109, 110]. The actin network in this model consists of a semiflexible region close to the membrane and a gel like region consisting of cross-linked filaments further away.

Membrane protrusions coupled to an excitable biochemical network have also been studied in the context of *Dictyostelium* morphodynamics [41, 94]. These studies used versions of the phase field method to track movements of cell boundaries. In [94], the positive and negative feedbacks were due to PIP2 phosphorylation and PIP3 dephosphorylation while actin was not explicitly modeled. The model in [41] included a slow excitable system, reflecting the behavior of the signal transduction excitable network and a fast oscillatory system, reflecting the behavior of the cytoskeletal oscillatory network. Future modeling work could investigate in more detail the similarities between *Dictyostelium* and animal cells, combining the models of signal networks with models of cytoskeletal flows, moving cell boundaries and models of biophysical regulation of actin polymerization [37, 89].

References

1. Abraham, V.C., Krishnamurthi, V., Taylor, D.L., Lanni, F.: The actin-based nanomachine at the leading edge of migrating cells. Biophysical Journal **77**, 1721–1732 (1999)
2. Adler, Y., Givli, S.: Closing the loop: Lamellipodia dynamics from the perspective of front propagation. Phys Rev E Stat Nonlin Soft Matter Phys **88**(4 Pt 1), 042,708 (2013)
3. Alexandrova, A.Y., Arnold, K., Schaub, S., Vasiliev, J.M., Meister, J.J., Bershadsky, A.D., Verkhovsky, A.B.: Comparative dynamics of retrograde actin flow and focal adhesions: formation of nascent adhesions triggers transition from fast to slow flow. PloS One **3**, e3234 (2008)
4. Allard, J., Mogilner, A.: Traveling waves in actin dynamics and cell motility. Current opinion in cell biology **25**, 107–115 (2013)
5. Anderson, T.W., Vaughan, A.N., Cramer, L.P.: Retrograde flow and myosin ii activity within the leading cell edge deliver f-actin to the lamella to seed the formation of graded polarity actomyosin ii filament bundles in migrating fibroblasts. Molecular biology of the cell **19**, 5006–5018 (2008)
6. Aroush, D.R.B., Ofer, N., Abu-Shah, E., Allard, J., Krichevsky, O., Mogilner, A., Keren, K.: Actin turnover in lamellipodial fragments. Current Biology **27**, 2963–2973 (2017)
7. Bailly, M., Macaluso, F., Cammer, M., Chan, A., Segall, J.E., Condeelis, J.S.: Relationship between arp2/3 complex and the barbed ends of actin filaments at the leading edge of carcinoma cells after epidermal growth factor stimulation. The Journal of cell biology **145**, 331–345 (1999)
8. Barnhart, E.L., Allard, J., Lou, S.S., Theriot, J.A., Mogilner, A.: Adhesion-dependent wave generation in crawling cells. Current biology : CB **27**, 27–38 (2017)
9. Bernstein, B.W., Bamburg, J.R.: Adf/cofilin: a functional node in cell biology. Trends in cell biology **20**, 187–195 (2010)
10. Blanchoin, L., Boujemaa-Paterski, R., Sykes, C., Plastino, J.: Actin dynamics, architecture, and mechanics in cell motility. Physiol Rev **94**(1), 235–263 (2014)
11. Burnette, D.T., Manley, S., Sengupta, P., Sougrat, R., Davidson, M.W., Kachar, B., Lippincott-Schwartz, J.: A role for actin arcs in the leading-edge advance of migrating cells. Nature cell biology **13**, 371–381 (2011)
12. Cai, L., Makhov, A.M., Schafer, D.A., Bear, J.E.: Coronin 1b antagonizes cortactin and remodels arp2/3-containing actin branches in lamellipodia. Cell **134**, 828–842 (2008)
13. Campàs, O., Mahadevan, L., Joanny, J.F.: Actin network growth under load. Biophysical journal **102**, 1049–1058 (2012)
14. Carrero, G., Crawford, E., Hendzel, M.J., de Vries, G.: Characterizing fluorescence recovery curves for nuclear proteins undergoing binding events. Bulletin of mathematical biology **66**, 1515–1545 (2004)
15. Chan, A.Y., Raft, S., Bailly, M., Wyckoff, J.B., Segall, J.E., Condeelis, J.S.: Egf stimulates an increase in actin nucleation and filament number at the leading edge of the lamellipod in mammary adenocarcinoma cells. Journal of cell science **111 (Pt 2)**, 199–211 (1998)
16. Chan, C., Beltzner, C.C., Pollard, T.D.: Cofilin dissociates arp2/3 complex and branches from actin filaments. Current biology : CB **19**, 537–545 (2009)
17. Cirit, M., Krajcovic, M., Choi, C.K., Welf, E.S., Horwitz, A.F., Haugh, J.M.: Stochastic model of integrin-mediated signaling and adhesion dynamics at the leading edges of migrating cells. PLoS computational biology **6**, e1000,688 (2010)
18. Craig, E.M., Van Goor, D., Forscher, P., Mogilner, A.: Membrane tension, myosin force, and actin turnover maintain actin treadmill in the nerve growth cone. Biophysical journal **102**, 1503–1513 (2012)
19. Cramer, L., Briggs, L., Dawe, H.: Use of fluorescently labelled deoxyribonuclease i to spatially measure g-actin levels in migrating and non-migrating cells. Cytoskeleton **51**(1), 27–38 (2002)

20. Danuser, G., Allard, J., Mogilner, A.: Mathematical modeling of eukaryotic cell migration: insights beyond experiments. Annu Rev Cell Dev Biol **29**, 501–528 (2013)
21. Doubrovinski, K., Kruse, K.: Cell motility resulting from spontaneous polymerization waves. Physical review letters **107**, 258,103 (2011)
22. Driscoll, M.K., McCann, C., Kopace, R., Homan, T., Fourkas, J.T., Parent, C., Losert, W.: Cell shape dynamics: From waves to migration. PLoS Computational Biology **8**, e1002,392 (2012)
23. Edwards, M., Liang, Y., Kim, T., Cooper, J.A.: Physiological role of the interaction between carmil1 and capping protein. Mol Biol Cell **24**(19), 3047–3055 (2013)
24. Enculescu, M., Sabouri-Ghomi, M., Danuser, G., Falcke, M.: Modeling of protrusion phenotypes driven by the actin-membrane interaction. Biophysical journal **98**, 1571–1581 (2010)
25. Engelke, H., Heinrich, D., Rädler, J.O.: Probing gfp-actin diffusion in living cells using fluorescence correlation spectroscopy. Physical biology **7**, 046,014 (2010)
26. Fan, Y., Eswarappa, S.M., Hitomi, M., Fox, P.L.: Myo1c facilitates g-actin transport to the leading edge of migrating endothelial cells. J Cell Biol **198**(1), 47–55 (2012)
27. Fujiwara, I., Remmert, K., Hammer 3rd, J.A.: Direct observation of the uncapping of capping protein-capped actin filaments by carmil homology domain 3. J Biol Chem **285**(4), 2707–2720 (2010)
28. Fujiwara, I., Remmert, K., Piszczek, G., Hammer, J.A.: Capping protein regulatory cycle driven by carmil and v-1 may promote actin network assembly at protruding edges. Proc Natl Acad Sci U S A **111**(19), E1970–E1979 (2014)
29. Giannone, G., Dubin-Thaler, B.J., Döbereiner, H.G., Kieffer, N., Bresnick, A.R., Sheetz, M.P.: Periodic lamellipodial contractions correlate with rearward actin waves. Cell **116**, 431–443 (2004)
30. Giannone, G., Dubin-Thaler, B.J., Rossier, O., Cai, Y., Chaga, O., Jiang, G., Beaver, W., Döbereiner, H.G., Freund, Y., Borisy, G., Sheetz, M.P.: Lamellipodial actin mechanically links myosin activity with adhesion-site formation. Cell **128**, 561–575 (2007)
31. Gov, N.S., Gopinathan, A.: Dynamics of membranes driven by actin polymerization. Biophysical journal **90**, 454–469 (2006)
32. Hecht, I., Kessler, D.A., Levine, H.: Transient localized patterns in noise-driven reaction-diffusion systems. Physical review letters **104**, 158,301 (2010)
33. Heinemann, F., Doschke, H., Radmacher, M.: Keratocyte lamellipodial protrusion is characterized by a concave force-velocity relation. Biophysical journal **100**, 1420–1427 (2011)
34. Henty, J.L., Bledsoe, S.W., Khurana, P., Meagher, R.B., Day, B., Blanchoin, L., Staiger, C.J.: Arabidopsis actin depolymerizing factor4 modulates the stochastic dynamic behavior of actin filaments in the cortical array of epidermal cells. The Plant cell **23**, 3711–3726 (2011)
35. Higashida, C., Suetsugu, S., Tsuji, T., Monypenny, J., Narumiya, S., Watanabe, N.: G-actin regulates rapid induction of actin nucleation by mdia1 to restore cellular actin polymers. Journal of cell science **121**, 3403–3412 (2008)
36. Higgs, H.N., Pollard, T.D.: Regulation of actin filament network formation through arp2/3 complex: activation by a diverse array of proteins. Annual review of biochemistry **70**, 649–676 (2001)
37. Holmes, W.R., Edelstein-Keshet, L.: A comparison of computational models for eukaryotic cell shape and motility. PLoS computational biology **8**, e1002,793 (2012)
38. Hotulainen, P., Paunola, E., Vartiainen, M.K., Lappalainen, P.: Actin-depolymerizing factor and cofilin-1 play overlapping roles in promoting rapid f-actin depolymerization in mammalian nonmuscle cells. Molecular biology of the cell **16**, 649–664 (2005)
39. Hu, L., Papoian, G.A.: Mechano-chemical feedbacks regulate actin mesh growth in lamellipodial protrusions. Biophys J **98**(8), 1375–1384 (2010)
40. Hu, L., Papoian, G.A.: How does the antagonism between capping and anti-capping proteins affect actin network dynamics? J Phys Condens Matter **23**(37), 374,101 (2011)

41. Huang, C.H., Tang, M., Shi, C., Iglesias, P.A., Devreotes, P.N.: An excitable signal integrator couples to an idling cytoskeletal oscillator to drive cell migration. Nature cell biology **15**, 1307–1316 (2013)
42. Huber, F., Käs, J., Stuhrmann, B.: Growing actin networks form lamellipodium and lamellum by self-assembly. Biophys J **95**(12), 5508–5523 (2008)
43. Inagaki, N., Katsuno, H.: Actin waves: Origin of cell polarization and migration? Trends in cell biology **27**, 515–526 (2017)
44. Iwasa, J.H., Mullins, R.D.: Spatial and temporal relationships between actin-filament nucleation, capping, and disassembly. Curr Biol **17**(5), 395–406 (2007)
45. Ji, L., Lim, J., Danuser, G.: Fluctuations of intracellular forces during cell protrusion. Nature cell biology **10**, 1393–1400 (2008)
46. Kapustina, M., Vitriol, E., Elston, T.C., Loew, L.M., Jacobson, K.: Modeling capping protein frap and cali experiments reveals in vivo regulation of actin dynamics. Cytoskeleton (Hoboken) **67**(8), 519–534 (2010)
47. Kawska, A., Carvalho, K., Manzi, J., Boujemaa-Paterski, R., Blanchoin, L., Martiel, J.L., Sykes, C.: How actin network dynamics control the onset of actin-based motility. Proc Natl Acad Sci U S A **109**(36), 14,440–14,445 (2012)
48. Keren, K., Pincus, Z., Allen, G.M., Barnhart, E.L., Marriott, G., Mogilner, A., Theriot, J.A.: Mechanism of shape determination in motile cells. Nature **453**, 475–480 (2008)
49. Kiuchi, T., Nagai, T., Ohashi, K., Mizuno, K.: Measurements of spatiotemporal changes in g-actin concentration reveal its effect on stimulus-induced actin assembly and lamellipodium extension. J Cell Biol **193**(2), 365–380 (2011)
50. Kiuchi, T., Ohashi, K., Kurita, S., Mizuno, K.: Cofilin promotes stimulus-induced lamellipodium formation by generating an abundant supply of actin monomers. The Journal of cell biology **177**, 465–476 (2007)
51. Koestler, S.A., Rottner, K., Lai, F., Block, J., Vinzenz, M., Small, J.V.: F- and g-actin concentrations in lamellipodia of moving cells. PloS one **4**, e4810 (2009)
52. Lai, F.P.L., Szczodrak, M., Block, J., Faix, J., Breitsprecher, D., Mannherz, H.G., Stradal, T.E.B., Dunn, G.A., Small, J.V., Rottner, K.: Arp2/3 complex interactions and actin network turnover in lamellipodia. EMBO J **27**(7), 982–992 (2008)
53. Le Clainche, C., Carlier, M.F.: Regulation of actin assembly associated with protrusion and adhesion in cell migration. Physiological reviews **88**, 489–513 (2008)
54. Lee, C.W., Vitriol, E.A., Shim, S., Wise, A.L., Velayutham, R.P., Zheng, J.Q.: Dynamic localization of g-actin during membrane protrusion in neuronal motility. Curr Biol **23**(12), 1046–1056 (2013)
55. Lee, K., Elliott, H.L., Oak, Y., Zee, C.T., Groisman, A., Tytell, J.D., Danuser, G.: Functional hierarchy of redundant actin assembly factors revealed by fine-grained registration of intrinsic image fluctuations. Cell systems **1**(1), 37–50 (2015)
56. Lewalle, A., Fritzsche, M., Wilson, K., Thorogate, R., Duke, T., Charras, G.: A phenomenological density-scaling approach to lamellipodial actin dynamics. Interface Focus **4**(6), 20140,006 (2014)
57. Lieber, A.D., Yehudai-Resheff, S., Barnhart, E.L., Theriot, J.A., Keren, K.: Membrane tension in rapidly moving cells is determined by cytoskeletal forces. Current biology : CB **23**, 1409–1417 (2013)
58. Liu, X., Welf, E.S., Haugh, J.M.: Linking morphodynamics and directional persistence of t lymphocyte migration. Journal of the Royal Society, Interface **12** (2015)
59. Machacek, M., Danuser, G.: Morphodynamic profiling of protrusion phenotypes. Biophysical journal **90**, 1439–1452 (2006)
60. Mahaffy, R.E., Pollard, T.D.: Kinetics of the formation and dissociation of actin filament branches mediated by arp2/3 complex. Biophysical journal **91**, 3519–3528 (2006)
61. McGrath, J.L., Tardy, Y., Dewey Jr, C., Meister, J.J., Hartwig, J.H.: Simultaneous measurements of actin filament turnover, filament fraction, and monomer diffusion in endothelial cells. Biophys J **75**(4), 2070–2078 (1998)

62. McMillen, L.M., Vavylonis, D.: Model of turnover kinetics in the lamellipodium: implications of slow- and fast- diffusing capping protein and arp2/3 complex. Physical biology **13**, 066,009 (2016)

63. Meinhardt, H., Gierer, A.: Pattern formation by local self-activation and lateral inhibition. BioEssays : news and reviews in molecular, cellular and developmental biology **22**, 753–760 (2000)

64. Michalski, P.J., Carlsson, A.E.: The effects of filament aging and annealing on a model lamellipodium undergoing disassembly by severing. Phys Biol **7**(2), 026,004 (2010)

65. Millius, A., Watanabe, N., Weiner, O.D.: Diffusion, capture and recycling of scar/wave and arp2/3 complexes observed in cells by single-molecule imaging. J Cell Sci **125**(Pt 5), 1165–1176 (2012)

66. Miyoshi, T., Tsuji, T., Higashida, C., Hertzog, M., Fujita, A., Narumiya, S., Scita, G., Watanabe, N.: Actin turnover-dependent fast dissociation of capping protein in the dendritic nucleation actin network: evidence of frequent filament severing. J Cell Biol **175**(6), 947–955 (2006)

67. Mogilner, A., Edelstein-Keshet, L.: Regulation of actin dynamics in rapidly moving cells: a quantitative analysis. Biophys J **83**(3), 1237–1258 (2002)

68. Mogilner, A., Keren, K.: The shape of motile cells. Curr Biol **19**(17), R762–R771 (2009)

69. Mogilner, A., Oster, G.: Cell motility driven by actin polymerization. Biophysical journal **71**, 3030–3045 (1996)

70. Moraru, I.I., Schaff, J.C., Slepchenko, B.M., Blinov, M.L., Morgan, F., Lakshminarayana, A., Gao, F., Li, Y., Loew, L.M.: Virtual cell modelling and simulation software environment. IET Systems Biology **2**(5), 352–362 (2008)

71. Mullins, R.D., Heuser, J.A., Pollard, T.D.: The interaction of arp2/3 complex with actin: nucleation, high affinity pointed end capping, and formation of branching networks of filaments. Proceedings of the National Academy of Sciences of the United States of America **95**, 6181–6186 (1998)

72. Novak, I.L., Slepchenko, B.M., Mogilner, A.: Quantitative analysis of g-actin transport in motile cells. Biophys J **95**(4), 1627–1638 (2008)

73. Ohashi, K., Fujiwara, S., Watanabe, T., Kondo, H., Kiuchi, T., Sato, M., Mizuno, K.: Lim kinase has a dual role in regulating lamellipodium extension by decelerating the rate of actin retrograde flow and the rate of actin polymerization. The Journal of biological chemistry **286**, 36,340–36,351 (2011)

74. Oser, M., Condeelis, J.: The cofilin activity cycle in lamellipodia and invadopodia. Journal of cellular biochemistry **108**, 1252–1262 (2009)

75. Pack, C., Saito, K., Tamura, M., Kinjo, M.: Microenvironment and effect of energy depletion in the nucleus analyzed by mobility of multiple oligomeric egfps. Biophysical journal **91**, 3921–3936 (2006)

76. Padrick, S.B., Rosen, M.K.: Physical mechanisms of signal integration by wasp family proteins. Annual review of biochemistry **79**, 707–735 (2010)

77. Parsons, J.T., Horwitz, A.R., Schwartz, M.A.: Cell adhesion: integrating cytoskeletal dynamics and cellular tension. Nature reviews. Molecular cell biology **11**, 633–643 (2010)

78. Peskin, C.S., Odell, G.M., Oster, G.F.: Cellular motions and thermal fluctuations: the brownian ratchet. Biophysical journal **65**, 316–324 (1993)

79. Pollard, T.D., Blanchoin, L., Mullins, R.D.: Molecular mechanisms controlling actin filament dynamics in nonmuscle cells. Annu Rev Biophys Biomol Struct **29**, 545–576 (2000)

80. Pollard, T.D., Borisy, G.G.: Cellular motility driven by assembly and disassembly of actin filaments. Cell **112**(4), 453–465 (2003)

81. Pollard, T.D., Cooper, J.A.: Actin, a central player in cell shape and movement. Science **326**(5957), 1208–1212 (2009)

82. Ponti, A., Matov, A., Adams, M., Gupton, S., Waterman-Storer, C.M., Danuser, G.: Periodic patterns of actin turnover in lamellipodia and lamellae of migrating epithelial cells analyzed by quantitative fluorescent speckle microscopy. Biophysical journal **89**, 3456–3469 (2005)

83. Prass, M., Jacobson, K., Mogilner, A., Radmacher, M.: Direct measurement of the lamellipodial protrusive force in a migrating cell. The Journal of cell biology **174**, 767–772 (2006)

84. Raynaud, F., Ambühl, M.E., Gabella, C., Bornert, A., Sbalzarini, I.F., Meister, J.J., Verkhovsky, A.B.: Minimal model for spontaneous cell polarization and edge activity in oscillating, rotating and migrating cells. Nature Physics **12**, 367–373 (2016)
85. Ridley, A.J., Schwartz, M.A., Burridge, K., Firtel, R.A., Ginsberg, M.H., Borisy, G., Parsons, J.T., Horwitz, A.R.: Cell migration: Integrating signals from front to back. Science **302**(5651), 1704–1709 (2003)
86. Ryan, G.L., Holz, D., Yamashiro, S., Taniguchi, D., Watanabe, N., Vavylonis, D.: Cell protrusion and retraction driven by fluctuations in actin polymerization: A two-dimensional model. Cytoskeleton (Hoboken, N.J.) (2017)
87. Ryan, G.L., Petroccia, H.M., Watanabe, N., Vavylonis, D.: Excitable actin dynamics in lamellipodial protrusion and retraction. Biophys J **102**(7), 1493–1502 (2012)
88. Ryan, G.L., Watanabe, N., Vavylonis, D.: A review of models of fluctuating protrusion and retraction patterns at the leading edge of motile cells. Cytoskeleton (Hoboken, N.J.) **69**, 195–206 (2012)
89. Shao, D., Rappel, W.J., Levine, H.: Computational model for cell morphodynamics. Physical review letters **105**, 108,104 (2010)
90. Smith, B.A., Daugherty-Clarke, K., Goode, B.L., Gelles, J.: Pathway of actin lament branch formation by arp2/3 complex revealed by single-molecule imaging. PNAS **110**, 1285–1290 (2013)
91. Smith, M.B., Karatekin, E., Gohlke, A., Mizuno, H., Watanabe, N., Vavylonis, D.: Interactive, computer-assisted tracking of speckle trajectories in fluorescence microscopy: application to actin polymerization and membrane fusion. Biophys J **101**(7), 1794–1804 (2011)
92. Smith, M.B., Kiuchi, T., Watanabe, N., Vavylonis, D.: Distributed actin turnover in the lamellipodium and frap kinetics. Biophys J **104**(1), 247–257 (2013)
93. Svitkina, T.M., Borisy, G.G.: Arp2/3 complex and actin depolymerizing factor/cofilin in dendritic organization and treadmilling of actin filament array in lamellipodia. The Journal of cell biology **145**, 1009–1026 (1999)
94. Taniguchi, D., Ishihara, S., Oonuki, T., Honda-Kitahara, M., Kaneko, K., Sawai, S.: Phase geometries of two-dimensional excitable waves govern self-organized morphodynamics of amoeboid cells. Proceedings of the National Academy of Sciences of the United States of America **110**, 5016–5021 (2013)
95. Tardy, Y., McGrath, J.L., Hartwig, J.H., Dewey, C.F.: Interpreting photoactivated fluorescence microscopy measurements of steady-state actin dynamics. Biophysical journal **69**, 1674–1682 (1995)
96. Theriot, J.A., Mitchison, T.J.: Actin microfilament dynamics in locomoting cells. Nature **352**, 126–131 (1991)
97. Tsuji, T., Miyoshi, T., Higashida, C., Narumiya, S., Watanabe, N.: An order of magnitude faster aip1-associated actin disruption than nucleation by the arp2/3 complex in lamellipodia. PLoS One **4**(3), e4921 (2009)
98. Van Goor, D., Hyland, C., Schaefer, A.W., Forscher, P.: The role of actin turnover in retrograde actin network flow in neuronal growth cones. PloS one **7**, e30,959 (2012)
99. Vitriol, E.A., McMillen, L.M., Kapustina, M., Gomez, S.M., Vavylonis, D., Zheng, J.Q.: Two functionally distinct sources of actin monomers supply the leading edge of lamellipodia. Cell Rep **11**(3), 433–445 (2015)
100. Vitriol, E.A., Uetrecht, A.C., Shen, F., Jacobson, K., Bear, J.E.: Enhanced egfp-chromophore-assisted laser inactivation using deficient cells rescued with functional egfp-fusion proteins. Proc Natl Acad Sci U S A **104**(16), 6702–6707 (2007)
101. Watanabe, N.: Inside view of cell locomotion through single-molecule: fast f-/g-actin cycle and g-actin regulation of polymer restoration. Proc Jpn Acad Ser B Phys Biol Sci **86**(1), 62–83 (2010)
102. Watanabe, N., Mitchison, T.J.: Single-molecule speckle analysis of actin filament turnover in lamellipodia. Science **295**(5557), 1083–1086 (2002)
103. Wolgemuth, C.W.: Lamellipodial contractions during crawling and spreading. Biophysical journal **89**, 1643–1649 (2005)

104. Xiong, Y., Huang, C.H., Iglesias, P.A., Devreotes, P.N.: Cells navigate with a local-excitation, global-inhibition-biased excitable network. Proceedings of the National Academy of Sciences of the United States of America **107**, 17,079–17,086 (2010)
105. Yamashiro, S., Mizuno, H., Smith, M.B., Ryan, G.L., Kiuchi, T., Vavylonis, D., Watanabe, N.: New single-molecule speckle microscopy reveals modification of the retrograde actin flow by focal adhesions at nanometer scales. Mol Biol Cell **25**(7), 1010–1024 (2014)
106. Yamashiro, S., Mizuno, H., Smith, M.B., Ryan, G.L., Kiuchi, T., Vavylonis, D., Watanabe, N.: New single-molecule speckle microscopy reveals modification of the retrograde actin flow by focal adhesions at nanometer scales. Molecular biology of the cell **25**, 1010–1024 (2014)
107. Yang, C., Czech, L., Gerboth, S., Kojima, S.i., Scita, G., Svitkina, T.: Novel roles of formin mdia2 in lamellipodia and filopodia formation in motile cells. PLoS biology **5**, e317 (2007)
108. Zicha, D., Dobbie, I.M., Holt, M.R., Monypenny, J., Soong, D.Y.H., Gray, C., Dunn, G.A.: Rapid actin transport during cell protrusion. Science **300**(5616), 142–145 (2003)
109. Zimmermann, J., Falcke, M.: On the existence and strength of stable membrane protrusions. New Journal of Physics **15**(1), 015,021 (2013)
110. Zimmermann, J., Falcke, M.: Formation of transient lamellipodia. PloS one **9**, e87,638 (2014)

Intracellular Membrane Trafficking: Modeling Local Movements in Cells

Ritvik Vasan, Matthew Akamatsu, Johannes Schöneberg, and Padmini Rangamani

Abstract Cells constantly exchange material and information with their environment through a variety of trafficking mechanisms. Membrane trafficking encompasses a broad range of biological processes, all of which are characterized by the local deformation and movement of the plasma membrane. These movements are orchestrated by a complex protein machinery and cytoskeletal rearrangements. While different membrane trafficking pathways use different sets of proteins, mathematical and computational models have been used with great success to identify some of the governing physical principles. Here, we review the different theoretical and computational models of local movements in cells and the insights obtained from them. We will also highlight the challenges in the field and discuss future directions.

1 Introduction

Cell movement can be understood at many different length scales. The obvious large length scale movement is that of cell motility, crawling, or other behaviors where the length scales of the movements are of the order of the length scale of the cell itself and the velocity of the movement is rapid, often tens of microns per minute [128]. These movements are categorized by the dynamic remodeling of the actin cytoskeleton and the generation of a pushing velocity against the plasma

R. Vasan · P. Rangamani (✉)
University of California, San Diego, 9500 Gilman Dr, 92093 La Jolla, CA, USA
e-mail: rvasan@eng.ucsd.edu; prangamani@eng.ucsd.edu

M. Akamatsu · J. Schöneberg
Department of Molecular and Cell Biology, University of California, 94720 Berkeley, CA, USA
e-mail: matt.akamatsu@berkeley.edu; joh.schoeneberg@berkeley.edu

membrane on the leading edge and the contraction of the rear end due to actomyosin
contractility (Table 1). However, even in a nonmotile cell, there are plenty of local
movements that take place at much smaller length scales and allow for the regulating
intake and egress of cargo into and out of the cell (Figure 1).

Table 1 List of abbreviations.

| Notation	Description
BAR	Bin-amphiphysin-rvs
BDP	BAR domain proteins
CME	Clathrin-mediated endocytosis
CPP	Cell penetrating peptides
CLIC	Clathrin-independent carriers
GEEC	GPI-enriched early endosomal compartments
GEF	Guanine nucleotide exchange factor
GTP	Guanosine-5'-triphosphate
GDP	Guanosine diphosphate
ATP	Adenosine triphosphate
ADP	Adenosine diphosphate
NPF	Nucleation promoting factor
Sla2	Src-like-adaptor 2
CDC42	Cell division control protein 42 homolog
Arp2/3	Actin-related proteins 2/3
Hip1R	Huntingtin-interacting protein 1-related protein
ADF	Actin depolymerizing factor
COPII	Coat protein II
N-WASP	Neuronal Wiskott-Aldrich syndrome protein
WASP	Wiskott-Aldrich syndrome protein
AP-2	Adaptor protein 2
SNX-9	Sorting nexin 9
AA	All-atom
MD	Molecular dynamics
CGMD	Coarse-grained molecular dynamics
MS-CG	Multiscale-coarse graining
SBCG	Shape based coarse-graining
POPC	Phosphatidylcholine
POPS	Phosphatidylserine
MWCNT-FITC	Multi-walled carbon nanotube functionalized with fluorescein isothiocyanate
cEND	Cerebral endothelial
HMMM	Highly mobile membrane mimetic
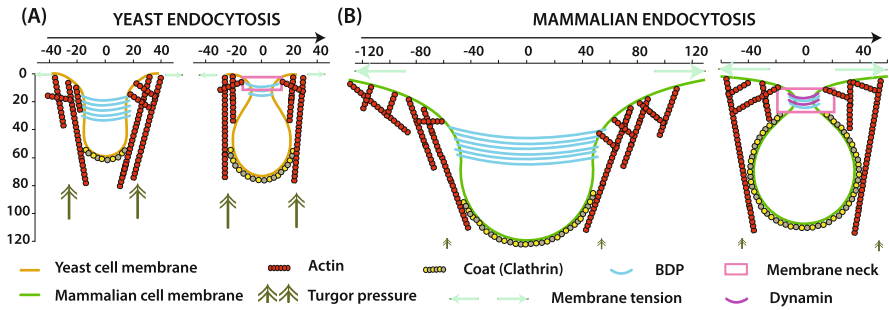
Fig. 1 Schematic of clathrin-mediated endocytosis in (A) yeast and (B) mammalian cells. Dimensions are in nanometer (nm). (A) Yeast endocytic buds have tubular necks that are generated by actin-mediated forces [63]. BAR (bin-amphiphysin-rvs)-domain proteins (BDPs) deform the membrane through protein-protein and lipid-protein binding [89]. (B) Mammalian endocytic buds have "U" or "Ω" shaped necks generated by clathrin and other proteins [123, 148]. Dynamin is required for scission in mammalian cells [49].

1.1 Membrane Trafficking as Local Movement

Membrane trafficking or vesicle trafficking refers to the movement of cargo, which can include proteins, lipids, and pathogens, across the plasma membrane from outside-in or inside-out. Vesicle trafficking has been a focus of intense study for the last four decades and multiple reviews [11, 123] and books [90, 121] have been dedicated to these processes. More recently James Rothman, Randy Schekman, and Thomas Südof received the Nobel Prize in 2013 for identifying the molecular components involved in cargo delivery, revealing an evolutionary relationship between the transport systems in yeast and mammalian cells [18, 143, 149]. Importantly, they also unraveled the precision and timing of the proteins involved in trafficking, which is critical to understanding many physiological disorders.

There are many different modes of trafficking, and protein-coated vesicles and the actin cytoskeleton play an important role in the movement of proteins and lipids [18, 64, 69, 99]. Irrespective of the pathway involved, the formation of these vesicles involves budding from one membrane followed by fusion with another membrane – movement of cargo into the cell is broadly termed endocytosis [84, 205] and movement of cargo towards the extracellular space is broadly termed exocytosis [92, 208]. Despite the complexity of timing, protein machinery, and lipid composition, these processes share common biophysical features – generation of membrane curvature [170], a morphological change, and fission/fusion, a topological change [48] – resulting in local movements within the cell (Figure 1).

1.2   Endocytosis

Endocytosis refers to the uptake of cargo from the extracellular *milieu* and can be broadly classified into two categories – clathrin-dependent and clathrin-independent endocytosis [90]. Clathrin-dependent endocytosis is the most widely studied form and has been characterized by five stages – endocytic patch nucleation, cargo selection, coat assembly, scission, and vesicle uncoating [123]. A range of proteins is involved in each stage from clathrin being central to coat assembly [148] to dynamin playing an important role during scission [49]. Curvature-inducing proteins, including BAR (bin-amphiphysin-rvs)-domain proteins (BDPs), are thought to sense and generate curvature, and couple the formation of the clathrin coat to the actin cytoskeleton through protein-protein binding [89]. Clathrin-independent endocytosis can be mediated through BAR-domain proteins through caveolins [103], macropinocytosis [74], and the CLIC/GEEC [76] (clathrin-independent carriers/GPI-enriched early endosomal compartments) pathways [79, 122]. Despite the diversity of mechanisms of endocytosis, it remains unclear how cargo selection proceeds and if the biophysical mechanisms are common to these different modes.

In addition to membrane curvature generation, actin polymerization is important for the progress of endocytosis. Actin remodeling at the endocytic patch provides the force required for the formation of tubular necks in endocytosis in yeast [63, 207] and for constriction of the neck [126, 230]. The particular role of actin in these two different cell types is still under investigation but we now know that in yeast cells, endocytosis will not occur in the absence of F-actin, while mammalian cells can be more flexible [11]. F-actin linkages are typically regulated through the Arp2/3 complex at the membrane and Huntingtin-interacting protein 1-related protein (Hip1R) at the clathrin coat [161]. Additionally, actin-associated motor proteins such as class I myosins also play a critical role in vesicle trafficking [96, 142]. Currently, there are three well-accepted models for force generation by myosin – *i*) membrane-bound myosin moves along existing F-actin [57], *ii*) myosin controls the organization of new F-actin [187], and *iii*) myosin leads to nucleation of new F-actin [11, 207]. Myosin is also known to respond to changes in membrane tension, thereby playing a critical role in communicating membrane tension to actin polymerization [108]. Thus, there is a mechanochemical feedback between the actomyosin machinery and the membrane during endocytosis.

Over the years there has been immense progress in our understanding of the molecular machinery underlying endocytosis [27, 51, 170], actin-membrane interactions [63, 73, 135, 221, 230], and the robust progression of endocytosis [79, 90, 122, 123]. However, there remain some fundamental gaps in our understanding of these processes. For instance, we still don't understand the role of lipid composition, actomyosin interactions, bulk fluid interactions with the membrane, and biochemical signaling in the progression of endocytosis. These open questions give rise to opportunities both in modeling and in experimental biology of trafficking. These are discussed in the perspectives section (Section 4).

1.3 Biophysical Modeling of Trafficking

Despite the particulars associated with each type of trafficking pathway, some common biophysical principles emerge as critical steps in their progression – membrane curvature sensing and generation by coat proteins, membrane bending, formation of a neck, and scission [51, 124]. Many of these steps lend themselves to mathematical and computational modeling to provide insight into the physical principles underlying each process and to generate experimentally testable hypotheses. The field of membrane modeling is a rich one and was pioneered by some of the early contributions by Helfrich and Canham more than four decades ago [33, 56, 83]. Since then, the advances in experiments and computational power have led to the development of detailed simulations of membrane trafficking. In this review, we focus on the role of mathematical and computational models in endocytosis and the insights gained from modeling, followed by a discussion on how these ideas can be extended to other trafficking processes.

2 Membrane Models of Endocytosis

Among all the participants in endocytosis, lipid bilayers and biological membranes have perhaps been the best-studied both theoretically and computationally. These models range from atomistic models of individual lipid rearrangements to large-scale bending models of the bilayer. It is easy to see why: lipids are amphiphilic molecules, are about 25 Å in length, and self-assemble to form a variety of mind-boggling structures geometrically and mechanically. But more than that, lipids are active participants in endocytosis. So how do the biophysical properties of lipid membranes and their interaction with membrane proteins regulate the endocytic pathway? We discuss the different modeling approaches, their advantages and disadvantages, and applicability in detail below (summarized in Table 2).

2.1 Atomistic Molecular Dynamics

At the atomistic scale, modeling the lipid bilayer requires a study of the proteins and lipids that constitute the cell membrane. Although experimental techniques such as grazing incidence and small angle X-ray scattering provide information on how lipid bilayers function at small length scale [127, 210, 226], obtaining complete information on lipid-lipid and lipid-protein interactions *in situ* remains a challenge. All-atom (AA) models can give insight into the detailed interactions between different conformations of atoms and can extract quantities such as solvation energy, heats of vaporization, spectroscopy data, and X-ray diffraction structures, to name a few. These models have also been used to extract the values of bending

Table 2 Membrane models in endocytosis.

Membrane model	Atomistic MD	Coarse-grained MD	Continuum
Advantages	*Computes detailed interactions between atoms. Extracts values and quantities like bending rigidity, lipid-bond orders, lipid-protein interactions, etc.*	*Simulates large systems of protein-lipid interactions by mapping individual atoms to coarse-grained beads. Achieves biologically relevant timescales.*	*Computationally inexpensive. Simulates large length scales of membrane deformation by approximating the lipid bilayer as a thin elastic shell.*
Limitations	*Computationally intensive. Cannot capture cellular length and time scales.*	*Choosing the nonessential degrees of freedom that can reduce computation time. Force fields may not be accurate enough.*	*Cannot capture smaller length scale deformations. Difficult to account for lipid and protein structures that alter the continuum properties of the membrane.*
Biological example	*A 250 ns AA simulation of membrane bending by single F-BAR domain proteins using the CHARMM27 force field [232].*	*A 200 micro CGMD simulation of membrane tubulation by multiple amphiphysin N-BAR domains, where each N-BAR dimer is represented by 50 CG beads [231].*	*A spontaneous curvature based Helfrich energy model of membrane bud formation during clathrin-mediated endocytosis [80].*

rigidity [100, 112, 233] and to study phase transitions in the bilayer [141, 213]. In recent years, atomistic simulations have been extended for studying more complex interactions such as protein-ligand interaction, protein folding, enzyme-binding, and protein-DNA interactions [29] and have successfully calculated realistic values for lipid bond orders, lipid-protein, and peptide-protein interactions [235] (Table 3).

2.1.1 The General Approach

The basis of atomistic models, similar to general molecular models, is to treat individual atoms in a classical sense, by integrating Newton's laws of motion in terms of potential energy functions. The governing equations for each particle can be written as

$$m_i \frac{\partial^2 r_i}{\partial t^2} = F_i, \tag{1}$$

$$F_i = -\frac{\partial U}{\partial r_i}, \ i = 1 \dots N, \tag{2}$$

Table 3 Notation used in all atom bilayer models.

Notation	Description	Units
U	Potential energy	$pN \cdot nm$
K	Kinetic energy	$pN \cdot nm$
N	Number of atoms	
N_{df}	Number of degrees of freedom	
r	Distance between atoms	nm
b	Bond length	nm
θ	Angle	
ϕ	Dihedral angle	
b^0	Equilibrium value of bond length	nm
θ^0	Equilibrium value of angle	
ϕ^0	Equilibrium value of dihedral angle	
k^θ	Force constant for bonds	pNnm
k^b	Force constant for angles	pN/nm
k^ϕ	Force constant for dihedrals	$pN \cdot nm$
u	Potential field	pNnm
T	Temperature	K

where m is the mass of an individual atom, N is the number of atoms, F is the force, and U is the potential energy of the system. An analytical solution is prohibitive since N atoms have $3N$ position coordinates (each atom is described by a set of Cartesian coordinates x, y, and z). To solve these equations numerically, an iterative scheme (finite-difference) is used such that the discrete time steps involved are typically no more than a few femtoseconds (10^{-15} s). Each time step updates the position and velocity of each atom and calculates a new force field. Since lipid molecules interact with water, including the solvent molecules is crucial to meaningful simulations. They are generally incorporated as either explicit or implicit boundary conditions. Explicit solvents can be incorporated as periodic boundary conditions while implicit solvents approximate the average effect of the solvent using mathematical models, which in turn reduces the number of degrees of freedom [55] (Figure 2).

Potential energy includes terms from bonded (atoms connected by a chemical bond) and nonbonded (atoms within a certain radius that experience van der Waals forces or electrostatic forces) interactions between any pair of atoms. Bonded interactions include terms for the angle, bond, and dihedral [212], while nonbonded interactions include pairwise interactions up to 2 body terms (three body interactions and higher are generally neglected) [7], simple examples of which are Lennard Jones potential and electrostatic interactions. Still, the number of pairwise interactions per atom is $N(N - 1)/2$, which requires large computation time. Mathematically, the potential energy due to both kinds of interactions can be written as

Fig. 2 Summary of basic equations in atomistic modeling.

> **Math box: Atomistic models**
>
> **Newton's laws**
>
> $m_i d^2 r_i / dt^2 = F_i$ $i = 1, 2 \ldots N$
>
> $F_i = -dU/dr_i$
>
> **Potential energy**
>
> $U(R)_{bonded} = \Sigma_{angles} 1/2 \, (k_{ijk}^\theta \, (\theta_{ijk} - \theta_{ijk}^0)^2)$
>
> $+ \, \Sigma_{bonds} 1/2 \, (k_{ij}^b \, (r_{ij} - b_{ij}^0)^2)$
>
> $+ \, \Sigma_{dihedrals} \, (k^\phi (1 + \cos(n(\phi - \phi^0))))$
>
> $U(R)_{non-bonded} = \Sigma_i \, u(r_i) + \Sigma_i \, \Sigma_{j>i} v(r_{ij}) + \ldots$

$$U(R)_{bonded} = \sum_{angles} \frac{1}{2} k_{ijk}^\theta (\theta_{ijk} - \theta_{ijk}^0)^2 + \sum_{bonds} \frac{1}{2} k_{ij}^b (r_{ij} - b_{ij}^0)^2$$

$$+ \sum_{dihedrals} k^\phi (1 + \cos(n(\phi - \phi^0))) \tag{3}$$

$$U(R)_{non-bonded} = \sum_i u(r_i) + \sum_i \sum_{j>i} v(r_{ij}) + \ldots, \tag{4}$$

where $R \in [1, 2, 3 \ldots N]$, r_{ij} is the distance between atoms i and j, k^θ, k^b, and k^ϕ are force constants for bonds, angles, and dihedrals, b^0, θ^0, and ϕ^0 are equilibrium values for bond lengths, angles, and dihedral angles and $u(r)$ is an externally applied potential field or effects due to the boundary wall [7, 29, 212]. These potential energy functions can be plugged into Equation (2) to calculate the force field. Some examples of force fields in the simulation of lipid bilayers are CHARMM [119] and GROMOS [179]. Kinetic energy for the system can be written as a function of temperature using

$$\frac{N_{df} kT}{2} = \frac{1}{2} \sum_i^N m \frac{\partial r_i}{\partial t} \frac{\partial r_i}{\partial t} = K(R), \tag{5}$$

where N_{df} is the number of degrees of freedom, T is temperature, and K is kinetic energy [29]. The total energy, which is sum of potential and kinetic energy, is conserved.

With the tremendous increase in computational capability, atomistic simulations are proving to be more impressive and realistic. Some of the most commonly used MD software packages are CHARMM [102], AMBER [220], GROMACS [216], Desmond [28], and NAMD [152]. Visual molecular dynamics (VMD) [87] is widely used for visualizing results from MD simulations. While the fundamental

physics behind MD is identical between the various packages, the choice of software package depends on the particular simulation or problem at hand. Some of the factors that need to be considered are the software features, computational efficiency, and the ability to reproduce the requisite protein-lipid interactions. For example, NAMD and GROMACS are generally computationally more efficient and thus faster [152, 216]. Often, atomistic systems are used as inputs to coarse-grained (CG) models, where the position of each CG bead is determined by taking the average of its constitutive atoms [118].

2.1.2 Applications to Endocytosis

Multiple groups have worked on using AA simulations to model complex biological processes such as membrane trafficking. Annex V trimer, a membrane-binding protein that is known to play an important role in trafficking, was modeled to bind to a POPC/POPS lipid bilayer using AA simulations incorporating the CHARMM27 force field [43]. From this work, the calcium bridge, hydrophobic interactions, and H-bond were found to be the main factors that control the protein-lipid binding. The same force field was also used to perform 250 ns AA simulations of membrane bending by single F-BAR domain proteins [232]. F-BAR domains are crucial to tubulation (the generation of a long cylindrical deformation) from an endocytic patch (Figure 1) and were found to curve membranes by a scaffolding mechanism [232]. Another member of the BAR domain family that has an N-terminal amphiphathic helix (N-BAR) was shown to curve membranes by binding completely to its concave surface [26, 151]. It was also shown to have a "curvature-sensing" ability – preferentially binding at angles that match the intrinsic curvature of the membrane [26]. This feature was experimentally shown in the *Drosophilia* amphyphysin BAR domain [151]. These results clarify the interdependence of proteins and membrane curvature during endocytosis at atomic length scales. More recently, 1,000 ps AA simulations using the Merck molecular force field tested the ability of multi-walled carbon nanotube functionalized with fluorescein isothiocyanate (MWCNT-FITC) to be a central nervous system targeted drug delivery system by directly releasing therapeutic or diagnostic cargo into the cytoplasm [186]. The study found that these carbon nanotubes were permeable to transport across microvascular cerebral endothelial (cEND) monolayers, providing evidence for a drug delivery mechanism.

While the length scales achievable in AA simulations are impressive, the time-scales are less so. This is especially evident when trying to capture the flow of membrane lipids using MD simulations, which are known to exhibit slow dynamics [16, 75, 145], requiring timescales of an order of magnitude more than the typical hundreds of nanoseconds. As we discuss later, the flow of lipids is closely coupled with membrane bending and deformations. An alternative approach called the highly mobile membrane mimetic (HMMM) model uses a combination of short-tailed lipids and biphasic solvents (selective fragmentation) [13, 145] to increase lipid diffusion within the bilayer by 1–2 orders of magnitude while maintaining

the precise description of protein-lipid interactions. The robustness of this method was demonstrated by capturing the insertion and binding of peripheral proteins into the membrane [145]. However, the limitation of the model is that mechanical parameters such as bending rigidity and area compressibility are only partially captured [145]. Despite these challenges, the potential to incorporate lipid diffusion into membrane models of endocytosis presents an exciting opportunity.

2.2 Coarse-Grained Molecular Dynamics

Interactions between different protein and lipid chains occur over a wide range of time and length scales, making all-atom simulations impractical for studying problems at the cellular length and time scales. Coarse-grained molecular dynamics (CGMD) models allow for simulating large systems of protein-lipid interactions at biologically relevant timescales by approximating the energetics of these interactions [200].

2.2.1 The General Approach

The general approach involves mapping individual atoms to coarse-grained/ mesoscopic "beads," which redefines the length scale of the system, makes computation faster, and achieves impressive levels of complexity. An example of this complexity can be seen in a recent work that simulates a cell membrane with nearly 20,000 lipids and 63 lipid species [88]. This idealized model of the mammalian plasma membrane showed a larger distribution of cholesterol on the outer leaflet while also detailing the diffusion rates and ordering of the lipids. Interestingly, they identify that the lipids are heterogeneously mixed without any clear phase separation, potentially providing some insight into the much-debated lipid raft hypothesis [31, 88, 188, 189]. Lipid rafts are dynamic, fluctuating nanodomains in cellular membranes that are thought to serve as signaling platforms [113, 190]. Recent reviews such as [29, 82] have focused on coarse-grained models and their application to protein-membrane and lipid-protein interactions. At the core of the CG model is the length scale, degrees of freedom being considered, and the property that is sought to be reproduced. Broadly, they can be divided into structure-based [136], force-based [223], and energy-based [120] (MARTINI) force fields that aim to reproduce the geometry, force distribution, and thermodynamics, respectively [29].

A major challenge with coarse-graining is choosing the important degrees of freedom that can reduce computation time without losing other important degrees of freedom. To tackle this, multiscale [91] and mixed-resolution [185] models have been developed. The multiscale-coarse graining method (MS-CG) combines an atomistic approach with coarse-grained simulations. It uses the atomistic trajectory from an atomistic simulation as an input to calculate the coarse-grained force field

in a force matching approach. Subsequently, this model was used to develop mixed all-atom and coarse-grained (AA-CG) [185] models that favorably compared to all-atom simulation results.

Models that bridge the gap between the quantum scale and other larger length scales have also been developed. In 2013, the Nobel Prize in chemistry was awarded to Michael Levitt, Ariel Warshel, and Martin Karplus for their work on developing multiscale models for complex chemical systems by combining a quantum chemical model at the core region with a classical model at the larger surroundings.

2.2.2   Applications to Endocytosis

The MARTINI force field is one of the most widely used explicit solvent coarse-grained models. It is based on a four-to-one mapping, where four heavy atoms are represented by one interaction center [120]. Nonbonded interactions are represented by a shifted Lennard Jones potential. The MARTINI model has been extended to include proteins [133] and has been used to study complex biological systems that simulate vesicle fusion and fission. For example, polyunsaturated phospholipids were shown to aid endocytosis by increasing the ability of dynamin and endophilin to deform the membrane [155]. In another study, the internalization of polyarginine peptides (R8) was shown to be affected by membrane tension [81]. R8 peptides are a class of cell-penetrating peptides (CCPs) known to penetrate the membrane through endocytic and non-endocytic means [68]. More recently, MARTINI-based MD combined with Monte Carlo simulations were used to study the metastability of lipid nanotubes, commonly seen in the endoplasmic reticulum [17]. A force-field based on a ten-to-one mapping instead of the four-to-one mapping seen in MARTINI named as the shape based coarse-grained (SBCG) method was developed in [15]. Figure 3 shows a SBCG simulation of membrane tubulation by N-BAR domains [231].

Another popular CG force field is GROMOS [146], where aliphatic CH_n groups are represented as a united atom. A recent model using a 50 ns MD simulation incorporating the GROMOS96 force field parameter set could track Rab21 and guanine nucleotide exchange factor (GEF) exchanges [183]. Rab21 belongs to the Rab family of proteins and plays an important role in vesicle trafficking [206]. The study found that GTP-bound Rab21 is more stable than the GDP-bound form and attributed it to the activation of the protein, potentially aiding in the development of anti-cancer therapeutics [183]. Another study of the influenza virus fusion peptide (FP), which is known to insert into the host membrane during fusion, adopted a CGMD simulation employing the GROMOS54A7 force field to show that the influenza FP has a substantial effect on the model bilayer and that it can adopt two configurations – a membrane-spanning configuration and an interfacial configuration [218].

Using the multiscale approach, a study of the effect of N-BAR domain proteins on membrane curvature found that the N-BAR domain proteins assemble into linear aggregates resulting in large endocytic bud-like formations [192]. The same group
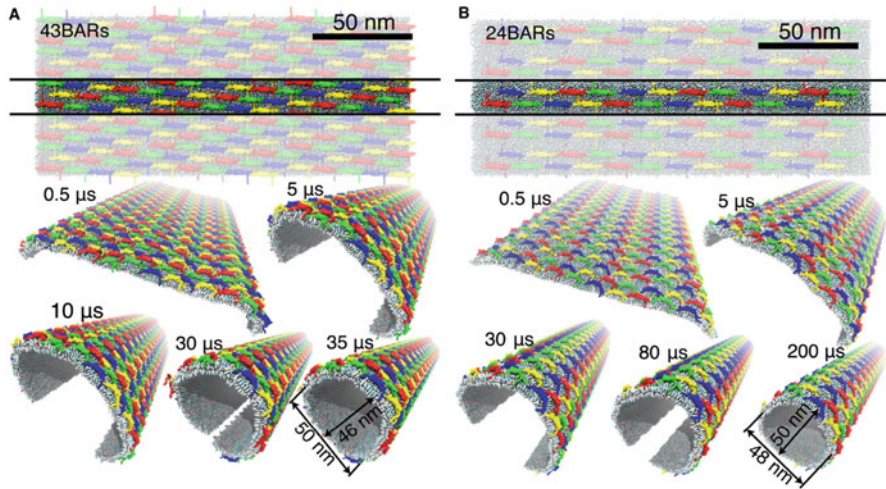
Fig. 3 Coarse-grained molecular dynamics (CGMD) simulations of tubulation of a 200 nm planar sheet of membrane induced by multiple amphiphysin N-BAR domains; figure from [231] (pending permission). Each N-BAR dimer is represented by 50 CG beads [15] and is colored as blue, green, yellow, and red. The membrane begins to bend from the edge at 0.5 μs and achieves complete tubulation between 30 and 200 μs [231]. Here, (A) and (B) are two independent simulations of 43 and 24 BAR domain proteins, respectively [231].

of researchers also analyzed the role of membrane tension in the recruitment of N-BAR domain proteins, finding that high tension inhibits protein interactions [191]. Direct experimental validation of the predictions from these simulations remains a challenge because of experimental resolution; a detailed review of the issues associated with experimental validation can be found in [78].

2.3 Continuum Treatment of the Lipid Bilayer

Continuum models treat the lipid bilayer as a thin elastic shell by assuming that the membrane curvature is much larger than the thickness of the bilayer [137]. This field traces its history back to a set of papers written in the 1970s – three main papers by Helfrich [83], Canham [33], and Jenkins [95] and the impact of this line of modeling is evident simply from a PubMed or Google scholar search for Helfrich energy. The most widely used continuum model is the Helfrich-Canham energy model [83], which proposes the free energy of a membrane as a function of its principal curvatures.

2.3.1 The General Approach

In its most basic form, for a homogenous membrane, the Helfrich energy can be written as

$$W = \kappa H^2 + \kappa_G K, \tag{6}$$

where W is the free energy density (per unit area), κ is the bending modulus, H is the mean curvature, κ_G is the Gaussian modulus, and K is the Gaussian curvature. We note here that Equation (6) differs from the standard Helfrich energy equation by a factor of 2, accounted for by using a κ that is twice the standard value. The typical value for κ is $\sim 20\,k_B T$ while the Gaussian modulus is a matter of significant debate [55, 105]. This is because the use of the Gauss Bonet theorem states that the term with Gaussian curvature in Equation (6) is a topological constant and appears only in boundary conditions [41, 55], so that the energy is invariant to the Gaussian modulus except in the boundary condition. Despite this, the Gaussian term is known to play an important role in phase separation, as shown in [19]. Here, the researchers calculated a ratio of bending moduli between lipid ordered and disordered phases of a GUV as $\kappa^{L_o}/\kappa^{L_d} \sim 5$ and a difference in Gaussian moduli as $(\kappa_G^{L_d} - \kappa_G^{L_o})/\kappa_{L_d}$ ~ 3.6.

The energy functional (Equation 6) can be plugged into the equilibrium equations obtained using elastic Kirchoff Love theory through variational principles [95, 137, 201, 202]. These equilibrium equations are first written out as a local force balance, given by (see Table 4 for notation)

$$\nabla \cdot \boldsymbol{\sigma} + p\mathbf{n} = \mathbf{f}, \tag{7}$$

where $\nabla\cdot$ is the surface divergence, $\boldsymbol{\sigma}$ is the stress tensor, p is the pressure difference between the inside and outside of the volume bounded by the membrane, and $\mathbf{f}$ is any externally applied force per unit area on the membrane [201]. The surface stresses in Equation (7) can be decomposed into normal and tangential components as

$$\sigma^\alpha = T^\alpha + S^\alpha \mathbf{n}, \tag{8}$$

where

$$\mathbf{T}^\alpha = T^{\alpha\beta}\mathbf{a}_\beta, \qquad T^{\alpha\beta} = \sigma^{\alpha\beta} + b_\mu^\beta M^{\mu\alpha}, \qquad S^\alpha = -M_{;\beta}^{\alpha\beta}. \tag{9}$$

The two tensors $\sigma^{\alpha\beta}$ (stress resultants) and $M^{\alpha\beta}$ (couple resultants) can be expressed by the derivative of F, the energy per unit mass, with respect to the coefficients of the first and second fundamental forms, $a_{\alpha\beta}$, $b_{\alpha\beta}$, respectively [165, 201] as

Table 4 Notation used in continuum models of lipid membranes.

Notation	Description	Units
E	Strain energy	pN $\cdot$ nm
γ	Lagrange multiplier for incompressibility constraint	pN/nm
p	Pressure difference across the membrane	pN/nm^2
σ	Surface stress tensor	pN/nm
C	Spontaneous curvature	nm^{-1}
D	Lipid bilayer thickness	nm
A	Mean area of the lipid monolayers	nm^2
ΔA	Global area difference between the monolayers	nm^2
ΔA_0	Area difference for the unstressed monolayers	nm^2
θ^α	Coordinates describing the surface	
W	Local energy per unit area	pN/nm
$\mathbf{r}$	Position vector	
$\mathbf{n}$	Normal to the membrane surface	unit vector
$\boldsymbol{\nu}$	Tangent to the membrane surface in direction of increasing arc length	unit vector
$\boldsymbol{\tau}$	Rightward normal in direction of revolution	unit vector
$\mathbf{a}_\alpha$	Basis vectors describing the tangent plane	
$a_{\alpha\beta}$	First fundamental form	
$b_{\alpha\beta}$	Second fundamental form	
β	Degree of ordering parameter	
λ	Membrane tension, $-(W + \gamma)$	pN/nm
H	Mean curvature of the membrane	nm^{-1}
K	Gaussian curvature of the membrane	nm^{-2}
κ	Bending modulus (rigidity)	pN $\cdot$ nm
κ_G	Gaussian modulus	pN $\cdot$ nm
s	Arc length	nm
θ	Azimuthal angle	
ψ	Angle between $\mathbf{e}_r$ and $\mathbf{a}_s$	
r	Radial distance	nm
z	Elevation from base plane	nm
$\mathbf{e}_r(\theta)$	Radial basis vector	unit vector
$\mathbf{e}_\theta$	Azimuthal basis vector	unit vector
$\mathbf{k}$	Altitudinal basis vector	unit vector
$\mathbf{f}$	Applied force per unit area	pN/nm^2
τ	Surface twist	nm^{-1}
M	Bending couple	pN $\cdot$ nm

Fig. 4 Summary of basic equations in continuum modeling.

$$\sigma^{\alpha\beta} = \rho\left(\frac{\partial F(\rho, H, K; x^\alpha)}{\partial a_{\alpha\beta}} + \frac{\partial F(\rho, H, K; x^\alpha)}{\partial a_{\beta\alpha}}\right), \tag{10}$$

$$M^{\alpha\beta} = \frac{\rho}{2}\left(\frac{\partial F(\rho, H, K; x^\alpha)}{\partial b_{\alpha\beta}} + \frac{\partial F(\rho, H, K; x^\alpha)}{\partial b_{\beta\alpha}}\right). \tag{11}$$

Here, ρ is the density of the membrane. The lipid bilayer has a high stretch modulus [86] and can be treated as effectively incompressible. Applying area incompressibility (requiring that the Jacobian J = 1) constraint using a Lagrange multiplier field [201], Equations (11, 7, 8, and 9) can be simplified to give the equations in normal (shape equation) and tangential direction as

$$p + \mathbf{f} \cdot \mathbf{n} = \Delta\frac{1}{2}W_H + (W_K)_{;\alpha\beta}\tilde{b}^{\alpha\beta} + W_H(2H^2 - K) + 2H(KW_K - W) - 2\lambda H, \tag{12}$$

and

$$N^{\beta\alpha}_{;\alpha} - S^\alpha b^\beta_\alpha = -(\gamma_{,\alpha} + W_K k_{,\alpha} + W_H H_{,\alpha})a^{\beta\alpha} = \left(\frac{\partial W}{\partial x^\alpha_{|exp}} + \lambda_{,\alpha}\right)a^{\beta\alpha} = -\mathbf{f} \cdot \mathbf{a}_s. \tag{13}$$

Here $()_;$ denotes the covariant derivative, $\tilde{b}^{\alpha\beta}$ denotes the contravariant cofactor of the curvature, $\Delta(\cdot)$ is the surface Laplacian (the Laplace-Beltrami operator), $()_{|exp}$ denotes the explicit derivative respect to coordinate θ^α, and $\mathbf{f} \cdot \mathbf{a}_s$ denotes the dot product of $\mathbf{f}$ with the tangent. For a more detailed derivation, see [95, 137, 201, 202] (Figure 4).

Equations (12 and 13) together constitute a boundary value problem that can be solved using an appropriate choice of surface parameterization (Monge, axisymmetry, etc.). To fully define the system, boundary conditions need to be

determined. However, these boundary terms only play an important role when the system under consideration is not a closed system as the energy required to maintain the edge is large [95]. Otherwise, edge conditions can simply be derived from a mechanical power balance between the energy of the film and the forces and moments at the surface boundary [165, 202] and are given by

$$\bar{\mathbf{f}} = \mathbf{T}^\alpha \nu_\alpha - (\mathbf{M}^{\alpha\beta} \tau_\alpha \nu_\beta n)' \quad \text{(distributed force on the edge)}, \tag{14}$$

$$\mathbf{M} = \mathbf{M}^{\alpha\beta} \nu_\alpha \nu_\beta \quad \text{(distributed bending couple on the edge)}, \tag{15}$$

where

$$\boldsymbol{\nu} = \nu_\alpha a^\alpha \quad \text{is the unit normal with the exterior}, \tag{16}$$

$$\boldsymbol{\tau} = n \times \boldsymbol{\nu} \quad \text{is the unit tangent}. \tag{17}$$

Since 1975, the model has been further expanded to account for membrane heterogeneity through spontaneous curvature, lateral stretching, and lipid tilt. Spontaneous curvature represents the intrinsic membrane curvature and asymmetry across the leaflets of the bilayer. It can be incorporated into the Helfrich energy as [167, 201]

$$W = \kappa (H - C(\theta^\alpha))^2 + \kappa_G K, \tag{18}$$

where C is the spontaneous curvature field along θ^α, the position coordinates. Effectively, spontaneous curvature captures the curvature at which the bending energy is minimized and is now used to represent the asymmetry between the lipid bilayers either due to the shape of the lipid [211, 236] or due to protein-induced bilayer asymmetry [167, 169].

The lateral stretching/area difference elasticity (ADE) [181] model incorporates the relative stretching and compression of the monolayers against each other and the energy functional for this is written as

$$E = \kappa \int (H - C(\theta^\alpha))^2 dA + \kappa_G \frac{\pi}{AD^2} (\Delta A - \Delta A_0)^2, \tag{19}$$

where E is the free energy (not to be confused with W, which is the free energy density or free energy per unit area), D is bilayer thickness, ΔA is the global area difference between the monolayers, ΔA_0 is the area difference for the unstressed monolayers, and A is the mean area of the monolayers [60, 181]. The second term in Equation (19) accounts for the area difference with respect to the relaxed state.

The lipid tilt model integrates two tilt director fields corresponding to each monolayer [182] and is an important outcome of lipid packing and frustration in biological processes such as vesicle fusion and scission. The notion of lipid tilt as an important physical variable for regulating membrane mechanics is supported by experiments in DPPC bilayers that determine a tilt angle of 32 ± 0.5 at $19°C$ [214].

Studies such as [138] argue for the need to include a secondary term for the tilt modulus in addition to the bending modulus. They do this by obtaining comparable values of bending moduli using theory, experiments, and simulation. The effect of monolayer tilt is to add an anisotropic curvature term to the energy density

$$W^{\pm} = \beta b_{\alpha\beta} m_{\pm}^{\alpha} m_{\pm}^{\beta}, \tag{20}$$

where "+" and "−" are the two monolayers (chosen such that the normal points from "−" to "+" side), m_{+} and m_{-} are tangent vector fields to each monolayer surface (describing the tilt), $b_{\alpha\beta}$ is the curvature tensor, and β is a new parameter depending on the degree of ordering [182]. Each monolayer has its own spontaneous curvature, stretch, and bending modulus [182]. The mathematics of such an implementation gets significantly more complex as discussed in [163, 166, 203].

2.3.2 Applications to Endocytosis

Continuum models have been applied to the study of various trafficking processes. The basic form of the Helfrich formulation (Equation 19) has widely been applied to the simulation and modeling of membrane tubules, which are commonly seen as long-lived connections between a vesicle and the membrane [42, 61, 180] during endocytosis. These membrane tethers are modeled by applying a point force to a flat membrane patch, mimicking the function of cellular motor proteins [173]. An important study by Derenyi [54] first showed the dependence of this point force on the membrane tension and bending rigidity. By plotting the equilibrium shapes of these tubes under an applied point force, they were also able to identify a neck region – now an area of active research both theoretically and experimentally. An analysis of a bilayer lipid membrane tubule stretched between two coaxial end rings as a model for the connection between a vesicle and the membrane during endocytosis further showed the existence of a bistability or a sudden breakage of the membrane connection [66]. This instability was shown by modeling the membrane tubule as a catenoid or a cylinder, an accepted model shape of the membrane neck [125].

The spontaneous curvature model (Equation 18) is another widely used continuum description of membrane remodeling in cellular processes. The versatility of this model is evident from the broad range of applications ranging from vesicle behaviors to endocytosis in cells. Early works dating back to the 1970s have successfully and extensively been used to study vesicle shapes [56, 104, 181]. Famously, the spontaneous curvature model explained the biconcave disc shape of red blood cells [56]. A few papers have also evaluated externally applied forces and line tensions of membranes in different biological contexts [6, 19, 109]. More recent studies have focussed on the effect of membrane tension, actin forces, and bending rigidity on vesiculation during endocytosis in a multivariate framework [80]. Actin forces specifically have been shown to induce instabilities during endocytosis and these instabilities can be stabilized to a finite extent by BAR proteins [219].

The area difference between the monolayers of a lipid membrane has also been used to study various aspects of endocytosis. A study of nanoparticle trafficking through asymmetric model membranes was recently performed in the context of both receptor-mediated and clathrin-mediated endocytosis [3]. This study derives relationships between nanoparticle size and membrane properties such as adhesion strength and spontaneous curvature. An understanding of these parameters can be crucial for applications such as drug delivery and intracellular sensing. The effect of shape and size of nanoparticles in endocytosis was further analyzed in [234]. Here, nanodiamonds (NDs) were classified into prickly (sharp edges) and round (smooth). Smooth NDs were found to internalize more in experiments. Continuum models suggested that factors like energy penalty of anchoring and surface area of contact could be responsible for the increased internalization of round NDs [234]. Nonspherical nanoparticle trafficking during the drug delivery of natural (viruses) and artificial (biomimetic) particles in receptor-mediated endocytosis has also been modeled [53]. This study identifies three distinct endocytic phases – no wrapping, partial wrapping or frustrated endocytosis, and complete wrapping (leading to endocytosis) based on the aspect ratio of the particle being engulfed [53].

Lipid tilt models are useful for the calculation of parameters such as line tension [107]. Studies such as [107] have also used the tilt model to predict domains of lipid raft formation, a debatable region of the lipid membrane that is thicker than its surroundings [31, 188, 189]. A 1D form of the lipid tilt model was applied to protein adsorption onto membranes in order to capture dynamics at the length scale of the bilayer thickness [166]. The results obtained using this model were favorably compared to CG simulations showing that the effect of lipid tilt due to protein insertion is of the same order of magnitude as the thickness of the bilayer. A more complex tilt model based on 3D liquid crystal theory has also been developed [203] and applied to the analysis of ripple phases and small deviations from the plane [163].

3 Modeling Membrane-Cytoskeleton Interactions in Endocytosis

Actin is one of the most abundant proteins in eukaryotic cells and actin filaments play an important role in coordinating functions such as intracellular membrane trafficking and cell motility [32, 158]. The directional polymerization of actin, coupled with severing, branching, and capping, gives rise to a multitude of actin structures that are implicated in a variety of cellular processes (Figure 5). Indeed, actin-membrane interaction is a workhorse of intracellular force generation [65]. Multiple reviews have focussed on the function of actin polymerization in endocytic vesicle formation [40, 73, 99, 115]. Actin is known to play important roles during internalization of the protein coat and subsequently in constriction and scission
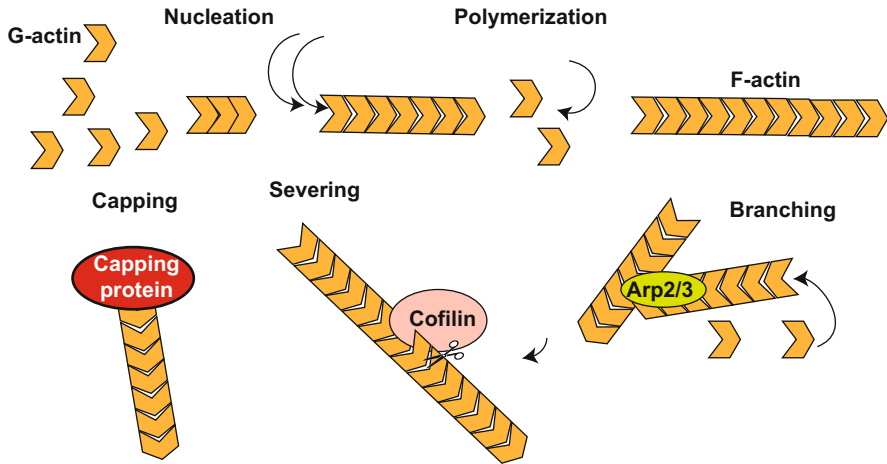
Fig. 5 Schematic of key actin remodeling events for single filaments. Actin is a directional polymer; monomeric actin or G-actin is shaped like an arrowhead and the polymerization rates are higher for the addition of monomers at the barbed end rather than the pointed end. Filaments can undergo capping, severing, or branching depending on the particular actin modulator.

events [97–99]. In mammalian cells, the actin cytoskeleton is necessary to maintain membrane tension during many cellular functions [47, 58]. Recent experimental evidence suggests that actin-generated forces during CME can function as a constricting force in a collar at the base (in yeast) [44, 80] or as an inward force with the actin network attached to the coat [80, 153]. In yeast endocytosis, branched actin structures exist as a cortical patch around the membrane invagination and are essential for endocytosis [171]. Membrane-cytoskeleton adhesion is also known to affect this force generation capacity [184].

One way to model the effect of actin and myosin is to consider it as an active force **f** in a Helfrich based continuum model, as described previously in Equation (7). The free energy of the system is then given by Equations (12 and 13). Early studies used an axial point force as a proxy for the actin polymerization force to model membrane tubulation or tether formation [54]. In cells with turgor pressure, a closer match between simulation profiles and experimentally observed shapes of tether formation was obtained by incorporating the effect of pressure in addition to the axial point load [59]. More recently, studies have also emphasized the role of actin forces (both axial and radial) in mediating snap-through instabilities during CME [80]. A snap-through instability occurs when the membrane that is in one equilibrium state must jump to another equilibrium state as a control parameter changes because the first equilibrium state either becomes unstable or ceases to exist [72]. Figure 6 shows the orientations of these actin forces in a schematic and Figure 7 shows a few example shapes obtained from a simulation of CME in the presence of these forces. Figure 7(A) shows the formation of a U-shaped invagination with increasing area of the protein coat. Figure 7(B) shows the response of this U shaped membrane to
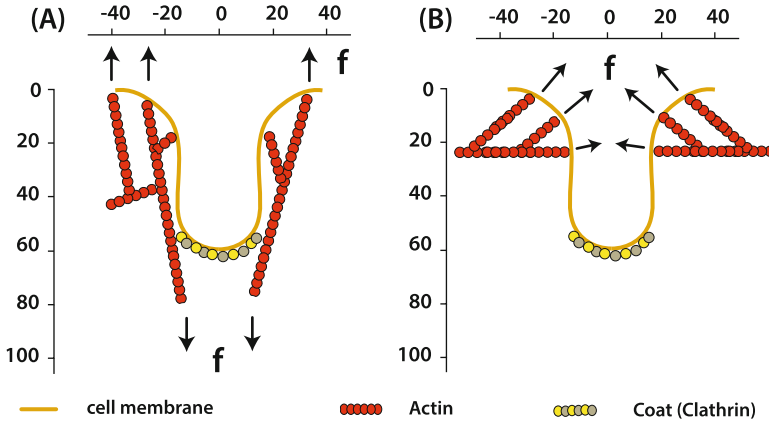
Fig. 6 Schematic of actin force orientation along a yeast cell membrane [80, 97, 153]. Dimensions are in nanometer (nm). (A) Actin network is attached to protein coat and forms a cone-shaped structure of interlinked filaments. Actin polymerization at the membrane assembles in the shape of a ring. It exerts a net inward force [153]. (B) Actin network exerts a constricting force at the neck by forming a collar [97].

applied axial forces (orientation shown in Figure 6(A)) and Figure 7(C) shows the response of the U-shaped membrane to radial forces (orientation in Figure 6(B)). Interestingly, increasing coat rigidity drastically reduced the actin force required to invaginate the membrane [80], suggesting a close relationship between bending rigidity, actin forces, and phase separation. We note here that all membrane shapes obtained using the continuum model are at mechanical equilibrium and are thus snapshots of "pseudo" time, which we discuss in the perspectives section (Section 4). The phase separation can be incorporated as a line tension at the interface that reduces the energy of the phase boundary [114]. Indeed, this approach has been used to compute equilibrium membrane shapes of vesicle formation in yeast endocytosis generated by the coordinated action of actin surface forces and protein-induced lipid phase separation [114]. The study found that this concerted action is sufficient for scission. However, there still remain many unanswered questions with respect to actin dynamics at endocytic sites – how does actin assemble and disassemble at endocytic sites? How do we specifically model actin-membrane interactions? How is the actin network organized? To answer these questions, we need to consider the dynamics of individual actin filaments and review some of the basics steps in actin remodeling.

Actin exists in two forms – G-actin (globular), and F-actin (filamentous). Each actin filament has a barbed (+ve) and pointed (−ve) end [224] with different critical concentrations (actin concentration that balances polymerization and depolymerization rates at one end), leading to addition of monomers at the barbed end and removal of monomers from the pointed end, a process known as actin treadmilling [209] (Figure 5). This treadmilling is traditionally characterized by 3 steps – nucleation, elongation, and steady state [225]. For polymerization to occur, the
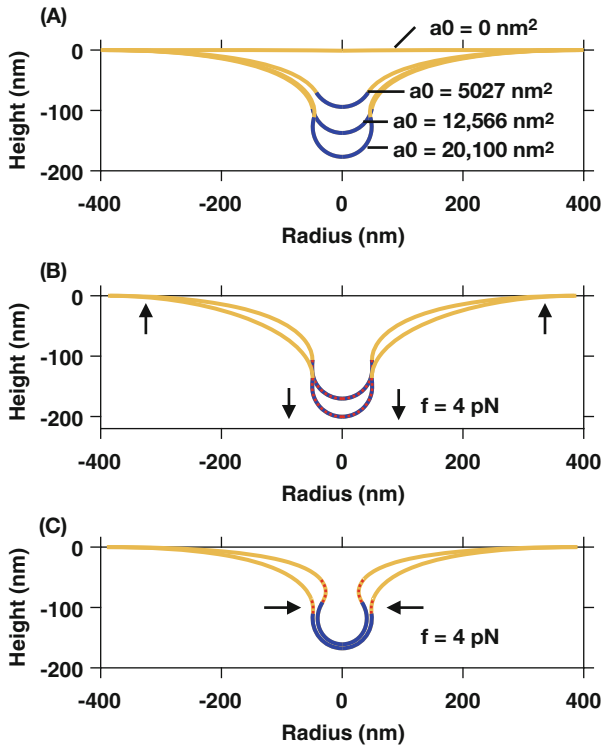
Fig. 7 Equilibrium shapes obtained from solving Equations (13 and 12) in an axisymmetric coordinate system for a spontaneous curvature based Helfrich energy (Equation 18) [80]. Spontaneous curvature $c = 0.02$ nm^{-1}. a0 is the dimensional protein coat area (nm^2). Total membrane area is 502650 nm^2. Membrane tension is 0.002 pN/nm (low tension). Coat and membrane rigidity are both set at 320 pNnm. (A) Equilibrium membrane shapes obtained for a0 = 0 nm^2, 5027 nm^2, 12566 nm^2, and 20100 nm^2 (increasing coat area). (B) Equilibrium membrane shape obtained by applying an axial force of 4 pN acting over an area equal to the coat area of 20100 nm^2. An upward force acts at the base of the bud. (C) Equilibrium membrane shape obtained by applying a radial force of 4 pN at the edge of the coat (a0 = 20100 nm^2). Orientations of the axial and radial force are shown in Figure 6 [80, 97, 153].

concentration of actin must be greater than the monomeric critical concentration [158]. The difference in critical concentration between the two ends reflects the fact that the system operates out of equilibrium [39], made possible by a reservoir of ATP, which is replenished in the cell and made available for actin polymerization by actin-binding proteins that catalyze the exchange of ADP to ATP [158]. This sequence of events is a remarkable explanation for the organization and coordinated dynamics of networks of actin filaments observed in cells. Polymerizing actin is responsible for force generation at the plasma membrane since the filaments are anchored at the membrane through actin-binding proteins [158].

Recent reviews such as [157] highlight the progress made in actin research and serve as an excellent summary of actin filament dynamics. At physiological concentrations, ATP-bound actin monomers associate rapidly with the barbed ends of actin filaments. ATP hydrolyzes over time, leaving "older" subunits in the filament bound to ADP. ADP-bound actin has a high dissociation rate from the pointed end. Filaments treadmill when ADP-actin depolymerization at the pointed end coincides with polymerization of ATP-actin from the barbed end. Higher concentrations of ATP-actin monomers increase the rate of polymerization.

Actin filaments in solution are disorganized and polymerize without control, but in cells actin-binding proteins can nucleate, crosslink, cap, and sever the filaments. For example, profilin and thymosin-β4 are the most prevalent actin monomer-binding proteins and can affect polymerization rates through steric hindrance. Profilin binds to the barbed end of monomers, which prevents those monomers from associating with an actin filament's pointed end but not barbed end. Once bound to filaments it rapidly dissociates [159]. Profilin exchanges ADP- for ATP-actin monomers in the solution, which increases the concentration of ATP-actin available for polymerization [129]. It was later shown to compete with severing proteins like cofilin to bind to actin monomers and to counter severing at high concentration [24]. In the last decade, profilin has been shown to have a high affinity for ADP-actin filament barbed ends [46] and to accelerate depolymerization at the barbed end [94].

While profilin plays a crucial role in elongation, it also inhibits nucleation, the first stage of polymerization. Spontaneous nucleation of actin filaments from monomers is energetically unfavorable in cells, but is sped up by filament nucleation proteins such as the Arp2/3 complex. Arp2/3 is a seven-protein complex [160] that binds to the sides of actin filaments and catalyzes the nucleation of a new filament at an angle of 70° from the side of the existing "mother" filament [134]. This was proposed as the "dendritic nucleation model" with 4 stages - (*i*) inactive Arp2/3 complex is recruited to the plasma membrane by membrane-bound activators, (*ii*) activated Arp2/3 complex nucleates the growth of new actin filaments at a defined angle from the sides of existing filaments, creating networks of branched filaments, (*iii*) growing filaments are rapidly capped, and (*iv*) phosphate hydrolysis and release promote disassembly of the pointed end of the branched network [134, 160]. Activators of the Arp2/3 complex, known as nucleation-promoting factors, include WASP family proteins such as SCAR and N-WASP [172]. WASP-family proteins bind membranes and are themselves activated by their membrane association and binding to GTP-binding proteins of the Rho-family such as Cdc42. ADF/Cofilin severs ADP-actin filaments, a critical step for replenishing the actin monomer pool [158, 160].

Incorporating all these biological features into a mathematical model requires a significant amount of parameter estimation. Elongation rate constants of single actin filaments were measured under electron microscopy and determined to be 10 μM^{-1} s^{-1} for ATP-actin association and 1 s^{-1} for ATP-actin dissociation at the barbed end [156]. This explains the critical concentration of 0.1 μM ATP-actin at the barbed end [39, 45]. ADP-actin, on the other hand, dissociates faster at the

barbed end and slower at the pointed end while the association rate was found to be slow at both ends, leading to a critical concentration 20x higher than for ATP-actin [156]. An impressive number of rate constants have been measured for many of the reactions described above [20, 67, 106] as well as their concentrations and numbers of molecules per structure, particularly in yeast [27, 154, 194, 227], which makes the system especially well suited for quantitative comparison between model and experiments.

3.1 Ratchet Models

Actin polymerization rates decrease when pushing against a membrane. One of the early models for load-dependent actin polymerization is the "Brownian ratchet" model [131] (Table 5).

Table 5 Notation used in the actin models.

Notation	Description	Units
v	Velocity	nm/s
δ	Actin monomer width	nm
M	Actin concentration	μM
β	Depolymerization rate	s^{-1}
α	Polymerization rate	s^{-1}
k_{on}	Polymerization rate constant	$\mu M^{-1}s^{-1}$
k_{off}	Depolymerization rate constant	s^{-1}
k_{cap}	Capping rate constant	s^{-1}
k_{branch}	Branching rate constant	$\mu M^{-1}s^{-1}$
k_{sever}	Severing rate constant	$\mu M^{-1}s^{-1}$
θ	Angle of actin filament impingement	s^{-1}
p	Probability of actin monomer addition	
G	Free actin monomer concentration	μM
a	Number of filaments attached to the surface	
w	Number of polymerizing filaments	
n	Nucleation rate of attached filaments	s^{-1}
κ	Filament capping rate	s^{-1}
ϵ_1	Dimensionless work done in breaking filaments	
ϵ_2	Dimensionless polymerization velocity	
ϵ_3	Dimensionless depolymerization velocity	
ϵ_4	Dimensionless work done by working filament against load	

3.1.1   The General Approach

The "Brownian ratchet" model assumed that individual actin filaments were rigid [150]. This model also assumed thermal fluctuations didn't affect the polymerizing filaments, which means that the gap width between the monomer and membrane could be determined by taking into account only the diffusion of the membrane. Using this model, the force-velocity relationship was determined to be

$$v = \delta[\alpha e^{-\omega} - \beta]. \tag{21}$$

Here, δ is actin monomer width, $\alpha = \mathrm{k}_{on}$ M is the polymerization rate of actin concentration M weighted by the probability that the dimensionless load ω will allow the addition of a monomer unit, and β is the depolymerization rate. This formula is a simplified version, valid for ideal ratchet velocity much larger than polymerization and depolymerization rates [150]. Correspondingly, the force needed to stop the ratchet is

$$f_0 = -\frac{k_B T}{\delta} \log(\frac{\beta}{\alpha}). \tag{22}$$

This model was further modified to include elasticity and thermal fluctuations [131]. In the revised "elastic Brownian ratchet" model, the actin filament was assumed to behave like a one-dimensional spring with a spring constant equivalent to the bending elasticity of a filament. The force-velocity relationship was obtained as

$$v \approx \delta \cos(\theta)[k_{on} M p(\theta, f) - k_{off}], \tag{23}$$

where f is the load, θ is the angle at which the actin filament impinges on the load, δ is the monomer width, and $p(\theta, f)$ is the steady-state probability that there exists a gap between the actin filament and the impinging force so as to allow monomer addition. A further update to the model was developed in [132] to incorporate the effects of both attaching and detaching/working filaments, known as the "tethered ratchet model." The dynamics of these filaments are given by

$$\frac{da}{dt} = n - \delta.a \quad \text{for attached filaments,} \tag{24}$$

$$\frac{dw}{dt} = \delta.a - \kappa.w \quad \text{for working filaments.} \tag{25}$$

$a(t)$ is the number of filaments attached to the surface, $w(t)$ is the number of polymerizing filaments or working filaments, n is nucleation rate of attached filaments, δ is filament dissociation rate, and κ is filament capping rate [132].

Fig. 8 Summary of the basic equations in the ratchet models.

Math box: Ratchet models

Brownian ratchet model

$$v = \delta[\alpha e^{-\omega} - \beta]$$

Elastic brownian ratchet model

$$v = \delta \cos(\theta)[k_{on} M p(\theta, f) - k_{off}]$$

Tethered ratchet model

$$v = \varepsilon_2[e^{-\varepsilon, v\omega(v)^2 - \varepsilon_4}] - \varepsilon_3$$

Incorporating these actin dynamics into Equation (23) results in a force-velocity relationship given by

$$v = \epsilon_2[e^{-\epsilon_1 v\omega(v)^2 - \epsilon_4}] - \epsilon_3, \tag{26}$$

where ϵ_i is a dimensionless quantity, ϵ_1 is the dimensionless work done in breaking the attachment between filaments, ϵ_2 is the dimensionless polymerization velocity, ϵ_3 is the dimensionless depolymerization velocity, and ϵ_4 is the dimensionless work done by the working filament against the load. This "tethered ratchet" model was used in an *in silico* reconstruction of *Listeria* propulsion for cell motility, taking into account both actin recycling and hydrolysis [5, 130] (Figure 8).

3.1.2 Applications to Endocytosis

A ratchet-based model for the role of clathrin in CME was proposed in [85], where the researchers suggested that instead of driving curvature generation, the clathrin coat forms a cage around the membrane invagination and stabilizes or traps any transient fluctuations [85]. In this case, the curvature is driven by thermal fluctuations with clathrin polymerization leading to the stability of more curved geometries. An earlier model for the endocytosis of proteins across the mitochondrial membrane in the presence of protein translocases TOM and TOM23 suggested that a targeted Brownian ratchet mechanism, with no backward motion, leads to spontaneous unfolding of these proteins and subsequently pushes them unidirectionally toward the mitochondrial matrix [140]. This counteracts another popular theory that the movement of proteins across the mitochondrial matrix is driven by a mechanical power stroke. A similar targeted ratchet mechanism labeled as the "Burnt bridge model" [12] based on probabilistic or biased diffusion of molecular motors provided an explanation for bacterial endospore engulfment [30].

3.2 Population-Based Stochastic Models of Actin

One of the drawbacks of ratchet models is that they do not account for the variation of a population of actin filaments in space and time. In fact, they assume that the loss of energy with actin growth is the same at every point along the membrane [131, 168]. However, the three-dimensional evolution of the actin network around the endocytic site is governed by spatial and temporal stochasticity of actin remodeling events [222]. How can we incorporate the stochastic behavior of actin polymerization into models of actin filament interactions while also including the membrane?

Figure 9 shows the available modeling approaches for a stochastic modeling of a reaction-diffusion system such as actin polymerization. If proteins are involved in high copy numbers, an individual molecule's contribution is less important to resolve and the species might be treated as a concentration evolution over time (left column). However, when the involved copy numbers are low, as in the case of endocytosis, individual molecules have to be resolved to account for stochasticity (right column). The next dimension to take into account for modeling is the spatial embedding: Is the entire reaction container well mixed (top row)? Are there spatial inhomogeneities on a large scale but small subvolumes can still be treated as well mixed (middle row)? Is there no spatial dimension in which well mixedness can be assumed and every particle has to be resolved explicitly in space (bottom row)? These considerations are not only important for reaching high modeling accuracy but also have computational cost and attainable simulation timescale implications. Naturally, models that incorporate more detail are computationally more expensive and differences in wall-clock time for a simulation on different detail levels can reach orders of magnitude. In most cases, a balance has to be found between desired modeling detail and the timescales of the studied process.

3.2.1 The General Approach

In stochastic models, the actin filament grows by monomer addition with a rate constant k_{on} at the barbed end and depolymerization with a rate constant k_{off} at the pointed end [38]. k_{cap} is the capping rate constant, which determines when a filament will stop growing. "Daughter" filaments are added to the side of existing branches with a rate constant k_{branch}. Severing of filaments through ADF/Cofilin is specified by rate constant k_{sever}. These rate constants are determined experimentally (biochemical assays). Branching can be either "end branching" or "side branching," depending on where Arp2/3 is located. A 3D stochastic simulation was performed in [38, 164, 229] and compared favorably to lamellipodium ultrastructure studies.

An "autocatalytic branching" theory was developed in [34], which stated that new branches of actin filaments are dependent on the number of existing branches. Contrary to this theory was the "nucleation" model, where new branch formation was independent of existing filaments. The "autocatalytic branching" model was
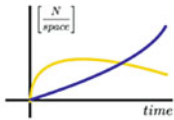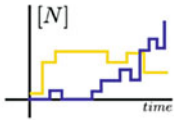
Fig. 9 Stochastic models in reference to different reaction-diffusion modeling approaches. Reaction-diffusion models can be differentiated into concentration based/deterministic (left column) and particle based/stochastic (right column). Depending on the system at hand, the spatial representation can be chosen to be well mixed (top row), well mixed in lattice based sub-volumes (middle row), or spatially fully resolved into individual particles. The underlying models are ordinary differential equations (ODEs) and partial differential equations (PDEs) for the concentration case and chemical master equation (ME), spatio-temporal chemical master equation (ST-ME), and particle-based reaction diffusion dynamics (iPRD) also known as agent based modeling.

found to be in better agreement with experimental measurements of force-velocity relationships [34]. In theory, this model would lead to a steep increase in actin density if not for the presence of capping protein. The effect of capping protein in end- versus side-branching by Arp2/3 was then modeled [37]. In side-branching, capping protein slows down growth while in end-branching, capping protein stops growth. The branching is described as

$$k_{br} = k_{br,0}[Arp2/3]([G] - G_c^B)^2, \tag{27}$$

where $[Arp2/3]$ is the concentration of activated Arp2/3, $[G]$ is free actin monomer concentration, G_C^B is critical actin concentration at the barbed end, and $k_{br,0}$ is a rate parameter. The results in [37] showed that side-branching is a better fit to experiments, assuming that branching is dominated by either branching mode alone. Additionally, monomers with a decaying branching ability showed a better fit [37] (Figure 10).

Fig. 10 Summary of basic
equations in population based
stochastic models.

<div style="border:1px solid">

Math box: Population models

Branching

$k_{br} = k_{br,0}[Arp2/3]([G] - G_{c,barbed})$

Severing

$\Delta G = (0.1 \ \mu M) \ k_{sev}^{1/2}/[CP]$

</div>

Severing or disassembly of actin filaments is equally important to free up
actin and drive propulsion. Severing of filaments by cofilin has been shown to
increase actin polymerization by freeing up barbed ends [71]. A model incorporating
severing and capping rates in addition to branching effects was developed in [35].
An analytic expression for severing, given by

$$\Delta G = (0.1 \mu M)\sqrt{k_{sev}}/[CP], \tag{28}$$

matched the stochastic growth simulations for high concentrations of $[CP]$ well.
Here, $[CP]$ is the concentration of capping protein, k_{sev} is the rate of severing,
and ΔG is the difference between treadmilling actin concentration and critical actin
concentration [35]. However, the same match was not obtained for lower values
of $[CP]$, indicating that severing enhances polymerization only in the presence of
barbed end capping [35].

The effects of annealing and disassembly for square/cubic geometries have also
been studied [36]. Here, different segments of filaments were characterized by nodes
that specify branch points. Random severing occurs when this link was broken and
annealing occurs when the links were stochastically restored. In the absence of
annealing, network density was found to decay inversely to severing rate [36]. In
the presence of a critical value of annealing, network density remained constant.

3.2.2 Agent-Based Actin Modeling

Another method to model actin dynamics is through agent-based models. Within
cell and developmental biology, agent-based models, also known as rule-based
or particle-based models, have mostly focused on collective cell migration and
behavior, treating individual cells as agents [8, 62, 117]. Recently, agent-based
models have been adopted to study cell biology at the "mesoscale" to model the
behavior of proteins or multi-protein complexes interacting within cells [4, 139,
217] providing mechanistic insight to cellular processes such as endocytosis and
cytokinesis [144, 178, 199].

Interacting particle-based reaction-diffusion (iPRD) simulations are the most
detailed of such models. Here, each protein or protein complex is treated as an object
with properties (e.g., position, size, excluded volume, diffusion coefficient, binding
status, membrane association) and rules (e.g., diffuse, react with another particle,

bind to a membrane, etc.) executed over successive time steps within a defined space. These models have many parameters and in order to be predictive, they must be minimal or have many of the relevant parameters measured, particularly reaction rate constants, positions, and numbers of molecules over time. The great advantage of these models is their ability to bridge first principle physics (microscopic diffusion constants, membrane viscosity, membrane bending rigidity, spatial constraints of the cell, etc.) with biological parameters that are accessible for experiments (e.g., fluorescent tagging of proteins can reveal macroscopic, i.e. crowded, diffusion constants, protein numbers, the systems overall time evolution, and reaction rates). Different approaches and software packages exist for iPRD that allow different levels of modeling detail, excluded volume incorporation, reactions between particles, membrane treatment, and 3D geometry embedding (see review [177]).

The structure of these models makes them well suited for studying actin dynamics, since the stochasticity of the model reflects the stochastic nature of molecular motion and interactions in the cell. This is particularly the case for a small number of discrete interacting structures, which is true for many cytoskeletal processes relative to the size of the cell [139].

Because each relevant entity (molecule or multiprotein structure) is explicitly represented in these models, the outputs of these simulations can be directly compared to experimental data and guide new measurements that will constrain or test model predictions. The modular nature of these models allows them to be modified by specialists and nonspecialists alike, and permits increases in model complexity as more parameter values become available from experiments. Their construction and use are complementary to the theory-driven mathematical models described above, and their increasing popularity promises to drive the identification and characterization of emergent behavior and self-organization in subcellular processes such as the cytoskeleton, particularly as more quantitative measurements are made in cells.

3.2.3   Applications to Endocytosis

Recent studies such as [221] use a Master Equation (ME) method to model 3D growth (using cylindrical coordinates) of F-actin filaments to deform a membrane in the context of yeast CME. This model incorporates branching induced by the nucleation-promoting factor (NPF Las17) that accumulates as a ring around the endocytic patch [135], spontaneous nucleation, and cofilin-driven severing [221]. Filament branching leads to a pushing force along the ring [221]. The yeast Hip1R homologue Sla2 is assumed to play a role in the pulling force which acts at the center of the ring [221]. This pulling force also requires spontaneous nucleation of actin filaments, an assumption made in the model. Filament dynamics incorporate a negative feedback loop of actin on Las17 – there is a probability that Las17 detaches from the membrane because of polymerizing actin [222]. The results obtained for the number of F-actin and Las17 matched well with experimentally

determined values [222] and other stochastic results [221]. This study provides strong evidence for the use of a statistically averaged actin network in order to reduce the computational load on calculating branching.

Studies such as [22] perform temporal simulations that support the "dendritic nucleation" model [99] of endocytic patch formation. Time course data was obtained from quantitative confocal microscopy measurements of purified protein in a dilute solution [195]. Simulation results show a good match to live cell experimental data only when (*i*) the ternary complex of actin monomer-WASP-Arp2/3 binds to actin filaments 400 times faster than the rate constant measured *in vitro* [21], (*ii*) cofilin-induced severing and fragmentation of actin filaments speeds up actin patch disassembly, and (*iii*) capping protein reaction rates are faster in cells. This work performed a large parameter sweep of reaction rates to determine the best fit to live cell measurements, besides identifying the crucial reactions that differentiate *in vitro* and *in vivo* endocytic patch formation.

Agent-based models have also been used to model actin filament growth, mechanics, and branching [111, 147, 197] with varying levels of sophistication. Agent-based models have contributed to the mechanistic understanding of several cytoskeletal cellular processes, including (microtubules) formation of bipolar microtubule bundles, mitotic spindle assembly, nuclear and division plane positioning, and (actin) bacterial actin-based motility [52, 93, 116, 144]. Popular modular implementations of agent-based modeling include Smoldyn [9, 10], which models diffusing and interacting particles; and Cytosim [139], which models dynamics, interactions, and forces of cytoskeletal filaments and their binding partners using Brownian dynamics. Several platforms combined agent-based models with ODE, stochastic, or spatial models on different length scales to make multiscale models [25, 62].

Schöneberg [23, 175] developed an iPRD software framework named ReaDDy, which includes interaction potentials to model space exclusion, particle interactions (e.g., binding and clustering), membrane interactions, and a particle-particle reaction framework. Most applicable to highly crowded systems, ReaDDy has been used to simulate Rhodopsin-G-protein interaction in the visual cascade [77, 176], SNARE clustering in the presynaptic active zone [215], and HIV maturation [174]. Recently, ReaDDy was combined with a spatio-temporal master equation (ST-ME) reaction-diffusion model [178] to investigate how endocytic proteins become partitioned into different regions of endocytic buds. The authors used this framework to model the diffusion of a BAR-domain protein named SNX9 in the context of clathrin-coated buds crowded by endocytic proteins [178]. Using realistic copy numbers and sizes of endocytic proteins positioned underneath a clathrin cage, their Brownian dynamics simulations revealed that a membrane lipid composition change in the highly competitive lipid binding environment of the clathrin coat can specifically recruit SNX9 to the membrane and that protein crowding excluded SNX9 from the bud in favor of the neck of the endocytic pit. This restriction of SNX9 to the edge of the clathrin lattice was confirmed experimentally [178, 198]. Including a weak end-to-end interaction potential between SNX9 molecules (found in many BAR-domain proteins) led to SNX9 oligomerizing in rings at the bud neck, at various stages
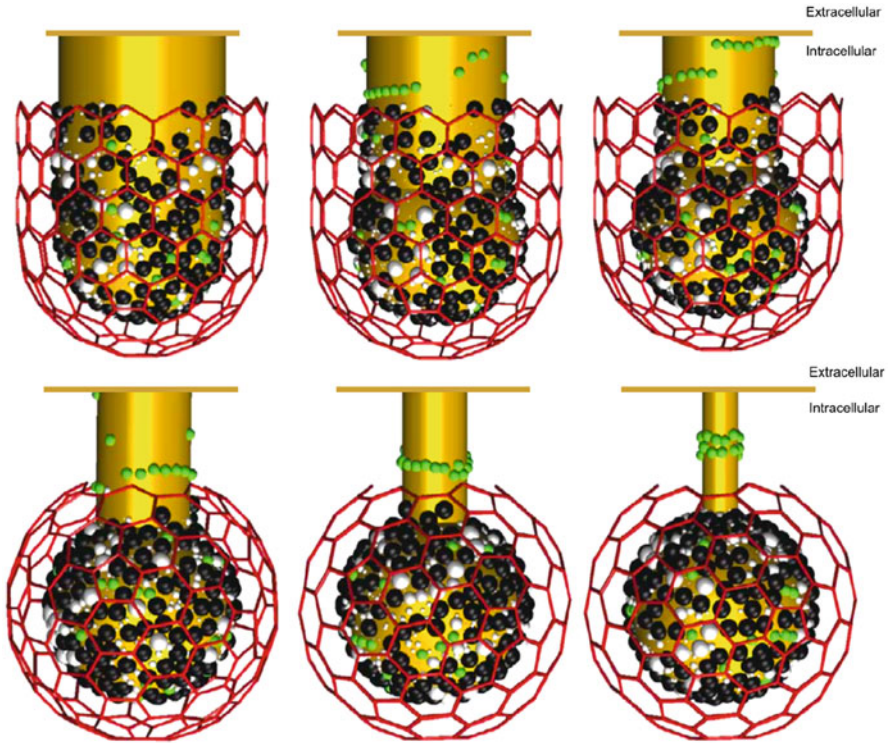
Fig. 11 Simulations of endocytic proteins diffusing and partitioning during clathrin-coated pit maturation. Underneath the clathrin coat (red), the clathrin-binding Adaptor Protein 2 (AP-2, black) the BAR-protein SNX9 (green) and all other present endocytosis proteins (white) are explicitly simulated using experimentally determined numbers and sizes. Newly recruited SNX9 is spatially excluded from underneath the coat due to crowding and partitions to the endocytic neck. A tip-to-tip interaction potential for SNX9 molecules induces their oligomerization into rings at the bud neck. Shown are snapshots of different simulations with different curvatures of the vesicle neck from [178]. Permission pending.

of neck constriction (Figure 11). The spatial patterning of SNX9 allows it to bind membranes of a particular curvature while recruiting dynamin and activating the nucleation-promoting factor NWASP [50]. This serves as a mechanism to coordinate membrane curvature, force generation via actin polymerization, and membrane scission via dynamin constriction.

4 Future Perspectives/Challenges

It is now evident that biophysical modeling of endocytosis has made great progress and we are able to glean insights into these complex biological processes and generate experimentally testable hypotheses. However, there remain many challenges

that require advances in mathematical and computational modeling of endocytosis. We highlight a few here:

- How can a continuum model incorporate the effects of any new molecules made over a given timescale? Recent works have highlighted the role of lipid structures in protein activation [70], which would, in turn, alter the continuum properties of the membrane. Since continuum models incorporate proteins using spontaneous curvature fields and variable elastic moduli, we need a framework that can account for nonlinear lipid-protein interactions such as the one shown in [110].
- Hybrid continuum-atomistic models can help bridge the gap between accuracy of MD and speed of continuum modeling [14]. Where continuum fails, MD simulations give insight into the nature of the lipid-protein interactions at a length scale smaller than that of the lipid bilayer, as shown in works like [75]. However, there remain computational challenges associated with a hybrid model. Whereas continuum simulations can easily compute energies over large systems, MD simulations require large computation time and storage and are practical only over small spatial domains. Mesoscale reaction-diffusion modeling such as iPRD is a promising approach in the right direction.
- Coupling mechanics with biochemistry in a model remains a continued challenge. Although some efforts have been made to couple the lipid composition to membrane mechanics [114], a complete mechanochemical model that couples signaling to membrane dynamics is still missing. Furthermore, the newly developed models should take the multiple time scales that govern the progression of endocytosis into account rather than assume mechanical equilibrium.
- Another major challenge is the relationship between actin and the membrane. A recent review on membrane bending by actin polymerization [40] discusses this issue in detail; identifying the relationship between actin dynamics and membrane deformation remains a continued challenge for mathematical and computational model development.
- Capturing in-plane diffusion of proteins and lipids is another emerging area of research. Recently, there has been a slew of models [2, 162, 165, 167, 204] that account for in-plane transport. However, despite recent evidence that inter-monolayer friction affects scission due to BAR domain proteins [193], these models are not the norm.
- Last, but not least, theory and computation need to work closely with experiments, so that the models can push closer towards experimentally accessible parameters and outputs. This will allow experimentalists to test predictions of the model and identify the key quantitative approaches that need to be developed in cellular experiments (measuring numbers of molecules at endocytic sites, cytoplasmic concentrations, membrane and coat rigidity, membrane tension, actin dimensions, and organization). While some of these methods have been developed in yeast [1, 101, 195, 196, 228], these methods emerge [178] but are less well established for mammalian cells.

Many of these issues can be addressed by strong interdisciplinary teams and cross-pollination of ideas from different fields. With advances in imaging and

computational tools, the time is right for us to make progress in leaps and bounds in the study of small-scale cellular movements.

References

1. Abe F, Hiraki T (2009) Mechanistic role of ergosterol in membrane rigidity and cycloheximide resistance in saccharomyces cerevisiae. Biochimica et Biophysica Acta (BBA)-Biomembranes 1788(3):743–752
2. Agrawal A, Steigmann DJ (2011) A model for surface diffusion of trans-membrane proteins on lipid bilayers. Zeitschrift für Angewandte Mathematik und Physik (ZAMP) 62(3):549–563
3. Agudo-Canalejo J, Lipowsky R (2015) Critical particle sizes for the engulfment of nanoparticles by membranes and vesicles with bilayer asymmetry. ACS nano 9(4):3704–3720
4. Akamatsu M, Berro J, Pu KM, Tebbs IR, Pollard TD (2014) Cytokinetic nodes in fission yeast arise from two distinct types of nodes that merge during interphase. The Journal of Cell Biology 204(6):977–988
5. Alberts JB, Odell GM (2004) In silico reconstitution of listeria propulsion exhibits nano-saltation. PLoS biology 2(12):e412
6. Alimohamadi H, Vasan R, Hassinger JE, Stachowiak JC, Rangamani P (2017) The role of traction in membrane curvature generation. arXiv preprint arXiv:170609926
7. Allen MP, et al (2004) Introduction to molecular dynamics simulation. Computational soft matter: from synthetic polymers to proteins 23:1–28
8. An G, Mi Q, Dutta-Moscato J, Vodovotz Y (2009) Agent-based models in translational systems biology. Wiley Interdisciplinary Reviews: Systems Biology and Medicine 1(2):159–171
9. Andrews SS, Bray D (2004) Stochastic simulation of chemical reactions with spatial resolution and single molecule detail. Physical biology 1(3–4):137–151
10. Andrews SS, Addy NJ, Brent R, Arkin AP (2010) Detailed simulations of cell biology with Smoldyn 2.1. PLoS computational biology 6(3):e1000,705
11. Anitei M, Hoflack B (2012) Bridging membrane and cytoskeleton dynamics in the secretory and endocytic pathways. Nature cell biology 14(1):11
12. Antal T, Krapivsky P (2005) "Burnt-bridge"İmechanism of molecular motor motion. Physical Review E 72(4):046,104
13. Arcario MJ, Ohkubo YZ, Tajkhorshid E (2011) Capturing spontaneous partitioning of peripheral proteins using a biphasic membrane-mimetic model. The Journal of Physical Chemistry B 115(21):7029–7037
14. Argudo D, Bethel NP, Marcoline FV, Grabe M (2016) Continuum descriptions of membranes and their interaction with proteins: Towards chemically accurate models. Biochimica et Biophysica Acta (BBA)-Biomembranes 1858(7):1619–1634
15. Arkhipov A, Yin Y, Schulten K (2008) Four-scale description of membrane sculpting by bar domains. Biophysical journal 95(6):2806–2821
16. Arkhipov A, Yin Y, Schulten K (2009) Membrane-bending mechanism of amphiphysin n-bar domains. Biophysical journal 97(10):2727–2735

17. Bahrami AH, Hummer G (2017) Formation and stability of lipid membrane nanotubes. ACS nano

18. Barlowe C, Orci L, Yeung T, Hosobuchi M, Hamamoto S, Salama N, Rexach MF, Ravazzola M, Amherdt M, Schekman R (1994) Copii: a membrane coat formed by sec proteins that drive vesicle budding from the endoplasmic reticulum. Cell 77(6):895–907

19. Baumgart T, Das S, Webb WW, Jenkins JT (2005) Membrane elasticity in giant vesicles with fluid phase coexistence. Biophysical journal 89(2):1067–1080

20. Beltzner CC, Pollard TD (2008) Pathway of actin filament branch formation by Arp2/3 complex. The Journal of biological chemistry 283(11):7135–7144

21. Beltzner CC, Pollard TD (2008) Pathway of actin filament branch formation by arp2/3 complex. Journal of Biological Chemistry 283(11):7135–7144

22. Berro J, Sirotkin V, Pollard TD (2010) Mathematical modeling of endocytic actin patch kinetics in fission yeast: disassembly requires release of actin filament fragments. Molecular biology of the cell 21(16):2905–2915

23. Biedermann J, Ullrich A, Schoneberg J, Noe F (2015) ReaDDyMM: Fast Interacting Particle Reaction-Diffusion Simulations Using Graphical Processing Units. Biophysj 108(3):457–461

24. Blanchoin L, Pollard TD (1998) Interaction of actin monomers with acanthamoebaactophorin (adf/cofilin) and profilin. Journal of Biological Chemistry 273(39):25,106–25,111

25. Blinov ML, Schaff JC, Vasilescu D, Moraru II, Bloom JE, Loew LM (2017) Compartmental and Spatial Rule-Based Modeling with Virtual Cell. Biophysj 113(7):1365–1372

26. Blood PD, Voth GA (2006) Direct observation of bin/amphiphysin/rvs (bar) domain-induced membrane curvature by means of molecular dynamics simulations. Proceedings of the National Academy of Sciences 103(41):15,068–15,072

27. Boeke D, Trautmann S, Meurer M, Wachsmuth M, Godlee C, Knop M, Kaksonen M (2014) Quantification of cytosolic interactions identifies Ede1 oligomers as key organizers of endocytosis. Molecular systems biology 10:756

28. Bowers KJ, Chow E, Xu H, Dror RO, Eastwood MP, Gregersen BA, Klepeis JL, Kolossvary I, Moraes MA, Sacerdoti FD, et al (2006) Scalable algorithms for molecular dynamics simulations on commodity clusters. In: Proceedings of the 2006 ACM/IEEE conference on Supercomputing, ACM, p 84

29. Bradley R, Radhakrishnan R (2013) Coarse-grained models for protein-cell membrane interactions. Polymers 5(3):890–936

30. Broder DH, Pogliano K (2006) Forespore engulfment mediated by a ratchet-like mechanism. Cell 126(5):917–928

31. Brown DA, Rose JK (1992) Sorting of gpi-anchored proteins to glycolipid-enriched membrane subdomains during transport to the apical cell surface. Cell 68(3):533–544

32. Bugyi B, Carlier MF (2010) Control of actin filament treadmilling in cell motility. Annual review of biophysics 39:449–470

33. Canham PB (1970) The minimum energy of bending as a possible explanation of the biconcave shape of the human red blood cell. Journal of theoretical biology 26(1):61IN777–76IN881

34. Carlsson A (2003) Growth velocities of branched actin networks. Biophysical journal 84(5):2907–2918

35. Carlsson A (2006) Stimulation of actin polymerization by filament severing. Biophysical journal 90(2):413–422

36. Carlsson A (2007) Disassembly of actin networks by filament severing. New Journal of Physics 9(11):418

37. Carlsson A, Wear M, Cooper J (2004) End versus side branching by arp2/3 complex. Biophysical journal 86(2):1074–1081

38. Carlsson AE (2001) Growth of branched actin networks against obstacles. Biophysical journal 81(4):1907–1923

39. Carlsson AE (2010) Actin dynamics: from nanoscale to microscale. Annual review of biophysics 39:91–110
40. Carlsson AE (2018) Membrane bending by actin polymerization. Current opinion in cell biology 50:1–7
41. Carmo Md (1993) Differential geometry of curves and surfaces. 1976. Prentice-Hall, Englewood Cliffs, New Jersey) Rehsteiner, F and Rewker, HJ Collision free five axis milling of twisted ruled surface Ann CIRP 42(1):457–461
42. Chabanon M, Stachowiak JC, Rangamani P (2017) Systems biology of cellular membranes: a convergence with biophysics. Wiley Interdisciplinary Reviews: Systems Biology and Medicine 9(5)
43. Chen Z, Mao Y, Yang J, Zhang T, Zhao L, Yu K, Zheng M, Jiang H, Yang H (2014) Characterizing the binding of annexin v to a lipid bilayer using molecular dynamics simulations. Proteins: Structure, Function, and Bioinformatics 82(2):312–322
44. Collins A, Warrington A, Taylor KA, Svitkina T (2011) Structural organization of the actin cytoskeleton at sites of clathrin-mediated endocytosis. Current Biology 21(14):1167–1175
45. Cooper JA, Walker SB, Pollard TD (1983) Pyrene actin: documentation of the validity of a sensitive assay for actin polymerization. Journal of muscle research and cell motility 4(2):253–262
46. Courtemanche N, Pollard TD (2013) Interaction of profilin with the barbed end of actin filaments. Biochemistry 52(37):6456–6466
47. Dai J, Sheetz MP (1999) Membrane tether formation from blebbing cells. Biophysical journal 77(6):3363–3370
48. Damke H, Baba T, Warnock DE, Schmid SL (1994) Induction of mutant dynamin specifically blocks endocytic coated vesicle formation. The Journal of cell biology 127(4):915–934
49. Damke H, Baba T, van der Bliek AM, Schmid SL (1995) Clathrin-independent pinocytosis is induced in cells overexpressing a temperature-sensitive mutant of dynamin. The Journal of Cell Biology 131(1):69–80
50. Daste F, Walrant A, Holst MR, Gadsby JR, Mason J, Lee JE, Brook D, Mettlen M, Larsson E, Lee SF, Lundmark R, Gallop JL (2017) Control of actin polymerization via the coincidence of phosphoinositides and high membrane curvature. The Journal of Cell Biology pp jcb.201704,061–21
51. Dawson JC, Legg JA, Machesky LM (2006) Bar domain proteins: a role in tubulation, scission and actin assembly in clathrin-mediated endocytosis. Trends in cell biology 16(10):493–498
52. Dayel MJ, Akin O, Landeryou M, Risca V, Mogilner A, Mullins RD (2009) In silico reconstitution of actin-based symmetry breaking and motility. PLoS biology 7(9):e1000,201
53. Decuzzi P, Ferrari M (2008) The receptor-mediated endocytosis of nonspherical particles. Biophysical journal 94(10):3790–3797
54. Derényi I, Jülicher F, Prost J (2002) Formation and interaction of membrane tubes. Physical review letters 88(23):238,101
55. Deserno M (2009) Mesoscopic membrane physics: concepts, simulations, and selected applications. Macromolecular rapid communications 30(9–10):752–771
56. Deuling H, Helfrich W (1976) Red blood cell shapes as explained on the basis of curvature elasticity. Biophysical journal 16(8):861–868
57. Dippold HC, Ng MM, Farber-Katz SE, Lee SK, Kerr ML, Peterman MC, Sim R, Wiharto PA, Galbraith KA, Madhavarapu S, et al (2009) Golph3 bridges phosphatidylinositol-4-phosphate and actomyosin to stretch and shape the golgi to promote budding. Cell 139(2):337–351
58. Diz-Muñoz A, Fletcher DA, Weiner OD (2013) Use the force: membrane tension as an organizer of cell shape and motility. Trends in cell biology 23(2):47–53
59. Dmitrieff S, Nédélec F (2015) Membrane mechanics of endocytosis in cells with turgor. PLoS computational biology 11(10):e1004,538
60. Döbereiner H (2000) Fluctuating vesicle shapes. John Wiley & Sons, New York pp 149–168
61. Duman JG, Pathak NJ, Ladinsky MS, McDonald KL, Forte JG (2002) Three-dimensional reconstruction of cytoplasmic membrane networks in parietal cells. Journal of cell science 115(6):1251–1258

62. Emonet T, Macal CM, North MJ, Wickersham CE, Cluzel P (2005) AgentCell: a digital single-cell assay for bacterial chemotaxis. Bioinformatics (Oxford, England) 21(11):2714–2721

63. Engqvist-Goldstein ÅE, Drubin DG (2003) Actin assembly and endocytosis: from yeast to mammals. Annual review of cell and developmental biology 19(1):287–332

64. Faini M, Beck R, Wieland FT, Briggs JA (2013) Vesicle coats: structure, function, and general principles of assembly. Trends in cell biology 23(6):279–288

65. Fletcher DA, Mullins RD (2010) Cell mechanics and the cytoskeleton. Nature 463(7280):485–492

66. Frolov VA, Lizunov VA, Dunina-Barkovskaya AY, Samsonov AV, Zimmerberg J (2003) Shape bistability of a membrane neck: a toggle switch to control vesicle content release. Proceedings of the National Academy of Sciences 100(15):8698–8703

67. Fujiwara I, Vavylonis D, Pollard TD (2007) Polymerization kinetics of adp-and adp-pi-actin determined by fluorescence microscopy. Proceedings of the National Academy of Sciences 104(21):8827–8832

68. Futaki S, Nakase I, Tadokoro A, Takeuchi T, Jones AT (2007) Arginine-rich peptides and their internalization mechanisms

69. Gaidarov I, Chen Q, Falck JR, Reddy KK, Keen JH (1996) A functional phosphatidylinositol 3, 4, 5-trisphosphate/phosphoinositide binding domain in the clathrin adaptor ap-2 α subunit. implications for the endocytic pathway. Journal of Biological Chemistry 271(34):20,922–20,929

70. Gawrisch K, Soubias O (2008) Structure and dynamics of polyunsaturated hydrocarbon chains in lipid bilayers – significance for gpcr function. Chemistry and physics of lipids 153(1):64–75

71. Ghosh M, Song X, Mouneimne G, Sidani M, Lawrence DS, Condeelis JS (2004) Cofilin promotes actin polymerization and defines the direction of cell motility. Science 304(5671):743–746

72. Gomez M, Moulton DE, Vella D (2016) Critical slowing down in purely elastic 'snap-through' instabilities. Nat Phys 13:142

73. Goode BL, Eskin JA, Wendland B (2015) Actin and endocytosis in budding yeast. Genetics 199(2):315–358

74. Grimmer S, van Deurs B, Sandvig K (2002) Membrane ruffling and macropinocytosis in a431 cells require cholesterol. Journal of cell science 115(14):2953–2962

75. Grossfield A, Feller SE, Pitman MC (2006) A role for direct interactions in the modulation of rhodopsin by ω-3 polyunsaturated lipids. Proceedings of the National Academy of Sciences of the United States of America 103(13):4888–4893

76. Guha A, Sriram V, Krishnan K, Mayor S (2003) Shibire mutations reveal distinct dynamin-independent and-dependent endocytic pathways in primary cultures of drosophila hemocytes. Journal of Cell Science 116(16):3373–3386

77. Gunkel M, Schöneberg J, Alkhaldi W, Irsen S, Noé F, Kaupp UB, Al-Amoudi A (2015) Higher-order architecture of rhodopsin in intact photoreceptors and its implication for phototransduction kinetics. Structure 23(4):628–638

78. van Gunsteren WF, Daura X, Hansen N, Mark AE, Oostenbrink C, Riniker LJ Sereina andn-Smith (2018) Validation of molecular simulation: An overview of issues. Angew Chem Int Ed 57(4):884–902

79. Hansen CG, Nichols BJ (2009) Molecular mechanisms of clathrin-independent endocytosis. Journal of cell science 122(11):1713–1721

80. Hassinger JE, Oster G, Drubin DG, Rangamani P (2017) Design principles for robust vesiculation in clathrin-mediated endocytosis. Proceedings of the National Academy of Sciences 114(7):E1118–E1127

81. He X, Lin M, Sha B, Feng S, Shi X, Qu Z, Xu F (2015) Coarse-grained molecular dynamics studies of the translocation mechanism of polyarginines across asymmetric membrane under tension. Scientific reports 5

82. Hedger G, Sansom MS (2016) Lipid interaction sites on channels, transporters and receptors: recent insights from molecular dynamics simulations. Biochimica et Biophysica Acta (BBA)-Biomembranes 1858(10):2390–2400

83. Helfrich W (1973) Elastic properties of lipid bilayers: theory and possible experiments. Zeitschrift für Naturforschung C 28(11–12):693–703

84. Heuser J, Reese T (1973) Evidence for recycling of synaptic vesicle membrane during transmitter release at the frog neuromuscular junction. The Journal of cell biology 57(2):315–344

85. Hinrichsen L, Meyerholz A, Groos S, Ungewickell EJ (2006) Bending a membrane: how clathrin affects budding. Proceedings of the National Academy of Sciences 103(23):8715–8720

86. Hochmuth RM, Mohandas N, Blackshear P (1973) Measurement of the elastic modulus for red cell membrane using a fluid mechanical technique. Biophysical journal 13(8):747–762

87. Humphrey W, Dalke A, Schulten K (1996) Vmd: visual molecular dynamics. Journal of molecular graphics 14(1):33–38

88. Ingolfsson HI, Melo MN, van Eerden FJ, Arnarez C, Lopez CA, Wassenaar TA, Periole X, de Vries AH, Tieleman DP, Marrink SJ (2014) Lipid organization of the plasma membrane. Journal of the american chemical society 136(41):14,554–14,559

89. Itoh T, Erdmann KS, Roux A, Habermann B, Werner H, De Camilli P (2005) Dynamin and the actin cytoskeleton cooperatively regulate plasma membrane invagination by bar and f-bar proteins. Developmental cell 9(6):791–804

90. Ivanov AI (2008) Exocytosis and endocytosis. Springer

91. Izvekov S, Voth GA (2005) A multiscale coarse-graining method for biomolecular systems. The Journal of Physical Chemistry B 109(7):2469–2473

92. Jahn R, Südhof TC (1999) Membrane fusion and exocytosis. Annual review of biochemistry 68(1):863–911

93. Janson ME, Loughlin R, Loiodice I, Fu C, Brunner D, Nedelec FJ, Tran PT (2007) Crosslinkers and motors organize dynamic microtubules to form stable bipolar arrays in fission yeast. Cell 128(2):357–368

94. Jégou A, Niedermayer T, Orbán J, Didry D, Lipowsky R, Carlier MF, Romet-Lemonne G (2011) Individual actin filaments in a microfluidic flow reveal the mechanism of atp hydrolysis and give insight into the properties of profilin. PLoS biology 9(9):e1001,161

95. Jenkins J (1977) Static equilibrium configurations of a model red blood cell. Journal of mathematical biology 4(2):149–169

96. Jung G, Wu X, Hammer JA (1996) Dictyostelium mutants lacking multiple classic myosin i isoforms reveal combinations of shared and distinct functions. The Journal of Cell Biology 133(2):305–323

97. Kaksonen M, Sun Y, Drubin DG (2003) A pathway for association of receptors, adaptors, and actin during endocytic internalization. Cell 115(4):475–487

98. Kaksonen M, Toret CP, Drubin DG (2005) A modular design for the clathrin-and actin-mediated endocytosis machinery. Cell 123(2):305–320

99. Kaksonen M, Toret CP, Drubin DG (2006) Harnessing actin dynamics for clathrin-mediated endocytosis. Nature reviews Molecular cell biology 7(6):404

100. Khelashvili G, Kollmitzer B, Heftberger P, Pabst G, Harries D (2013) Calculating the bending modulus for multicomponent lipid membranes in different thermodynamic phases. Journal of chemical theory and computation 9(9):3866–3871

101. Kilmartin J, Adams A (1984) Structural rearrangements of tubulin and actin during the cell cycle of the yeast saccharomyces. The Journal of cell biology 98(3):922–933

102. Klauda JB, Venable RM, Freites JA, O'Connor JW, Tobias DJ, Mondragon-Ramirez C, Vorobyov I, MacKerell Jr AD, Pastor RW (2010) Update of the charmm all-atom additive force field for lipids: validation on six lipid types. The journal of physical chemistry B 114(23):7830–7843

103. Kovtun O, Tillu VA, Ariotti N, Parton RG, Collins BM (2015) Cavin family proteins and the assembly of caveolae. J Cell Sci 128(7):1269–1278

104. Kozlov M, Leikin S, Chernomordik L, Markin V, Chizmadzhev YA (1989) Stalk mechanism of vesicle fusion. European Biophysics Journal 17(3):121–129

105. Kreyszig E (1968) Introduction to differential geometry and Riemannian geometry. University of Toronto Press
106. Kuhn JR, Pollard TD (2007) Single molecule kinetic analysis of actin filament capping. Polyphosphoinositides do not dissocate capping proteins. The Journal of biological chemistry 282(38):28,014–28,024
107. Kuzmin PI, Akimov SA, Chizmadzhev YA, Zimmerberg J, Cohen FS (2005) Line tension and interaction energies of membrane rafts calculated from lipid splay and tilt. Biophysical journal 88(2):1120–1133
108. Laakso JM, Lewis JH, Shuman H, Ostap EM (2008) Myosin i can act as a molecular force sensor. Science 321(5885):133–136
109. Lee HJ, Peterson EL, Phillips R, Klug WS, Wiggins PA (2008) Membrane shape as a reporter for applied forces. Proceedings of the National Academy of Sciences 105(49):19,253–19,257
110. Lee KI, Pastor RW, Andersen OS, Im W (2013) Assessing smectic liquid-crystal continuum models for elastic bilayer deformations. Chemistry and physics of lipids 169:19–26
111. Letort G, Politi AZ, Ennomani H, THERY M, Nédélec F, Blanchoin L (2015) Geometrical and mechanical properties control actin filament organization. PLoS computational biology 11(5):e1004,245
112. Levine ZA, Venable RM, Watson MC, Lerner MG, Shea JE, Pastor RW, Brown FL (2014) Determination of biomembrane bending moduli in fully atomistic simulations. Journal of the American Chemical Society 136(39):13,582–13,585
113. Lingwood D, Simons K (2010) Lipid rafts as a membrane-organizing principle. Science 327(5961):46–50
114. Liu J, Kaksonen M, Drubin DG, Oster G (2006) Endocytic vesicle scission by lipid phase boundary forces. Proceedings of the National Academy of Sciences 103(27):10,277–10,282
115. Liu J, Sun Y, Oster GF, Drubin DG (2010) Mechanochemical crosstalk during endocytic vesicle formation. Current opinion in cell biology 22(1):36–43
116. Loughlin R, Wilbur JD, McNally FJ, Nedelec FJ, Heald R (2011) Katanin contributes to interspecies spindle length scaling in Xenopus. Cell 147(6):1397–1407
117. Macal CM, North MJ (2010) Tutorial on agent-based modelling and simulation. Journal of Simulation 4(3):151–162
118. MacDermaid CM, Kashyap HK, DeVane RH, Shinoda W, Klauda JB, Klein ML, Fiorin G (2015) Molecular dynamics simulations of cholesterol-rich membranes using a coarse-grained force field for cyclic alkanes. The Journal of chemical physics 143(24):12B625_1
119. MacKerell Jr AD, Bashford D, Bellott M, Dunbrack Jr RL, Evanseck JD, Field MJ, Fischer S, Gao J, Guo H, Ha S, et al (1998) All-atom empirical potential for molecular modeling and dynamics studies of proteins. The journal of physical chemistry B 102(18):3586–3616
120. Marrink SJ, Risselada HJ, Yefimov S, Tieleman DP, De Vries AH (2007) The martini force field: coarse grained model for biomolecular simulations. The journal of physical chemistry B 111(27):7812–7824
121. Maxfield FR, McGraw TE (2004) Endocytic recycling. Nature reviews Molecular cell biology 5(2):121
122. Mayor S, Pagano RE (2007) Pathways of clathrin-independent endocytosis. Nature reviews Molecular cell biology 8(8):603–612
123. McMahon HT, Boucrot E (2011) Molecular mechanism and physiological functions of clathrin-mediated endocytosis. Nature reviews Molecular cell biology 12(8):517
124. McMahon HT, Gallop JL (2005) Membrane curvature and mechanisms of dynamic cell membrane remodelling. Nature 438(7068):590–596
125. Melikyan G, Kozlov M, Chernomordik L, Markin V (1984) Fission of the bilayer lipid tube. Biochimica et Biophysica Acta (BBA)-Biomembranes 776(1):169–175
126. Merrifield CJ, Feldman ME, Wan L, Almers W (2002) Imaging actin and dynamin recruitment during invagination of single clathrin-coated pits. Nature cell biology 4(9):691–698
127. Miller CE, Majewski J, Gog T, Kuhl TL (2005) Characterization of biological thin films at the solid-liquid interface by x-ray reflectivity. Physical review letters 94(23):238,104

128. Miller MJ, Wei SH, Cahalan MD, Parker I (2003) Autonomous t cell trafficking examined in vivo with intravital two-photon microscopy. Proceedings of the National Academy of Sciences 100(5):2604–2609

129. Mockrin SC, Korn ED (1980) Acanthamoeba profilin interacts with g-actin to increase the rate of exchange of actin-bound adenosine 5'-triphosphate. Biochemistry 19(23):5359–5362

130. Mogilner A (2006) On the edge: modeling protrusion. Current opinion in cell biology 18(1):32–39

131. Mogilner A, Oster G (1996) Cell motility driven by actin polymerization. Biophysical journal 71(6):3030–3045

132. Mogilner A, Oster G (2003) Force generation by actin polymerization ii: the elastic ratchet and tethered filaments. Biophysical journal 84(3):1591–1605

133. Monticelli L, Kandasamy SK, Periole X, Larson RG, Tieleman DP, Marrink SJ (2008) The martini coarse-grained force field: extension to proteins. Journal of chemical theory and computation 4(5):819–834

134. Mullins RD, Heuser JA, Pollard TD (1998) The interaction of arp2/3 complex with actin: nucleation, high affinity pointed end capping, and formation of branching networks of filaments. Proceedings of the National Academy of Sciences 95(11):6181–6186

135. Mund M, van der Beek JA, Deschamps J, Dmitrieff S, Monster JL, Picco A, Nedelec F, Kaksonen M, Ries J (2017) Systematic analysis of the molecular architecture of endocytosis reveals a nanoscale actin nucleation template that drives efficient vesicle formation. bioRxiv p 217836

136. Murtola T, Karttunen M, Vattulainen I (2009) Systematic coarse graining from structure using internal states: Application to phospholipid/cholesterol bilayer. The Journal of chemical physics 131(5):08B601

137. Naghdi PM (1973) The theory of shells and plates. In: Linear Theories of Elasticity and Thermoelasticity, Springer, pp 425–640

138. Nagle JF, Jablin MS, Tristram-Nagle S, Akabori K (2015) What are the true values of the bending modulus of simple lipid bilayers? Chemistry and physics of lipids 185:3–10

139. Nédélec F, Foethke D (2007) Collective Langevin dynamics of flexible cytoskeletal fibers. New Journal of Physics 9(11):427

140. Neupert W, Brunner M (2002) The protein import motor of mitochondria. Nature reviews Molecular cell biology 3(8):555–565

141. Niemelä PS, Ollila S, Hyvönen MT, Karttunen M, Vattulainen I (2007) Assessing the nature of lipid raft membranes. PLoS computational biology 3(2):e34

142. Novak KD, Peterson MD, Reedy MC, Titus MA (1995) Dictyostelium myosin i double mutants exhibit conditional defects in pinocytosis. The Journal of Cell Biology 131(5):1205–1221

143. Novick P, Field C, Schekman R (1980) Identification of 23 complementation groups required for post-translational events in the yeast secretory pathway. Cell 21(1):205–215

144. Odell GM, Foe VE (2008) An agent-based model contrasts opposite effects of dynamic and stable microtubules on cleavage furrow positioning. The Journal of Cell Biology 183(3):471–483

145. Ohkubo YZ, Pogorelov TV, Arcario MJ, Christensen GA, Tajkhorshid E (2012) Accelerating membrane insertion of peripheral proteins with a novel membrane mimetic model. Biophysical journal 102(9):2130–2139

146. Oostenbrink C, Villa A, Mark AE, Van Gunsteren WF (2004) A biomolecular force field based on the free enthalpy of hydration and solvation: the gromos force-field parameter sets 53a5 and 53a6. Journal of computational chemistry 25(13):1656–1676

147. Pauleweit S, Nebe JB, Wolkenhauer O (2013) Modelling Molecular Processes by Individual-Based Simulations Applied to Actin Polymerisation

148. Pearse B (1976) Clathrin: a unique protein associated with intracellular transfer of membrane by coated vesicles. Proceedings of the National Academy of Sciences 73(4):1255–1259

149. Perin MS, Fried VA, Mignery GA, Jahn R, Südhof TC (1990) Phospholipid binding by a synaptic vesicle protein homologous to the regulatory region of protein kinase c. Nature 345(6272):260–263

150. Peskin CS, Odell GM, Oster GF (1993) Cellular motions and thermal fluctuations: the brownian ratchet. Biophysical journal 65(1):316–324

151. Peter BJ, Kent HM, Mills IG, Vallis Y, Butler PJG, Evans PR, McMahon HT (2004) Bar domains as sensors of membrane curvature: the amphiphysin bar structure. Science 303(5657):495–499

152. Phillips JC, Braun R, Wang W, Gumbart J, Tajkhorshid E, Villa E, Chipot C, Skeel RD, Kale L, Schulten K (2005) Scalable molecular dynamics with namd. Journal of computational chemistry 26(16):1781–1802

153. Picco A, Mund M, Ries J, Nédélec F, Kaksonen M (2015) Visualizing the functional architecture of the endocytic machinery. Elife 4:e04,535

154. Picco A, Mund M, Ries J, Nédélec F, Kaksonen M (2015) Visualizing the functional architecture of the endocytic machinery. eLife 4

155. Pinot M, Vanni S, Pagnotta S, Lacas-Gervais S, Payet LA, Ferreira T, Gautier R, Goud B, Antonny B, Barelli H (2014) Polyunsaturated phospholipids facilitate membrane deformation and fission by endocytic proteins. Science 345(6197):693–697

156. Pollard TD (1986) Rate constants for the reactions of atp-and adp-actin with the ends of actin filaments. The Journal of cell biology 103(6):2747–2754

157. Pollard TD (2016) Actin and actin-binding proteins. Cold Spring Harbor perspectives in biology 8(8):a018,226

158. Pollard TD, Borisy GG (2003) Cellular motility driven by assembly and disassembly of actin filaments. Cell 112(4):453–465

159. Pollard TD, Cooper JA (1984) Quantitative analysis of the effect of Acanthamoeba profilin on actin filament nucleation and elongation. Biochemistry 23(26):6631–6641

160. Pollard TD, Blanchoin L, Mullins RD (2000) Molecular mechanisms controlling actin filament dynamics in nonmuscle cells. Annual review of biophysics and biomolecular structure 29(1):545–576

161. Poupon V, Girard M, Legendre-Guillemin V, Thomas S, Bourbonniere L, Philie J, Bright NA, McPherson PS (2008) Clathrin light chains function in mannose phosphate receptor trafficking via regulation of actin assembly. Proceedings of the National Academy of Sciences 105(1):168–173

162. Rahimi M, Arroyo M (2012) Shape dynamics, lipid hydrodynamics, and the complex viscoelasticity of bilayer membranes. Physical Review E 86(1):011,932

163. Rangamani P, Steigmann D (2014) Variable tilt on lipid membranes. Proc R Soc A 470(2172):20140,463

164. Rangamani P, Fardin MA, Xiong Y, Lipshtat A, Rossier O, Sheetz MP, Iyengar R (2011) Signaling network triggers and membrane physical properties control the actin cytoskeleton-driven isotropic phase of cell spreading. Biophysical journal 100(4):845–857

165. Rangamani P, Agrawal A, Mandadapu KK, Oster G, Steigmann DJ (2013) Interaction between surface shape and intra-surface viscous flow on lipid membranes. Biomechanics and modeling in mechanobiology pp 1–13

166. Rangamani P, Benjamini A, Agrawal A, Smit B, Steigmann DJ, Oster G (2014) Small scale membrane mechanics. Biomechanics and modeling in mechanobiology 13(4):697–711

167. Rangamani P, Mandadap KK, Oster G (2014) Protein-induced membrane curvature alters local membrane tension. Biophysical journal 107(3):751–762

168. Rangamani P, Xiong GY, Iyengar R (2014) Multiscale modeling of cell shape from the actin cytoskeleton. Progress in molecular biology and translational science 123:143

169. Ray S, Kassan A, Busija AR, Rangamani P, Patel HH (2016) The plasma membrane as a capacitor for energy and metabolism. American Journal of Physiology-Cell Physiology 310(3):C181–C192

170. Ringstad N, Gad H, Löw P, Di Paolo G, Brodin L, Shupliakov O, De Camilli P (1999) Endophilin/sh3p4 is required for the transition from early to late stages in clathrin-mediated synaptic vesicle endocytosis. Neuron 24(1):143–154

171. Rodal AA, Kozubowski L, Goode BL, Drubin DG, Hartwig JH (2005) Actin and septin ultrastructures at the budding yeast cell cortex. Molecular biology of the cell 16(1):372–384

172. Rohatgi R, Ma L, Miki H, Lopez M, Kirchhausen T, Takenawa T, Kirschner MW (1999) The interaction between n-wasp and the arp2/3 complex links cdc42-dependent signals to actin assembly. Cell 97(2):221–231

173. Roux A, Cappello G, Cartaud J, Prost J, Goud B, Bassereau P (2002) A minimal system allowing tubulation with molecular motors pulling on giant liposomes. Proceedings of the National Academy of Sciences 99(8):5394–5399

174. Sadiq SK (2016) Reaction–diffusion basis of retroviral infectivity. Phil Trans R Soc A 374(2080):20160,148

175. Schoneberg J, Noe F (2013) ReaDDy - A Software for Particle-Based Reaction-Diffusion Dynamics in Crowded Cellular Environments. PloS one 8(9):e74,261–14

176. Schöneberg J, Heck M, Hofmann KP, Noé F (2014) Explicit spatiotemporal simulation of receptor-g protein coupling in rod cell disk membranes. Biophysical journal 107(5):1042–1053

177. Schöneberg J, Ullrich A, Noé F (2014) Simulation tools for particle-based reaction-diffusion dynamics in continuous space. BMC biophysics 7(1):11

178. Schoneberg J, Lehmann M, Ullrich A, Posor Y, Lo WT, Lichtner G, Schmoranzer J, Haucke V, Noé F (2017) Lipid-mediated px-bar domain recruitment couples local membrane constriction to endocytic vesicle fission. Nature communications 8:15,873

179. Schuler LD, Daura X, Van Gunsteren WF (2001) An improved gromos96 force field for aliphatic hydrocarbons in the condensed phase. Journal of Computational Chemistry 22(11):1205–1218

180. Sciaky N, Presley J, Smith C, Zaal KJ, Cole N, Moreira JE, Terasaki M, Siggia E, Lippincott-Schwartz J (1997) Golgi tubule traffic and the effects of brefeldin a visualized in living cells. The Journal of cell biology 139(5):1137–1155

181. Seifert U, Berndl K, Lipowsky R (1991) Shape transformations of vesicles: Phase diagram for spontaneous-curvature and bilayer-coupling models. Physical Review A 44(2):1182

182. Seifert U, Shillcock J, Nelson P (1996) Role of bilayer tilt difference in equilibrium membrane shapes. Physical review letters 77(26):5237

183. Shahbaaz M, Amir M, Rahman S, Mustafa Hasan G, Dohare R, Bisetty K, Ahmad F, Kim J, Hassan MI (2017) Structural insights into rab21 gtpase activation mechanism by molecular dynamics simulations. Molecular Simulation pp 1–11

184. Sheetz MP (2001) Opinion: Cell control by membrane-cytoskeleton adhesion. Nature reviews Molecular cell biology 2(5):392

185. Shi Q, Izvekov S, Voth GA (2006) Mixed atomistic and coarse-grained molecular dynamics: simulation of a membrane-bound ion channel. The Journal of Physical Chemistry B 110(31):15,045–15,048

186. Shityakov S, Salvador E, Pastorin G, Förster C (2015) Blood–brain barrier transport studies, aggregation, and molecular dynamics simulation of multiwalled carbon nanotube functionalized with fluorescein isothiocyanate. International journal of nanomedicine 10:1703

187. e Silva MS, Depken M, Stuhrmann B, Korsten M, MacKintosh FC, Koenderink GH (2011) Active multistage coarsening of actin networks driven by myosin motors. Proceedings of the National Academy of Sciences 108(23):9408–9413

188. Silvius JR (2003) Role of cholesterol in lipid raft formation: lessons from lipid model systems. Biochimica et Biophysica Acta (BBA)-Biomembranes 1610(2):174–183

189. Simons K, Ikonen E (1997) Functional rafts in cell membranes. nature 387(6633):569

190. Simons K, Vaz WLC (2004) MODEL SYSTEMS, LIPID RAFTS, AND CELL MEMBRANES 1. Annu Rev Biophys Biomol Struct 33(1):269–295

191. Simunovic M, Voth GA (2015) Membrane tension controls the assembly of curvature-generating proteins. Nature communications 6

192. Simunovic M, Srivastava A, Voth GA (2013) Linear aggregation of proteins on the membrane as a prelude to membrane remodeling. Proceedings of the National Academy of Sciences 110(51):20,396–20,401

193. Simunovic M, Manneville JB, Renard HF, Evergren E, Raghunathan K, Bhatia D, Kenworthy AK, Voth GA, Prost J, McMahon HT, et al (2017) Friction mediates scission of tubular membranes scaffolded by bar proteins. Cell 170(1):172–184

194. Sirotkin V, Berro J, Macmillan K, Zhao L, Pollard TD (2010) Quantitative analysis of the mechanism of endocytic actin patch assembly and disassembly in fission yeast. Molecular Biology of the Cell 21(16):2894–2904
195. Sirotkin V, Berro J, Macmillan K, Zhao L, Pollard TD (2010) Quantitative analysis of the mechanism of endocytic actin patch assembly and disassembly in fission yeast. Molecular biology of the cell 21(16):2894–2904
196. Smith AE, Zhang Z, Thomas C (2000) Wall material properties of yeast cells: Part 1. cell measurements and compression experiments. Chemical Engineering Science 55(11):2031–2041
197. Sneddon MW, Faeder JR, Emonet T (2010) Efficient modeling, simulation and coarse-graining of biological complexity with NFsim. Nature methods 8(2):177–183
198. Sochacki KA, Dickey AM, Strub MP, Taraska JW (2017) Endocytic proteins are partitioned at the edge of the clathrin lattice in mammalian cells. Nat Cell Biol 12:517–41
199. Stachowiak MR, Laplante C, Chin HF, Guirao B, Karatekin E, Pollard TD, O'Shaughnessy B (2014) Mechanism of Cytokinetic Contractile Ring Constriction in Fission Yeast. Developmental Cell 29(5):547–561
200. Stansfeld PJ, Sansom MS (2011) From coarse grained to atomistic: a serial multiscale approach to membrane protein simulations. Journal of Chemical Theory and Computation 7(4):1157–1166
201. Steigmann D (1999) Fluid films with curvature elasticity. Archive for Rational Mechanics and Analysis 150(2):127–152
202. Steigmann D (1999) On the relationship between the cosserat and kirchhoff-love theories of elastic shells. Mathematics and Mechanics of Solids 4(3):275–288
203. Steigmann DJ (2013) A model for lipid membranes with tilt and distension based on three-dimensional liquid crystal theory. International Journal of Non-Linear Mechanics 56:61–70
204. Steigmann DJ (2018) Mechanics and physics of lipid bilayers. In: The Role of Mechanics in the Study of Lipid Bilayers, Springer, pp 1–61
205. Steinman RM, Mellman IS, Muller WA, Cohn ZA (1983) Endocytosis and the recycling of plasma membrane. The Journal of cell biology 96(1):1–27
206. Stenmark H (2009) Rab gtpases as coordinators of vesicle traffic. Nature reviews Molecular cell biology 10(8):513–525
207. Sun Y, Martin AC, Drubin DG (2006) Endocytic internalization in budding yeast requires coordinated actin nucleation and myosin motor activity. Developmental cell 11(1):33–46
208. Sutton RB, Fasshauer D, Jahn R, Brunger AT (1998) Crystal structure of a snare complex involved in synaptic exocytosis at 2.4 å resolution. Nature 395(6700):347–353
209. Svitkina TM, Borisy GG (1999) Arp2/3 complex and actin depolymerizing factor/cofilin in dendritic organization and treadmilling of actin filament array in lamellipodia. The Journal of cell biology 145(5):1009–1026
210. Tayebi L, Ma Y, Vashaee D, Chen G, Sinha SK, Parikh AN (2012) Long-range interlayer alignment of intralayer domains in stacked lipid bilayers. Nature materials 11(12):1074–1080
211. Templer R, Seddon J, Warrender N (1994) Measuring the elastic parameters for inverse bicontinuous cubic phases. Biophysical chemistry 49(1):1–12
212. Tieleman DP, Marrink SJ, Berendsen HJ (1997) A computer perspective of membranes: molecular dynamics studies of lipid bilayer systems. Biochimica et Biophysica Acta (BBA)-Reviews on Biomembranes 1331(3):235–270
213. Tieleman DP, MacCallum JL, Ash WL, Kandt C, Xu Z, Monticelli L (2006) Membrane protein simulations with a united-atom lipid and all-atom protein model: lipid–protein interactions, side chain transfer free energies and model proteins. Journal of Physics: Condensed Matter 18(28):S1221
214. Tristram-Nagle S, Zhang R, Suter R, Worthington C, Sun W, Nagle J (1993) Measurement of chain tilt angle in fully hydrated bilayers of gel phase lecithins. Biophysical journal 64(4):1097–1109

215. Ullrich A, Böhme MA, Schöneberg J, Depner H, Sigrist SJ, Noé F (2015) Dynamical organization of syntaxin-1a at the presynaptic active zone. PLoS computational biology 11(9):e1004,407
216. Van Der Spoel D, Lindahl E, Hess B, Groenhof G, Mark AE, Berendsen HJ (2005) Gromacs: fast, flexible, and free. Journal of computational chemistry 26(16):1701–1718
217. Vavylonis D, Wu JQ, Hao S, O'Shaughnessy B, Pollard TD (2008) Assembly Mechanism of the Contractile Ring for Cytokinesis by Fission Yeast. Science 319(5859):97–100
218. Victor BL, Lousa D, Antunes JM, Soares CM (2015) Self-assembly molecular dynamics simulations shed light into the interaction of the influenza fusion peptide with a membrane bilayer. Journal of chemical information and modeling 55(4):795–805
219. Walani N, Torres J, Agrawal A (2015) Endocytic proteins drive vesicle growth via instability in high membrane tension environment. Proceedings of the National Academy of Sciences 112(12):E1423–E1432
220. Wang J, Wolf RM, Caldwell JW, Kollman PA, Case DA (2004) Development and testing of a general amber force field. Journal of computational chemistry 25(9):1157–1174
221. Wang X, Carlsson AE (2017) A master equation approach to actin polymerization applied to endocytosis in yeast. PLoS computational biology 13(12):e1005,901
222. Wang X, Galletta BJ, Cooper JA, Carlsson AE (2016) Actin-regulator feedback interactions during endocytosis. Biophysical journal 110(6):1430–1443
223. Wang Y, Noid W, Liu P, Voth GA (2009) Effective force coarse-graining. Physical Chemistry Chemical Physics 11(12):2002–2015
224. Wang YL (1985) Exchange of actin subunits at the leading edge of living fibroblasts: possible role of treadmilling. The Journal of cell biology 101(2):597–602
225. Wegner A, Engel J (1975) Kinetics of the cooperative association of actin to actin filament. Biophysical chemistry 3(3):215–225
226. Wiener M, Suter R, Nagle J (1989) Structure of the fully hydrated gel phase of dipalmitoylphosphatidylcholine. Biophysical journal 55(2):315–325
227. Wu JQ, Pollard TD (2005) Counting cytokinesis proteins globally and locally in fission yeast. Science 310(5746):306–310
228. Wu JQ, Pollard TD (2005) Counting cytokinesis proteins globally and locally in fission yeast. Science 310(5746):310–314
229. Xiong Y, Rangamani P, Fardin MA, Lipshtat A, Dubin-Thaler B, Rossier O, Sheetz MP, Iyengar R (2010) Mechanisms controlling cell size and shape during isotropic cell spreading. Biophysical journal 98(10):2136–2146
230. Yarar D, Waterman-Storer CM, Schmid SL (2005) A dynamic actin cytoskeleton functions at multiple stages of clathrin-mediated endocytosis. Molecular biology of the cell 16(2):964–975
231. Yin Y, Arkhipov A, Schulten K (2009) Simulations of membrane tubulation by lattices of amphiphysin n-bar domains. Structure 17(6):882–892
232. Yu H, Schulten K (2013) Membrane sculpting by f-bar domains studied by molecular dynamics simulations. PLoS computational biology 9(1):e1002,892
233. Zemel A, Ben-Shaul A, May S (2008) Modulation of the spontaneous curvature and bending rigidity of lipid membranes by interfacially adsorbed amphipathic peptides. The Journal of Physical Chemistry B 112(23):6988–6996
234. Zhang B, Feng X, Yin H, Ge Z, Wang Y, Chu Z, Raabova H, Vavra J, Cigler P, Liu R, et al (2017) Anchored but not internalized: shape dependent endocytosis of nanodiamond. Scientific Reports 7
235. Zimmerberg J, Gawrisch K (2006) The physical chemistry of biological membranes. Nature chemical biology 2(11):564–567
236. Zimmerberg J, Kozlov MM (2006) How proteins produce cellular membrane curvature. Nature reviews Molecular cell biology 7(1):9–19